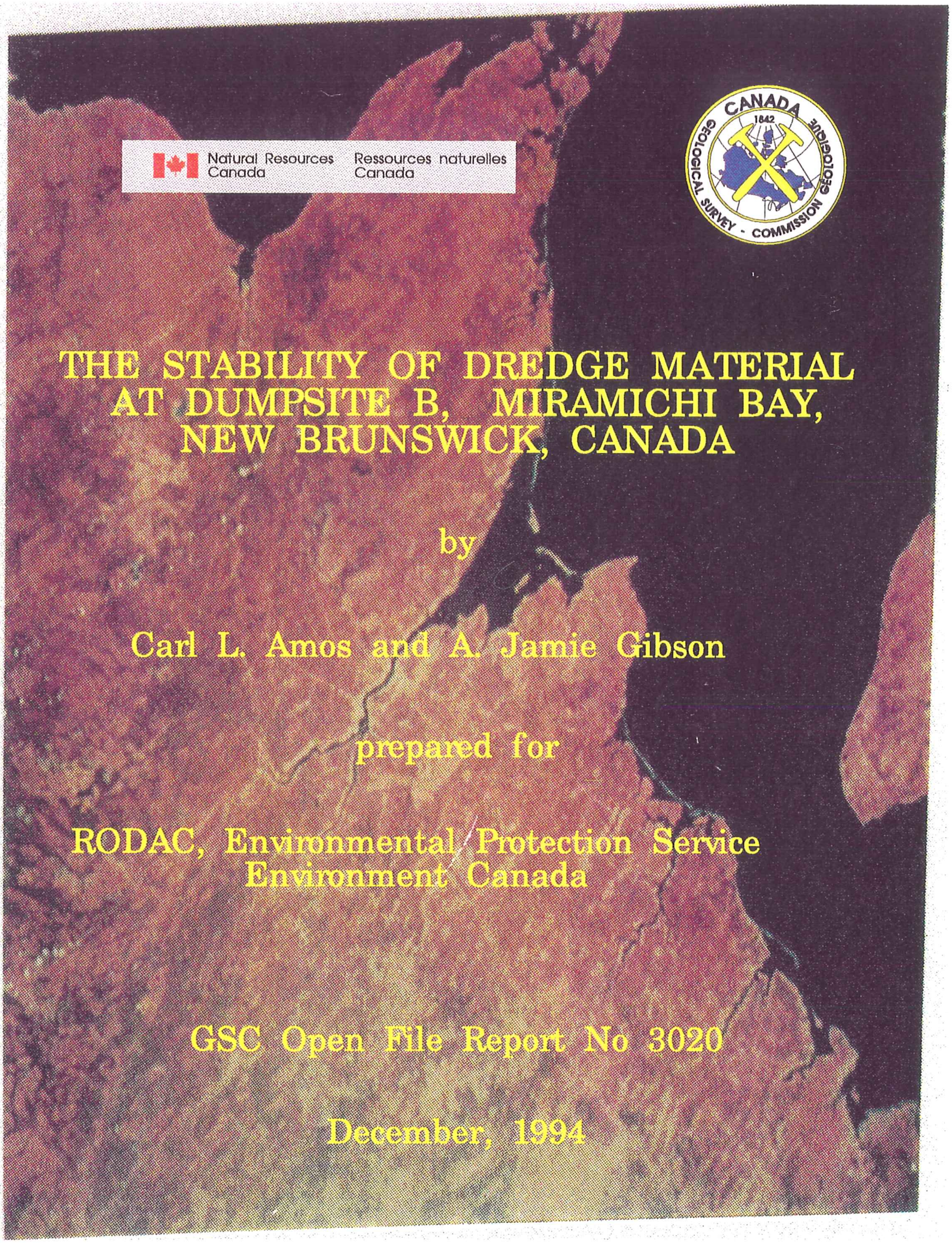

Natural Resources Canada / Ressources naturelles Canada

THE STABILITY OF DREDGE MATERIAL AT DUMPSITE B, MIRAMICHI BAY, NEW BRUNSWICK, CANADA

by

Carl L. Amos and A. Jamie Gibson

prepared for

RODAC, Environmental Protection Service
Environment Canada

GSC Open File Report No 3020

December, 1994

THE STABILITY OF DREDGE MATERIAL AT DUMPSITE B, MIRAMICHI BAY, NEW BRUNSWICK, CANADA.

by

Carl L. Amos[1] and A. Jamie Gibson[2]

1. Geological Survey of Canada
Atlantic Geoscience Centre
Bedford Institute of Oceanography
P.O. Box 1006, Dartmouth
Nova Scotia, CANADA, B2Y 4A2

2. Acadia Centre for Estuarine Research
Acadia University, Wolfville,
Nova Scotia, CANADA, B0P 1H0

prepared for

RODAC, Environmental Protection Service
Queen Square, 45 Alderney Drive
Dartmouth, Nova Scotia, CANADA
B2Y 2N6

Geological Survey of Canada Open File Report # 3020

December, 1994

TABLE OF CONTENTS

Appendix 1 (grain size results)

Appendix 2 (plots of shear strength versus depth, Miramichi dumpsite gravity core analysis)

Appendix 3 (biological sampling program)

Appendix 4 (a rapid technique to determine bulk density of fine-grained sediments by x-ray computed tomography).

Appendix 5 (gravity core photographs)

EXECUTIVE SUMMARY

This report summarises three studies on the fate and stability of material dumped at dumpsite B, Miramichi bay, New Brunswick. These three studies are (1) the 1993 *in situ* survey outlined in Amos, Brylinski *et al.* (1994); (2) the 1994 *in situ* survey outlined in Amos, Gibson *et al.* (1994); and (3) a laboratory study of dumpsite B material outlined in this report. The information on seabed stability gained from these three studies helps elucidate important trends in the development of stability of dumpsite material with time. The most significant finding of the study was the time variability in dumpsite stability that is linked to biostabilization, seawater temperature, and therefore season. Peak stability may be expected in late summer, lowest stability may be expected in late winter and early spring. The early spring 1994 dumpsite survey showed dumpsite B to be less stable than the late summer survey of 1993 (only 1 week after dumping).

The erosion at the dumpsite changed from a largely unstable but surface biostabilised seabed in 1993 to a stable seabed in 1994. That is, notwithstanding a decrease in erosion threshold, the strength of the sediment with depth increased at a greater rate (higher friction angle) in 1994 than in 1993. The potential for liquefaction is thus lower in 1994. Erosion changed from being dominantly Type II (chronic) in 1993 to being dominantly Type I (benign) in 1994. That is, the seabed is self-armouring and the erosion process is limited. A laboratory study of dumpsite B material showed a rapid increase in erosion threshold with time due to biostabilization. This strengthening was partially reversed during the transition from oxygenated to anoxic conditions due to the collapse of the microphytobenthos. The remnant strength may be linked to bacterial colonization. Initial results using a CT Scanner showed that sediment bulk density ρ_b varied considerably in the topmost 1 cm of sediment. This variation is linked to the macrostructure of the sediment and to biostabilization and so is not predictable at present.

The erosion rate was found to be an exponential function of the absolute applied bed shear stress. This rate was modified by the effects of biostabilization. Sediment mass settling rate (W_s) was found to be constant at suspended sediment concentrations (SSC) in excess of 2000 mg/L ($W_s = 1.2 \times 10^{-3}$ m/s). At lower values of SSC, W_s appeared to vary in proportion to SSC.

The sidescan survey of dumpsite B showed that the material dumped in 1993 was largely intact 1 year later. However, material dumped in previous years had been largely reworked into current parallel ribbons. There have been no significant changes in grain size, organic content, or mass physical properties of dumpsite B material in the year between the 1993 and 1994 surveys. This again suggests that little seabed reworking has taken place.

There have been no significant changes in the macrofaunal diversity and abundances. By contrast, chlorophyll *a* concentration is lower than in 1993. The distribution of chlorophyll with sediment depth appears to conform with the strength profiles derived from the Sea Carousel.

LIST OF FIGURES

FIGURE 3.2.1.5. A time-series plot of the Sea Carousel deployment at station MIR3, dumpsite B, Miramichi bay.(A) azimuthal and vertical current speed (m/s); (B) suspended sediment concentration (mg/L); and (C) erosion rate ($kg/m^2/s$). In this case the data have been filtered through a 20-second time average.

FIGURE 3.2.1.6. A time-series plot of the Sea Carousel deployment at station MIR3, dumpsite B, Miramichi bay.(A) azimuthal and vertical current speed (m/s); (B) suspended sediment concentration (mg/L); and (C) erosion rate ($kg/m^2/s$). In this example the data have been filtered through a 60-second time average.

FIGURE 3.2.1.7. A time-series plot of the Sea Carousel deployment at station MIR4, dumpsite B, Miramichi bay.(A) azimuthal and vertical current speed (m/s); (B) suspended sediment concentration (mg/L); and (C) erosion rate ($kg/m^2/s$).

FIGURE 3.2.1.8. A time-series plot of the Sea Carousel deployment at station MIR5, dumpsite B, Miramichi bay.(A) azimuthal and vertical current speed (m/s); (B) suspended sediment concentration (mg/L); and (C) erosion rate ($kg/m^2/s$).

FIGURE 3.2.1.9. A time-series plot of the Sea Carousel deployment at station MIR6, dumpsite B, Miramichi bay.(A) azimuthal and vertical current speed (m/s); (B) suspended sediment concentration (mg/L); and (C) erosion rate ($kg/m^2/s$).

FIGURE 3.2.1.10. A time-series plot of the Sea Carousel deployment at station MIR7, dumpsite B, Miramichi bay.(A) azimuthal and vertical current speed (m/s); (B) suspended sediment concentration (mg/L); and (C) erosion rate ($kg/m^2/s$).

FIGURE 3.2.1.11. A time-series plot of the Sea Carousel deployment at station MIR8, dumpsite B, Miramichi bay.(A) azimuthal and vertical current speed (m/s); (B) suspended sediment concentration (mg/L); and (C) erosion rate ($kg/m^2/s$).

FIGURE 3.2.1.12. A time-series plot of the Sea Carousel deployment at station MIR9, dumpsite B, Miramichi bay.(A) azimuthal and vertical current speed (m/s); (B) suspended sediment concentration (mg/L); and (C) erosion rate ($kg/m^2/s$).

FIGURE 3.2.1.13. A time-series plot of the Sea Carousel deployment at station MIR10, dumpsite B, Miramichi bay.(A) azimuthal and vertical current speed (m/s); (B) suspended sediment concentration (mg/L); and (C) erosion rate ($kg/m^2/s$).

FIGURE 3.2.1.14. A time-series plot of the Sea Carousel deployment at station MIR11, dumpsite B, Miramichi bay.(A) azimuthal and vertical current speed (m/s); (B) suspended sediment concentration (mg/L); and (C) erosion rate ($kg/m^2/s$).

FIGURE 3.2.1.15. A time-series plot of the Sea Carousel deployment at station MIR12, dumpsite B, Miramichi bay.(A) azimuthal and vertical current speed (m/s); (B) suspended sediment concentration (mg/L); and (C) erosion rate ($kg/m^2/s$).

FIGURE 3.2.1.16. A time-series plot of the Sea Carousel deployment at station MIR13, dumpsite B, Miramichi bay.(A) azimuthal and vertical current speed (m/s); (B) suspended sediment concentration (mg/L); and (C) erosion rate ($kg/m^2/s$).

FIGURE 3.2.2.1. A synthetic core from station MIR1 computed from the Sea Carousel time-series data on eroded mass. The erosion threshold is 0.5 Pa; the maximum strength is 0.9 Pa and is found 0.0005 m below the mudline.

FIGURE 3.2.2.2. A synthetic core from station MIR1A computed from the Sea Carousel time-series data on eroded mass. The erosion threshold is 0.5 Pa, and the substrate is stable yielding a friction angle of 32°.

FIGURE 3.2.2.3. A synthetic core from station MIR2 computed from the Sea Carousel time-series data on eroded mass. The erosion threshold is 0.7 Pa, and the substrate is stable yielding a friction angle of 32°.

FIGURE 3.2.2.4. A synthetic core from station MIR3 computed from the Sea Carousel time-series data on eroded mass. The erosion threshold is 0.6 Pa, and the substrate is stable yielding a friction angle of 45°.

FIGURE 3.2.2.5. A synthetic core from station MIR4 computed from the Sea Carousel time-series data on eroded mass. The erosion threshold is 0.5 Pa, and the substrate is stable yielding friction angles of 18° and 53°.

FIGURE 3.2.2.6. A synthetic core from station MIR5 computed from the Sea Carousel time-series data on eroded mass. The erosion threshold is 0.6 Pa, and the substrate is of variable stability yielding a friction angle of 32° and 46° separated by a "soft" at a depth of 0.002 m.

FIGURE 3.2.2.7. A synthetic core from station MIR6 computed from the Sea Carousel time-series data on eroded mass. The erosion threshold is 0.4 Pa, and the substrate is stable yielding a friction angle of 84°.

FIGURE 3.2.2.8. A synthetic core from station MIR7 computed from the Sea Carousel time-series data on eroded mass. The erosion threshold is 0.5 Pa.

FIGURE 3.2.2.9. A synthetic core from station MIR8 computed from the Sea Carousel time-series data on eroded mass. The erosion threshold is 0.5 Pa, and the substrate is stable yielding a friction angle of 51°.

FIGURE 3.2.2.10. A synthetic core from station MIR9 computed from the Sea Carousel time-series data on eroded mass. The erosion threshold is 0.7 Pa, and the substrate is stable yielding a friction angle of 42°.

FIGURE 3.2.2.11. A synthetic core from station MIR10 computed from the Sea Carousel time-series data on eroded mass. The erosion threshold is 0.7 Pa, and the substrate is of variable stability yielding friction angles of 45° and 7° separated by a "soft" at a depth of 0.0015 m.

FIGURE 3.2.2.12. A synthetic core from station MIR11 computed from the Sea Carousel time-series data on eroded mass. The erosion threshold is 1.0 Pa, and the substrate is stable yielding a friction angle of 87°.

FIGURE 3.2.2.13. A synthetic core from station MIR12 computed from the Sea Carousel time-series data on eroded mass. The erosion threshold is 0.4 Pa and the friction angle is 69°.

FIGURE 3.2.2.14. A synthetic core from station MIR13 computed from the Sea Carousel time-series data on eroded mass. The erosion threshold is 0.7 Pa, and the substrate is of variable stability yielding friction angles of 49° and 45° separated by a "soft" at a depth of 0.0015 m.

FIGURE 3.2.3.1. A scattergram of current speed (U_y) versus peak seabed erosion rate ($\delta M/\delta t$; $kg/m^2/s$) for the control sites (MIR1 - MIR3) and for stations MIR4 - MIR6. These stations exhibited Type I erosion. A positive exponential relationship was evident of the form $\delta M/\delta t = 0.006 + 0.006[\log_{10}(U_y)]$; $r^2 = 0.49$.

FIGURE 3.2.3.2. A scattergram of bed shear stress (τ) versus peak seabed erosion rate ($\delta M/\delta t$; $kg/m^2/s$) for the control sites (MIR1 - MIR3) and for stations MIR4 - MIR6. These stations exhibited Type I erosion. A positive exponential relationship was evident of the form $\delta M/\delta t = 0.003 + 0.003[\log_{10}(\tau)]$; $r^2 = 0.32$.

FIGURE 3.2.4.1. The still-water settling of material eroded from the seabed in stations (A) MIR1 - MIR7, and (B) MIR8 - MIR13. The concentration change with time falls into three phases (1) an initial period of inhibited settling; (2) a period of rapid settling; and (3) a final period of low settling.

FIGURE 3.2.6.1. A sidescan mosaic of the eastern margin of dumpsite B.

FIGURE 3.2.6.2. A detailed example of the sidescan record of the 1993 scow-dumps. The distance between fixes is approximately 100 m. The channel swath width is 100 m per channel. The two traces give results from two frequencies (120 - left, and 320 kHz - right).

FIGURE 3.2.6.3. A detailed inset of the dumpsite B exclusion zone monitored in this study. The Sea Carousel stations are shown on and around the major region of dumping in 1993. The crosses show the positions at the beginning of dumping and the arrows show the scow paths. The location of the majority of the dumped material is shown by the solid curved oblongs. The

northeast-southwest trending lineaments in the mosaic are interpreted to be scallop trawl marks. Notice one such marks appears to cross the 1993 dump material.

FIGURE 4.1.1. The calibration of the three Optical Backscatter Sensors (OBS) in the Laboratory Carousel against suspended sediment concentration for experiment LE4.

FIGURE 4.1.2. The calibration of the three Optical Backscatter Sensors (OBS) in the Laboratory Carousel against suspended sediment concentration for experiments LE5 and LE6.

FIGURE 4.2.1.1. A time-series of erosion threshold derived from the Laboratory Carousel analysis of dumpsite B material. Notice the linear increase in erosion threshold with time over the first 7 days. The reveral in trends after 8 days reflects a change from oxygenated to anoxic conditions, associated with the collapse of the benthic macrofauna and development of anaerobic bacteria.

FIGURE 4.2.1.2. A time-series plot of the Laboratory Carousel experiment LE4, on dumpsite B material, Miramichi bay. (A) azimuthal and vertical current speed (m/s); (B) suspended sediment concentration (mg/L); and (C) erosion rate (kg/m^2/s).

FIGURE 4.2.1.3. A time-series plot of the Laboratory Carousel experiment LE5, on dumpsite B material, Miramichi bay. (A) azimuthal and vertical current speed (m/s); (B) suspended sediment concentration (mg/L); and (C) erosion rate (kg/m^2/s).

FIGURE 4.2.1.4. A time-series plot of the Laboratory Carousel experiment LE6, on dumpsite B material, Miramichi bay. (A) azimuthal and vertical current speed (m/s); (B) suspended sediment concentration (mg/L); and (C) erosion rate (kg/m^2/s).

FIGURE 4.2.1.5. A time-series plot of the Laboratory Carousel experiment LE7, on dumpsite B material, Miramichi bay. (A) azimuthal and vertical current speed (m/s); (B) suspended sediment concentration (mg/L); and (C) erosion rate (kg/m^2/s).

FIGURE 4.2.1.6. A time-series plot of the Laboratory Carousel experiment LE8, on dumpsite B material, Miramichi bay. (A) azimuthal and vertical current speed (m/s); (B) suspended sediment concentration (mg/L); and (C) erosion rate (kg/m^2/s).

FIGURE 4.2.2.1. A synthetic core from experiment LE4 computed from the Laboratory Carousel time-series data on eroded mass. The experiment was undertaken after 7 days of consolidation/biostabilization. The erosion threshold is 1.2 Pa. Notice the peak in bed strength (1.9 Pa) within the topmost 2 mm, which is diagnostic of biostabilization.

FIGURE 4.2.2.2. A synthetic core from experiment LE5 computed from the Laboratory Carousel time-series data on eroded mass. The experiment was undertaken after 4 days of consolidation/biostabilization. The erosion threshold is 0.8 Pa. Notice the peak in bed strength (1.2 Pa) within the topmost 2 mm, which is diagnostic of biostabilization.

FIGURE 4.2.2.3. A synthetic core from experiment LE6 computed from the Laboratory Carousel time-series data on eroded mass. The experiment was undertaken after 2 days of consolidation/biostabilization. The erosion threshold is 0.4 Pa. Notice the peak in bed strength (0.8 Pa) within the topmost 2 mm, which is diagnostic of biostabilization.

FIGURE 4.2.2.4. A synthetic core from experiment LE7 computed from the Laboratory Carousel time-series data on eroded mass. The experiment was undertaken after 1 day of consolidation/biostabilization. The erosion threshold is 0.3 Pa. Notice the peak in bed strength (0.7 Pa) within the topmost 1 mm, which is diagnostic of biostabilization.

FIGURE 4.2.2.5. A synthetic core from experiment LE8 computed from the Laboratory Carousel time-series data on eroded mass. The experiment was undertaken after 11 days of consolidation/biostabilization and the system had gone anoxic. The erosion threshold is 0.8 Pa. Notice the peak in bed strength (0.7 Pa) within the topmost 1 mm, which is diagnostic of biostabilization.

FIGURE 4.2.2.6. A time-series of the friction angle derived from the Laboratory Carousel analysis of dumpsite B material. The decrease in value with time is diagnostic of a systematic development of a biofilm (surface strengthening). The reveral in trends after 8 days reflects a change from oxygenated to anoxic conditions, associated with the collapse of the benthic macrofauna and development of anaerobic bacteria.

FIGURE 4.2.3.1. A synthetic core developed from Laboratory Carousel experiment LE4 showing the erosion rate ($\delta M/\delta t$) as a function of eroded depth. Notice that $\delta M/\delta t$ is virtually constant at 1×10^{-3} kg/m^2/s.

FIGURE 4.2.3.2. A synthetic core developed from Laboratory Carousel experiment LE5 showing the erosion rate ($\delta M/\delta t$) as a function of eroded depth. No clear trends emerged.

FIGURE 4.2.3.3. A synthetic core developed from Laboratory Carousel experiment LE6 showing the erosion rate ($\delta M/\delta t$) as a function of eroded depth.

FIGURE 4.2.3.4. A synthetic core developed from Laboratory Carousel experiment LE7 showing the erosion rate ($\delta M/\delta t$) as a function of eroded depth. $\delta M/\delta t$ appears to increase with depth due to the lack of sediment consolidation (1 day only) but the data are scattered.

FIGURE 4.2.3.5. A synthetic core developed from Laboratory Carousel experiment LE8 showing the erosion rate ($\delta M/\delta t$) as a function of eroded depth. Notice that $\delta M/\delta t$ is virtually constant at 2×10^{-4} kg/m^2/s.

FIGURE 4.2.3.6. A scattergram of current speed against erosion rate ($\delta M/\delta t$) for Laboratory Carousel experiment LE4. $\delta M/\delta t$ appears to increase exponentially with current speed.

FIGURE 4.2.3.7. A scattergram of current speed against erosion rate ($\delta M/\delta t$) for Laboratory Carousel experiment LE5. $\delta M/\delta t$ appears to increase exponentially with current speed.

FIGURE 4.2.3.8. A scattergram of current speed against erosion rate ($\delta M/\delta t$) for Laboratory Carousel experiment LE6. $\delta M/\delta t$ appears to increase exponentially with current speed.

FIGURE 4.2.3.9. A scattergram of current speed against erosion rate ($\delta M/\delta t$) for Laboratory Carousel experiment LE7. $\delta M/\delta t$ appears to increase exponentially with current speed.

FIGURE 4.2.3.10. A scattergram of current speed against erosion rate ($\delta M/\delta t$) for Laboratory Carousel experiment LE8. $\delta M/\delta t$ appears to increase exponentially with current speed.

FIGURE 4.2.4.1. A time-series of still-water settling in the Laboratory Carousel for experiments LE4 - LE8. Notice they all show similar trends with time. These are: (1) an initial period of inhibited settling; (2) a period of rapid exponentially-decaying settling; and (3) a period of slow settling. These trends mirror those from the Sea Carousel *in situ* surveys.

FIGURE 4.2.4.2. A scattergram of suspended sediment concentration against the settling decay constant (K_1). The Sea Carousel data indicates that settling was much greater *in situ* than was found under laboratory conditions.

FIGURE 4.2.4.3. A scattergram of suspended sediment concentration (SSC) against mean mass settling velocity (W_s). Notice that W_s appears to reach a constant value of 0.0012 m/s at SSC's > 2000 mg/L, and is scattered, but less, at lower concentrations.

FIGURE 5.1. A scattergram of the erosion thresholds for Sea Carousel stations occupied on dumpsite B during 1993 and 1994. Notice that the seabed has become weaker during the year or so between surveys, even though no obvious change in physical bed properties was detected. This is attributed to seasonal fluctuations in bed strength related to benthic biological productivity.

FIGURE 5.2. A scattergram of the friction angles for Sea Carousel stations occupied on dumpsite B during 1993 and 1994. Notice that the seabed has become more consolidated during the year or so between surveys as would be expected. This appears to have little effect on the erosion threshold as evidenced in Figure 5.1.

FIGURE 5.3. The observed increase in bed strength for three surveys of dumpsite B material: (1) the *in situ* 1993 Sea Carousel survey (water temp = 16°C); (2) the *in situ* 1994 Sea Carousel survey (water temp = 6°C); and (3) the laboratory study reported herein (water temp = 24°C). The solid lines show the best-fit increase in bed strengths for surveys (1) and (3). Notice that strength increase appears to be related to water temperature, which would agree with the concept of biostabilization.

LIST OF TABLES

TABLE 4.2.4.1. A summary of mass settling of dumpsite B material in the Lab Carousel.

TABLE 4.2.4.2. A summary of mass settling rates of dumpsite B material in the Lab Carousel (W_f is the frontal settling velocity and W_s is the mass settling velocity).

TABLE 5.1. A summary of the surface erosion thresholds and internal friction angles of Sea Carousel stations occupied on dumpsite B in 1993 and then re-occupied in 1994.

1.0 INTRODUCTION

A meeting on Ocean Disposal regulation, held in Halifax on 13 December, 1993, provided the framework for research and monitoring through the 90's. The context for this work comes largely from presentations given at that meeting. The theme appeared to be towards developing a sustained ecosytem and the protection of coastal waters. Approximately 250 applications to dump at sea are made each year (160 of which are in the Maritimes). These applications fall broadly into: (1) artificial reefs; (2) fish waste; (3) dredge material; and (4) ship disposal.

About 6 x 10^6 m^3/year of material is dredged in Canada each year. 4 x 10^6 m^3 a^{-1} comes from the Fraser River, the remainder comes largely from the Maritimes. All dredging and dumping activities are subject to Ocean Disposal Regulations under the Canadian Environmental Protection Act. Of particular concern to regulators are the potential impacts of:

- o habitat destruction, acute and chronic effects;
- o chemical contamination; and
- o conflicts with other uses (J. Osbourne, 1993).

In order to evaluate a dumping application, information is required pertaining to: general site conditions; physical environment; dumping specifications; chemical and biological compositions; alternative sites; historical data; as well as monitoring strategies (K. Tay and A. McDonald, 1993).

The physical conditions at a potential dumpsite are central to the evaluation of the above-stated impacts, as they largely control the dispersal rate and dilution of dumped material, and the potential pathways of noxious substances (organo-halogens; nuclear waste; PAH's; Hg; cadmium; PCB's; amongst others; after C. Duerden, 1993; also see Basco *et al.* 1974; Johanson *et al.* 1976; and Pequegnat *et al.* 1981). Dispersal of dumped material may be viewed as a three-phase flow, the three phases being: sediment; water; and contaminants. The three phases are invariably linked. Unfortunately the way in which they are linked is often extremely complex, and often mediated by biological processes. The purpose of this study is to examine the linkages between the hydrodynamic forces acting on dumped material at dumpsite B, Miramichi bay, and the sediment response to these forces. A second purpose has been to evaluate the role of benthic biostabilization and bioturbation in controlling the water-sediment linkages. The ultimate goal of this work is to provide regulators with a more accurate means to evaluate dumpsite longterm stability.

The dispersal of dumped material (sediment transport) may be viewed at a range of scales (Figure 1.1) from the transport of a single particle (particle-by-particle transport) to the mass movement associated with slumping. Although we conveniently view sediment transport as a binary phenomenon, it is in fact a continuum wherein dispersal may take place at a number of scales either in concert or sequentially. Particle-by-particle transport is largely a surface phenomenon. It is often chronic in its effect, and tends to be long-lived. It is the consequence of day-to-day hydrodynamic forces at the seabed brought about by waves, tidal currents, ship passages, and bioturbation. It is a skin phenomenon, pertaining to the very surface of the dumped material and the material exposed by the erosion process. An example of this type of transport is found at dumpsite B, Miramichi bay, where tidal reworking has dispersed much the original dumped material (Kranck and Milligan, 1989). Mass movement, by contrast, is brought about by failure within the body of the sediment resulting in liquefaction and motion due to gravity. It is usually short-lived and can be catastrophic. Examples of liquefaction and mass movement of dumped material are found off Black Point, St John Harbour, where 50% of the material has flowed downslope into deeper water of the Bay of Fundy (Canadian Seabed Research Ltd., 1994).

An approach taken by the Geological Survey of Canada in the evaluation of the sediment transport phenomenon is illustrated in Figure 1.2. The approach combines data collection (remote sensing), sample collection and analysis, and process/response modelling. These aspects have been expanded upon in a report to Environment Canada by Hodgins and Harper (1994). Such an intergrated approach is essential to the developments of maps and models of seabed stability. We are concerned here with aspects of process/response modelling and prediction.

The prediction of particle-by-particle transport of dumped material requires knowledge of a number of factors which are illustrated in Figure 1.3. For cohesive sediments these factors are: the critical shear stress for erosion (erosion threshold) and the change in this threshold with sediment depth; the rate of erosion; the critical shear stress for deposition, the particle settling rate; and the rate of consolidation/bed strengthening. For non-cohesive sediments these factors are: the critical shear stress for traction; the traction (bedload) rate; the critical shear stresses for saltation/suspension/sheet flow; the total load transport; and the genesis and stability of bedforms. While much work has been done on sand transport under currents, virtually nothing is known about cohesive sediments (which typifies much dumped material) under complex combined flows (waves and currents together). Yet dispersal of dumpsite material usually takes place under complex flows. As a consequence, the ability to predict the fate of dumped material is limited.

The assessment of mass movement of cohesive sediments depends on the undrained and drained strengths, the stress history of the material, and the time-dependent properties of the seabed (such as pore pressure; Figure 1.4). These properties have been measured at dumpsite B and they can be significant (Amos, Brylinski, *et al.* 1994). The slopes of the seabed at this site preclude significant sediment transport by this mechanism.

In the past, the results from the above analyses of seabed stability have been used in two ways: for environmental Impact Assessment and for Engineering Risk Analysis. There is a basic need for such information in both of these tasks (Figure 1.5). However, this information must be accurate and specific. New *in situ* technologies have been developed in Canada over the last 5 years that allows us to monitor seabed stability. Results from this instrumentation will produce better information on dumpsite responses under complex conditions of flow, and thus better predictions of the fate of such material.

The purpose of this study was to provide information on the particle-by-particle transport of dumpsite material in order to assess dispersal or stability potential for a given set of environmental factors. This has been achieved by application of new *in situ* technologies to measure directly dumpsite stability. Also, through the selective laboratory analysis of dumpsite material under controlled conditions. The site chosen for investigation was dumpsite B, Miramichi bay, New Brunswick (Figure 1.6). It was chosen on the basis of discussions with staff at Environment Canada and Dept. Fisheries and Oceans, and on the basis of a review of dredging in this bay (Acadia Centre for Estuarine Research, 1990). As far as we are aware, this represents the first time that the evolution of the stability of a dumpsite has been monitored by direct measurement. The results of this work will provide a rational basis for future study of dump material stability, and will help in the regulation of the dumpsite in question.

2.0 BACKGROUND

The Miramichi bay is a shallow, broad coastal plain estuary (Figure 2.1). Vilks and Krauel (1982) and Willis (1990) showed that the Miramichi estuary may be divided into five parts: (1) the rivers; (2) the Miramichi river; (3) the inner bay; (4) the tidal deltas and coastal barrier complex (described by Reinson, 1976; 1980); and (5) Miramichi bay. The bay follows an antecendent drainage channel that has been modified by glacial deposits that are up to 8 m thick (Howells and McKay, 1977), and by post-glacial transgression. The eastern part of the bay is underlain by sand, while silt and clay predominate in the central and western regions.

The Miramichi is a wide shallow stratified estuary, subject to 2 m semi-diurnal tides, and a mean annual fresh water inflow of 300 m^3/s. Consequently, the estuary is strongly stratified in the inner narrow parts, become moderately stratified seawards due to wave and tidal mixing (Krauel, 1975). As a result, currents are predominantly landward at the bed and seawards at the surface. Superimposed on this, there is a strong cyclonic residual circulation in the bay. Tidal currents vary up to 1.0 m/s, and waves can reach heights up to *circa* 2.5 m and periods up to 8 seconds. The bay is ice-covered from December to March each year, and so the seabed is subject to wide fluctuations in water temperature (0 - 16°C) and exposure to winds.

The majority of sediment entering the bay (approximately 6,000 m^3/day, Philpott, 1978) comes from the rivers. The majority of this load comes during the spring freshet (100,000 m^3) in the form of silt and clay. The sediment is derived from a river catchment of 14,000 km^2. Despite this influx, the suspended sediment concentration exceeds 90 mg/L only during storms (Winters *et al.* 1978; Winters, 1981) and are typically around 10 mg/L. According to Buckley (1990), the influx of sediment leads to a net accretion of 0.03 cm/a. Over the last 200 years, wood waste products have also been released into the estuary at a rate of *circa* 20,000 tonnes/a (Philpott and Duncan, 1977). Consequently the organic content of bottom sediments is high. It is 7% in the river section, 2% in the bay (Buckley and Winters, 1983), and up to 15% in the navigation channel (Amos, Brylinksi *et al.* 1994).

Dredging of the navigation channel in Miramichi bay has been taking place since 1872. Until 1930, only 510,000 m^3 of material had been dredged. Between 1981 and 1983, major capital dredging took place (6.2×10^6 metric tonnes) to bring the channel depth to 8 m (Solomon, 1990). The material from this dredging operation was dumped at three dumpsites in the bay (A, B, and C). According to Buckley (1990), 10% of the inner bay is covered with spoils from dumping of this material.

A total of 4.9 x 10^6 m^3 of material from the capital dredging program was dumped on dumpsite B over an area of 3 x 7 km. Much of this material, according to Kranck and Milligan (1989) was dispersed...

"The similarity in grain size of the material on the bottom and in suspension under the normal weather conditions during which the suspended sediment sampling occurred as well as the very fine size and low density are evidence that these [Grande Dune Flats] mud deposits were relatively unstable and easily resuspended".

Perhaps the most controversial statement regarding dredging and dumping in Miramichi came from Kranck and Milligan (1989) who stated that...

"the sedimentary environment of the Miramichi estuary appears to have undergone a change since 1981-82. Scientific evidence is available which indicates that dredged spoils at dumpsites are not stable. The instability of the dumpsites may be a contributary cause of the environmental changes which appear to be taking place in Miramichi.".

The environmental changes were based on evidence of foraminifera changes presented by Schafer *et al.* (1977), Scott *et al.* (1977), and Schafer and Smith (1988). Furthermore, Philpott (1978) postulated that...

"there may be a negative impact on the lobster populations in the vicinity of dumpsite B due to changing the conditions of the bottom and to increased levels of turbidity.".

Worms and Bates (1990) suggest that the impact from dredging is felt in three ways: (1) through higher suspended loads; (2) through nutrient loading; and (3) through increased bio-availability of pollutants. Before 1983 a cutter-suction technique was employed in dredging. The losses of material through spillage from the trailing hopper amounted to 75% by volume (Kranck and Milligan, 1989) with the production of a bottom turbidity (fluff) layer over much of the bay, which was apparently mobile. This material was assumed to be ultimately transported to the turbidity maximum at the head of the bay. Since 1983 a clam-shell bucket dredge has been used, which reduced turbidity by 30-70% (Herbich and Brahme, 1991). The consequence of the changes in dredging method had two impacts: (1) reduced potential for fluid mud generation; and (2) lower potential for reworking of dumpsite material. But are these potential effects still significant ?

MacGregor and Packman (1983) believe that, in the absence of waves, dumpsite B is stable. Landva (1976) has speculated that waves liquefy material at the dumpsite rendering it unstable, yet provides no evidence on which to base the conclusion. Two surveys have been carried out at dumpsite B to monitor the effects of dredging and dumping on turbidity, and to evaluate dumpsite stability. The first study (undertaken in 1991), using the *in situ* flume Sea

Carousel, showed that the seabed of dumpsite B was then as stable as the surrounding material (Brylinski *et al.* 1992). No fluid mud layers were detected in that study. The second study, undertaken during channel dredging in 1993 showed virtually no turbidity increases during dredging or dumping, and a rapidly stabilising seabed after dumping (Amos, Brylinski *et al.* 1994). However, there were signs of fluid mud development adjacent to dumpsite B during periods of high wave activity. It was not possible to say if the material had come from dumpsite B, and the question of its stability under waves remained contentious.

This study provided the opportunity to examine dumpsite B for a third year (1 year after the last dumping took place). The objectives of this study were as follows:

(1) to determine the long-term (1 year) change in seabed stability at dumpsite B, and to evaluate the performance of clamshell disposal material to resist resuspension;

(2) to map the distribution in bed strength over the dumpsite and define the heterogeneity in this attribute;

(3) to look for fluid mud layers;

(4) to collect seabed samples and to examine the physical properties of the sediments in order to assess changes with time;

(5) to undertake a preliminary sidescan survey of dumpsite B to map the 1993 dump sites; and

(6) to undertake controlled laboratory experiments on dumpsite B sediment in order to define the processes of stabilization for purposes of improving our predictive capability in this matter.

3.0 FIELD SURVEY

A major field survey was carried out at dumpsite B, Miramichi bay, under this project. A detailed description of the field work is given in Amos, Gibson *et al.* (1994). The purpose of the survey was to measure seabed stability using Sea Carousel approximately 1 year after the dumping of 4100 m^3 of material dredged from area 22-28 of reach 22 in the main navigation channel. These results were compiled to provide information on long-term trends on dumpsite stability to supplement the results obtained during a similar survey during 1993 (Amos, Brylinski *et al.* 1994).

3.1 Equipment and methods

3.1.1 Sea Carousel

Sea Carousel is a benthic annular flume capable of submarine monitoring of seabed erosion (Amos, Grant *et al.*, 1992). The annulus is 2 m in diameter, 0.3 m high and 0.15 m wide. It is equipped with three optical backscatter sensors to monitor water turbidity, a Marsh-

McBirney® current meter to monitor azimuthal and vertical flow, a lid rotation sensor and an underwater camera that views the eroding bed through a window in the side of the annulus. The system is operated from the surface through an RS-232 communication link to a submerged data logger/controller. The digital driver motor is controlled by a similar link to a second computer. Real time video is monitored on a video display and logged on VHS tape.

Flow is induced by rotation of the lid, to which are attached eight paddles. Azimuthal flow is transformed to bed stress based on velocity gradients derived in a series of laboratory tests. Bed stress is increased in the flume in a series of steps to a maximum value, and then rotation is stopped. Erosion rate is defined as the increase in suspended mass through time. Eroded depth is derived assuming spatially-constant erosion under the flume, and by measures of bulk density made at the site (*circa* 1300 kg/m^3). The profile of shear strength with depth is derived by assuming that the applied fluid shear stress (τ_o) is equivalent to the shear strength (τ_b) of the sediment when erosion ceases, and that this strength is the critical value (τ_c) at which sediment at that depth will begin to be eroded $\tau_o = \tau_b = \tau_c$. The critical shear stress for incipient erosion of the sediment surface is evaluated as the surface (z = 0) intercept of the best-fit line of shear strength versus depth. See Amos, Daborn *et al.* (1992) for a detailed description of the methods and results.

3.1.2 Seabed sampling

A medium Van Veen grab was used to collect bulk samples of the seabed at each station. Two small syringe cores were collected from the surface of each grab for purposes of examining microfabric and macrostructure. The syringe cores were held vertically to prevent disturbance, and frozen onboard using dry ice. Small unit volumes of sediment were also collected from the for CHN ratios, polysaccharides, and chlorophyll-a content (see appendix 3). These were collected from three depths in each grab sample: 1, 8 and 15 cm. Thereafter, the bulk sample was retained for future analysis of resuspension and biostabilization within the Laboratory Carousel at Acadia University (see section 4.0).

A wide-barrel AGC gravity corer was deployed at each site. The corer was equipped with 50 lbs of lead and a 1 m long barrel. The barrel was equipped with a one-way valve at the top (to prevent draw-out on removal) and a leaf core catcher at the base. The corer was allowed to free fall from 1 - 2 m above the seabed. The purpose was to obtain undisturbed samples of the sediment surface and about 0.6 to 0.8 m of the underlying material. Cores were stored vertically, packed to prevent motion, and sealed with wax to prevent loss of moisture. The cores were collected for analysis of the major physical properties. These properties are: water content; grain size; bulk density; acoustic velocity; vane shear strength; and sediment texture, lithology, and structure.

Benthic invertebrate samples were collected at each site using a 15 x 15 cm Eckman grab sampler. The bulk sample was wet seived through a 710 μm sieve, and the retained macrofauna was stored for enumeration and identification of species. Sediment chlorophyll *a* was determined from sub-samples pumped from Sea Carousel at regular intervals throughout each deployment.

A 60-ml syringe with a Swinnex® disk filter holder were used to extract the samples onto MSF GF75 borosilicate filters. Water temperature, salinity, and density were monitored at each Sea Carousel site using an Applied Microsystems Ltd. EMP2000. Detailed descriptions of the analytical methods used in this study can be found in Amos, Brylinski *et al.* (1994).

3.1.3 Sidescan sonar

A sidescan mosaic of dumpsite B was compiled using a Simrad® MS992 system. The system works at frequencies of 120 and 320 kHz, and is fully digital. The incoming signals are displayed on a TDU 1200 graphic recorder and colour video monitor. All records were slant-range corrected and the water column was removed. Signals were digitized and logged with a Geoacoustics® SE880 Digitizer. A swath width of 100 m/channel was used throughout the survey. The system was deployed from the starboard side of the ship and towed about 10 m aft, at a height of 4 m above the seabed.

3.2 Results

3.2.1 Summary

The following were the major achievements of the Miramichi 1994 survey: (1) completion of four (4) Sea Carousel stations at Miramichi inner bay Control site (reach 22); (2) completion of ten (10) Sea Carousel stations at Miramichi inner bay disposal site B; (3) collection of thirteen (13) gravity cores, bulk samples and biological samples from each Sea Carousel site; (4) completion of a sidescan sonar survey of Miramichi bay navigation channel from Newcastle to M47; and (5) a preliminary sidescan survey of eastern and central Miramichi bay dumpsite B.

Good results were obtained at all stations. The time-series of results from the 14 Sea Carousel deployments are shown in Figures 3.2.1.1 to 3.2.1.17. Stations MIR1 to MIR3 and MIR14 were occupied on the 1993 control site (north of the main channel); the remaining stations were occupied on dumpsite B stations originally occupied in 1993 (see Table 3.2.1.1). Results from stations MIR1, MIR2, and MIR3 were used as controls; those from stations MIR4-MIR13 re-occupied dumpsite stations first occupied in 1993; and MIR14 was undertaken to evaluate leakage of sediment from Sea Carousel. In each case, the raw data has been time-averaged over 10 seconds, and transformed into scientific units based on calibrations described in Amos, Gibson *et al* (1994). The effect of time-averaging on the results is seen in Figures 3.2.1.3 to 3.2.1.6. These figures show respectively time-averages over 5, 10, 20, and 60 seconds. Notice that the 10-second average yields the optimum in signal display; that is, the minimum noise and the maximum signal. All stations are plotted, therefore, using a 10-second time-average.

ST # (1994)	ST # (1993)	LAT.	LONG.	DEPTH (m)	TEMP (C)	SAL (ppt)	SAMP #
MIR1	MIR13	47 08.06	65 09.54	6.3	5.8	17.1	5

ST # (1994)	ST # (1993)	LAT.	LONG.	DEPTH (m)	TEMP (C)	SAL (ppt)	SAMP #
MIR1A	MIR13	47 08.14	65 09.40	6.3	5.8	17.1	7
MIR2	MIR13	47 08.09	65 09.47	6.1	6.0	16.3	12
MIR3	MIR13	47 08.12	65 09.40	5.8	--	--	12
MIR4	MIR7	47 06.99	65 10.17	5.0	6.0	20.5	11
MIR5	MIR18	47 06.82	65 10.29	6.0	5.7	20.7	11
MIR6	MIR19	47 06.85	65 10.24	5.8	5.7	20.8	9
MIR7	MIR9	47 06.85	65 10.18	5.2	--	--	11
MIR8	MIR10	47 06.90	65 10.26	5.2	--	--	12
MIR9	MIR15	47 07.02	65 10.13	5.3	6.5	21.1	12
MIR10	MIR16	47 07.04	65 10.14	5.3	6.0	21.5	12
MIR11	MIR11	47 06.89	65 10.23	4.8	6.4	18.3	11
MIR12	MIR8	45 06.85	65 10.28	5.3	--	--	12
MIR13	MIR20	47 06.87	65 10.31	5.6	--	--	12
MIR14	MIR13	47 08.02	65 09.40	5.3	--	--	--

Table 3.2.1.1. A summary table of the stations occupied by Sea Carousel in 1994. These stations are cross-referenced to those occupied during the 1993 survey of dumpsite B for comparative purposes.

The control stations (MIR1 to MIR3) were typified by Type I erosion (asymptotic with time). Clear peaks in erosion rate (EP) occurred at the onset of each speed increment. These peaks showed systematic increases with increasing current speed. Such peaks were also evident at stations MIR4, MIR5, and MIR6. Remaining dumpsite stations showed considerable scatter with no clearly defined peaks. The process of erosion at these stations is thus more complex than a simple exponential decay with time. The following is a general survey of the erosion process, based on observations of super-VHS video recordings at the control site.

General site description: highly bioturbated and browsed by amphipods and gastropods. Abundant organic flocs on a flat substrate with a roughness of *circa* 0.5 cm.

current speed (m/s)	description
0.02	no motion
0.03	resuspension of organic flocs (Type Ia erosion)
0.12	onset of Type Ib erosion with erosion of inorganic, disaggregated particles (smooth flow)
0.16	onset of 3-D circulation and development of turbid boils from the bed (rough flow)
0.19	significant suspended sediment concentration, no definite aggregates visible
0.23	onset of aggregate surface creep and saltation (0.5 cm diameter)
0.27	larger aggregates moving as bedload (1-2 cm); aggregates in suspension (0.5 cm)
0.30	all aggregates undergoing saltation/suspension with significant bed impacts
0.35	abundant aggregates in saltation/suspension, bed impacts increasing
0.38	dramatic increase in size and number of rip-up clasts (2-3 cm diameter)
0.40	introduction of shell fragments moving in saltation.

3.2.2 Threshold stresses for bed erosion

The time-series of suspended solids concentration (SSC) is used to computed total eroded mass (M) throughout each experiment. This may be transformed into a mean eroded depth because the sediment bulk density (ρ_s) is measured from core samples. This transform is described in recently submitted papers on the Sea Carousel (Amos, Sutherland and Zevenhuizen, in review). Eroded depth (z) is determined as:

$$z = M/0.873\rho_s \text{ (in mks units)}$$

z is determined by dividing the suspended sediment dry mass by the sediment dry bulk density (which is determined from samples collected by coring) and the flume footprint area (0.873 m^2). The resistance of sediments to erosion with depth below the mudline or the sediment/water interface ($\tau_c(z)$) is determined by equating the applied shear stress (τ_o) to bed shear strength ($\tau_b(z)$) at the point of cessation of erosion ($\delta M/\delta t(z) = 0$). The line that defines $\tau_c(z)$ on a depth plot is interpreted as the linear failure envelope of the sediment profile (the increase in sediment strength with depth, Terzaghi and Peck, 1967). It is proportional to the internal friction angle of the sediment. The friction angle Φ is calculated by transforming depth into effective stress $\sigma' = \gamma z - P$ (where γ is the unit bulk weight of the sediment, z is the depth, and P is the excess pore pressure, assumed to be zero). Thus the internal friction angle is defined as:

$$\Phi = \tan^{-1}(\tau/\sigma')$$

The method given above cannot be used in the case of Type II erosion, as continuous erosion implies, by definition, that τ_o is greater than $\tau_c(z)$. The reproduceability of the method was shown by Amos, Brylinski *et al.* (1994) to be ± 0.1 Pa at the control site in inner Miramichi bay.

We now have enough information to create synthetic cores from the time-series of Sea Carousel. These are produced by plotting applied bed shear stress against computed eroded depth. Two major parameters governing sediment stability can be derived from such synthetic cores. The surface intercept of the failure envelope is a measure of the **erosion threshold** and the friction angle traces the **increase in strength with depth.**

The plots of the synthetic cores are shown in Figures 3.2.2.1 to 3.2.2.14. A summary of erosion character for each station (derived from these plots) is given in Table 3.2.2.1. The interpretations of bed state follows Amos, Brylinski *et al.* (1994).

Notice that at the control site the friction angle is positive and between 30 and 40° (stable), and shows a steady increase with depth. This trend is typical of self-weight consolidation of sediments with little evidence of a surface biofilm. The mean erosion threshold is 0.57 Pa and the standard deviation of this parameter is only 0.08 Pa. The low scatter in results also typified the controls in the 1993 survey, and adds confidence to the trends discussed below. **Note that the 1994 erosion threshold at the control site is less than 50% of that derived in 1993. Also note the evolution of the seabed at the dumpsite from a largely unstable and biostabilised condition to a dominantly stable one. That is, there is a greater potential for particle-by-particle erosion, but a lower potential for liquefaction.**

STATION #	EROSION THRESHOLD (Pa)	FRICTION ANGLE Φ (degrees)	EROSION TYPE	BED STATE
MIR1(CO)	0.5	--	I	STABLE
MIR1A(CO)	0.5	32	I	STABLE
MIR2(CO)	0.7	32	I	STABLE
MIR3(CO)	0.6	45	I	STABLE
MIR4(D)	0.5	18 53	I I	STABLE STABLE
MIR5(D)	0.6	32 -- 46	I -- I	STABLE UNSTABLE STABLE
MIR6(D)	0.4	84	I	STABLE
MIR7(D)	0.5	--	--	--
MIR8(D)	0.5	51	II	STABLE
MIR9(D)	0.7	42	I/II	STABLE

STATION #	EROSION THRESHOLD (Pa)	FRICTION ANGLE Φ (degrees)	EROSION TYPE	BED STATE
MIR10(D)	0.7	45 -- 7	I -- --	STABLE UNSTABLE NEUTRAL
MIR11(D)	1.0	87	I	STABLE
MIR12(D)	0.4	69	I/II	STABLE
MIR13(D)	0.7	49 -- 45	I -- II	STABLE UNSTABLE STABLE

Table 3.2.2.1. A summary of the erosion characteristics of Sea Carousel stations occupied on dumpsite B during June, 1994. (CO refers to the control sites and D refers to the dump sites. Bed state is herein subdivided into five major groups on the basis of erosion threshold and friction angle Φ. These are (1) stable beds where $\Phi > 10°$; (2) unstable beds where $\Phi < -10°$; (3) neutral beds where $-10° > \Phi > 10°$; (4) fluidized beds where $-10° > \Phi > 10°$ and where $\tau_o \Rightarrow 0$; and (5) surface bed strengthening attributed to biostabilization.

3.2.3 Erosion Rates

Erosion rates ($kg/m^2/s$) are determined by computing the differential of suspended mass per unit time divided by the area of the annulus. The Type of erosion (Type I or II) is determined from trends in erosion rate through time (10 minutes). Type I erosion shows an asymptotic decrease in erosion rate with time; Type II erosion shows continuous erosion rate with time. Two indices of erosion rate are used in this study following Amos, Brylinksi *et al.* (1994): the peak (10-second averaged) erosion rate (EP); and the base erosion rate (EB). The peak erosion rate is typically the maximum value at the onset of flow under Type I erosion. The base erosion rate is the asymptote of Type I erosion or the mean value of Type II erosion. A summary of EP is given below in Table 3.2.3.1.

STATION/ TIME (GMT)	EROSION RATE ($kg/m^2/s$)	CURRENT SPEED (m/s)	BED SHEAR STRESS (Pa)
1/15.55	3.31×10^{-5}	0.15	0.39
1/15.63	1.33×10^{-3}	0.20	0.66
1/15.72	1.31×10^{-3}	0.25	0.93
2/18.20	1.47×10^{-4}	0.15	0.39

STATION/ TIME (GMT)	EROSION RATE ($kg/m^2/s$)	CURRENT SPEED (m/s)	BED SHEAR STRESS (Pa)
2/18.29	2.73×10^{-3}	0.20	0.61
2/18.39	1.08×10^{-3}	0.25	0.93
2/18.48	2.04×10^{-3}	0.30	1.18
2/18.56	1.75×10^{-3}	0.35	1.51
2/18.64	1.00×10^{-3}	0.40	1.85
2/18.73	5.32×10^{-3}	0.49	1.88
2/18.82	6.43×10^{-3}	0.59	2.02
2/18.89	5.29×10^{-3}	0.69	3.21
3/19.86	1.39×10^{-5}	0.10	0.17
3/19.93	4.78×10^{-4}	0.15	0.39
3/20.04	1.85×10^{-3}	0.20	0.64
3/20.15	1.90×10^{-3}	0.25	0.93
3/20.22	2.76×10^{-3}	0.30	1.10
3/20.31	3.60×10^{-3}	0.35	1.40
3/20.39	1.86×10^{-3}	0.40	1.80
3/20.47	7.77×10^{-3}	0.49	1.91
3/20.55	3.72×10^{-3}	0.59	2.33
3/20.64	4.75×10^{-3}	0.69	3.67
4/13.93	9.08×10^{-5}	0.10	0.18
4/14.01	1.91×10^{-3}	0.15	0.38
4/14.10	3.56×10^{-3}	0.20	0.57
4/14.18	5.90×10^{-3}	0.25	0.65
4/14.30	4.80×10^{-3}	0.30	0.98
4/14.42	4.65×10^{-3}	0.35	1.07
4/14.51	4.66×10^{-3}	0.40	1.16

STATION/ TIME (GMT)	EROSION RATE ($kg/m^2/s$)	CURRENT SPEED (m/s)	BED SHEAR STRESS (Pa)
4/14.68	6.22×10^{-3}	0.49	2.02
4/14.76	3.49×10^{-3}	0.59	2.02
4/14.84	5.55×10^{-3}	0.69	2.84
5/17.40	1.97×10^{-5}	0.05	0.04
5/17.48	3.60×10^{-5}	0.10	0.17
5/17.59	2.09×10^{-4}	0.15	0.39
5/17.63	2.58×10^{-3}	0.20	0.62
5/17.73	3.98×10^{-3}	0.25	0.65
5/17.81	4.66×10^{-3}	0.30	0.87
5/17.91	3.62×10^{-3}	0.35	1.35
5/17.98	3.69×10^{-3}	0.40	1.61
5/18.06	9.43×10^{-3}	0.49	1.88
5/18.14	7.39×10^{-3}	0.59	2.28
5/18.23	5.97×10^{-3}	0.69	2.97
6/19.23	3.58×10^{-5}	0.05	0.05
6/19.34	1.09×10^{-5}	0.10	0.18
6/19.41	4.47×10^{-4}	0.15	0.39
6/19.50	3.99×10^{-4}	0.20	0.69
6/19.59	5.35×10^{-4}	0.25	1.05
6/19.68	5.10×10^{-4}	0.30	1.47
6/19.76	3.66×10^{-4}	0.35	1.99
6/19.84	5.72×10^{-4}	0.40	2.51
6/19.93	1.34×10^{-3}	0.49	3.56

Table 3.2.3.1. A summary of (EP) erosion rates for Sea Carousel deployments MIR1 to MIR6. No other stations were summarised due to the highly scattered data on erosion.

The majority of erosion is Type Ib, that is, floc erosion. There was little evidence, in the time-series plots, for Type Ia erosion (resuspension of a surface, organic rich, fluff layer as seen in the videos). The low quantities of "fluff" may be due to the season in which our survey was carried out (spring). There appear to be weak positive correlations between peak sediment erosion rate (EP) and current speed (Figure 3.2.3.1) and bed shear stress (Figure 3.2.3.2). These relationships have the following exponential forms:

$$EP = 0.006 + 0.006[\log_{10}(U)] \text{ kg/m}^2\text{/s}; \; r^2 = 0.49; \; n = 52$$
$$EP = 0.003 + 0.003[\log_{10}(\tau_o)] \text{ kg/m}^2\text{/s}; \; r^2 = 0.32; \; n = 52$$

The erosion rates at the control and dumpsite stations are similar, with no obvious differences in their dependencies on current speed or bed shear stress. Maximum erosion rates were also similar at *circa* 10^{-2} kg/m^2/s. Also, the range of values of EP is the same as that encountered during the 1993 survey of the dumpsite. The decay to the base erosion rate was also rapid, occuring within 60 seconds of EP. The base erosion rate in this survey differed from that of the previous year in being close to zero at almost all applied shear stresses (classic Type I erosion). By contrast, in the 1993 survey EB increased significantly in proportion to the applied bed shear stress to values in excess of 5×10^{-4} kg/m^2/s (transitional Type I/II and Type II erosion). This fundamental difference in erosion trends has a significant impact on the potential, net amount of material eroded from the dumpsite. Under present conditions (1994), the bed would become stable and cease erosion much more rapidly than would have been the case during 1993, even assuming the same erosion threshold, friction angle, and applied bed shear stress. **A major conclusion of this study is that dumped material may change with time from that dominated by Type II erosion (chronic) to that where Type I erosion (benign) prevails**. It is speculated that consolidation is the dominant factor in this process (in the near absence of biofilms), and that the time-scale is on the order of 1 year. However, focussed research on this subject could prove fruitful in defining this important transition, and the factors which influence it.

3.2.4 Deposition rates

Deposition from suspension was monitored immediately after the bed erosion phase during a period of still water. The trends in SSC with time are plotted in Figure 4.2.4.1. Notice that all trends are similar, showing three phases to settling. The first phase lasts about 100 seconds. Here, settling takes place very slowly. Next comes a phase of rapid settling (phase 2) whereby SSC follows an exponentially-decaying trend of the form:

$$SSC(t) = SSC_o - K_1 \log_{10}(t)$$

where SSC_o is the suspended sediment concentration at time = 0 (that is, the time at which $U_y \Rightarrow 0$). The third period of settling follows a less rapid settling rate and consequently, a much lower value of W_s than would be derived from the mean value. It typifies low SSC's and represents disaggregated fine material and organic debris. The decay constant (K_1) for settling is presented in Table 3.2.4.1. Note that the units of K_1 are reciprocal seconds.

STATION #	SSC_o (mg/L)	SSC(t) (mg/L)	Δt (s)	K_1
MIR1	1185	2	640	1418
MIR2	1561	96	320	1373
MIR3	1245	72	520	680
MIR4	1014	50	290	1052
MIR5	1210	2	850	896
MIR6	--	--	--	--
MIR7	1460	195	320	2242
MIR8	435	144	530	106
MIR9	982	340	530	505
MIR10	1211	135	500	397
MIR11	154	5	440	56
MIR12	475	47	420	163
MIR13	960	40	510	340

Table 3.2.4.1. A summary of mass settling in Sea Carousel during the dumpsite B survey in 1994 (Amos, Gibson *et al.* 1994).

The table reviews results from the 1994 Miramichi study (Amos, Gibson *et al.* 1994). The time-series are plotted in Figure 3.2.4.1A and B. K_1 was found to vary in direct proportion with the starting SSC (Figure 4.2.4.2). This is precisely what was found in a similar study of *in situ* settling made in Manitounuk Sound, Hudson Bay (Amos *et al.* in review). The *in situ* experiments show a rapid increase in K_1, and hence settling rate, above 1000 mg/L that is not reflected in the lab experiments (see later). Results presented by ACER (1993) show that K_1 and W_s continue to increase with SSC to *circa* 20,000 mg/L. The values of K_1, determined in Sea Carousel, were generally greater than those detected by ACER (*ibid*) who worked on laboratory samples.

The mean mass settling rates have been evaluated from the SSC time-series in two ways. In the first case, the development and downward migration (W_f) of a lutocline (where evident) was used. In the second case, the mean settling velocity (W_s) was determined based on a transform of the settling equation of Krone (1962), whereby:

$$SSC(t) = SSC_o \exp[-ptW_s/y]$$

where p is the probability of sediment settling (p = 1 in still water), and y is the depth of the measurements of SSC. We can evaluate W_s considering the concentration half-life of the suspension ($t_{0.5}$):

$$W_s = [-\ln(0.5)/pt_{0.5}].y$$

W_s is thus independent of SSC and time, and thus assumes a single settling velocity for the suspended population. In general, the two methods yield similar results, though there is a greater scatter in W_f than in W_s. W_s is plotted against SSC_o in Figure 4.2.4.3. Notice that W_s determined in the Sea Carousel is comparable to that from the laboratory experiments under similar SSC's, and that there appears to be a maximum settling rate of *circa* 1.5 x 10^{-3} m/s. This maximum rate appears to be valid for 2000 < SSC_o < 8000 mg/L. This suggests that the mass settling rate may be approximated by a single mean value (1.2 x 10^{-3} m/s), when the material in suspension has been eroded from the bed, such as during a storm.

Settling rates are about an order of magnitude greater than has been reported in the literature from laboratory experiments (Amos and Mosher, 1985). However, the results are equivalent to those measured *in situ* at Windsor causeway, Bay of Fundy (Amos and Mosher, *ibid*). The inference is that settling rate in nature is much greater than would be expected based purely on laboratory results. Again, it would appear that aggregation, flocculation, and pelletization influence the natural settling rate at dumpsite B.

STATION #	SSC_o (mg/L)	W_f (m/s)	W_s (m/s)
MIR1	1185	1.0 x 10^{-3}	1.3 x 10^{-3}
MIR2	1561	1.8 x 10^{-3}	1.3 x 10^{-3}
MIR3	1245	3.6 x 10^{-3}	5.4 x 10^{-4}
MIR4	1014	2.7 x 10^{-3}	1.3 x 10^{-3}
MIR5	1210	1.6 x 10^{-3}	8.4 x 10^{-4}
MIR7	1460	5.8 x 10^{-3}	1.1 x 10^{-3}
MIR8	435	--	3.8 x 10^{-4}
MIR9	982	--	2.5 x 10^{-4}
MIR10	1211	--	4.5 x 10^{-4}
MIR11	154	--	6.9 x 10^{-4}
MIR12	475	--	5.1 x 10^{-4}
MIR13	960	--	9.5 x 10^{-4}

Table 3.2.4.2. A summary of mass settling rates from Sea Carousel deployments during the 1994 survey of dumpsite B.

3.2.5 Sediment physical properties

The composition of surface sediments from each station is summarised in Table 3.2.5.1. The mean size falls within the silt range (from very fine to coarse), although there is a significant proportion of sand at all stations. The dump sites have a higher sand content and lower clay content than the control site. The material at the dump site is poorly sorted showing a wide range in sizes from gravel to clay material (see plots in Appendix 1). Notice the station-to-station variation in composition. This appears to typify material from dumpsites and is diagnostic of heterogeneous conditions at the seafloor. Of note was the highly diatomaceous nature of the sand fraction of stations MIR7 to MIR12 and MIR1. This contrasts with the dominantly siliceous composition (with iron staining) of sand from stations MIR5, MIR6, and MIR13. The range in sizes and textures matches that found during the 1993 survey. There appears to be a marginal increase in sand content and associated decrease in clay content which may be diagnostic of slight seabed winnowing over winter 1993/94.

STATION #	GRAVEL %	SAND %	SILT %	CLAY %	MEAN SIZE (mm)	SORTING
MIR1	0	10	50	40	5.08×10^{-3}	2.78
MIR4	0	16	48	36	6.94×10^{-3}	2.89
MIR5	0	62	22	16	4.18×10^{-2}	3.09
MIR6	8	56	20	16	6.84×10^{-2}	3.72
MIR7	0	16	47	37	6.21×10^{-3}	2.92
MIR8	0	15	47	38	5.68×10^{-3}	2.91
MIR9	0	29	43	28	1.14×10^{-2}	3.05
MIR10	0	27	45	28	1.18×10^{-2}	2.93
MIR11	1	9	47	42	4.88×10^{-3}	2.95
MIR12	0	34	40	25	1.45×10^{-2}	3.09
MIR13	1	55	26	17	3.47×10^{-2}	3.19

Table 3.2.5.1. A summary of the grain size analysis of surface samples from the Sea Carousel stations.

The shear strength measures on the gravity cores from each station are plotted in Figures given in appendix 2. Notice that these strengths (τ, measured using a Soiltest® Torevane) yielded values which are consistently 3 orders of magnitude greater than values determined with Sea Carousel. Computations of dry weight bulk density, effective stress (σ), and friction angle for each station are summarised in Table 3.2.5.2.

STATION #	BULK DENSITY (kg/m^3)	SEDIMENT DEPTH (m)	$\Delta\sigma$ (Pa)	$\Delta\tau$ (Pa)	LAB Φ	IN SITU Φ
MIR1	1330	0.60	1789	2750	57	32
MIR4	1340	0.59	1817	1960	47	18-53
MIR5	1346	0.51	1600	2550	57	32-46
MIR6	1464 1464	0.35 0.80	1504 1718	-2930 1500	-63 45	84
MIR7	1448	0.81	2559	10500	76	--
MIR8	1303	0.42	1553	4000	69	51
MIR9	1360	0.69	2261	14500	81	42
MIR10	1360	0.70	2293	9500	76	7-45
MIR11	1398	0.68	2481	13500	79	87
MIR12	1345	0.70	2190	10500	78	69
MIR13	1325	0.52	1525	11000	83	49

Table 3.2.5.2. A summary of laboratory measures of sediment shear strength from the Sea Carousel stations, together with the estimates of friction angle (Φ). ($\Delta\sigma$ is the differential effective stress i.e. over a given range in sediment depths; $\Delta\tau$ is the differential shear strength for the equivalent range in depths).

The plots show that τ increases steadily with depth. The friction angles for the material are generally high and are diagnostic of a consolidating sedimentary column. The values of Φ are generally greater than those derived from Sea Carousel (*in situ* Φ, Table 3.2.5.2). The inference from this is that the surface material is less consolidated than the material beneath. This conforms to the picture of the dumpsite seabed where blocks of dumped material occur retaining their original strength, and that these blocks are covered with a veneer of newly-deposited sediment.

STATION/ DEPTH(cm)	ORGANIC CONT (%)	STATION/ DEPTH(cm)	ORGANIC CONT (%)	STATION/ DEPTH(cm)	ORGANIC CONT (%)
1/5	2.82	4/5	2.04	5/5	1.56
1/15	2.78	4/15	1.91	5/19	3.15
1/25	2.62	4/25	2.88	5/30	2.84
1/35	2.84	4/35	2.87	5/46	2.24
1/50	2.59	4/45	2.89		
1/64	2.63	4/55	2.75		
6/4	2.02	7/4	2.19	8/2	3.47
6/10	2.36	7/16	2.26	8/10	2.16
6/20	3.00	7/28	1.17	8/22	0.62
6/30	2.81	7/40	1.47	8/31	2.87
6/40	2.52	7/50	3.25	8/39	1.70
6/50	1.93	7/60	3.16		
6/60	2.27	7/70	2.54		
6/72	1.50	7/81	2.06		
6/80	2.19				
9/4	3.57	10/10	2.14	11/2	3.19
9/13	2.26	10/20	2.36	11/13	2.09
9/26	3.03	10/30	2.83	11/28	2.44
9/35	2.61	10/40	2.46	11/37	1.79
9/45	2.25	10/50	1.98	11/48	2.39
9/55	2.18	10/60	2.07	11/58	2.25
9/67	2.26	10/70	2.96	11/68	2.40
12/2	2.81	13/2	2.25		
12/10	1.48	13/8	1.54		
12/20	2.30	13/18	1.26		
12/37	2.57	13/27	3.31		

STATION/ DEPTH(cm)	ORGANIC CONT (%)	STATION/ DEPTH(cm)	ORGANIC CONT (%)	STATION/ DEPTH(cm)	ORGANIC CONT (%)
12/47	2.02	13/38	2.35		
12/60	2.67	13/47	3.49		
12/70	2.57	13/58	2.57		

Table 3.2.5.3. A summary of the analysis of organic carbon content of samples taken from gravity cores collected at dumpsite B in 1994.

The organic content of surface sediments was between 3 and 6% (Table 3.2.5.3). This is the same range of values detected during the 1993 survey. The water content varied between 100 and 200% (Table 3.2.5.4) which is the also same range found during the 1993 survey. In general, therefore, there appears to be little change in the mass physical properties at dumpsite B over the year subsequent to 1993 dumping.

STATION/ DEPTH(cm)	BULK DENSITY (kg/m^3)	WATER CONTENT (%)	STATION/ DEPTH(cm)	BULK DENSITY (kg/m^3)	WATER CONTENT (%)
1/35	1324	194	4/25	1376	153
1/50	1337	151	4/35	1322	170
			4/54	1322	167
5/19	1283	194	6/3	1434	121
5/46	1410	138	6/20	1321	164
			6/30	1346	173
7/16	1412	121	6/40	1320	163
7/50	1262	214	6/50	1420	133
7/60	1344	168	6/60	1420	115
7/70	1312	169	6/72	1622	71
7/81	1411	135	6/80	1415	120
8/2	1272	233	9/13	1362	143
8/10	1448	99	9/26	1310	192
8/22	1567	45	9/35	1313	173

STATION/ DEPTH(cm)	BULK DENSITY (kg/m^3)	WATER CONTENT (%)	STATION/ DEPTH(cm)	BULK DENSITY (kg/m^3)	WATER CONTENT (%)
8/31	1291	186	9/45	1395	143
8/39	1440	118	9/55	1343	150
			9/67	1436	124
10/10	1388	141	11/28	1298	177
10/20	1363	141	11/37	1463	108
10/30	1317	163	11/48	1415	116
10/40	1331	175	11/58	1428	115
10/50	1357	142	11/68	1388	126
10/60	1449	121			
10/70	1314	169			
12/10	1413	118	13/8	1370	143
12/20	1331	176	13/18	1338	151
12/37	1289	185	13/27	1321	180
12/47	1431	123	13/38	1320	159
12/60	1265	201	13/47	1239	282
12/70	1339	176	13/58	1362	143

Table 3.2.5.4. A summary of the analysis of dry weight bulk density and water content of samples taken from gravity cores collected at dumpsite B in 1994.

3.2.6. Sidescan sonar

The sidescan sonar survey was undertaken for a preliminary examination of (1) the navigation channel (at the request of DPW), and (2) dumpsite B (at the request of Environment Canada). The surveys were carried out aboard MV Navicula (Amos, Gibson *et al.*, 1994) which did not carry differential GPS. This system was to be provided by DPW, but was unavailable at the time of the cruise. Consequently, a last-minute interface was made between the digital SE880 sidescan recorder and the ship-board GPS. Unfortunately, the navigation was intermittent and subject to drift. The sidescan data, on the other hand, were of good quality, and can be used in a qualitative sense to interpret seabed conditions.

The survey of the channel was from Newcastle wharf (channel marker M97) to reach 22 (channel marker M37), a distance of 40 km. Despite the poor navigation, the channel markers are clear in the records, allowing precise registration of the records to position. The records show that the channel from M97 to M91 is littered with strong reflectors diagnostic of bedrock outcrop, boulders and possibly submerged logs. Seawards of M91 the channel appears less littered, except along the channel inner banks where again bedrock crops out. This region also shows evidence of lineations parallel to the channel that are 2-3 m wide. Seawards of the highway 8 bridge, the channel becomes smooth and featureless with no obvious obstructions visible in the records. The low reflectivity of the signals suggests a soft, muddy channel floor. At M73, the floor becomes "harder" (sandier) with the appearance of channel-parallel lineations. The smaller lineations appear to be tidal current lineations; the larger ones may be anthropogenic. At M71, the presence of a pycnocline masks the seabed reflections, and introduces water column reflections. Nevertheless, bedrock appears to crop out in the channel margins from M67 to M65. Again, there appear to be no obstructions in the channel itself. From M65 to M56 the channel is largely featureless (muddy) with rare traces of current lineations. The most significant feature appears between M56 and M54. Here, bedrock appears to crop out in the channel itself although there is no evidence for shoals. From this point to the end of the survey (M37) the channel is featureless, and there are no signs of any boulders, or bedrock cropping out.

The dumpsite B sidescan survey was incomplete as the water depth of the entire western end of the site was near the draft of the vessel (4 m). Consequently, only the sites of the 1993 dumping and the region to the east were surveyed. The survey covered completely the 1993 exclusion zone, the site of test dumping during July, 1993, and the eastern part of the alternate dumpsite during July, 1993. The mosaic of this survey is shown in Figure 3.2.6.1. The erratic nature of the mosaic is a function of the erratic nature of the navigation. The sidescan records were, nevertheless, of good quality depite the presence of wave noise. The scow-loads of material dumped in 1993 at the alternate site are still clear almost 1 year later. The imprints of the dumps have well-defined edges suggesting that little dispersal took place either during dumping or subsequently (Figure 3.2.6.2). The region to the north of the dumpsite shows strong evidence for tidal current reworking. Current lineations are evident parallel with the navigation channel. To the east of the exclusion zone, there is also evidence for sediment reworking. The coarse (more reflective) remnants of earlier scow-loads are visible, though not as common as in the western part. These remnants are elongated northeast-southwest. It thus appears that reworking of this dumped material has taken place, although the age of this material is unknown. The reworking has not removed the criss-cross pattern of older dumps that surround the exclusion zone (Figure 3.2.6.3).

The exclusion zone shows a distinct reflector that is the same shape and size as the mound of dump material mapped in Amos, Brylinski *et al.* (1994; their Figure 2.1 and Figure 3.2.6.3). The reflector is however offset to the southwest by 213 m from our survey. This difference is due to a systematic error in the Navicula 1994 survey navigation. The well-defined margins to the mound indicate that virtually no reworking has taken place since dumping. Lineations in the lowermost part of Figure 3.2.6.3 are interpreted to be scallop drag marks. They are well within dumpsite B, and one even appears to overlie the 1993 dumped material mound. The inference is that scallop dragging is still taking place in this region.

The positions of the Sea Carousel stations are given in relation to the 1993 dump mound in Figure 3.2.6.3. Notice that stations MIR9, MIR8, MIR6 and MIR11 are situated in the mound. The remaining stations are situated adjacent to the mound (but nevertheless still on dumped material). No difference is evident between the two sets of stations in either the erosion threshold or the physical properties.

4.0 LABORATORY STUDY

4.1 Equipment and methods

The Lab Carousel is an annular flume located at Acadia Centre for Estuarine Research, Acadia University, Wolfville. It is used to undertake calibration and manipulative experiments on natural sediments examined *in situ* using Sea Carousel. Consequently, it is of the same dimensions as Sea Carousel. That is, it is 2 m in diameter with an annulus width of 0.15 m. It may be filled with seawater to a maximum depth of 0.50 m, but is nominally maintained at 0.30 m to mimic the flume depth in Sea Carousel. It is fitted with a rotating lid that sits at the water surface with 8 paddles beneath that are spaced equidistantly around the lid. The speed of lid rotation is controlled by a Empire® 0.75 Hp DC motor and Focus® controller and power supply. The speed of flow is detected by a model 523 (0.5" head size) Marsh-McBirney® electromagnetic current meter. The meter is situated 0.20 m above the base of the flume, where it records azimuthal (tangential) and vertical components of the flow field. The meter is situated in the outer part of the benthic boundary layer. The relationship between lid rotation (U_r, in Hertz) and index azimuthal current speed (U_y) is:

$$U_y = 1.46 + 300U_r \text{ cm/s}; \ r^2 = 0.98$$

The relationship between voltage output (V, in mVolts) from the EM flow meter and U_y is:

$$U_y = 3.02 - 0.222V \text{ cm/s}; \ r^2 = 0.98$$

Three Optical Backscatter Sensors (OBS's) are housed in the wall of the flume at heights of 0.02 (OBS2), 0.09 (OBS1), and 0.20 m (OBS3) above the base of the flume. The OBS's are calibrated to suspended sediment mass by analysis of pumped samples taken from three ports in the side of Lab Carousel at the heights of the OBS's. Samples were collected approximately 2 minutes after each increase in lid rotation. Approximately 200 ml were filtered through Millipore®, glass fibre filters. The tared dry weight was plotted against OBS voltage output and a least-squares, best-fit regression derived. The results from experiment LE4 and experiments LE5 and LE6 are shown in Figures 4.1.1 and 4.1.2 respectively. In both plots SSC increases as an exponential function of voltage. The OBS calibrations for LE4 are as follows:

$$\log_{10}(SSC_1) = 0.2 + 9.2 \times 10^{-3}(OBS_1); \ r^2 = 1.0$$

$$\log_{10}(SSC_2) = -0.2 + 8.8 \times 10^{-3}(OBS_2);\ r^2 = 1.0$$
$$\log_{10}(SSC_3) = -0.1 + 8.2 \times 10^{-3}(OBS_3);\ r^2 = 1.0$$

Notice the excellent regression coefficients in all cases. Also, the water column in the flume appears to have been well mixed throughout the experiments.

Data on the two components of current speed and the three OBS channels are logged at 1 Hz using a Campbell Scientific® CR10 data logger. All data are stored on a PC which is interfaced to the data logger via an RS232 link. A Hi8 Sony® video camera records bed erosion and flow in the lowermost 30 mm of the water column. The video is used to examine the depth of bed erosion, the size of material eroded from the bed, the mechanics of bed erosion, the presence and nature of bedload transport (surface creep or saltation), the presence or absence of a viscous sub-layer, and the velocity gradient in the lowermost part of the benthic boundary layer (0 to 5 cm). Also, the observed current speed was compared to that determined by the EM flow meter as a check. Each experiment was carried out in a manner similar to that adopted for Sea Carousel. That is, the current speed was increased incrementally in a series of steps, each step lasting 15-20 minutes. The experiment terminated when saturation of the OBS sensors took place; at which point the flow was stopped and a period of mass settling was monitored.

A series of experiments was undertaken using natural seawater collected at Hall's Harbour, Bay of Fundy, Nova Scotia. The water at Hall's Harbour was of the same salinity as the Miramichi experiments (30 ppt). The sediment bed was created from a composite of grab samples collected at dumpsite B, Miramichi inner bay during MV Navicula cruise 94-350 (Amos, Gibson *et al.*, 1994). The composite was remoulded into a suspended slurry and allowed to deposit from suspension in still water. No attempt was made to suppress the growth of microorganisms.

4.2 Results

4.2.1 Summary

Five (5) experiments were carried out on the composite sample. A summary of these experiments, the consolidation times, and the erosive characteristics is given in Table 4.2.1.

EXPERIMENT #	CONSOLIDATION TIME (days)	WATER TEMP (C)	EROSION THRESHOLD (Pa)	FRICTION ANGLE (Φ)
LE4	7	24	1.9	-39
LE5	4	21	1.2	-27
LE6	2	21	0.8	-28
LE7	1	23	0.7	-43

EXPERIMENT #	CONSOLIDA-TION TIME (days)	WATER TEMP (C)	EROSION THRESHOLD (Pa)	FRICTION ANGLE (Φ)
LE8	11	23	0.8	-28

Table 4.2.1. A summary of results on the erosion of dump site B sediments using the Lab Carousel.

Deposited sediments behaved as fluid muds for 1-2 hours after settling, at which time they assumed properties of an elasto-plastic solid. Fluid muds were manifested by the development of Kelvin-Helmholtz waves on the sediment/water interface upon application of a bed shear stress. Under such conditions, there was no detectible erosion threshold, and bed material was easily resuspended. The internal friction angle was consequently zero. The solid bed responded to applied bed shear stress in a elasto-plastic fashion, whereby aggregates or individual particles were ejected into the flow at stresses in excess of a measureable erosion threshold. This erosion threshold increased steadily over 7 days of consolidation/biostabilization of the solid bed, reaching a value that matched the maximum strength detected *in situ* using Sea Carousel during the 1993 and 1994 surveys (1.2 Pa; Figure 4.2.1.1). The observed trend took place in oxygenated seawater with an active microphytobenthos due to high water temperatures (24°C). The reversal in the trend (LE8) corresponded to the development of anoxic conditions with consequent eutrophication and sulphur production. In all experiments, the solid bed was characterised by negative friction angles that reflected a decrease in sediment strength with depth in the sediment below a maximum in the topmost mm. The magnitude of Φ increased with time for the first 7 days. This reflected a steady increase in the surface strength of the sediment with no change in strength beneath. The strengthened surface layer was typically 2 mm thick and corresponded well with the depth of active algal activity as described by Paterson (1994). **The inference is that biostabilization is the dominant process in bed stabilization at dumpsite B immediately after dumping, and that redox potential, and water temperature are important factors controlling the degree and rate of stabilization.**

4.2.2 Threshold stresses for bed erosion

The time-series of results from each of the 5 experiments (LE4 to LE8) are plotted in Figures 4.2.1.2 to 4.2.1.6. Each experiment comprised a period of incremental increases in current speed to the point where erosion resulted in a turbidity level that saturated the OBS sensors. Each increment of speed lasted *circa* 20 minutes. In the latter part of each experiment, the lid was stopped, and still-water settling was monitored until the suspended concentration was *circa* 5% of the peak value.

A complete set of results was obtained. Data were logged at 1 Hz, and filtered by 10-second time-averaging for plotting purposes, and to conform with the Sea Carousel plots. Our results showed that the induced current speed was largely constant with time during each increment of speed. The radial component of flow was very small (less than 10% of the azimuthal value). However, it increased in proportion with the azimuthal current speed and also with the SSC. All experiments showed an initial period of no detectible erosion (up to between 0.2 to 0.3 m/s), followed by rapid erosion and resuspension (to a maximum current speed of 0.4 m/s). Settling also took place very rapidly.

The erosion threshold for bed erosion, and the bed strength as a function of depth below the mudline, were determined by the development of synthetic cores. These cores awere produced by firstly computing the mean eroded depth (z). This was done on the basis of the following equation and assumes continuity of mass (M):

$$z = (M/A).1/\rho_b$$

where A is the area of bed of the laboratory flume (0.873 m^2) and ρ_b is the dry weight bulk density of the deposited sediment. ρ_b was evaluated using an indirect method as follows: the elevation of the bed (ζ) was measured at regular intervals throughout each experiment by reference to a vernier scale in the window of the lab flume. At the same time, the total suspended mass (M) was measured (the product of SSC (kg/m^3) and flume volume, 0.218 m^3): M = 0.218SSC kg. The volume of bed material eroded (V) was determined as the product of z (in m) and V = 0.873z m^3. Finally the mean dry weight bulk density for the depth increment of the eroded bed was determined as:

$$\rho_b = 0.218SSC/0.873z \text{ kg/m}^3.$$

Table 4.2.2.1 summarises the results for experiments LE6 and LE7. Notice that the dry bulk densities vary by up to a factor of 5 with depth in the sediment. Significant changes were detected over vertical changes of less than 1 mm. The average bulk density of the bed during experiment LE6 was 472 kg/m^3, and for LE7 was 494 kg/m^3. This is equivalent to buoyant saturated unit weights of 1096 kg/m^3 and 1094 kg/m^3 respectively. These values are very low compared to typical marine sediments reported in the literature (1500 - 2000 kg/m^3, see Terzaghi and Peck, 1967). The results from the two experiments are remarkably consistent, and are significantly below the typical values of dry weight bulk density derived from standard geotechnical laboratory analysis (Amos, Daborn *et al.* 1992; Amos, Brylinksi *et al.* 1994). The geotechnical analyses were made on samples taken *circa* 1 - 5 cm below the mudline, as no reliable techniques are available to obtain smaller samples closer to the mudline. Over-estimates of ρ_b are therefore inevitable. **The results from the indirect method suggest that there is a strong density gradient in the topmost 1 cm of the bed that cannot be ignored when dealing with seabed sediment transport and stability.** The impact of using the higher bulk density values is that the predicted eroded depth can be a factor of 3 less than in reality, and the computed friction angle would be over-predicted. **The macrofabric of the topmost 1 cm of the bed and the associated bulk density is a key area for future research.** We are using Catscan imagery in order begin this area of research (Amos, Sutherland *et al.* in review). Initial results show that ρ_b can be mapped to the mudline with a spatial resolution of 1 mm and with a density discrimination of ±2%.

TIME (GMT)	BED ELEV (ξ; mm)	EROSION (Δz; m)	M (kg)	ΔM (kg)	ρ_b (kg/m^3)
LE6/1633	12.5	5×10^{-4}	0.164	0.164	376
LE6/1647	12.0	5×10^{-4}	0.280	0.116	266
LE6/1710	11.5	5×10^{-4}	0.603	0.323	740
LE6/1723	7.5	4×10^{-3}	1.488	0.885	507
LE6/1738	15.0	-7.5×10^{-3}	-1.488	1.488	227*
LE7/1456	12.5	5×10^{-4}	0.147	0.147	337
LE7/1521	12.0	5×10^{-4}	0.253	0.106	243
LE7/1531	11.5	5×10^{-4}	0.493	0.240	550
LE7/1553	11.0	5×10^{-4}	1.085	0.592	1356
LE7/1600	10.0	1×10^{-3}	1.350	0.265	303
LE7/1610	7.0	3×10^{-3}	1.589	0.239	182
LE7/1630	13.5	-6.5×10^{-3}	-1.589	1.589	280*

Table 4.2.2.1 A summary of the determination of deposited bed dry weight bulk density from Lab Carousel for experiments LE6 and LE7 (* negative values signify bed accretion during still water settling).

Synthetic cores have been constructed based on the bulk density values measured in the laboratory studies described above (Figures 4.2.2.1 to 4.2.2.5). These cores show the prevailing bed shear stress (τ_o) within the flume against the depth of bed erosion, z. To re-state an earlier concept, under Type I erosion, the prevailing bed shear stress may be equated with the erosive strength of the sediment ($\tau_e(z)$; see Amos, Sutherland and Zevenhuizen, in review). In all cases, this strength is greatest at the surface and decreases steadily with depth in the sediment. The region of strengthening is within 2 mm of the mudline, which corresponds with the depth of activity of algae (Paterson, 1994). The peak strength is not at the sediment surface but *circa* 1 mm below it. The magnitude and thickness of this peak grows with time. It is best developed for LE4 (7 days of consolidation; Figure 4.2.2.1). Below the peak value, the strength drops off in an exponential decaying fashion to virtually zero. This indicates that **there is little sediment strength below the surface biofilm. The inference is that all the strength gains with time are the result of biostabilization within the topmost 2 mm of the bed, and that strengthening due to consolidation and cohesion development is negligible.**

The surface value of shear strength ($\tau_b(0)$) is equated with the erosion threshold (shown in Figure 4.2.1.1). The linear increase in strength with time corresponds with the growth of microphytobenthos. Selected observations made by Dr G. Daborn (pers. comm.) of the surface material showed an active and abundant group of diatoms in the form of a surface biofilm. The collapse of the benthic population took place when the system became anoxic, and corresponded with a decrease in erosion threshold (LE8). There was still a significant strengthening of the surface over underlying material which may be caused by the rapid growth of a bacterial population feeding on the collapsed diatoms. **The relative contributions of bacteria and algae to bed stabilization appear to be significant and rapidly felt. This merits further research with emphasis placed on the biofilm character.** Such work is presently being undertaken in part by T.F. Sutherland in completion of a Ph.D. thesis at Dalhousie University.

The significance of biofilm growth is evident in the trends in sediment internal friction angle (Φ) given in Table 4.2.1 and plotted in Figure 4.2.2.6. This angle expresses the rate of change in sediment strength with sediment geostatic load. Notice that Φ is consistently negative, and that there is a progressive decrease in the value through time during the oxygenated portion of the study. This reflects an increasing difference between the surface strength and that of the sediment below. **We propose that it is a product of the developing algal biofilm in the absence of any significant consolidation. The collapse of the algal biofilm during anoxic conditions is mirrored by a reduction in Φ. A series of controlled experiments should be carried out on dumpsite material. This material should be "seeded" with biostabilisers and the changes in bed character and resulting strength (as biostabilization develops) determined under laboratory conditions.**

4.2.3 Erosion Rates

The trends in bed erosion are distinct from those observed *in situ*. The erosion rates for the five lab experiments are shown in Figures 4.2.1.2 to 4.2.1.6 (panel C). The laboratory results showed a rapid increase in erosion rate, once the erosion threshold was exceeded, to values in excess of 3×10^{-3} kg/m^2/s. **These values are between 3 and 30 times greater than those observed *in situ*.** The lack of clear trends when compared to natural sediments is noted, and may be due to the lack of consolidation and the remoulded nature of the laboratory substrate. The erosion trends showed a maximum (EP) at the start of each speed increment (Figure 4.2.1.6C), and thereafter it decreased with time (Type I erosion). The erosion rate did not fall back to zero, but maintained a constant, though lower, erosion level (EB). This trend is diagnostic of a transition to Type II erosion and is similar to field results obtained at dumpsite B during 1993, immediately after dumping. The rapid release of bed material resulted in sensor saturation at low current speeds (0.2 to 0.3 m/s).

The erosion rate was least in the very surface layer (where organic bonding is presumed to be strongest) and was greatest immediately beneath this surface layer. The rate of erosion was generally constant with the depth of erosion (Figures 4.2.3.1 to 4.2.3.5). There is, however, considerable scatter in the data making general interpretations difficult. The high erosion rates within the sediment support the results of sediment strength presented in section 4.2.2. That is, that there was little gain in strength due to consolidation with depth.

The rate of erosion of bed sediment ($\delta M/\delta t$) shows a positive correlation with the applied current speed (U) in the carousel. These correlations are shown in Figures 4.2.3.6 to 4.3.2.10. The wide scatter in the data may be related to the complex influences of SSC which may suppress turbulence and increase the thickness of the viscous sub-layer as well as changes in bed strength with sediment depth. Thus, erosion should decrease with time (at a constant current speed) as SSC and z increases. Such an effect was not evident in our results and so this interpretation must be considered speculative. Interestingly, some models of sediment transport use stress reduction to limit bed erosion at a constant current speed (Sheng and Villaret, 1989). The correlations of current speed and erosion rate are log-linear for experiments LE5 (4 days consolidation), LE6 (2 days consolidation) and LE7 (1 day consolidation). The exponential forms of the correlation are respectively:

$$\delta M/\delta t(LE5) = 1 \times 10^{-6}.10^{10.0U_y} \text{ kg/m}^2\text{/s}$$
$$\delta M/\delta t(LE6) = 1 \times 10^{-6}.10^{9.4U_y} \text{ kg/m}^2\text{/s}$$
$$\delta M/\delta t(LE7) = 1 \times 10^{-6}.10^{9.4U_y} \text{ kg/m}^2\text{/s}$$

where U is the mean current speed (in m/s). The trends show that $\delta M/\delta t$ increases as an exponential function of U_y. LE4 (7 days consolidation) departs from the above trends by showing a low erosion rate at low currents, but returning to high values at the higher speeds. We suggest that the lower erosion rates correspond to the region of biostabilization; once this biofilm is broken, erosion proceeds at rates typical of those given above. The relationships established above become obscure for the final experiment on anoxic material (LE8). Even so, a positive (if poor) correlation between $\delta M/\delta t$ and U_y is still evident (Figure 4.2.3.10).

The next step in the evaluation of erosion rate of bed material at dumpsites is to define the relationship between $\delta M/\delta t$ and ρ_b within the topmost 1 mm of the developed bed. At the same time to determine how ρ_b changes with time and sediment depth, firstly under still water conditions, then under conditions of tidal flow and wave motion. Information is now available that shows how biofilms affect the erosion threshold, yet there are virtually no studies that deal with the effect biofilms on the erosion rate.

4.2.4 Deposition rates

Deposition from suspension was monitored immediately after the bed erosion phase during the still-water phase of each experiment. The resulting trends in SSC are summarised in Figure 4.2.4.1. Time t = 0 was defined when $U_y \Rightarrow 0$. Notice that all trends are similar showing the same three phases of settling as was detected in Sea Carousel. That is: (1) an initial phase of low settling rate lasting *circa* 100 seconds; (2) a phase of rapid settling during which the trend in SSC follows an exponential-decay form; and (3) an extended period of low settling rate. A summary of settling observations is given in Table 4.2.4.1. The decay constant, K_1, varies in direct proportion to the starting SSC, and appears to be in continuity with results from the 1994 Sea

Carousel survey. This is evident in Figure 4.2.4.2. Notice that the Lab Carousel trend appears to be linear over the range of SSC values measured, whereas the *in situ* trends are not. The hypothesis is that the markedly higher values of K_1 from the *in situ* experiments (for 1000 > SSC > 2000 mg/L) reflect the size and density of aggregates resuspended during the erosion process. That is, they are larger and more dense in the field than is the case of the material eroded from the remoulded bed in the laboratory.

STATION #	SSC_o (mg/L)	SSC(t) (mg/L)	Δt (s)	K_1
LE4	7103	2000	150	2345
LE5	4414	858	140	1657
LE6	5006	859	170	1859
LE7	5243	1222	160	1824
LE8	836	360	190	216

Table 4.2.4.1. A summary of mass settling of dumpsite B material in the Lab Carousel.

The mass settling rates W_f and W_s for the laboratory study are summarised in Table 4.2.4.2. They are determined following the method given in section 3.2.4. Values fall within a narrow range between 5.4 x 10^{-4} and 1.5 x 10^{-3} m/s. The results suggest that a mean value for W_s of 1.2 x 10^{-3} m/s is valid for SSC > 2000 mg/L, and that a lower value might be appropriate to lower sediment concentrations. Insofar as it is the density and size of the eroded aggregates that control W_s, **we need to better define the size spectra of eroding bed material. This size spectrum appears to be a function of the macrostructure and bed density of dumped material, which is itself spatial and time variable. A series of field experiments focussing on the size spectrum of eroding material would be invaluable to such a study.**

STATION #	SSC_o (mg/L)	W_f (m/s)	W_s (m/s)
LE4	7103	1.6 x 10^{-3}	1.1 x 10^{-3}
LE5	4414	1.6 x 10^{-3}	9.5 x 10^{-4}
LE6	5006	--	1.5 x 10^{-3}
LE7	5243	--	1.3 x 10^{-3}
LE8	836	7.3 x 10^{-4}	5.4 x 10^{-4}

Table 4.2.4.2. A summary of mass settling rates of dumpsite B material in the Lab Carousel (W_f is the front settling velocity and W_s is the mass settling velocity).

5.0 TRENDS IN EROSION THRESHOLD

The trends in the physical properties and stability of dredge material at dumpsite B are quite evident when results from the 1993 and 1994 surveys are compared. A total of 14 stations were surveyed with Sea Carousel during each of the two periods. A summary of the results of the two surveys is given in Table 5.1. The table summarises both the surface erosion thresholds (ET = $\tau_e(0)$) and the internal friction angle (Φ).

1993 STATION #	1994 STATION #	$\tau_e(0)$ 1993	Φ 1993	$\tau_e(0)$ 1994	Φ 1994
13	1	1.4	-18	0.5	--
12	1A	1.3	-21	0.5	32
14	2	1.4	-22	0.7	32
13	3	1.4	-18	0.6	45
18	5	1.2	-27	0.6	32
19	6	0.9	-34	0.4	84
9	7	0.6	-13	0.5	--
10	8	0.5	29	0.5	51
15	9	0.8	-8	0.7	42
16	10	0	70	0.7	45
11	11	1.0	29	1.0	87
8	12	0.3	-34	0.4	69
20	13	1.1	-34	0.7	49
7	4	0.7	-8	0.5	18

Table 5.1. A summary of the surface erosion thresholds and internal friction angles of Sea Carousel stations occupied on dumpsite B in 1993 and then re-occupied in 1994.

Figure 5.1 shows a comparative plot of the erosion thresholds at dumpsite B from the two Sea Carousel surveys. Notice that in almost all cases the sediment has become weaker with time by 50% on average. At the same time the internal friction angle (Figure 5.2) has increased over the same period. The original strengthening of newly-dumped material was postulated to be due to biofilm development. This has been bourne out by the laboratory work reported herein. It is to be expected that benthic biological activity will be dependent on water temperature and light availability. This is expected to be at a maximum during late summer, and at a minimum during later winter (when the site is ice covered). **Thus we suggest that the rate and magnitude of dumpsite sediment strengthening and sediment erosion threshold will vary seasonally.** In the case of the Sea Carousel measurements, the 1993 results were collected in late summer (water temperature = 16°C) whereas the 1994 data were collected in early summer (water temperature = 6°C). Thus it would be expected that biofilm development would be greater in the 1993 survey. The general increase in friction angle (from negative to positive values) also indicates a destruction of the surface strengthening, giving way to a systematic increase in strength with depth. Thus, although the 1994 dumpsite has a lower surface strength, self-weight consolidation has stabilized the sub-surface material, possibly reducing the likelihood of liquefaction. This trend may also be inferred from the progression of dumpsite B from Type II erosion in 1993 to Type I erosion in 1994.

The above may be summarised by reference to Figure 5.3, which examines surface erosion threshold versus "age" of dumped material. The late summer survey shows a rapid build up in strength with time (solid dots) in the following form:

$$\tau_e(0) = 0.823 + 0.371\log_{10}(t) \text{ Pa}; \ r^2 = 0.65$$

where t is time in days. The laboratory data shows a comparable increase in $\tau_e(0)$, but at a faster rate (inverted open triangles):

$$\tau_e(0) = 0.302 + 0.714\log_{10}(t) \text{ Pa}; \ r^2 = 0.83.$$

The faster rate of strengthening in the laboratory case, was presumeably due to the high water temperature of 24°C. **The scatter in results from 1994 is large (inverted solid triangles), suggesting that dumpsite B is still highly heterogeneous with respect to seabed stability.** We are left to conclude that the strength of the dumped material at dumpsite B varies seasonally and was less 1 year after disposal took place that it was 1 week after disposal. The seasonal changes in dumpsite stability need to be explored in greater detail in future work. A possible outcome of such work could be a recommendation to dump material when benthic biological productivity is at a maximum.

6.0 SUMMARY AND CONCLUSIONS

This report summarises three studies on the fate and stability of material dumped at dumpsite B, Miramichi bay, New Brunswick. These three studies are (1) the 1993 *in situ* survey outlined in Amos, Brylinski *et al.* (1994); (2) the 1994 *in situ* survey outlined in Amos, Gibson *et al.* (1994); and (3) a laboratory study of dumpsite B material outlined in this report. The information on seabed stability gained from these three studies help elucidate important trends in the development of stability of dumpsite B material with time. Several major conclusions have been developed which are as follows:

(1) the most significant finding is the time variability in dumpsite B stability that is linked to biostabilization, seawater temperature, and therefore season. Peak stability may be expected in

late summer, lowest stability may be expected in late winter and early spring. The early spring 1994 survey showed dumpsite B to be less stable than the late summer survey of 1993 (only 1 week after dumping).

(2) The erosion at the dumpsite changed from a largely unstable and biostabilised seabed in 1993 to a stable seabed in 1994. That is, notwithstanding a decrease in erosion threshold, the strength of the sediment with depth increased at a greater rate (higher friction angle) in 1994. The potential for liquefaction is thus lower in 1994.

(3) Erosion changed from being dominantly Type II (chronic) in 1993 to being dominantly Type I (benign) in 1994. That is, the seabed is self-armouring and the erosion process is limited.

(4) The 1994 results from dumpsite B showed the seabed to be heterogeneous with respect to seabed stability. That is, a large number of sites (10-20) would be required in order to map adequately the spatial trends in dumpsite stability.

(5) The erosion rate was found to be an exponential function of the absolute applied bed shear stress. This rate was modified by the effects of biostabilization.

(6) Sedimentation rate was found to be constant for suspended sediment concentrations (SSC) in excess of 2000 mg/L ($W_s = 1.2 \times 10^{-3}$ m/s). At lower values of SSC, W_s appeared to vary in proportion to SSC.

(7) The sidescan survey of dumpsite B showed that the material dumped in 1993 was largely in tact 1 year later. However, material dumped in previous years had been largely reworked into current parallel ribbons.

(8) Initial results using a Catscan GE9800 showed sediment bulk density ρ_b varied considerably in the topmost 1 cm of sediment. This variation is linked to the macrostructure of the sediment and to biostabilization and is not predictable at present.

(9) A laboratory study of dumpsite B material showed a rapid increase in erosion threshold with time due to biostabilization. This strengthening was partially reversed by the change from oxygenated to anoxic conditions, possibly due to the collapse of the microphytobenthos. The remnant strength may be linked to bacterial colonization.

(10) An indirect method to determine ρ_b in the Lab Carousel showed much lower values than have been determined by standard geotechnical methods. This has an impact on the evaluation of erosion threshold which may be significantly over-predicted if standard methods only are employed.

(11) There have been no significant changes in grain size, organic content, or mass physical properties of dumpsite B material in the year between the 1993 and 1994 surveys. This suggests that little seabed reworking has taken place.

7.0 RECOMMENDATIONS

(1) The seasonal variation in dumpsite stability needs to be defined closely in order to define the amplitude of strength changes. Also, the phasing of major storm events needs to be compared to the cycle of strength changes in order to determine the susceptibility for reworking.

(2) Sedimentation rates (and the potential for fluid mud development) are strongly dependent on the size and density of the material eroded into suspension. This is largely a function of the macrostructure and ρ_b of the sediment itself within the topmost cms of the sediment. A program to define the range of density macrostructure, and the evolution of it with time after dumping, should be undertaken and the results compared to *in situ* measures of the size spectra of material eroded from dumpsite material.

(3) The effects of bacteria and algae in stabilizing dumpsite B material can be strong. So much so, that it could be used to promote and even manage stabilization. Unfortunately, biostabilization is species and location specific. A detailed study on the role of indigenous benthic species on sediment stabilization should be undertaken using dumpsite material. This should be undertake under controlled conditions where both the bed physical character and the benthic communities are monitored carefully with time.

(4) The effects of anoxia on sediment stability must be evaluated carefully as it appears to herald a reduction in seabed stability. This is especially true in regions of high organic content where anoxic sediments prevail.

(5) The effects of waves on the erosion and resuspension of dumped material has been shown to be very important in the Miramichi bay. Controlled experiments on wave erosion are, however, limited. We need to begin to examine wave liquefaction and resuspension by waves under controlled conditions and then through controlled *in situ* experiments. Finally, we must examine the erosion of cohesive sediments under the complex effects of waves and currents in combination.

(6) DPW have undertaken swath bathymetric surveys of dumpsite B each year for the last several years. A careful comparison of bathymetric changes (using these data sets) with time would be very useful to provide insight into longterm dumpsite reworking and stability.

8.0 REFERENCES

ACER. 1990. Review of impacts of channel dredging on biological resources of the Miramichi system. Unpublished Internal Report

ACER. 1993. Report of sediment settling rate analysis. Acadia Centre for Estuarine Research Publication No. 26: 29p.

Amos, C.L. and Mosher, D.C. 1985. Erosion and deposition of fine-grained sediments from the Bay of Fundy. Sedimentology 32: 815-832.

Amos, C.L., Daborn, G.R. Christian, H.A., Atkinson, A. and Robertson, A. 1992. *In situ* erosion measurements on fine-grained sediments from the Bay of Fundy. Marine Geology 108: 175-196.

Amos, C.L., Gibson, A.J. and Brylinski, M. 1992. Sediment settling rate analyses for a sediment stability study of the inner Miramichi bay. Acadia Centre for Estuarine Research Publication No. 23: 16p.

Amos, C.L., Grant, J., Daborn, G.R. and Black, K. 1992. Sea Carousel - a benthic annular flume. Estuarine, Coastal and Shelf Science 34: 557-577.

Amos, C.L., Brylinski, M., Christian, H.A. and Daborn, G.R. 1994. Seabed stability, liquefaction and the development of fluid mud during dredging and dumping at Miramichi inner bay. Acadia Centre for Estuarine Research Publication No. 32: 347p.

Amos, C.L., Gibson, A.J., Partridge, V., Atkinson, A. and Jodrey, F. 1994. MV Navicula Cruise - Miramichi bay, New Brunswick. Geological Survey of Canada Open File Report 2939: 55p.

Amos, C.L., Sutherland, T.F., and Zevenhuizen, J. in review. The stability of fine-grained sediment in Manitounuk Sound, Hudson Bay, Canada. Sedimentology.

Amos, C.L., Sutherland, T.F., Radzijewski, B., and Doucette, M. in review. A rapid technique to determine bulk density of fine-grained sediments from catscan computed tomography. Journal of Sedimentary Research.

Basco, D.R., Bouma, A.H. and Dunlap, W.A. 1974. Assessment of the factors controlling the long-term fate of dredged material deposited in unconfined subaqueous disposal areas. US Army Engineer Waterways Experiment Station Contract Report D-74-8: 238p.

Brylinski, M., Gibson, A.J., Daborn, G.R., Amos, C.L. and Christian, H.A. 1992. Miramichi inner bay sediment stability study. Acadia Centre for Estuarine Research Publication No. 22:

Buckley, D.E. 1990. Sedimentary geology of the Miramichi estuary system in relation to dredging and dumping activities: a review. in Review of Impacts of Channel Dredging on Biological Resources of the Miramichi System. G.R. Daborn (ed). Publ. Acadia Centre for Estuarine Research, Wolfville: 10p.

Buckley, D.E. and Winters, G.V. 1983. Geochemical transport through the Miramichi estuary. Canadian Journal of Fisheries and Aquatic Sciences 40: 162-182.

Herbich, J.B. and Brahme, S.B. 1991. Literature review and technical evaluation of sediment resuspension during dredging. US Army Engineers Waterways Experiment Station Contract Report HL-91-1: 87p.

Hodgins, D.O. and Harper, J.R. 1994. Technical guidelines for physical monitoring at ocean disposal sites. Consultant Report submitted to Environment Canada, Quebec: 85p.

Howells, K. and McKay, A.G. 1977. Seismic profiling in Miramichi bay, New Brunswick. Canadian Journal of Fisheries and Aquatic Sciences 14: 2909-2927.

Johanson, E.E., Bowen, S.P., and Henry, G. 1976. State-of-the-art survey and evaluation of open-water dredged material placement methodology. US Army Engineer Waterways Experiment Station Contract Report D-76-3: 145p.

Kranck, K. and Milligan, T.G. 1989. Effects of a major dredging program on the sedimentary environment of Miramichi Bay, New Brunswick. Canadian Technical Report of Hydrography and Ocean Science No. 112: 61p.

Krauel, D.P. 1975. The physical oceanography of the Miramichi River estuary., September-October, 1973. Fisheries Marine Service Technical Report No. 571: 184p.

Krone, R.B. 1962. Flume studies of the transport of sediment in estuarial shoaling processes. Final Report of Hydraulic Engineering Laboratory and Sanitation Engineering Research Laboratory, University of California, Berkley.

Landva, A.O. 1976. Miramichi channel study, Miramichi inner bay. Geotechnical investigations. Consultant Report submitted to Dept. Public Works: 24p.

MacGregor, C. and Packman, S.D. 1983. Winter water quality studies in Miramichi estuary. in Report on Ocean Dumping Research and development Fund, Atlantic Region, 1981-1982. Surveillance Report EPS-5-AR-83-9: 48-56.

Paterson, D.M. 1994. Microbial mediation of sediment structure and behaviour. NATO ASI Series G35: 97-109.

Pequegnat, W.E., Pequegnat, L.H., James, B.M., Kennedy, E.A. Fay, R.R., and Fredericks, A.D. 1981. Procedural guide for designation surveys of ocean dredged material disposal sites. US Army Engineer Waterways Experiment Station Technical Report EL-81-1: 268p.

Philpott, K.L. 1978. Miramichi Channel Study. Contract Report submitted to Dept. of Public Works, Halifax: 284p.

Philpott, K.L. and Duncan, G.R. 1977. Initial environmental evaluation, Miramichi channel study. Contract Report submitted to Dept. Public Works.

Reinson, G.E. 1976. Surficial sediment distribution in the Miramichi estuary, New Brunswick. Geological Survey of Canada Paper 76-1C: 41-44.

Reinson, G.E. 1980. Variations in tidal-inlet morphology and stability, northeast New Bruswick. in The Coastline of Canada, Littoral Processes and Shore Morphology. S.B. McCann (ed). Geological Survey of Canada Paper 80-10: 23-39.

Schafer, C.T., Cole, F.E. and Wagner, F.J.E. 1977. Relationship of Foraminifera distribution patterns to sedimentary processes in the Miramichi estuary, New Brunswick. Geological Survey of Canada Paper 77-1C: 1-7.

Schafer, C.T. and Smith, J.N. 1983. River discharge, sedimentation and benthic environmental variations in Miramichi inner bay, New Brunswick. Canadian Journal of Earth Sciences 20: 388-398.

Scott. D.B., Medioli, F.S. and Schafer, C.T. 1977. Temporal changes in foraminiferal distributions in Miramichi River estuary, New Brunswick. Canadian Journal of Earth Sciences 14: 1566-1587.

Sheng, Y.P. and Villaret, C. 1989. Modeling the effect of suspended sediment stratification on bottom exchange processes. Journal of Geophysical Research 94: 14,429-14,444.

Solomon, S. 1990. Suspended particulate material in the Miramichi estuary, New Brunswick: summary of pre- and post-dredging data. in Review of Impacts of Channel Dredging on Biological Resources of the Miramichi System. G.R. Daborn (ed). Publ. Acadia Centre for Estuarine Research, Wolfville: 14p.

Vilks, G. and Krauel, D.P. 1982. Environmental geology of the Miramichi estuary: physical oceanography. Geological Survey of Canada Paper 81-24:

Terzaghi, K. and Peck, R.B. 1967. Soil Mechanics in Engineering Practice. Publ. John Wiley and Sons: 729.

Willis, D.H. 1990. Miramichi estuary - physical oceanography. in Review of Impacts of Channel Dredging on Biological Resources of the Miramichi System. G.R. Daborn (ed). Publ. Acadia Centre for Estuarine Research, Wolfville: 10p.

Winters, G.V. 1981. Environmental geology of the Miramichi estuary: suspended sediment transport. Geological Survey of Canada Paper 81-16: 12p.

Winters, G.V. 1983. Modeling suspended sediment dynamics of the Miramichi estuary, New Brunswick, Canada. Canadian Journal of Fisheries and Aquatic Sciences 40: 105-116.

Winters, G.V., Fitzgerald, R.A. and Buckley, D.E. 1978. Analysis of water column and bottom sediment samples from the Miramichi Estuary, New Brunswick. Bedford Institute of Oceanography Data Series Report BI-D-78-8: 81p.

Worms, J. and Bates, S.S. 1990. Review of the impact of Miramichi dredging on primary production. in Review of Impacts of Channel Dredging on Biological Resources of the Miramichi System. G.R. Daborn (ed). Publ. Acadia Centre for Estuarine Research, Wolfville: 13p.

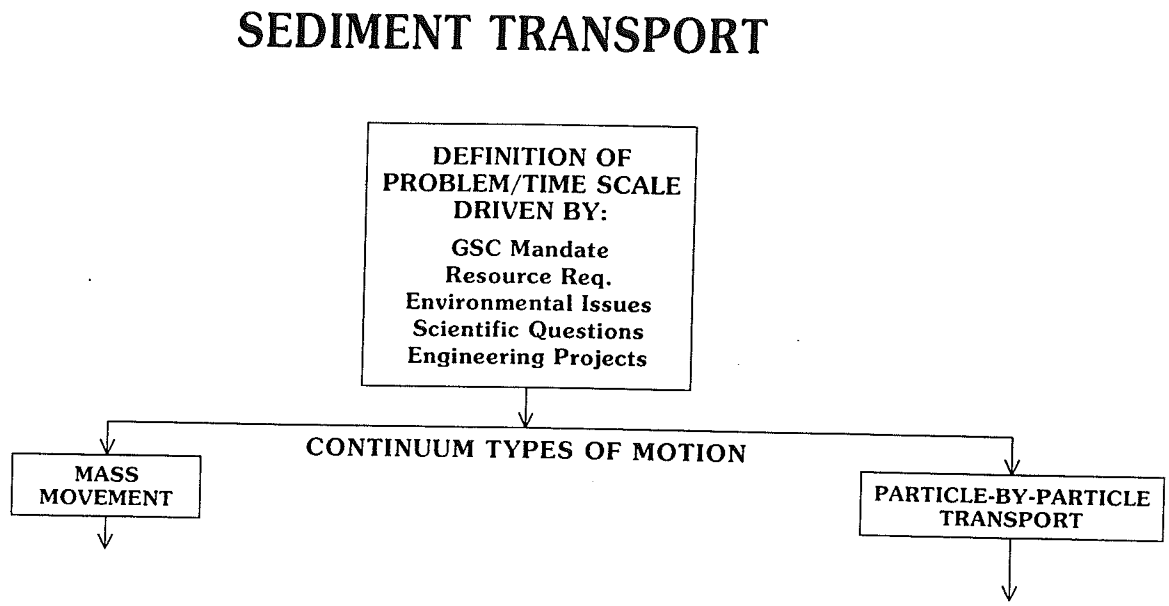

FIGURE 1.1. A schematic representation of the sediment transport process. It shows that erosion takes place over a continuum of scales from individual particles (particle-by-particle transport) to mass movements on the km scale.

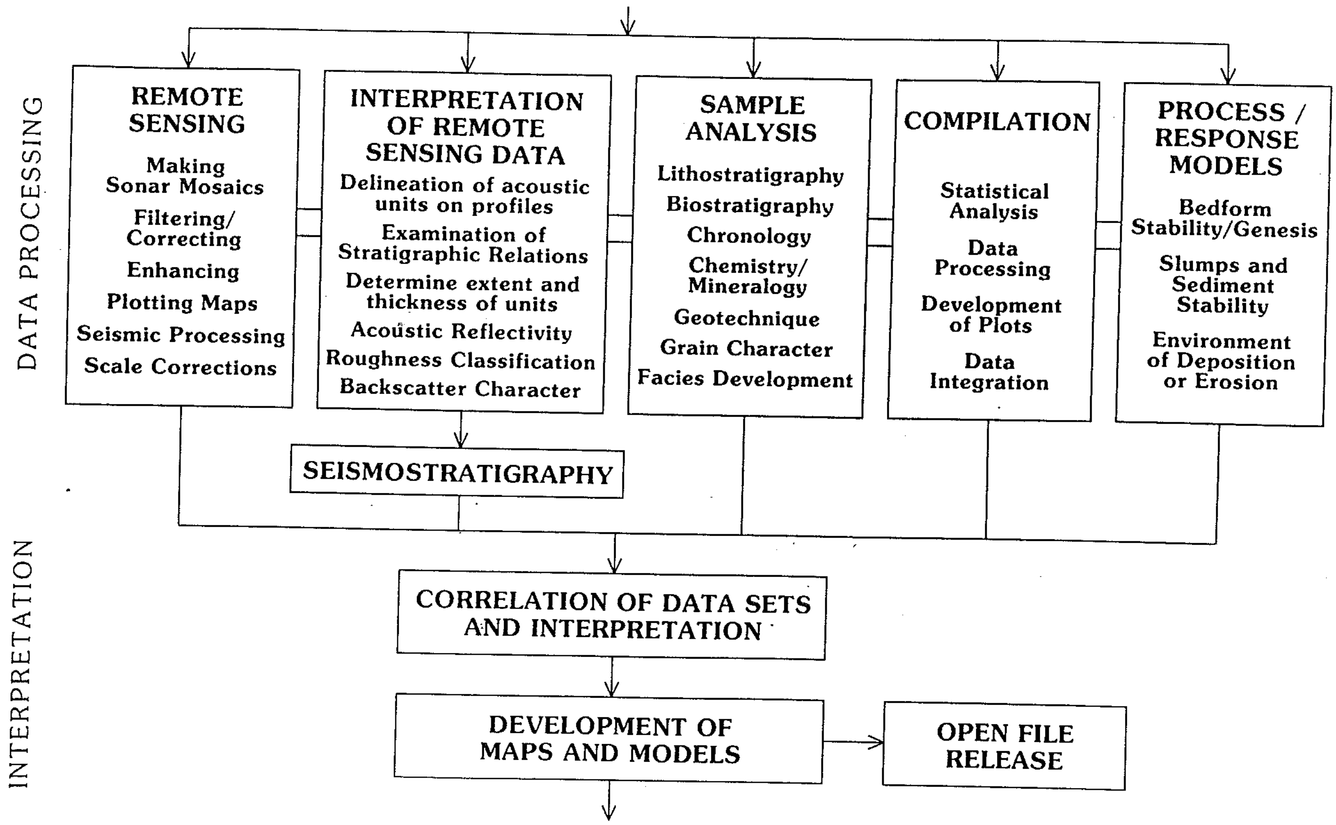

FIGURE 1.2. A scheme adopted by the Geological Survey of Canada to undertake surficial geological mapping. The scheme is applicable to the evaluation of dumpsites. The process/response module is the subject of this report.

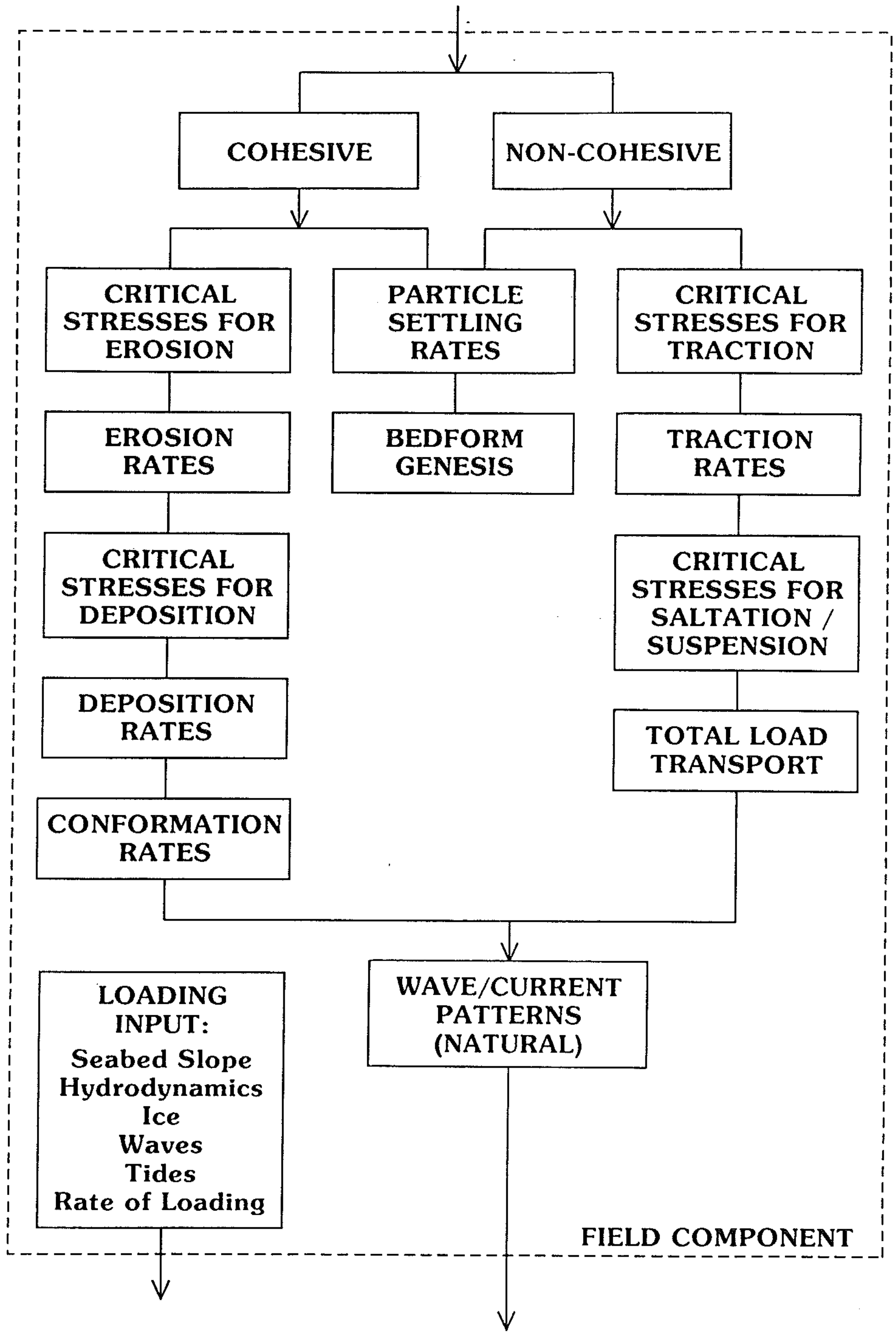

FIGURE 1.3. A detailed breakdown of elements involved in the modelling of sediment process\response. Sediments are broadly classified into either (1) cohesive, or (2) non-cohesive responses.

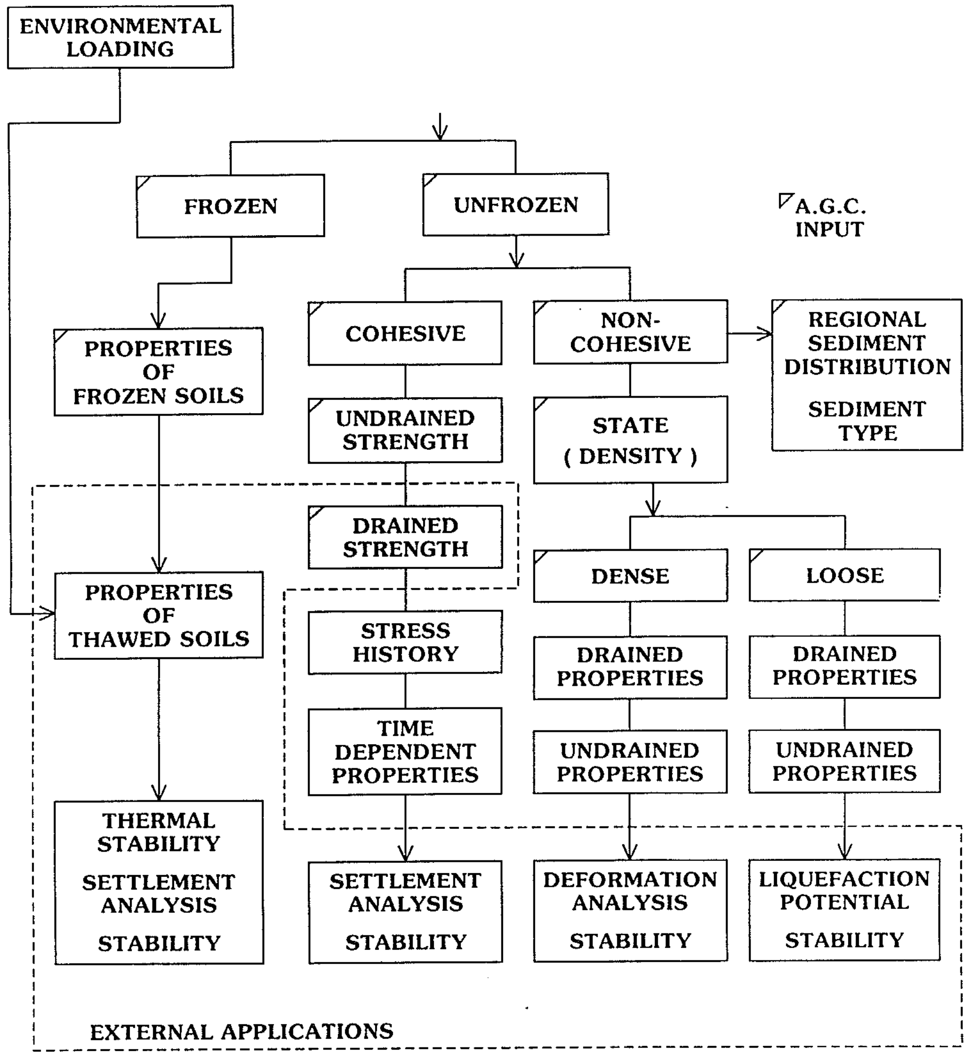

FIGURE 1.4. A detailed breakdown of the elements involved in the evaluation of mass movement of seabed sediments.

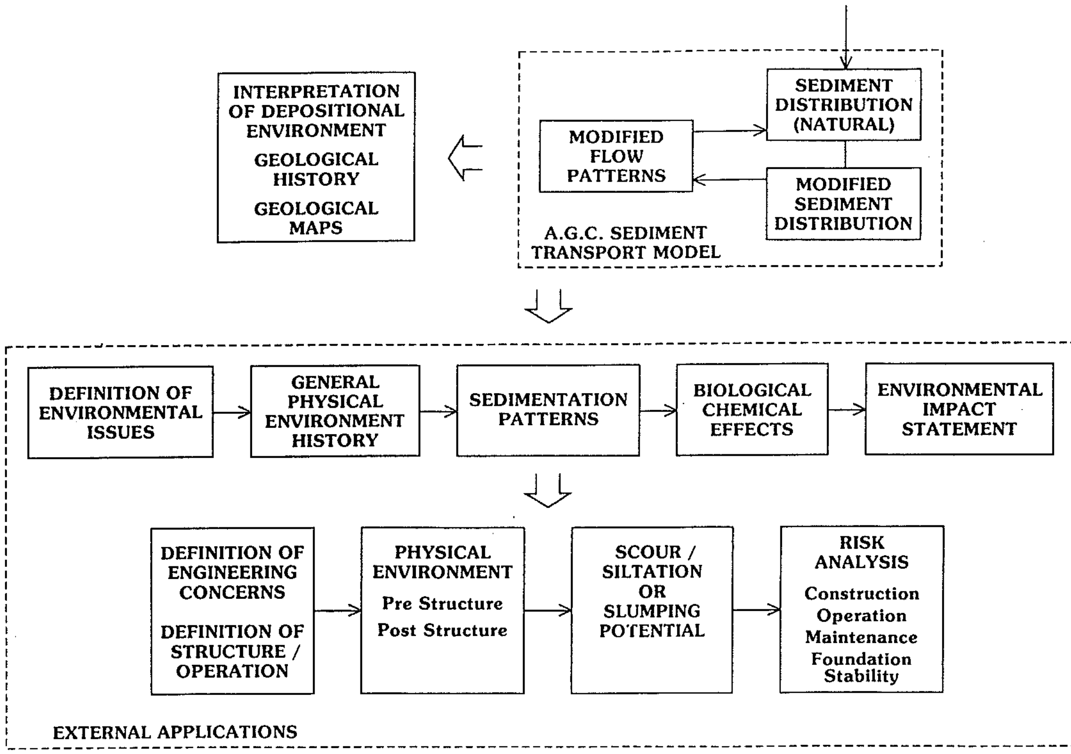

FIGURE 1.5. A schematic representation of the role of seabed stability studies in (1) environmental impact assessment, and (2) engineering risk analysis.

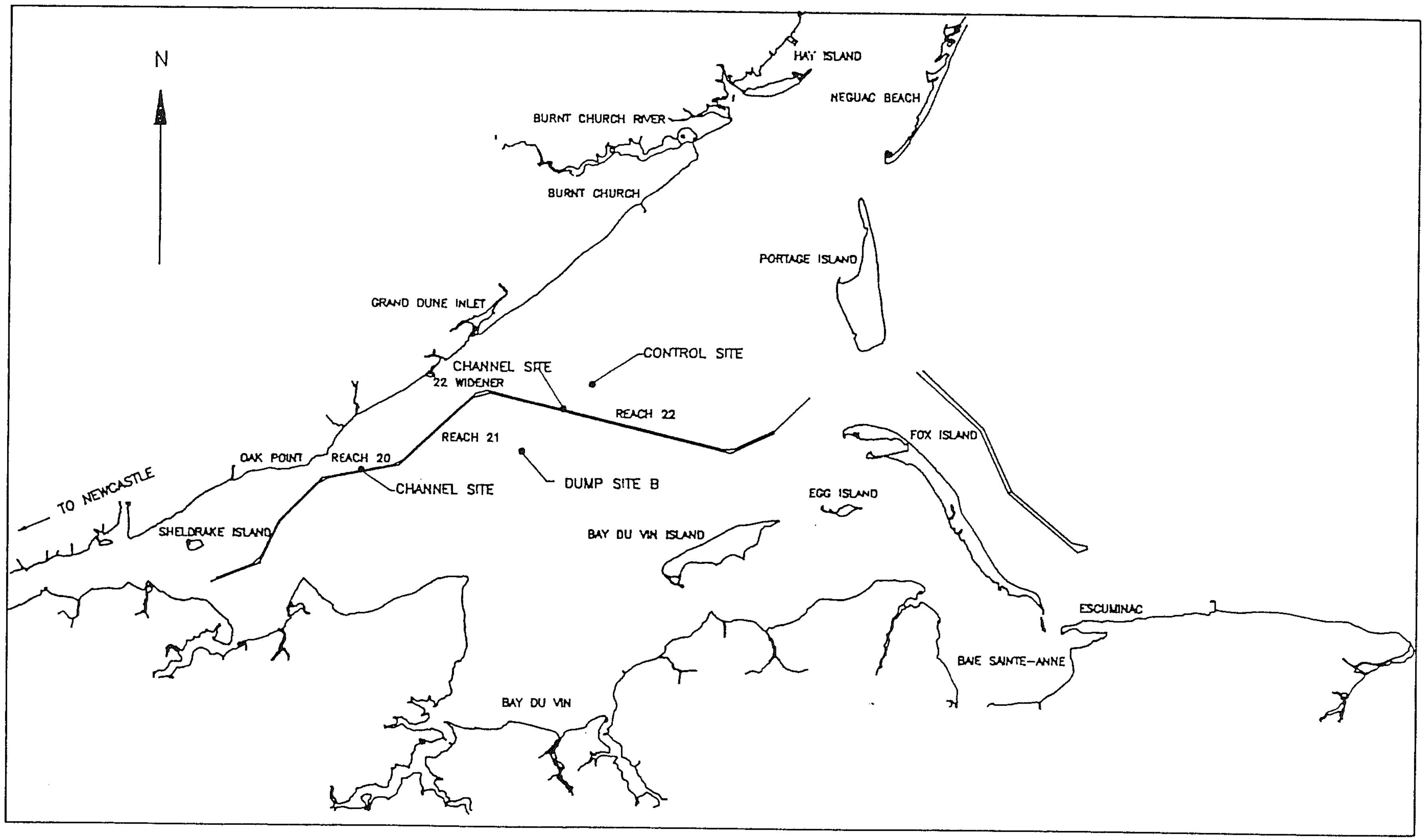

FIGURE 1.6. A location diagram of the Miramichi bay, New Brunswick.

FIGURE 3.2.1.1. A time-series plot of the Sea Carousel deployment at station MIR1, dumpsite B, Miramichi bay.(A) azimuthal and vertical current speed (m/s); (B) suspended sediment concentration (mg/L); OBS1 is the upper sensor, OBS3 is the lower one. Note the erratic lower sensor signal, produced by the saltation of large grains and aggregates; and (C) erosion rate (kg/m^2/s). The data have been filtered by a 10-second time average. The asymptotic trend in SSC is diagnostic of Type I erosion.

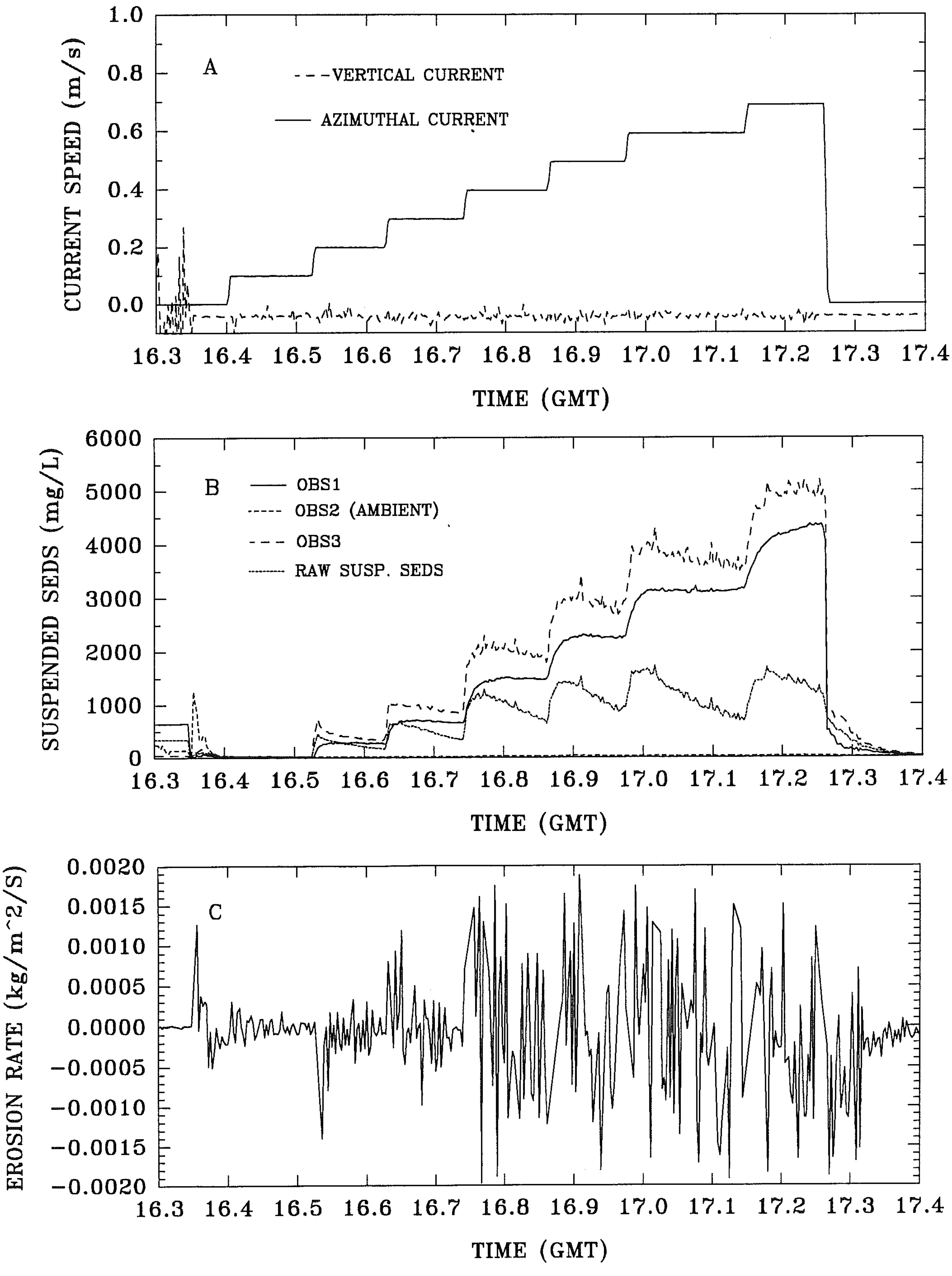

FIGURE 3.2.1.2. A time-series plot of the Sea Carousel deployment at station MIR2, dumpsite B, Miramichi bay.(A) azimuthal and vertical current speed (m/s); (B) suspended sediment concentration (mg/L); and (C) erosion rate ($kg/m^2/s$).

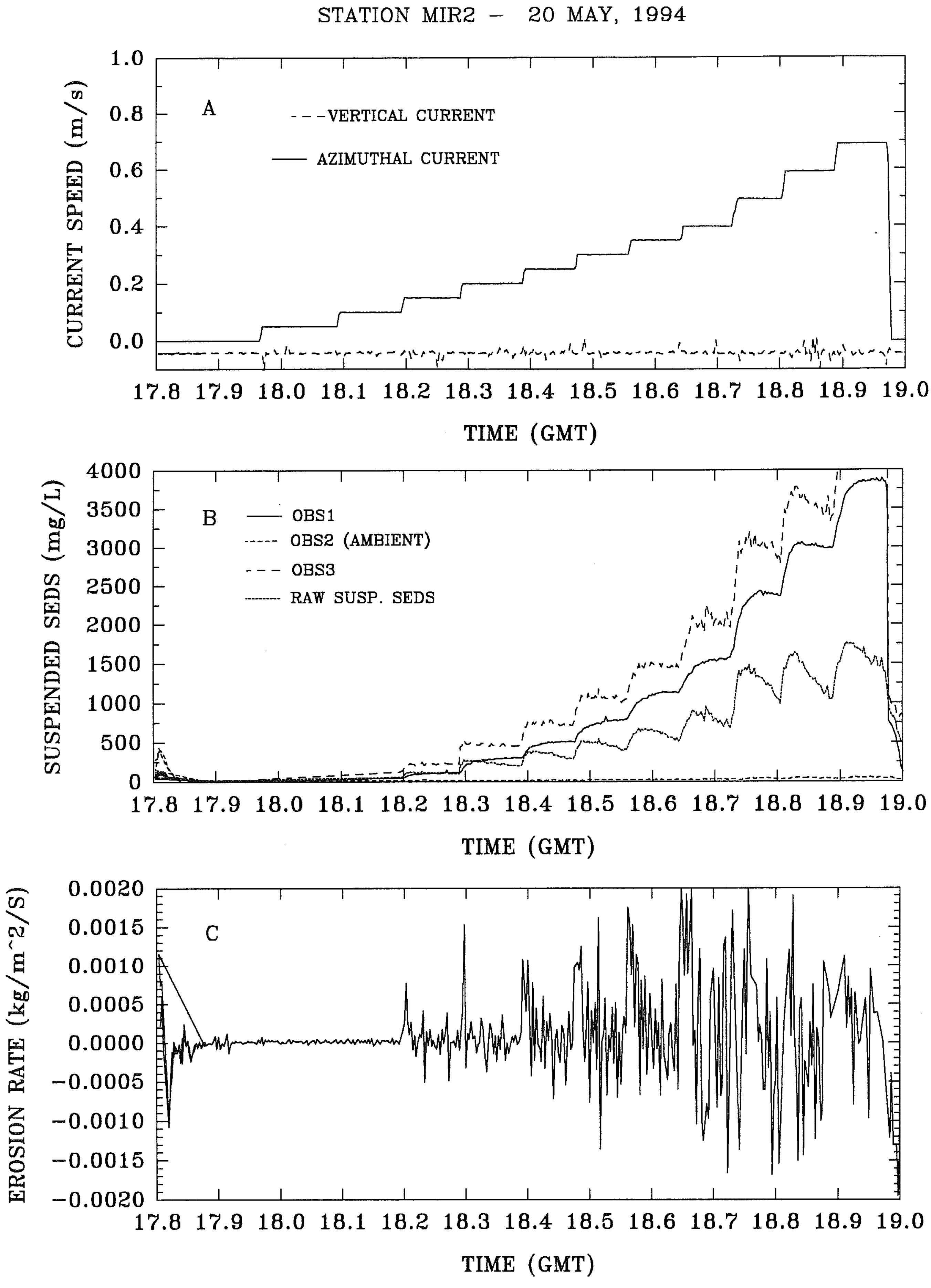

FIGURE 3.2.1.3. A time-series plot of the Sea Carousel deployment at station MIR3, dumpsite B, Miramichi bay.(A) azimuthal and vertical current speed (m/s); (B) suspended sediment concentration (mg/L); and (C) erosion rate (kg/m^2/s). In this example the data have been filtered through a 5-second time average.

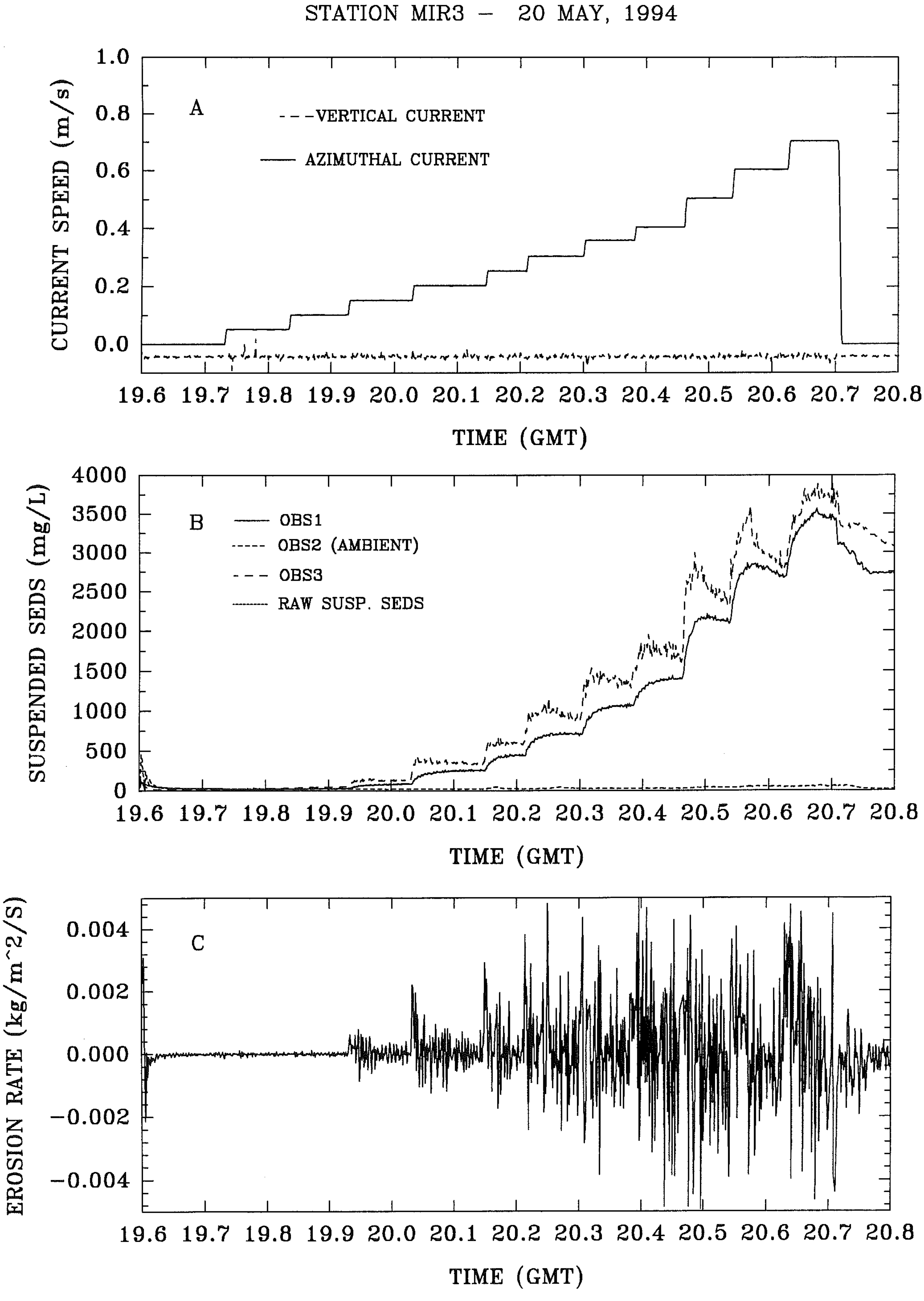

FIGURE 3.2.1.4. A time-series plot of the Sea Carousel deployment at station MIR3, dumpsite B, Miramichi bay.(A) azimuthal and vertical current speed (m/s); (B) suspended sediment concentration (mg/L); and (C) erosion rate (kg/m^2/s). In this example the data have been filtered through a 10-second time average.

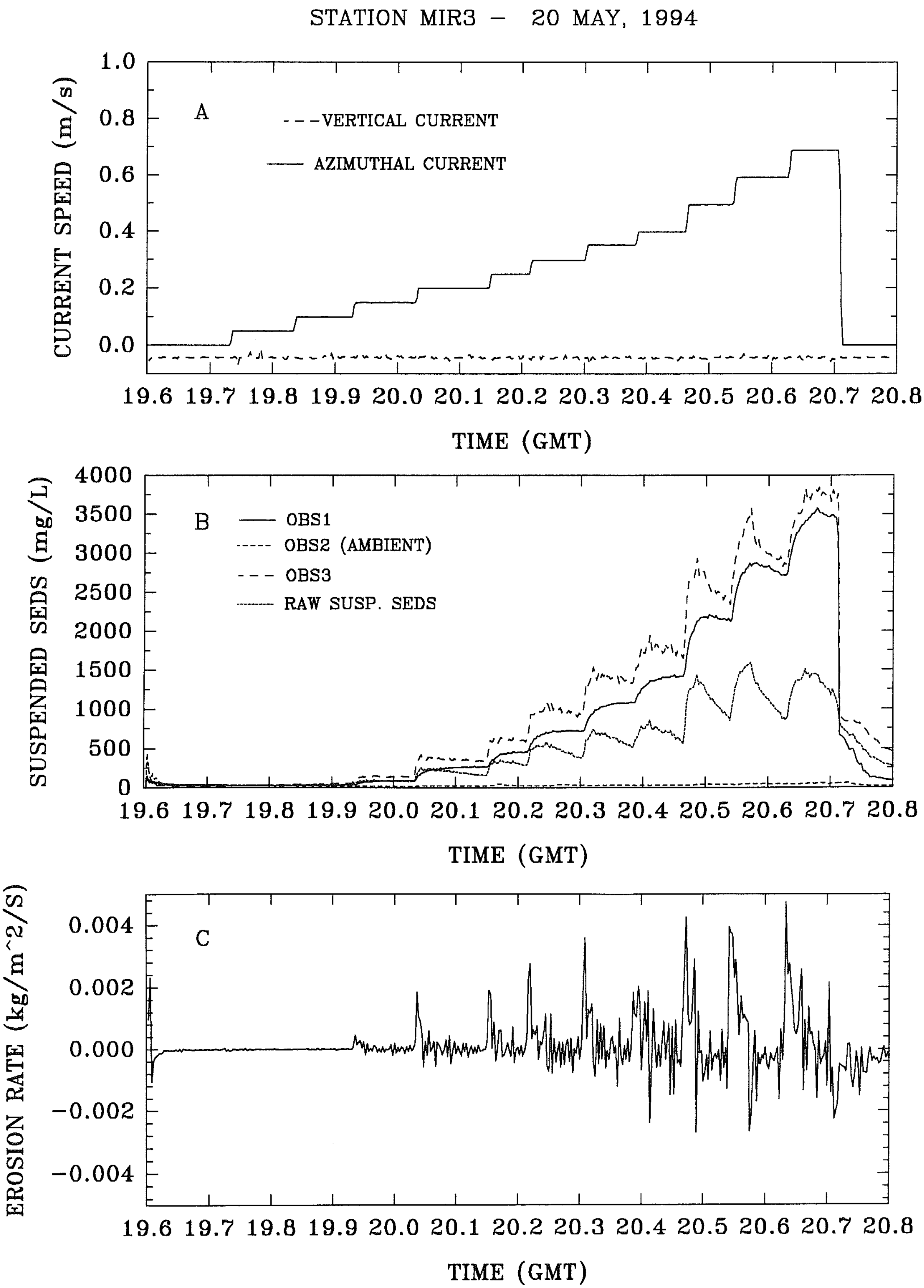

FIGURE 3.2.1.5. A time-series plot of the Sea Carousel deployment at station MIR3, dumpsite B, Miramichi bay.(A) azimuthal and vertical current speed (m/s); (B) suspended sediment concentration (mg/L); and (C) erosion rate (kg/m^2/s). In this case the data have been filtered through a 20-second time average.

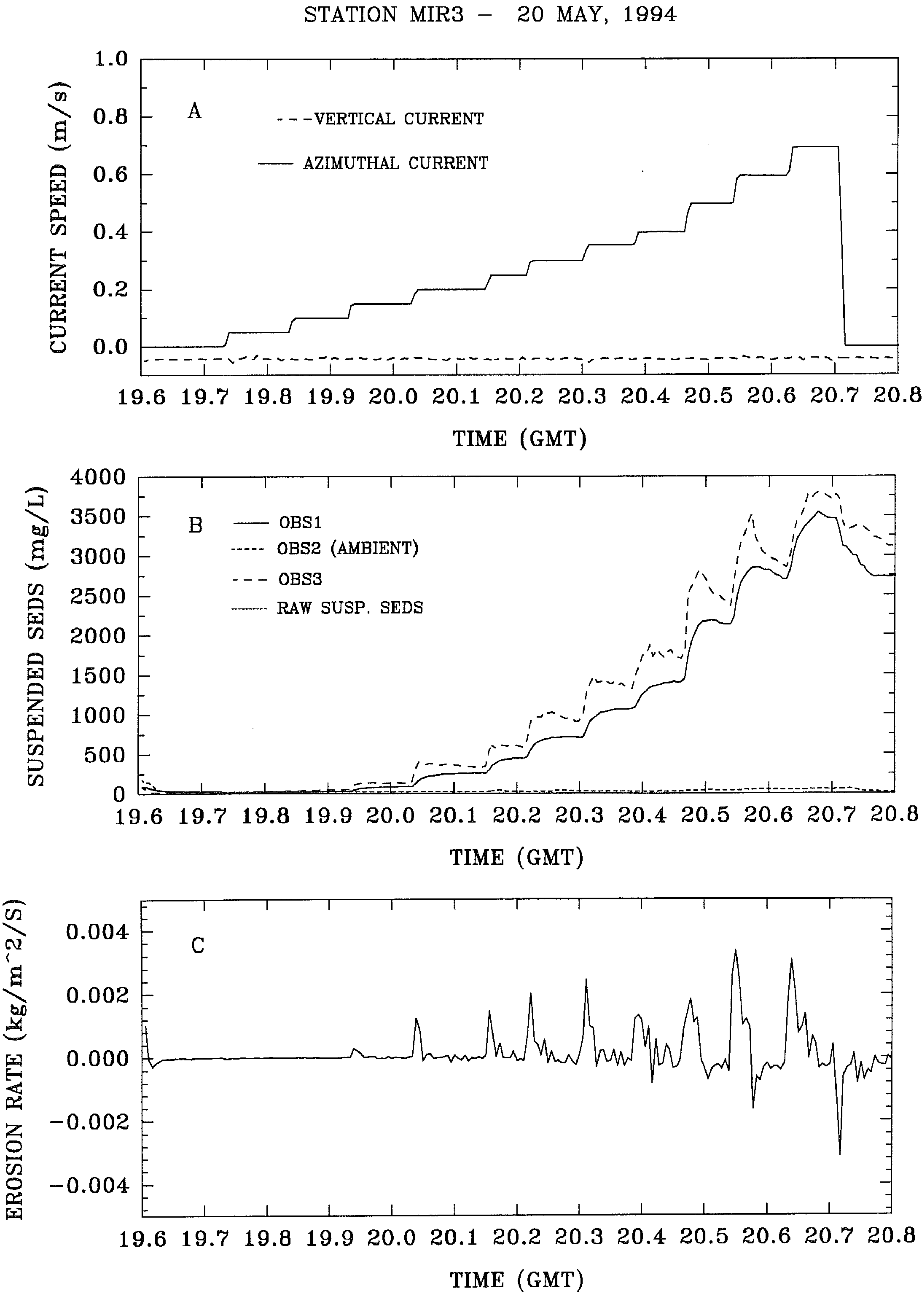

FIGURE 3.2.1.6. A time-series plot of the Sea Carousel deployment at station MIR3, dumpsite B, Miramichi bay.(A) azimuthal and vertical current speed (m/s); (B) suspended sediment concentration (mg/L); and (C) erosion rate (kg/m^2/s). In this example the data have been filtered through a 60-second time average.

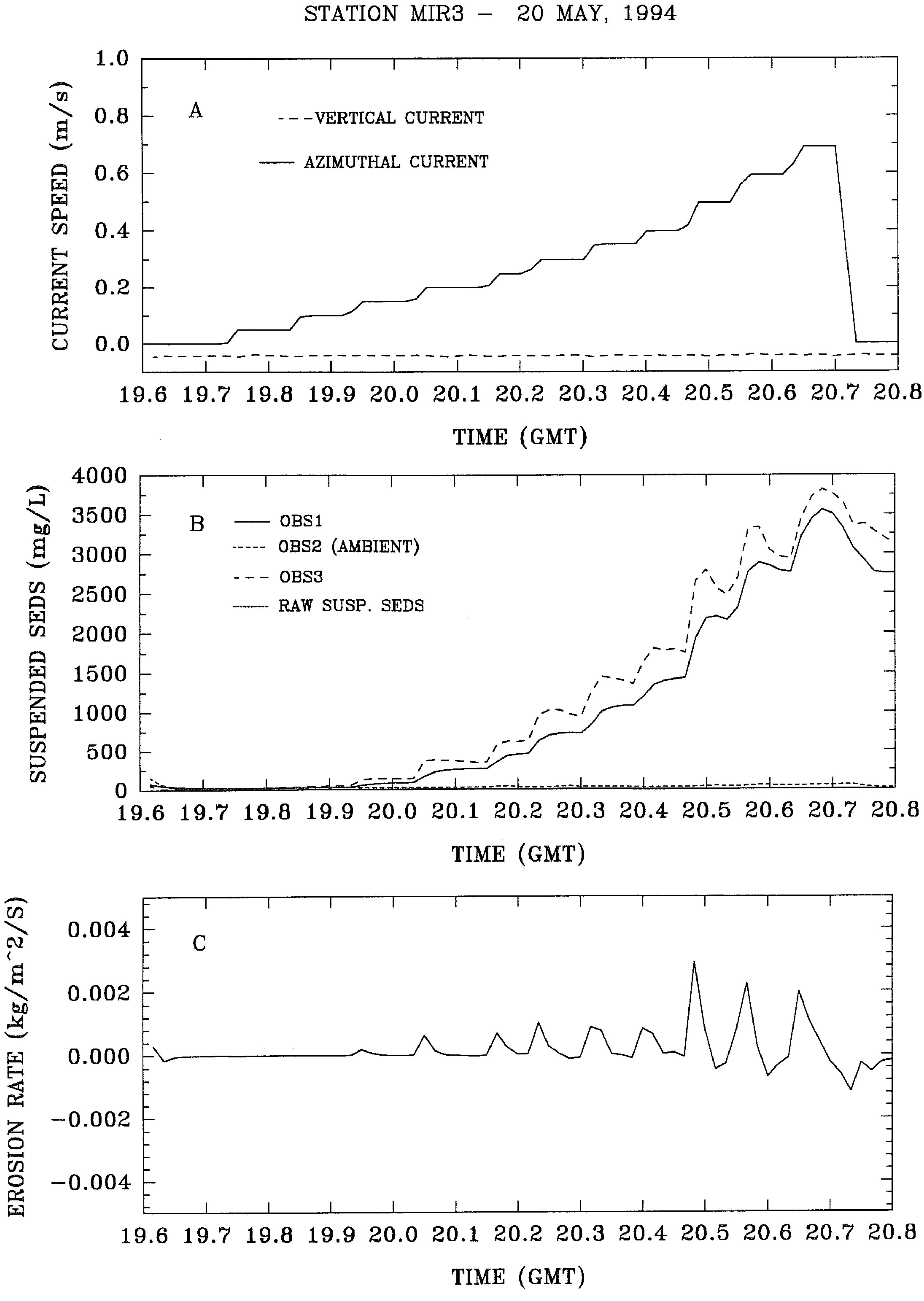

FIGURE 3.2.1.7. A time-series plot of the Sea Carousel deployment at station MIR4, dumpsite B, Miramichi bay.(A) azimuthal and vertical current speed (m/s); (B) suspended sediment concentration (mg/L); and (C) erosion rate (kg/m^2/s).

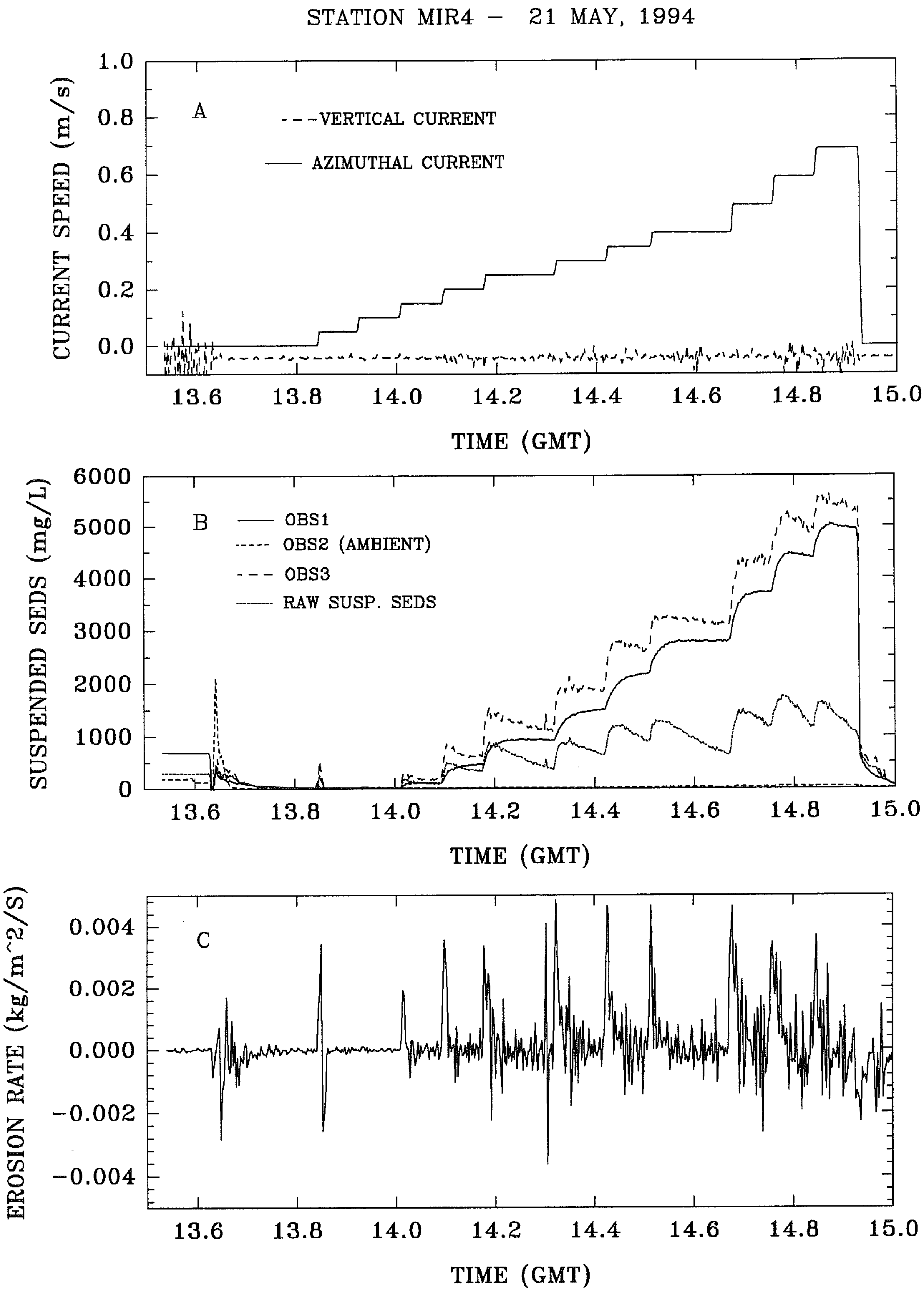

FIGURE 3.2.1.8. A time-series plot of the Sea Carousel deployment at station MIR5, dumpsite B, Miramichi bay.(A) azimuthal and vertical current speed (m/s); (B) suspended sediment concentration (mg/L); and (C) erosion rate (kg/m^2/s).

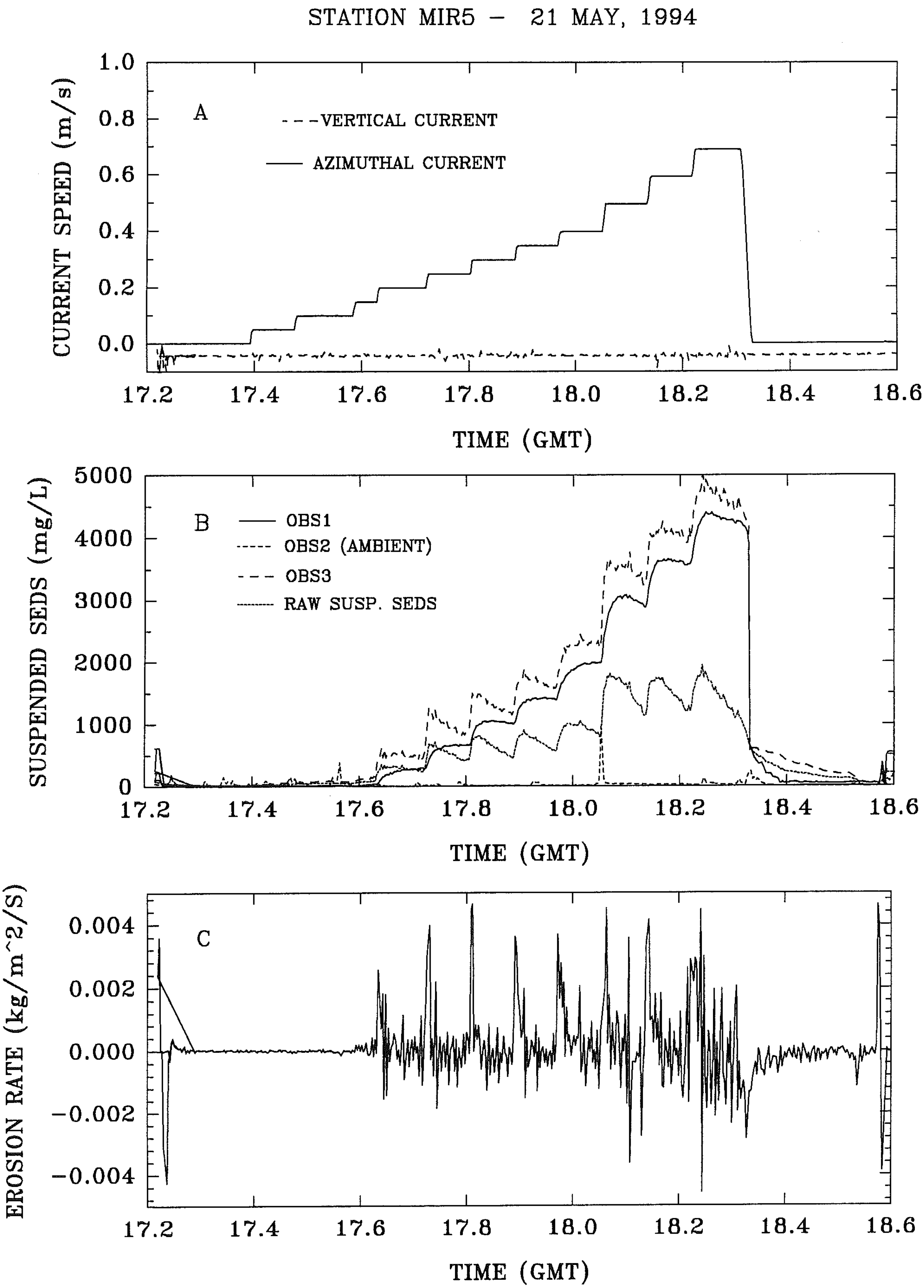

FIGURE 3.2.1.9. A time-series plot of the Sea Carousel deployment at station MIR6, dumpsite B, Miramichi bay.(A) azimuthal and vertical current speed (m/s); (B) suspended sediment concentration (mg/L); and (C) erosion rate (kg/m^2/s).

10 sec aver ?

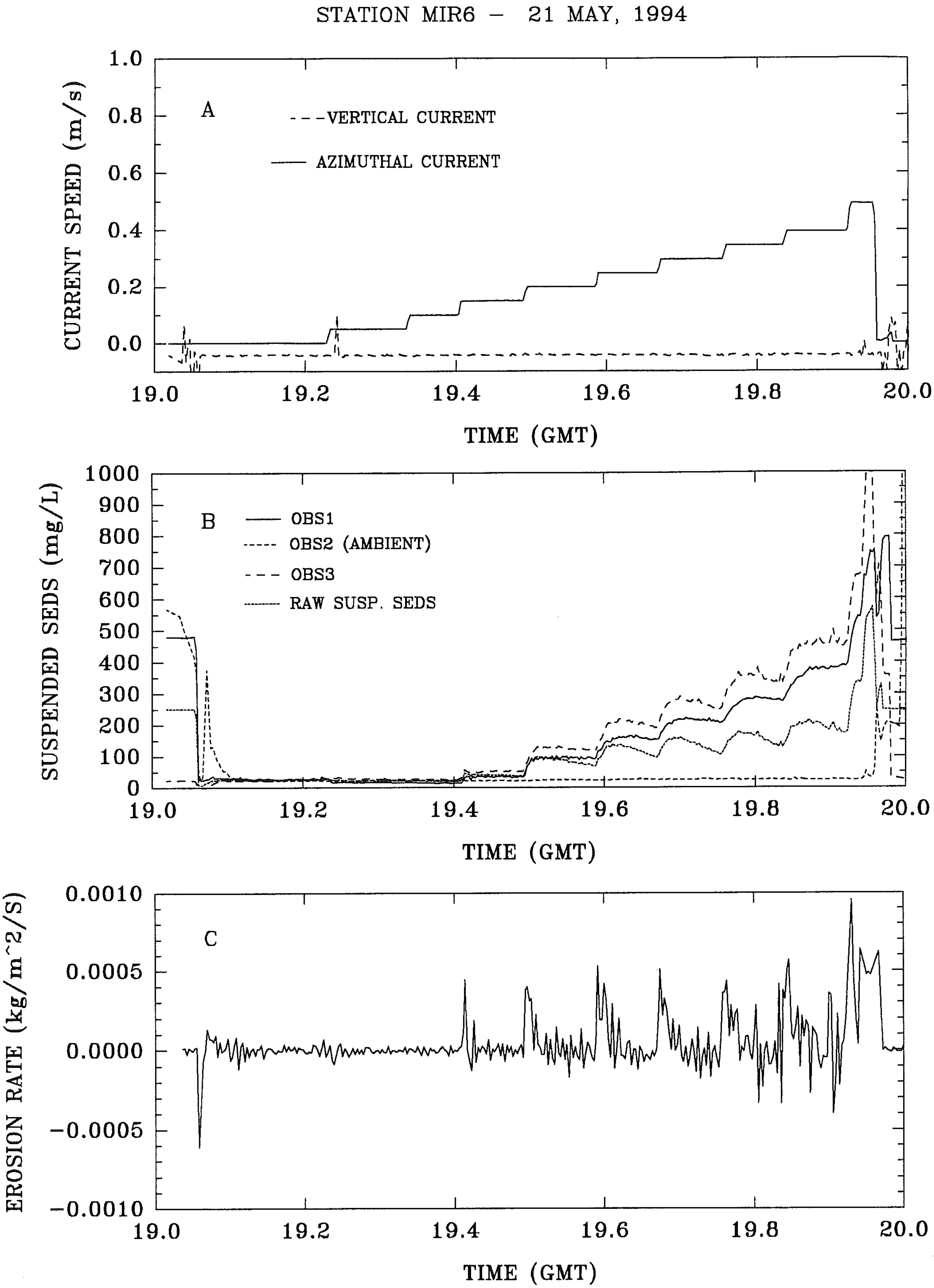

FIGURE 3.2.1.10. A time-series plot of the Sea Carousel deployment at station MIR7, dumpsite B, Miramichi bay.(A) azimuthal and vertical current speed (m/s); (B) suspended sediment concentration (mg/L); and (C) erosion rate ($kg/m^2/s$).

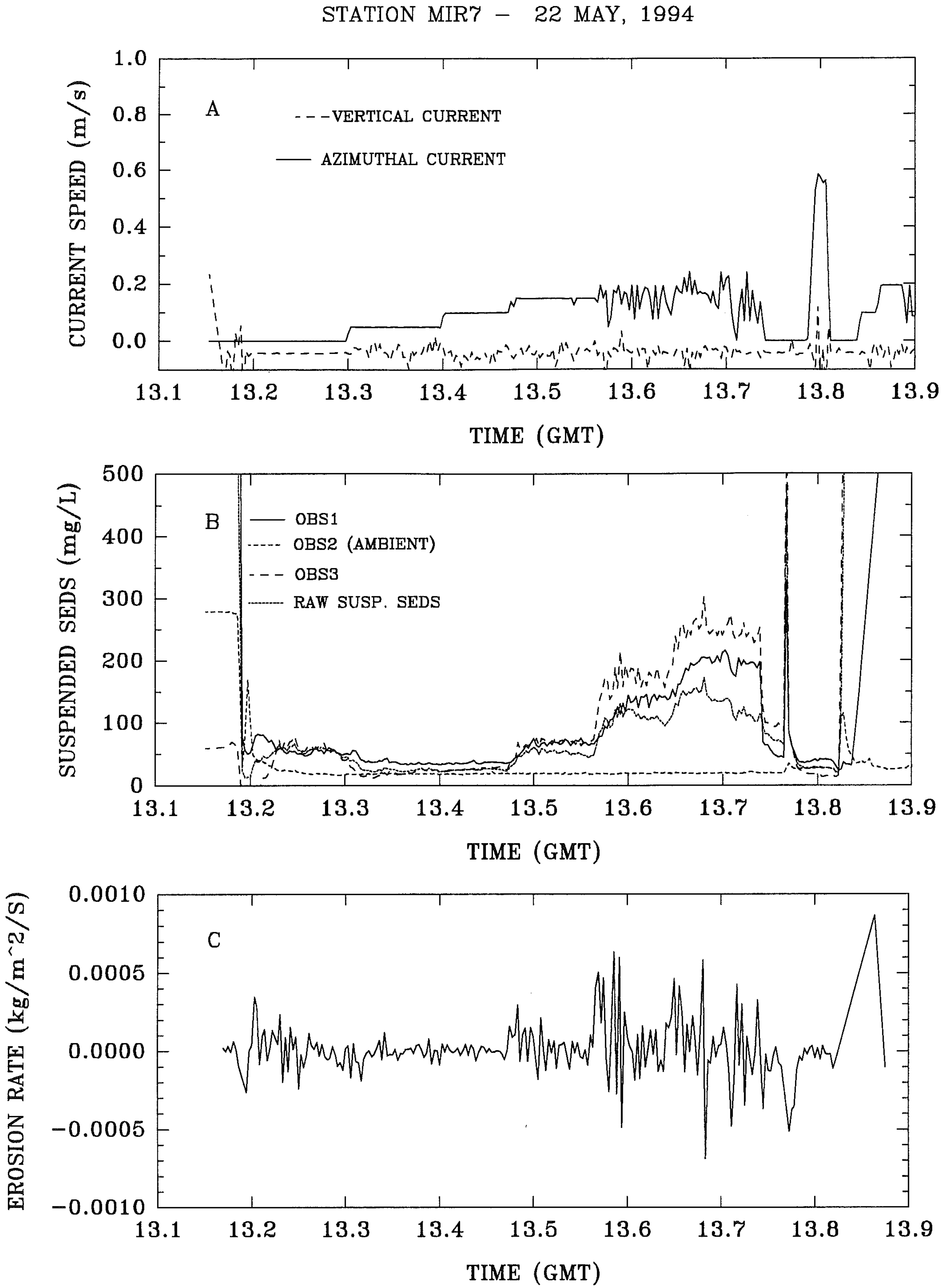

FIGURE 3.2.1.11. A time-series plot of the Sea Carousel deployment at station MIR8, dumpsite B, Miramichi bay.(A) azimuthal and vertical current speed (m/s); (B) suspended sediment concentration (mg/L); and (C) erosion rate (kg/m²/s).

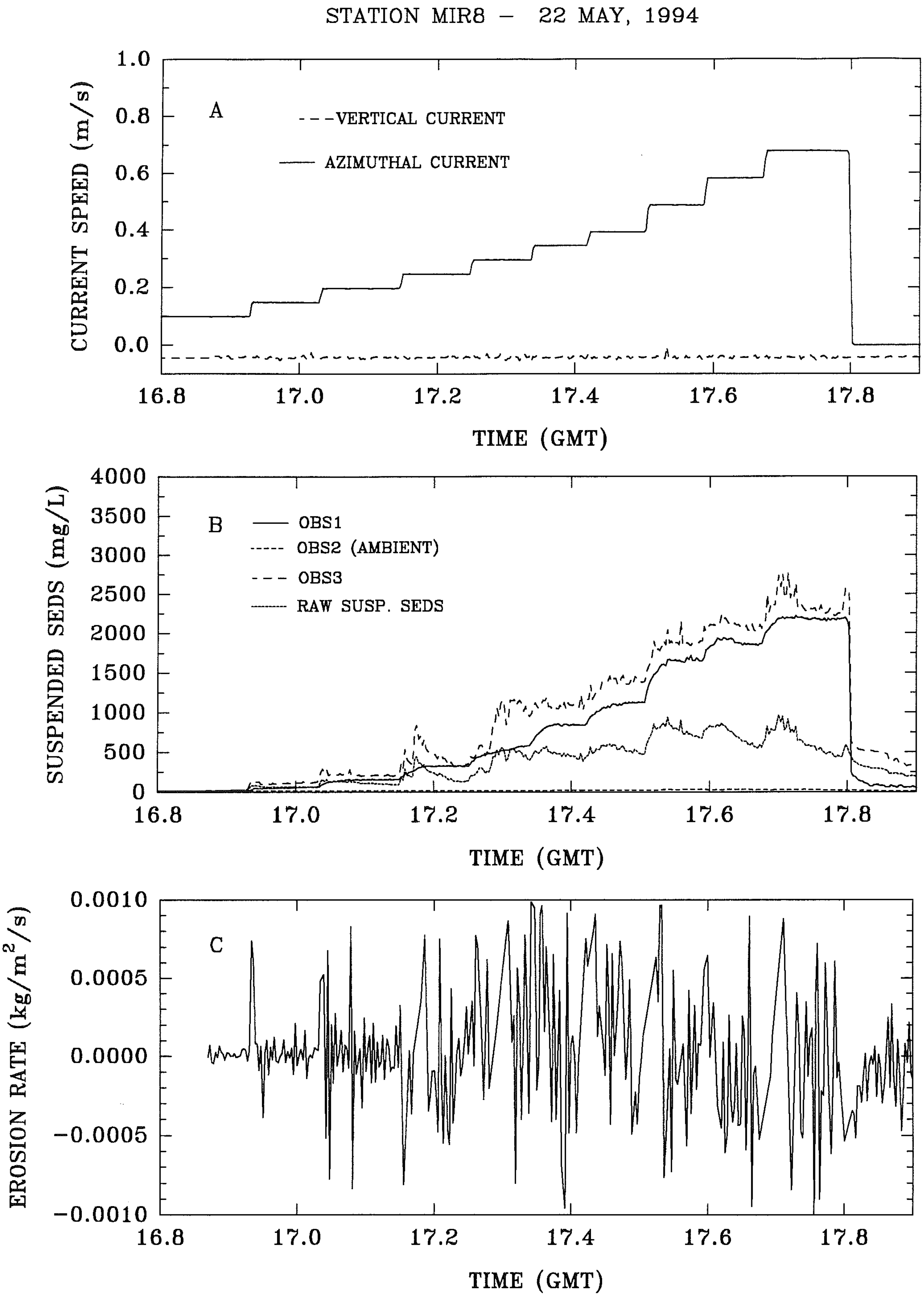

FIGURE 3.2.1.12. A time-series plot of the Sea Carousel deployment at station MIR9, dumpsite B, Miramichi bay.(A) azimuthal and vertical current speed (m/s); (B) suspended sediment concentration (mg/L); and (C) erosion rate (kg/m²/s).

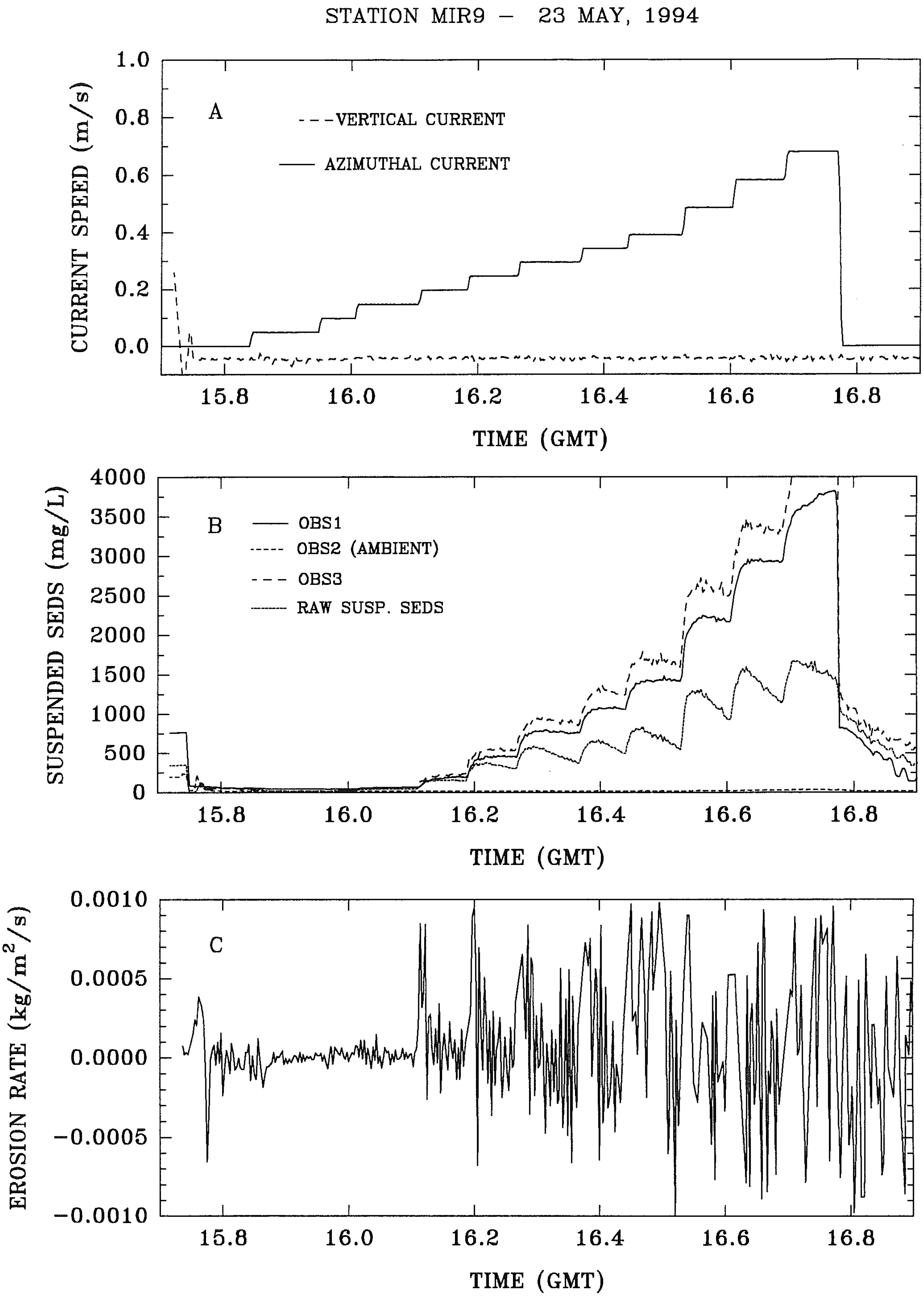

FIGURE 3.2.1.13. A time-series plot of the Sea Carousel deployment at station MIR10, dumpsite B, Miramichi bay.(A) azimuthal and vertical current speed (m/s); (B) suspended sediment concentration (mg/L); and (C) erosion rate (kg/m²/s).

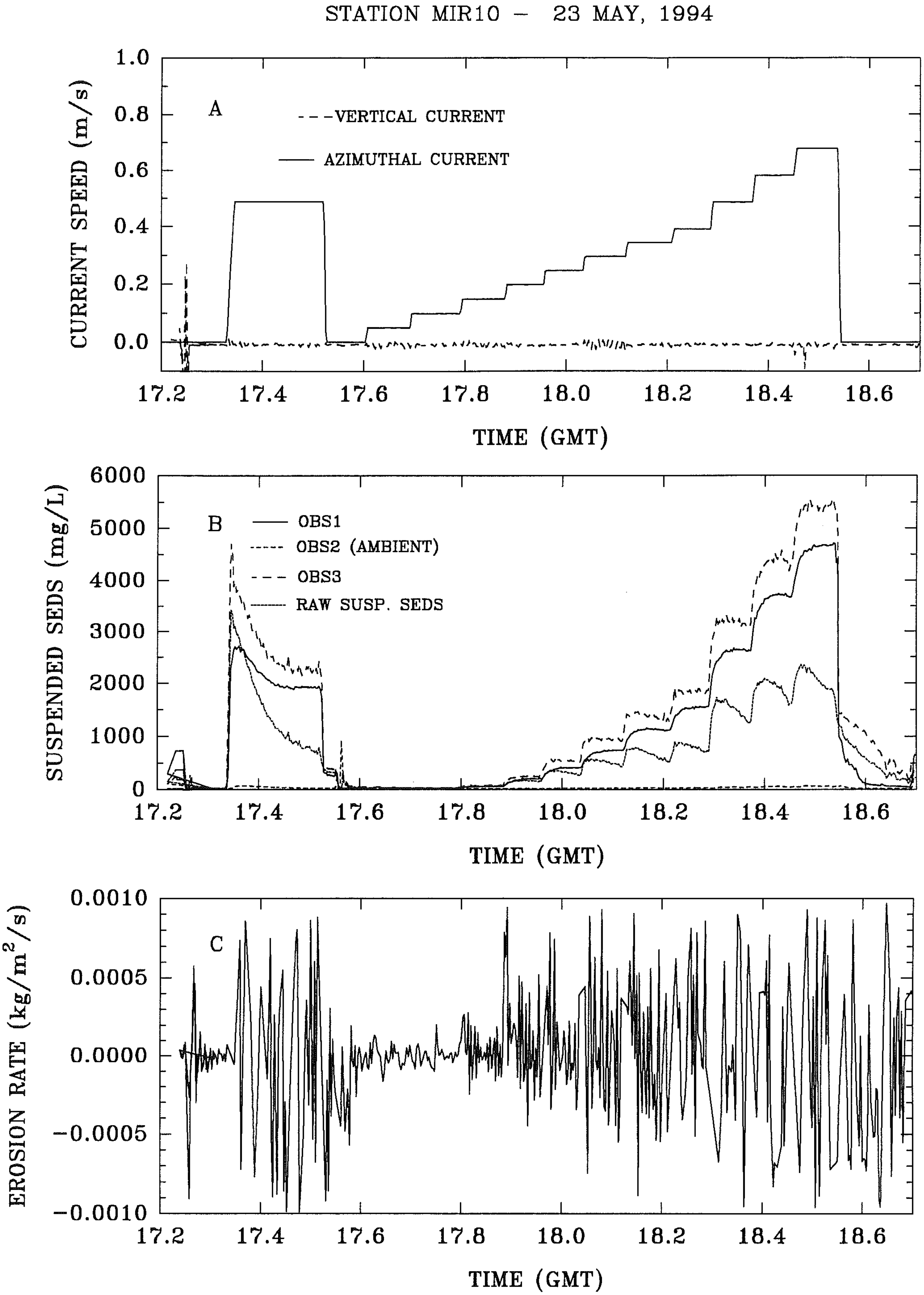

FIGURE 3.2.1.14. A time-series plot of the Sea Carousel deployment at station MIR11, dumpsite B, Miramichi bay.(A) azimuthal and vertical current speed (m/s); (B) suspended sediment concentration (mg/L); and (C) erosion rate ($kg/m^2/s$).

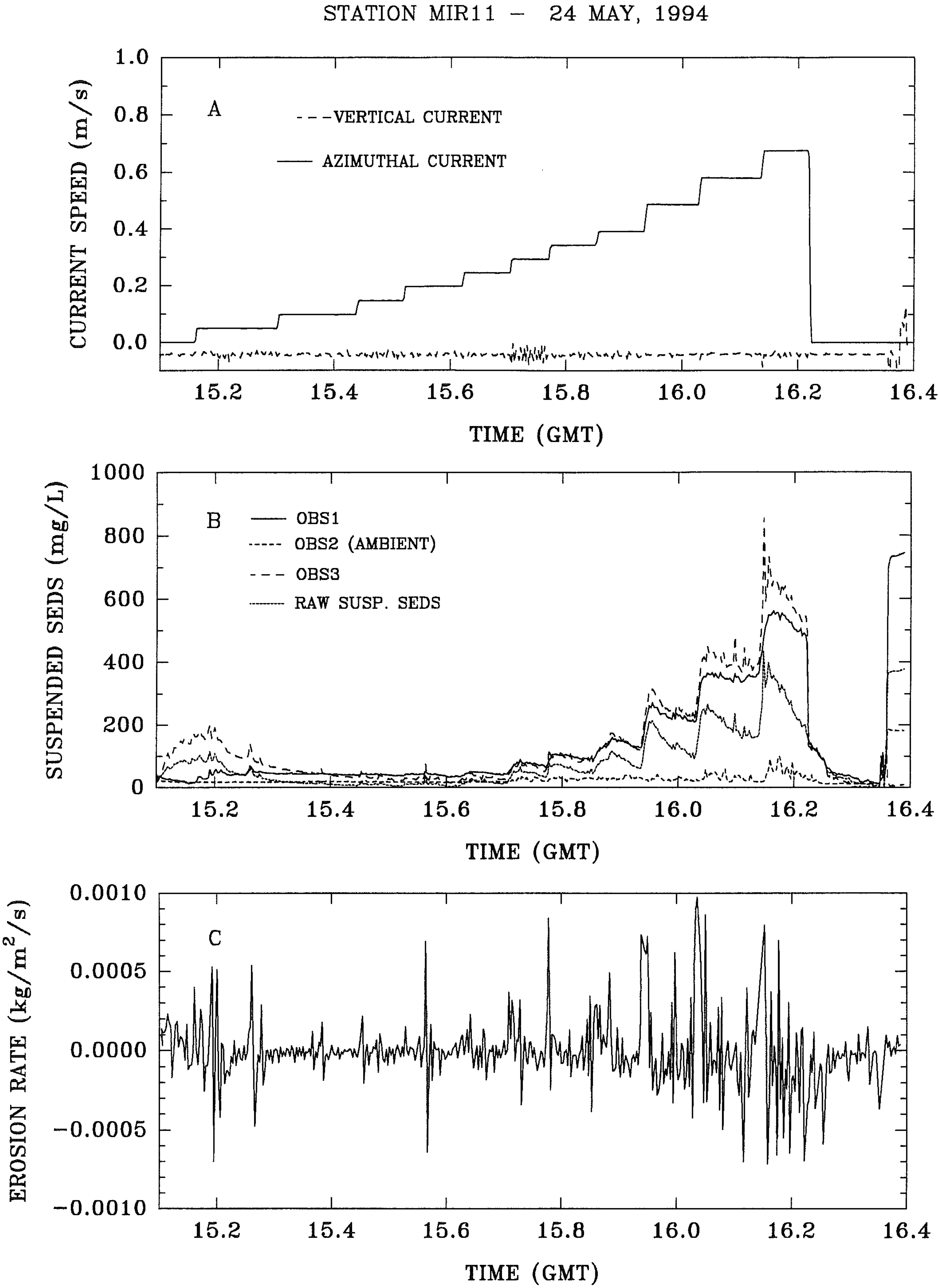

FIGURE 3.2.1.15. A time-series plot of the Sea Carousel deployment at station MIR12, dumpsite B, Miramichi bay.(A) azimuthal and vertical current speed (m/s); (B) suspended sediment concentration (mg/L); and (C) erosion rate (kg/m²/s).

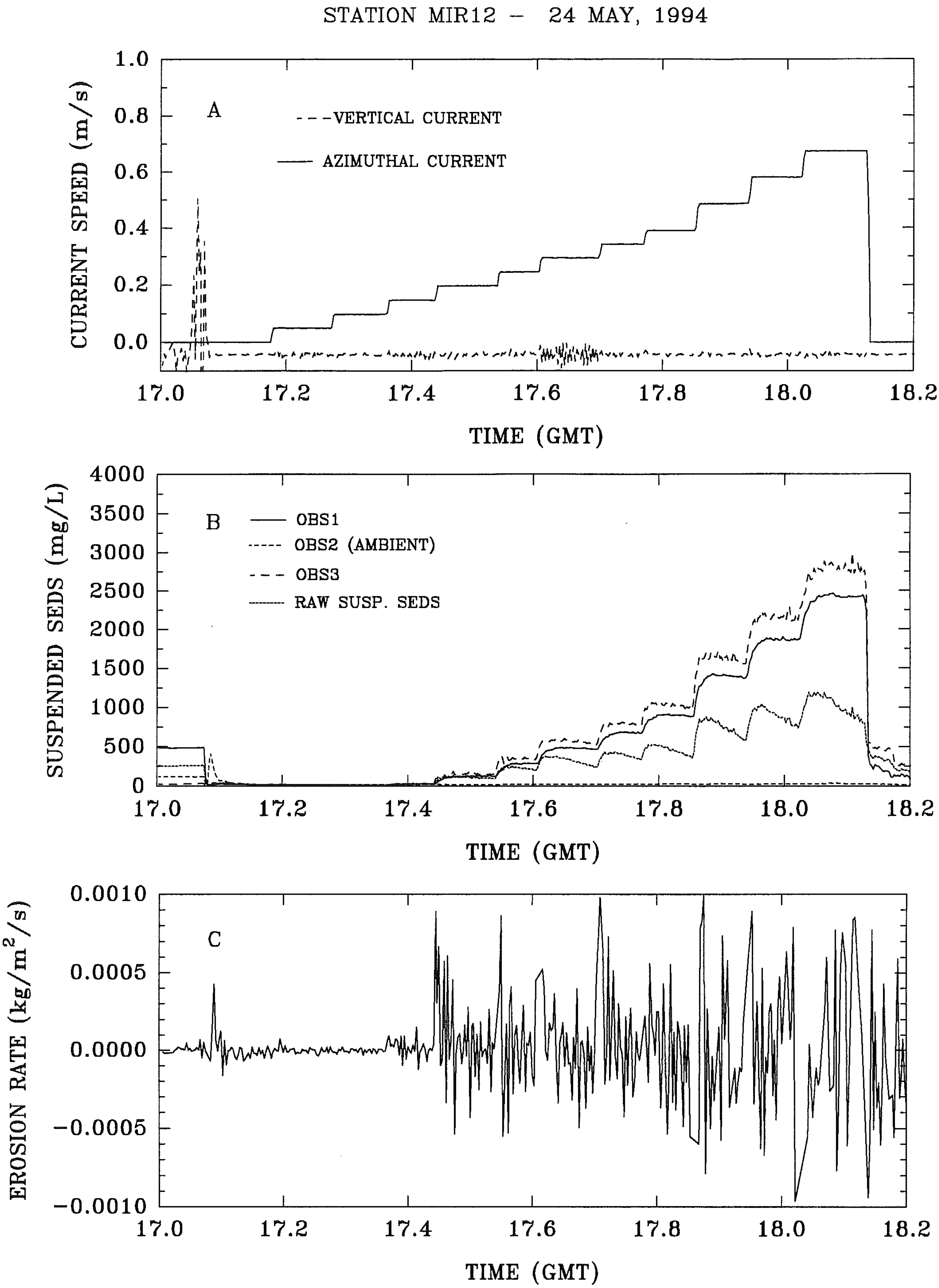

FIGURE 3.2.1.16. A time-series plot of the Sea Carousel deployment at station MIR13, dumpsite B, Miramichi bay.(A) azimuthal and vertical current speed (m/s); (B) suspended sediment concentration (mg/L); and (C) erosion rate (kg/m²/s).

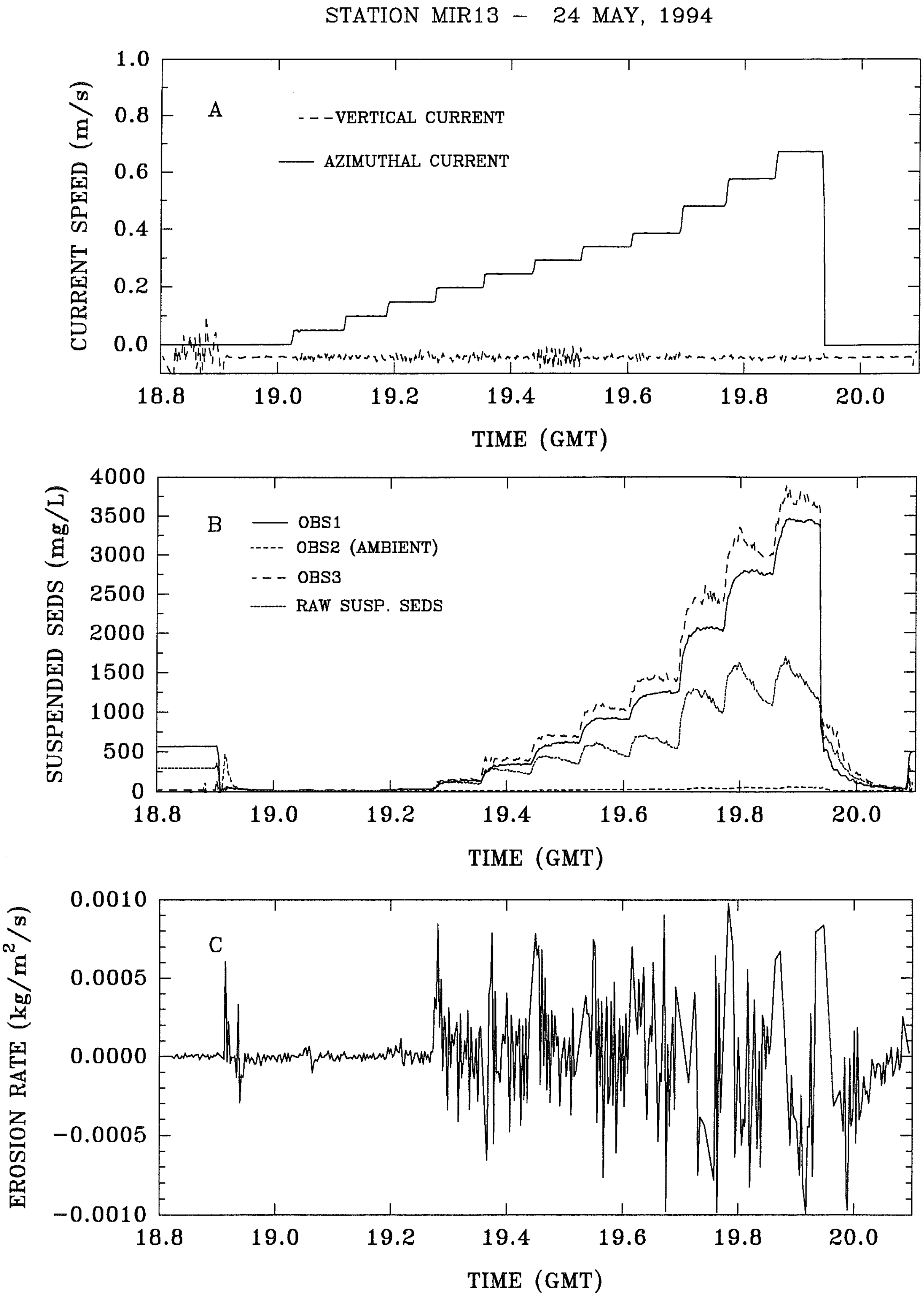

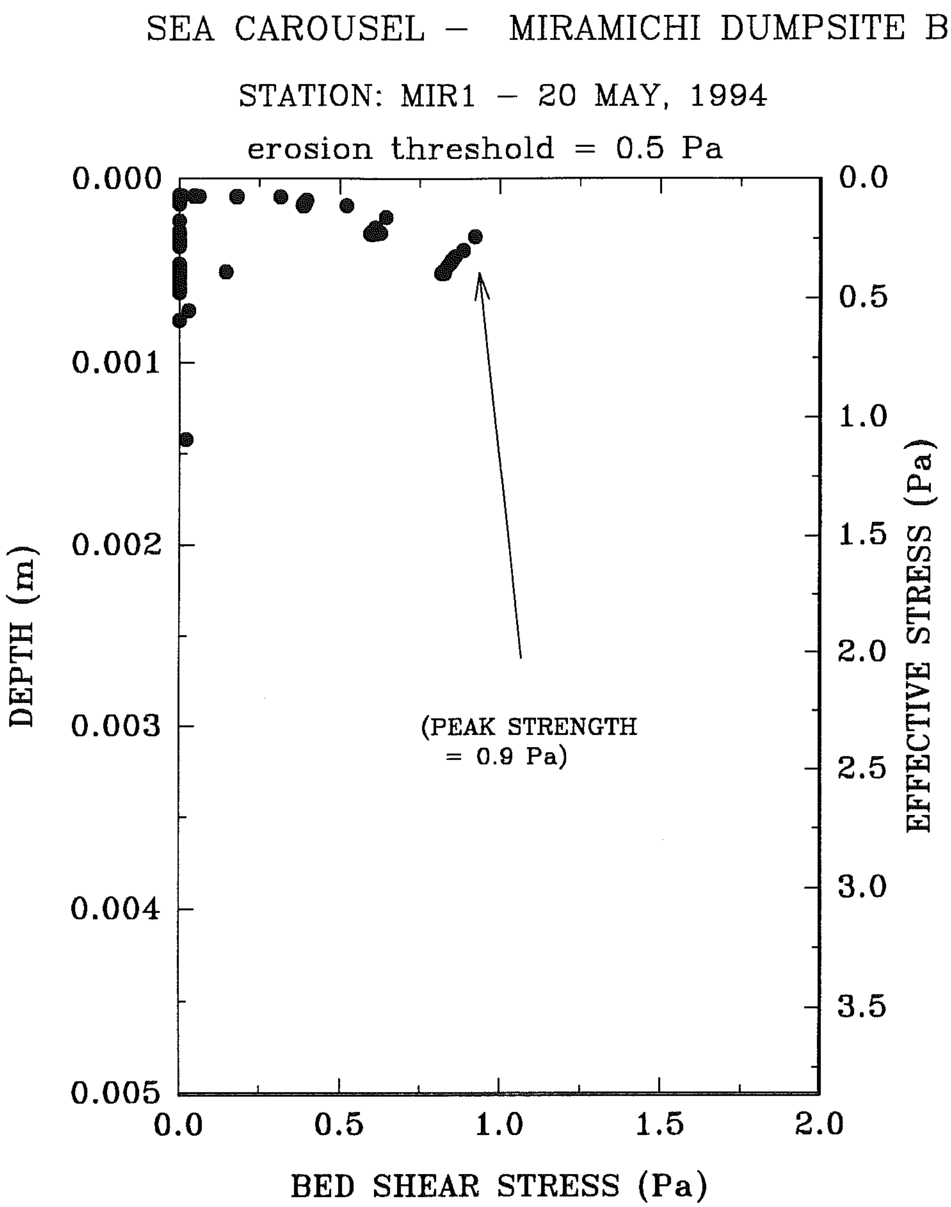

FIGURE 3.2.2.1. A synthetic core from station MIR1 computed from the Sea Carousel time-series data on eroded mass. The erosion threshold is 0.5 Pa; the maximum strength is 0.9 Pa and is found 0.0005 m below the mudline.

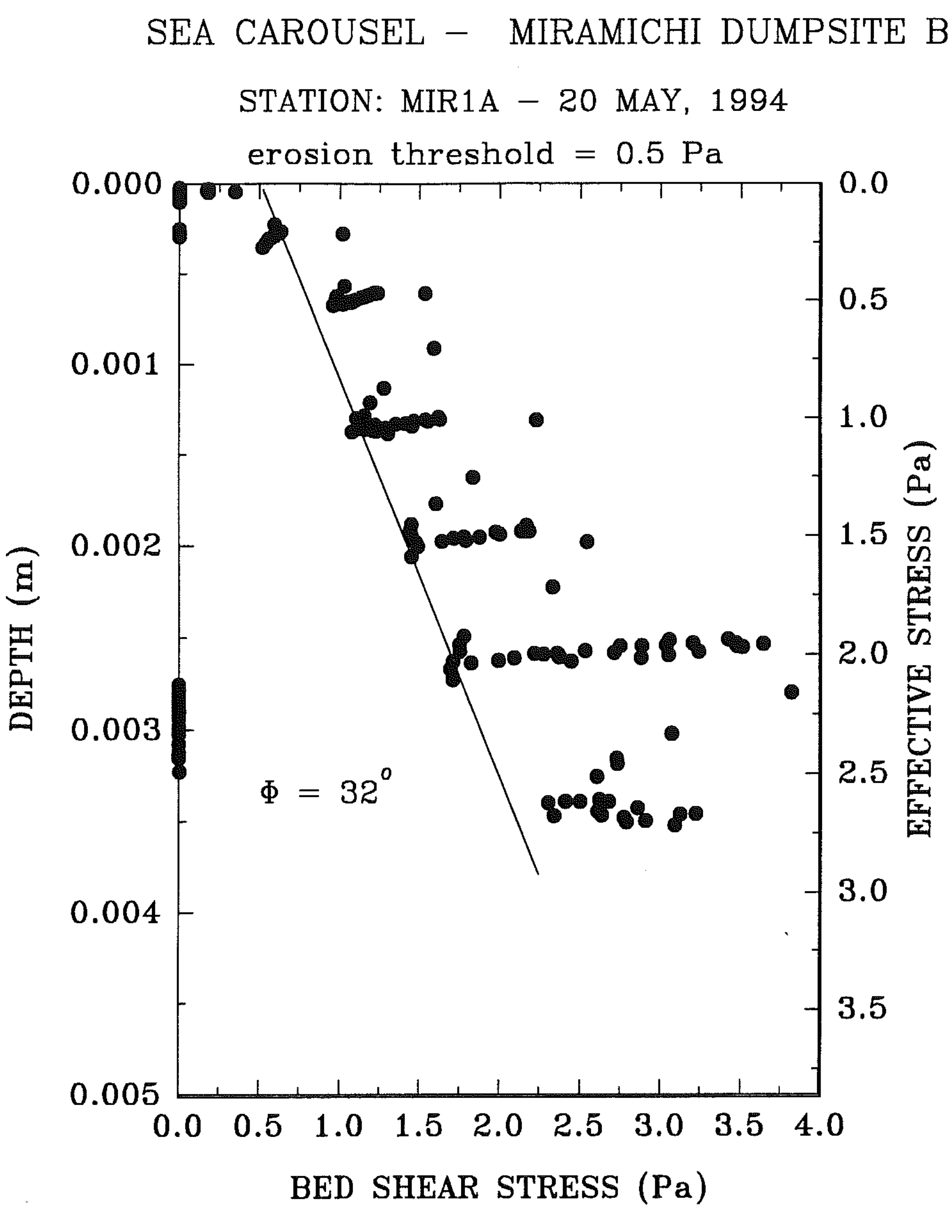

FIGURE 3.2.2.2. A synthetic core from station MIR1A computed from the Sea Carousel time-series data on eroded mass. The erosion threshold is 0.5 Pa, and the substrate is stable yielding a friction angle of 32°.

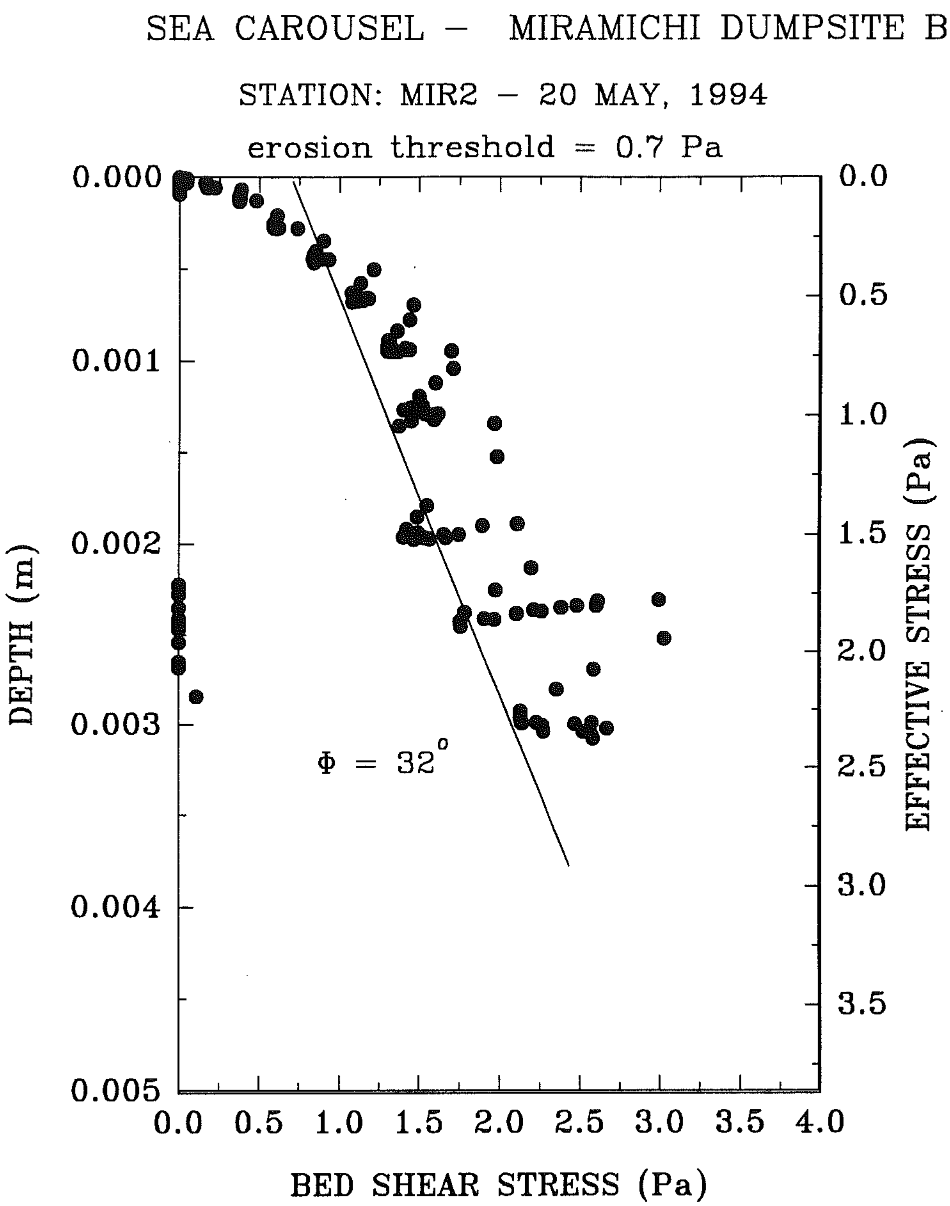

FIGURE 3.2.2.3. A synthetic core from station MIR2 computed from the Sea Carousel time-series data on eroded mass. The erosion threshold is 0.7 Pa, and the substrate is stable yielding a friction angle of 32°.

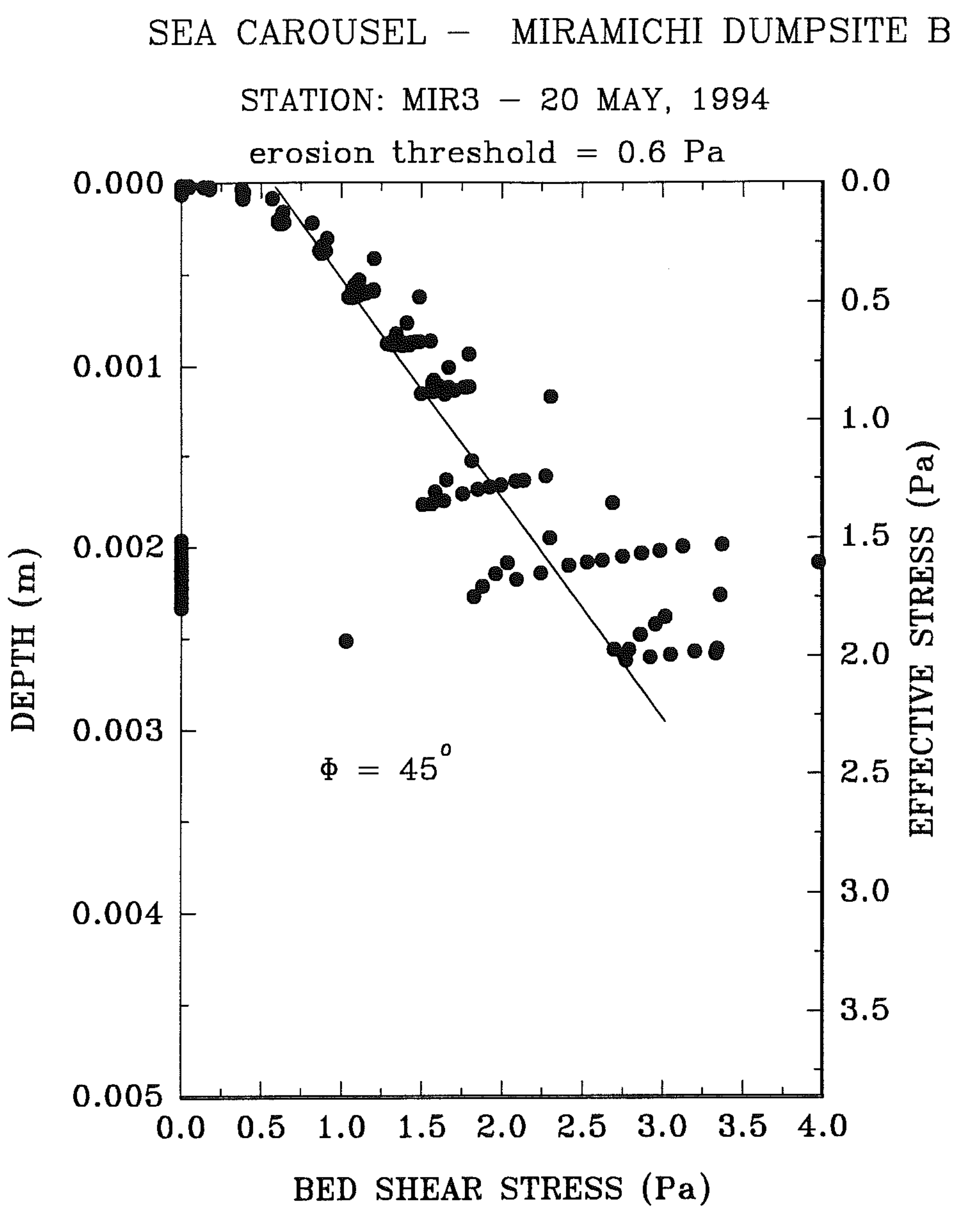

FIGURE 3.2.2.4. A synthetic core from station MIR3 computed from the Sea Carousel time-series data on eroded mass. The erosion threshold is 0.6 Pa, and the substrate is stable yielding a friction angle of 45°.

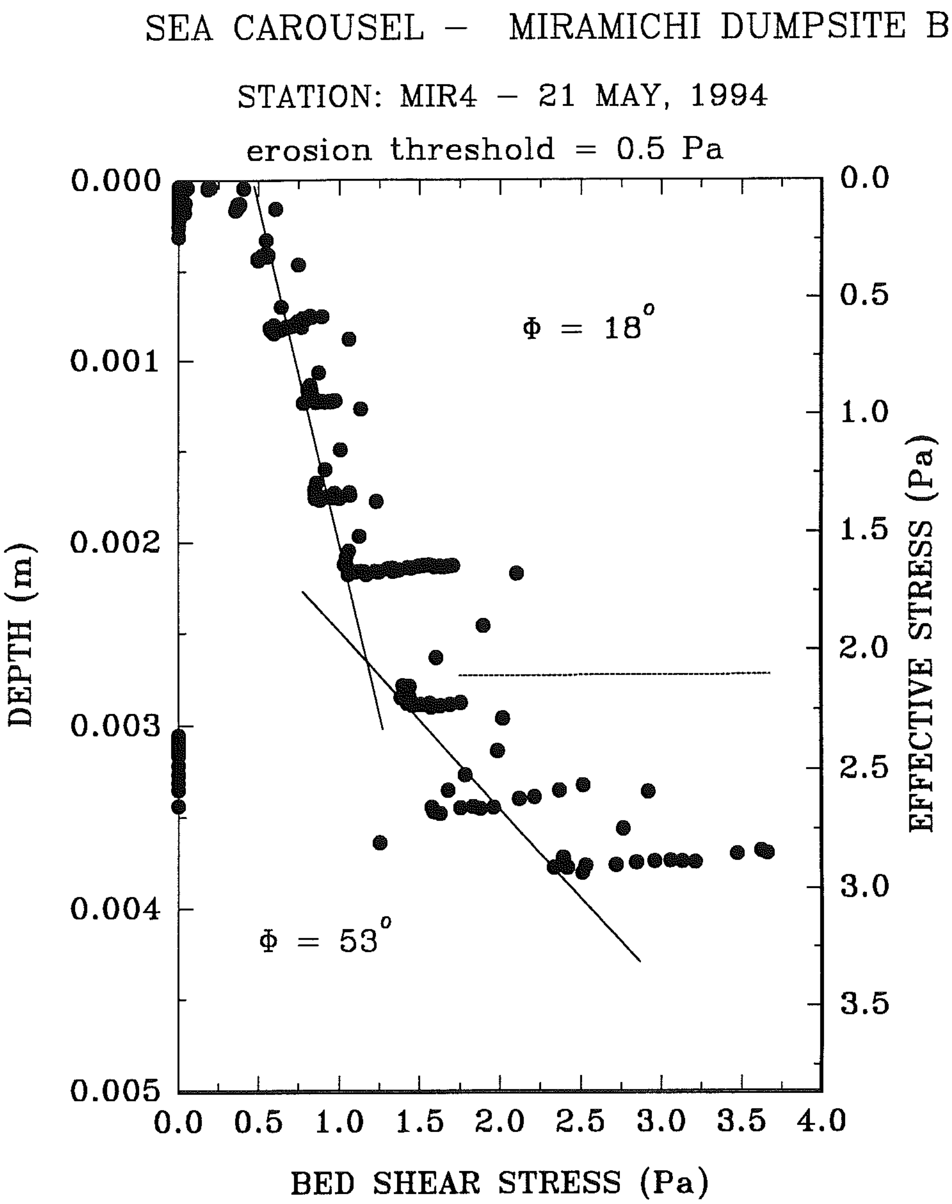

FIGURE 3.2.2.5. A synthetic core from station MIR4 computed from the Sea Carousel time-series data on eroded mass. The erosion threshold is 0.5 Pa, and the substrate is stable yielding friction angles of 18° and 53°.

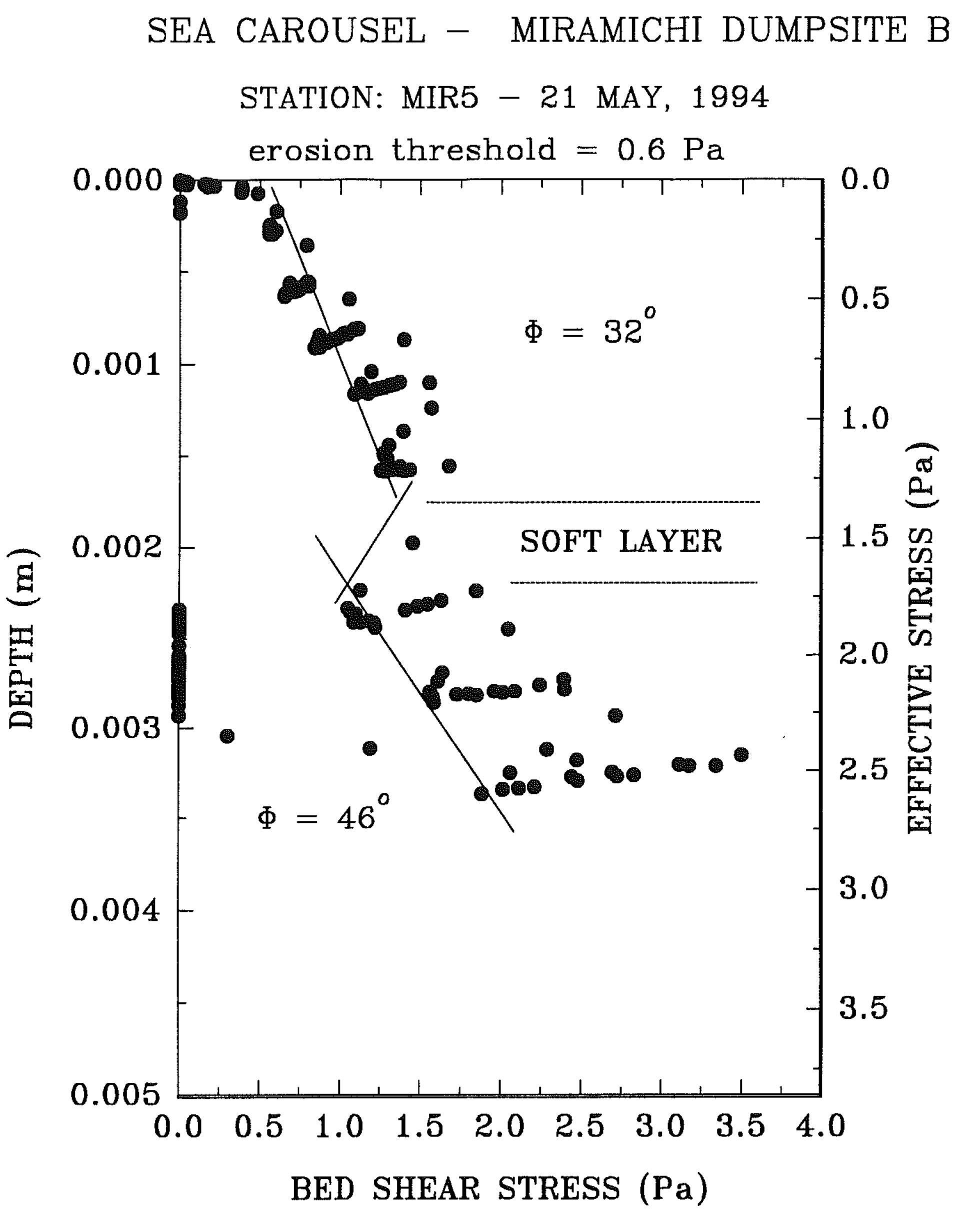

FIGURE 3.2.2.6. A synthetic core from station MIR5 computed from the Sea Carousel time-series data on eroded mass. The erosion threshold is 0.6 Pa, and the substrate is of variable stability yielding a friction angle of 32° and 46° separated by a "soft" at a depth of 0.002 m.

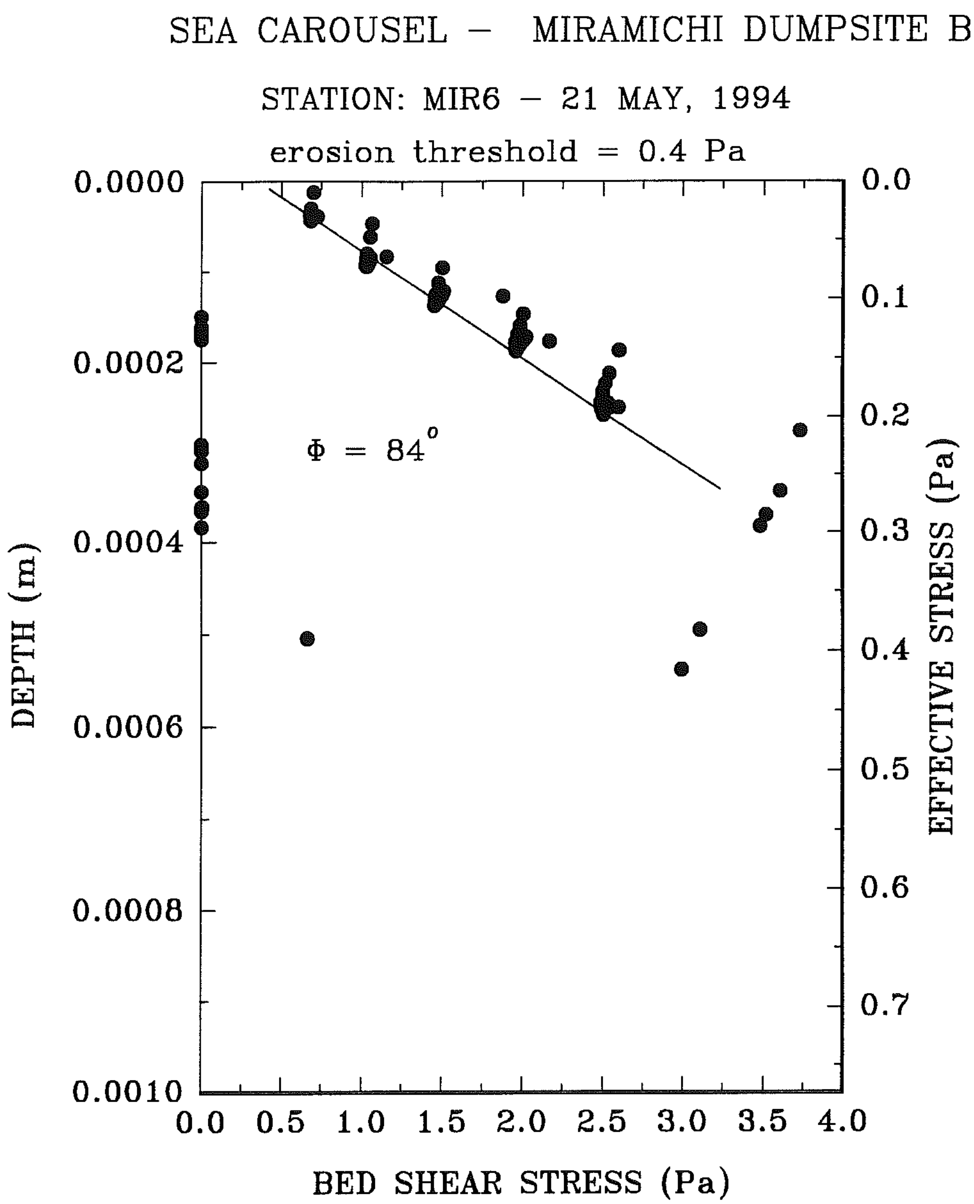

FIGURE 3.2.2.7. A synthetic core from station MIR6 computed from the Sea Carousel time-series data on eroded mass. The erosion threshold is 0.4 Pa, and the substrate is stable yielding a friction angle of 84°.

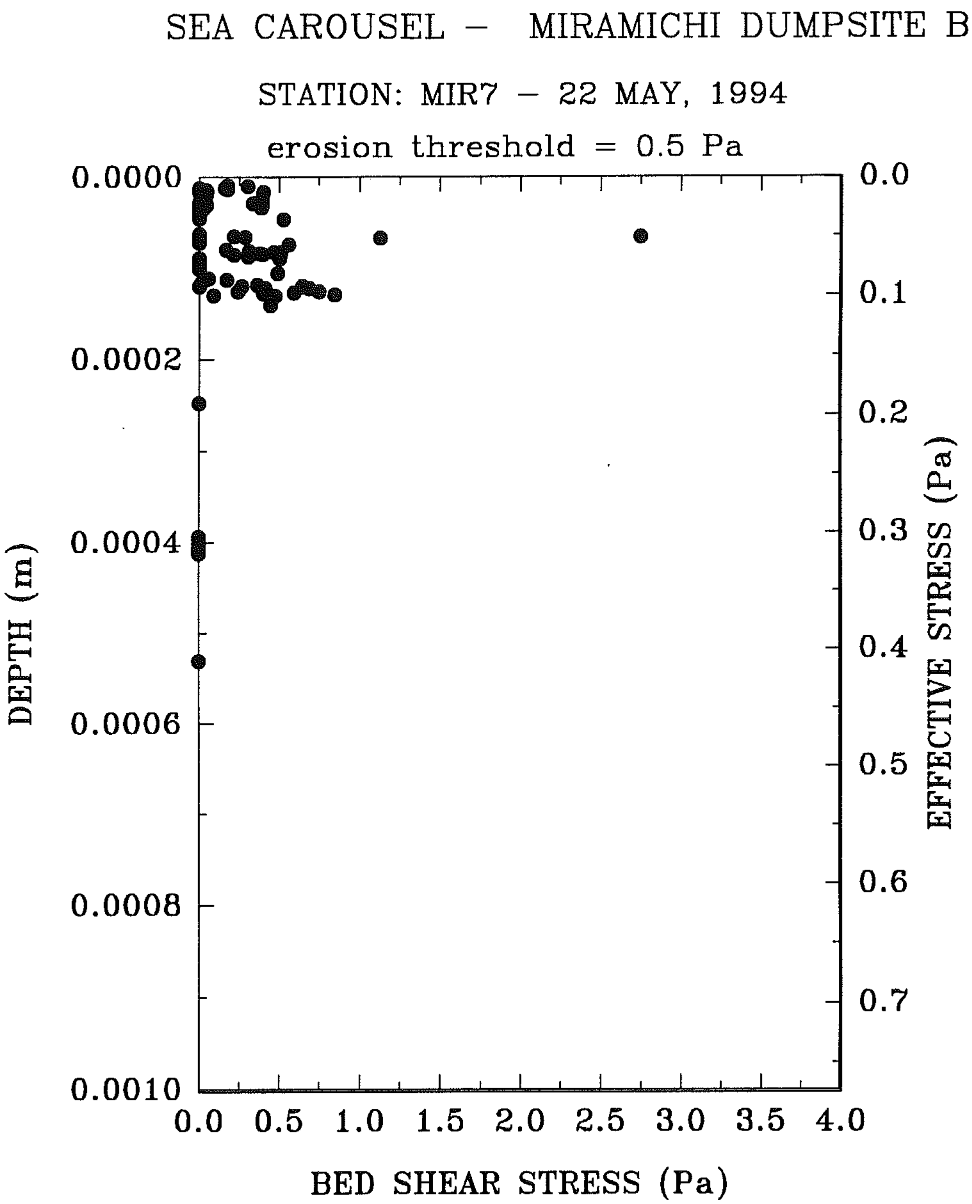

FIGURE 3.2.2.8. A synthetic core from station MIR7 computed from the Sea Carousel time-series data on eroded mass. The erosion threshold is 0.5 Pa.

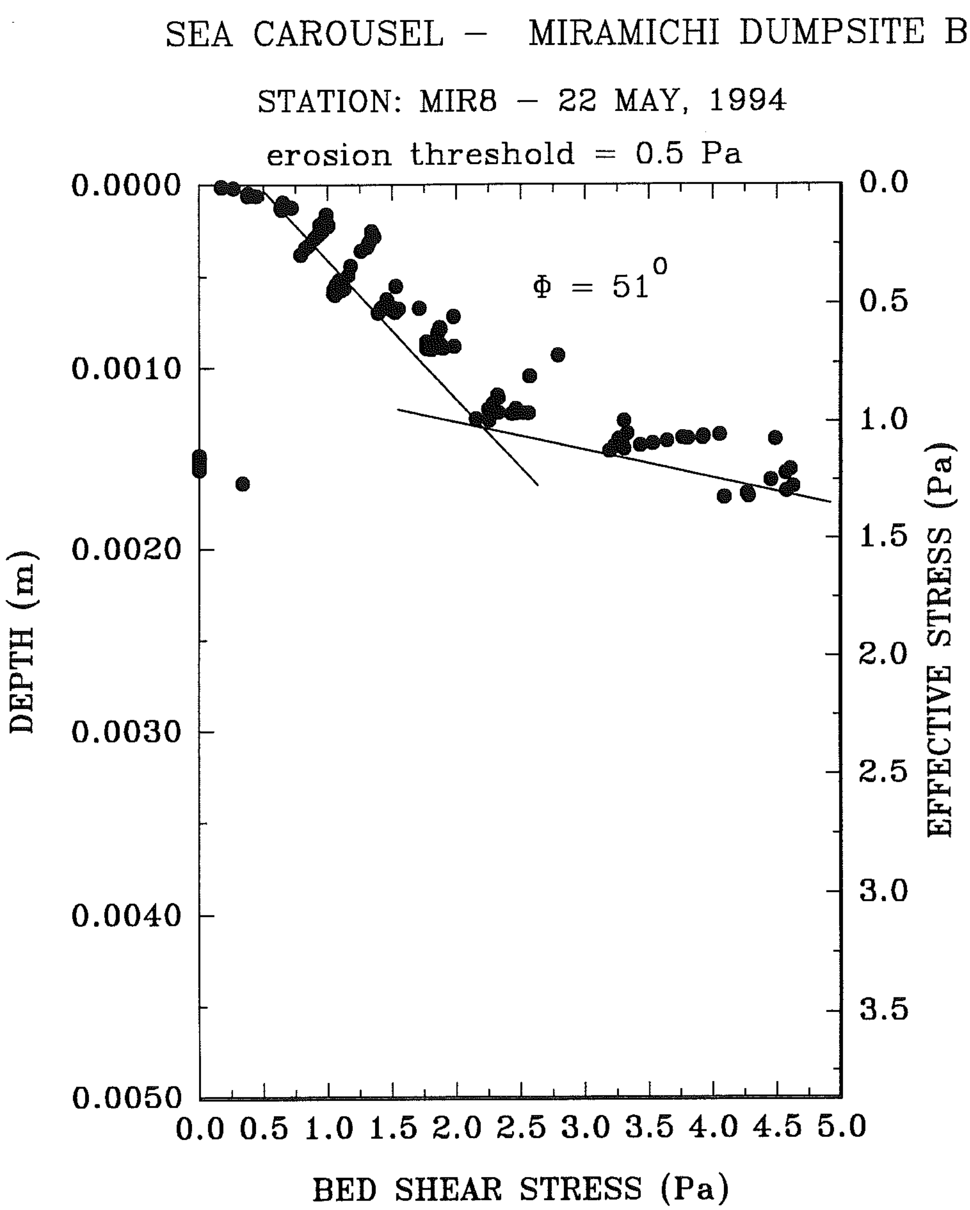

FIGURE 3.2.2.9. A synthetic core from station MIR8 computed from the Sea Carousel time-series data on eroded mass. The erosion threshold is 0.5 Pa, and the substrate is stable yielding a friction angle of 51°.

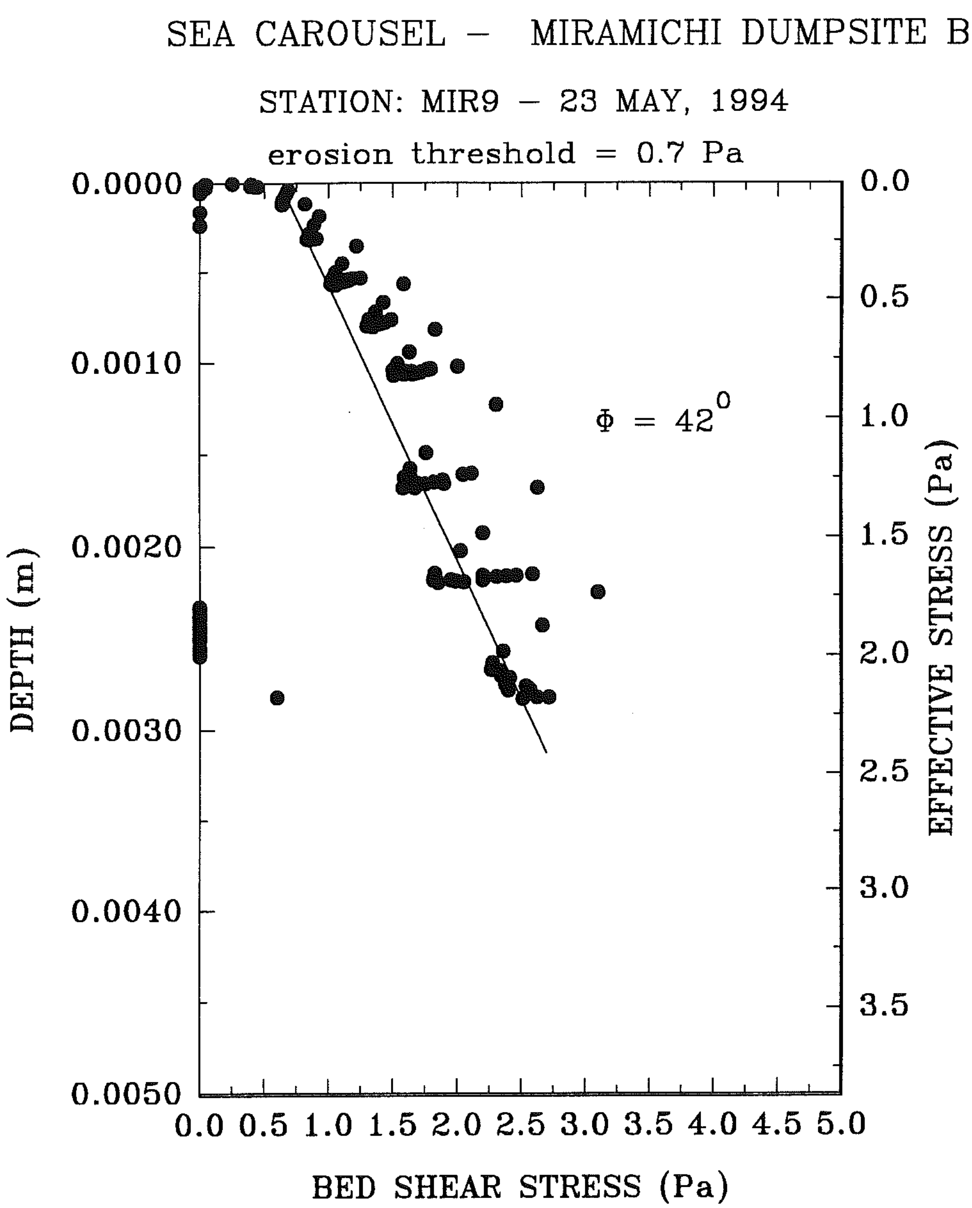

FIGURE 3.2.2.10. A synthetic core from station MIR9 computed from the Sea Carousel time-series data on eroded mass. The erosion threshold is 0.7 Pa, and the substrate is stable yielding a friction angle of 42°.

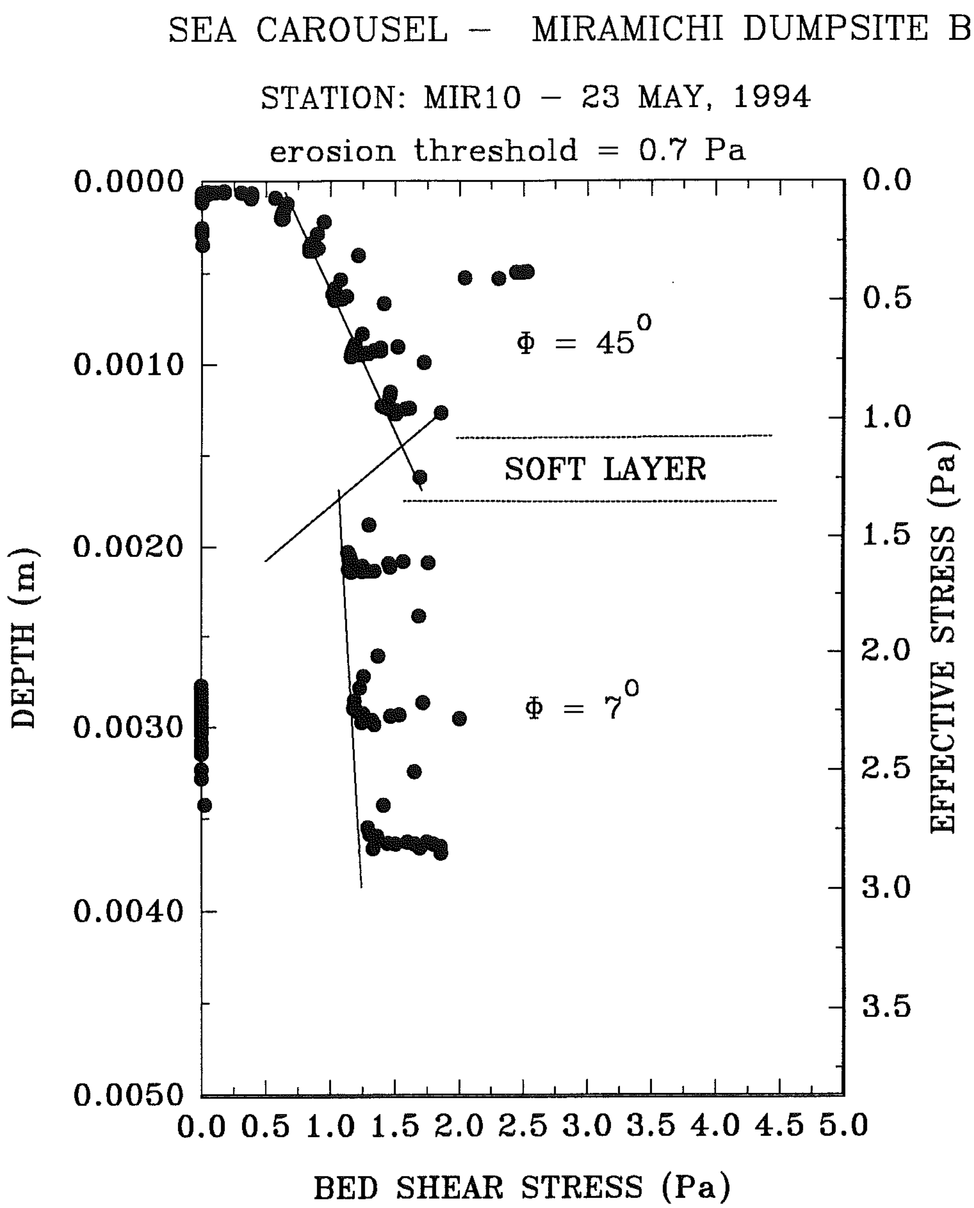

FIGURE 3.2.2.11. A synthetic core from station MIR10 computed from the Sea Carousel time-series data on eroded mass. The erosion threshold is 0.7 Pa, and the substrate is of variable stability yielding friction angles of 45° and 7° separated by a "soft" at a depth of 0.0015 m.

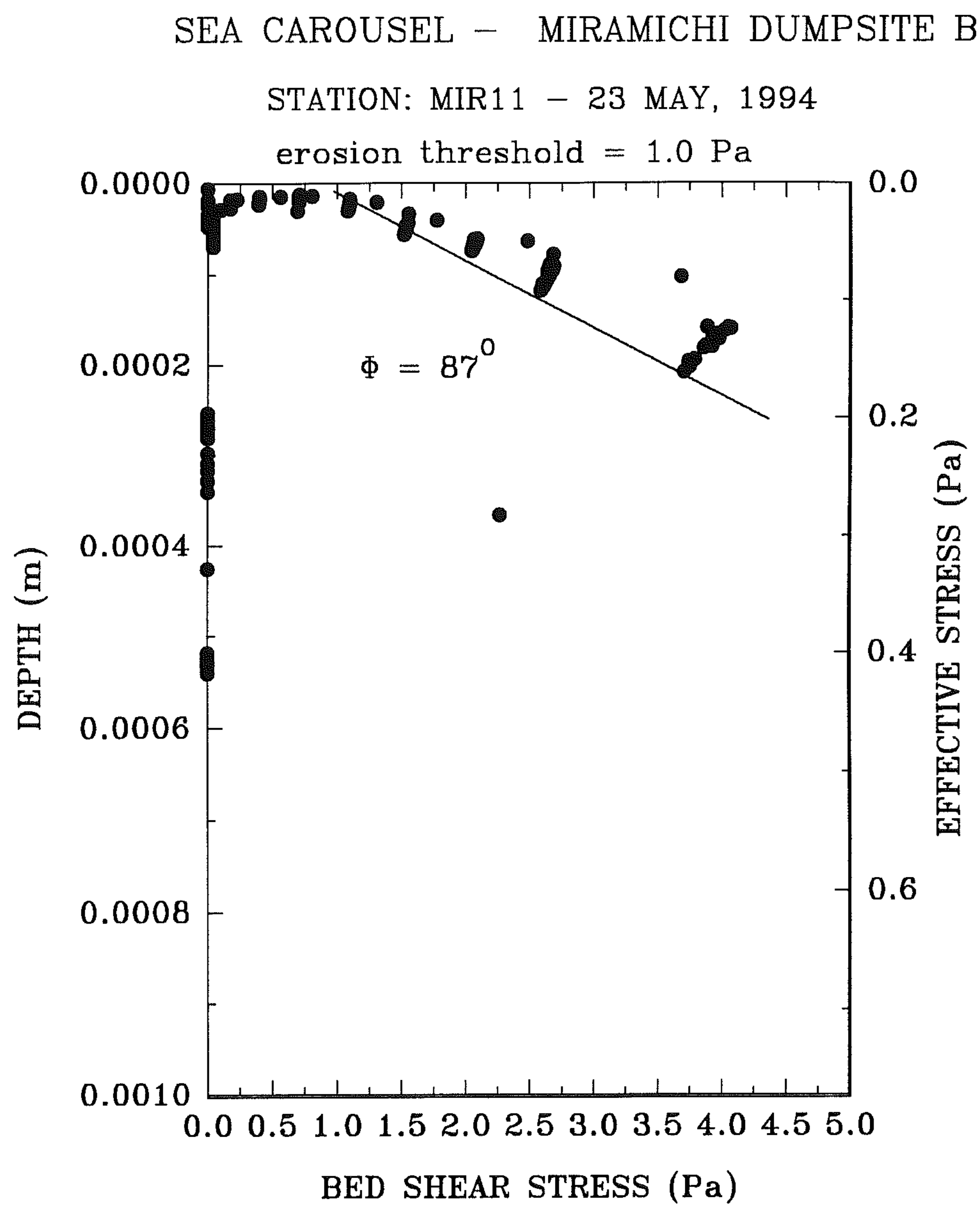

FIGURE 3.2.2.12. A synthetic core from station MIR11 computed from the Sea Carousel time-series data on eroded mass. The erosion threshold is 1.0 Pa, and the substrate is stable yielding a friction angle of 87°.

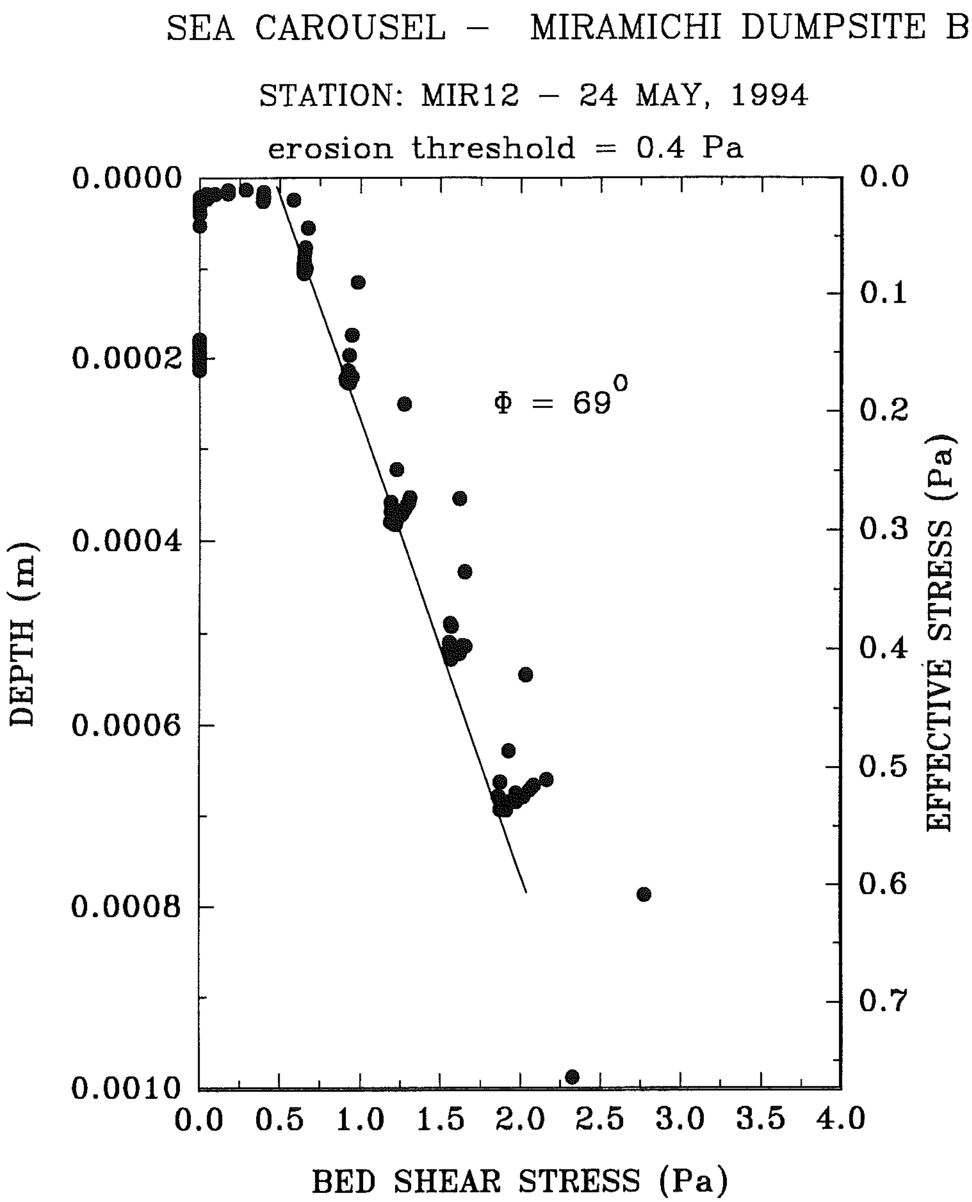

FIGURE 3.2.2.13. A synthetic core from station MIR12 computed from the Sea Carousel time-series data on eroded mass. The erosion threshold is 0.4 Pa and the friction angle is 69°.

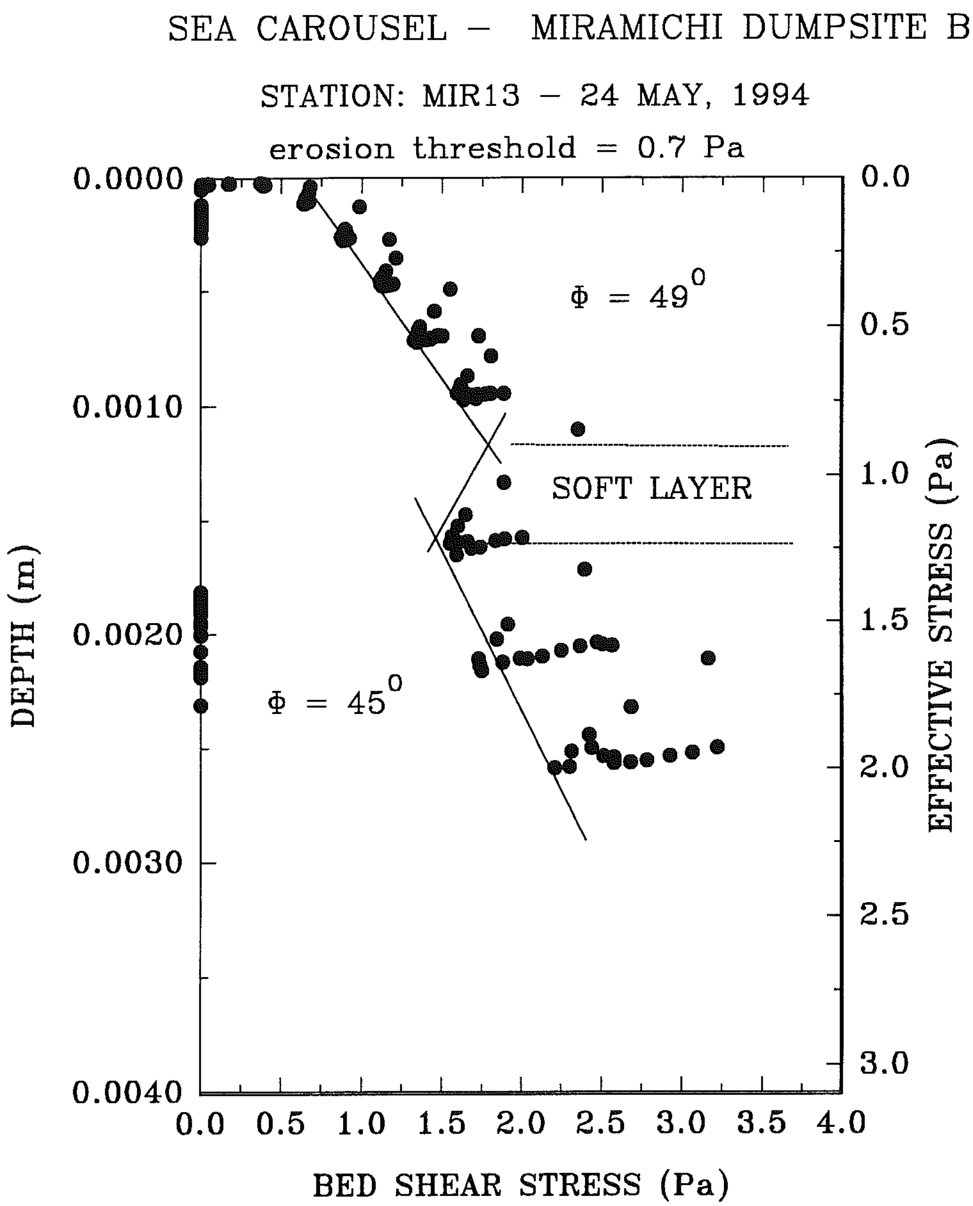

FIGURE 3.2.2.14. A synthetic core from station MIR13 computed from the Sea Carousel time-series data on eroded mass. The erosion threshold is 0.7 Pa, and the substrate is of variable stability yielding friction angles of 49° and 45° separated by a "soft" at a depth of 0.0015 m.

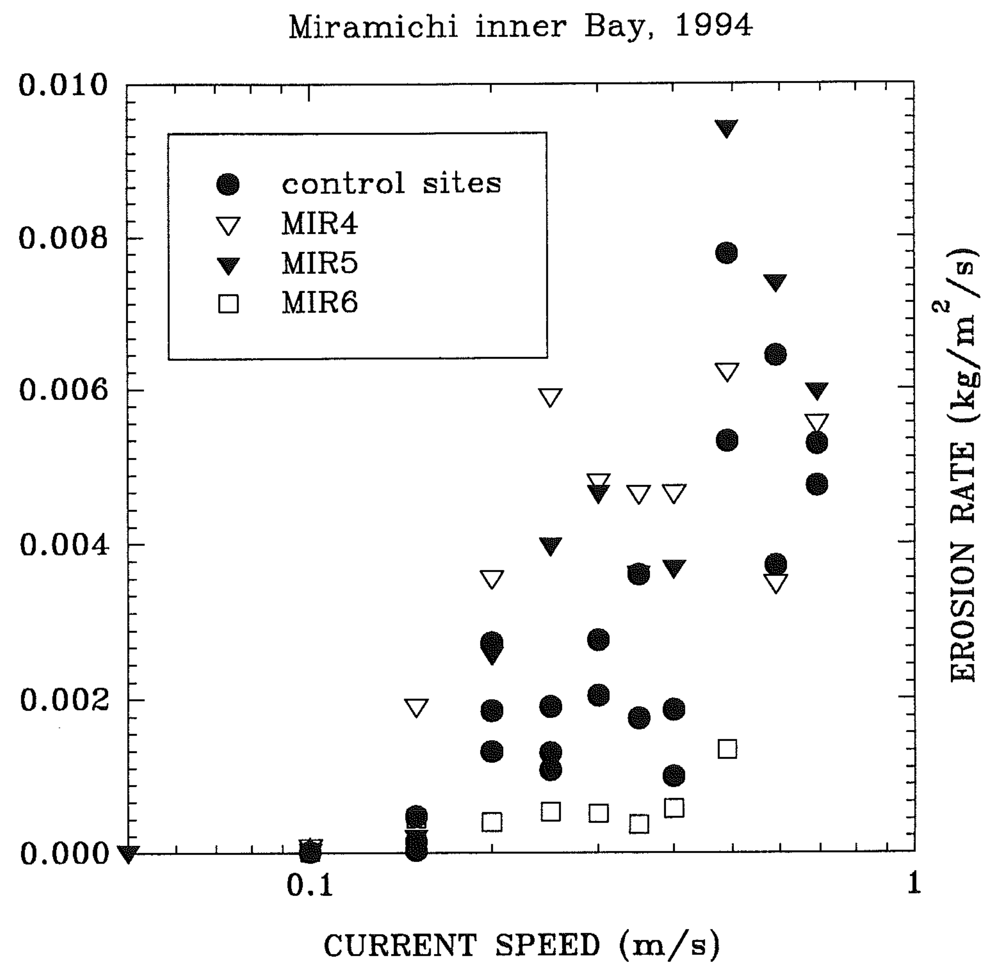

FIGURE 3.2.3.1. A scattergram of current speed (U_y) versus peak seabed erosion rate ($\delta M/\delta t$; $kg/m^2/s$) for the control sites (MIR1 - MIR3) and for stations MIR4 - MIR6. These stations exhibited Type I erosion. A positive exponential relationship was evident of the form $\delta M/\delta t = 0.006 + 0.006[\log_{10}(U_y)]$; $r^2 = 0.49$.

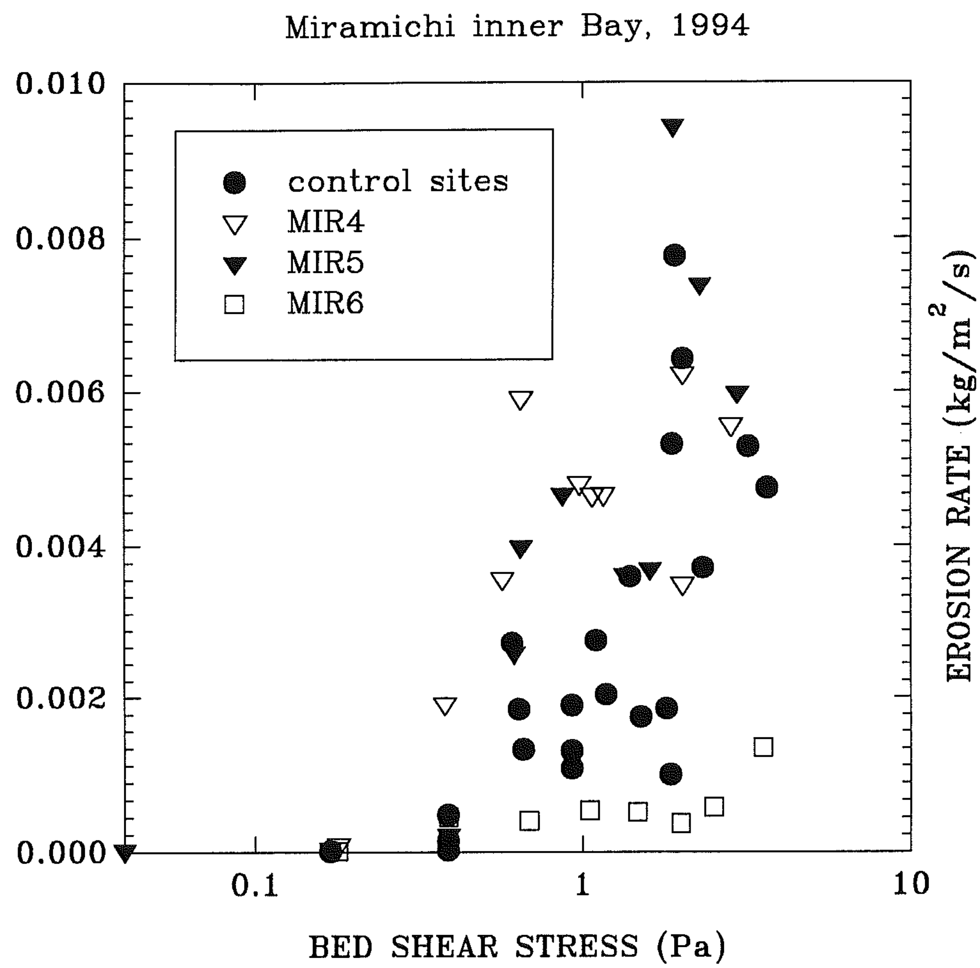

FIGURE 3.2.3.2. A scattergram of bed shear stress (τ) versus peak seabed erosion rate ($\delta M/\delta t$; $kg/m^2/s$) for the control sites (MIR1 - MIR3) and for stations MIR4 - MIR6. These stations exhibited Type I erosion. A positive exponential relationship was evident of the form $\delta M/\delta t = 0.003 + 0.003[\log_{10}(\tau)]$; $r^2 = 0.32$.

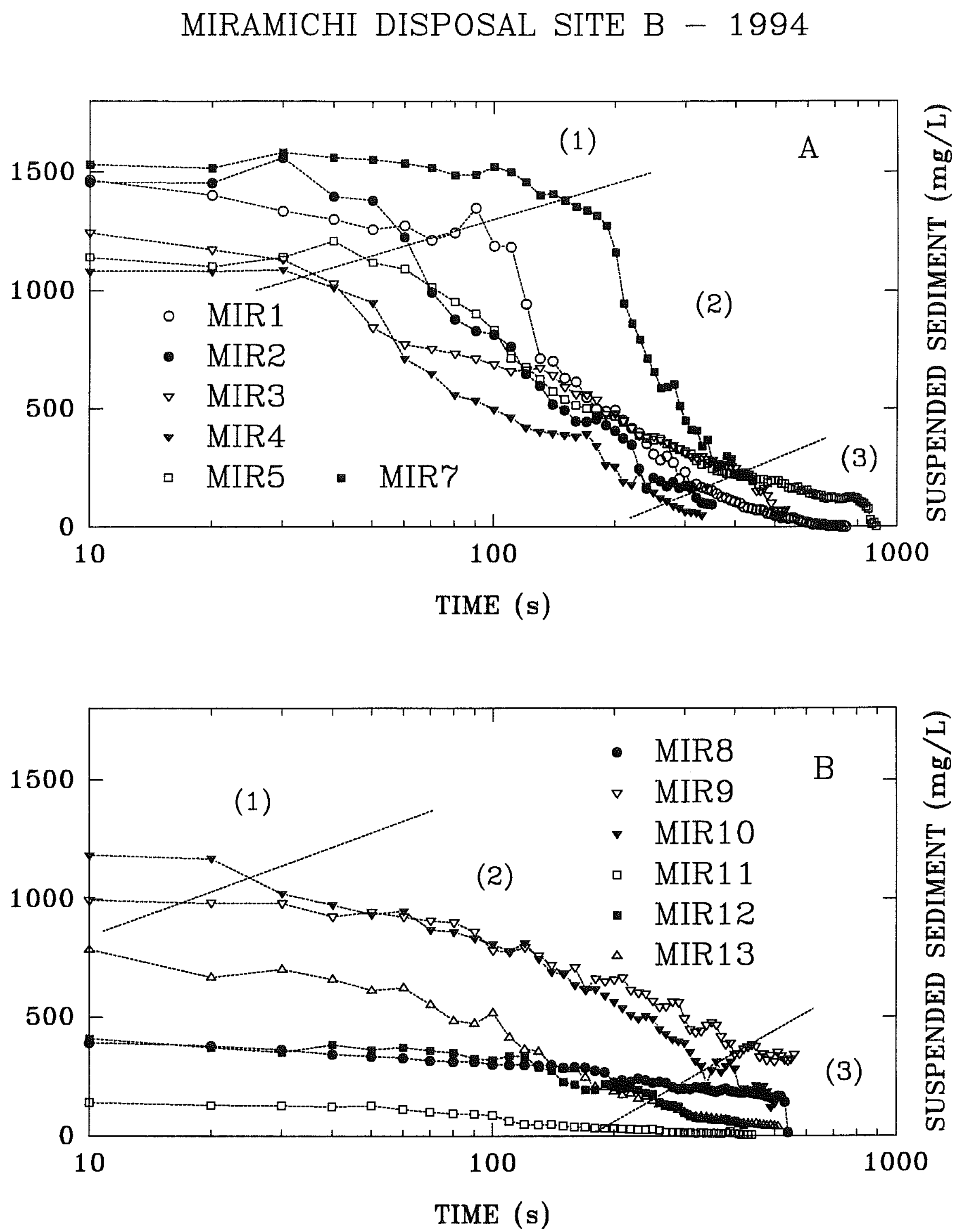

FIGURE 3.2.4.1. The still-water settling of material eroded from the seabed in stations (A) MIR1 - MIR7, and (B) MIR8 - MIR13. The concentration change with time falls into three phases (1) an initial period of inhibited settling; (2) a period of rapid settling; and (3) a final period of low settling.

fig 3.2.6.1

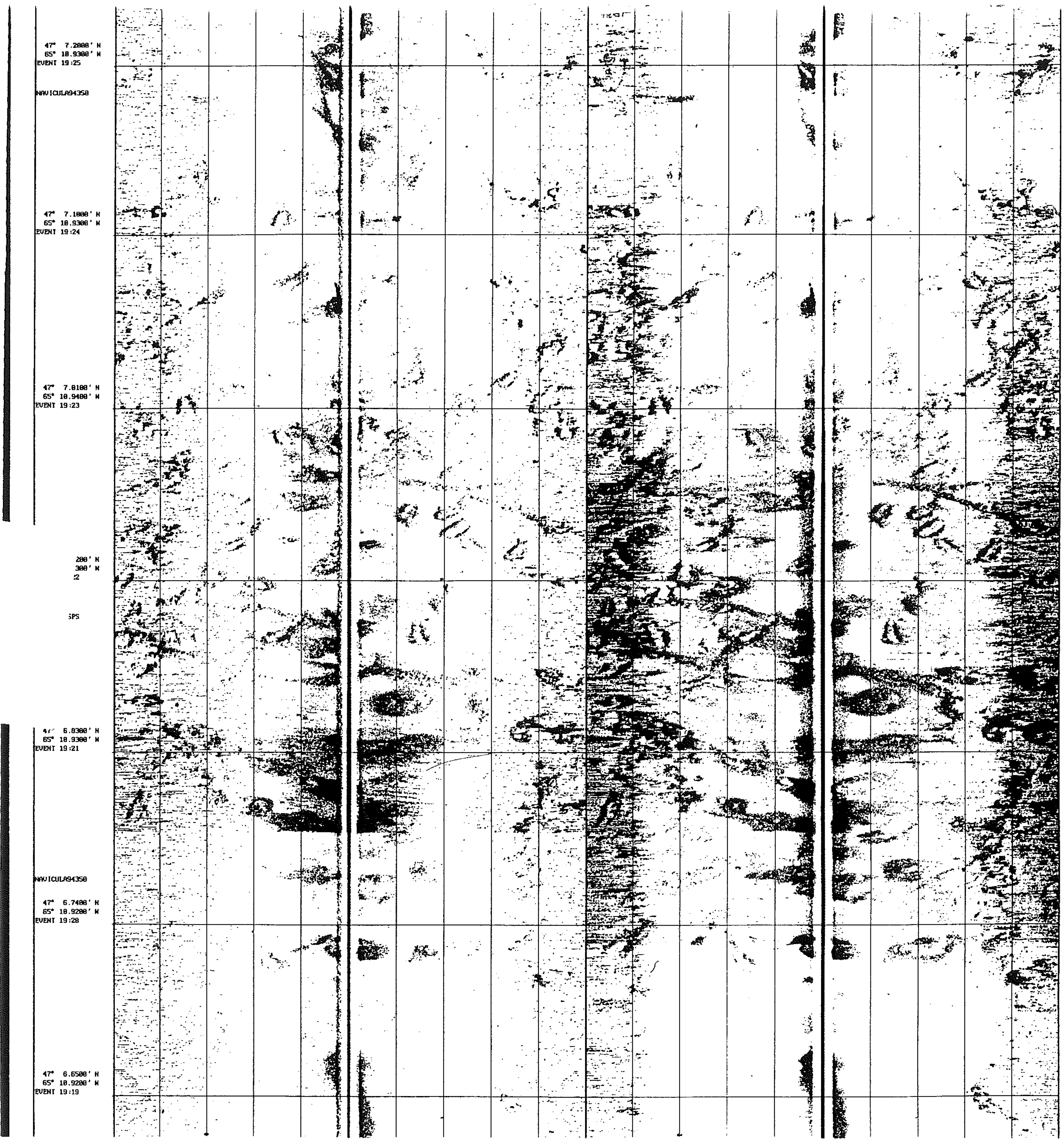

FIGURE 3.2.6.2. A detailed example of the sidescan record of the 1993 scow-dumps. The distance between fixes is approximately 100 m. The channel swath width is 100 m per channel. The two traces give results from two frequencies (120 - left, and 320 kHz - right).

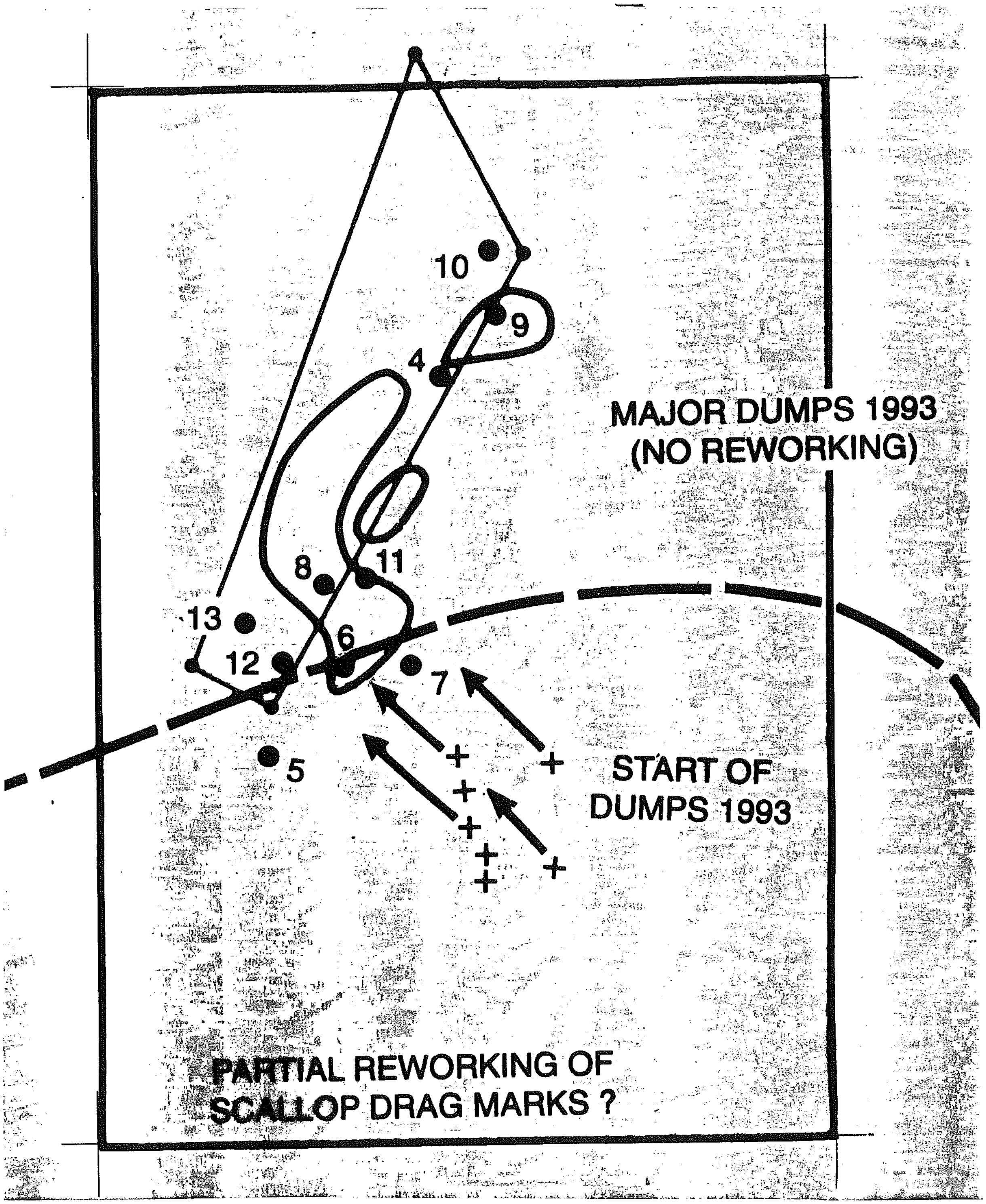

FIGURE 3.2.6.3. A detailed inset of the dumpsite B exclusion zone monitored in this study. The Sea Carousel stations are shown on and around the major region of dumping in 1993. The crosses show the positions at the beginning of dumping and the arrows show the scow paths. The location of the majority of the dumped material is shown by the solid curved oblongs. The northeast-southwest trending lineaments in the mosaic are interpreted to be scallop trawl marks. Notice one such marks appears to cross the 1993 dump material.

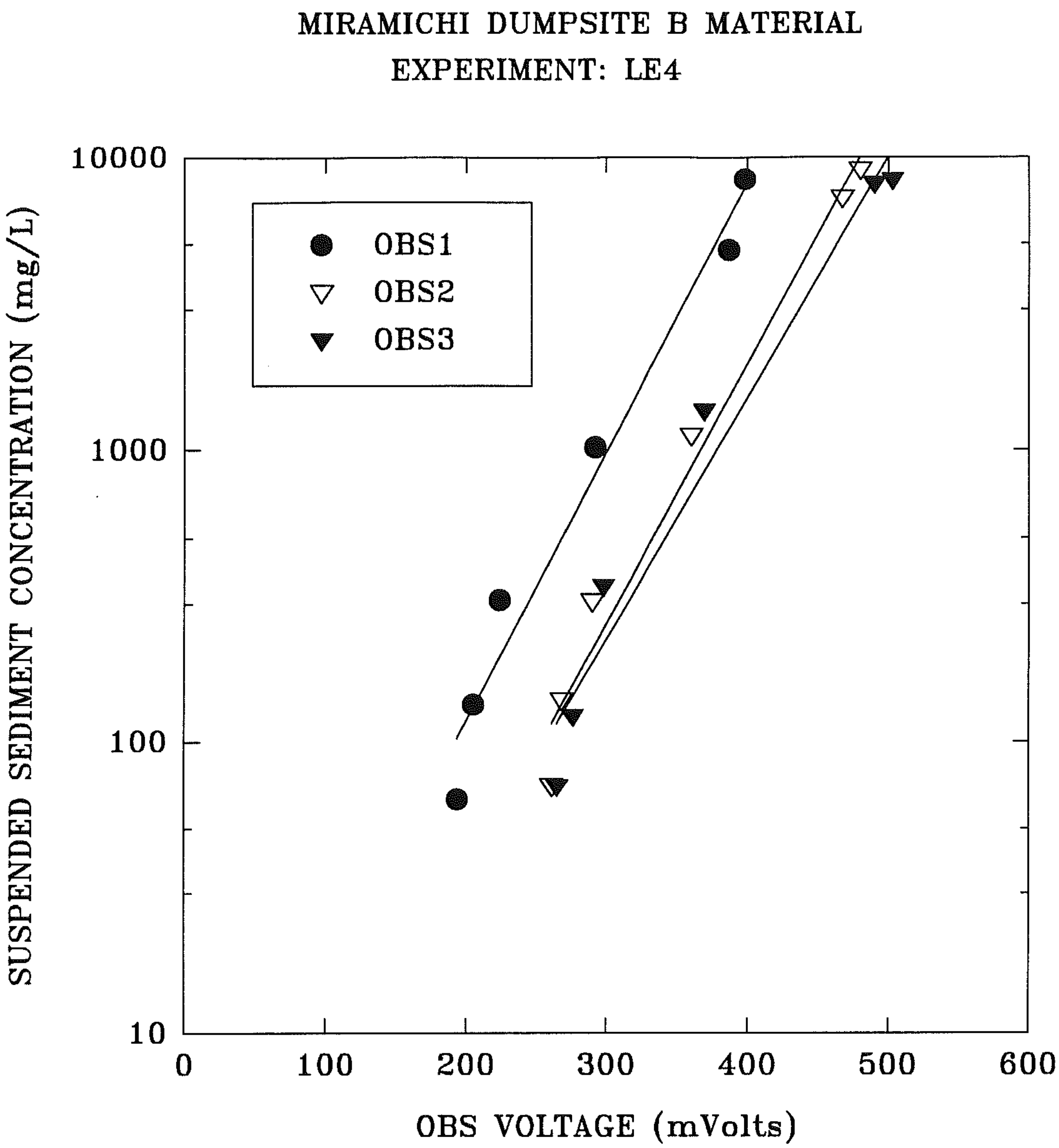

FIGURE 4.1.1. The calibration of the three Optical Backscatter Sensors (OBS) in the Laboratory Carousel against suspended sediment concentration for experiment LE4.

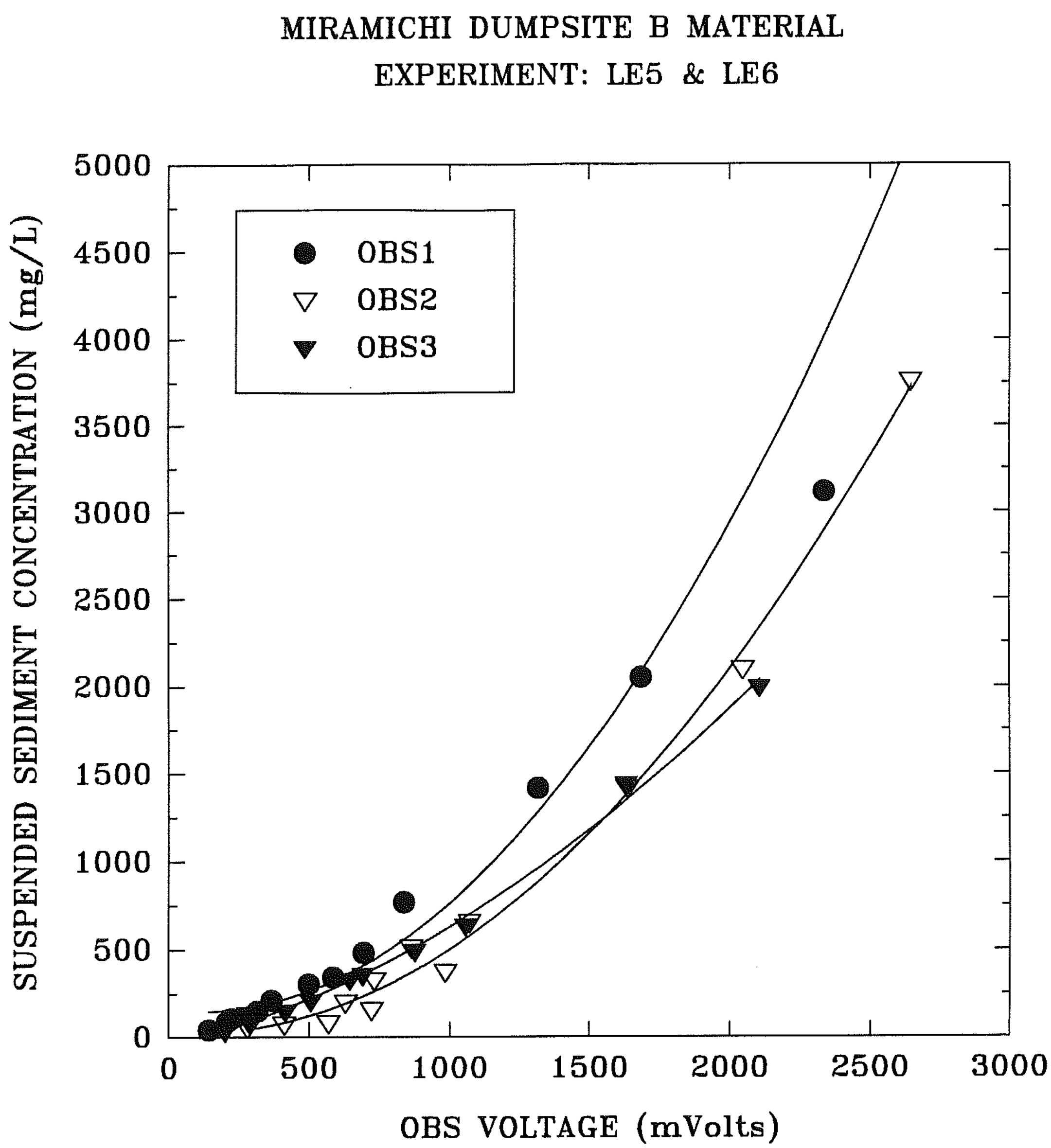

FIGURE 4.1.2. The calibration of the three Optical Backscatter Sensors (OBS) in the Laboratory Carousel against suspended sediment concentration for experiments LE5 and LE6.

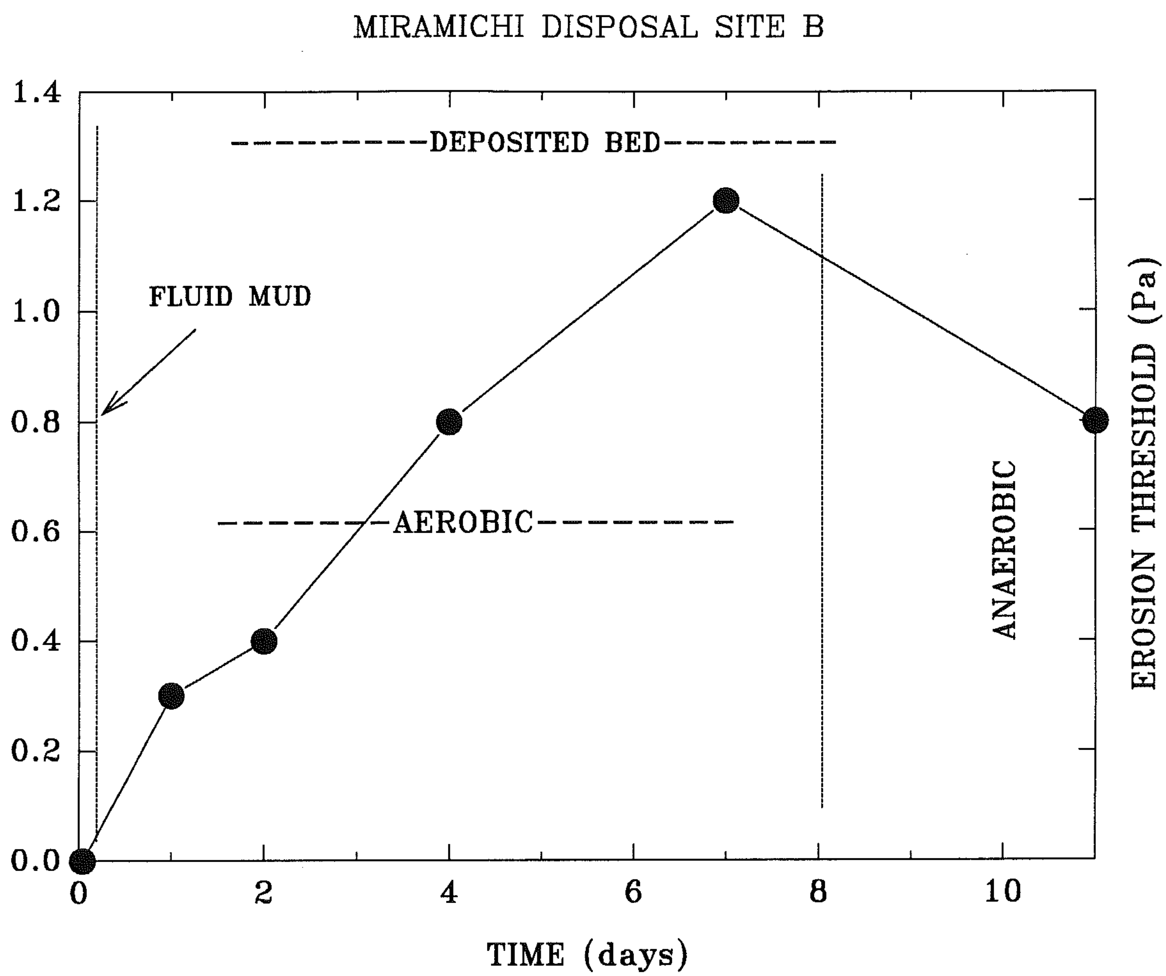

FIGURE 4.2.1.1. A time-series of erosion threshold derived from the Laboratory Carousel analysis of dumpsite B material. Notice the linear increase in erosion threshold with time over the first 7 days. The reveral in trends after 8 days reflects a change from oxygenated to anoxic conditions, associated with the collapse of the benthic macrofauna and development of anaerobic bacteria.

FIGURE 4.2.1.2. A time-series plot of the Laboratory Carousel experiment LE4, on dumpsite B material, Miramichi bay. (A) azimuthal and vertical current speed (m/s); (B) suspended sediment concentration (mg/L); and (C) erosion rate (kg/m^2/s).

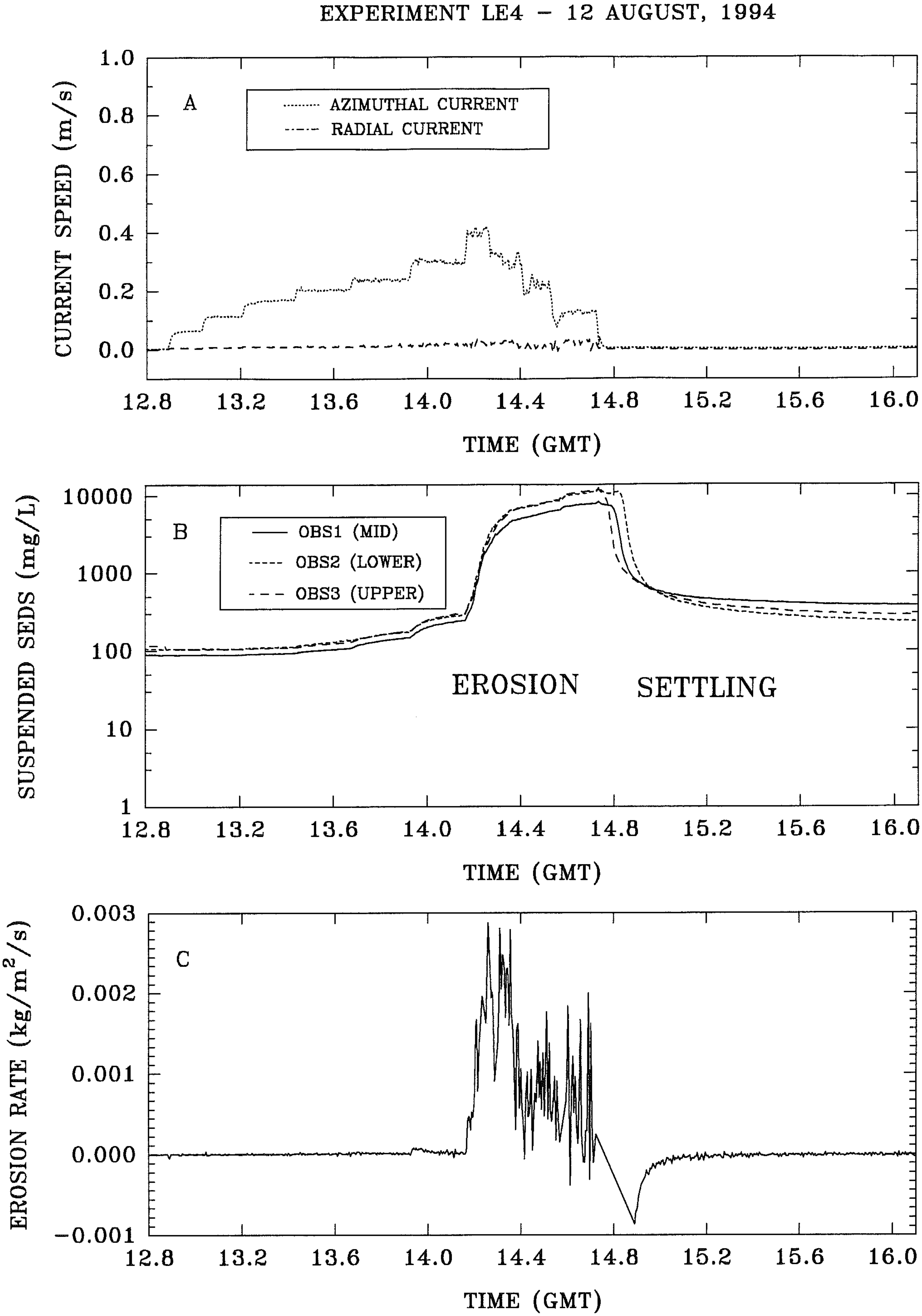

FIGURE 4.2.1.3. A time-series plot of the Laboratory Carousel experiment LE5, on dumpsite B material, Miramichi bay. (A) azimuthal and vertical current speed (m/s); (B) suspended sediment concentration (mg/L); and (C) erosion rate (kg/m²/s).

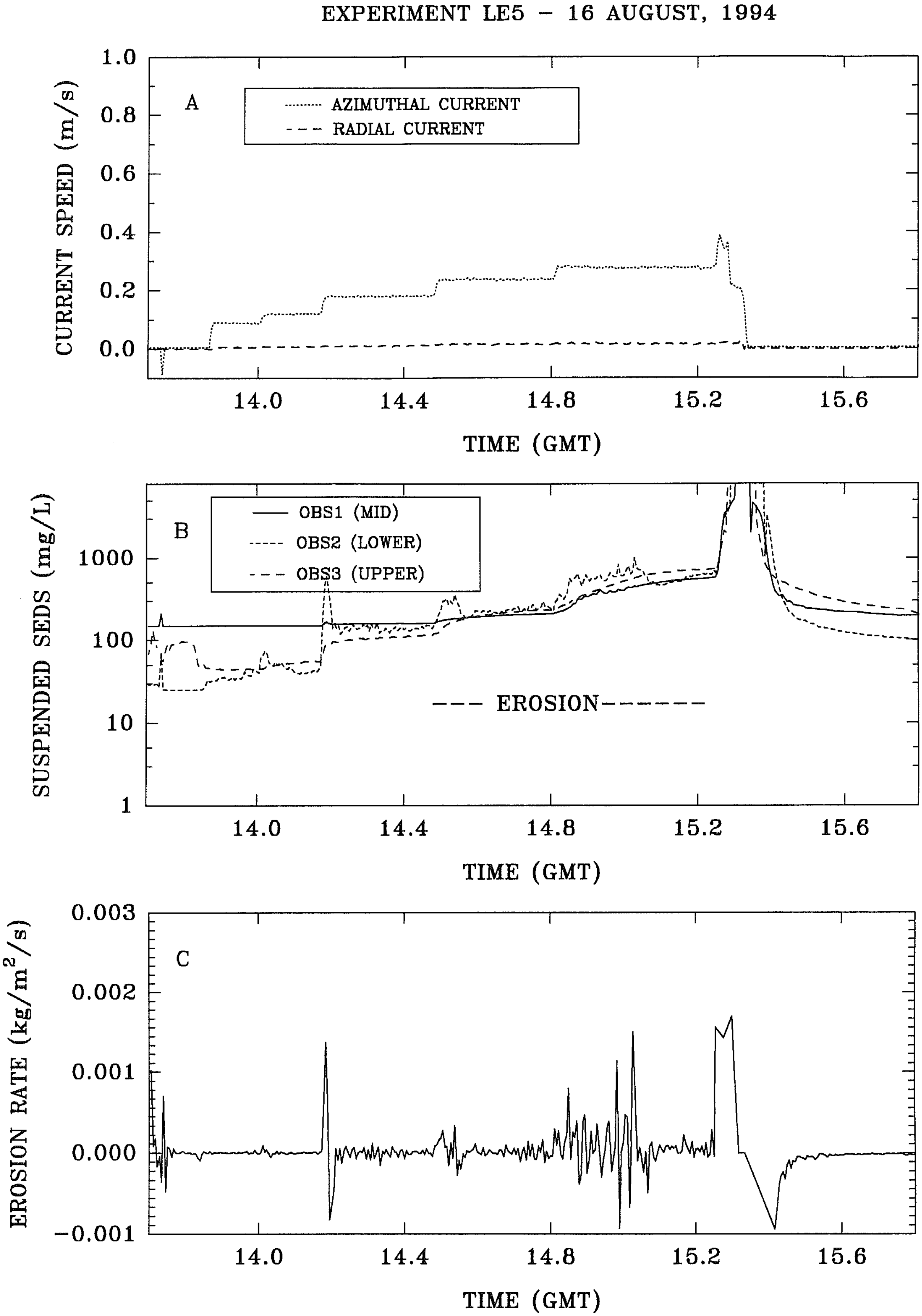

FIGURE 4.2.1.4. A time-series plot of the Laboratory Carousel experiment LE6, on dumpsite B material, Miramichi bay. (A) azimuthal and vertical current speed (m/s); (B) suspended sediment concentration (mg/L); and (C) erosion rate ($kg/m^2/s$).

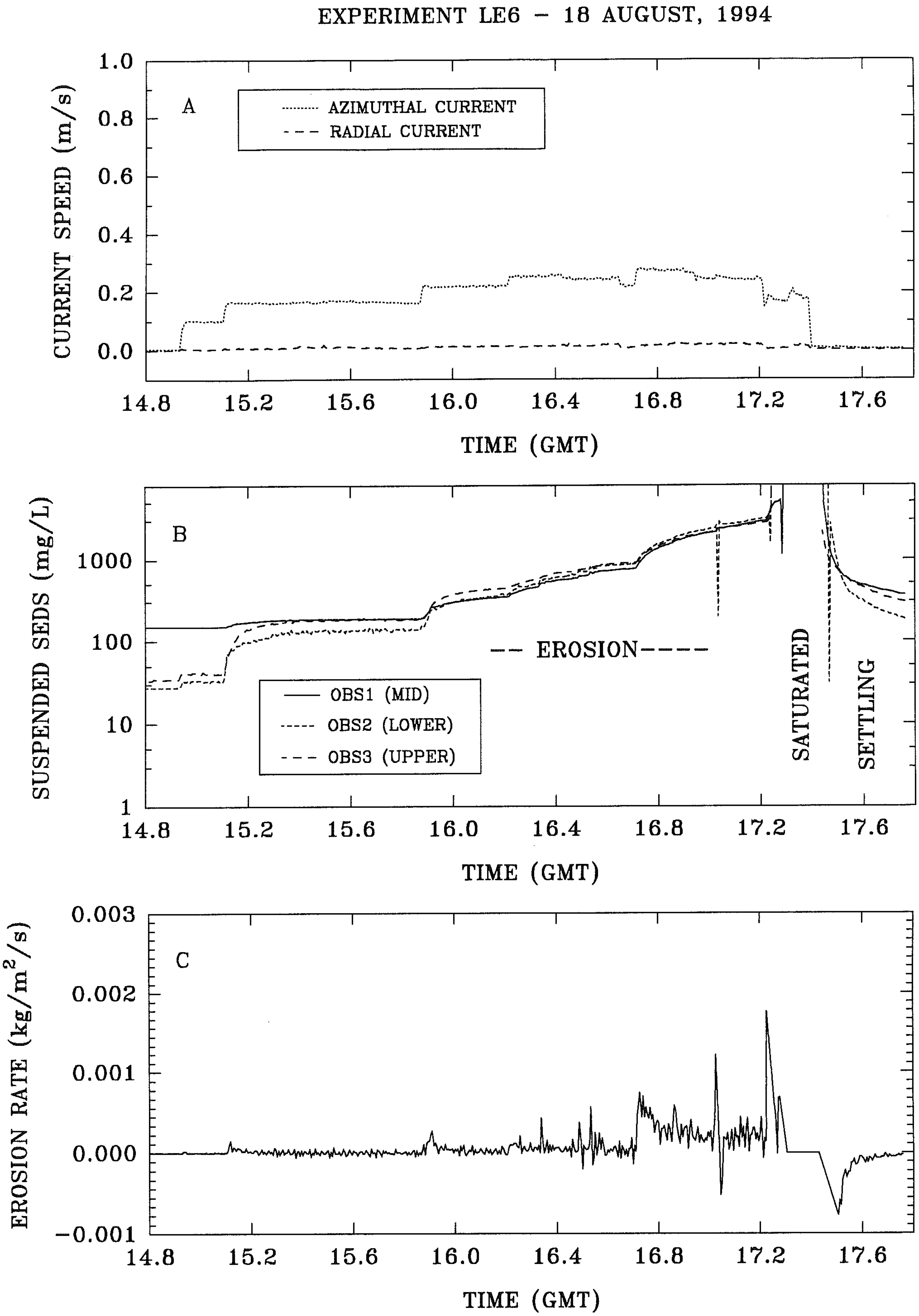

FIGURE 4.2.1.5. A time-series plot of the Laboratory Carousel experiment LE7, on dumpsite B material, Miramichi bay. (A) azimuthal and vertical current speed (m/s); (B) suspended sediment concentration (mg/L); and (C) erosion rate (kg/m²/s).

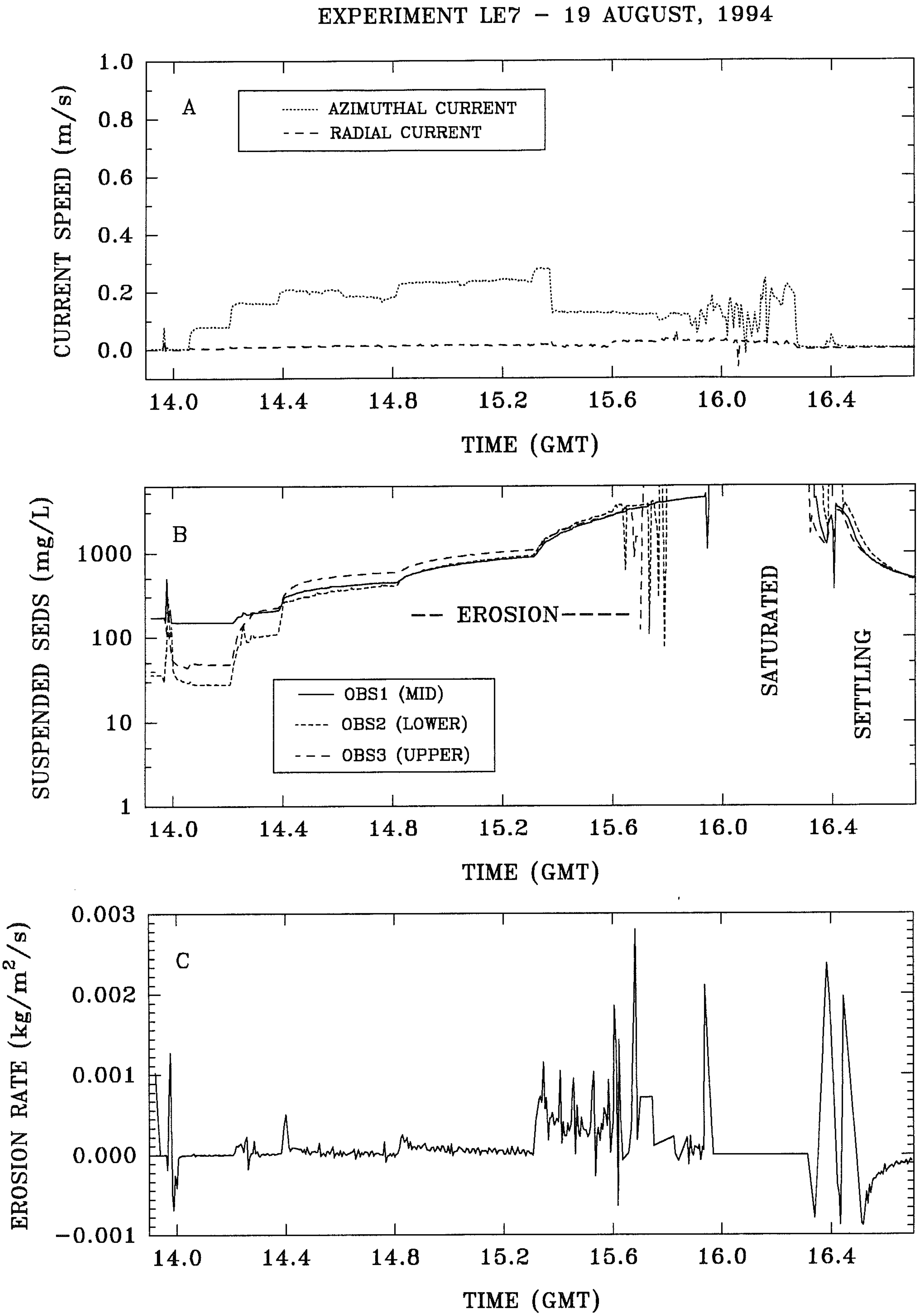

FIGURE 4.2.1.6. A time-series plot of the Laboratory Carousel experiment LE8, on dumpsite B material, Miramichi bay. (A) azimuthal and vertical current speed (m/s); (B) suspended sediment concentration (mg/L); and (C) erosion rate (kg/m^2/s).

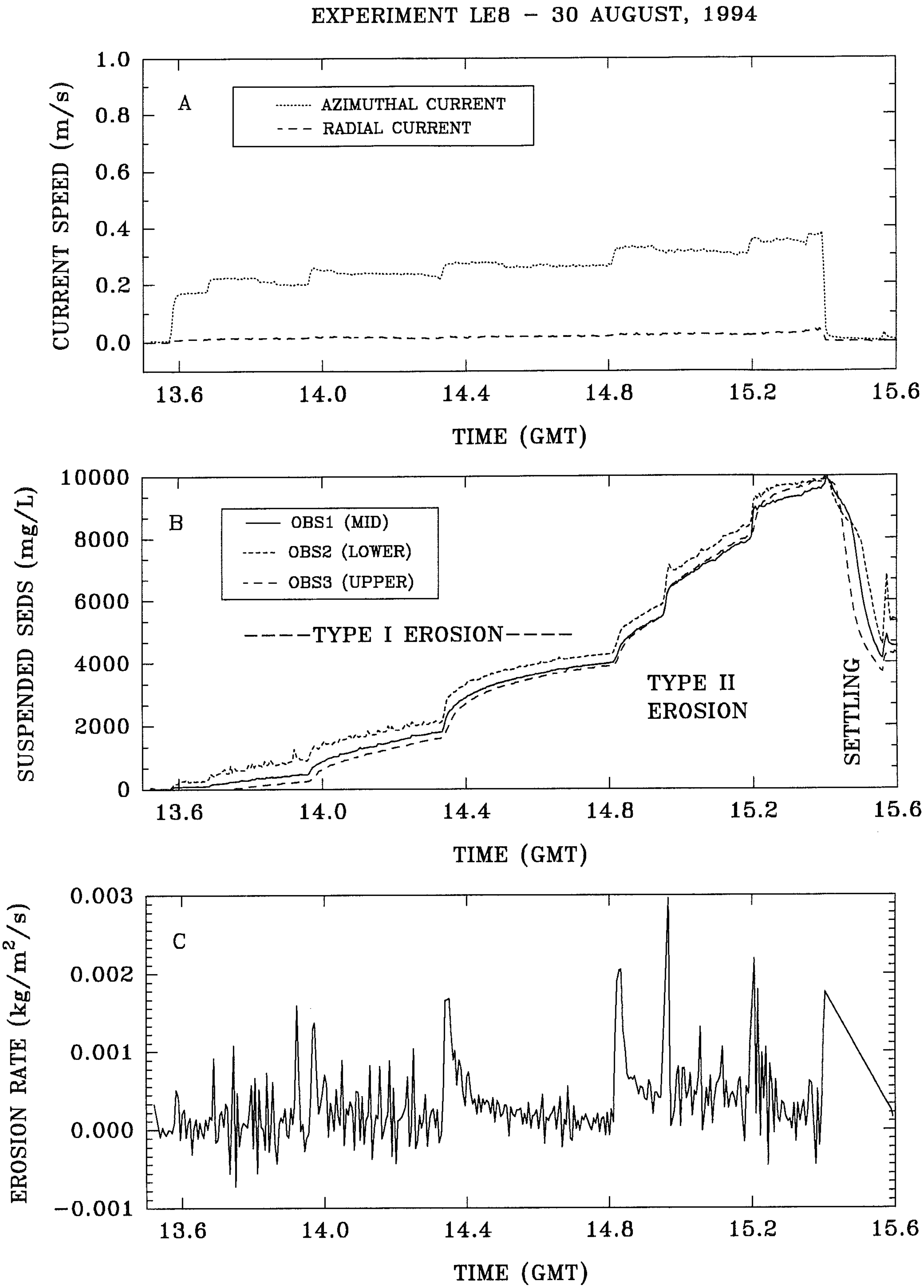

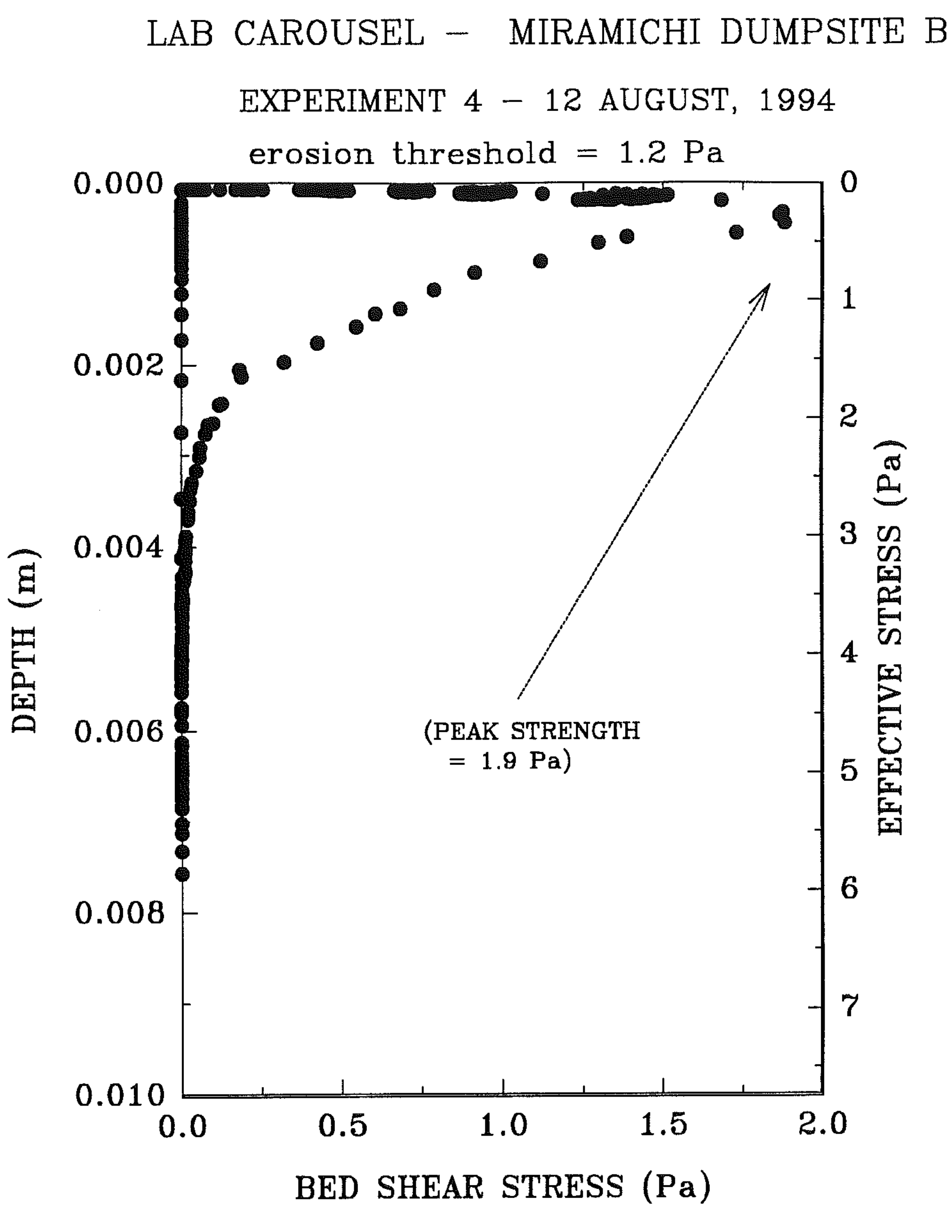

FIGURE 4.2.2.1. A synthetic core from experiment LE4 computed from the Laboratory Carousel time-series data on eroded mass. The experiment was undertaken after 7 days of consolidation/biostabilization. The erosion threshold is 1.2 Pa. Notice the peak in bed strength (1.9 Pa) within the topmost 2 mm, which is diagnostic of biostabilization.

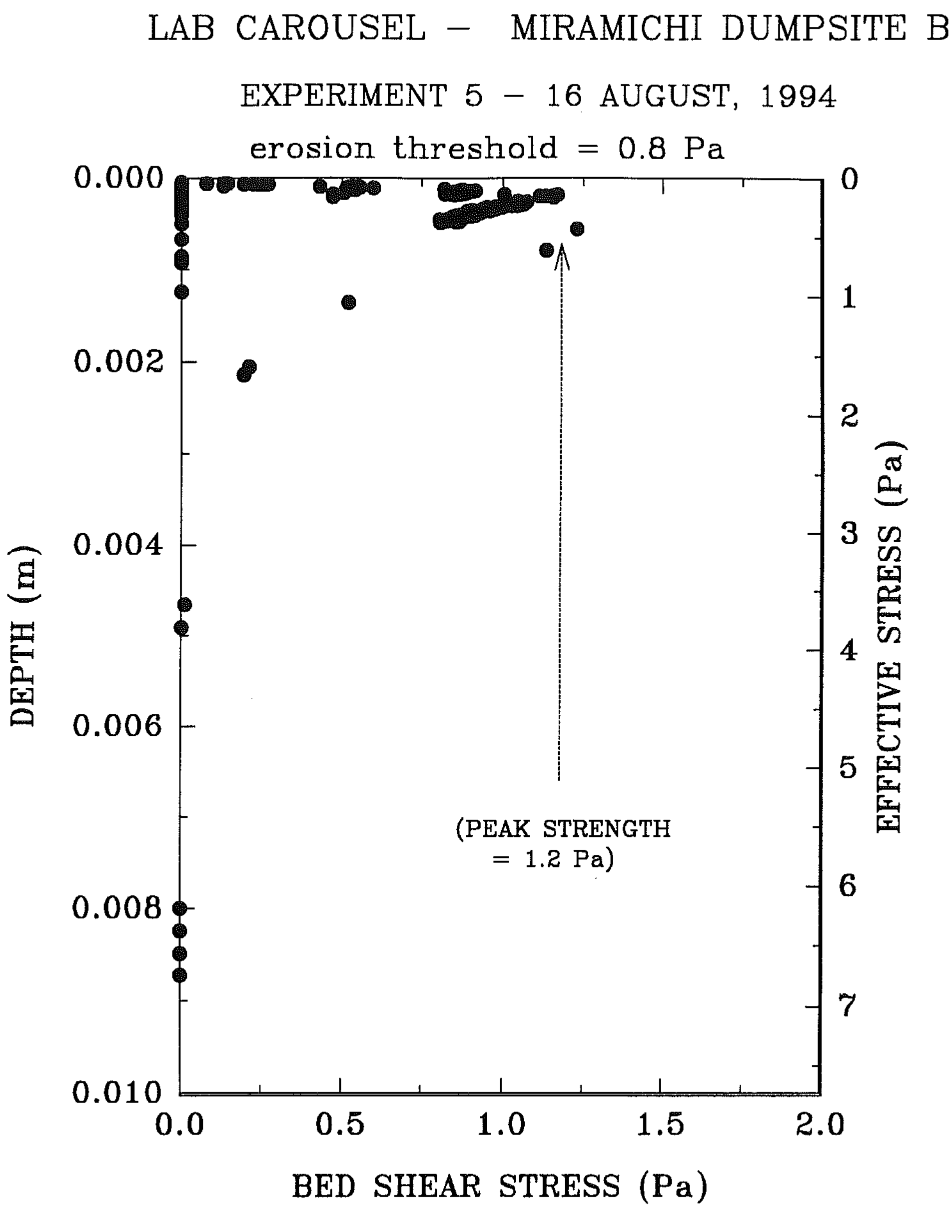

FIGURE 4.2.2.2. A synthetic core from experiment LE5 computed from the Laboratory Carousel time-series data on eroded mass. The experiment was undertaken after 4 days of consolidation/biostabilization. The erosion threshold is 0.8 Pa. Notice the peak in bed strength (1.2 Pa) within the topmost 2 mm, which is diagnostic of biostabilization.

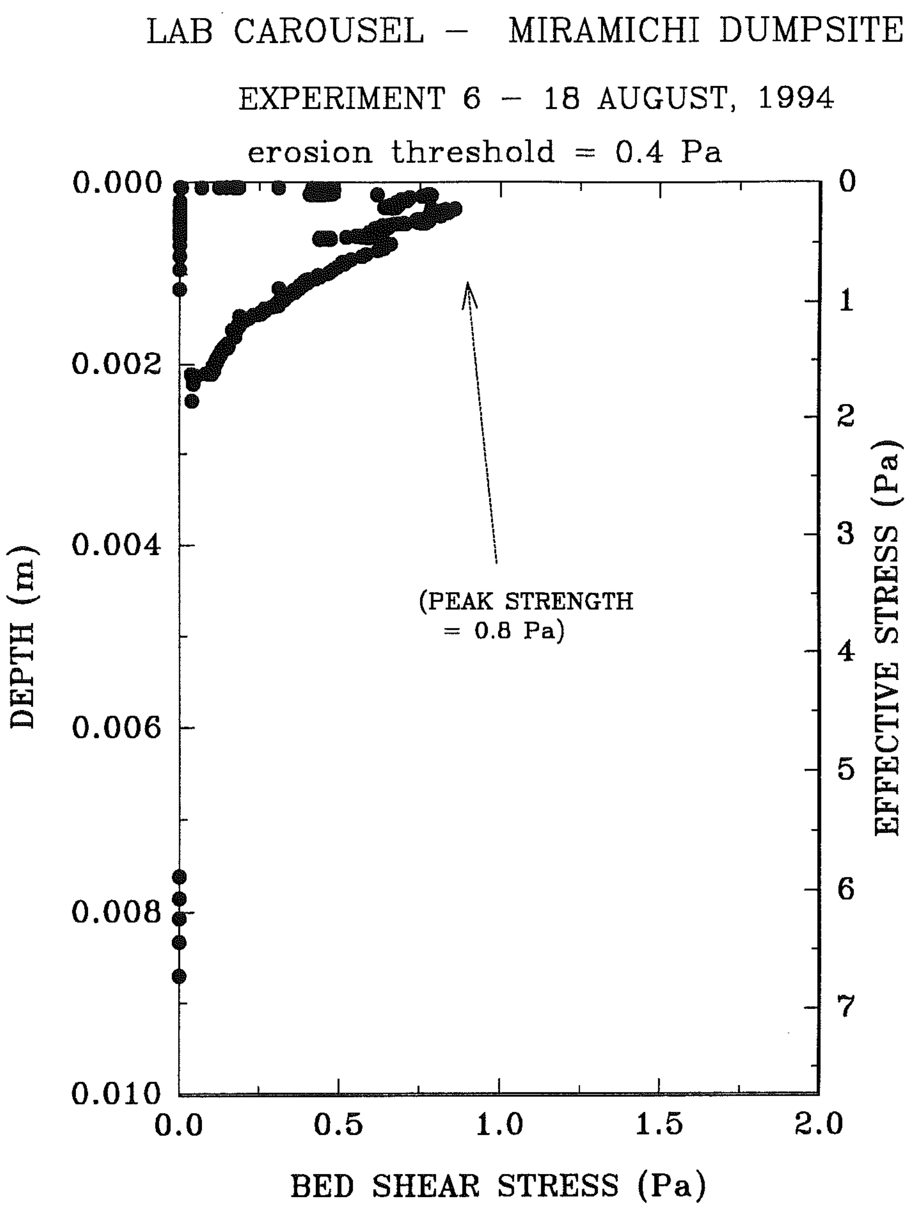

FIGURE 4.2.2.3. A synthetic core from experiment LE6 computed from the Laboratory Carousel time-series data on eroded mass. The experiment was undertaken after 2 days of consolidation/biostabilization. The erosion threshold is 0.4 Pa. Notice the peak in bed strength (0.8 Pa) within the topmost 2 mm, which is diagnostic of biostabilization.

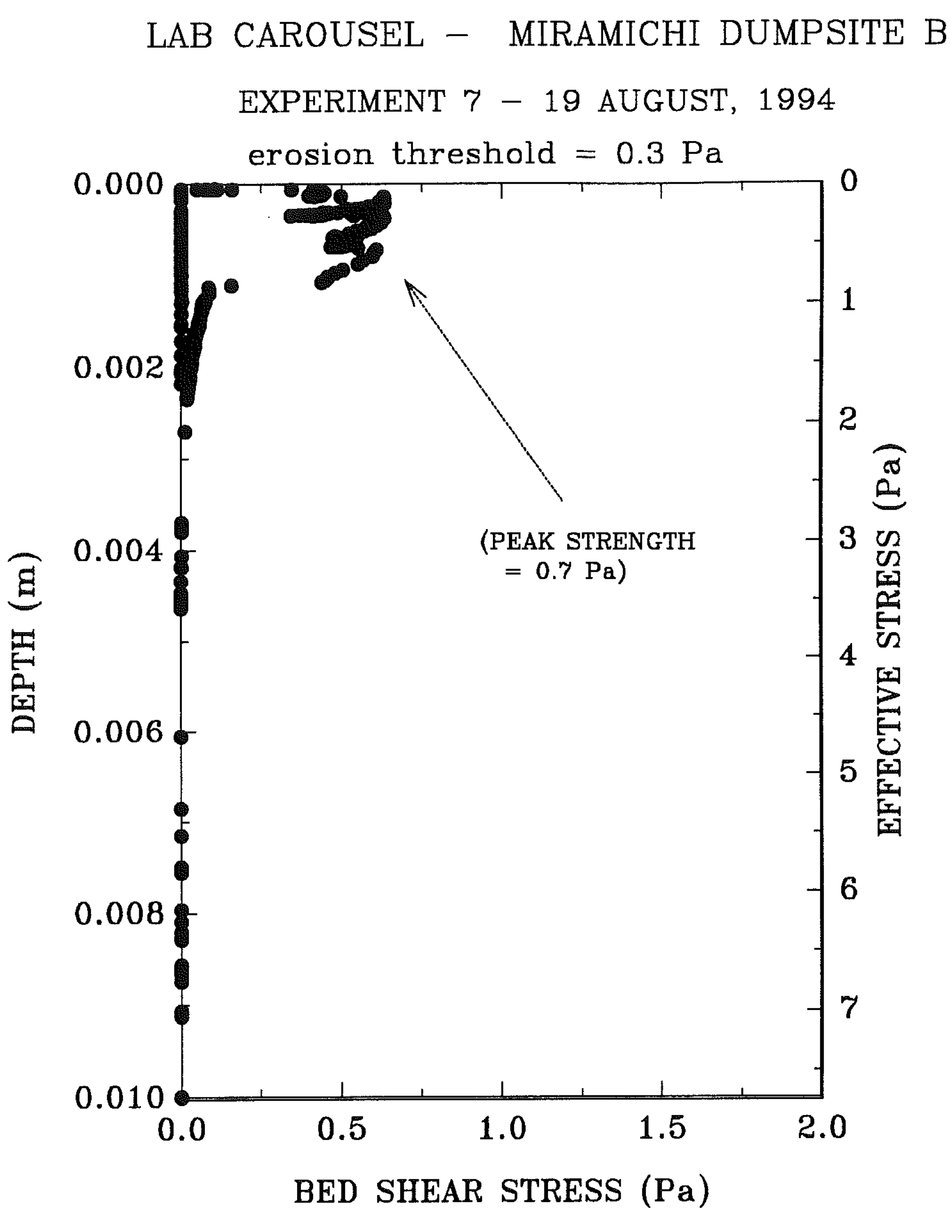

FIGURE 4.2.2.4. A synthetic core from experiment LE7 computed from the Laboratory Carousel time-series data on eroded mass. The experiment was undertaken after 1 day of consolidation/biostabilization. The erosion threshold is 0.3 Pa. Notice the peak in bed strength (0.7 Pa) within the topmost 1 mm, which is diagnostic of biostabilization.

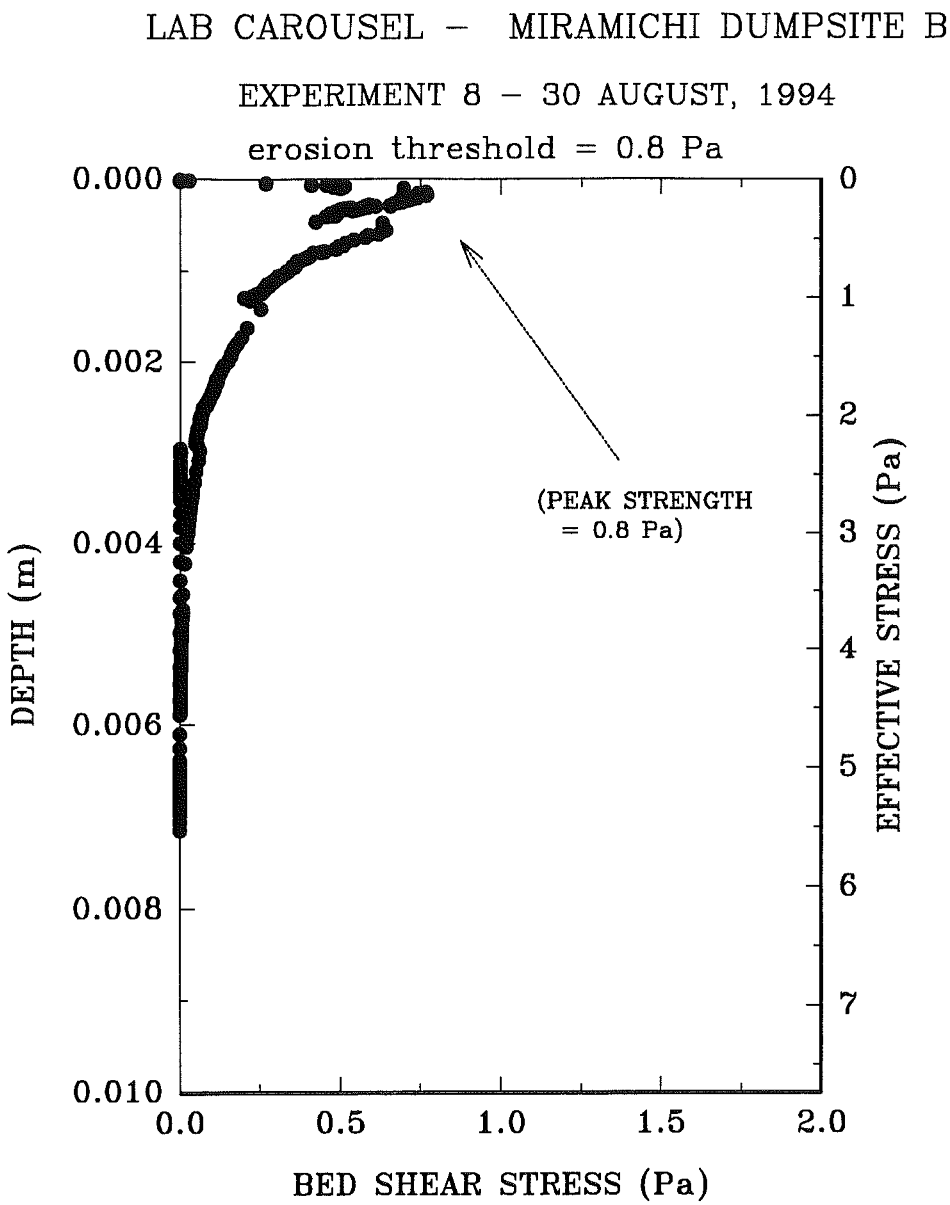

FIGURE 4.2.2.5. A synthetic core from experiment LE8 computed from the Laboratory Carousel time-series data on eroded mass. The experiment was undertaken after 11 days of consolidation/biostabilization and the system had gone anoxic. The erosion threshold is 0.8 Pa. Notice the peak in bed strength (0.7 Pa) within the topmost 1 mm, which is diagnostic of biostabilization.

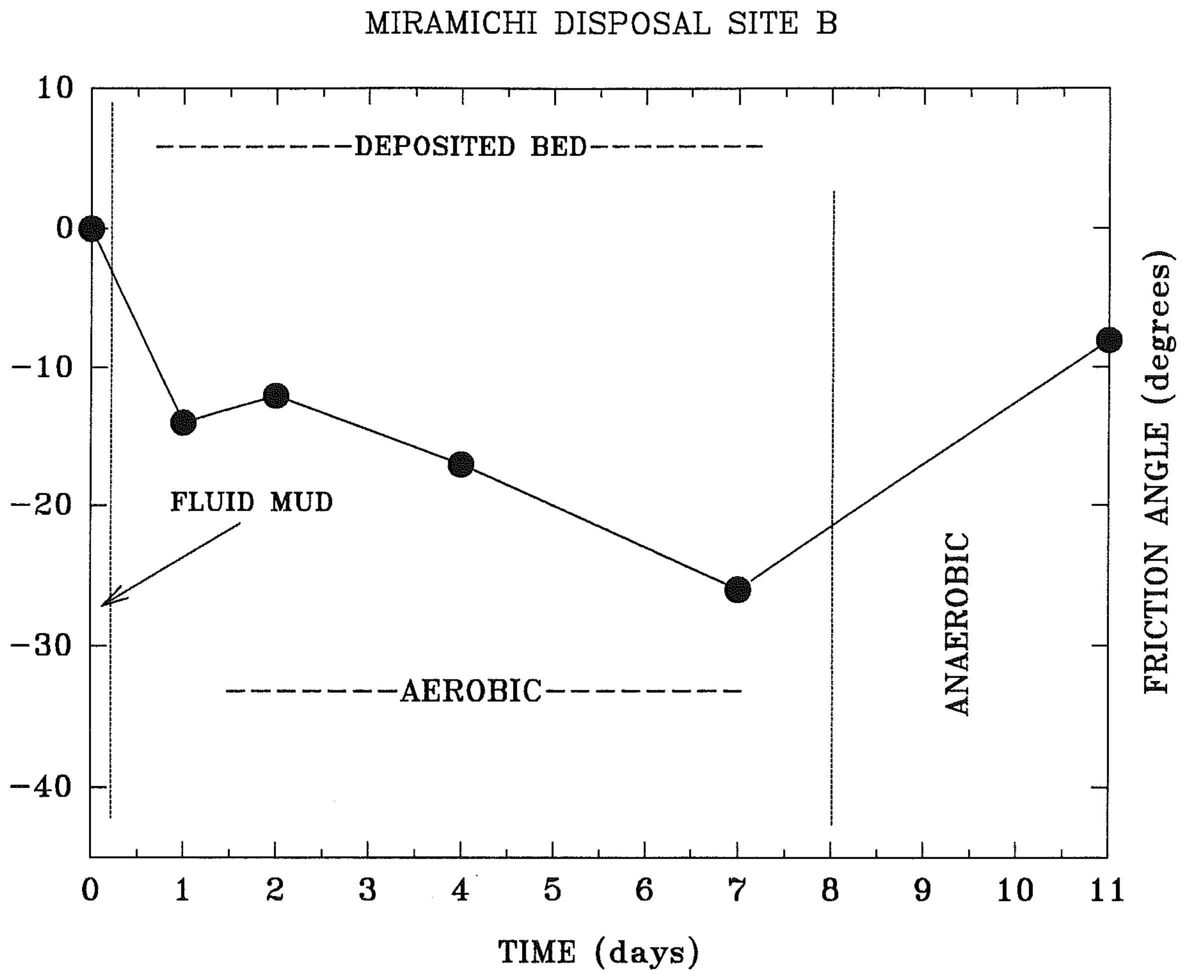

FIGURE 4.2.2.6. A time-series of the friction angle derived from the Laboratory Carousel analysis of dumpsite B material. The decrease in value with time is diagnostic of a systematic development of a biofilm (surface strengthening). The reveral in trends after 8 days reflects a change from oxygenated to anoxic conditions, associated with the collapse of the benthic macrofauna and development of anaerobic bacteria.

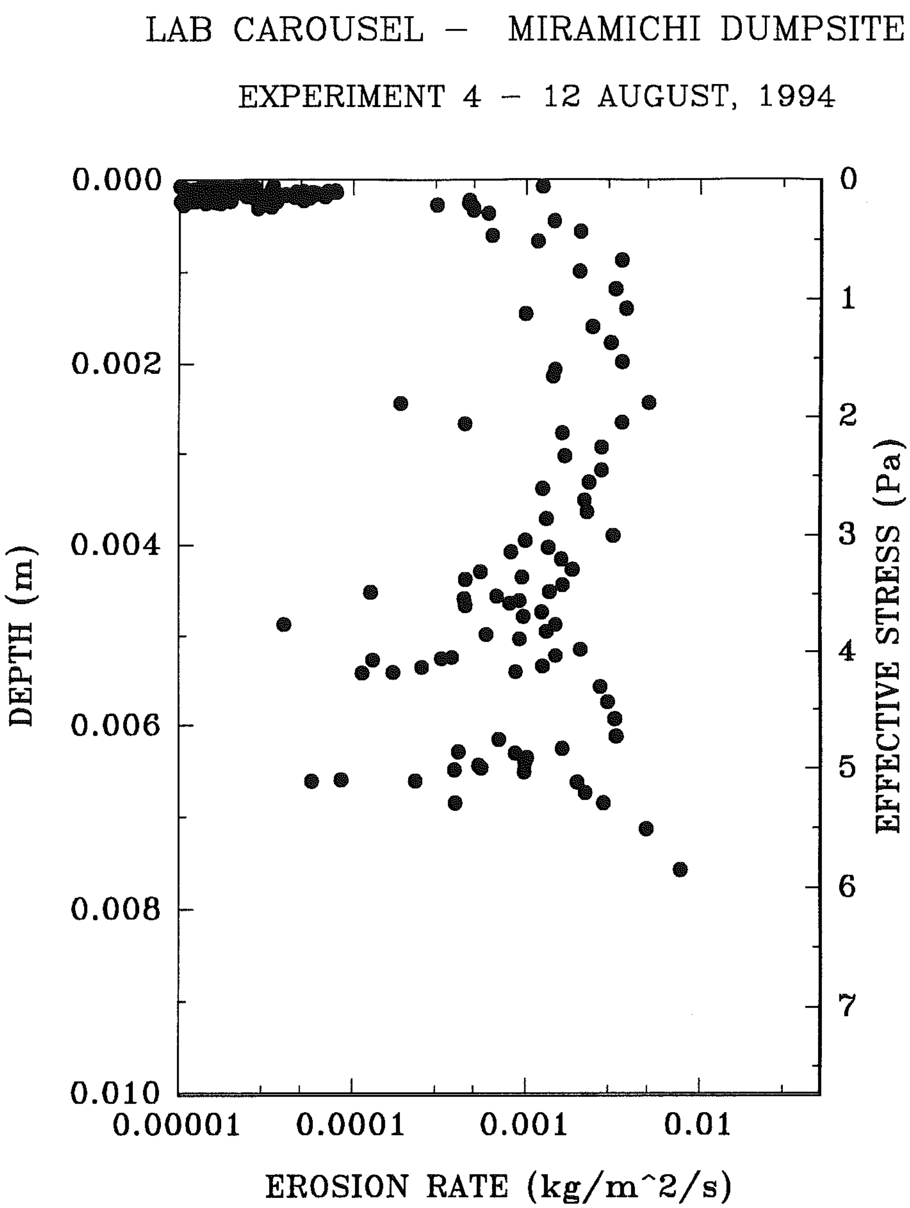

FIGURE 4.2.3.1. A synthetic core developed from Laboratory Carousel experiment LE4 showing the erosion rate ($\delta M/\delta t$) as a function of eroded depth. Notice that $\delta M/\delta t$ is virtually constant at 1×10^{-3} kg/m^2/s.

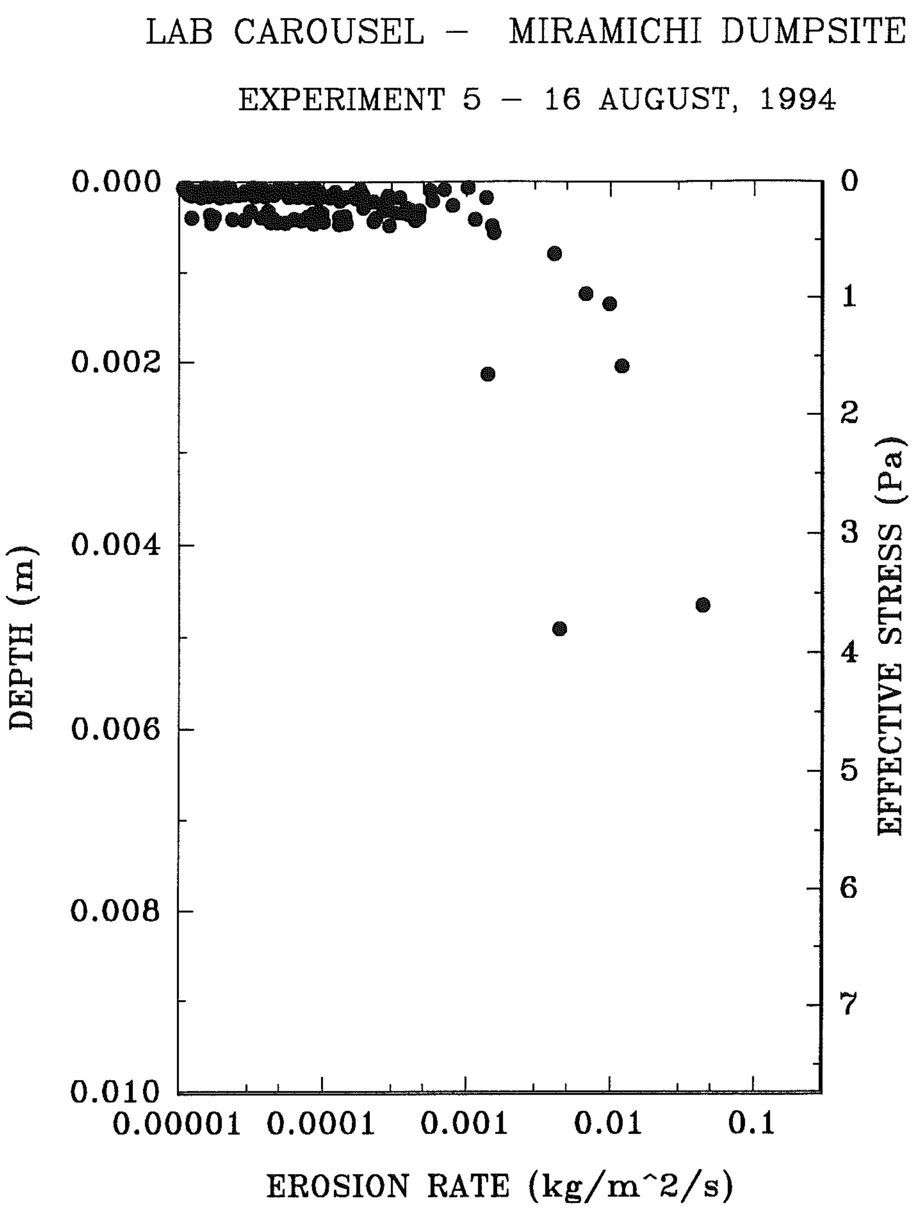

FIGURE 4.2.3.2. A synthetic core developed from Laboratory Carousel experiment LE5 showing the erosion rate (δM/δt) as a function of eroded depth. No clear trends emerged.

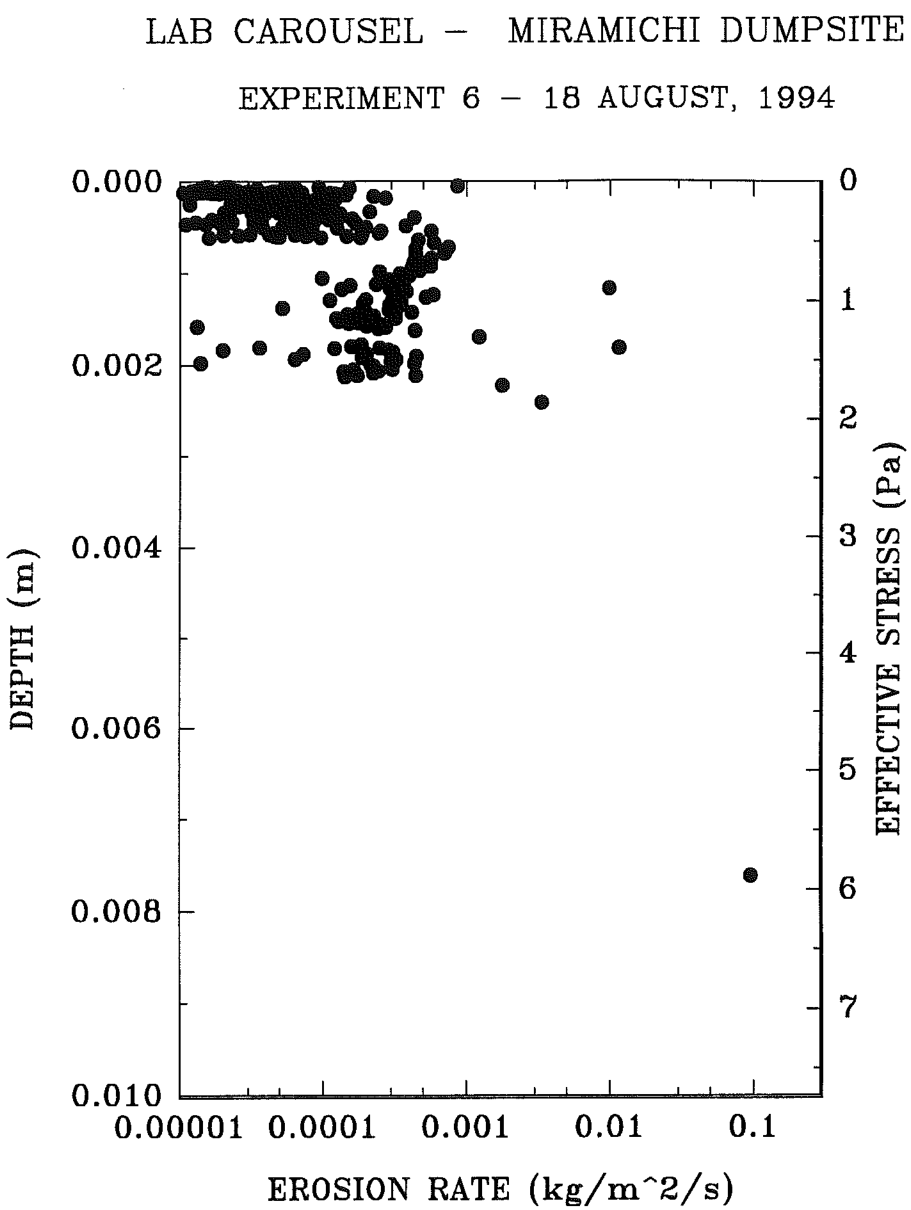

FIGURE 4.2.3.3. A synthetic core developed from Laboratory Carousel experiment LE6 showing the erosion rate (δM/δt) as a function of eroded depth.

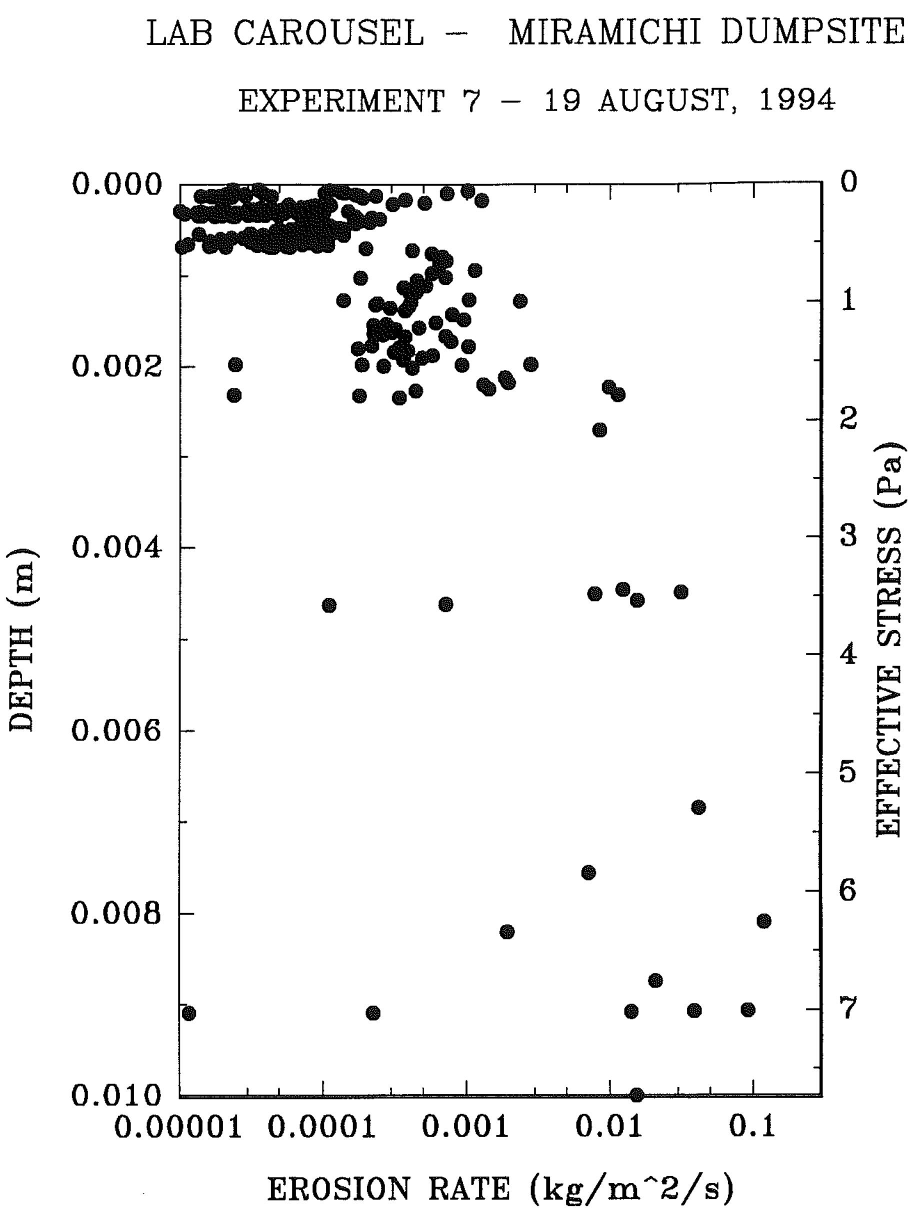

FIGURE 4.2.3.4. A synthetic core developed from Laboratory Carousel experiment LE7 showing the erosion rate (δM/δt) as a function of eroded depth. δM/δt appears to increase with depth due to the lack of sediment consolidation (1 day only) but the data are scattered.

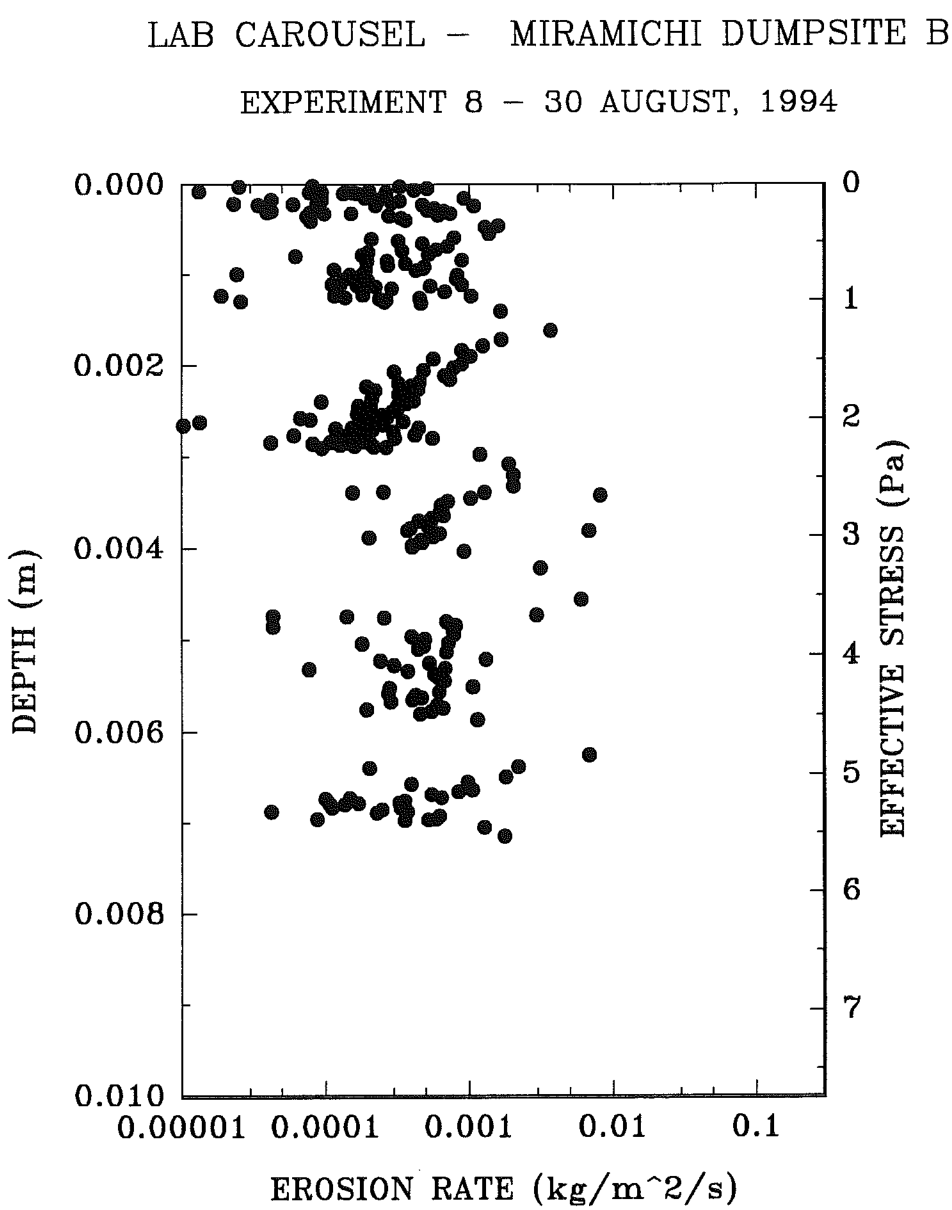

FIGURE 4.2.3.5. A synthetic core developed from Laboratory Carousel experiment LE8 showing the erosion rate ($\delta M/\delta t$) as a function of eroded depth. Notice that $\delta M/\delta t$ is virtually constant at 2×10^{-4} kg/m^2/s.

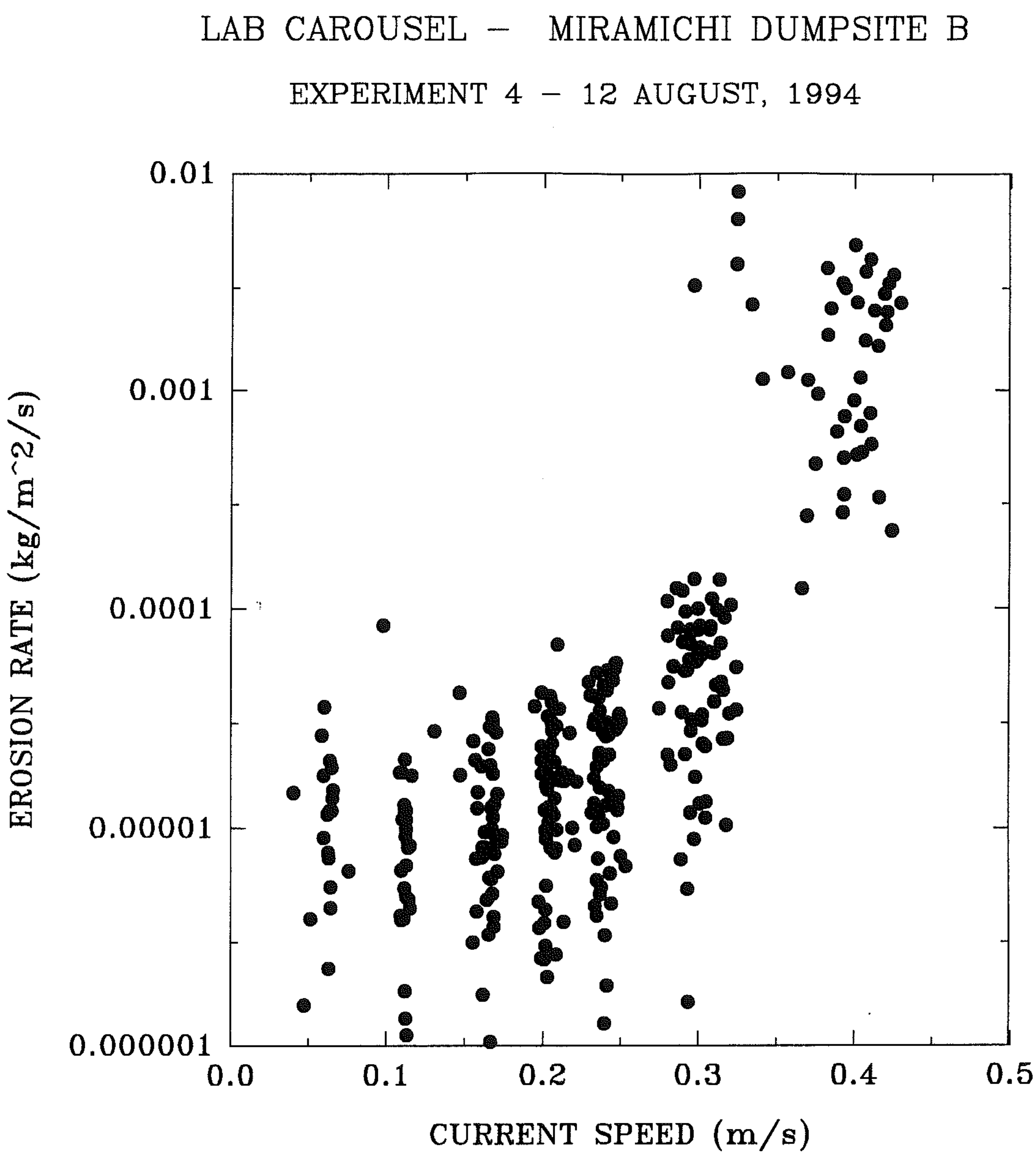

FIGURE 4.2.3.6. A scattergram of current speed against erosion rate ($\delta M/\delta t$) for Laboratory Carousel experiment LE4. $\delta M/\delta t$ appears to increase exponentially with current speed.

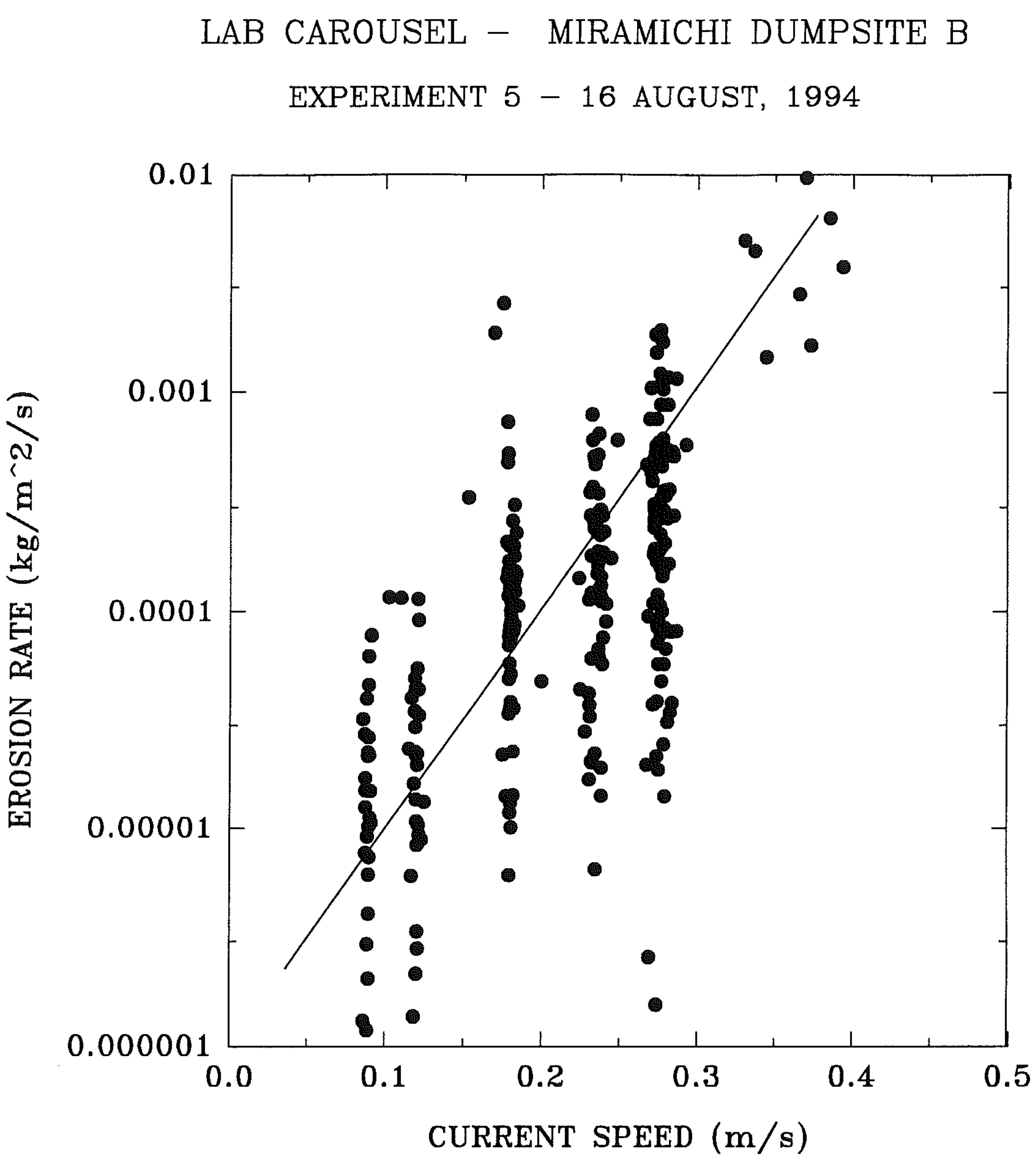

FIGURE 4.2.3.7. A scattergram of current speed against erosion rate ($\delta M/\delta t$) for Laboratory Carousel experiment LE5. $\delta M/\delta t$ appears to increase exponentially with current speed.

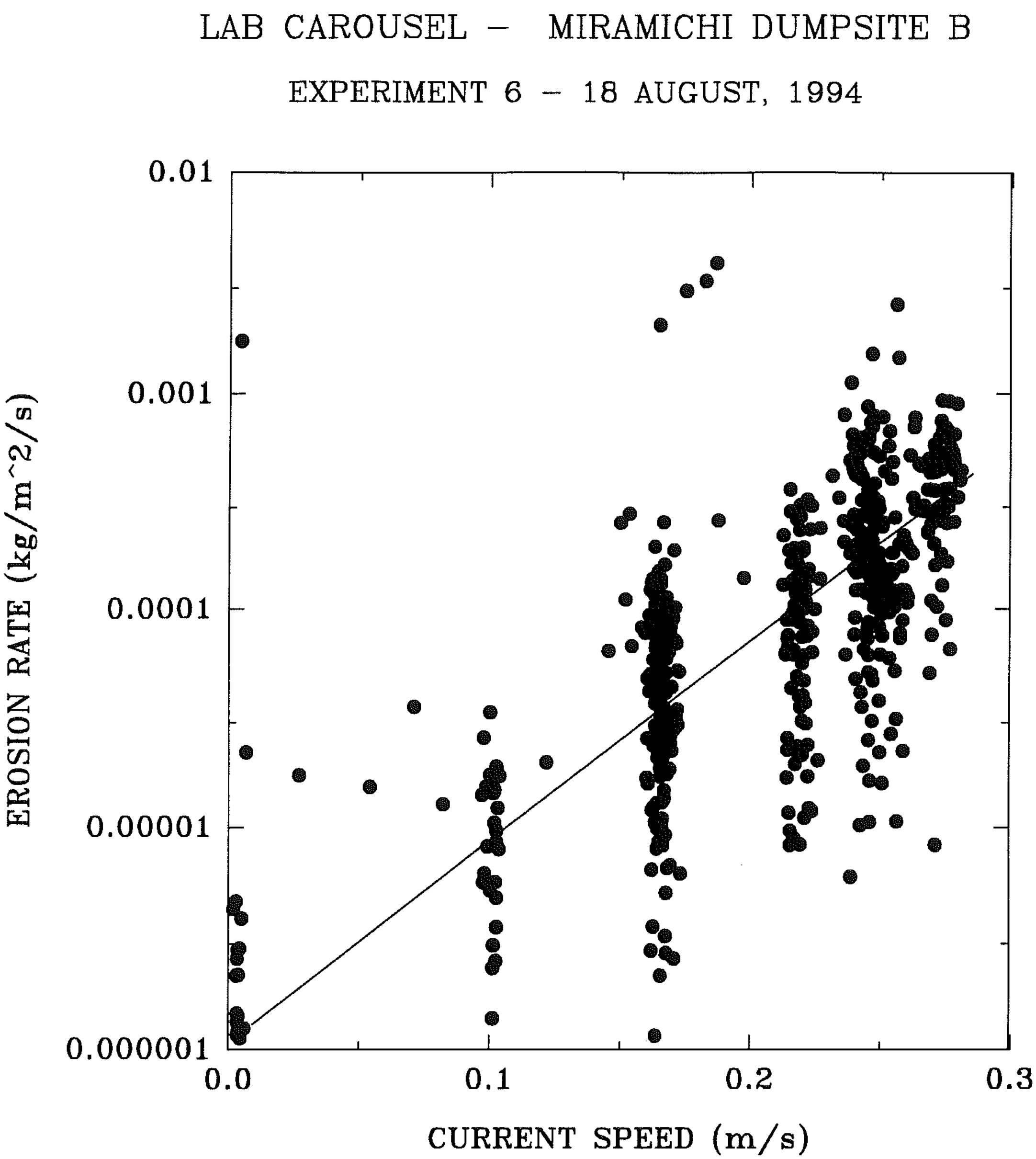

FIGURE 4.2.3.8. A scattergram of current speed against erosion rate (δM/δt) for Laboratory Carousel experiment LE6. δM/δt appears to increase exponentially with current speed.

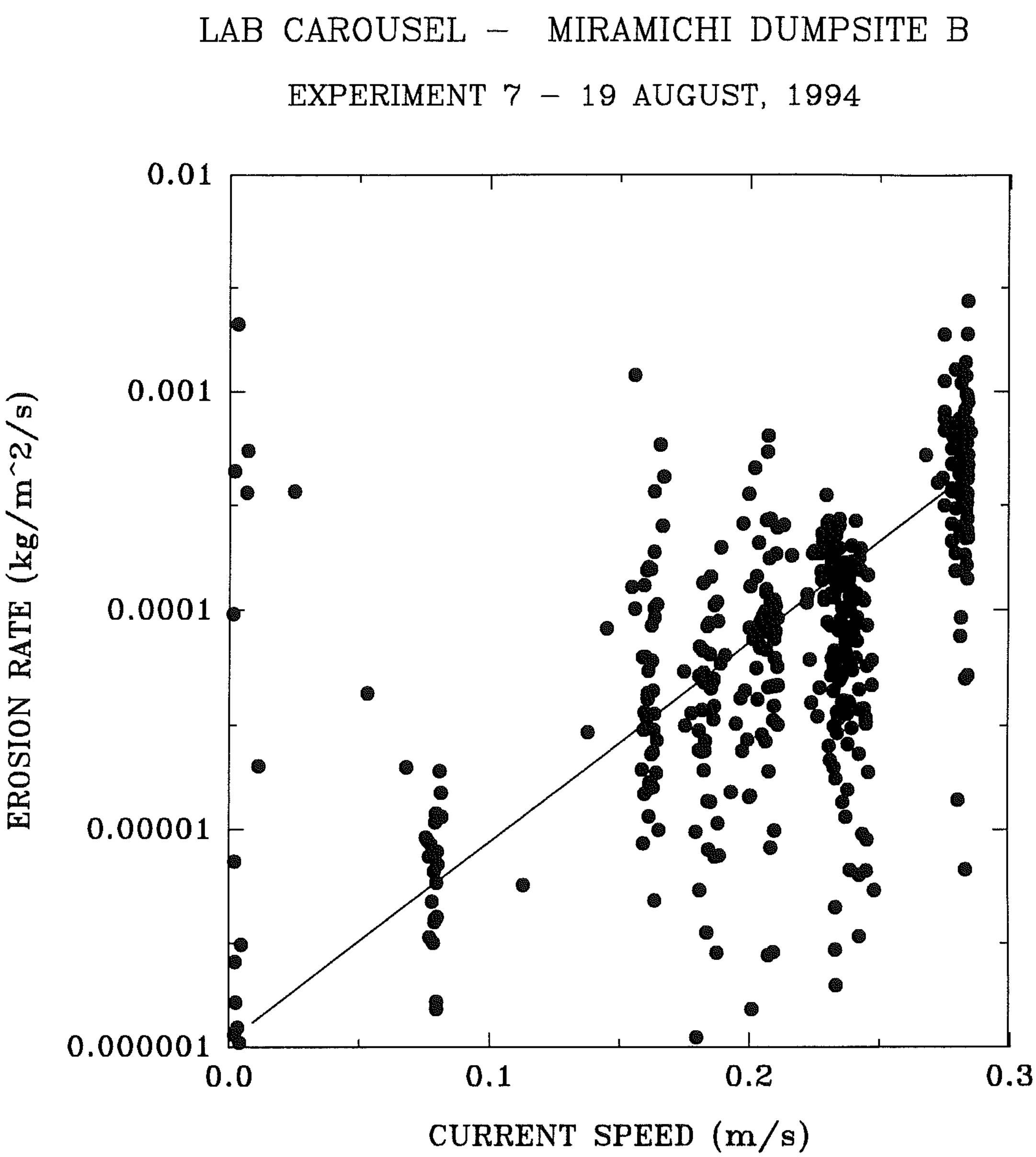

FIGURE 4.2.3.9. A scattergram of current speed against erosion rate (δM/δt) for Laboratory Carousel experiment LE7. δM/δt appears to increase exponentially with current speed.

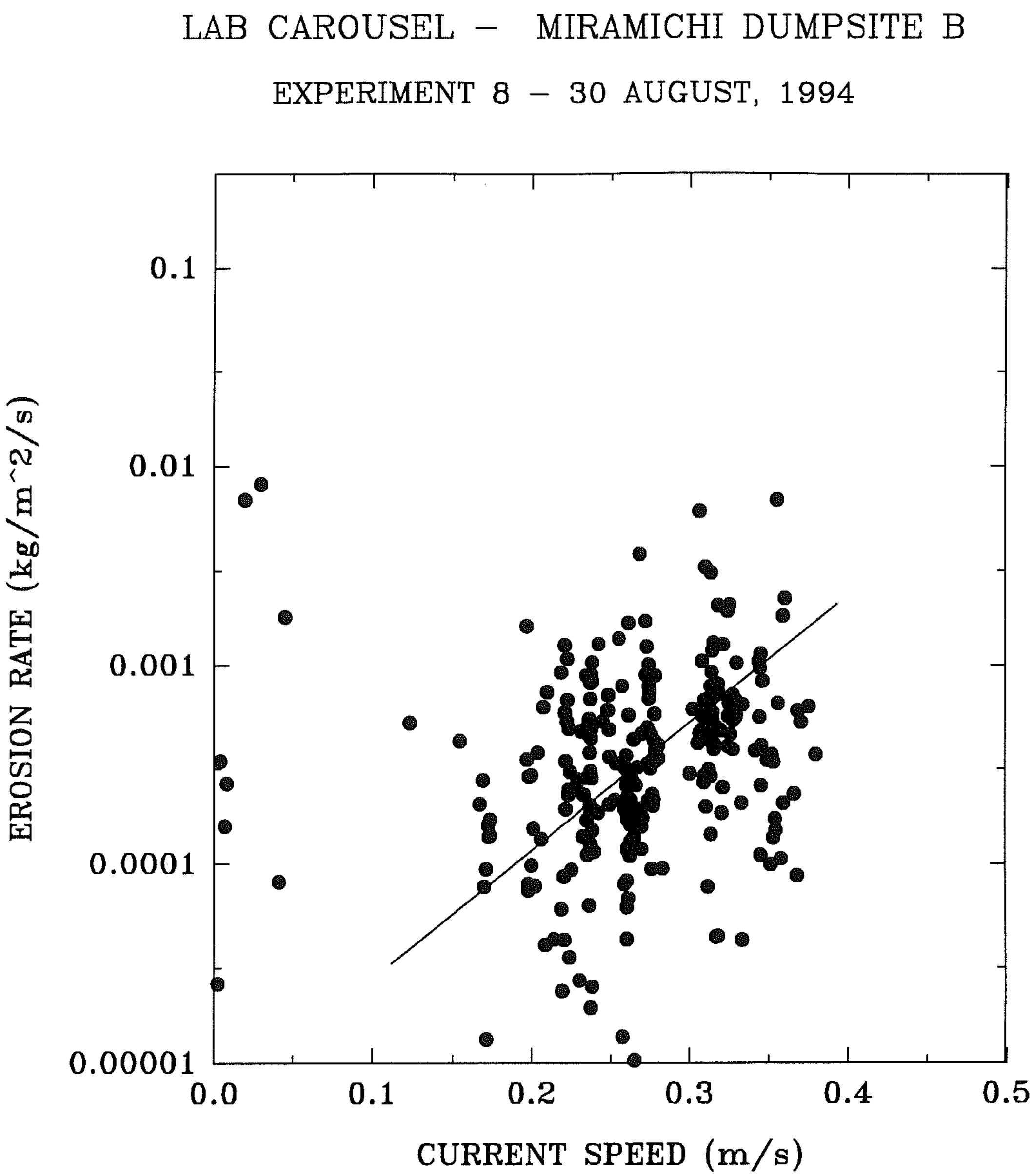

FIGURE 4.2.3.10. A scattergram of current speed against erosion rate ($\delta M/\delta t$) for Laboratory Carousel experiment LE8. $\delta M/\delta t$ appears to increase exponentially with current speed.

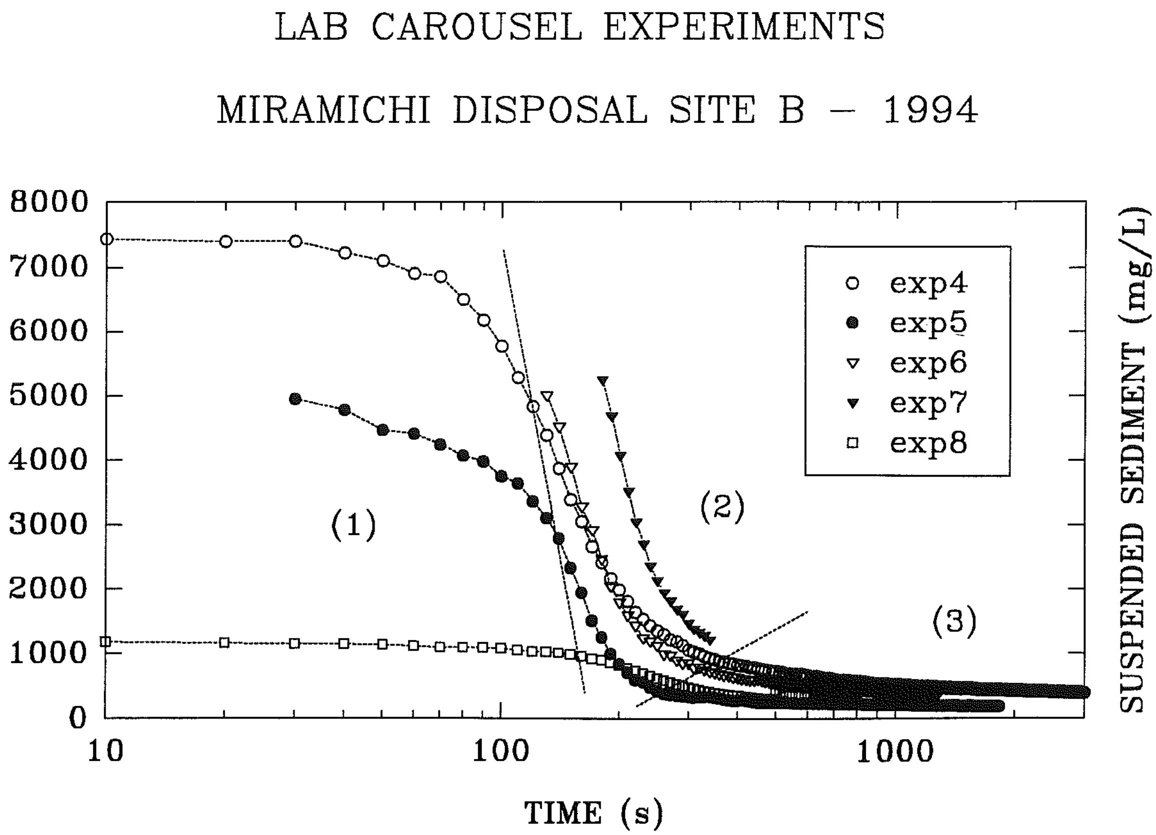

FIGURE 4.2.4.1. A time-series of still-water settling in the Laboratory Carousel for experiments LE4 - LE8. Notice they all show similar trends with time. These are: (1) an initial period of inhibited settling; (2) a period of rapid exponentially-decaying settling; and (3) a period of slow settling. These trends mirror those from the Sea Carousel *insitu* surveys.

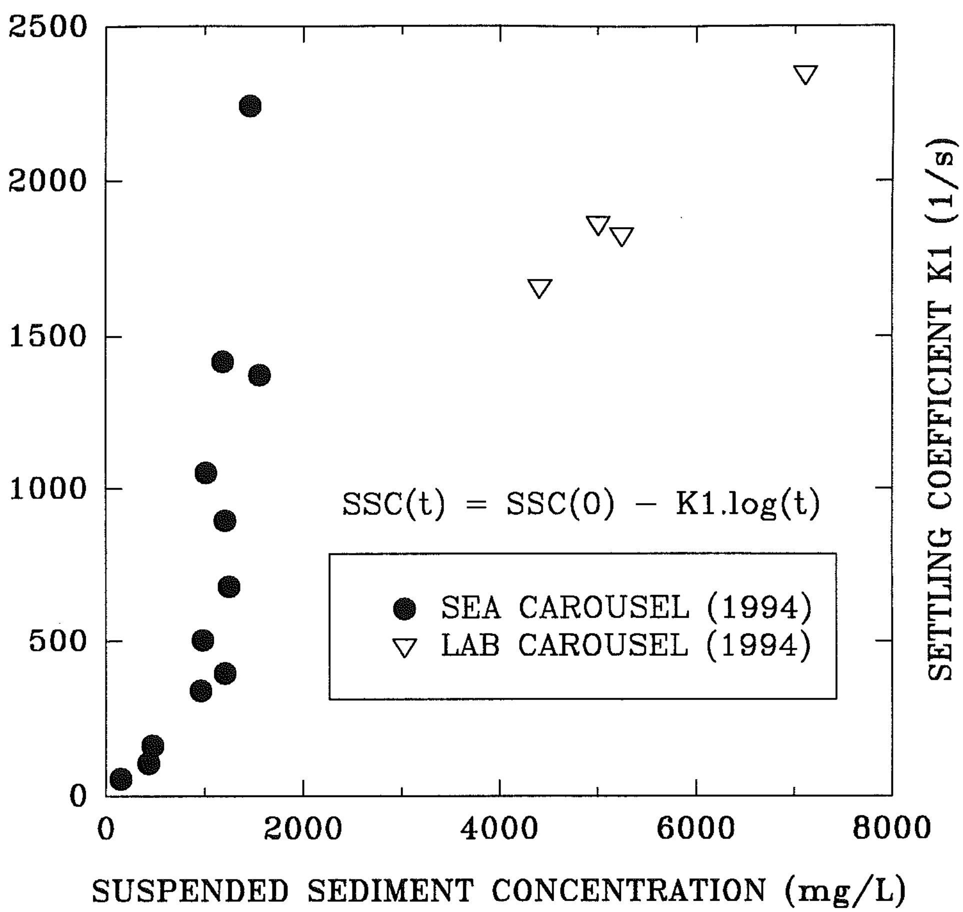

FIGURE 4.2.4.2. A scattergram of suspended sediment concentration against the settling decay constant (K_1). The Sea Carousel data indicates that settling was much greater *in situ* than was found under laboratory conditions.

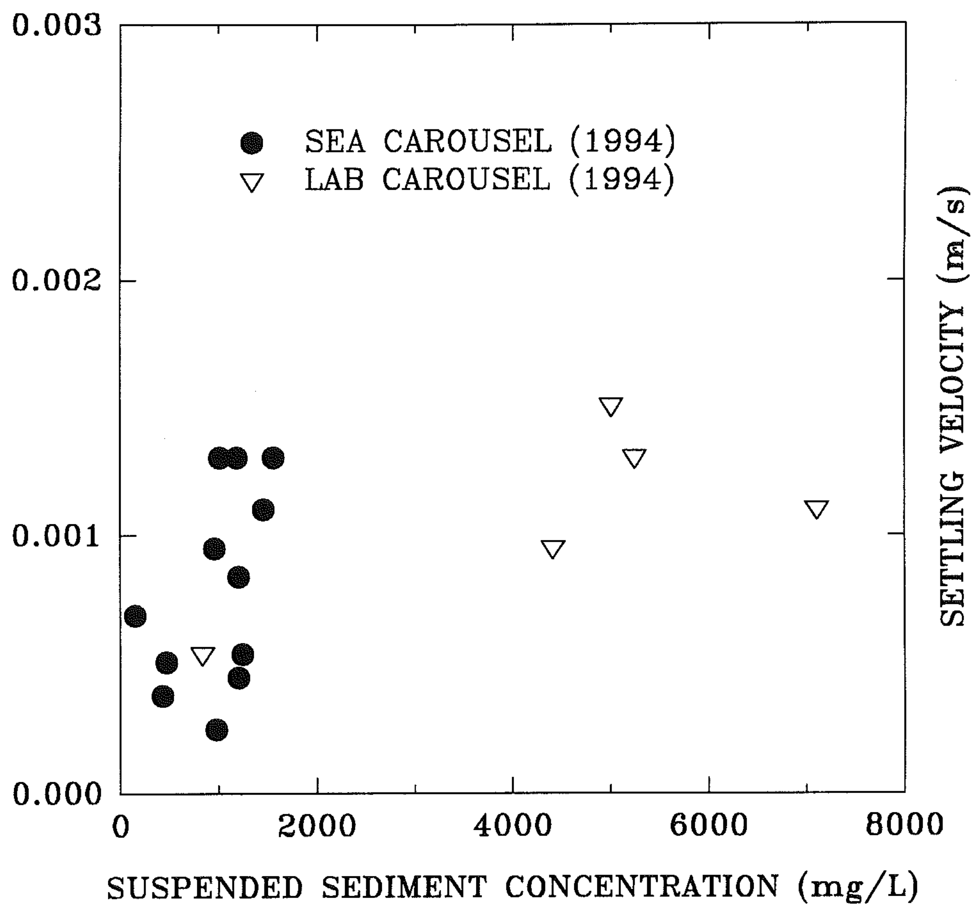

FIGURE 4.2.4.3. A scattergram of suspended sediment concentration (SSC) against mean mass settling velocity (W_s). Notice that W_s appears to reach a constant value of 0.0012 m/s at SSC's > 2000 mg/L, and is scattered, but less, at lower concentrations.

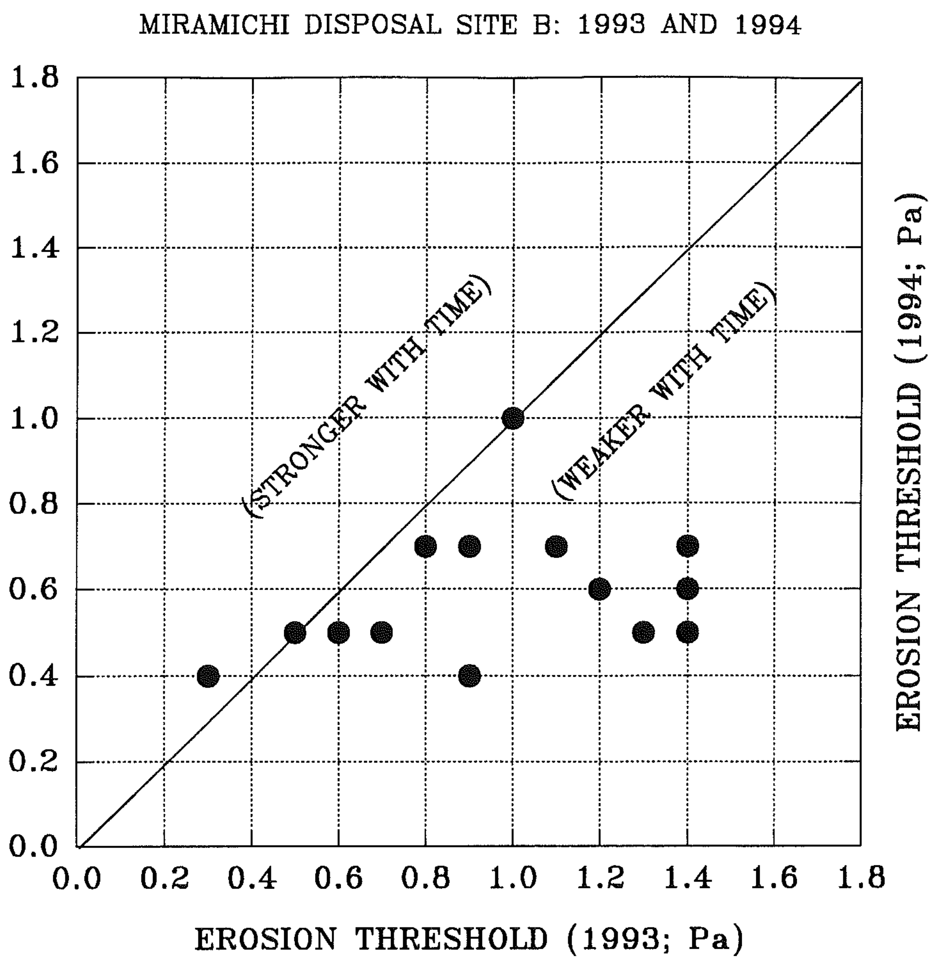

FIGURE 5.1. A scattergram of the erosion thresholds for Sea Carousel stations occupied on dumpsite B during 1993 and 1994. Notice that the seabed has become weaker during the year or so between surveys, even though no obvious change in physical bed properties was detected. This is attributed to seasonal fluctuations in bed strength related to benthic biological productivity.

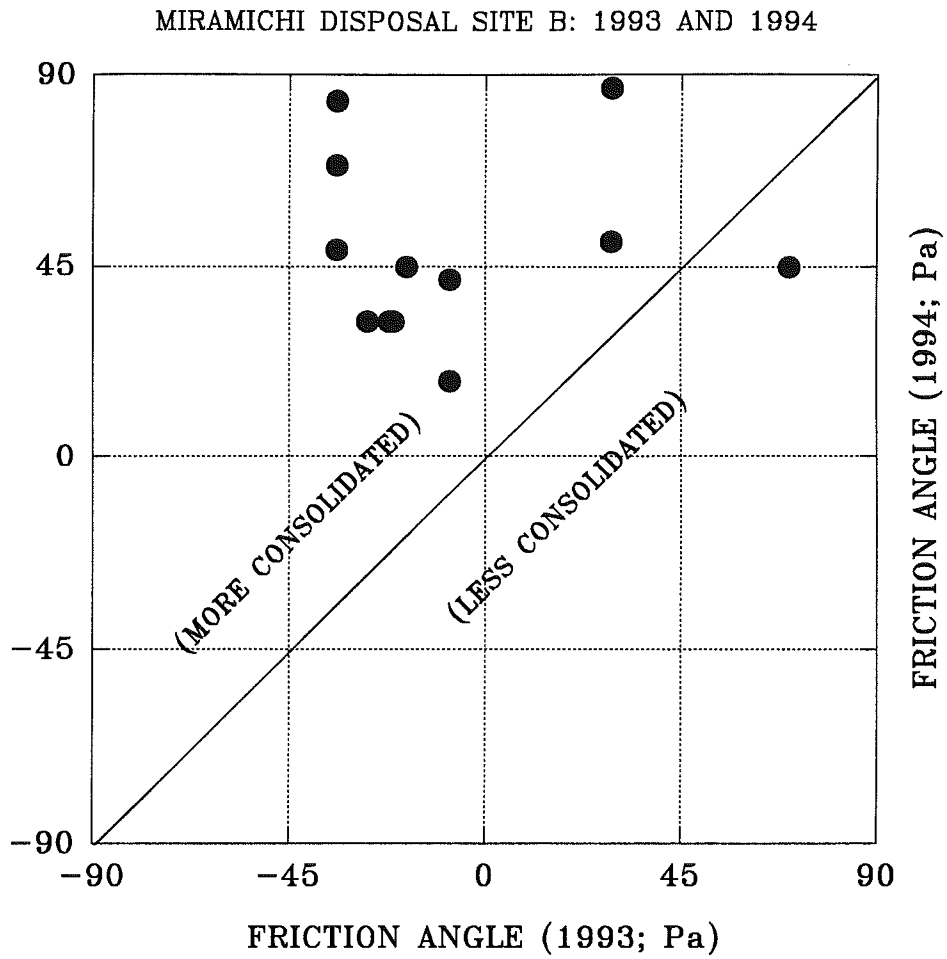

FIGURE 5.2. A scattergram of the friction angles for Sea Carousel stations occupied on dumpsite B during 1993 and 1994. Notice that the seabed has become more consolidated during the year or so between surveys as would be expected. This appears to have little effect on the erosion threshold as evidenced in Figure 5.1.

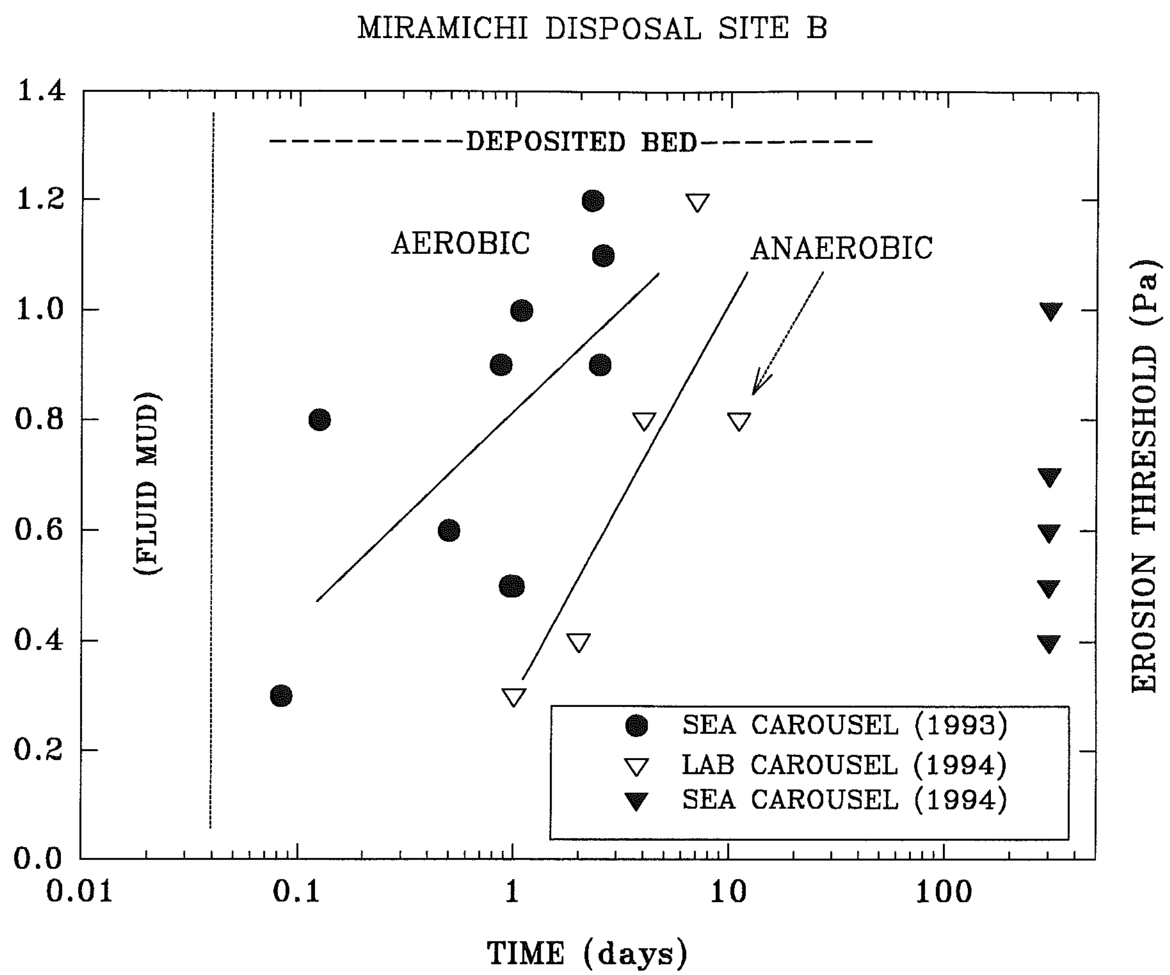

FIGURE 5.3. The observed increase in bed strength for three surveys of dumpsite B material: (1) the *insitu* 1993 Sea Carousel survey (water temp = 16°C); (2) the *insitu* 1994 Sea Carousel survey (water temp = 6°C); and (3) the laboratory study reported herein (water temp = 24°C). The solid lines show the best-fit increase in bed strengths for surveys (1) and (3). Notice that strength increase appears to be related to water temperature, which would agree with the concept of biostabilization.

APPENDIX 1

GRAIN SIZE RESULTS

MIRAMICHI DUMPSITE B GRAB SAMPLES

CALCULATION RESULTS FOR
THE SAMPLE WITH THE IDENTIFIER:

94350-001A C 0-2,RD009353, Dr. Carl Amos
,00205, AGC GRAVITY CORE, MIRAMICHI BAY

RESULTS

MIDPOINTS MM	PHI	RELATIVE FREQUENCY PERCENTAGES	CUMULATIVE FREQUENCY PERCENTAGES
8.0	-3.00	0.00	0.00
.93	0.10	0.00	0.00
.81	0.30	0.00	0.00
.71	0.50	0.01	0.01
.62	0.70	0.05	0.06
.54	0.90	0.06	0.12
.47	1.10	0.05	0.16
.41	1.30	0.13	0.29
.35	1.50	0.10	0.39
.31	1.70	0.09	0.48
.27	1.90	0.12	0.60
.23	2.10	0.11	0.71
.20	2.30	0.09	0.81
.18	2.50	0.10	0.91
.15	2.70	0.11	1.02
.13	2.90	0.10	1.12
.12	3.10	0.20	1.32
.10	3.30	0.95	2.27
.88E-01	3.50	4.21	6.48
.77E-01	3.70	1.83	8.31
.67E-01	3.90	1.79	10.10
.58E-01	4.10	1.57	11.68
.51E-01	4.30	1.23	12.91
.44E-01	4.50	1.25	14.16
.38E-01	4.70	1.82	15.98
.33E-01	4.90	2.15	18.13
.29E-01	5.10	2.99	21.11
.25E-01	5.30	2.84	23.95
.22E-01	5.50	2.43	26.38
.19E-01	5.70	3.14	29.53
.17E-01	5.90	3.08	32.61
.15E-01	6.10	3.29	35.90
.13E-01	6.30	3.26	39.15
.11E-01	6.50	2.90	42.05
.96E-02	6.70	2.73	44.78
.84E-02	6.90	2.59	47.37
.73E-02	7.10	2.51	49.88
.63E-02	7.30	2.71	52.59
.55E-02	7.50	2.57	55.16
.48E-02	7.70	2.55	57.71

.42E-02	7.90	2.37	60.08
.36E-02	8.10	2.06	62.14
.32E-02	8.30	1.63	63.78
.28E-02	8.50	1.46	65.23
.24E-02	8.70	1.65	66.88
.21E-02	8.90	1.53	68.41
.18E-02	9.10	1.31	69.72
.16E-02	9.30	1.24	70.96
.14E-02	9.50	1.51	72.48
.12E-02	9.70	1.73	74.21
.10E-02	9.90	1.50	75.71
.91E-03	10.10	1.34	77.05
.79E-03	10.30	1.28	78.32
.69E-03	10.50	1.48	79.80
.60E-03	10.70	1.76	81.56
.52E-03	10.90	1.54	83.09
.24E-03	12.00	16.91	100.00

GRAIN SIZE BREAKDOWN

% GRAVEL	% SAND	% SILT	% CLAY	% MUD
0.00	10.10	49.98	39.92	89.90

STATISTICAL MEASURES

MEAN (PHI)	STANDARD DEVIATION (PHI)	KURTOSIS (NO DIM.)	SKEWNESS (NO DIM.)
7.62	2.77	1.98	0.21

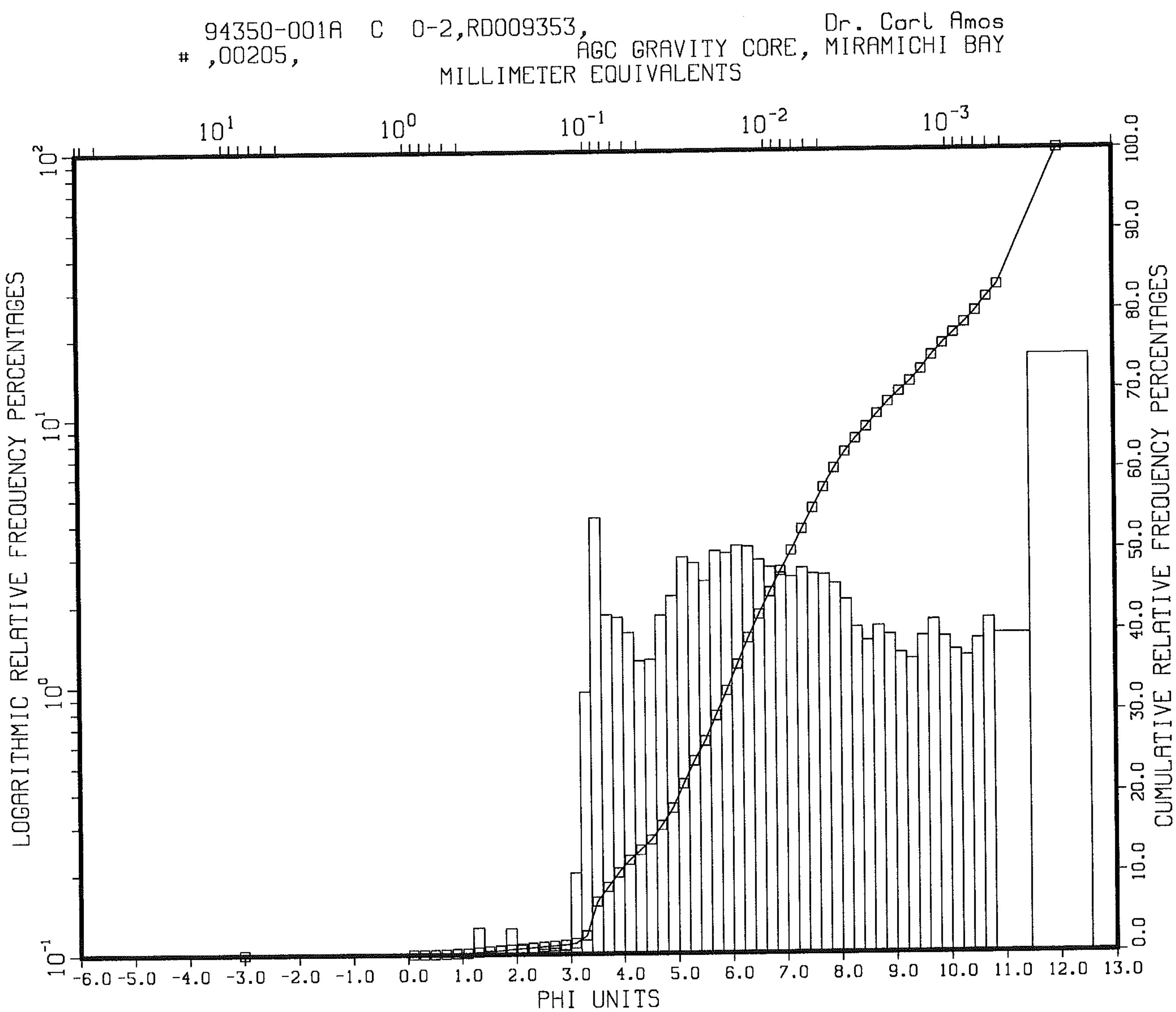
94350-001A C 0-2,RD009353,
,00205,
Dr. Carl Amos
AGC GRAVITY CORE, MIRAMICHI BAY
MILLIMETER EQUIVALENTS
10^{1}
10^{0}
10^{-1}
10^{-2}
10^{-3}
LOGARITHMIC RELATIVE FREQUENCY PERCENTAGES
10^{2}
10^{1}
10^{0}
10^{-1}
CUMULATIVE RELATIVE FREQUENCY PERCENTAGES
0.0
10.0
20.0
30.0
40.0
50.0
60.0
70.0
80.0
90.0
100.0
-6.0 -5.0 -4.0 -3.0 -2.0 -1.0 0.0 1.0 2.0 3.0 4.0 5.0 6.0 7.0 8.0 9.0 10.0 11.0 12.0 13.0
PHI UNITS

CALCULATION RESULTS FOR
THE SAMPLE WITH THE IDENTIFIER:

94350-004A C 0-2,RD009354, Dr. Carl Amos
,00205, AGC GRAVITY CORE, MIRAMICHI BAY

RESULTS

MIDPOINTS MM	PHI	RELATIVE FREQUENCY PERCENTAGES	CUMULATIVE FREQUENCY PERCENTAGES
8.0	-3.00	0.04	0.04
.93	0.10	0.00	0.04
.81	0.30	0.00	0.04
.71	0.50	0.03	0.07
.62	0.70	0.02	0.09
.54	0.90	0.04	0.13
.47	1.10	0.09	0.22
.41	1.30	0.15	0.37
.35	1.50	0.23	0.59
.31	1.70	0.24	0.84
.27	1.90	0.29	1.13
.23	2.10	0.30	1.43
.20	2.30	0.45	1.88
.18	2.50	0.77	2.66
.15	2.70	0.92	3.58
.13	2.90	1.20	4.78
.12	3.10	2.09	6.87
.10	3.30	2.61	9.47
.88E-01	3.50	2.65	12.12
.77E-01	3.70	2.08	14.21
.67E-01	3.90	1.68	15.89
.58E-01	4.10	1.22	17.11
.51E-01	4.30	1.28	18.39
.44E-01	4.50	1.52	19.90
.38E-01	4.70	2.54	22.44
.33E-01	4.90	3.04	25.49
.29E-01	5.10	2.95	28.44
.25E-01	5.30	2.89	31.33
.22E-01	5.50	2.77	34.09
.19E-01	5.70	2.95	37.04
.17E-01	5.90	2.72	39.76
.15E-01	6.10	2.44	42.21
.13E-01	6.30	2.29	44.50
.11E-01	6.50	2.35	46.85
.96E-02	6.70	2.38	49.23
.84E-02	6.90	2.60	51.83
.73E-02	7.10	2.46	54.29
.63E-02	7.30	2.51	56.80
.55E-02	7.50	2.65	59.45
.48E-02	7.70	2.52	61.97

.42E-02	7.90	1.94	63.92
.36E-02	8.10	1.88	65.79
.32E-02	8.30	1.72	67.51
.28E-02	8.50	1.40	68.91
.24E-02	8.70	1.36	70.26
.21E-02	8.90	1.44	71.71
.18E-02	9.10	1.24	72.94
.16E-02	9.30	1.20	74.14
.14E-02	9.50	1.34	75.48
.12E-02	9.70	1.88	77.36
.10E-02	9.90	1.88	79.25
.91E-03	10.10	1.58	80.83
.79E-03	10.30	1.13	81.95
.69E-03	10.50	1.41	83.37
.60E-03	10.70	1.84	85.20
.52E-03	10.90	1.44	86.64
.24E-03	12.00	13.36	100.00

GRAIN SIZE BREAKDOWN

% GRAVEL	% SAND	% SILT	% CLAY	% MUD
0.04	15.85	48.03	36.08	84.11

STATISTICAL MEASURES

MEAN (PHI)	STANDARD DEVIATION (PHI)	KURTOSIS (NO DIM.)	SKEWNESS (NO DIM.)
7.17	2.89	2.08	0.21

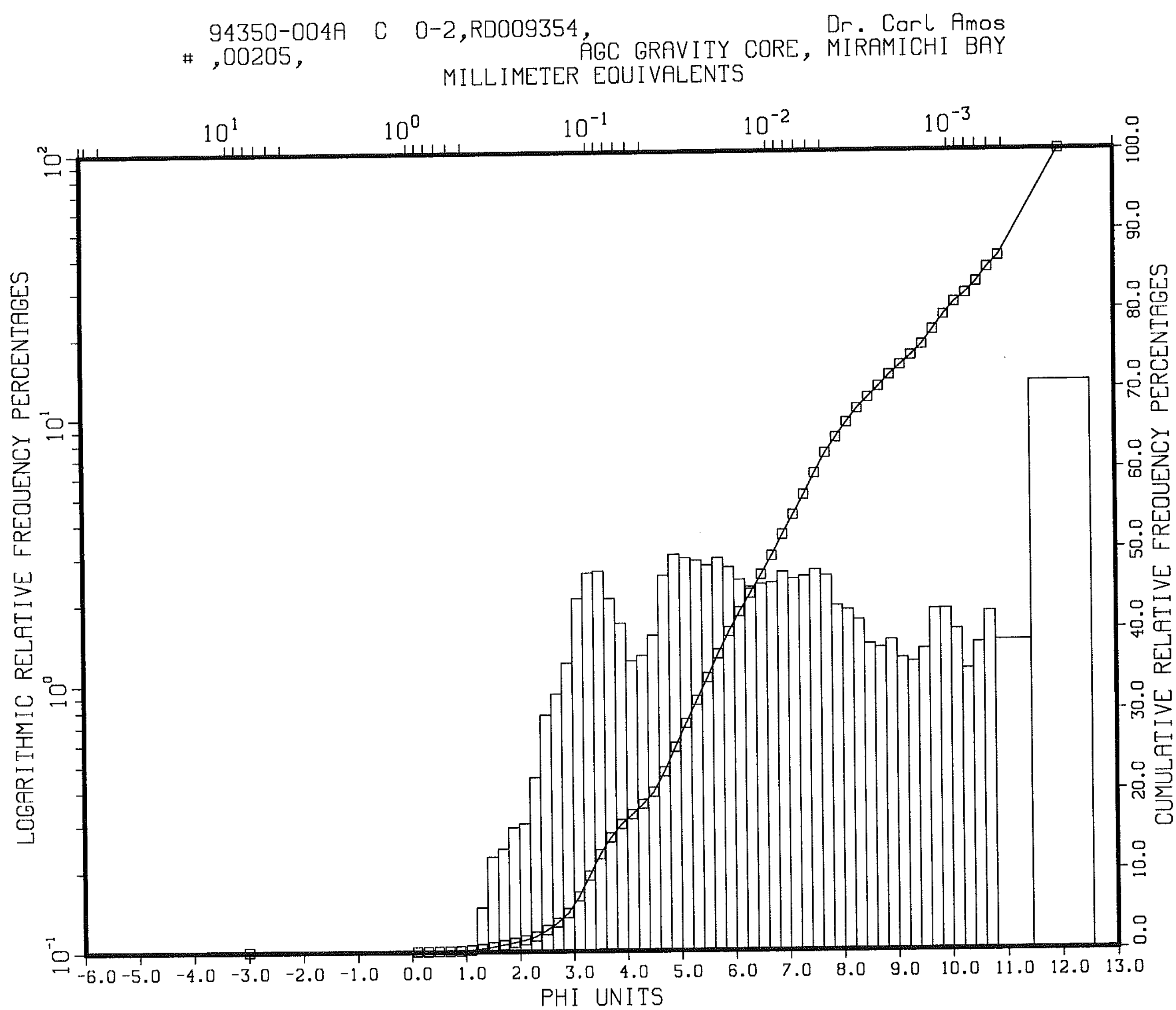
94350-004A C 0-2,RD009354,
,00205,
Dr. Carl Amos
AGC GRAVITY CORE, MIRAMICHI BAY
MILLIMETER EQUIVALENTS
LOGARITHMIC RELATIVE FREQUENCY PERCENTAGES
CUMULATIVE RELATIVE FREQUENCY PERCENTAGES
PHI UNITS

CALCULATION RESULTS FOR
THE SAMPLE WITH THE IDENTIFIER:

94350-005A C 0-2,RD009355, Dr. Carl Amos
,00205, AGC GRAVITY CORE, MIRAMICHI BAY

RESULTS

MIDPOINTS MM	PHI	RELATIVE FREQUENCY PERCENTAGES	CUMULATIVE FREQUENCY PERCENTAGES
8.0	-3.00	0.13	0.13
.93	0.10	0.00	0.13
.81	0.30	0.00	0.13
.71	0.50	0.00	0.13
.62	0.70	0.00	0.13
.54	0.90	0.00	0.13
.47	1.10	0.22	0.35
.41	1.30	0.52	0.87
.35	1.50	1.41	2.28
.31	1.70	3.33	5.61
.27	1.90	6.37	11.98
.23	2.10	6.47	18.45
.20	2.30	6.05	24.50
.18	2.50	11.14	35.64
.15	2.70	8.91	44.55
.13	2.90	5.05	49.60
.12	3.10	3.49	53.09
.10	3.30	3.39	56.48
.88E-01	3.50	2.21	58.69
.77E-01	3.70	1.74	60.43
.67E-01	3.90	1.38	61.82
.58E-01	4.10	0.83	62.65
.51E-01	4.30	0.67	63.32
.44E-01	4.50	0.83	64.15
.38E-01	4.70	1.20	65.35
.33E-01	4.90	1.25	66.60
.29E-01	5.10	1.32	67.92
.25E-01	5.30	1.20	69.12
.22E-01	5.50	1.11	70.23
.19E-01	5.70	1.27	71.51
.17E-01	5.90	1.34	72.84
.15E-01	6.10	1.51	74.35
.13E-01	6.30	1.22	75.57
.11E-01	6.50	1.14	76.71
.96E-02	6.70	1.04	77.76
.84E-02	6.90	1.04	78.80
.73E-02	7.10	1.09	79.90
.63E-02	7.30	1.18	81.07
.55E-02	7.50	1.22	82.29
.48E-02	7.70	1.09	83.38

.42E-02	7.90	0.86	84.25
.36E-02	8.10	0.72	84.97
.32E-02	8.30	0.70	85.67
.28E-02	8.50	0.57	86.24
.24E-02	8.70	0.65	86.88
.21E-02	8.90	0.75	87.64
.18E-02	9.10	0.64	88.28
.16E-02	9.30	0.41	88.69
.14E-02	9.50	0.36	89.04
.12E-02	9.70	0.51	89.56
.10E-02	9.90	0.60	90.16
.91E-03	10.10	0.69	90.85
.79E-03	10.30	0.65	91.49
.69E-03	10.50	0.62	92.11
.60E-03	10.70	0.63	92.75
.52E-03	10.90	0.50	93.24
.24E-03	12.00	6.76	100.00

GRAIN SIZE BREAKDOWN

% GRAVEL	% SAND	% SILT	% CLAY	% MUD
0.13	61.69	22.43	15.75	38.18

STATISTICAL MEASURES

MEAN (PHI)	STANDARD DEVIATION (PHI)	KURTOSIS (NO DIM.)	SKEWNESS (NO DIM.)
4.58	3.09	3.21	1.16

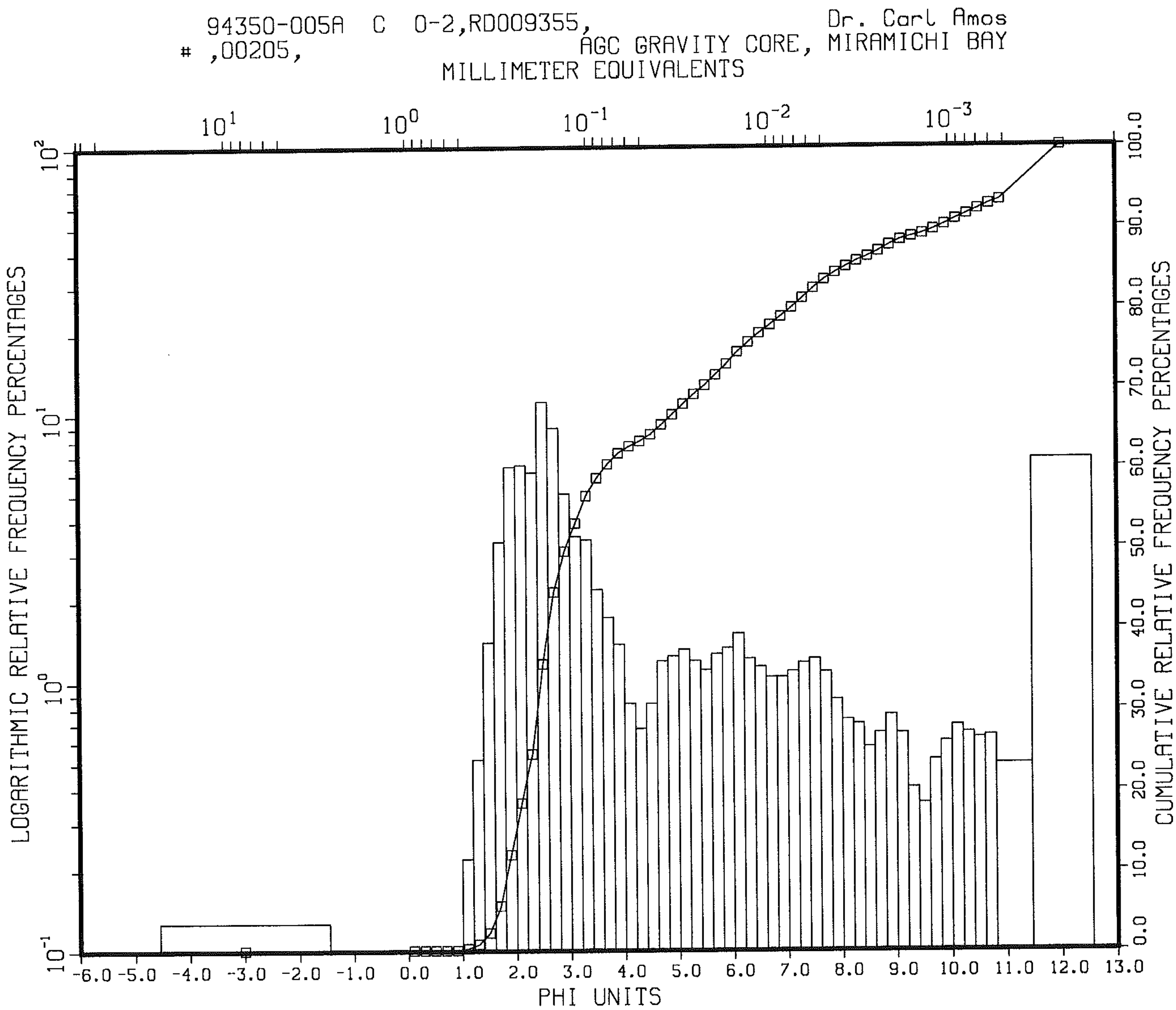
94350-005A C 0-2,RD009355,
,00205,
Dr. Carl Amos
AGC GRAVITY CORE, MIRAMICHI BAY
MILLIMETER EQUIVALENTS
LOGARITHMIC RELATIVE FREQUENCY PERCENTAGES
CUMULATIVE RELATIVE FREQUENCY PERCENTAGES
PHI UNITS

CALCULATION RESULTS FOR
THE SAMPLE WITH THE IDENTIFIER:

94350-006A C 0-2,RD009356, Dr. Carl Amos
,00205, AGC GRAVITY CORE, MIRAMICHI BAY

RESULTS

MIDPOINTS MM	PHI	RELATIVE FREQUENCY PERCENTAGES	CUMULATIVE FREQUENCY PERCENTAGES
8.0	-3.00	11.30	11.30
.93	0.10	0.01	11.31
.81	0.30	0.37	11.67
.71	0.50	1.06	12.73
.62	0.70	1.77	14.50
.54	0.90	1.95	16.45
.47	1.10	2.09	18.54
.41	1.30	2.70	21.24
.35	1.50	3.05	24.29
.31	1.70	3.54	27.83
.27	1.90	4.06	31.88
.23	2.10	3.71	35.60
.20	2.30	5.40	41.00
.18	2.50	5.51	46.51
.15	2.70	3.75	50.25
.13	2.90	3.29	53.54
.12	3.10	2.95	56.49
.10	3.30	2.27	58.76
.88E-01	3.50	2.09	60.85
.77E-01	3.70	1.71	62.56
.67E-01	3.90	1.40	63.95
.58E-01	4.10	0.97	64.92
.51E-01	4.30	1.03	65.95
.44E-01	4.50	0.97	66.92
.38E-01	4.70	1.21	68.13
.33E-01	4.90	1.18	69.31
.29E-01	5.10	1.39	70.70
.25E-01	5.30	1.27	71.97
.22E-01	5.50	1.28	73.24
.19E-01	5.70	1.32	74.56
.17E-01	5.90	1.04	75.60
.15E-01	6.10	0.94	76.54
.13E-01	6.30	0.91	77.45
.11E-01	6.50	0.87	78.32
.96E-02	6.70	0.90	79.21
.84E-02	6.90	0.88	80.09
.73E-02	7.10	0.73	80.82
.63E-02	7.30	0.78	81.60
.55E-02	7.50	0.89	82.48
.48E-02	7.70	0.76	83.24

.42E-02	7.90	0.75	84.00
.36E-02	8.10	0.79	84.79
.32E-02	8.30	0.69	85.48
.28E-02	8.50	0.56	86.04
.24E-02	8.70	0.50	86.54
.21E-02	8.90	0.60	87.14
.18E-02	9.10	0.54	87.67
.16E-02	9.30	0.53	88.20
.14E-02	9.50	0.42	88.62
.12E-02	9.70	0.41	89.03
.10E-02	9.90	0.51	89.54
.91E-03	10.10	0.64	90.19
.79E-03	10.30	0.59	90.78
.69E-03	10.50	0.59	91.37
.60E-03	10.70	0.82	92.18
.52E-03	10.90	0.66	92.84
.24E-03	12.00	7.16	100.00

GRAIN SIZE BREAKDOWN

% GRAVEL	% SAND	% SILT	% CLAY	% MUD
11.30	52.66	20.04	16.00	36.05

STATISTICAL MEASURES

MEAN (PHI)	STANDARD DEVIATION (PHI)	KURTOSIS (NO DIM.)	SKEWNESS (NO DIM.)
3.70	3.97	2.83	0.41

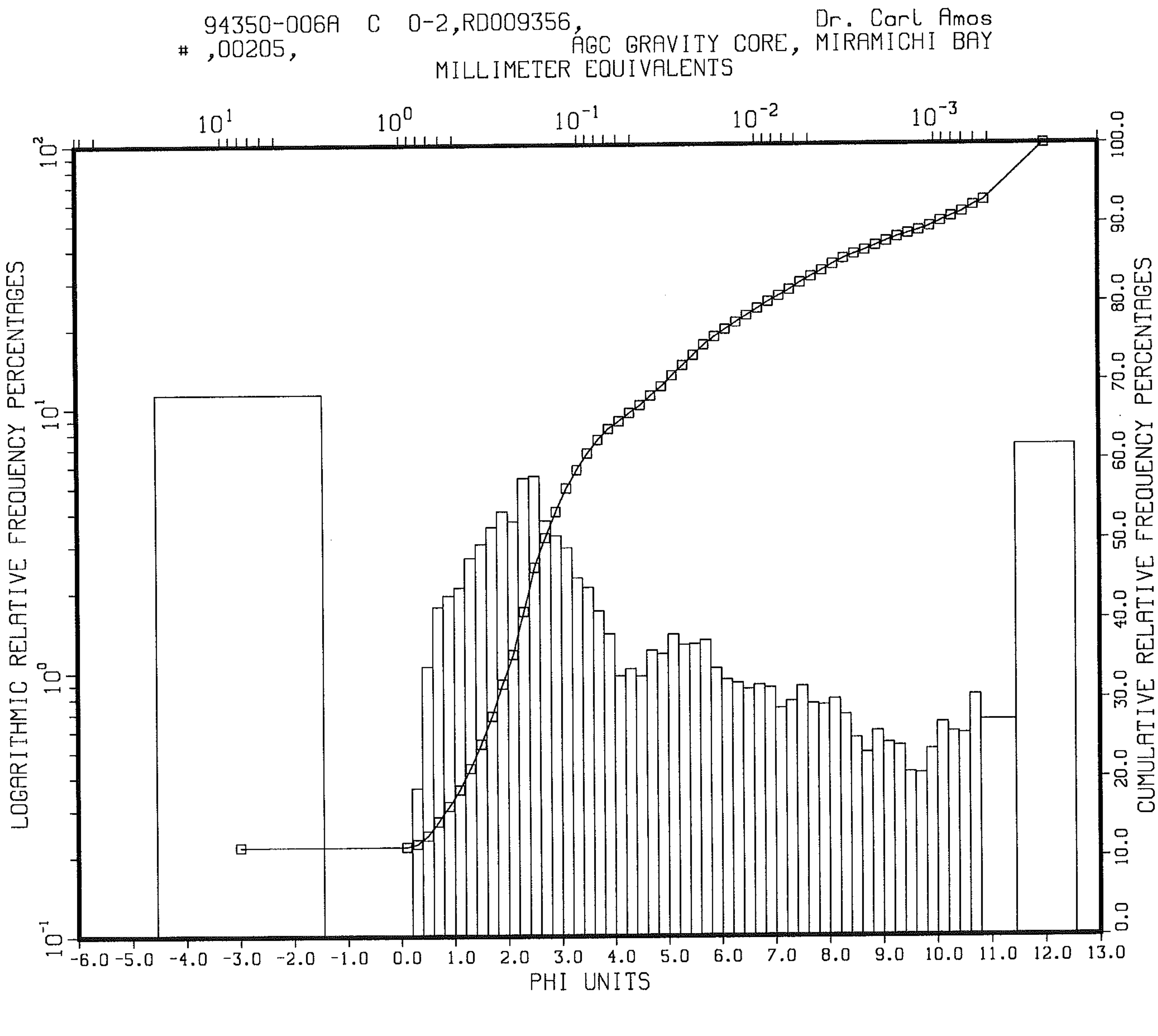

94350-006A C 0-2,RD009356,
,00205,
Dr. Carl Amos
AGC GRAVITY CORE, MIRAMICHI BAY
MILLIMETER EQUIVALENTS
LOGARITHMIC RELATIVE FREQUENCY PERCENTAGES
CUMULATIVE RELATIVE FREQUENCY PERCENTAGES
PHI UNITS

CALCULATION RESULTS FOR
THE SAMPLE WITH THE IDENTIFIER:

94350-006B C 0-4 ,RD009357, Dr. Carl Amos
,00205, AGC GRAVITY CORE, MIRAMICHI BAY

RESULTS

MIDPOINTS MM	PHI	RELATIVE FREQUENCY PERCENTAGES	CUMULATIVE FREQUENCY PERCENTAGES
8.0	-3.00	4.68	4.68
.93	0.10	0.01	4.69
.81	0.30	0.06	4.75
.71	0.50	0.20	4.95
.62	0.70	0.99	5.93
.54	0.90	1.52	7.45
.47	1.10	2.20	9.65
.41	1.30	3.25	12.91
.35	1.50	4.16	17.07
.31	1.70	3.89	20.96
.27	1.90	2.98	23.94
.23	2.10	2.41	26.35
.20	2.30	3.07	29.41
.18	2.50	3.41	32.82
.15	2.70	2.67	35.50
.13	2.90	2.18	37.68
.12	3.10	2.58	40.25
.10	3.30	2.66	42.91
.88E-01	3.50	1.81	44.72
.77E-01	3.70	1.59	46.31
.67E-01	3.90	1.19	47.50
.58E-01	4.10	0.68	48.19
.51E-01	4.30	0.50	48.69
.44E-01	4.50	0.82	49.51
.38E-01	4.70	1.36	50.87
.33E-01	4.90	1.51	52.38
.29E-01	5.10	1.90	54.29
.25E-01	5.30	1.65	55.94
.22E-01	5.50	1.55	57.49
.19E-01	5.70	1.51	59.00
.17E-01	5.90	1.60	60.60
.15E-01	6.10	1.72	62.32
.13E-01	6.30	2.02	64.34
.11E-01	6.50	1.82	66.17
.96E-02	6.70	1.53	67.70
.84E-02	6.90	1.35	69.05
.73E-02	7.10	1.32	70.37
.63E-02	7.30	1.29	71.66
.55E-02	7.50	1.40	73.06
.48E-02	7.70	1.52	74.58

.42E-02	7.90	1.39	75.97
.36E-02	8.10	1.26	77.23
.32E-02	8.30	1.14	78.37
.28E-02	8.50	1.13	79.50
.24E-02	8.70	0.88	80.39
.21E-02	8.90	0.74	81.12
.18E-02	9.10	0.56	81.68
.16E-02	9.30	0.74	82.43
.14E-02	9.50	0.81	83.23
.12E-02	9.70	0.83	84.06
.10E-02	9.90	0.80	84.86
.91E-03	10.10	0.95	85.81
.79E-03	10.30	0.92	86.73
.69E-03	10.50	0.99	87.72
.60E-03	10.70	0.95	88.68
.52E-03	10.90	0.77	89.44
.24E-03	12.00	10.56	100.00

GRAIN SIZE BREAKDOWN

% GRAVEL	% SAND	% SILT	% CLAY	% MUD
4.68	42.82	28.47	24.03	52.50

STATISTICAL MEASURES

MEAN (PHI)	STANDARD DEVIATION (PHI)	KURTOSIS (NO DIM.)	SKEWNESS (NO DIM.)
5.09	3.90	2.37	0.19

94350-006B C 0-4 ,RD009357,
,00205,

Dr. Carl Amos
AGC GRAVITY CORE, MIRAMICHI BAY

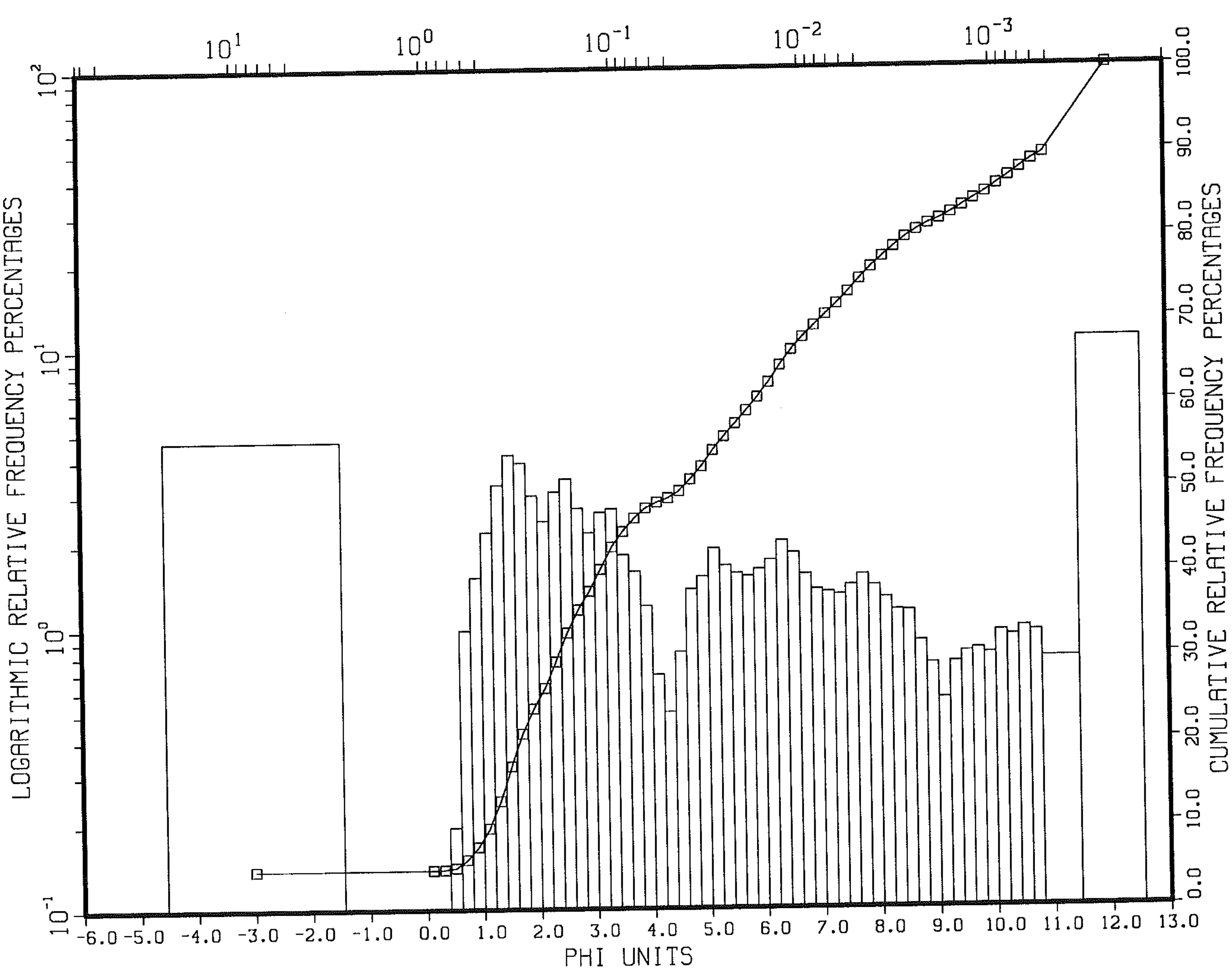

CALCULATION RESULTS FOR
THE SAMPLE WITH THE IDENTIFIER:

94350-007A C 0-2 ,RD009358, Dr. Carl Amos
,00205, AGC GRAVITY CORE, MIRAMICHI BAY

RESULTS

MIDPOINTS MM	PHI	RELATIVE FREQUENCY PERCENTAGES	CUMULATIVE FREQUENCY PERCENTAGES
8.0	-3.00	0.04	0.04
.93	0.10	0.00	0.04
.81	0.30	0.00	0.04
.71	0.50	0.01	0.05
.62	0.70	0.02	0.08
.54	0.90	0.11	0.18
.47	1.10	0.07	0.26
.41	1.30	0.15	0.41
.35	1.50	0.24	0.65
.31	1.70	0.27	0.91
.27	1.90	0.25	1.17
.23	2.10	0.22	1.39
.20	2.30	0.20	1.59
.18	2.50	0.21	1.80
.15	2.70	0.24	2.03
.13	2.90	0.36	2.40
.12	3.10	0.93	3.33
.10	3.30	3.03	6.35
.88E-01	3.50	4.53	10.88
.77E-01	3.70	2.82	13.71
.67E-01	3.90	2.00	15.70
.58E-01	4.10	1.56	17.26
.51E-01	4.30	1.76	19.02
.44E-01	4.50	1.34	20.36
.38E-01	4.70	1.53	21.89
.33E-01	4.90	1.67	23.56
.29E-01	5.10	2.39	25.94
.25E-01	5.30	2.43	28.37
.22E-01	5.50	2.71	31.08
.19E-01	5.70	3.26	34.34
.17E-01	5.90	3.05	37.39
.15E-01	6.10	3.35	40.75
.13E-01	6.30	2.82	43.57
.11E-01	6.50	2.54	46.11
.96E-02	6.70	2.51	48.62
.84E-02	6.90	2.19	50.81
.73E-02	7.10	2.32	53.13
.63E-02	7.30	2.45	55.58
.55E-02	7.50	2.33	57.91
.48E-02	7.70	2.33	60.23

.42E-02	7.90	2.44	62.67
.36E-02	8.10	1.92	64.59
.32E-02	8.30	1.40	65.99
.28E-02	8.50	1.29	67.28
.24E-02	8.70	1.40	68.68
.21E-02	8.90	1.81	70.49
.18E-02	9.10	1.52	72.01
.16E-02	9.30	1.20	73.21
.14E-02	9.50	0.86	74.07
.12E-02	9.70	0.95	75.02
.10E-02	9.90	1.10	76.12
.91E-03	10.10	1.46	77.58
.79E-03	10.30	1.66	79.24
.69E-03	10.50	1.80	81.03
.60E-03	10.70	1.78	82.81
.52E-03	10.90	1.26	84.08
.24E-03	12.00	15.92	100.00

GRAIN SIZE BREAKDOWN

% GRAVEL	% SAND	% SILT	% CLAY	% MUD
0.04	15.66	46.97	37.33	84.30

STATISTICAL MEASURES

MEAN (PHI)	STANDARD DEVIATION (PHI)	KURTOSIS (NO DIM.)	SKEWNESS (NO DIM.)
7.33	2.92	2.01	0.21

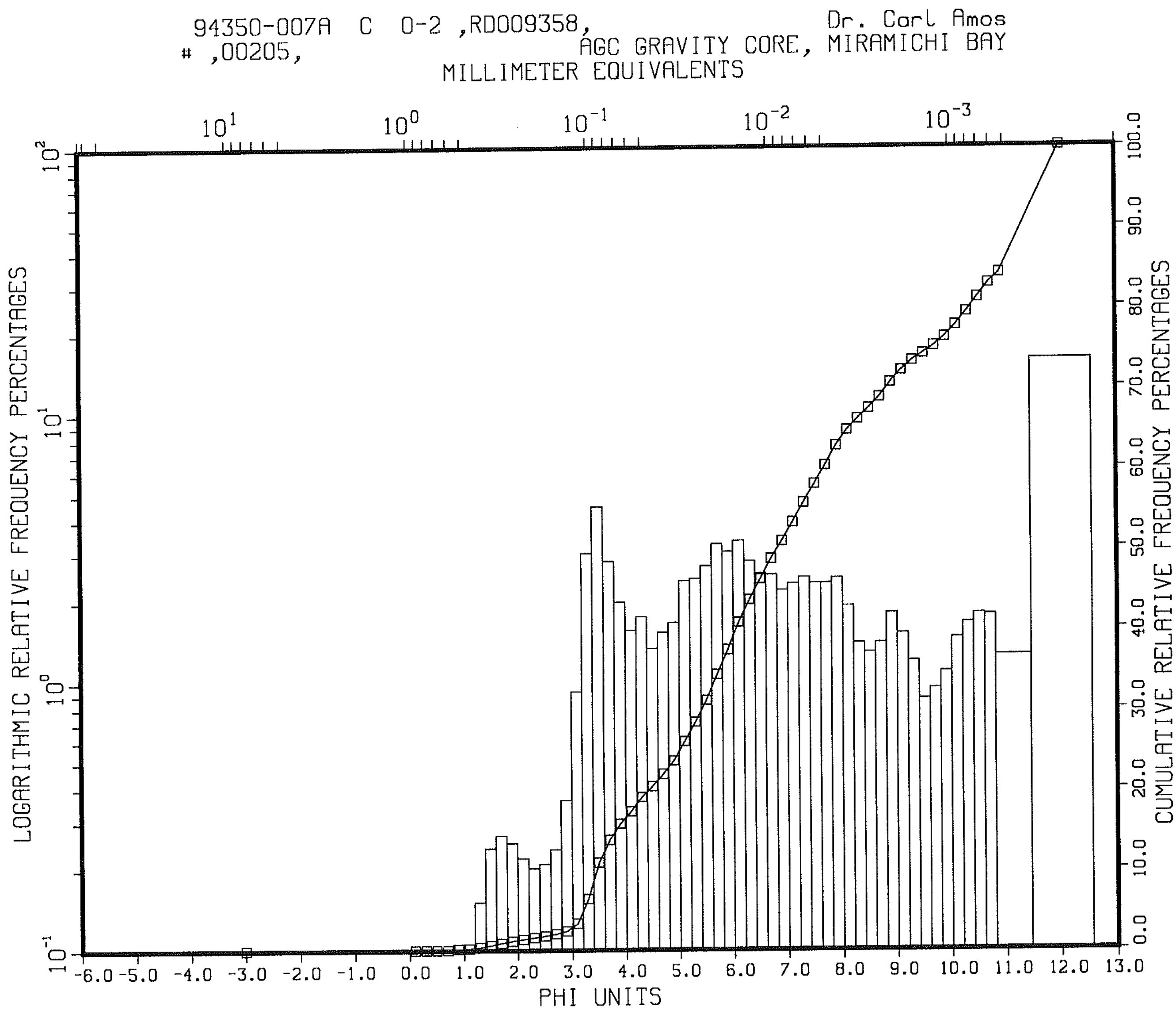

94350-007A C 0-2 ,RD009358,
,00205,
Dr. Carl Amos
AGC GRAVITY CORE, MIRAMICHI BAY
MILLIMETER EQUIVALENTS
10^1 10^0 10^-1 10^-2 10^-3
LOGARITHMIC RELATIVE FREQUENCY PERCENTAGES
10^2 10^1 10^0 10^-1
CUMULATIVE RELATIVE FREQUENCY PERCENTAGES
100.0 90.0 80.0 70.0 60.0 50.0 40.0 30.0 20.0 10.0 0.0
-6.0 -5.0 -4.0 -3.0 -2.0 -1.0 0.0 1.0 2.0 3.0 4.0 5.0 6.0 7.0 8.0 9.0 10.0 11.0 12.0 13.0
PHI UNITS

CALCULATION RESULTS FOR
THE SAMPLE WITH THE IDENTIFIER:

94350-008A C 0-2 ,RD009359, Dr. Carl Amos
,00205, AGC GRAVITY CORE, MIRAMICHI BAY

RESULTS

MIDPOINTS MM	PHI	RELATIVE FREQUENCY PERCENTAGES	CUMULATIVE FREQUENCY PERCENTAGES
8.0	-3.00	0.00	0.00
.93	0.10	0.00	0.00
.81	0.30	0.00	0.00
.71	0.50	0.00	0.00
.62	0.70	0.00	0.00
.54	0.90	0.00	0.00
.47	1.10	0.01	0.01
.41	1.30	0.03	0.04
.35	1.50	0.08	0.12
.31	1.70	0.07	0.19
.27	1.90	0.10	0.29
.23	2.10	0.12	0.41
.20	2.30	0.18	0.59
.18	2.50	0.42	1.01
.15	2.70	0.81	1.82
.13	2.90	1.14	2.96
.12	3.10	1.71	4.67
.10	3.30	3.23	7.90
.88E-01	3.50	3.66	11.55
.77E-01	3.70	2.04	13.59
.67E-01	3.90	1.55	15.14
.58E-01	4.10	1.38	16.53
.51E-01	4.30	1.41	17.94
.44E-01	4.50	1.03	18.97
.38E-01	4.70	1.49	20.47
.33E-01	4.90	1.66	22.12
.29E-01	5.10	2.39	24.51
.25E-01	5.30	2.90	27.42
.22E-01	5.50	2.68	30.09
.19E-01	5.70	2.77	32.86
.17E-01	5.90	3.05	35.90
.15E-01	6.10	3.63	39.53
.13E-01	6.30	2.47	42.00
.11E-01	6.50	2.45	44.45
.96E-02	6.70	2.60	47.05
.84E-02	6.90	3.00	50.05
.73E-02	7.10	2.61	52.66
.63E-02	7.30	2.30	54.96
.55E-02	7.50	2.60	57.56
.48E-02	7.70	2.34	59.90

.42E-02	7.90	1.83	61.73
.36E-02	8.10	1.31	63.04
.32E-02	8.30	1.31	64.35
.28E-02	8.50	1.58	65.93
.24E-02	8.70	1.47	67.41
.21E-02	8.90	1.52	68.92
.18E-02	9.10	1.36	70.28
.16E-02	9.30	1.23	71.51
.14E-02	9.50	1.30	72.81
.12E-02	9.70	1.40	74.22
.10E-02	9.90	1.28	75.50
.91E-03	10.10	1.29	76.79
.79E-03	10.30	1.27	78.07
.69E-03	10.50	1.56	79.63
.60E-03	10.70	1.76	81.39
.52E-03	10.90	1.96	83.35
.24E-03	12.00	16.65	100.00

GRAIN SIZE BREAKDOWN

% GRAVEL	% SAND	% SILT	% CLAY	% MUD
0.00	15.14	46.59	38.27	84.86

STATISTICAL MEASURES

MEAN (PHI)	STANDARD DEVIATION (PHI)	KURTOSIS (NO DIM.)	SKEWNESS (NO DIM.)
7.43	2.91	1.90	0.21

94350-008A C 0-2 ,RD009359, # ,00205,

Dr. Carl Amos

AGC GRAVITY CORE, MIRAMICHI BAY

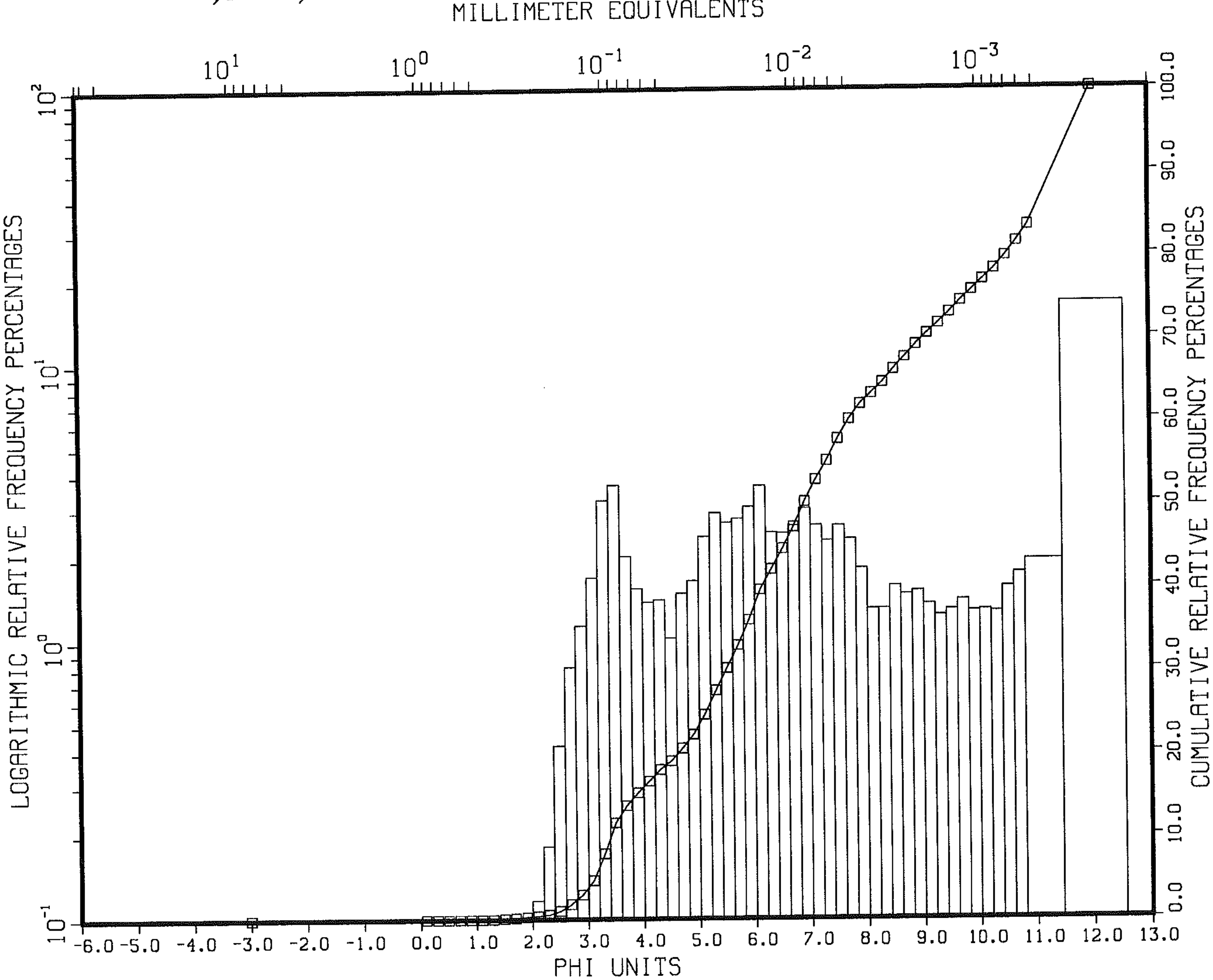

CALCULATION RESULTS FOR
THE SAMPLE WITH THE IDENTIFIER:

94350-009A C 0-2 ,RD009360, Dr. Carl Amos
,00205, AGC GRAVITY CORE, MIRAMICHI BAY

RESULTS

MIDPOINTS MM	PHI	RELATIVE FREQUENCY PERCENTAGES	CUMULATIVE FREQUENCY PERCENTAGES
8.0	-3.00	0.07	0.07
.93	0.10	0.00	0.07
.81	0.30	0.00	0.07
.71	0.50	0.00	0.07
.62	0.70	0.09	0.16
.54	0.90	0.12	0.27
.47	1.10	0.17	0.44
.41	1.30	0.32	0.76
.35	1.50	0.49	1.25
.31	1.70	0.46	1.71
.27	1.90	0.43	2.15
.23	2.10	0.56	2.71
.20	2.30	0.77	3.48
.18	2.50	1.34	4.81
.15	2.70	1.98	6.79
.13	2.90	3.25	10.04
.12	3.10	5.58	15.62
.10	3.30	4.43	20.05
.88E-01	3.50	3.52	23.58
.77E-01	3.70	3.20	26.77
.67E-01	3.90	2.13	28.90
.58E-01	4.10	1.29	30.20
.51E-01	4.30	1.00	31.19
.44E-01	4.50	1.30	32.49
.38E-01	4.70	2.45	34.94
.33E-01	4.90	2.52	37.46
.29E-01	5.10	3.26	40.71
.25E-01	5.30	2.81	43.53
.22E-01	5.50	2.67	46.19
.19E-01	5.70	2.37	48.56
.17E-01	5.90	2.25	50.82
.15E-01	6.10	2.39	53.21
.13E-01	6.30	2.05	55.26
.11E-01	6.50	2.44	57.70
.96E-02	6.70	1.97	59.68
.84E-02	6.90	1.99	61.67
.73E-02	7.10	1.82	63.49
.63E-02	7.30	2.13	65.61
.55E-02	7.50	2.09	67.70
.48E-02	7.70	2.17	69.88

.42E-02	7.90	1.71	71.59
.36E-02	8.10	1.48	73.07
.32E-02	8.30	1.29	74.36
.28E-02	8.50	1.16	75.52
.24E-02	8.70	1.04	76.56
.21E-02	8.90	1.04	77.60
.18E-02	9.10	1.24	78.83
.16E-02	9.30	1.01	79.85
.14E-02	9.50	0.69	80.54
.12E-02	9.70	0.61	81.14
.10E-02	9.90	0.73	81.88
.91E-03	10.10	1.08	82.96
.79E-03	10.30	1.35	84.31
.69E-03	10.50	1.39	85.69
.60E-03	10.70	1.37	87.07
.52E-03	10.90	1.44	88.51
.24E-03	12.00	11.49	100.00

GRAIN SIZE BREAKDOWN

% GRAVEL	% SAND	% SILT	% CLAY	% MUD
0.07	28.84	42.68	28.41	71.10

STATISTICAL MEASURES

MEAN (PHI)	STANDARD DEVIATION (PHI)	KURTOSIS (NO DIM.)	SKEWNESS (NO DIM.)
6.44	3.05	2.15	0.44

94350-009A C 0-2 ,RD009360, Dr. Carl Amos
,00205, AGC GRAVITY CORE, MIRAMICHI BAY

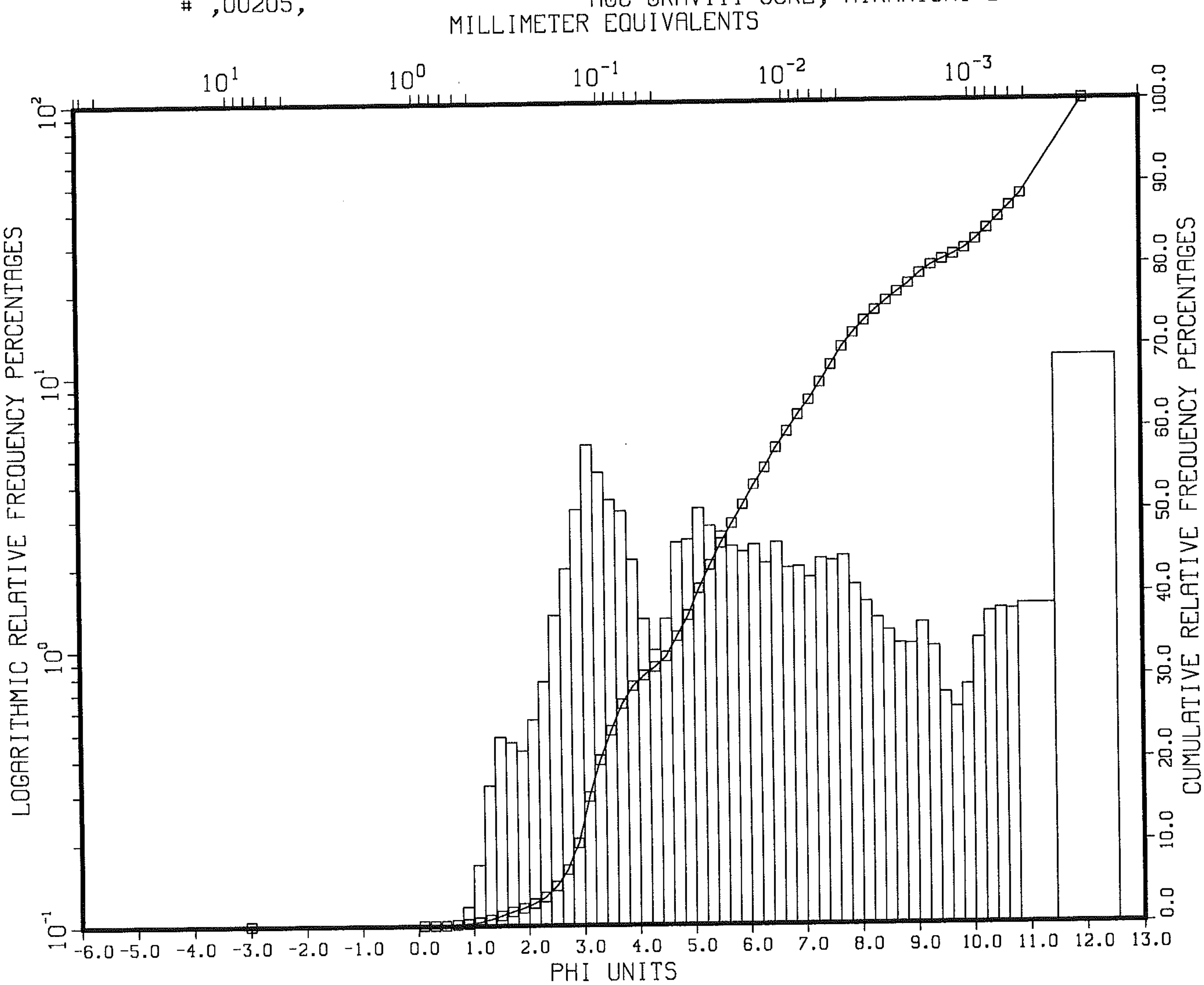

CALCULATION RESULTS FOR
THE SAMPLE WITH THE IDENTIFIER:

94350-010A C 0-2 ,RD009361, Dr. Carl Amos
,00205, AGC GRAVITY CORE, MIRAMICHI BAY

RESULTS

MIDPOINTS MM	PHI	RELATIVE FREQUENCY PERCENTAGES	CUMULATIVE FREQUENCY PERCENTAGES
8.0	-3.00	0.16	0.16
.93	0.10	0.00	0.16
.81	0.30	0.00	0.16
.71	0.50	0.00	0.16
.62	0.70	0.00	0.16
.54	0.90	0.01	0.16
.47	1.10	0.07	0.23
.41	1.30	0.16	0.39
.35	1.50	0.26	0.65
.31	1.70	0.31	0.97
.27	1.90	0.33	1.30
.23	2.10	0.58	1.87
.20	2.30	0.78	2.65
.18	2.50	1.05	3.70
.15	2.70	1.67	5.37
.13	2.90	2.48	7.85
.12	3.10	4.49	12.34
.10	3.30	5.16	17.50
.88E-01	3.50	4.91	22.41
.77E-01	3.70	2.79	25.20
.67E-01	3.90	2.34	27.54
.58E-01	4.10	1.62	29.16
.51E-01	4.30	1.94	31.10
.44E-01	4.50	1.94	33.04
.38E-01	4.70	2.62	35.66
.33E-01	4.90	2.53	38.20
.29E-01	5.10	2.56	40.76
.25E-01	5.30	2.94	43.70
.22E-01	5.50	2.83	46.53
.19E-01	5.70	2.54	49.07
.17E-01	5.90	2.66	51.73
.15E-01	6.10	2.54	54.27
.13E-01	6.30	2.37	56.64
.11E-01	6.50	2.16	58.81
.96E-02	6.70	2.17	60.98
.84E-02	6.90	2.01	62.99
.73E-02	7.10	1.90	64.90
.63E-02	7.30	1.77	66.66
.55E-02	7.50	1.76	68.42
.48E-02	7.70	2.00	70.42

.42E-02	7.90	1.81	72.23
.36E-02	8.10	1.53	73.76
.32E-02	8.30	1.41	75.17
.28E-02	8.50	0.93	76.10
.24E-02	8.70	0.81	76.91
.21E-02	8.90	0.94	77.85
.18E-02	9.10	1.05	78.90
.16E-02	9.30	1.01	79.91
.14E-02	9.50	1.02	80.93
.12E-02	9.70	1.11	82.04
.10E-02	9.90	1.17	83.22
.91E-03	10.10	1.27	84.49
.79E-03	10.30	1.42	85.91
.69E-03	10.50	1.74	87.65
.60E-03	10.70	1.95	89.61
.52E-03	10.90	1.44	91.05
.24E-03	12.00	8.95	100.00

GRAIN SIZE BREAKDOWN

% GRAVEL	% SAND	% SILT	% CLAY	% MUD
0.16	27.39	44.68	27.77	72.46

STATISTICAL MEASURES

MEAN (PHI)	STANDARD DEVIATION (PHI)	KURTOSIS (NO DIM.)	SKEWNESS (NO DIM.)
6.40	2.93	2.26	0.45

94350-010A C 0-2 ,RD009361, Dr. Carl Amos
,00205, AGC GRAVITY CORE, MIRAMICHI BAY

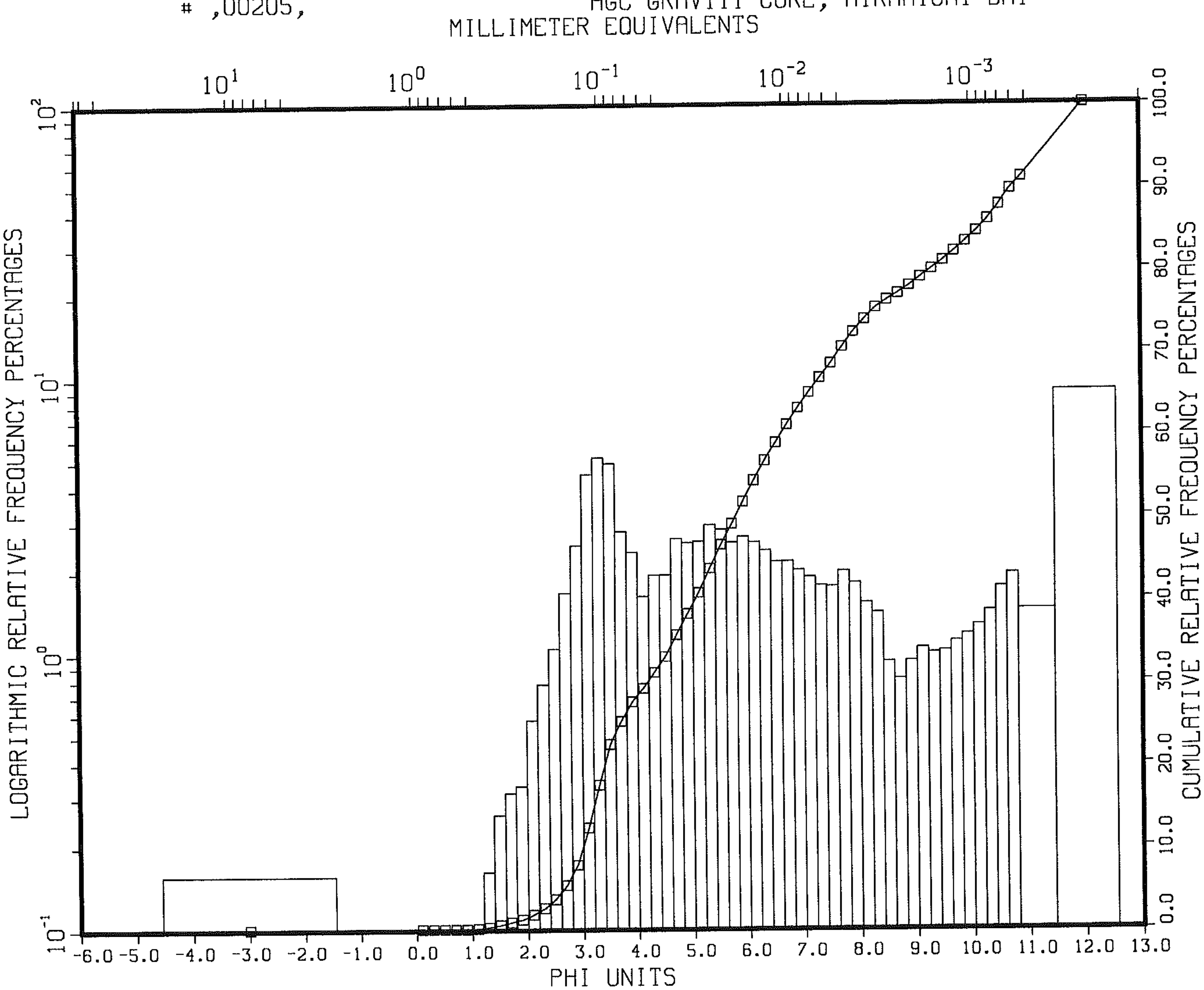

CALCULATION RESULTS FOR
THE SAMPLE WITH THE IDENTIFIER:

94350-011A C 0-2 ,RD009362, Dr. Carl Amos
,00205, AGC GRAVITY CORE, MIRAMICHI BAY

RESULTS

MIDPOINTS MM	PHI	RELATIVE FREQUENCY PERCENTAGES	CUMULATIVE FREQUENCY PERCENTAGES
8.0	-3.00	0.72	0.72
.93	0.10	0.00	0.72
.81	0.30	0.01	0.73
.71	0.50	0.00	0.73
.62	0.70	0.04	0.77
.54	0.90	0.06	0.83
.47	1.10	0.13	0.96
.41	1.30	0.20	1.16
.35	1.50	0.24	1.40
.31	1.70	0.26	1.66
.27	1.90	0.23	1.89
.23	2.10	0.17	2.06
.20	2.30	0.15	2.21
.18	2.50	0.14	2.35
.15	2.70	0.15	2.50
.13	2.90	0.16	2.67
.12	3.10	0.35	3.01
.10	3.30	1.74	4.75
.88E-01	3.50	2.62	7.37
.77E-01	3.70	1.76	9.13
.67E-01	3.90	1.10	10.22
.58E-01	4.10	1.05	11.28
.51E-01	4.30	1.32	12.60
.44E-01	4.50	1.42	14.02
.38E-01	4.70	1.60	15.62
.33E-01	4.90	2.33	17.94
.29E-01	5.10	2.16	20.10
.25E-01	5.30	2.24	22.34
.22E-01	5.50	2.73	25.07
.19E-01	5.70	3.06	28.13
.17E-01	5.90	3.16	31.29
.15E-01	6.10	2.81	34.10
.13E-01	6.30	3.03	37.13
.11E-01	6.50	2.60	39.72
.96E-02	6.70	2.47	42.19
.84E-02	6.90	2.68	44.88
.73E-02	7.10	2.74	47.62
.63E-02	7.30	2.44	50.06
.55E-02	7.50	2.42	52.49
.48E-02	7.70	2.64	55.12

.42E-02	7.90	2.44	57.56
.36E-02	8.10	2.05	59.61
.32E-02	8.30	1.94	61.55
.28E-02	8.50	1.61	63.16
.24E-02	8.70	1.48	64.64
.21E-02	8.90	1.59	66.23
.18E-02	9.10	1.66	67.90
.16E-02	9.30	1.79	69.69
.14E-02	9.50	1.59	71.28
.12E-02	9.70	1.38	72.66
.10E-02	9.90	1.09	73.75
.91E-03	10.10	1.19	74.94
.79E-03	10.30	1.52	76.46
.69E-03	10.50	1.85	78.31
.60E-03	10.70	2.11	80.42
.52E-03	10.90	1.73	82.14
.24E-03	12.00	17.86	100.00

GRAIN SIZE BREAKDOWN

% GRAVEL	% SAND	% SILT	% CLAY	% MUD
0.72	9.51	47.34	42.44	89.78

STATISTICAL MEASURES

MEAN (PHI)	STANDARD DEVIATION (PHI)	KURTOSIS (NO DIM.)	SKEWNESS (NO DIM.)
7.68	2.95	2.90	-0.20

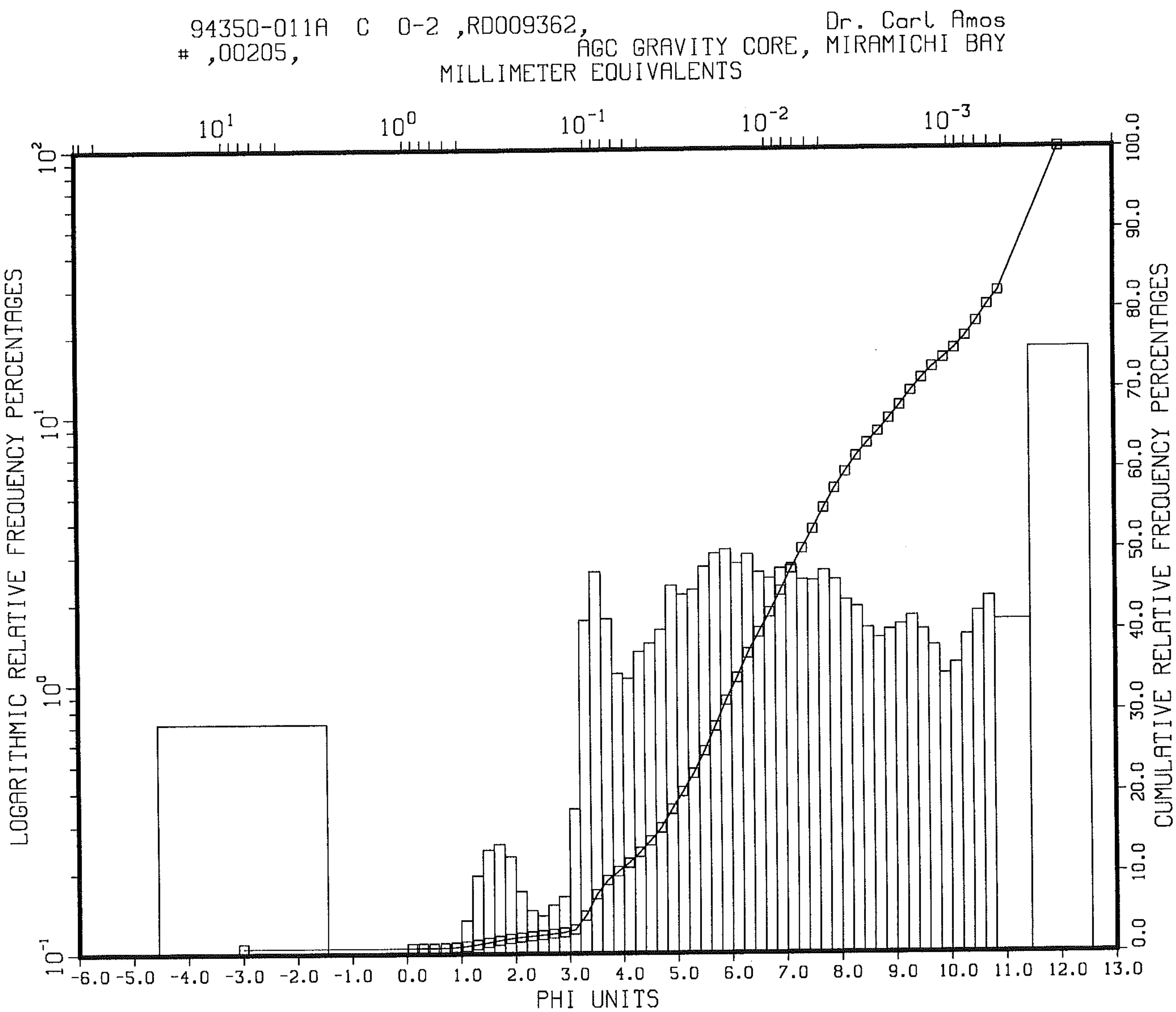
94350-011A C 0-2 ,RD009362,
,00205,
Dr. Carl Amos
AGC GRAVITY CORE, MIRAMICHI BAY
MILLIMETER EQUIVALENTS
LOGARITHMIC RELATIVE FREQUENCY PERCENTAGES
CUMULATIVE RELATIVE FREQUENCY PERCENTAGES
PHI UNITS

CALCULATION RESULTS FOR
THE SAMPLE WITH THE IDENTIFIER:

94350-012A C 0-2 ,RD009363, Dr. Carl Amos
,00205, AGC GRAVITY CORE, MIRAMICHI BAY

RESULTS

MIDPOINTS MM	PHI	RELATIVE FREQUENCY PERCENTAGES	CUMULATIVE FREQUENCY PERCENTAGES
8.0	-3.00	0.16	0.16
.93	0.10	0.00	0.16
.81	0.30	0.00	0.16
.71	0.50	0.00	0.16
.62	0.70	0.00	0.16
.54	0.90	0.00	0.16
.47	1.10	0.06	0.22
.41	1.30	0.32	0.53
.35	1.50	0.45	0.98
.31	1.70	0.62	1.60
.27	1.90	0.63	2.23
.23	2.10	0.75	2.98
.20	2.30	1.18	4.17
.18	2.50	2.34	6.51
.15	2.70	4.09	10.60
.13	2.90	5.00	15.60
.12	3.10	4.96	20.56
.10	3.30	4.85	25.41
.88E-01	3.50	4.21	29.63
.77E-01	3.70	2.89	32.51
.67E-01	3.90	2.17	34.68
.58E-01	4.10	1.21	35.89
.51E-01	4.30	0.86	36.75
.44E-01	4.50	1.74	38.49
.38E-01	4.70	2.03	40.52
.33E-01	4.90	2.16	42.68
.29E-01	5.10	2.47	45.15
.25E-01	5.30	2.42	47.57
.22E-01	5.50	2.62	50.19
.19E-01	5.70	2.99	53.18
.17E-01	5.90	2.68	55.86
.15E-01	6.10	2.81	58.66
.13E-01	6.30	2.32	60.98
.11E-01	6.50	2.25	63.24
.96E-02	6.70	2.10	65.33
.84E-02	6.90	1.86	67.19
.73E-02	7.10	1.62	68.81
.63E-02	7.30	1.51	70.32
.55E-02	7.50	1.64	71.95
.48E-02	7.70	1.49	73.44

.42E-02	7.90	1.36	74.80
.36E-02	8.10	1.16	75.96
.32E-02	8.30	1.10	77.07
.28E-02	8.50	0.84	77.90
.24E-02	8.70	0.68	78.58
.21E-02	8.90	0.72	79.30
.18E-02	9.10	0.91	80.22
.16E-02	9.30	0.74	80.95
.14E-02	9.50	0.65	81.61
.12E-02	9.70	0.88	82.49
.10E-02	9.90	1.13	83.62
.91E-03	10.10	1.20	84.82
.79E-03	10.30	1.06	85.88
.69E-03	10.50	1.10	86.99
.60E-03	10.70	1.15	88.13
.52E-03	10.90	0.82	88.96
.24E-03	12.00	11.04	100.00

GRAIN SIZE BREAKDOWN

% GRAVEL	% SAND	% SILT	% CLAY	% MUD
0.16	34.53	40.12	25.20	65.32

STATISTICAL MEASURES

MEAN (PHI)	STANDARD DEVIATION (PHI)	KURTOSIS (NO DIM.)	SKEWNESS (NO DIM.)
6.11	3.09	2.30	0.57

94350-012A C 0-2 ,RD009363, Dr. Carl Amos
,00205, AGC GRAVITY CORE, MIRAMICHI BAY

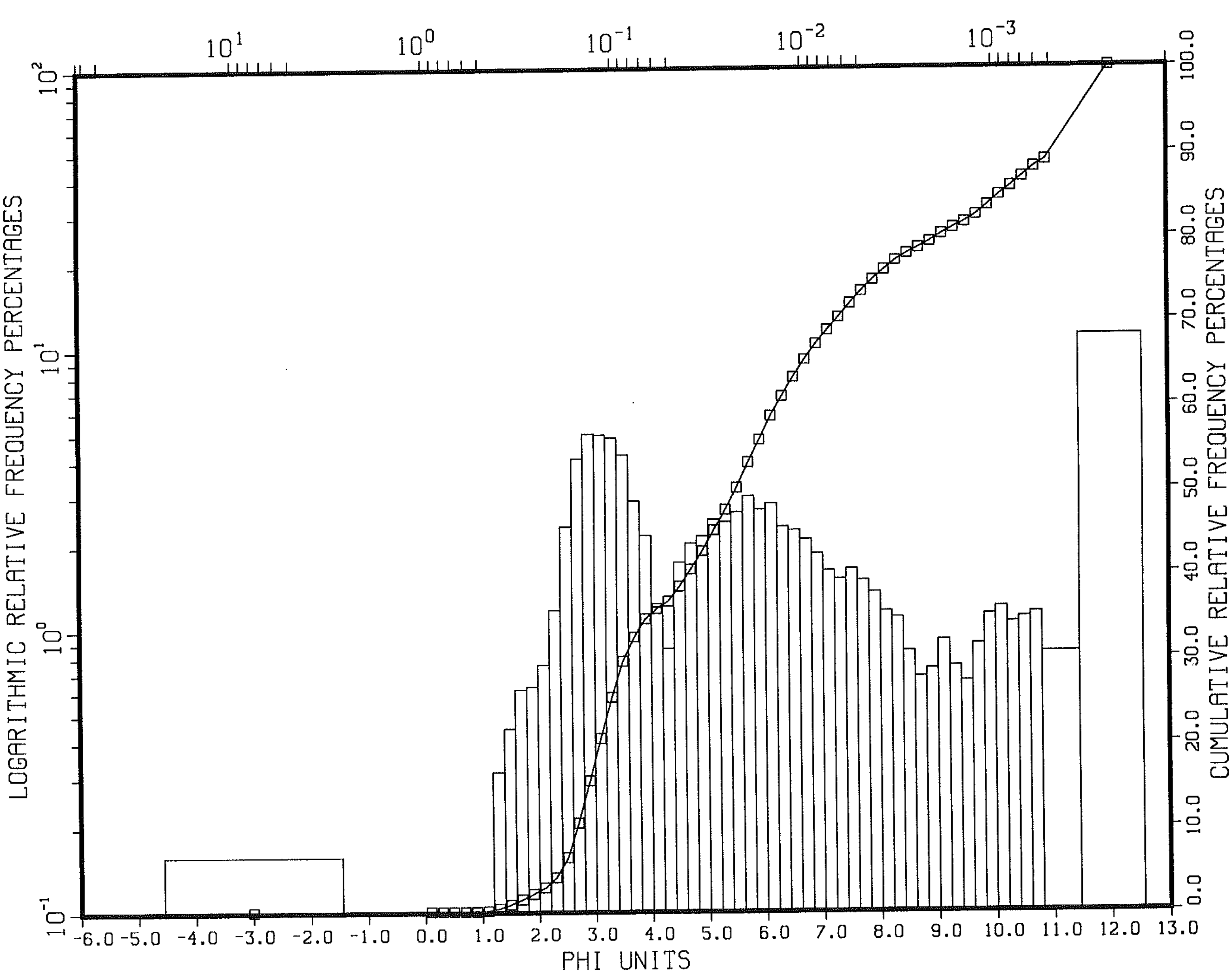

CALCULATION RESULTS FOR
THE SAMPLE WITH THE IDENTIFIER:

94350-013A C 0-2 ,RD009364, Dr. Carl Amos
,00205, AGC GRAVITY CORE, MIRAMICHI BAY

RESULTS

MIDPOINTS MM	MIDPOINTS PHI	RELATIVE FREQUENCY PERCENTAGES	CUMULATIVE FREQUENCY PERCENTAGES
8.0	-3.00	1.97	1.97
.93	0.10	0.00	1.97
.81	0.30	0.09	2.07
.71	0.50	0.11	2.17
.62	0.70	0.10	2.27
.54	0.90	0.21	2.48
.47	1.10	0.46	2.94
.41	1.30	0.61	3.55
.35	1.50	0.82	4.38
.31	1.70	1.14	5.52
.27	1.90	1.33	6.85
.23	2.10	1.85	8.70
.20	2.30	3.02	11.72
.18	2.50	6.51	18.23
.15	2.70	12.03	30.26
.13	2.90	9.11	39.37
.12	3.10	6.07	45.44
.10	3.30	3.43	48.87
.88E-01	3.50	3.25	52.12
.77E-01	3.70	2.58	54.70
.67E-01	3.90	1.84	56.54
.58E-01	4.10	1.72	58.25
.51E-01	4.30	1.27	59.52
.44E-01	4.50	0.95	60.48
.38E-01	4.70	1.22	61.69
.33E-01	4.90	1.43	63.12
.29E-01	5.10	1.60	64.72
.25E-01	5.30	1.58	66.30
.22E-01	5.50	1.76	68.07
.19E-01	5.70	1.86	69.93
.17E-01	5.90	1.74	71.67
.15E-01	6.10	1.59	73.26
.13E-01	6.30	1.49	74.75
.11E-01	6.50	1.33	76.08
.96E-02	6.70	1.12	77.20
.84E-02	6.90	1.22	78.42
.73E-02	7.10	0.95	79.36
.63E-02	7.30	0.87	80.23
.55E-02	7.50	0.81	81.05
.48E-02	7.70	0.86	81.91

.42E-02	7.90	0.68	82.59
.36E-02	8.10	0.70	83.30
.32E-02	8.30	0.75	84.05
.28E-02	8.50	0.76	84.81
.24E-02	8.70	0.67	85.48
.21E-02	8.90	0.61	86.09
.18E-02	9.10	0.58	86.67
.16E-02	9.30	0.43	87.09
.14E-02	9.50	0.37	87.46
.12E-02	9.70	0.42	87.89
.10E-02	9.90	0.60	88.48
.91E-03	10.10	0.77	89.26
.79E-03	10.30	0.72	89.98
.69E-03	10.50	0.68	90.67
.60E-03	10.70	0.66	91.32
.52E-03	10.90	0.48	91.80
.24E-03	12.00	8.20	100.00

GRAIN SIZE BREAKDOWN

% GRAVEL	% SAND	% SILT	% CLAY	% MUD
1.97	54.57	26.05	17.41	43.46

STATISTICAL MEASURES

MEAN (PHI)	STANDARD DEVIATION (PHI)	KURTOSIS (NO DIM.)	SKEWNESS (NO DIM.)
4.83	3.24	3.28	0.77

94350-013A C 0-2 ,RD009364, Dr. Carl Amos
,00205, AGC GRAVITY CORE, MIRAMICHI BAY
MILLIMETER EQUIVALENTS

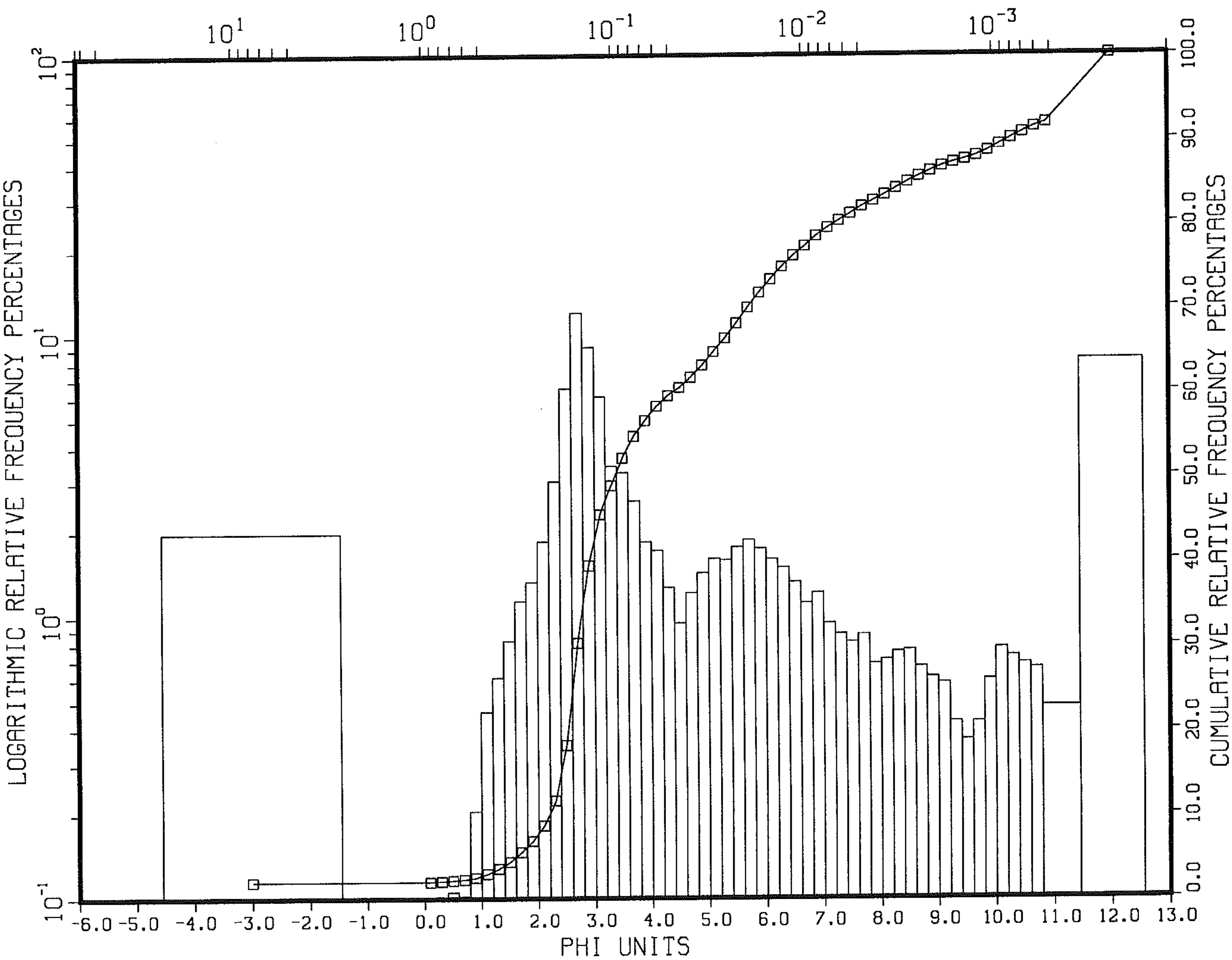

APPENDIX 2

PLOTS OF SHEAR STRENGTH VERSUS DEPTH

MIRAMICHI DUMPSITE GRAVITY CORE ANALYSIS

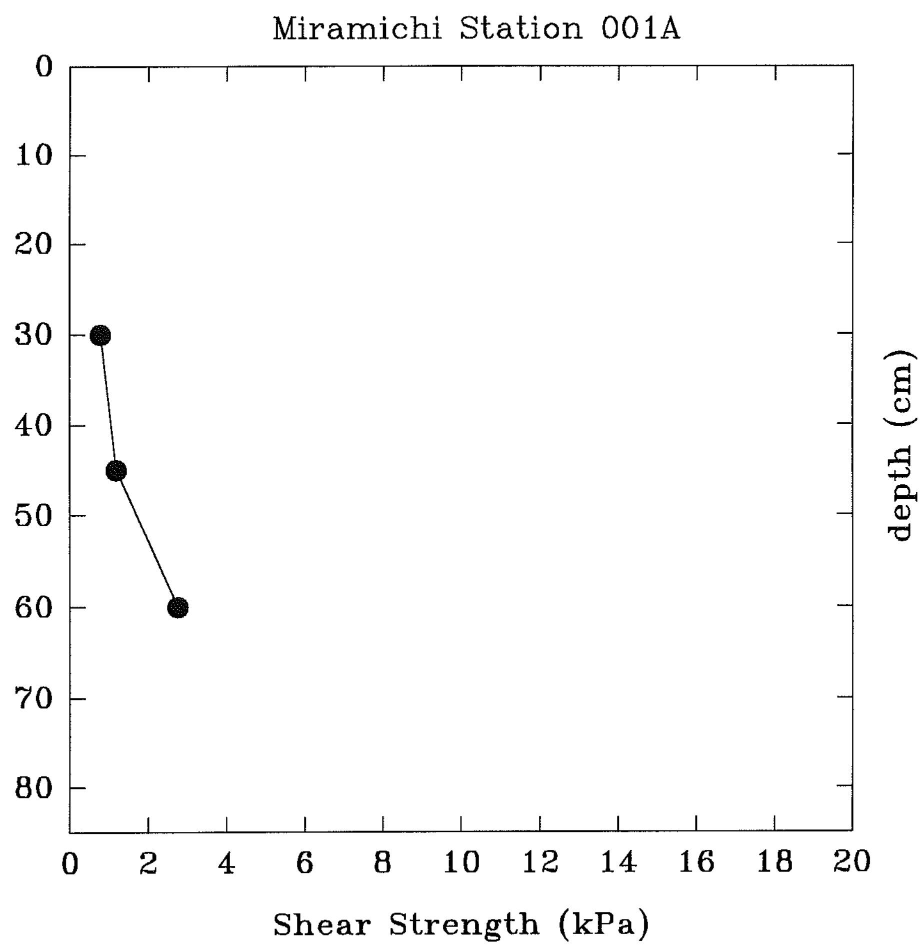

Note: Shear strength measured with the sensitive vane of the Soilotest CL 600 Torvane.

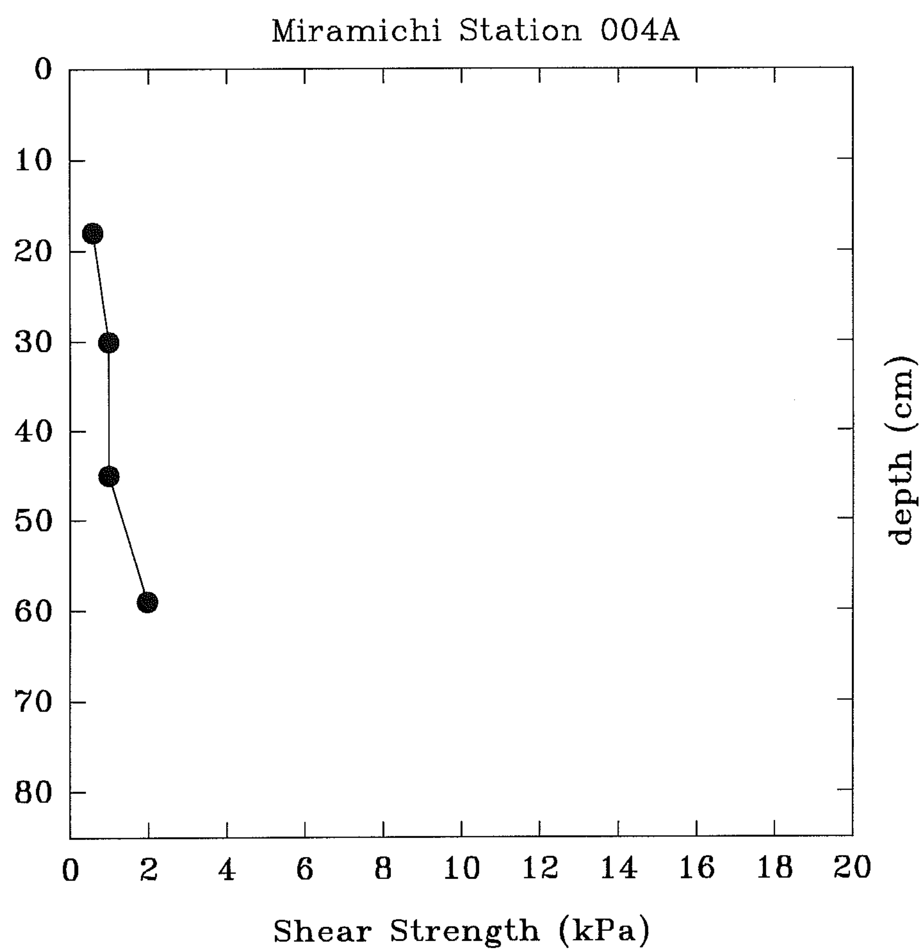

Note: Shear strength measured with the sensitive vane of the Soilotest CL 600 Torvane.

Miramichi Station 05A

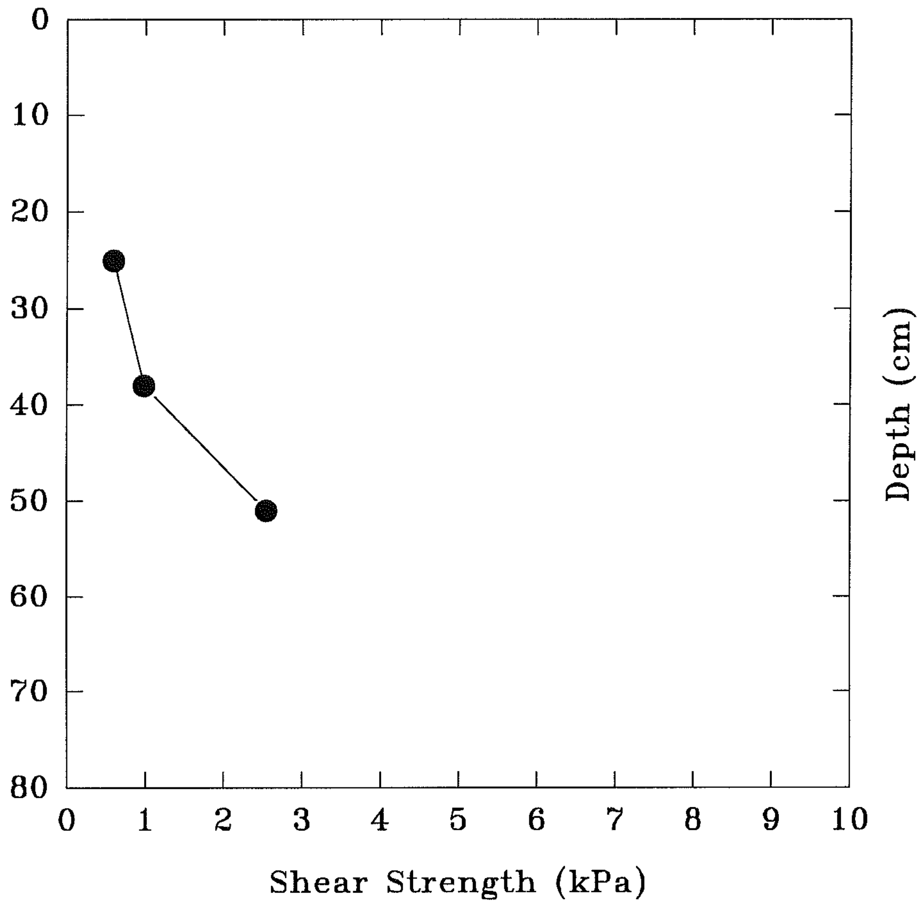

Note: Shear strength measured with the 25mm Controls Penetrometer.

Miramichi Station 006B

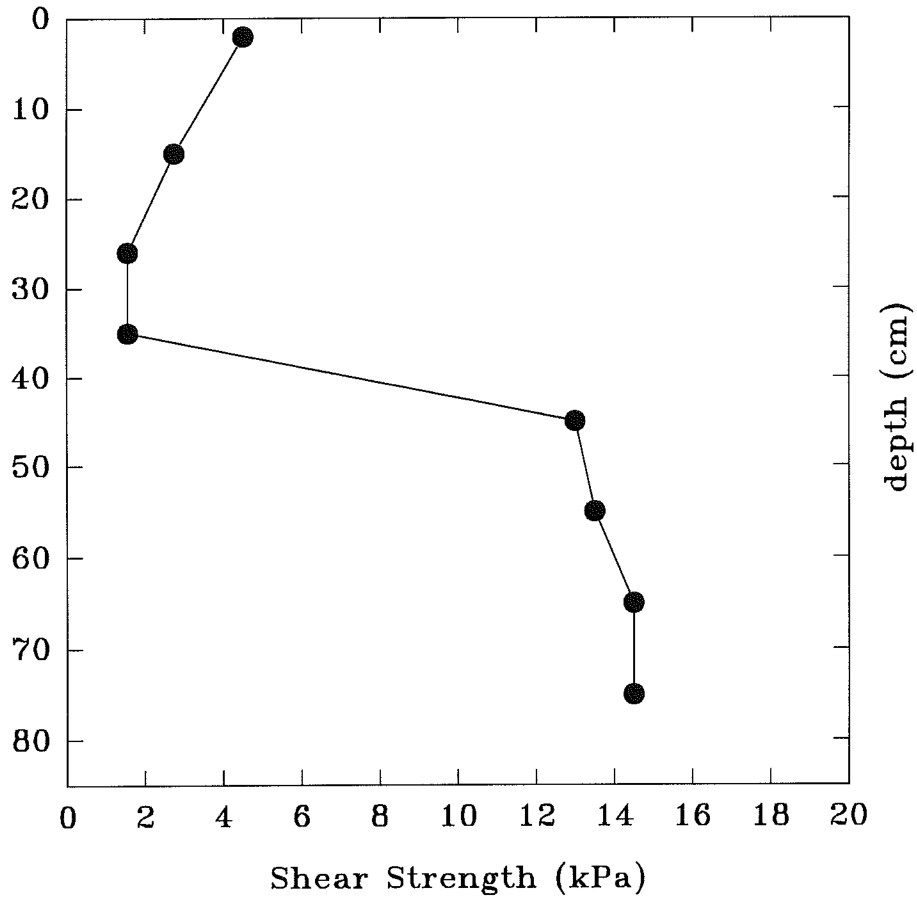

Note: Shear strength measurements for 15 cm, 26 cm, and 35 cm depths were taken with the sensitive vane Soiltest CL 600 Torvane. The remaining measurements were taken with the 25mm Controls Penetrometer.

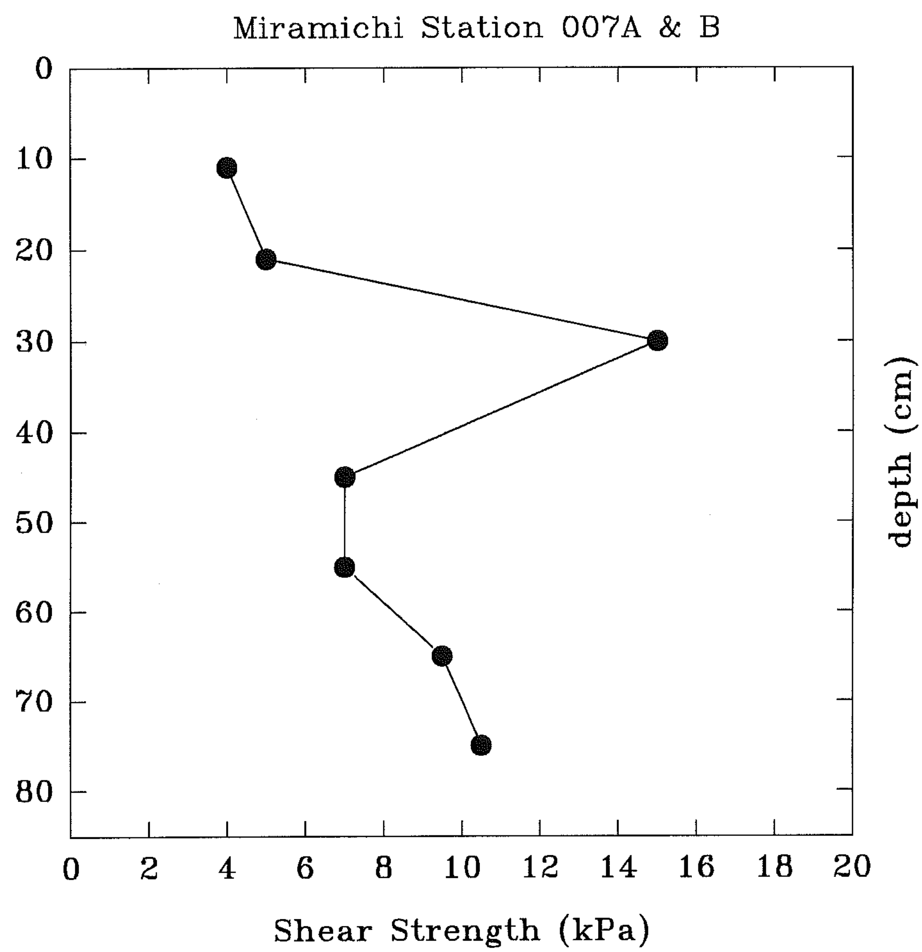

NOte: Shear strength measurements taken with the
25mm Controls Penetrometer.

Miramichi Station 008A

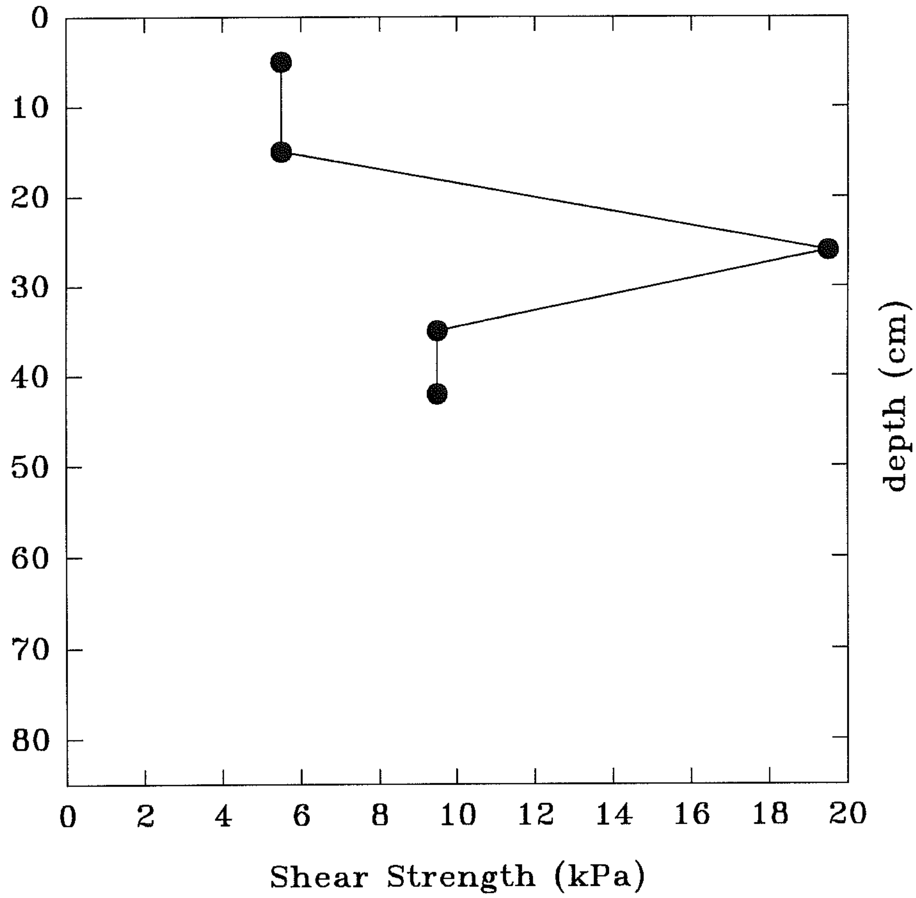

Note: Shear strength measurements taken with the
25mm Controls Penetrometer.

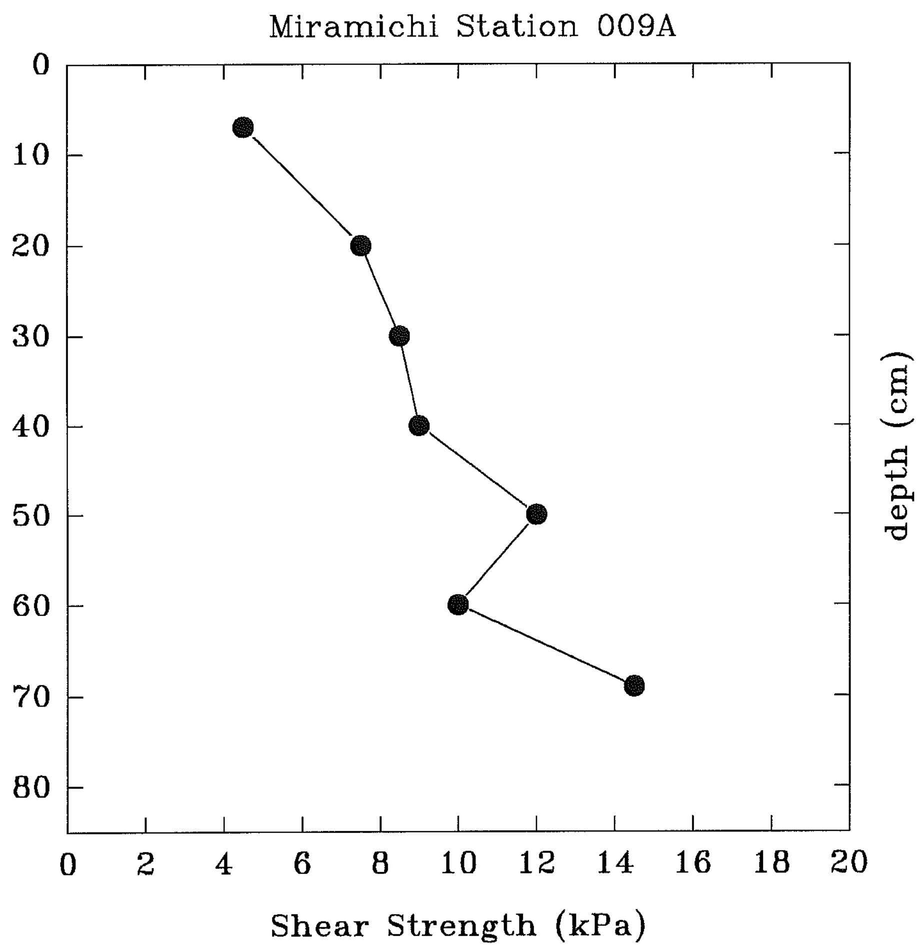

NOte: Shear strength measurements taken with the
25mm Controls Penetrometer.

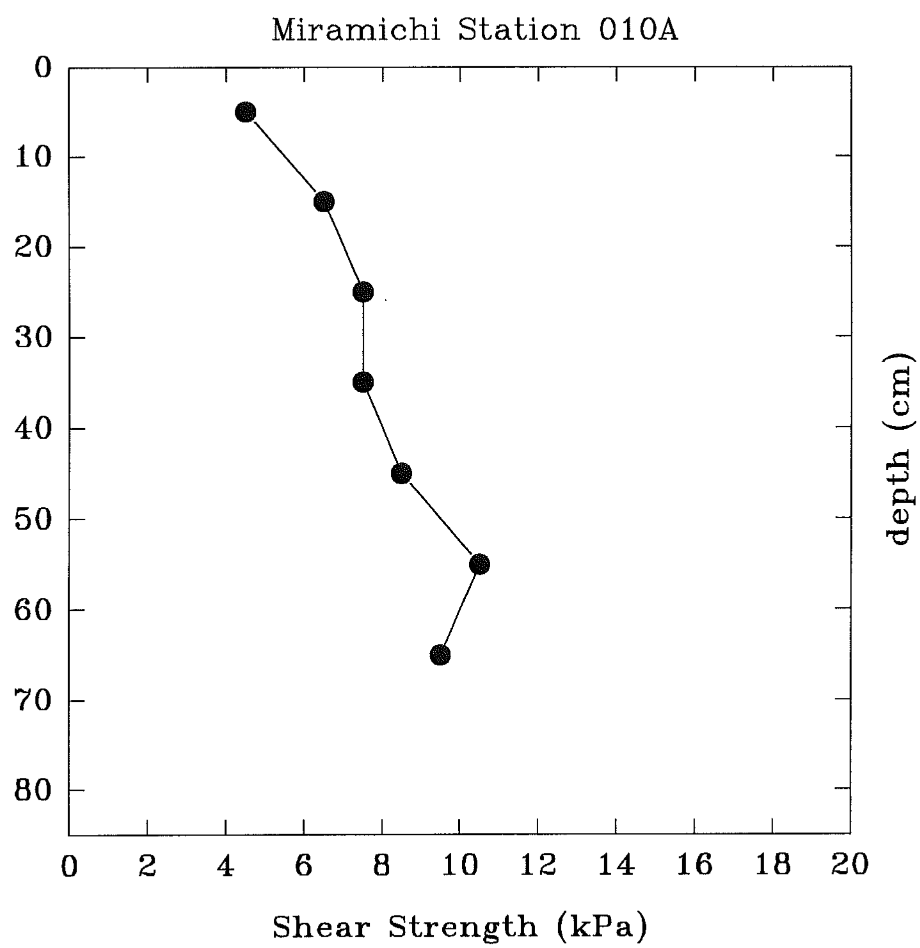

Note: Shear strength measured with the sensitive vane of the Soilotest CL 600 Torvane.

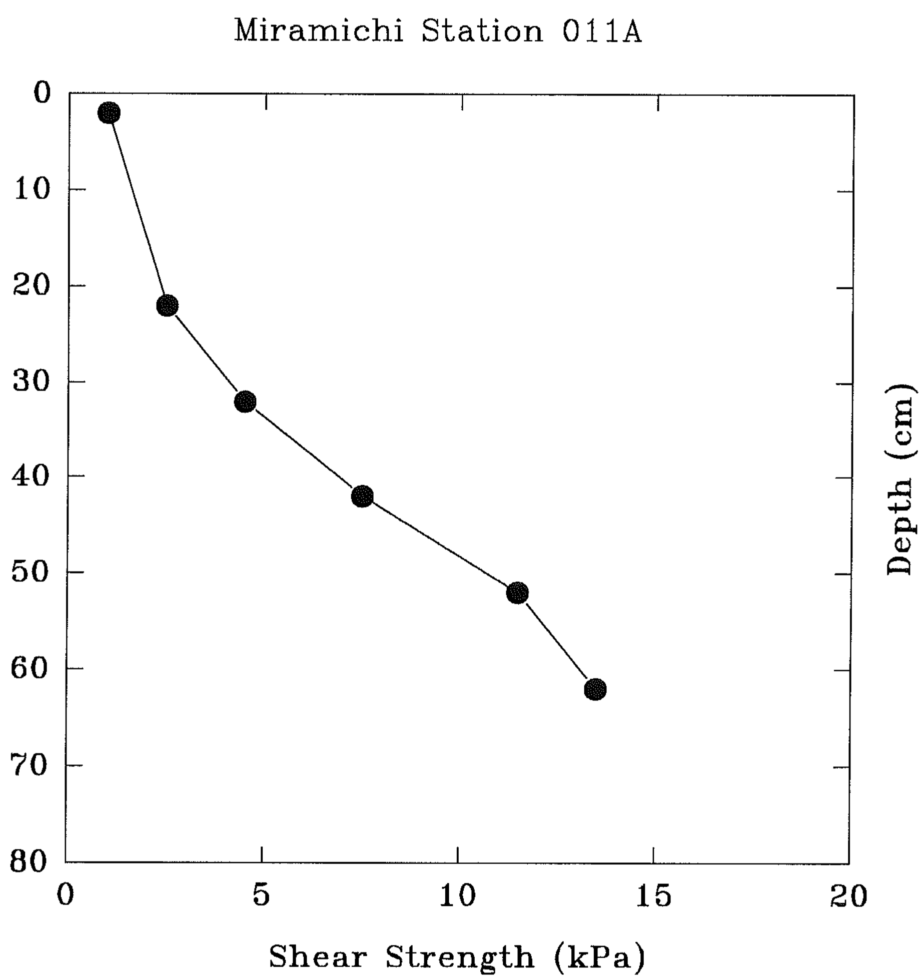

Note: Shear strength measured with the 25mm Controls Penetrometer.

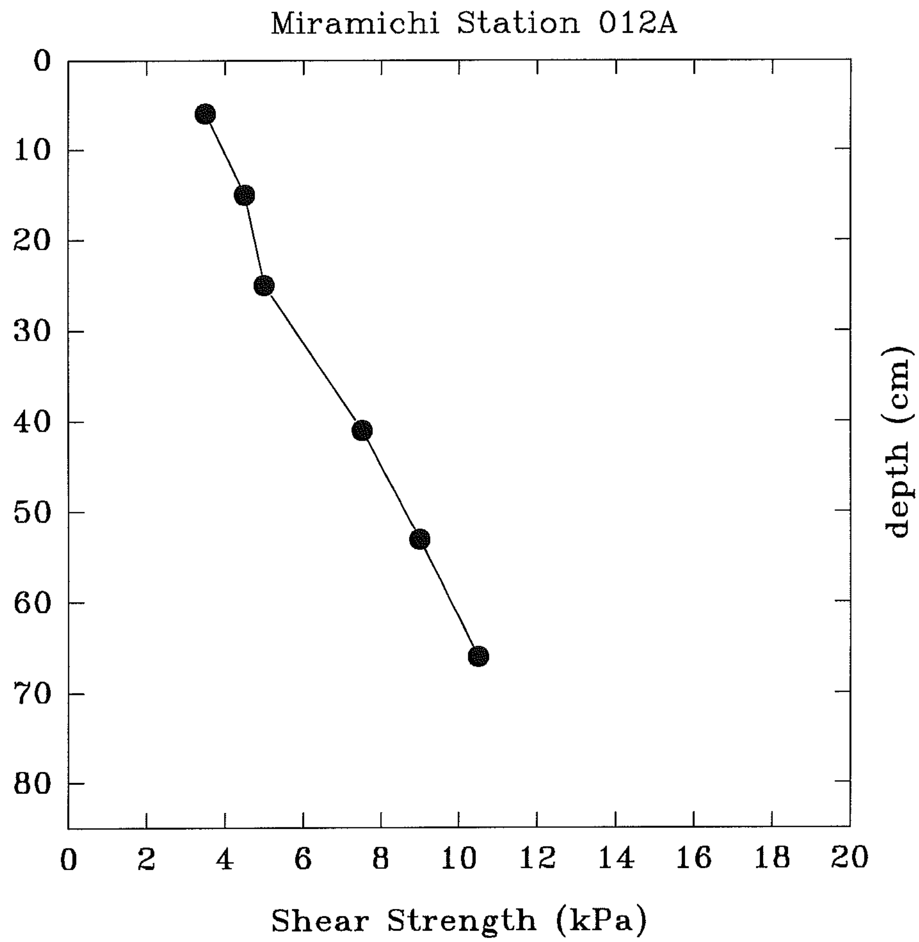

NOte: Shear strength measurements taken with the
25mm Controls Penetrometer.

Miramichi Station 013A

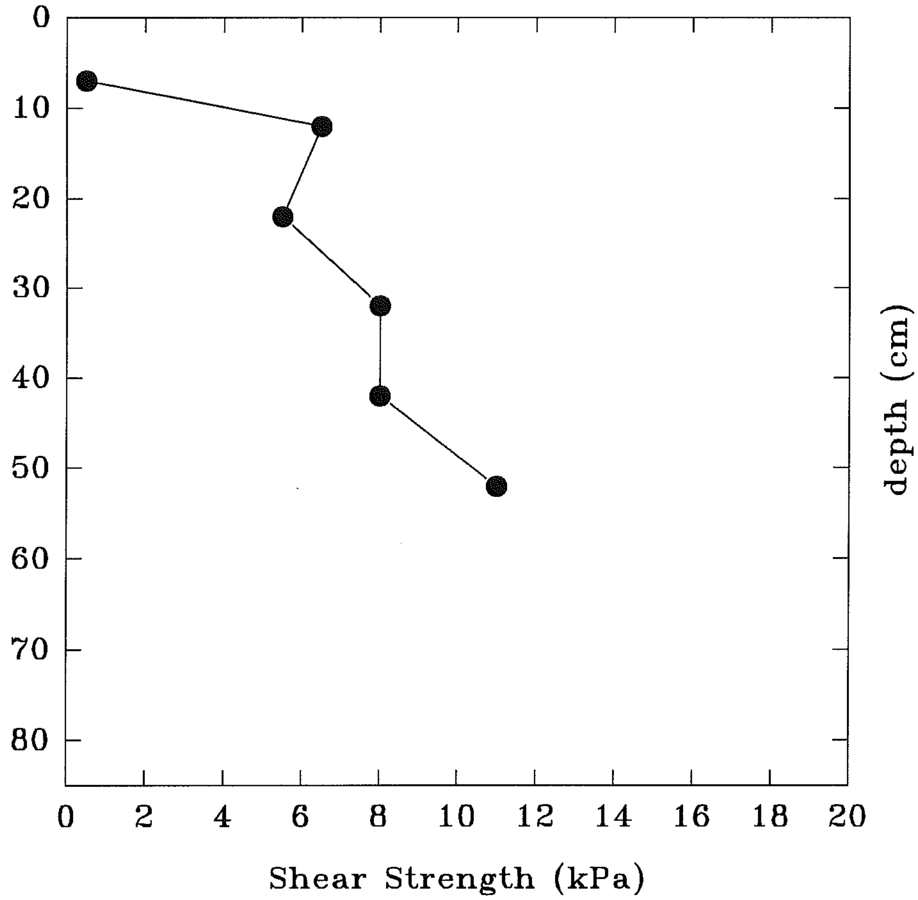

NOte: Shear strengthmeasurements taken with the
25mm Controls Penetrometer.

APPENDIX 3

PLOTS OF BIOLOGICAL SAMPLING PROGRAM

NAVICULA CRUISE 94-350 (1994)

1.0 INTRODUCTION

The investigation of biological characterisitics during this study was limited to a survey of species composition and abundance of the benthic macrofaunal community, and to measurements of sediment chlorophyll *a* concentrations. These factors are known to influence, and be infuenced by, sediment composition and dynamics. The macrofaunal community was examined through the analysis of samples collected with a 15 x 15 cm Eckman grab. Sediment chlorophyll *a* concentrations were investigated in two ways: by sub-sampling the water samples pumped at regular intervals from the Sea Carousel during each deployment; and by sub-sampling the upper 5 mm of sediment collected with a Van Veen grab using a 1.2 cm diameter syringe core. Sampling the sediment from the grabs gives an indication of the total amount of chlorophyll *a* associated with that surface layer, while the samples collected from the Sea Carousel were used to determine the chlorophyll *a* eroded from the bed during the deployment.

2.0 METHODOLOGY

2.1 Sediment Chlorophyll *a*

The syringe cores, collected for chlorophyll *a* analysis, were stored frozen prior to analysis. Chlorophyll *a* concentrations were determined photometrically after extraction in 90% acetone and centrifugation. The concentrations were standardized by the dry weight of the sediment in the sample.

2.2 Vertical Distribution of Sediment Chlorophyll *a*

Samples collected from Sea Carousel filtered onto MSF GF75 borosilicate filters held by a Swinnex disk filter holder attached to the end of a 60 ml syringe. The filters were stored frozed in 5 cm Petri dishes until analysis in the laboratory. The chlorophyll *a* was extracted by soaking the filters in 15 ml of 90% acetone for 24 hours. The chlorophyll *a* concentration in the extract was determined photometrically and then normalized to the volume of the sub-sample.

The resulting time-series was treated as a stepwise function and the change in concentration of chlorophyll *a* within the Sea Carousel due to sediment erosion beween each sample ($CONC_t$) was calculated as the difference between the concentration of the sample at time t (SCONCt) and the previous sample ($SCONC_{t-1}$) after correcting the latter term for diffusion of chlorophyll *a* from the annulus. This correction was made using a diffusion coefficient (k) of 1/700 s^{-1}.

$$CONC_t = SCONC_t - SCONC_{t-1} \ (e^{-kDt})$$

The depth of erosion associated with each increment of concentration was determined following methods described in the main text. Synthetic cores have been constructed for each station by plotting eroded depth against $CONC_t$.

2.3 Benthic Macrofauna

Benthic macrofauna samples, collected from the Eckmann grab, were sieved through a 710 mm screen and stored for identification and enumeration in the laboratory. Two samples were collected at each station.

3.0 RESULTS

3.1 Sediment Chlorophyll *a*

Sediment chlorophyll *a* concentrations exhibited little variability between the control area and the dumpsite (Fig. 1A). An analysis of variance show this variability to be statistically insignificant ($p = 0.115$, d.f. = 38). The dumpsite stations showed a wide scatter in results, but again there was no significance to the scatter ($p = 0.149$, d.f. = 38). The mean chlorophyll *a* concentrations measured during this study (22.87 and 18.2 mg/g of dry sediment for the control area and the dumpsite respectively) are lower than those reported Brylinsky *et al* (1992) (*circa* 26 and 10 mg/g dry sediment for the same areas). This is in keeping with the lower sediment strengths detected by Sea Carousel. It would appear that the low water temperature and early season were contributing factors tot he low detected values of chlorophyll.

3.2 Vertical Distribution of Chlorophyll *a*

The sediment chlorophyll *a* concentrations in the synthetic cores are low. These results are plotted in Figures 2.1 to 2.12 for stations MIR2 to MIR13 respectively. In all cases the lowest concentrations of chlorophyll are in the surface layer, and the level is greatest at a depth of between 2 and 3 mm. This suggests the absence of a significant biofilm and the relatively low influence of biostabilization. The maxima in chlorophyll seems to be associated with the change in strength exhibited in the synthetic cores of bed strength. Any direct associations between changes in strength and changes in chlorophyll must wait for future analyses of bulk density (from the Catscan analyses, see appendix 4) and from LTSEM analyses.

3.3 Benthic Macrofauna

A total of 26 species were identified during the benthic macrofauna survey. These species are listed in Table 1. While there was little difference in the mean number of benthic organisms per sample between the control area and the dumpsite (Fig. 3A), there was statistically significant variability between stations ($p = 0.013$, d.f. = 13) indicating a high degree of patchiness among stations. This was particularly evident at the dumpsite (Fig. 3B).

The most abundant species were the polycheates *Aglaophanus neotenus*, *Scoloplos robustus* and *Ninoe nigripes*. This was also the case reported by Brylinsky *et al* (1992). The mean numbers of organisms per sample were higher in this survey, however. This is probably due to the use of a finer mesh screen to seive the samples rather than any real difference in population densities between these years.

PHYLUM ANNELIDA

Class Polychaeta

Ninoe nigripes
Scoloplos robustus
Aglaophanus neotenus
Eteone lactea
Nereis diversicolor
Prionospio steenstrupi
Nereis viriens

PHYLUM MOLLUSCA

Class Gastropoda

Retusa canaliculata
Retusa obtusa
Nassarius trivitatus
Littorina obtusata
Littorina littorea
Littorina saxatilis
Turbonilla interrupta

Class Bivalvia

Spisula solidissima
Tellina agilis
Mytilis edulis
Yoldia limatula

Phylum Rhyncocoela

Cerebratulus lacteus

PHYLUM ARTHROPODA

Class Crustacea

Crangon septemspinosa
Ampelisca declivitatus
Pontoporeia femorata
Leptocheirus pinguis
Phoxocephalus holbolli
Harpinia propinqua

PHYLUM ECHINODERMATA

Class Echinoidea

Echinarachnius parma

Table 1 . Benthic macrofauna species list.

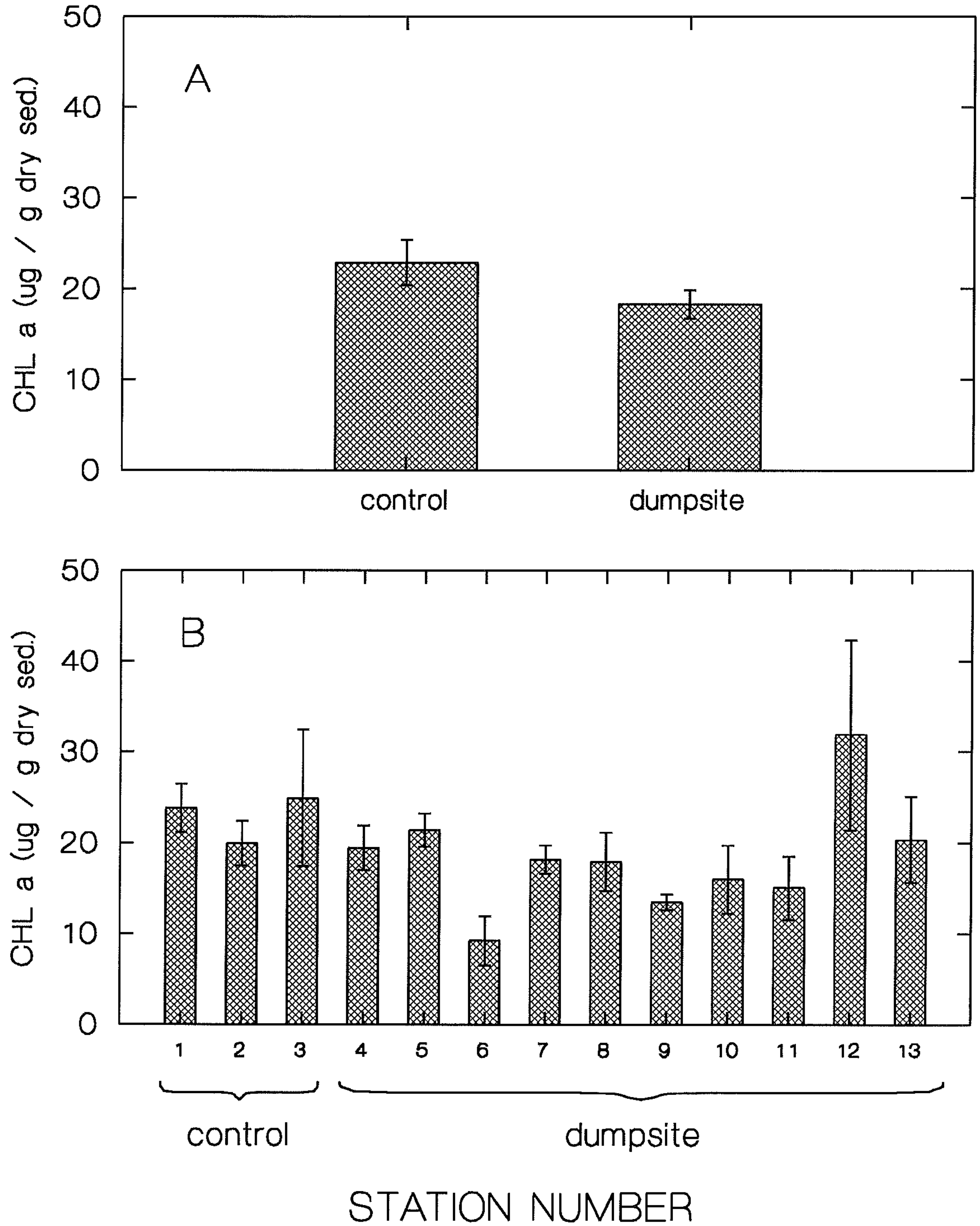

Figure 1. A) Comparision of mean sediment chlorophyll *a* concentrations between the control area and the dumpsite. B). Comparision of mean sediment chlorophyll *a* concentrations between stations. Error bars are standard error of the mean.

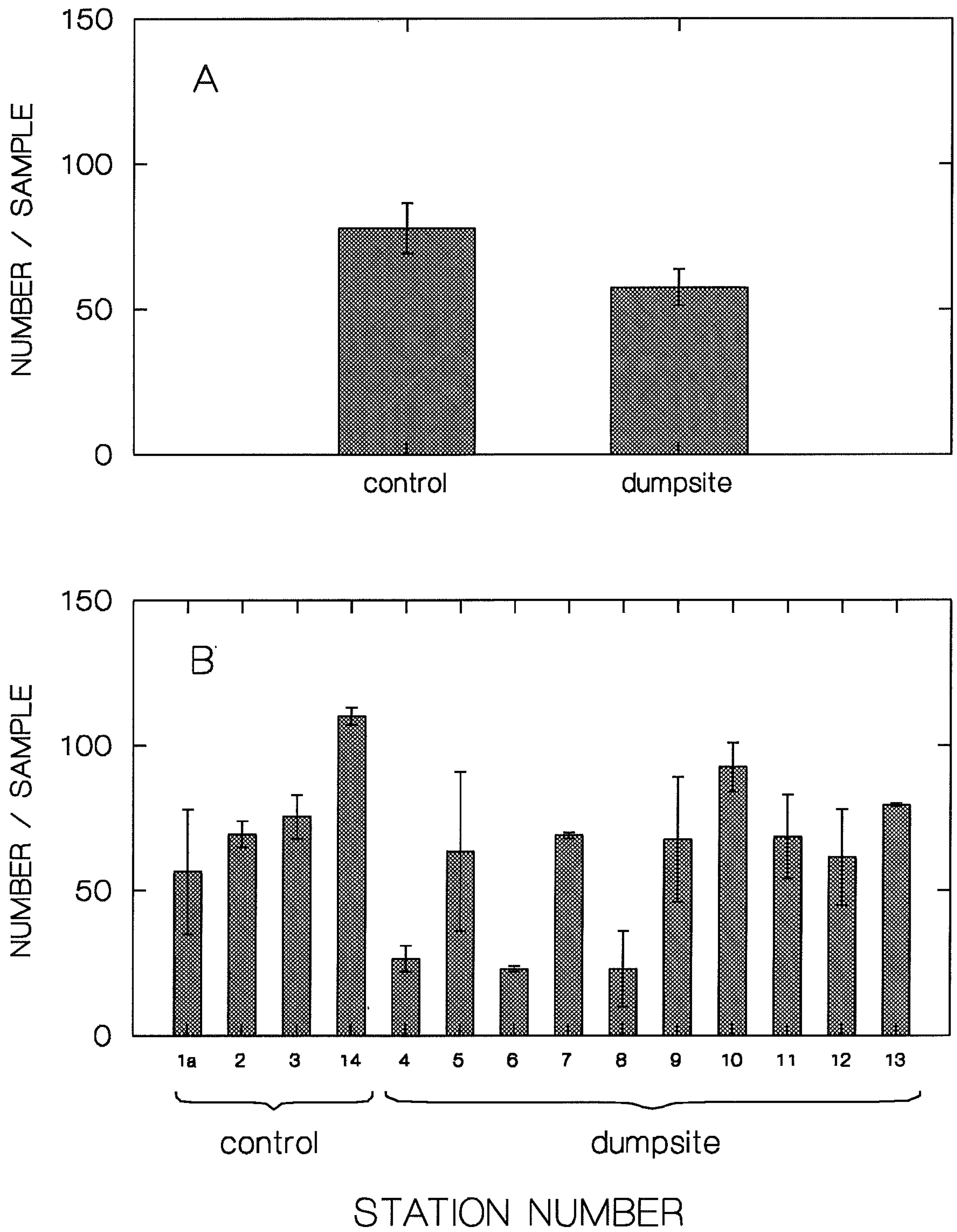

Figure 3. A) Comparision of mean number of organisms between the control area and the dumpsite. B). Comparision of mean number of organisms between stations. Error bars are standard error of the mean.

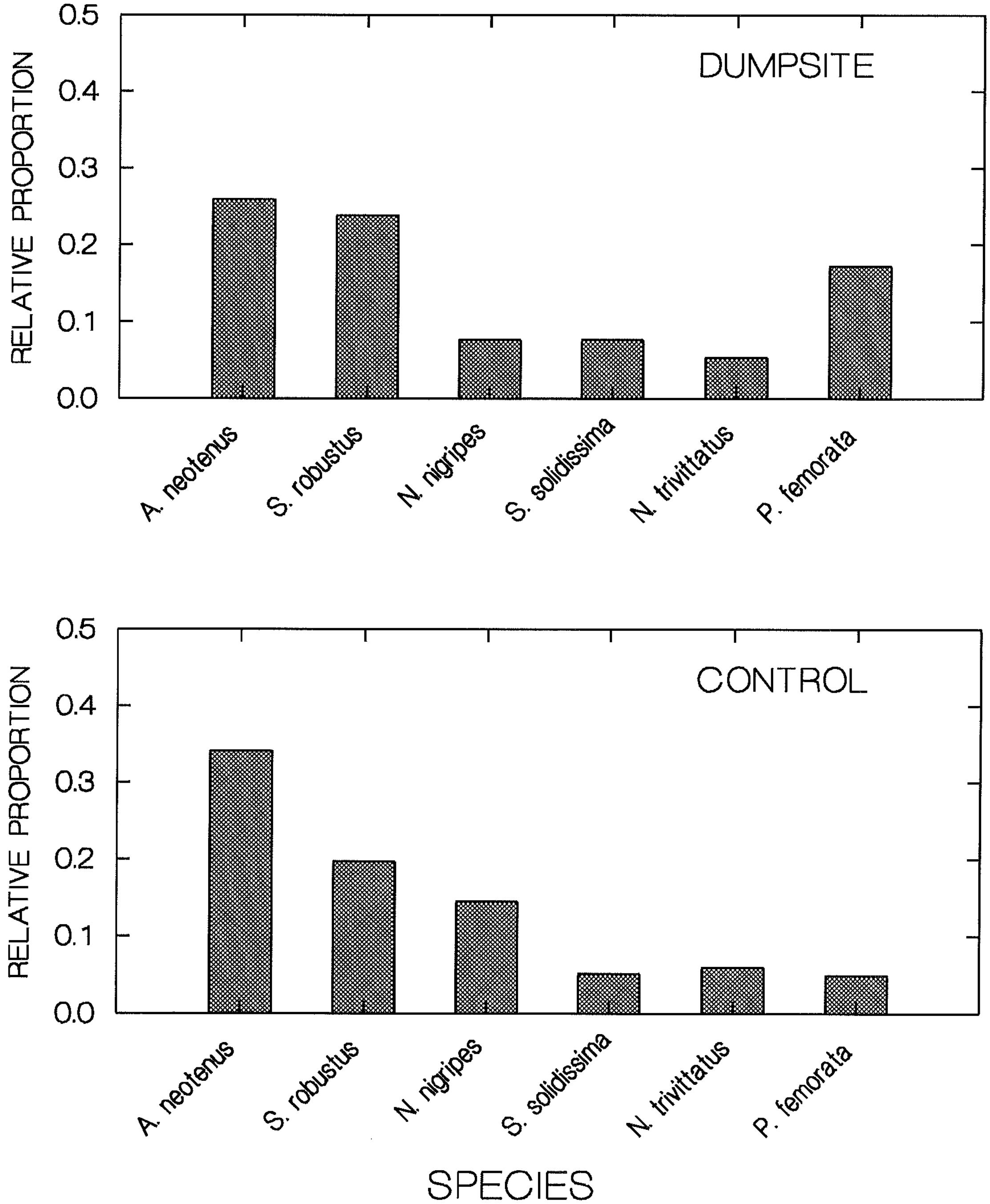

Figure 4. Relative abundance of the 6 most common species collected from the control area and the dumpsite.

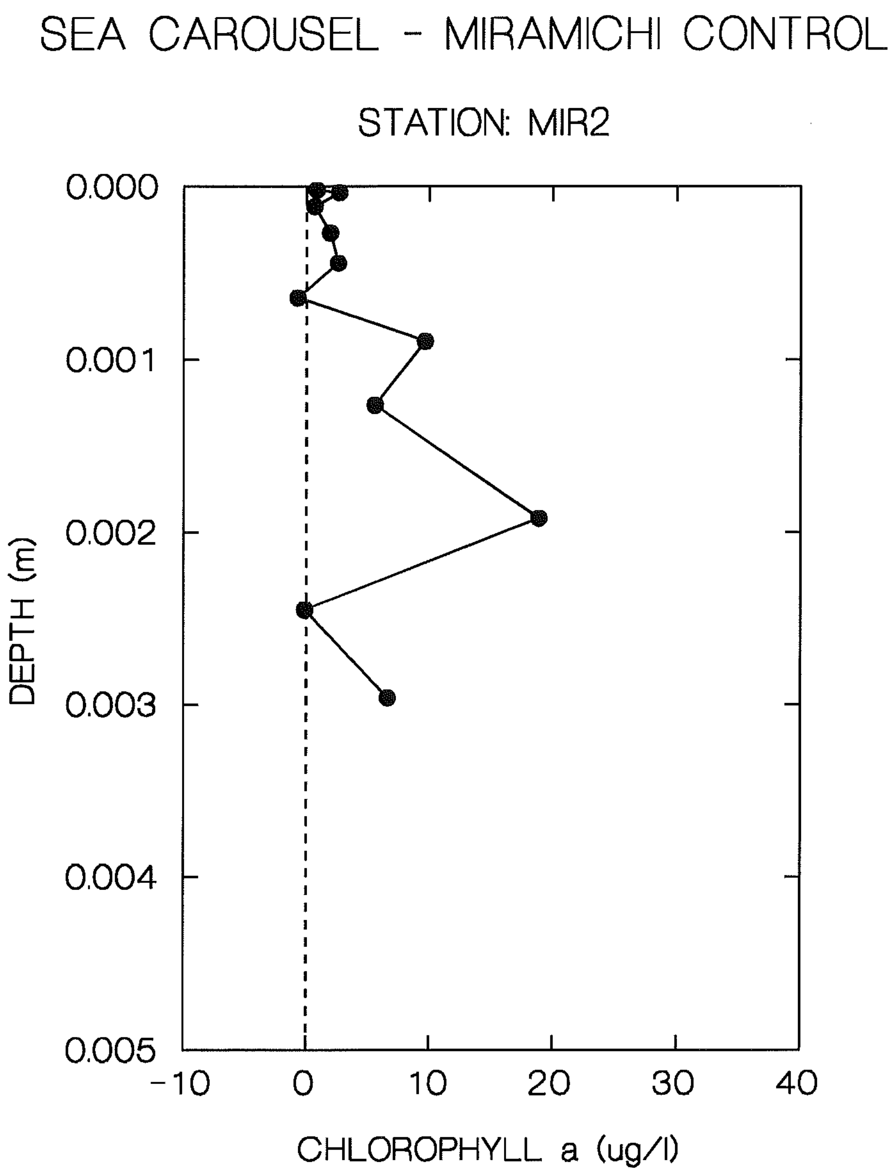

Figure 2.1. Relationship of relative chlorophyll *a* concentration and depth at station: MIR2.

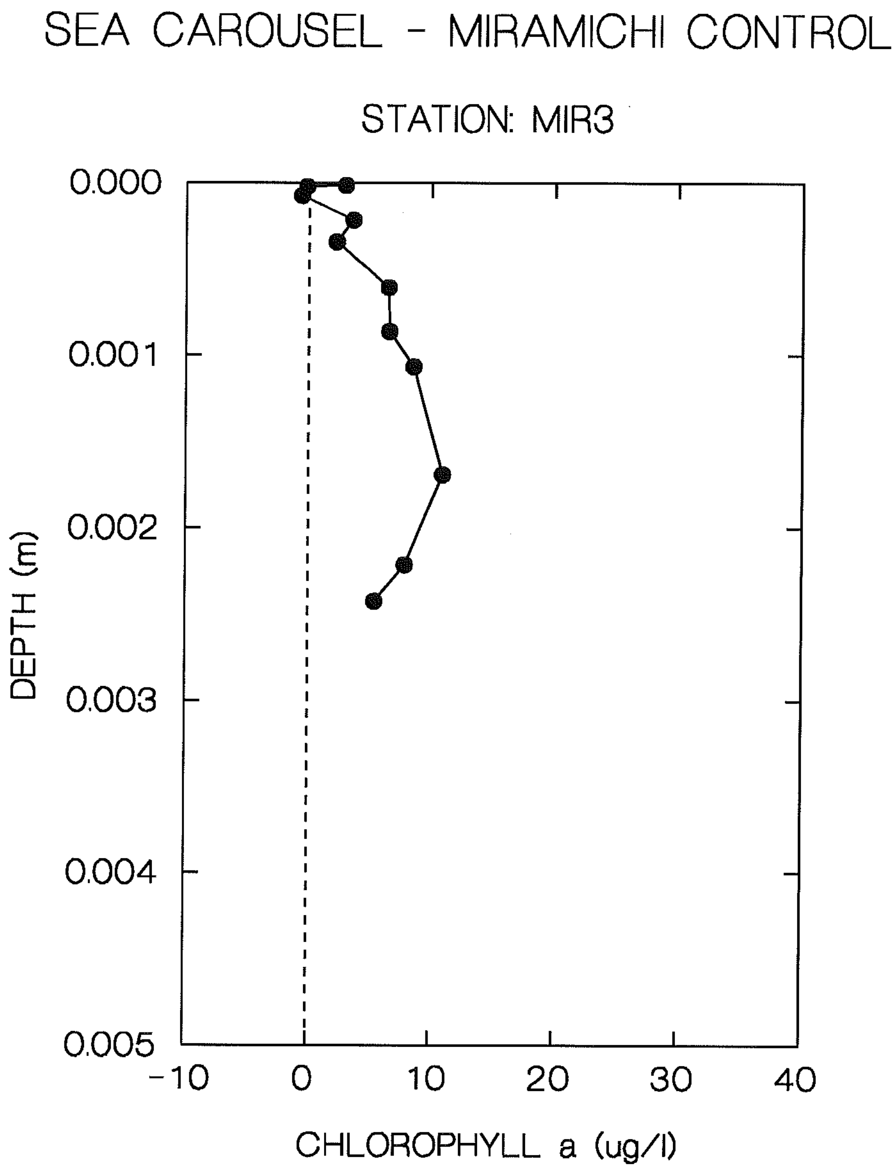

Figure 2.2. Relationship of relative chlorophyll *a* concentration and depth at station: MIR3.

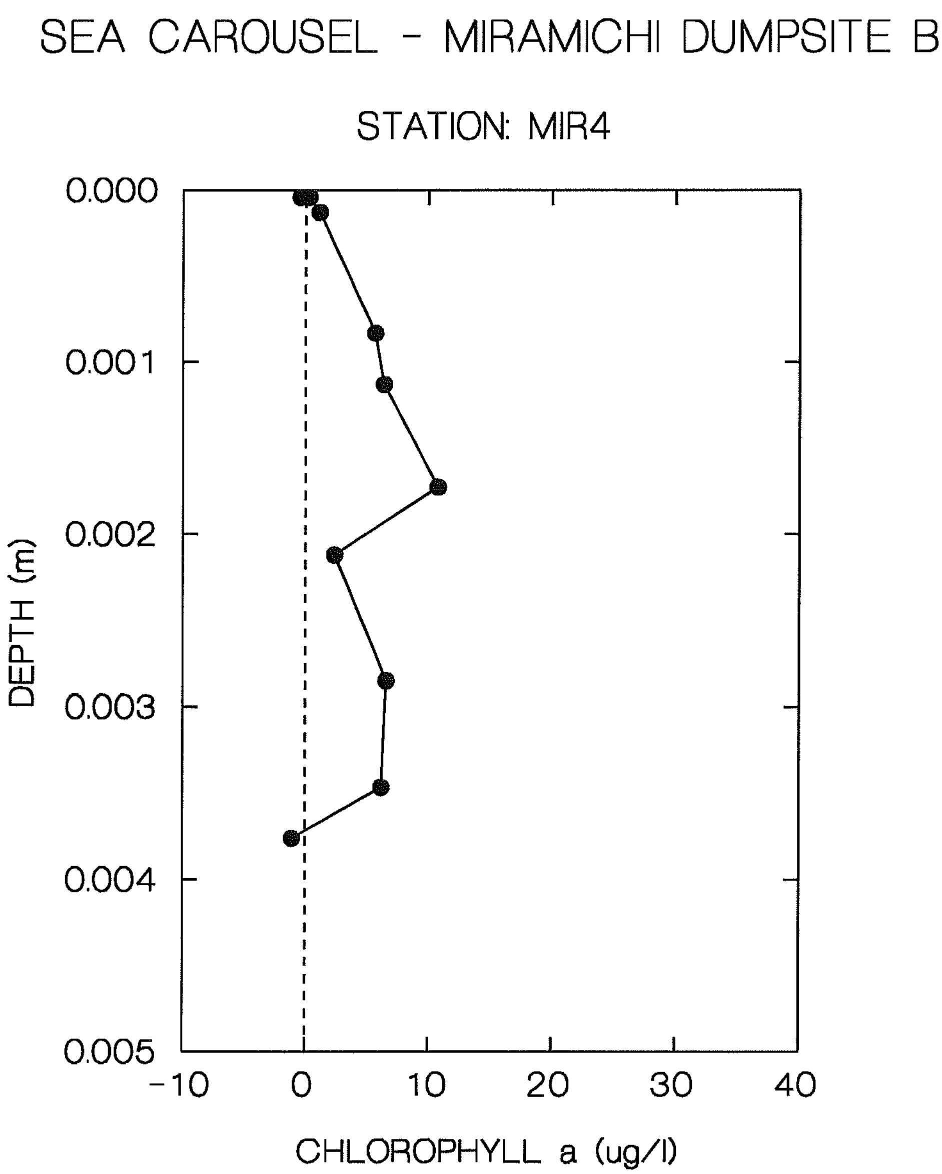

Figure 2.3. Relationship of relative chlorophyll *a* concentration and depth at station: MIR4.

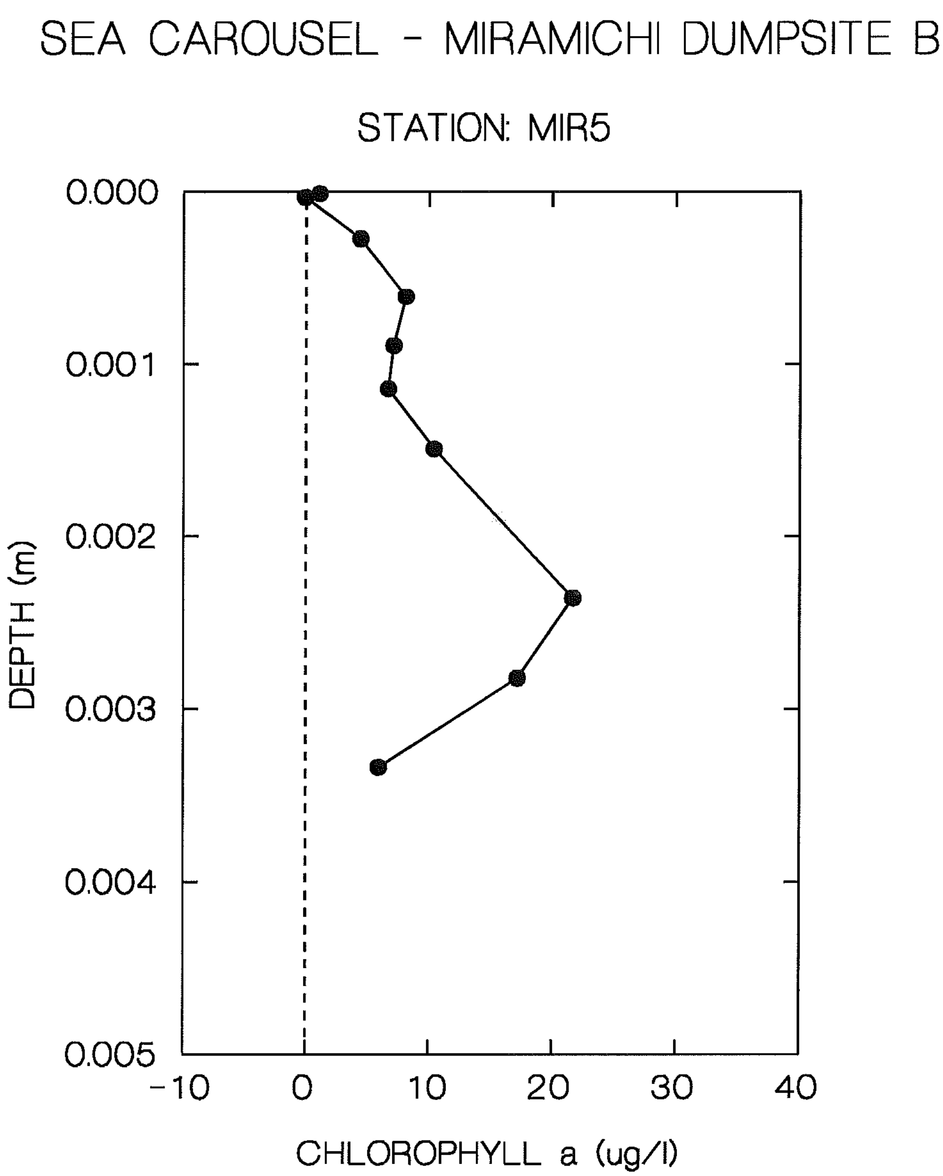

Figure 2.4. Relationship of relative chlorophyll *a* concentration and depth at station: MIR5.

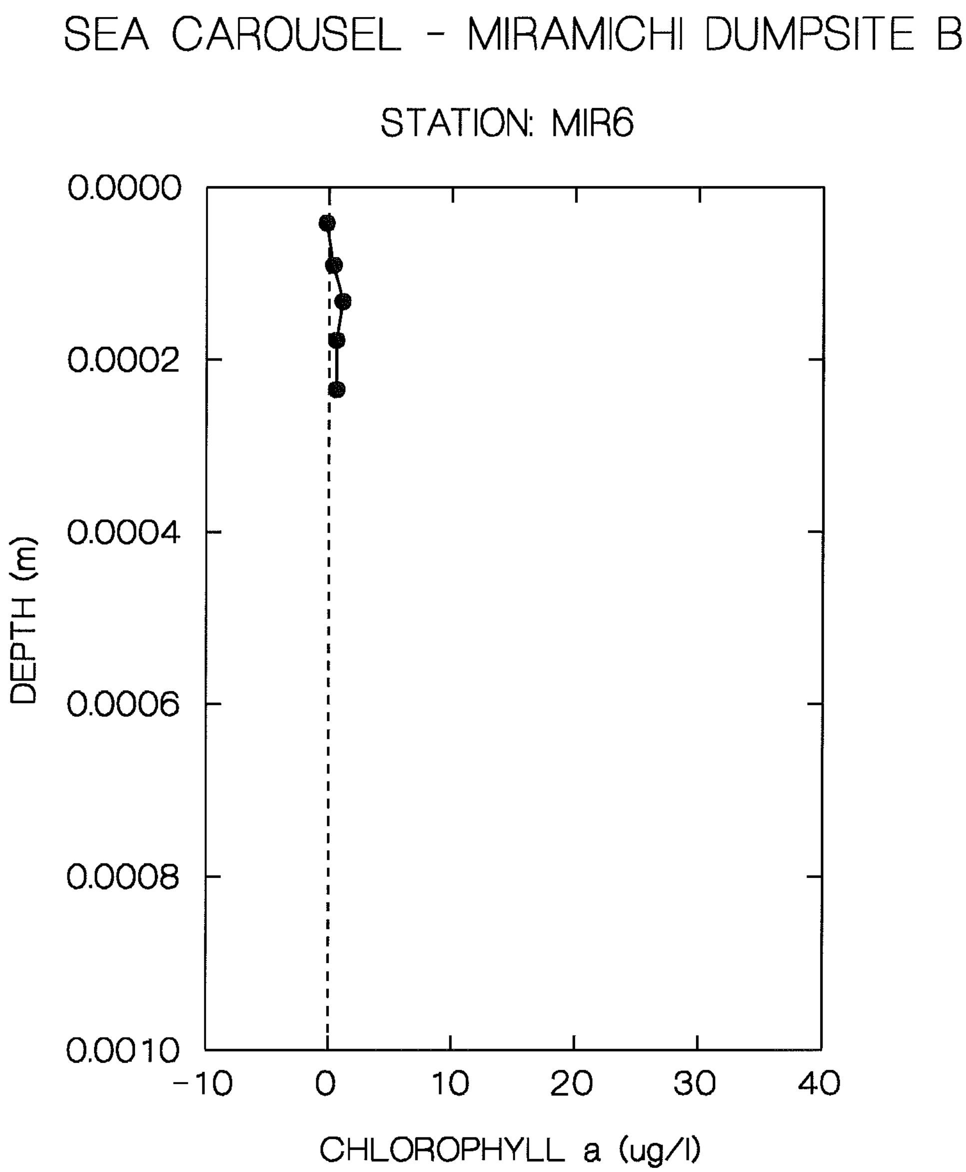

Figure 2.5. Relationship of relative chlorophyll *a* concentration and depth at station: MIR6.

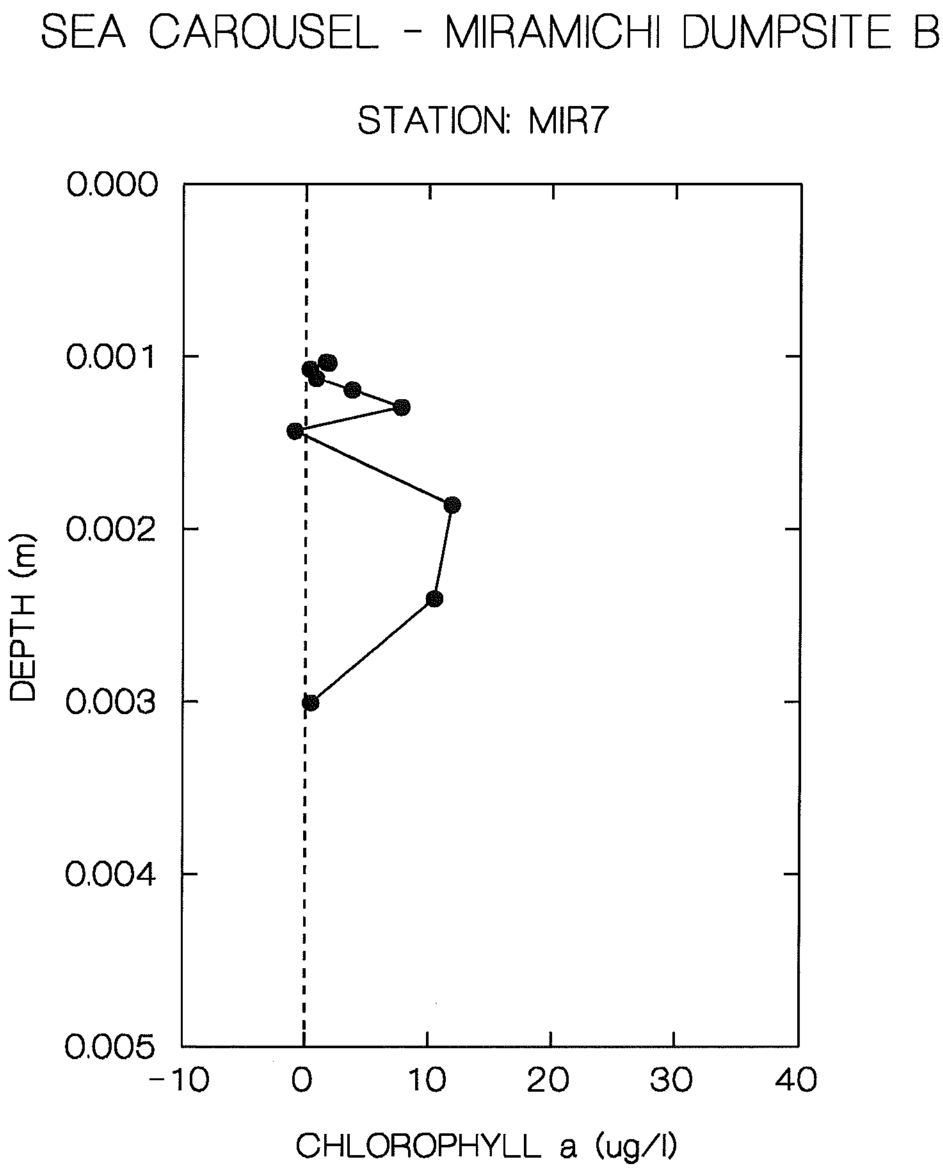

Figure 2.6. Relationship of relative chlorophyll *a* concentration and depth at station: MIR7.

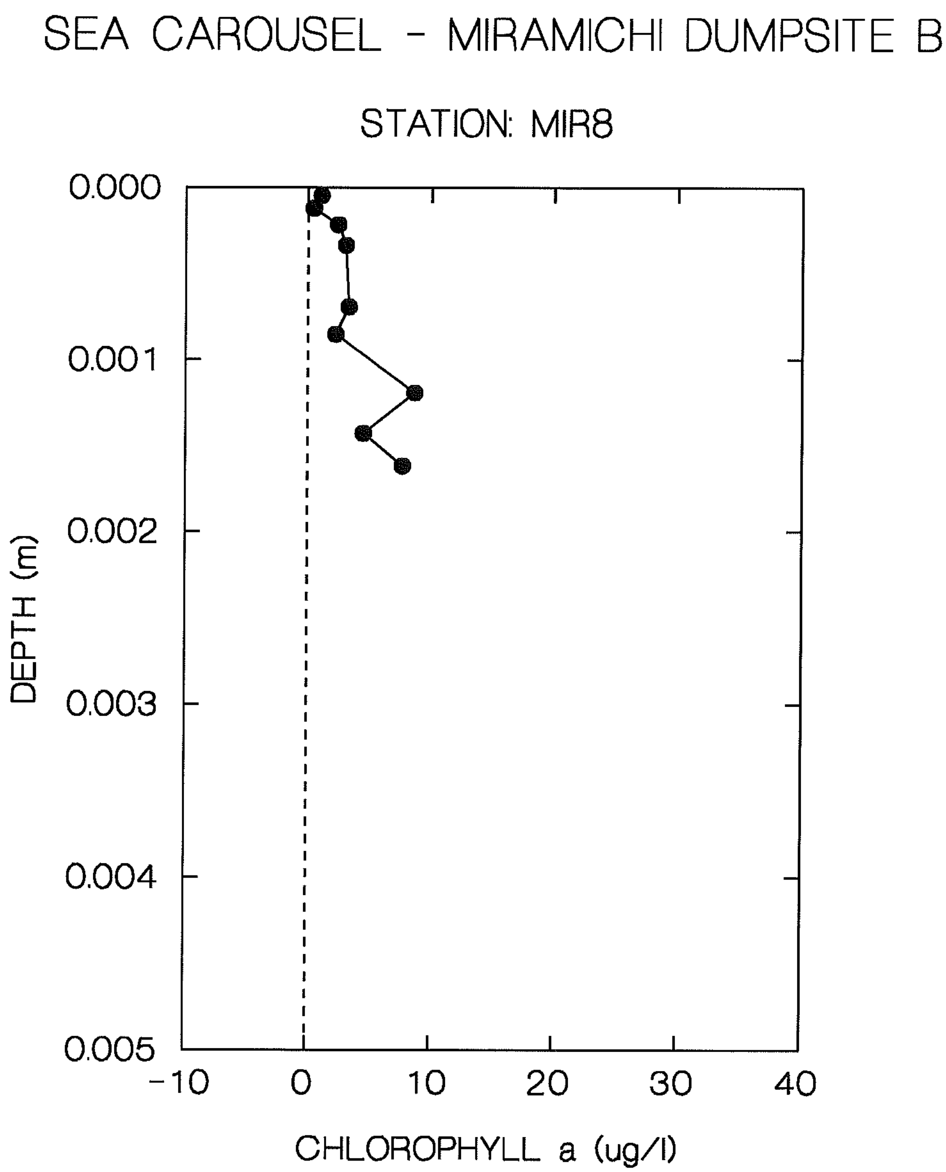

Figure 2.7. Relationship of relative chlorophyll *a* concentration and depth at station: MIR8.

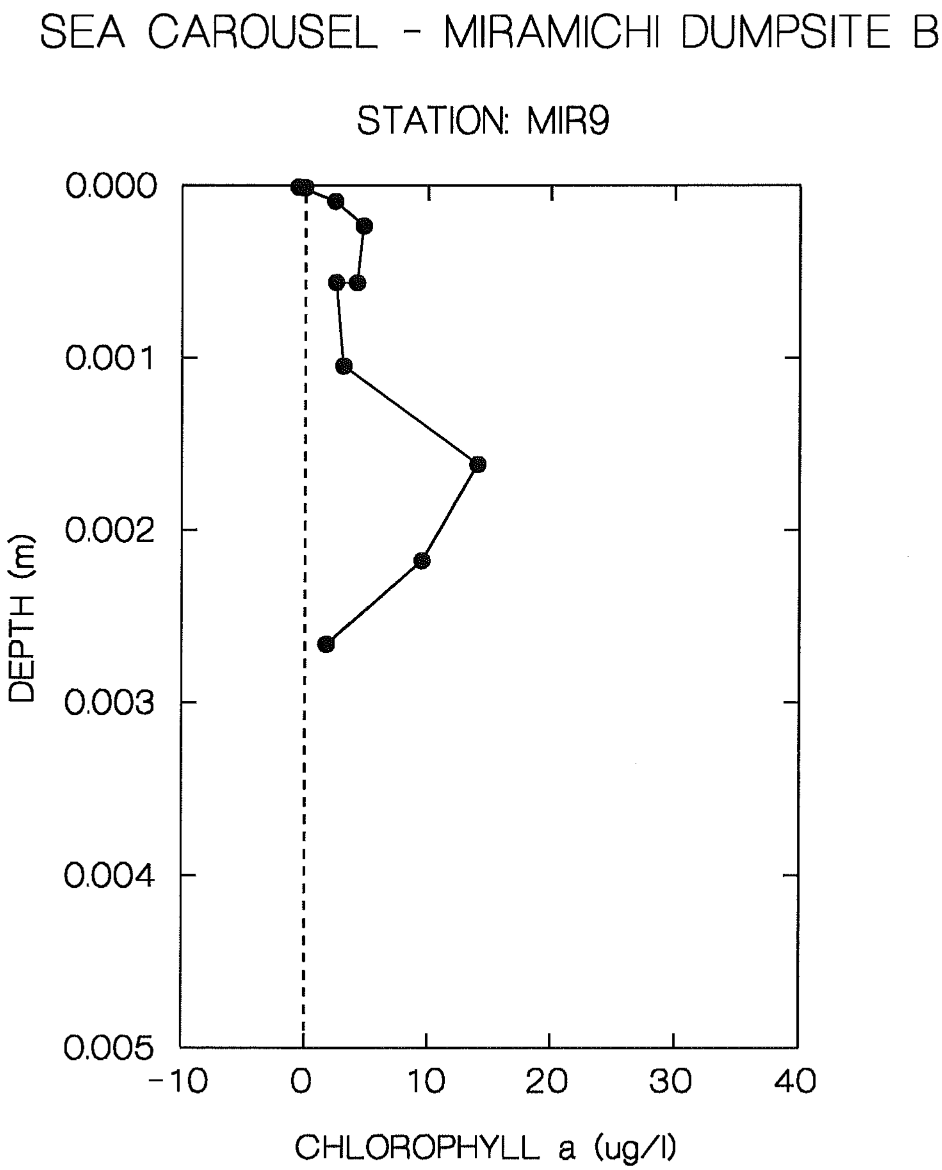

Figure 2.8. Relationship of relative chlorophyll *a* concentration and depth at station: MIR9.

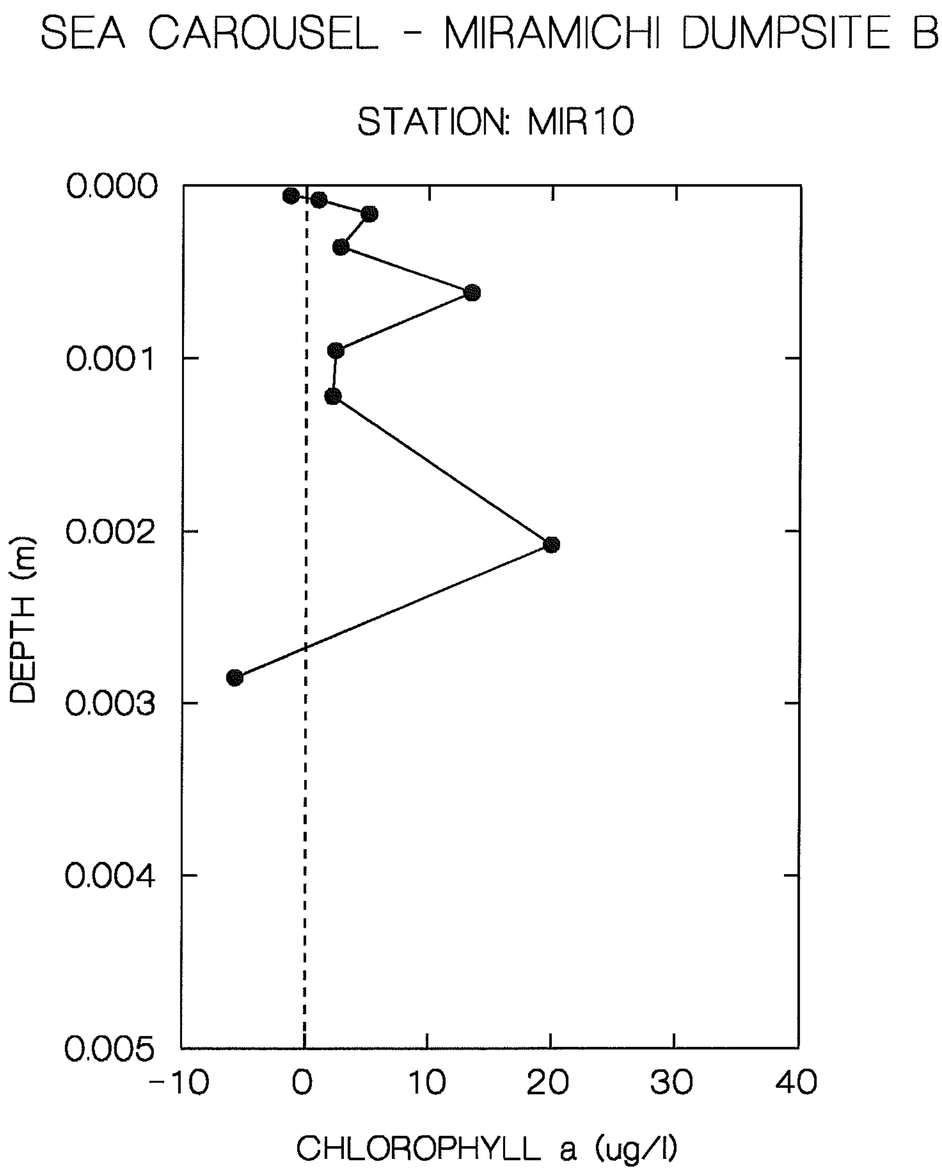

Figure 2.9. Relationship of relative chlorophyll *a* concentration and depth at station: MIR10.

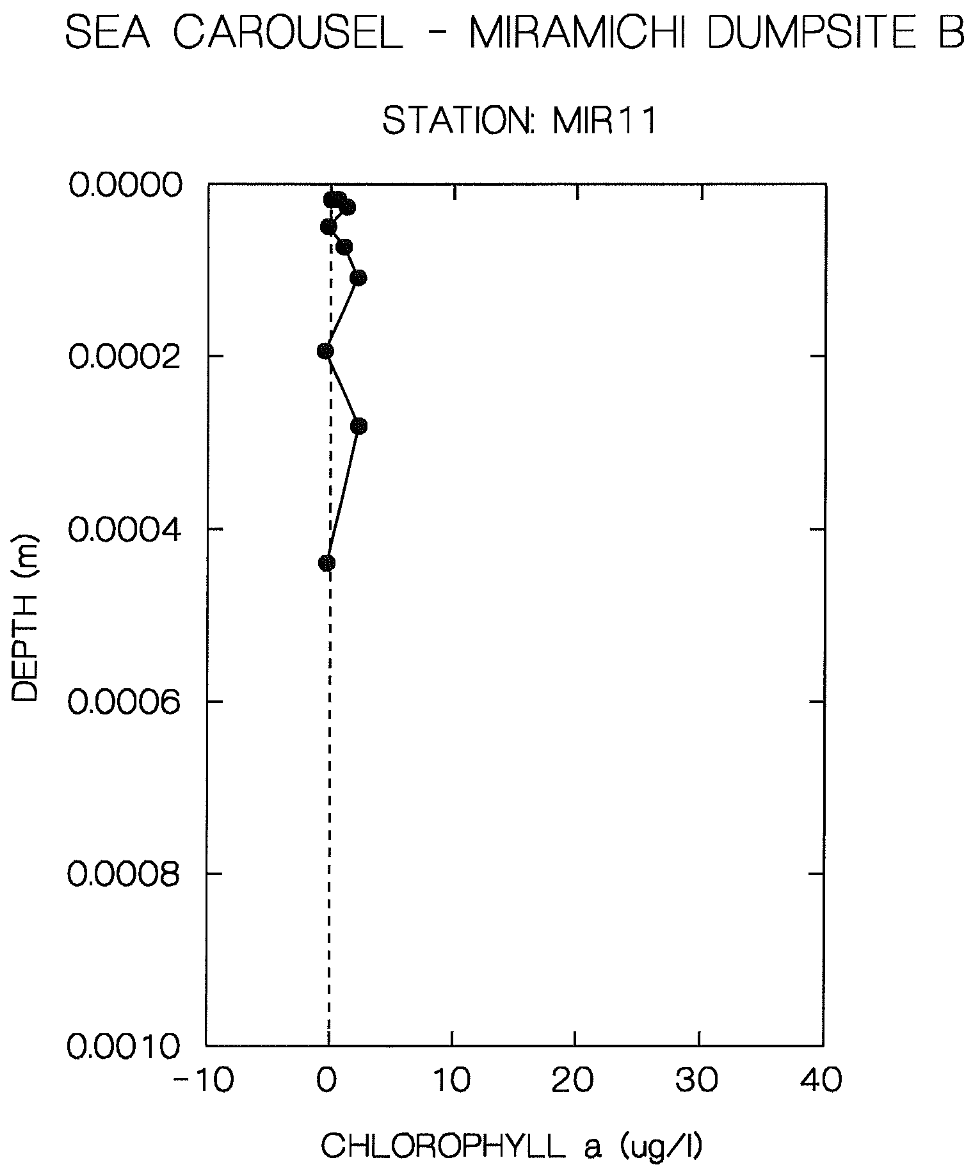

Figure 2.10. Relationship of relative chlorophyll *a* concentration and depth at station: MIR11.

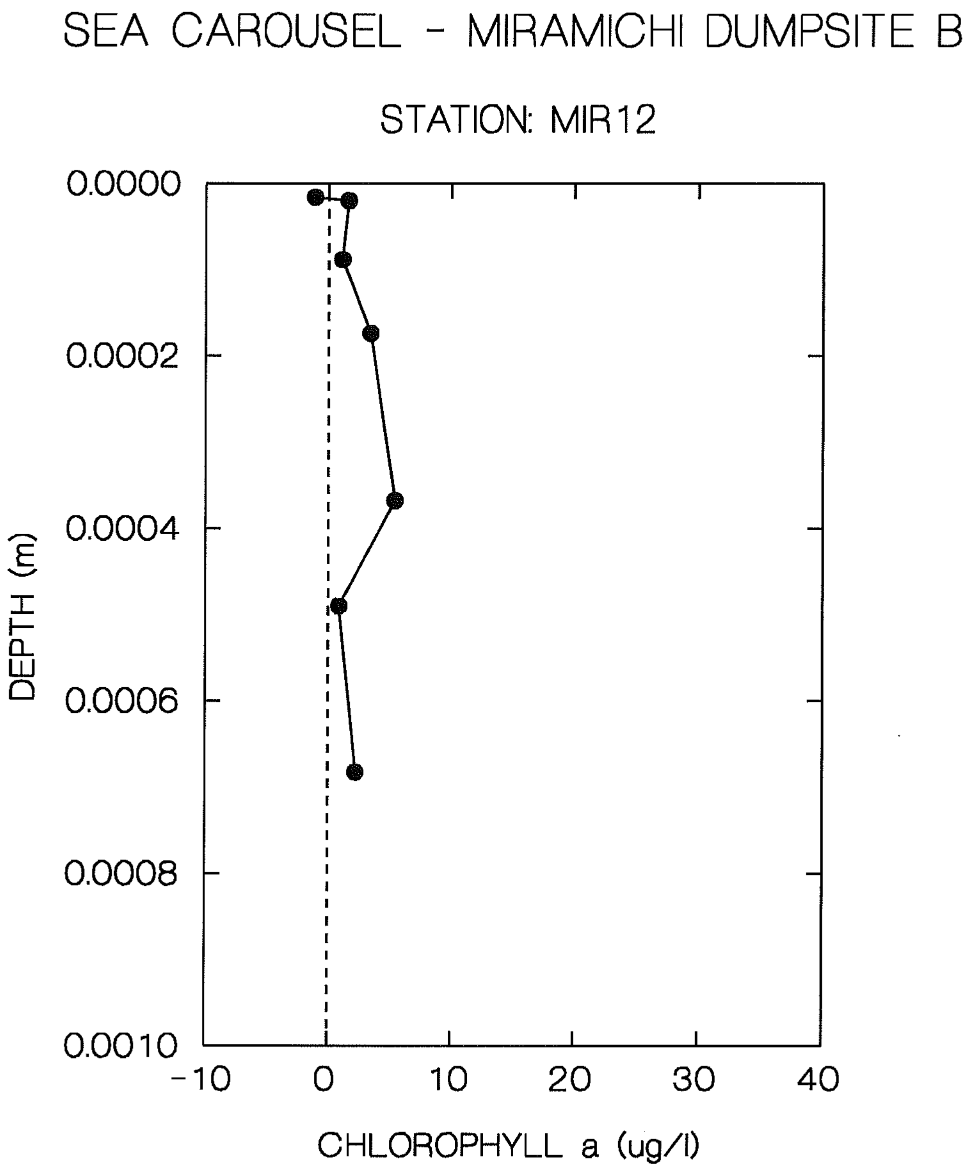

Figure 2.11. Relationship of relative chlorophyll *a* concentration and depth at station: MIR12.

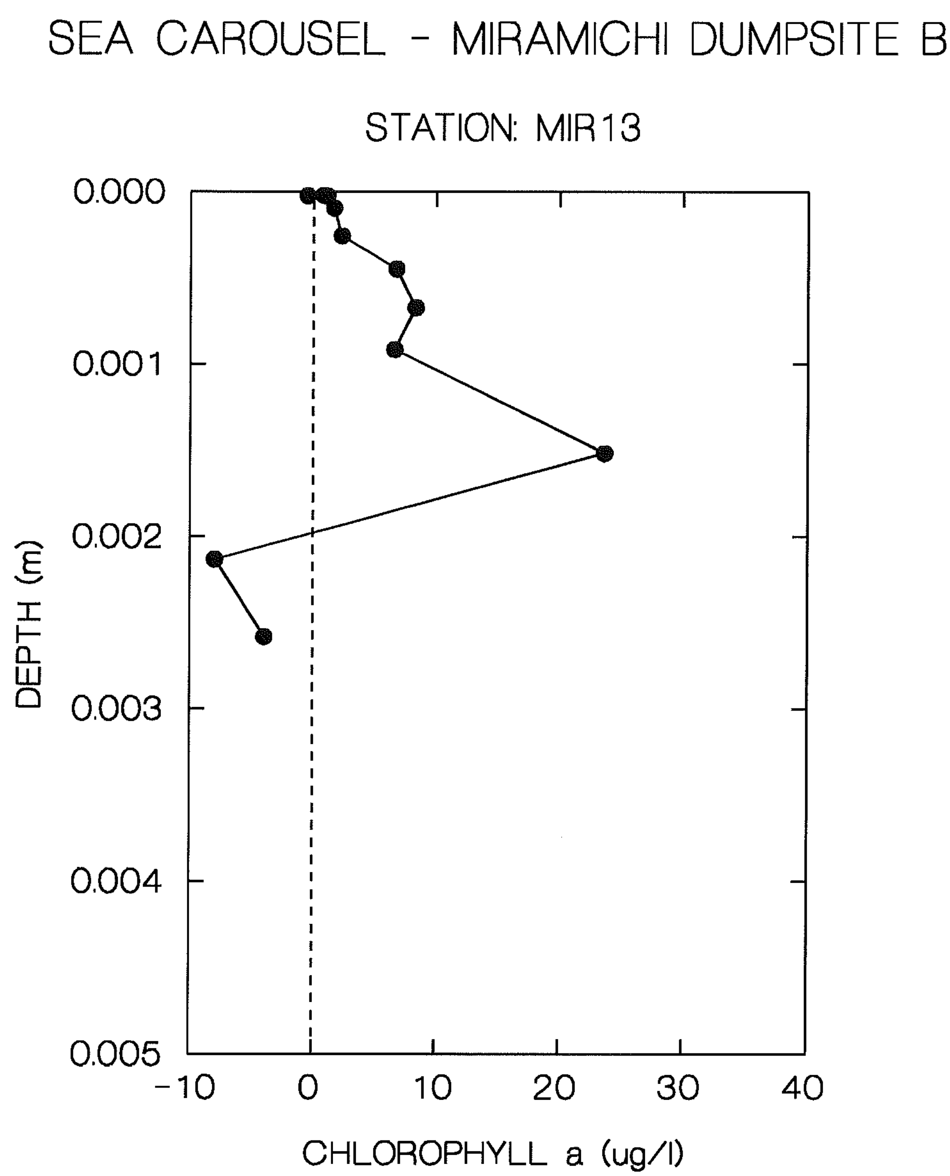

Figure 2.12 Relationship of relative chlorophyll *a* concentration and depth at station: MIR13.

PHYLUM ANNELIDA

Class Polychaeta

Ninoe nigripes
Scoloplos robustus
Aglaophanus neotenus
Eteone lactea
Nereis diversicolor
Prionospio steenstrupi
Nereis viriens

PHYLUM MOLLUSCA

Class Gastropoda

Retusa canaliculata
Retusa obtusa
Nassarius trivitatus
Littorina obtusata
Littorina littorea
Littorina saxatilis
Turbonilla interrupta

Class Bivalvia

Spisula solidissima
Tellina agilis
Mytilis edulis
Yoldia limatula

Phylum Rhyncocoela

Cerebratulus lacteus

PHYLUM ARTHROPODA

Class Crustacea

Crangon septemspinosa
Ampelisca declivitatus
Pontoporeia femorata
Leptocheirus pinguis
Phoxocephalus holbolli
Harpinia propinqua

PHYLUM ECHINODERMATA

Class Echinoidea

Echinarachnius parma

Table 1 . Benthic macrofauna species list.

APPENDIX 4

A RAPID TECHNIQUE TO DETERMINE BULK DENSITY OF FINE-GRAINED SEDIMENTS BY X-RAY COMPUTED TOMOGRAPHY

a manuscript submitted to Journal of Sedimentary Research

(this paper describes a technique that we wish to use to examine bulk density of dumpsite material at the microscale. This will help examine the sediment properties that govern sediment stability)

A RAPID TECHNIQUE TO DETERMINE BULK DENSITY OF FINE-GRAINED SEDIMENTS BY X-RAY COMPUTED TOMOGRAPHY

by

C. L. Amos[1], T. F. Sutherland[2], B. Radzijewski[3], and M. Doucette[3]

1. Geological Survey of Canada
Bedford Institute of Oceanography
P.O. Box 1006, Dartmouth
Nova Scotia, Canada, B2Y 4A2

2. Department of Oceanography
Dalhousie University
Halifax, Nova Scotia
Canada, B3H 3J5

3. Camp Hill Medical Centre
Halifax Infirmary, 1335 Queen St
Halifax, Nova Scotia, B3J 2H6

INTRODUCTION

The macrostructure of a cohesive seabed plays an important role in the erosion threshold, erosion rate, and erosion type of that seabed (Faas *et al.*, 1993). Sediment strength, a manifestation of macrostructure, is a critical component in seabed reaction to hydrodynamic forces. Microbial mediation of natural sediments within the topmost 2 mm can alter significantly sediment properties and hence seabed stability (Paterson, 1994). Such properties are strongly reflected in changes in sediment bulk density or unit wet weight, an important index to sediment strength (Einstein and Krone, 1962). Orsi (1994) and Orsi and Anderson (1994) have mapped significant bulk density changes within the topmost few cm's of cores, using x-ray comuted tomography, to a density resolution of 4 kg/m^3 (*circa* 0.2%) and to a sum-millimetre spatial resolution. Standard techniques for the analysis of bulk density in sediment cores use either raw data from gamma-ray attenuance (Grandy, 1987) or standard geotechnical sampling (Bowles, 1978). Neither have the spatial resolution nor the discrimination of x-ray attenuance to resolve details of near-surface macrostructure. X-ray computed tomography offers advantages over standard methods of analysis by being digital (yielding spectra of the Hounsfield Unit), being 3-dimensional, and being able to resolve to a voxel volume of 0.06 mm^3 anywhere within the sample. The Hounsfield Unit (HU) for any voxel is defined as:

$$HU = 1000[(\mu_s - \mu_w)/\mu_w] \quad (1)$$

where μ_s and μ_w are the x-ray linear attenuance coefficients of sediment and freshwater respectively. According to Beer's Law, μ_s is a function of sediment bulk density, ρ_s. Thus for a constant photoelectric effect, HU should vary in direct proportion to ρ_s. To eliminate negative numbers, and to approxate bulk density, Orsi (1994) transformed HU into a computed tomographic number (CT) by the expression:

$$CT = 1 + [HU/1000] \quad (2)$$

so that air has a CT $\approx$ 0, water has a CT $\approx$ 1, and natural, fine-grained sediment varies between 1 and 3.

The transform of CT to ρ_s has been evaluated by Orsi *et al.*(1994), Warner *et al* (1990), and Anderson *et al.* (1988) amongst others. It is not constant, but may vary with sediment composition due to the photo-electric effect (Orsi, pers. comm., 1994). So, it appears that each group of sediments needs independent calibration against CT to ensure accuracy. This paper presents a rapid and accurate means of preparing and analyzing a calibration sample of natural marine sediment for the purpose of transforming CT scanner values to sediment bulk density.

METHODS

A GE® Hilite Advantage CT scanner was used to examine a sample of silty clay. The scanner was operated at 120 Kv at 40 mA with zero tilt and 2 seconds of exposure. The thickness (d) of the computed tomograms was 1.5 mm with an in-plane resolution of 0.035 mm^2. The distance between tomograms was 5 mm (Figure 1A). The sample was contained within a syringe 26.5 mm in diameter (area = 551 mm^2). The sample was wedge-shaped in profile (Figure 1A). Thus, when viewed as a tomogram, two segments of a circle were evident: a sediment segment and an open segment (Figure 1B).

Firstly, a circular region of interest (ROI) was set within the syringe plastic liner (of inner radius r = 13.25 mm) which had an area of 482 mm^2 (Figure 1C). This corresponded to *circa* 13,700 voxels from which the image and a histogram of HU intensities for each tomogram were derived. The histogram in Figure 1D is from the ROI in Figure 1C. It is bimodal: the first population (around HU = -1000) represents air in the open segment; the second broader population (600 < HU < 1300) is of the seawater-saturated, sediment segment. The moment measure of the mean value of HU for this ROI is:

$$HU_{roi} = (\Sigma(HU_i N_i/N)) \quad (3)$$

where HU_i is the HU value of class i, and N_i is the number of voxels within class i.

HU_{roi}, or its transform CT_{roi}, is the CT scanner parameter that is compared with the mean (ROI-averaged) bulk density (ρ_{roi}) corresponding to the tomographic image.

Secondly, HU histograms of tomograms of pure air, saltwater (35 ppt), and fresh water were measured, yielding mean HU values of -994 (± 9), 54 (± 11), and 6 (± 11), respectively. A separate syringe was filled with distilled water in order to check for beam hardening and edge effects of the plastic syringe. If the areas of the sediment and air segments of the tomogram are

A_s and A_a, respectively, then the mean bulk density of the ROI is defined as $(A_s\rho_s)/(A_s + A_a)$, where the density of the air is assumed to be negligible relative to that of the sediment. Thirdly, the chord length (l) that defines the segment width in the sediment/air tomogram (see Figure 1B) was measured. This length, together with the inner radius of the syringe sampler, defines the area of the sediment segment of the syringe core:

$$A_s = 0.5\Theta r^2 + 0.5(\sin\Theta)r^2 \qquad (4)$$

where Θ is the radian measure of the angle subtended by the segment from the centre of the sectioned syringe:

$$\Theta = 2\cos^{-1}(r - l/r). \qquad (5)$$

Thus, $A_a = 551 - A_s\ mm^2$ (6)

and the calculated ROI-averaged wet bulk density (ρ_{roi}) is:

$$\rho_{roi} = (A_s\rho_s + A_a\rho_w)/(A_s + A_a) \qquad (7)$$

where ρ_w is the density of water (seawater = 1026 kg/m^3; freshwater = 1000 kg/m^3) and ρ_s is the density of the sediment (2650 kg/m^3). The mode in the HU histograms corresponding to the air segment (HU < -900) was shifted to a saltwater equivalent by adding 1048 and recomputing HU_{mean} and CT_{roi} using equations 3 and 2 respectively. The shift was possible as "...the average mass attenuance coefficient is equal to the sum of the weighted mass attenuance coefficients of the constituent elements of the material;" (Anderson *et al.* 1988). A freshwater equivalent was determined by adding 1000 to the air histogram values and again recomputing HU_{mean} and CT_{roi}.

SAMPLE PREPARATION

The material used in this calibration was surface sediment collected from Amundsen Basin in 4200 m of water beneath the North Pole (Futterer, 1992). The sediment was composed of 38%

sand, 24% silt, and 38% clay. It was remoulded to produce a uniform sample and slabbed so that the surface was flat and planar. The slab was sampled at three locations along its length for wet and dry bulk densities (Table 1) using standard geotechnical procedures (that is, the gravimetric weight, W, per unit volume, V; Bowles, 1978). The procedure involved a correction of sample weight (W) because of interstitial saline water (of salinity 0.035 g/cm^3):

$$W = [0.965(\rho_w V_w) + \rho_s V_s]g \tag{8}$$

where V_s and V_w are the respective volumes of sediment and water in the sample.

depth (mm)	sample volume (mm^3)	sample wet weight (g)	sample dry weight (g)	wet bulk density (kg/m^3)
10	950	19.87	15.01	2072
50	979	19.84	15.65	2012
100	974	19.98	15.49	2035

Table 1. The standard measures of wet weight bulk density taken from the remoulded, slabbed sediment used in the CT calibration.

The mean sample wet bulk density was 2040 (±30) kg/m^3. The sample was considered fully saturated for the purpose of the calculations. (This was verified later by the CT scanner results on the sediment sample.) A syringe core was taken oblique to the flat surface so that a semicircular wedge of sediment was trapped in the syringe. Coring was done in air to prevent sample disturbance. The resulting core comprised three portions: (1) air space at the top; (2) a mid-portion comprising the sediment wedge; and (3) a lower sediment-filled section. Tomograms were taken in the air-filled section (CT slice 1) to provide the mean HU value for air, at 11 intervals along the wedge (CT slices 2 to 12) to provide a range in section-averaged bulk density for calibration purposes, and in the sediment-filled lower portion of the core (CT slices 13 and

14) as a control.

RESULTS AND CONCLUSIONS

The 11 tomograms of the sediment wedge yielded a range in ρ_{roi} from 1450 to 1990 kg/m^3 in intervals of *circa* 50 kg/m^3. The wet bulk density value for each tomogram is given in Table 2, together with the mean CT_{roi} values. These densities have been estimated for both freshwater and saltwater saturation.

CT slice #	chord length h (mm)	sediment volume (mm^2)	air volume (mm^2)	saltwater wet bulk density (kg/m^3)	freshwater wet bulk density (kg/m^3)	fresh water CT_{roi}	salt water CT_{roi}
2	12	241	739	1450	1430	1.60	1.70
3	13	269	710	1496	1478	1.67	1.81
4	15	321	653	1589	1572	1.79	1.87
5	16	348	624	1636	1620	1.85	2.00
6	19	423	543	1768	1754	1.99	2.14
7	20	446	518	1808	1795	2.13	2.24
8	22	489	472	1883	1871	2.23	2.31
9	23	509	451	1918	1905	2.31	2.32
10	25	539	418	1970	1960	2.32	2.39
11	26	548	408	1986	1977	2.39	2.41
12	26.5	551	405	1992	1982	2.41	2.59

Table 2. A summary of the results computed from each tomographic image of the remoulded sediment wedge.

An almost perfect correlation was found between the transformed saltwater CT_{roi} values and saltwater wet bulk density (Figure 2). The relationship took the linear form:

$$\rho_{roi} = 272 + 694(CT_{roi}) \text{ kg/m}^3;\ r^2 = 0.992;\ n = 11 \qquad (9)$$

The results from our test fall almost exactly on the trend found by Orsi (1994) using seawater-saturated, silicon dioxide and Ottawa sand mixtures, and by Orsi *et al.* (1994) using material from a sediment core from the Louisiana continental shelf, northern Gulf of Mexico. The regression line for freshwater CT_{roi} and freshwater wet bulk density showed a similar trend to that for saltwater, but was offset from it:

$$\rho_{roi} = 390 + 670(CT_{roi})\ kg/m^3;\ r^2 = 0.992;\ n = 11 \qquad (10)$$

Our results suggest that a 4% difference in CT values would result from analysis of sediments saturated with freshwater as compared to saltwater. The major error in the determination of sediment bulk density comes from the change in chord length (l) across the 1.5 mm thickness of the tomogram, and in the estimation of sediment segment area. The change in chord length is 26.5*1.5/60 = 0.66 mm. Figure 3 shows the error bars in sediment area (normalised to total area) in terms of the chord length normalised to syringe diameter (l/2r). Notice that these errors are only *circa* ± 2%. We conclude that the use of a wedge of remoulded sediment in air is a valid and accurate technique for calibrating CT number to sediment bulk density. Importantly, the method is rapid, and eliminates the need to subsample to the scale of the tomographic slice (1.5 mm), thus avoiding sampling errors.

ACKNOWLEDGEMENTS

We wish to thank the Halifax Infirmary (Drs. J. Rees and G. Murphy) for the use of the GE9800 catscan. Sample analysis was provided by D. Clattenburg. Guidance throughout was provided by Dr. T. Orsi.

REFERENCES

Anderson, S.H., Gantzer, C.J., Boone, J.M., and Tully, R.J. 1988. Rapid nondestructive bulk density and soil-water content determination by computed tomography. Soil Science Society of America Journal 52: 35-40.

Bowles, J.E. 1978. Engineering Properties of Soils and their Measurement. Publ. McGraw-Hill International Book Company: 213p.

Einstein, H.A. and Krone, R.B. 1962. Experiments to determine modes of cohesive sediment transport in salt water. Journal of Geophysical Research 67(4): 1451-1461.

Faas, R.W., Christian, H.A., Daborn, G.R. and Brylinski, M. 1993. Biological control of mass properties of surficial sediments: an example from Starr's Point tidal flat. Minas Basin, Bay of Fundy. in A.J. Mehta (ed). Nearshore and Estuarine Cohesive Sediment Transport. Publ. American Geophysical Union 42: 360-377.

Futterer, A.W. 1992. Berichte Zur Polarforschung. Arctic91: The expedition ARK-VIII/3 of RV Polarstern in 1991. Publ. Alfred Wegener Institute fur Polar- und Meersesforschung, Bremerhaven.

Grandy, C.C. 1987. Bulk density determinations of fabricated soil cores using X-radiation. Unpublished B.Sc. Thesis. Memorial University of Newfoundland: 75p.

Orsi, T.H. 1994. Computed tomography of macrostructure and physical property variability of seafloor sediments. Unpublished Ph. D. Thesis, Texas A&M University: 181p.

Orsi, T.H. and Anderson, A.L. 1994. Bubble characteristics in gassy sediments. Transactions of the Gulf Coast Association of Geological Societies, 44: 533-540.

Orsi, T.H., Edwards, C.M., and Anderson, A.L. 1994. X-ray computed tomography: a nondestructive method for quantitative analysis of sediment cores. Journal of Sedimentary Research A64(3): 690-693.

Paterson, D.M. 1994. Microbiological mediation of sediment structure and behaviour. in L.J. Stal and P. Caumette (eds). Microbial Mats, Publ Springer-Verlag: 97-109.

Warner, G.S., Nieber, J.L., Moore, I.D., and Geise, R.A. 1990. Characterizing macropores in soil by computed tomography. Soil Science Society of America Journal 53: 653-660.

FIGURE 1. Prints from the GE® Hilite Advantage CT scanner. (A) "Scouts" of 13 CT slices (2 to 14, increasing from left to right) of the sediment wedge; (B) the tomogram of CT slice 4 showing the chord (l = 15 mm) of the sediment segment and the air segment above; (C) the enscribed ROI of CT slice 4; and (D) the bimodal histogram of HU values within the ROI of panel C.

FIGURE 2. A scattergram of the computed saltwater wet bulk density (ROI-averaged) and transformed computed tomography (CT_{roi}) number for the calibration wedge. Note the excellent linear relationship that falls on the line established by Orsi (1994) and Orsi *et al.* (1994). We conclude that the calibration wedge is a valid and accurate method of calibrating CT number to bulk density for the analysis of macrostructure in sediment cores.

FIGURE 3. A scattergram of nomalised chord length (l/2r) and normalised sediment area (A_s/A_{tot}) for the sediment wedge. Also shown are the maximum errors in estimation of A_s due to changes in chord length across the 1.5 mm depth of the tomogram.

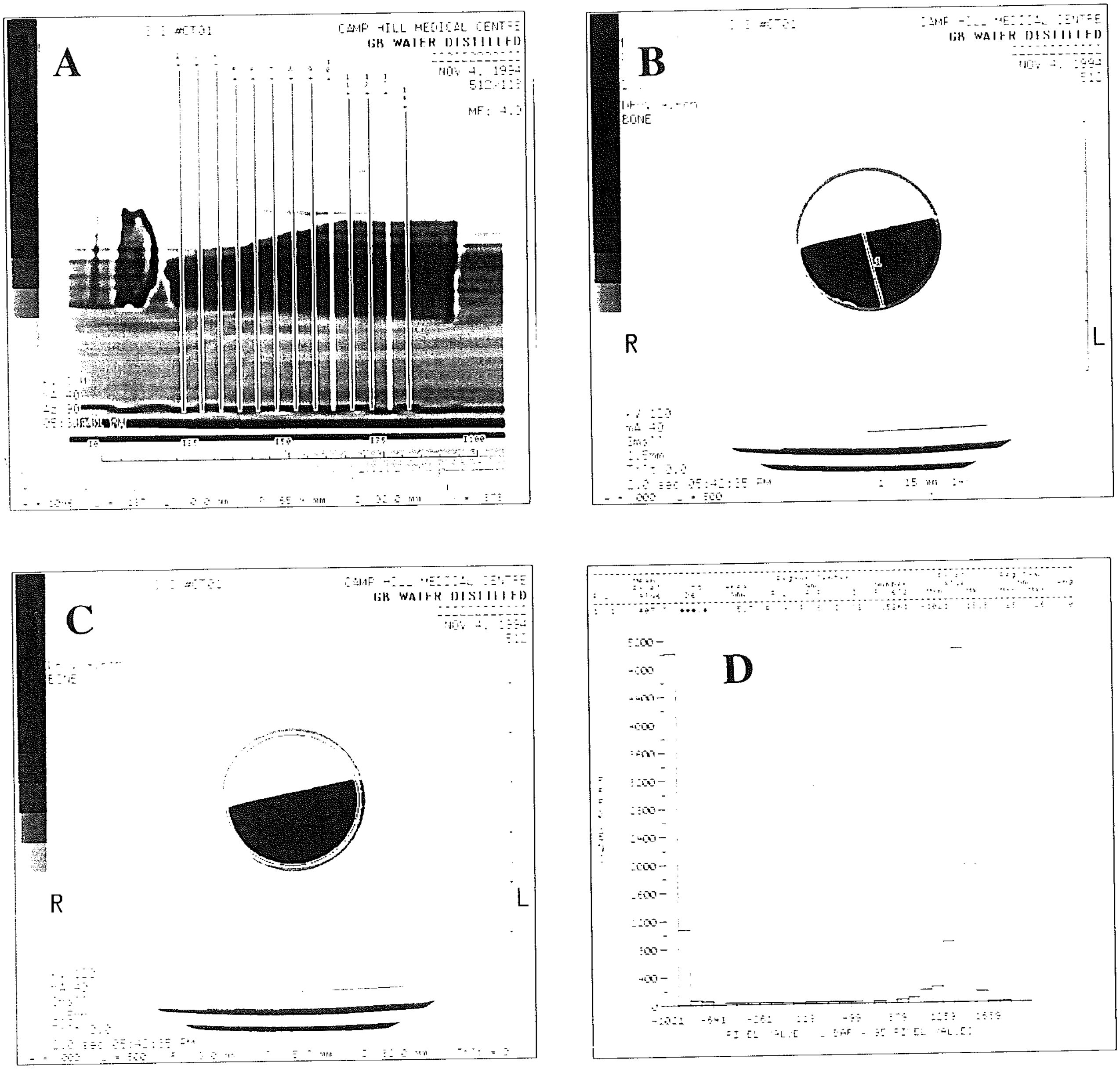
A
CAMP HILL MEDICAL CENTRE
GB WATER DISTILLED
NOV 4, 1994
B
CAMP HILL MEDICAL CENTRE
GB WATER DISTILLED
NOV 4, 1994
BONE
R
L
C
CAMP HILL MEDICAL CENTRE
GB WATER DISTILLED
NOV 4, 1994
R
L
D
PIXEL VALUE

Figure 1

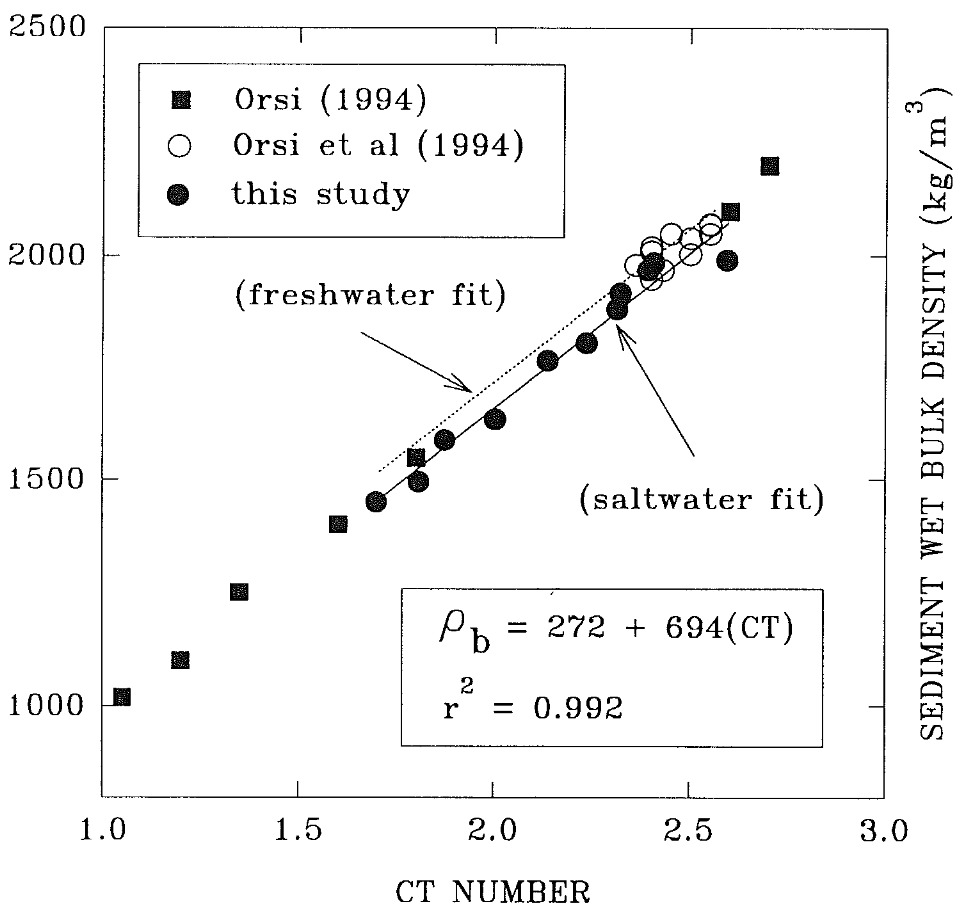

2500
2000
1500
1000
1.0
1.5
2.0
2.5
3.0
CT NUMBER
SEDIMENT WET BULK DENSITY (kg/m³)
Orsi (1994)
Orsi et al (1994)
this study
(freshwater fit)
(saltwater fit)
ρb = 272 + 694(CT)
r² = 0.992

50-263

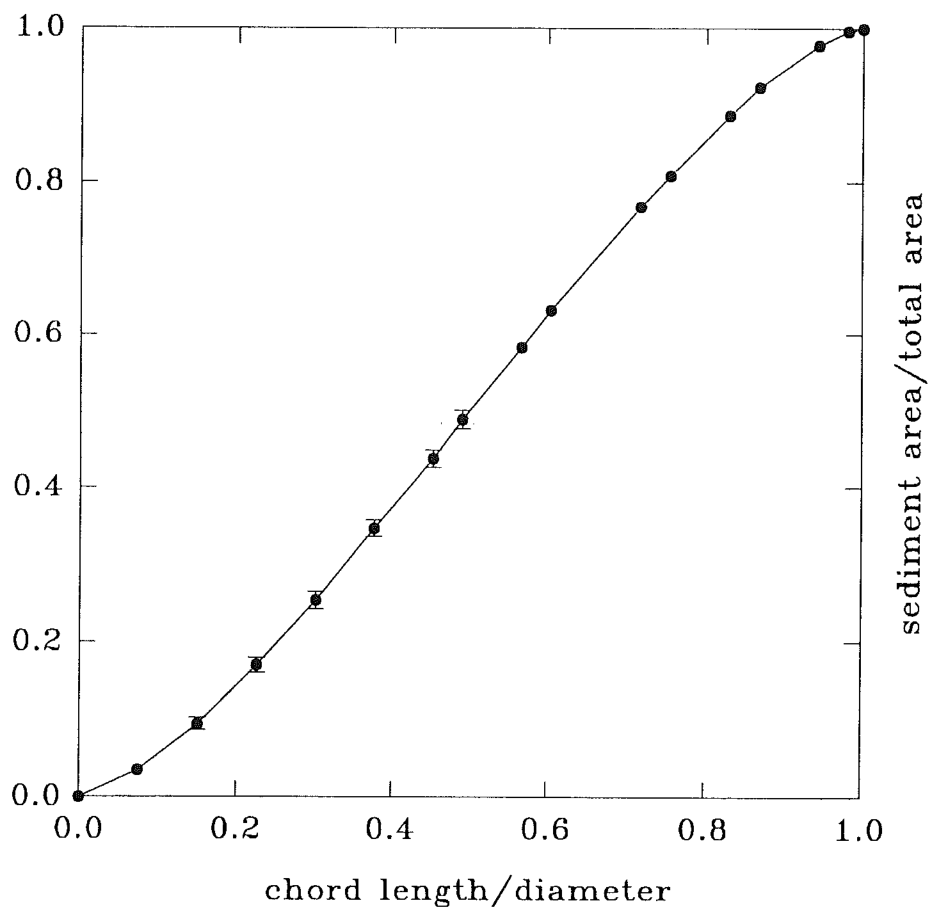
1.0
0.8
0.6
0.4
0.2
0.0
0.0
0.2
0.4
0.6
0.8
1.0
chord length/diameter
sediment area/total area

APPENDIX 5

GRAVITY CORE PHOTOGRAPHS

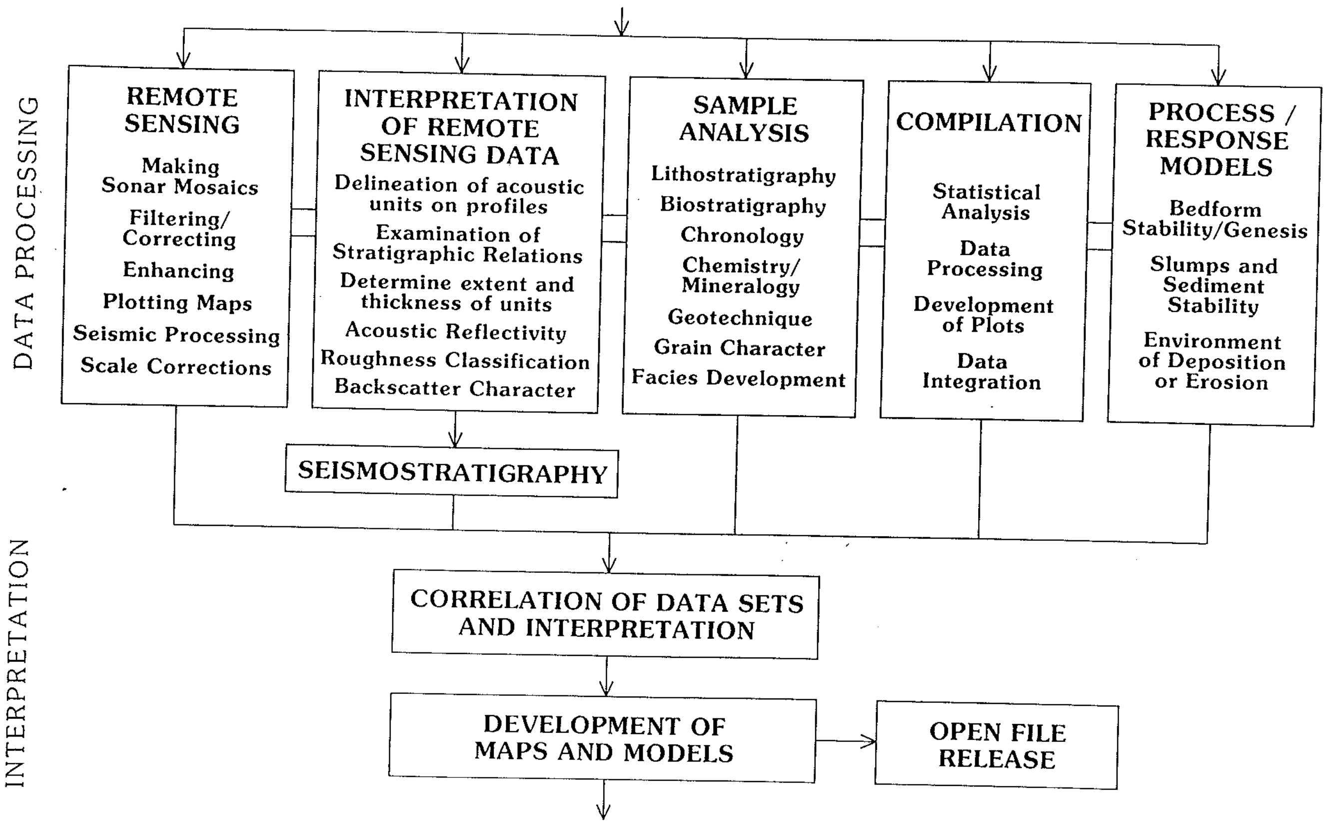

FIGURE 1.2. A scheme adopted by the Geological Survey of Canada to undertake surficial geological mapping. The scheme is applicable to the evaluation of dumpsites. The process/response module is the subject of this report.

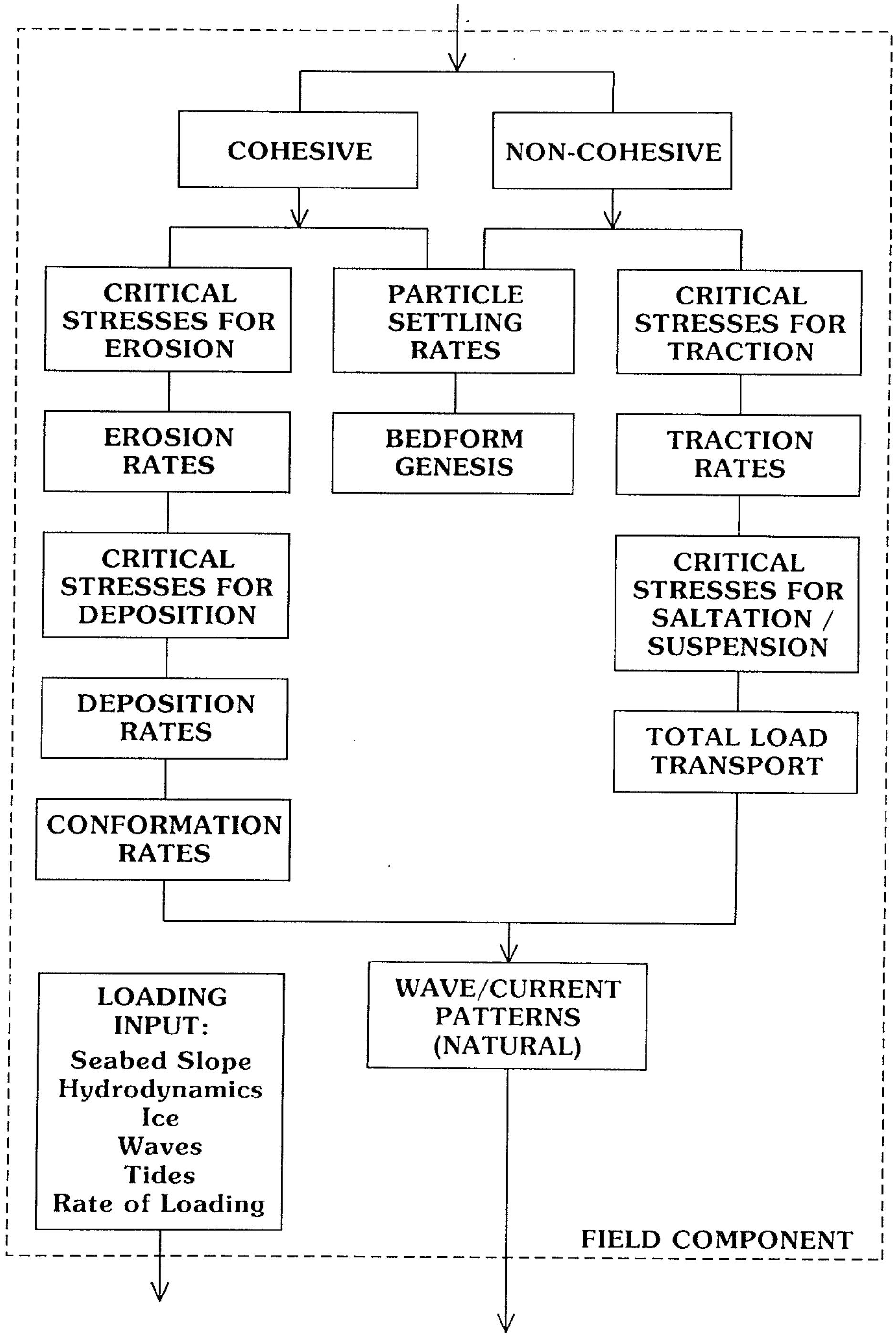

FIGURE 1.3. A detailed breakdown of elements involved in the modelling of sediment process\response. Sediments are broadly classified into either (1) cohesive, or (2) non-cohesive responses.

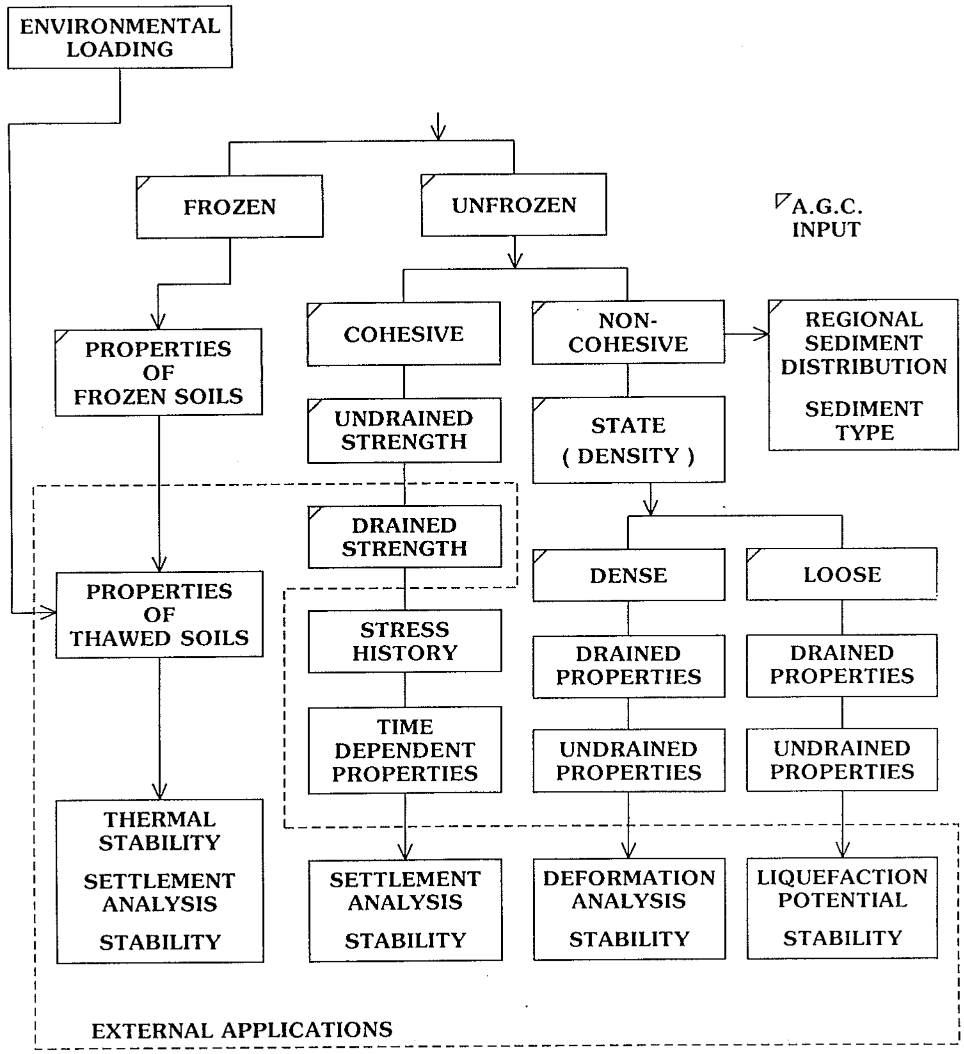

FIGURE 1.4. A detailed breakdown of the elements involved in the evaluation of mass movement of seabed sediments.

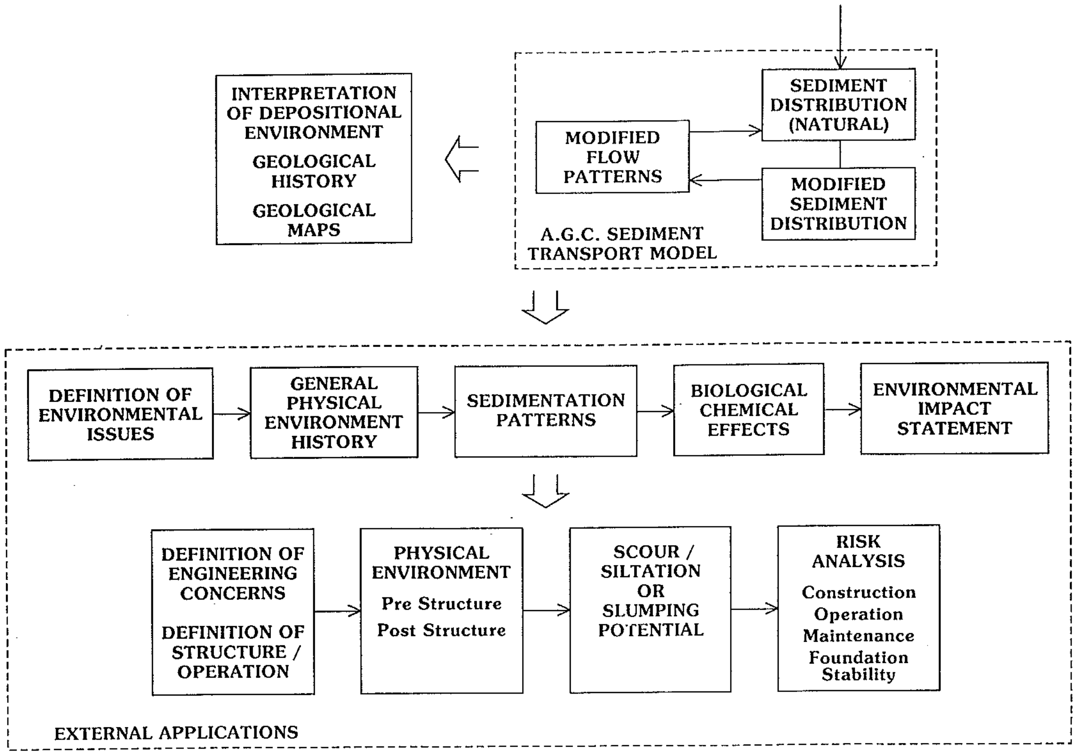

FIGURE 1.5. A schematic representation of the role of seabed stability studies in (1) environmental impact assessment, and (2) engineering risk analysis.

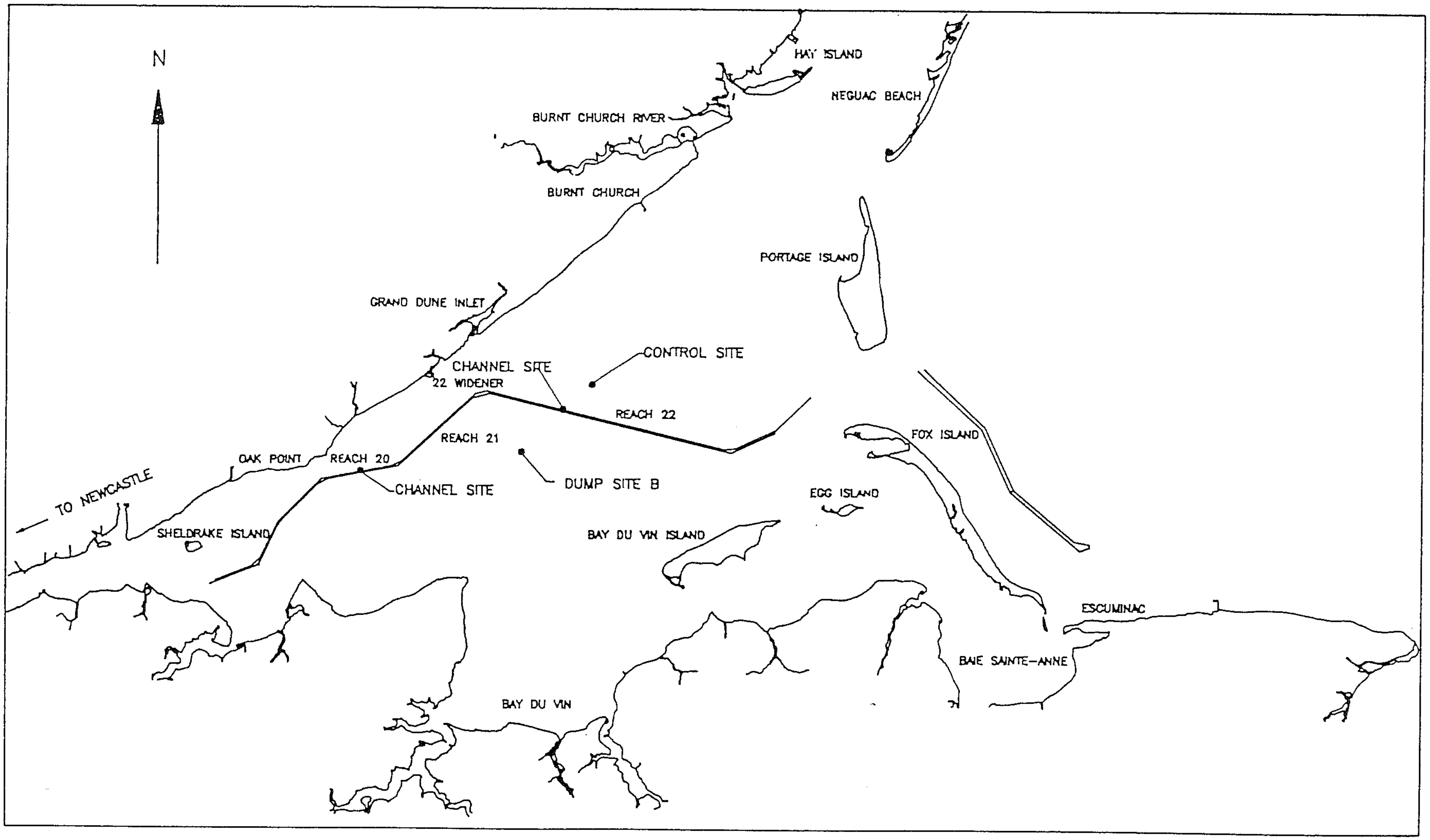

FIGURE 1.6. A location diagram of the Miramichi bay, New Brunswick.

FIGURE 3.2.1.2. A time-series plot of the Sea Carousel deployment at station MIR2, dumpsite B, Miramichi bay.(A) azimuthal and vertical current speed (m/s); (B) suspended sediment concentration (mg/L); and (C) erosion rate (kg/m^2/s).

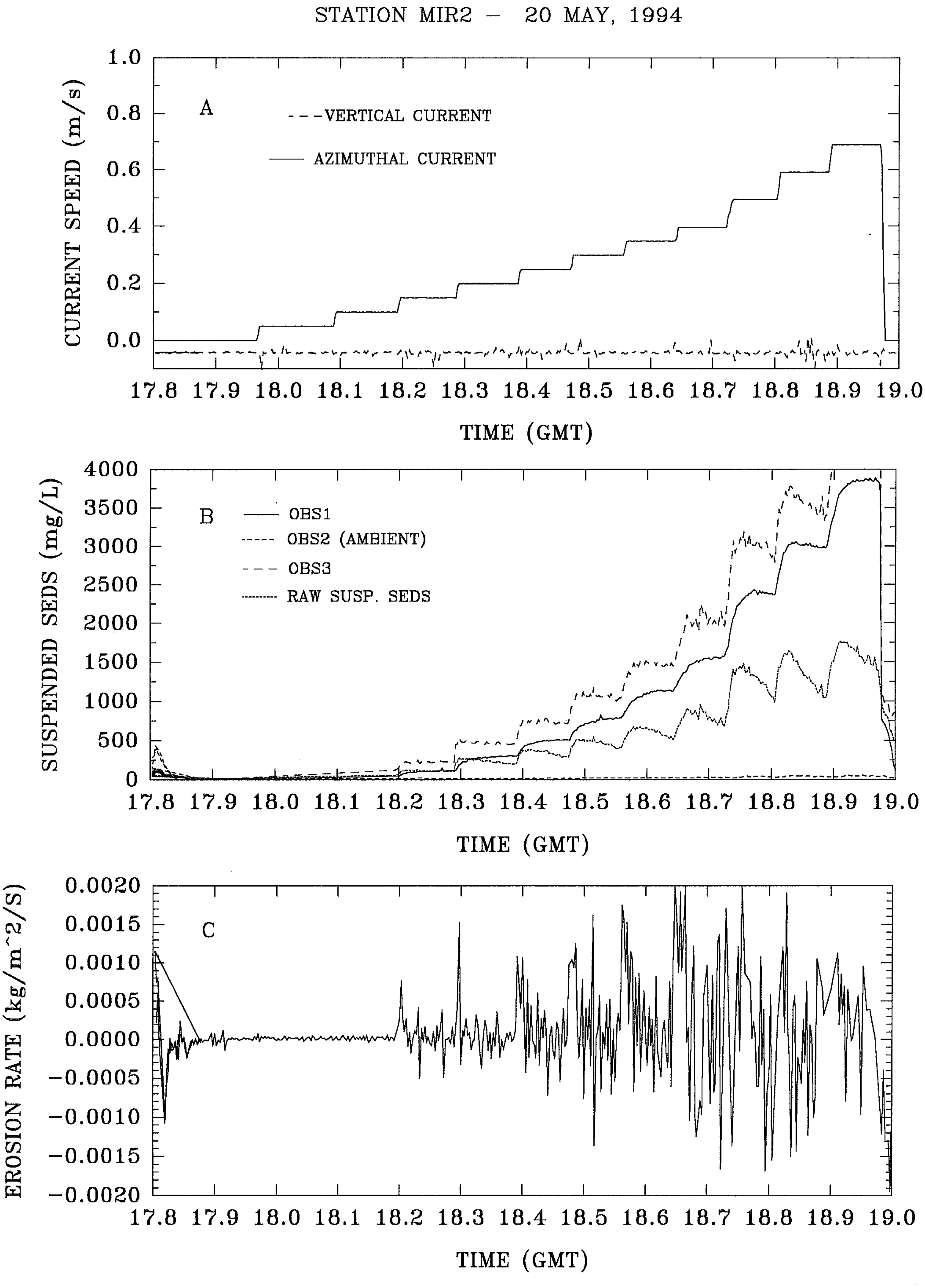

FIGURE 3.2.1.1. A time-series plot of the Sea Carousel deployment at station MIR1, dumpsite B, Miramichi bay.(A) azimuthal and vertical current speed (m/s); (B) suspended sediment concentration (mg/L); OBS1 is the upper sensor, OBS3 is the lower one. Note the erratic lower sensor signal, produced by the saltation of large grains and aggregates; and (C) erosion rate (kg/m^2/s). The data have been filtered by a 10-second time average. The asymptotic trend in SSC is diagnostic of Type I erosion.

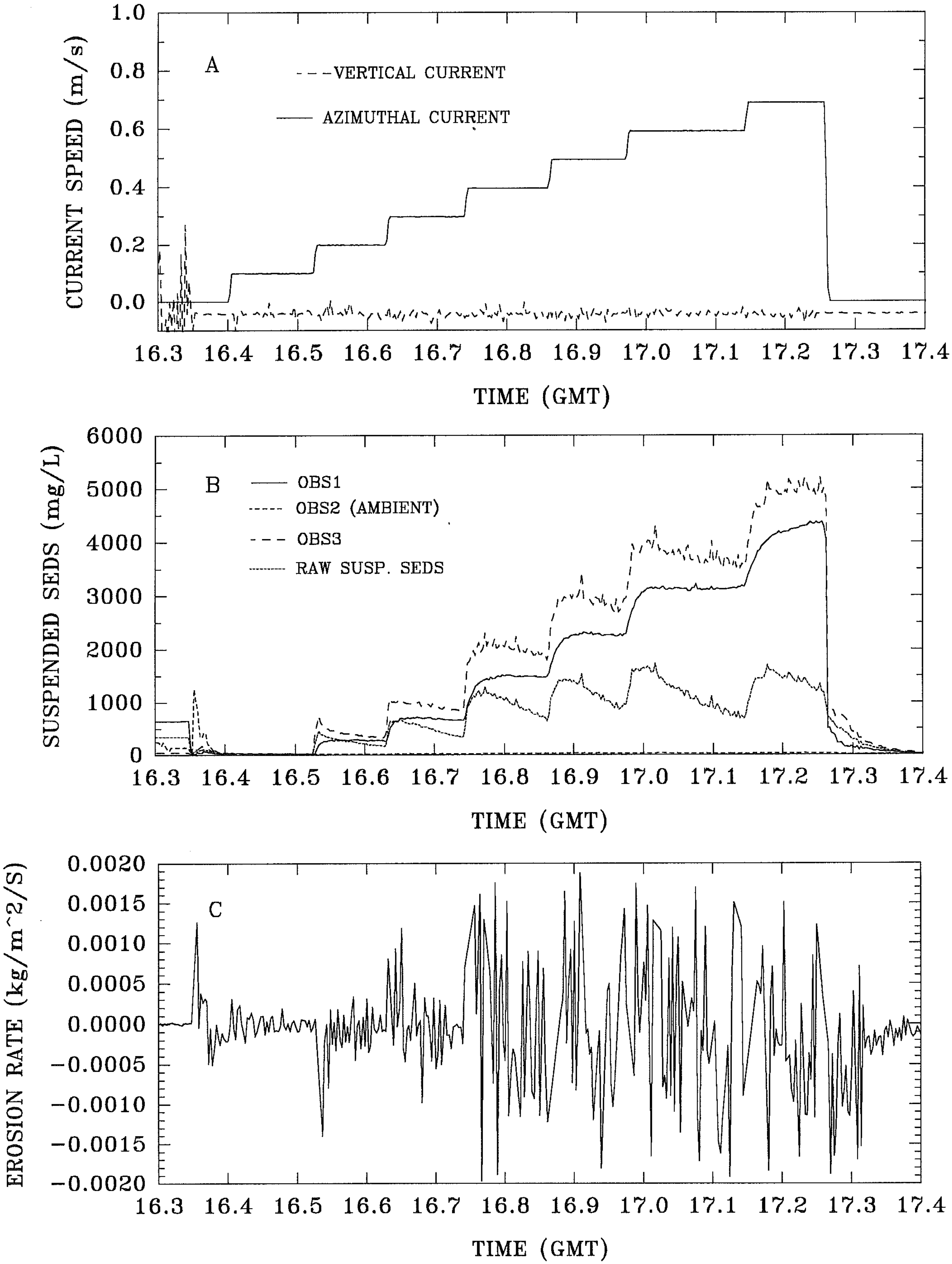

FIGURE 3.2.1.3. A time-series plot of the Sea Carousel deployment at station MIR3, dumpsite B, Miramichi bay.(A) azimuthal and vertical current speed (m/s); (B) suspended sediment concentration (mg/L); and (C) erosion rate (kg/m^2/s). In this example the data have been filtered through a 5-second time average.

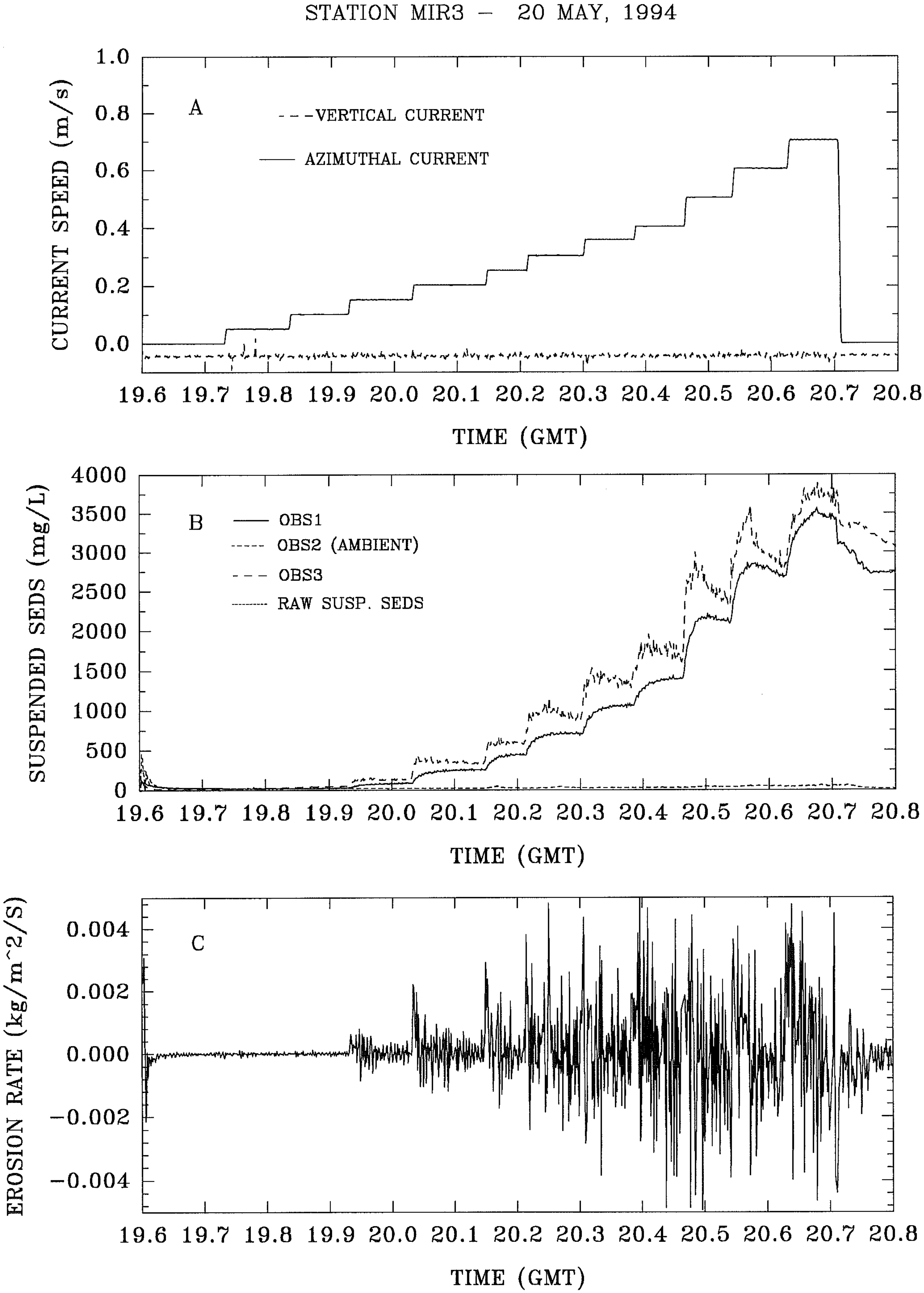

FIGURE 3.2.1.4. A time-series plot of the Sea Carousel deployment at station MIR3, dumpsite B, Miramichi bay.(A) azimuthal and vertical current speed (m/s); (B) suspended sediment concentration (mg/L); and (C) erosion rate (kg/m^2/s). In this example the data have been filtered through a 10-second time average.

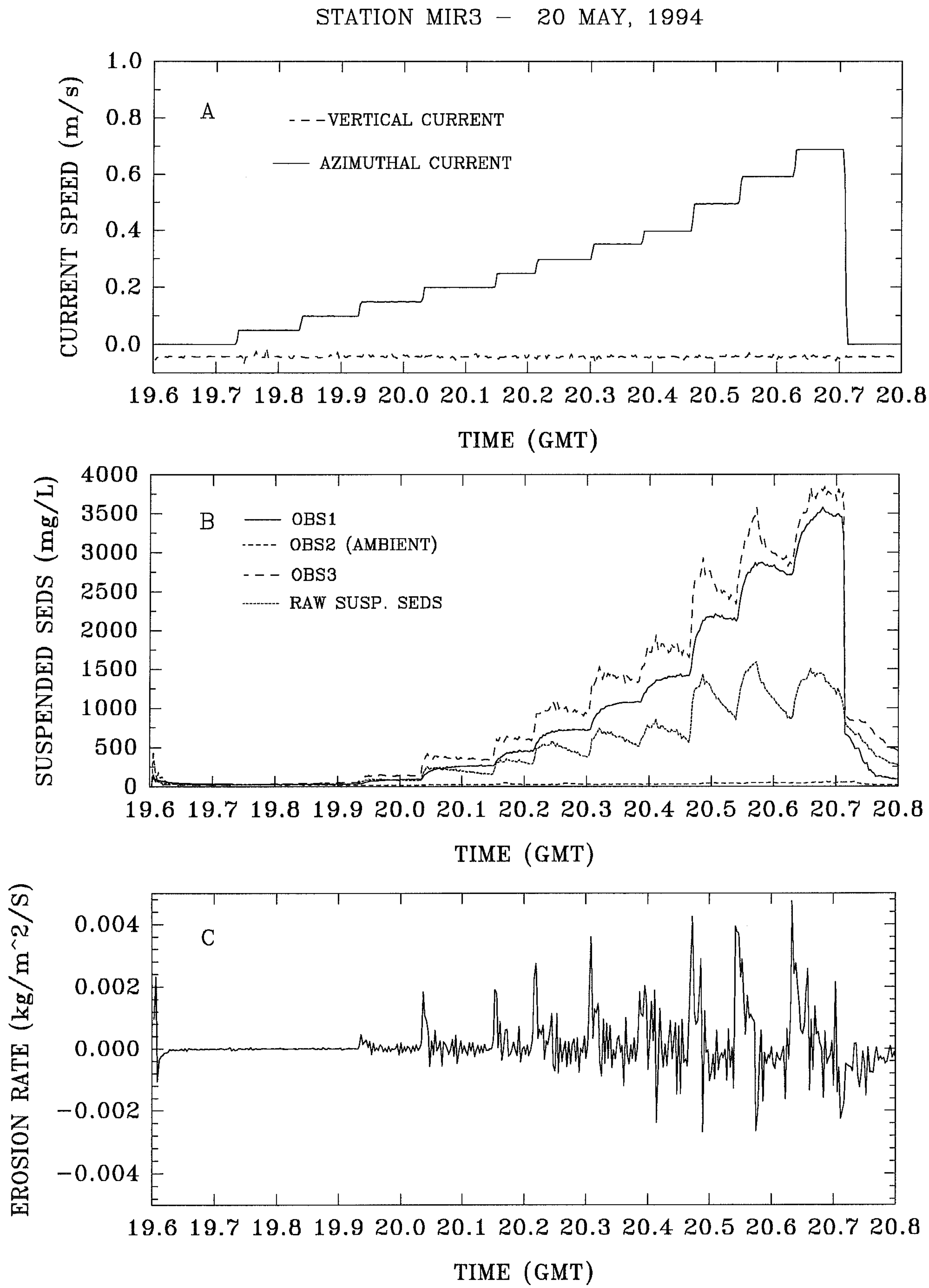

FIGURE 3.2.1.5. A time-series plot of the Sea Carousel deployment at station MIR3, dumpsite B, Miramichi bay.(A) azimuthal and vertical current speed (m/s); (B) suspended sediment concentration (mg/L); and (C) erosion rate (kg/m^2/s). In this case the data have been filtered through a 20-second time average.

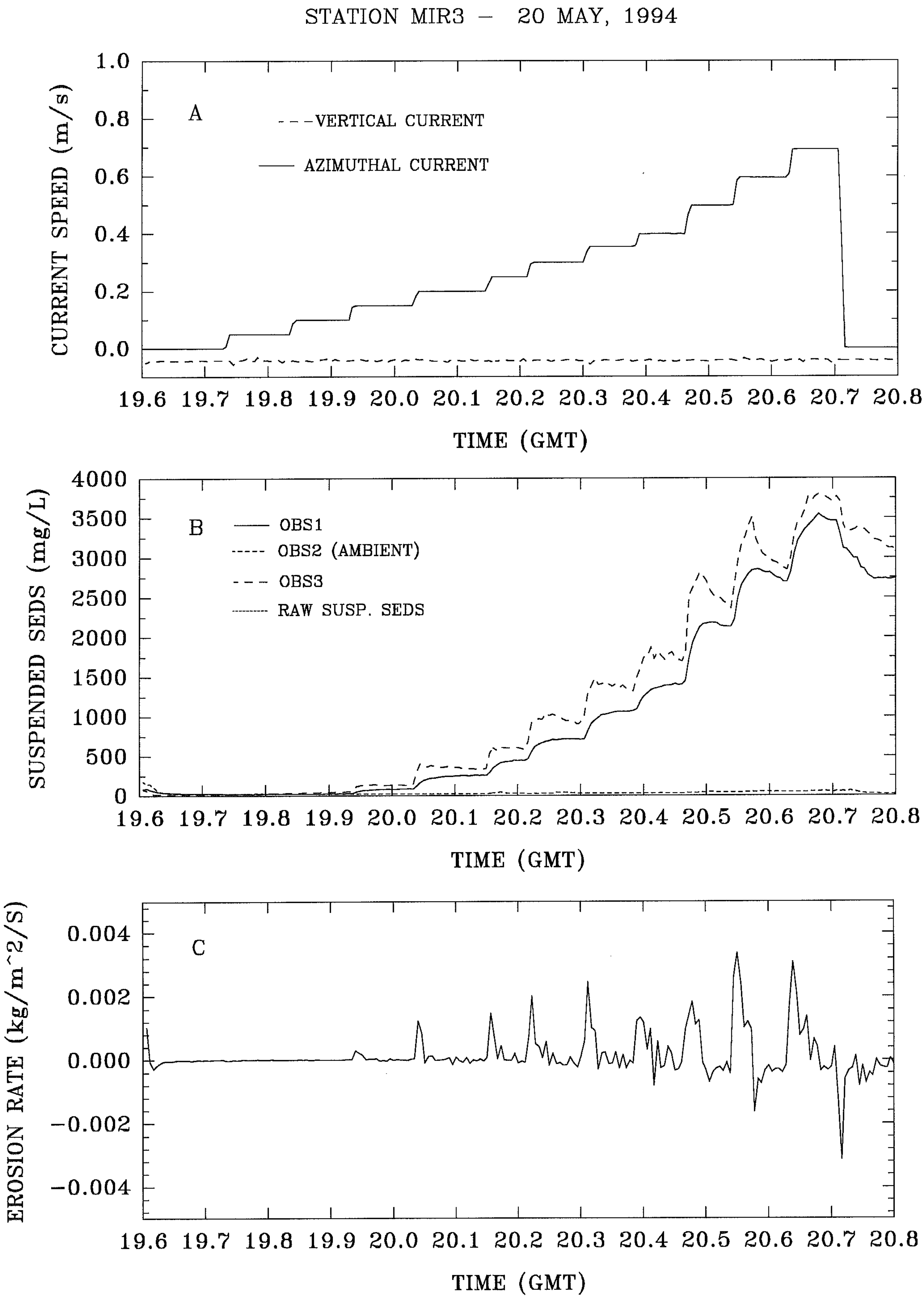

FIGURE 3.2.1.6. A time-series plot of the Sea Carousel deployment at station MIR3, dumpsite B, Miramichi bay.(A) azimuthal and vertical current speed (m/s); (B) suspended sediment concentration (mg/L); and (C) erosion rate (kg/m^2/s). In this example the data have been filtered through a 60-second time average.

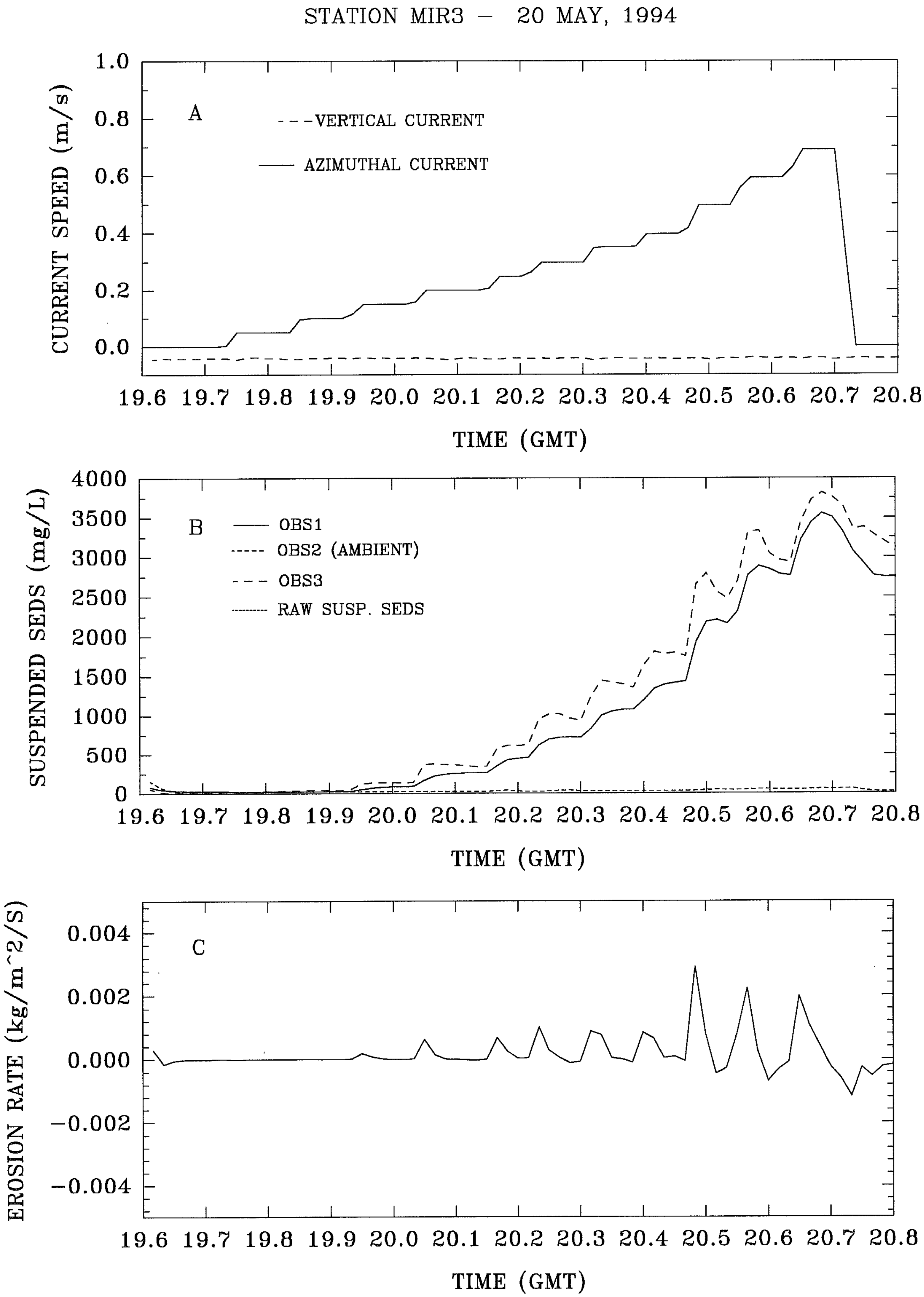

FIGURE 3.2.1.7. A time-series plot of the Sea Carousel deployment at station MIR4, dumpsite B, Miramichi bay.(A) azimuthal and vertical current speed (m/s); (B) suspended sediment concentration (mg/L); and (C) erosion rate ($kg/m^2/s$).

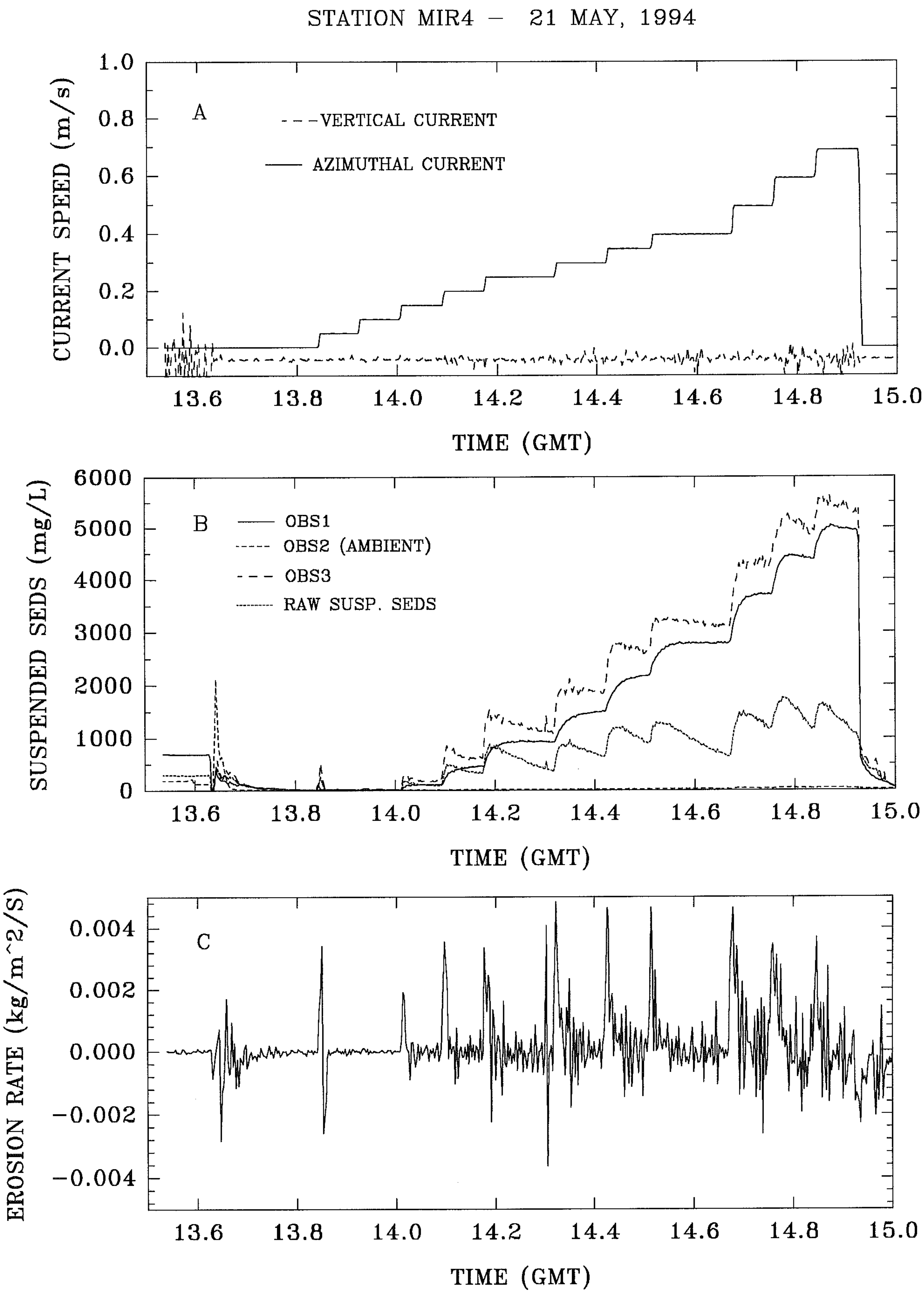

FIGURE 3.2.1.8. A time-series plot of the Sea Carousel deployment at station MIR5, dumpsite B, Miramichi bay.(A) azimuthal and vertical current speed (m/s); (B) suspended sediment concentration (mg/L); and (C) erosion rate (kg/m^2/s).

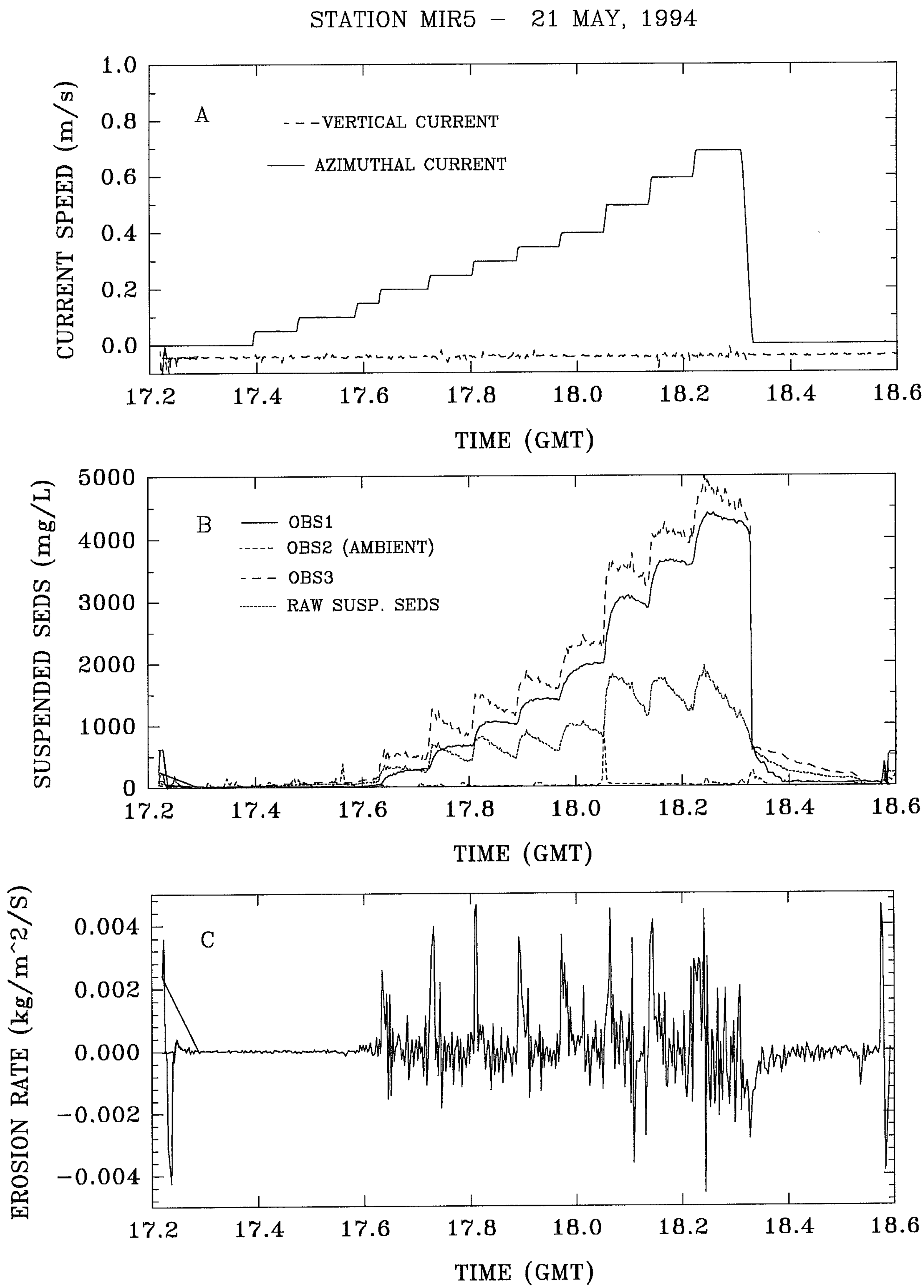

FIGURE 3.2.1.9. A time-series plot of the Sea Carousel deployment at station MIR6, dumpsite B, Miramichi bay.(A) azimuthal and vertical current speed (m/s); (B) suspended sediment concentration (mg/L); and (C) erosion rate (kg/m^2/s). 10 sec ave ?

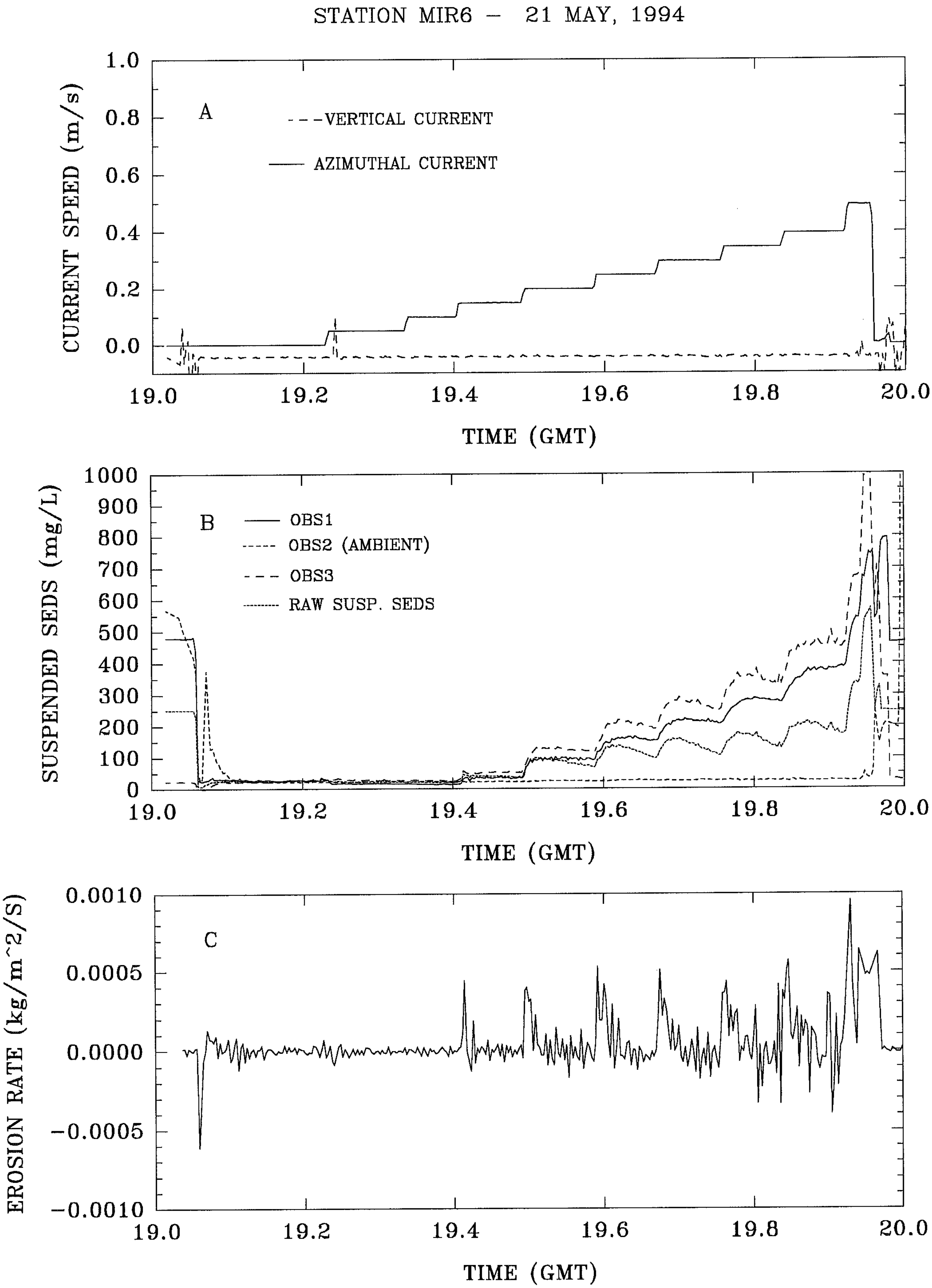

FIGURE 3.2.1.10. A time-series plot of the Sea Carousel deployment at station MIR7, dumpsite B, Miramichi bay.(A) azimuthal and vertical current speed (m/s); (B) suspended sediment concentration (mg/L); and (C) erosion rate (kg/m^2/s).

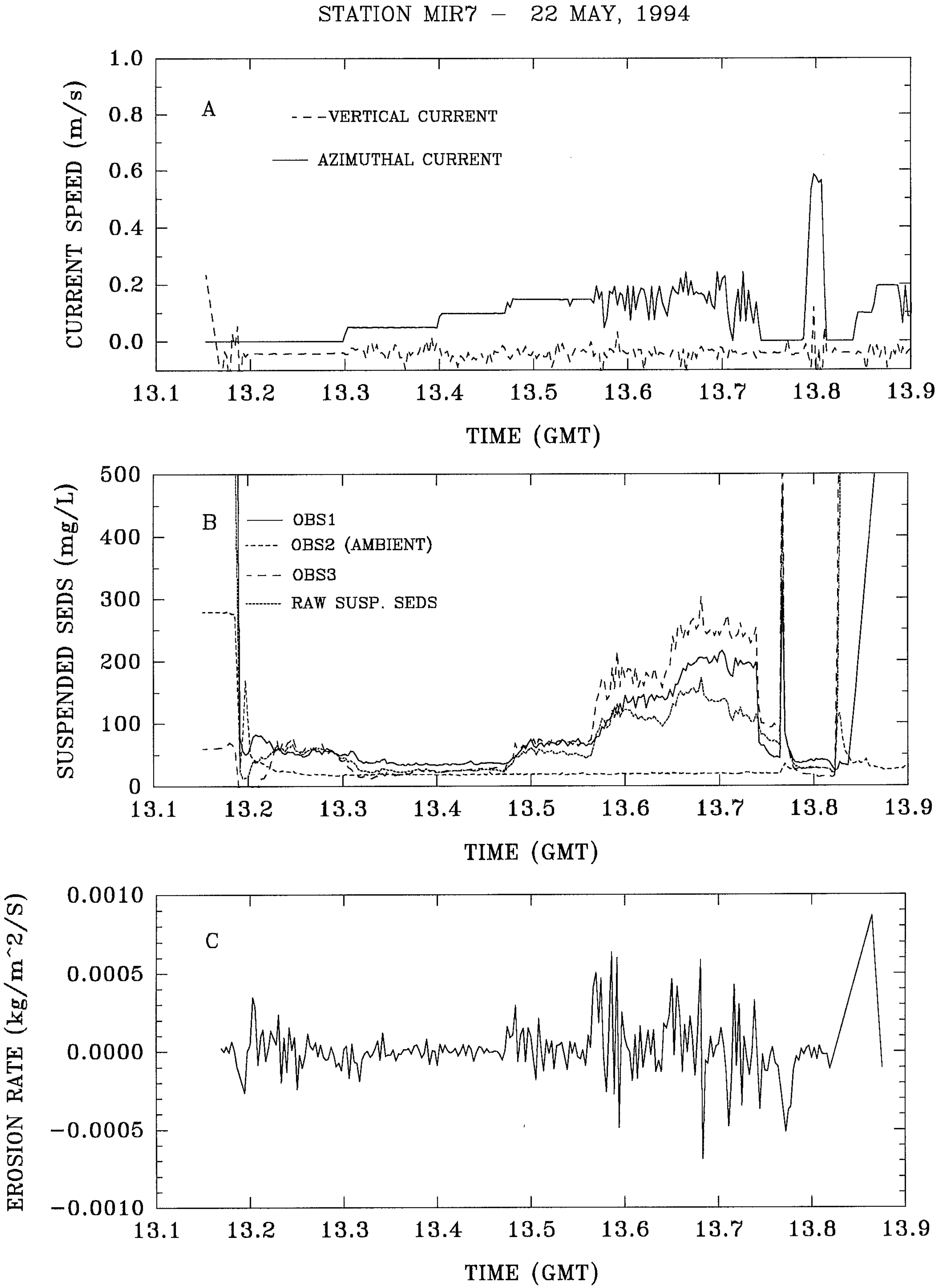

FIGURE 3.2.1.11. A time-series plot of the Sea Carousel deployment at station MIR8, dumpsite B, Miramichi bay.(A) azimuthal and vertical current speed (m/s); (B) suspended sediment concentration (mg/L); and (C) erosion rate (kg/m²/s).

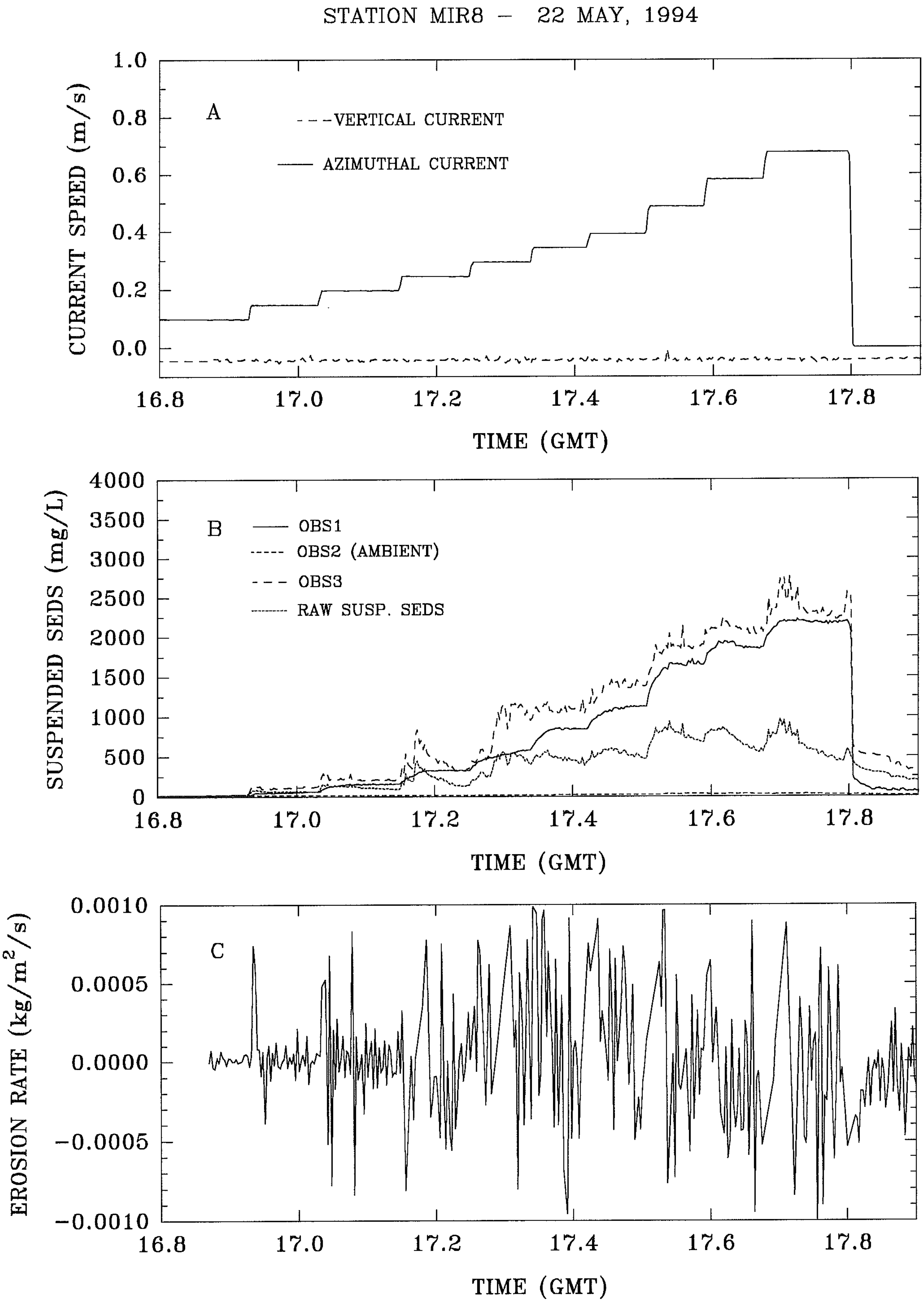

FIGURE 3.2.1.12. A time-series plot of the Sea Carousel deployment at station MIR9, dumpsite B, Miramichi bay.(A) azimuthal and vertical current speed (m/s); (B) suspended sediment concentration (mg/L); and (C) erosion rate ($kg/m^2/s$).

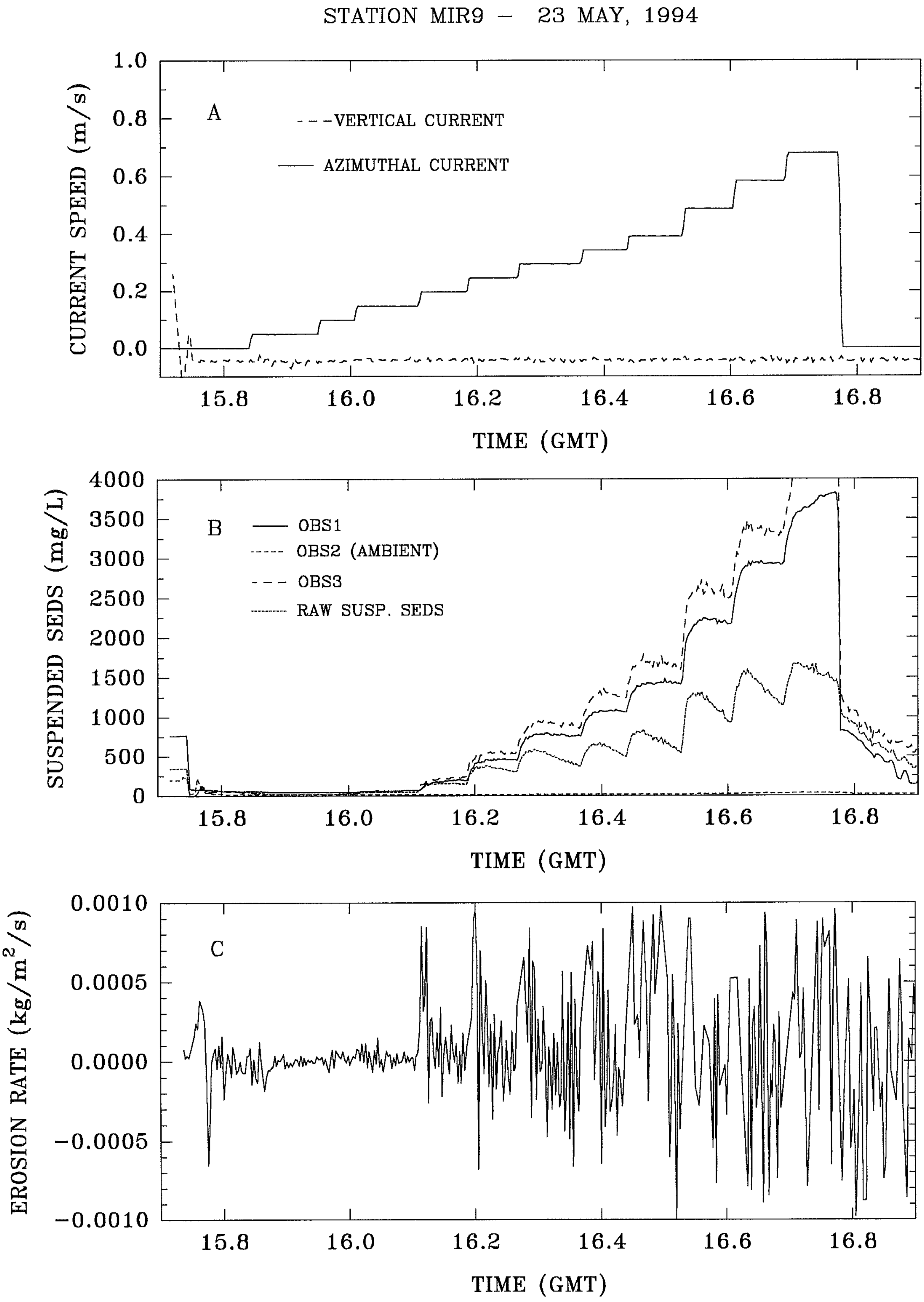

FIGURE 3.2.1.13. A time-series plot of the Sea Carousel deployment at station MIR10, dumpsite B, Miramichi bay.(A) azimuthal and vertical current speed (m/s); (B) suspended sediment concentration (mg/L); and (C) erosion rate (kg/m^2/s).

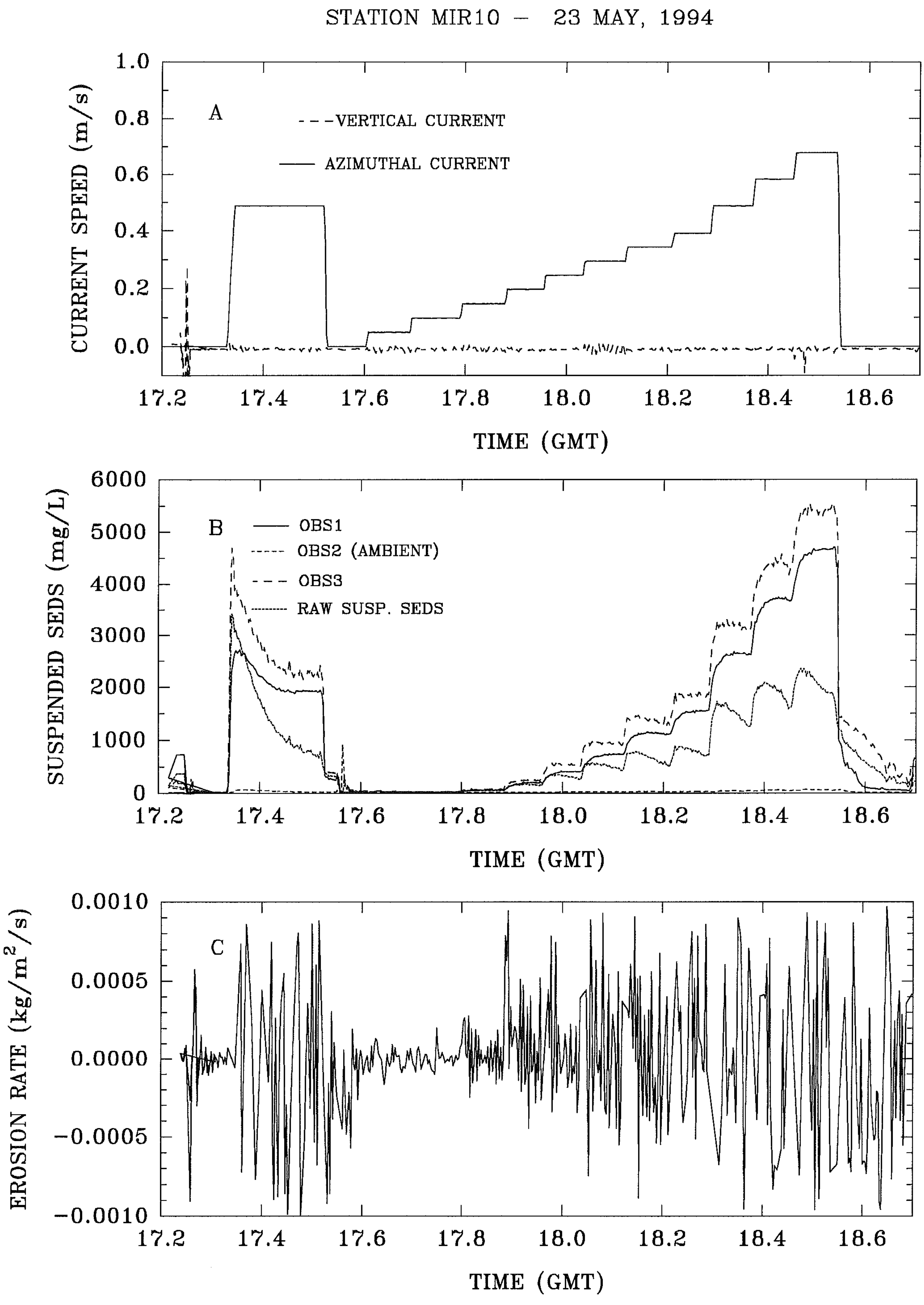

FIGURE 3.2.1.14. A time-series plot of the Sea Carousel deployment at station MIR11, dumpsite B, Miramichi bay.(A) azimuthal and vertical current speed (m/s); (B) suspended sediment concentration (mg/L); and (C) erosion rate (kg/m^2/s).

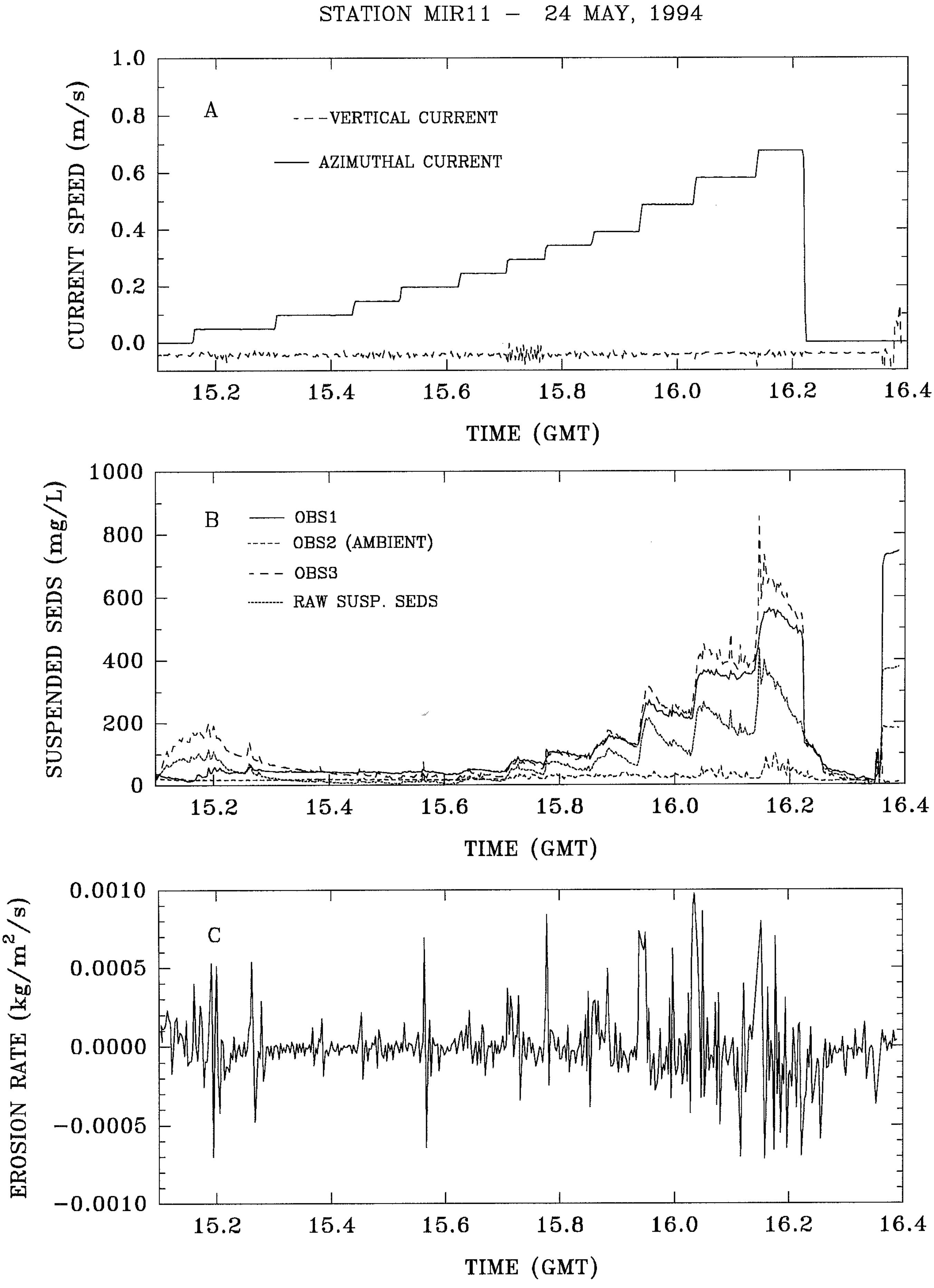

FIGURE 3.2.1.15. A time-series plot of the Sea Carousel deployment at station MIR12, dumpsite B, Miramichi bay.(A) azimuthal and vertical current speed (m/s); (B) suspended sediment concentration (mg/L); and (C) erosion rate (kg/m^2/s).

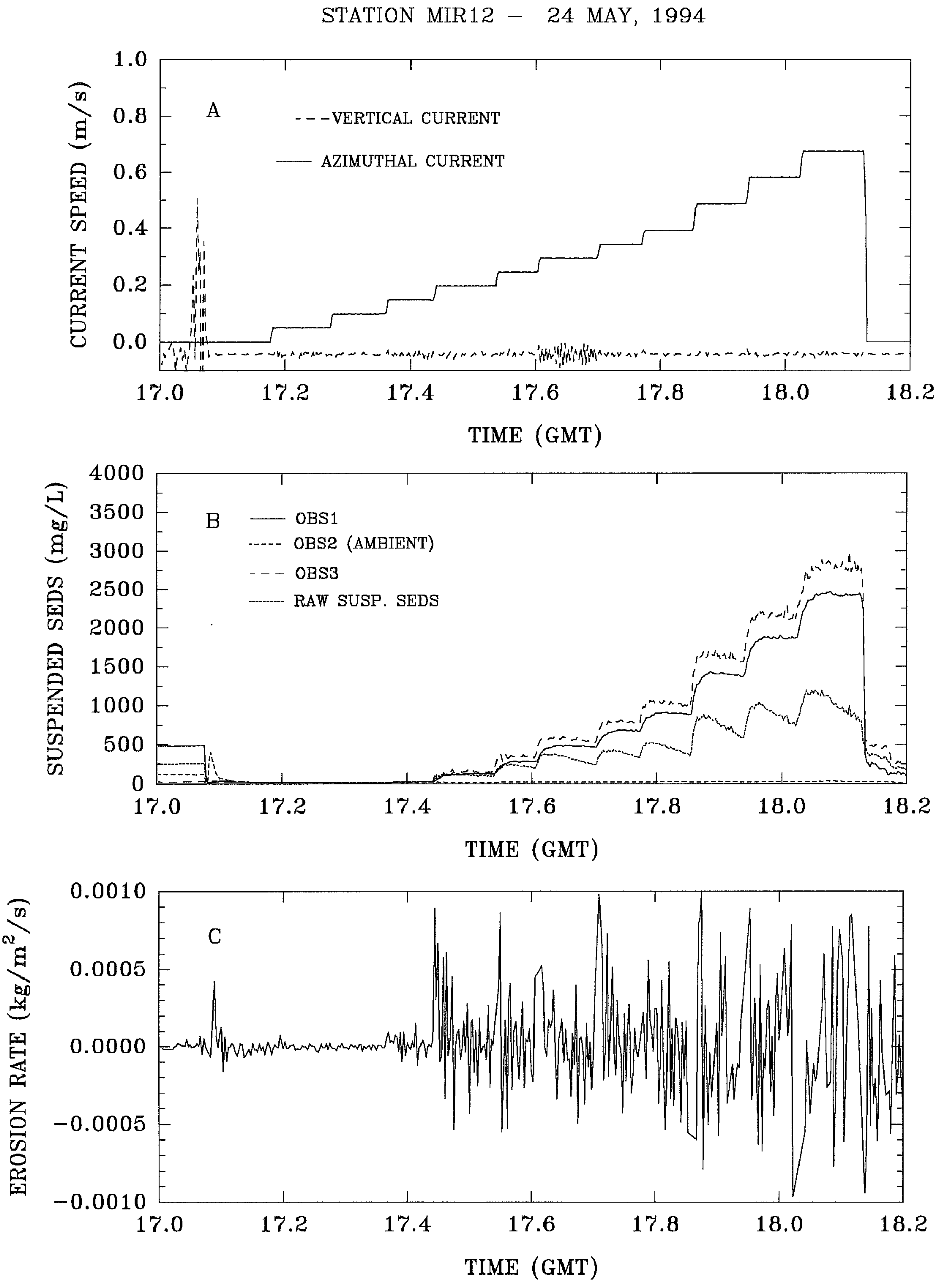

FIGURE 3.2.1.16. A time-series plot of the Sea Carousel deployment at station MIR13, dumpsite B, Miramichi bay.(A) azimuthal and vertical current speed (m/s); (B) suspended sediment concentration (mg/L); and (C) erosion rate ($kg/m^2/s$).

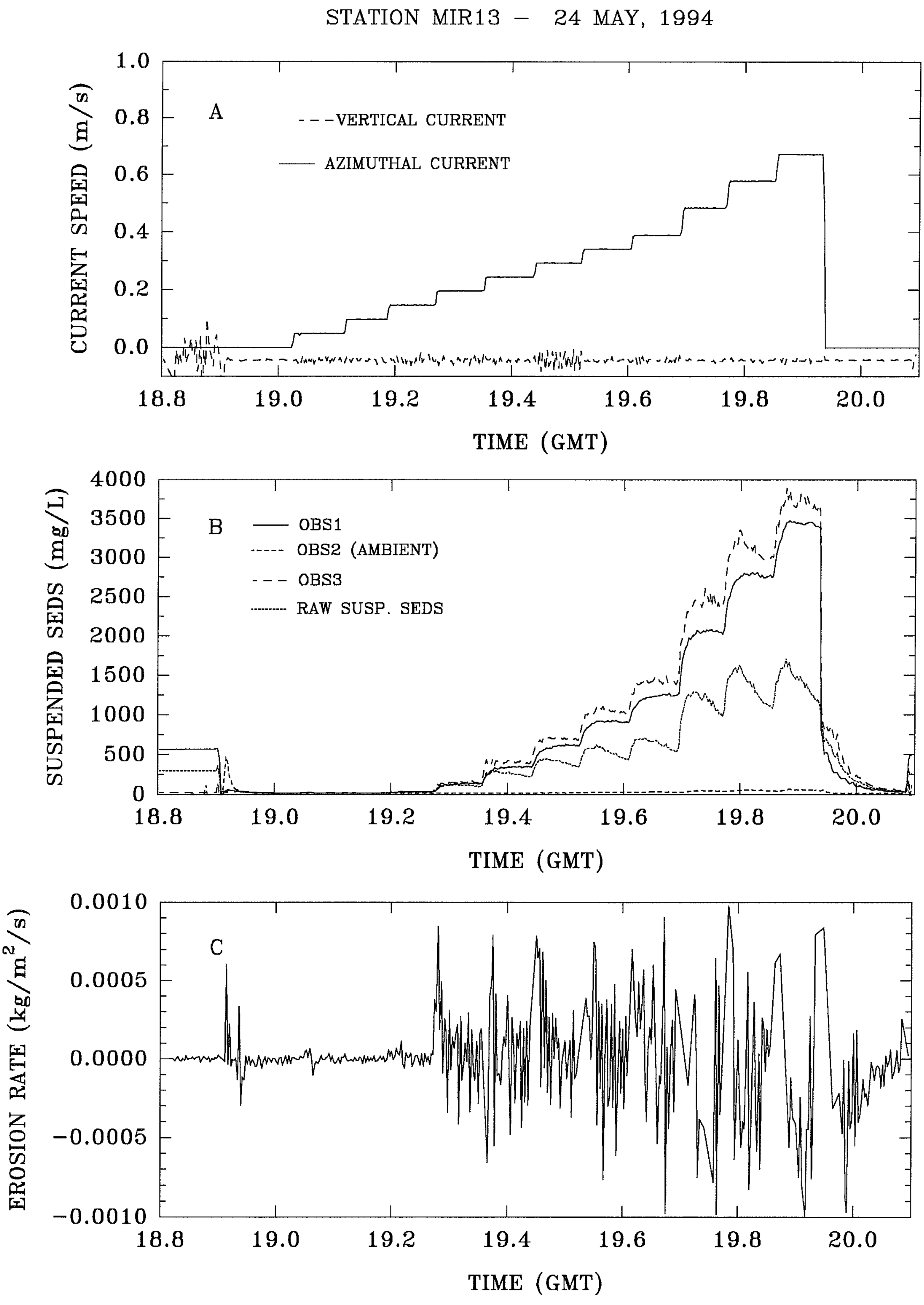

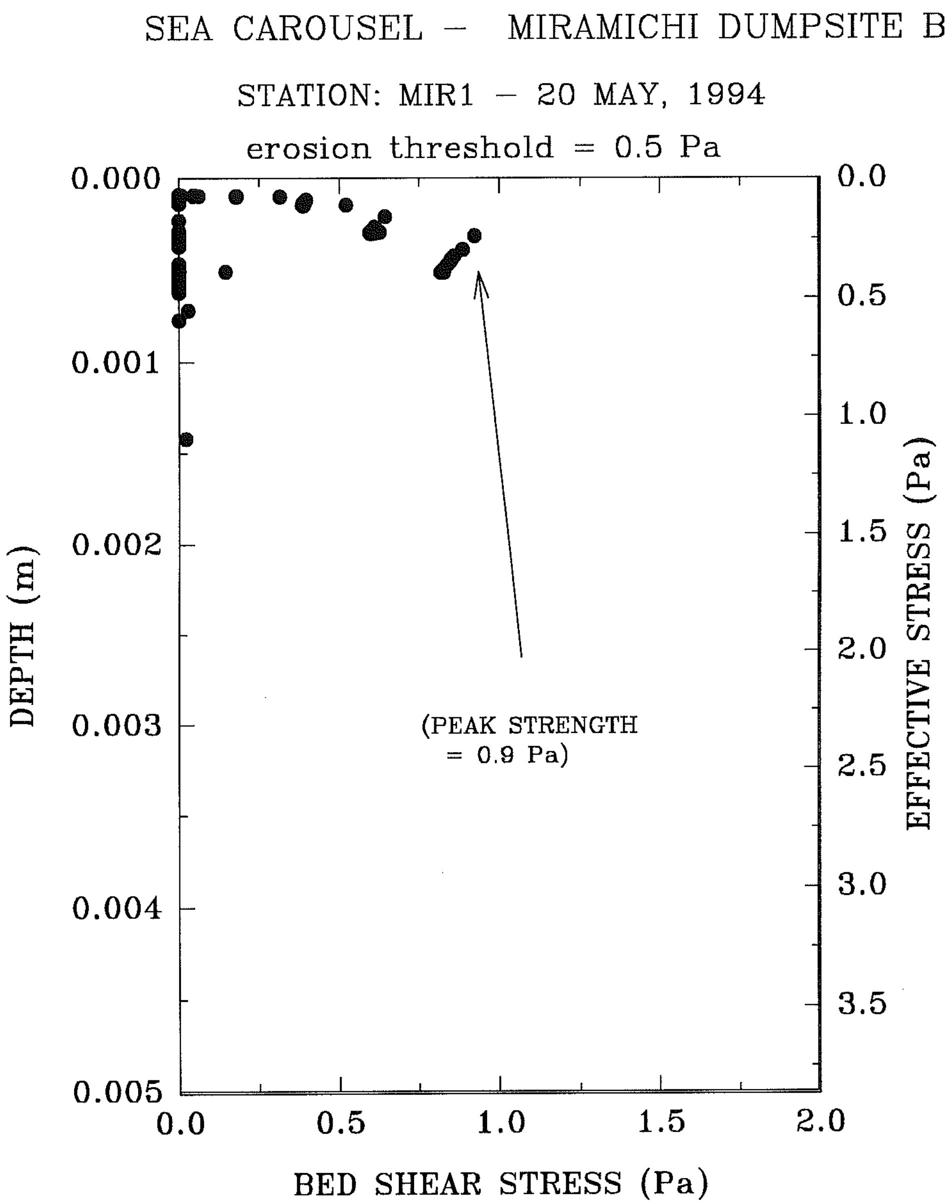

FIGURE 3.2.2.1. A synthetic core from station MIR1 computed from the Sea Carousel time-series data on eroded mass. The erosion threshold is 0.5 Pa; the maximum strength is 0.9 Pa and is found 0.0005 m below the mudline.

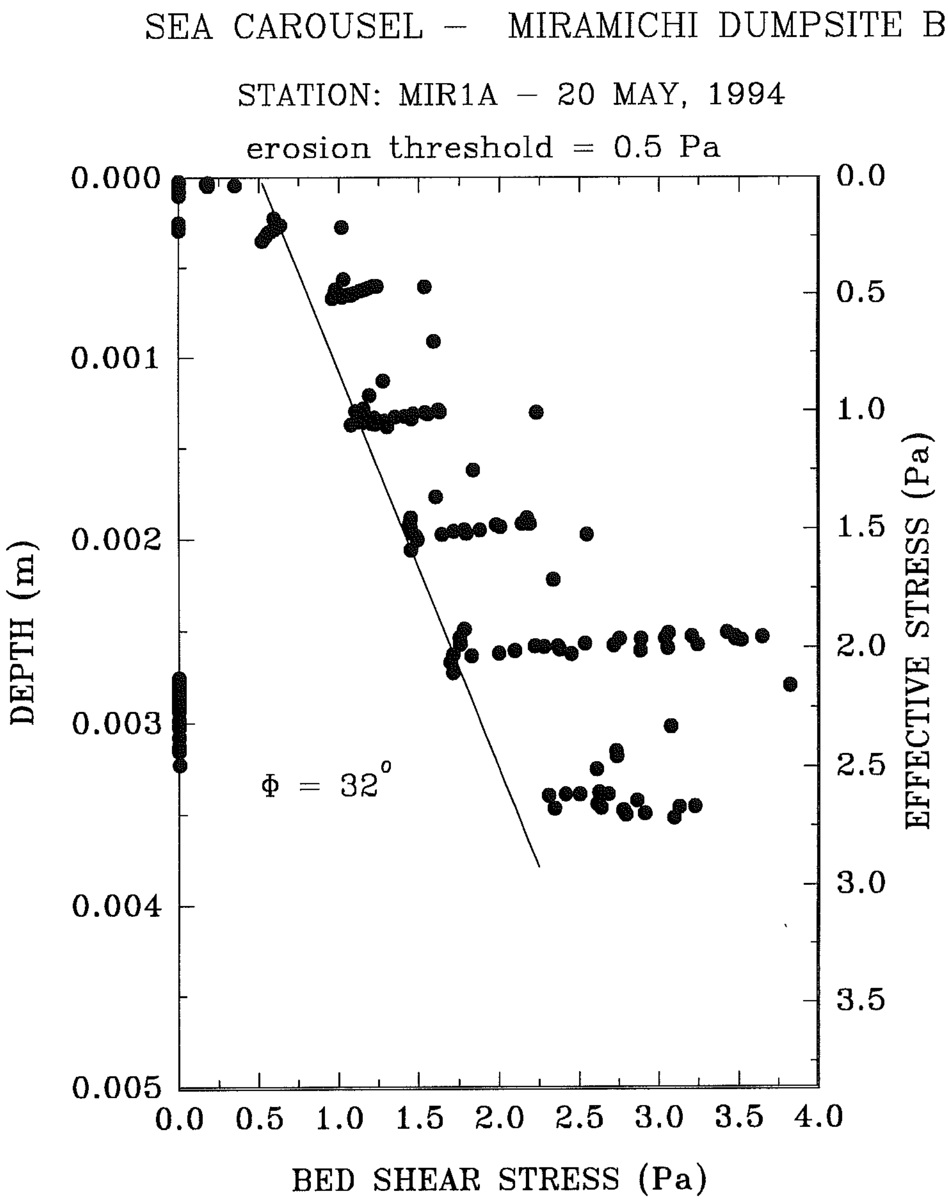

FIGURE 3.2.2.2. A synthetic core from station MIR1A computed from the Sea Carousel time-series data on eroded mass. The erosion threshold is 0.5 Pa, and the substrate is stable yielding a friction angle of 32°.

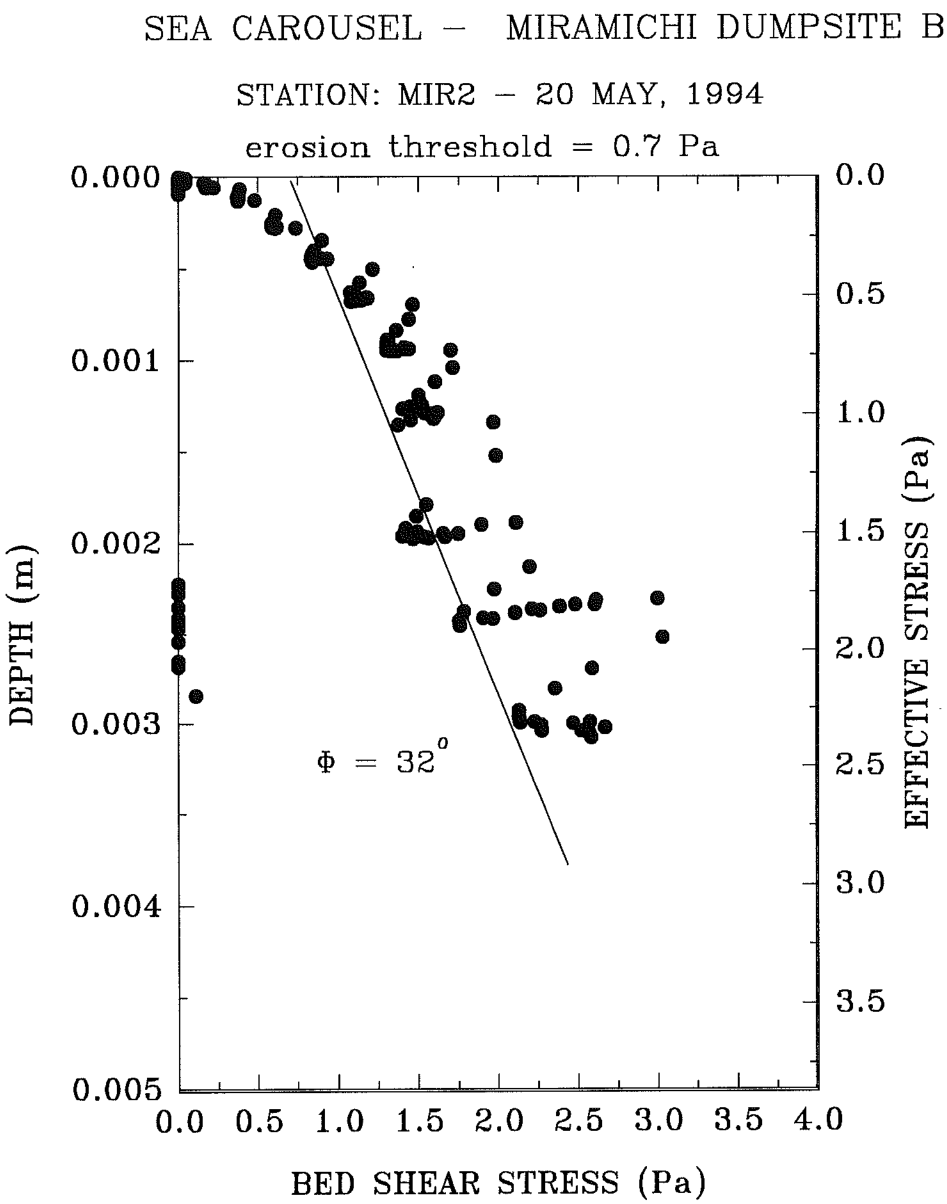

FIGURE 3.2.2.3. A synthetic core from station MIR2 computed from the Sea Carousel time-series data on eroded mass. The erosion threshold is 0.7 Pa, and the substrate is stable yielding a friction angle of 32°.

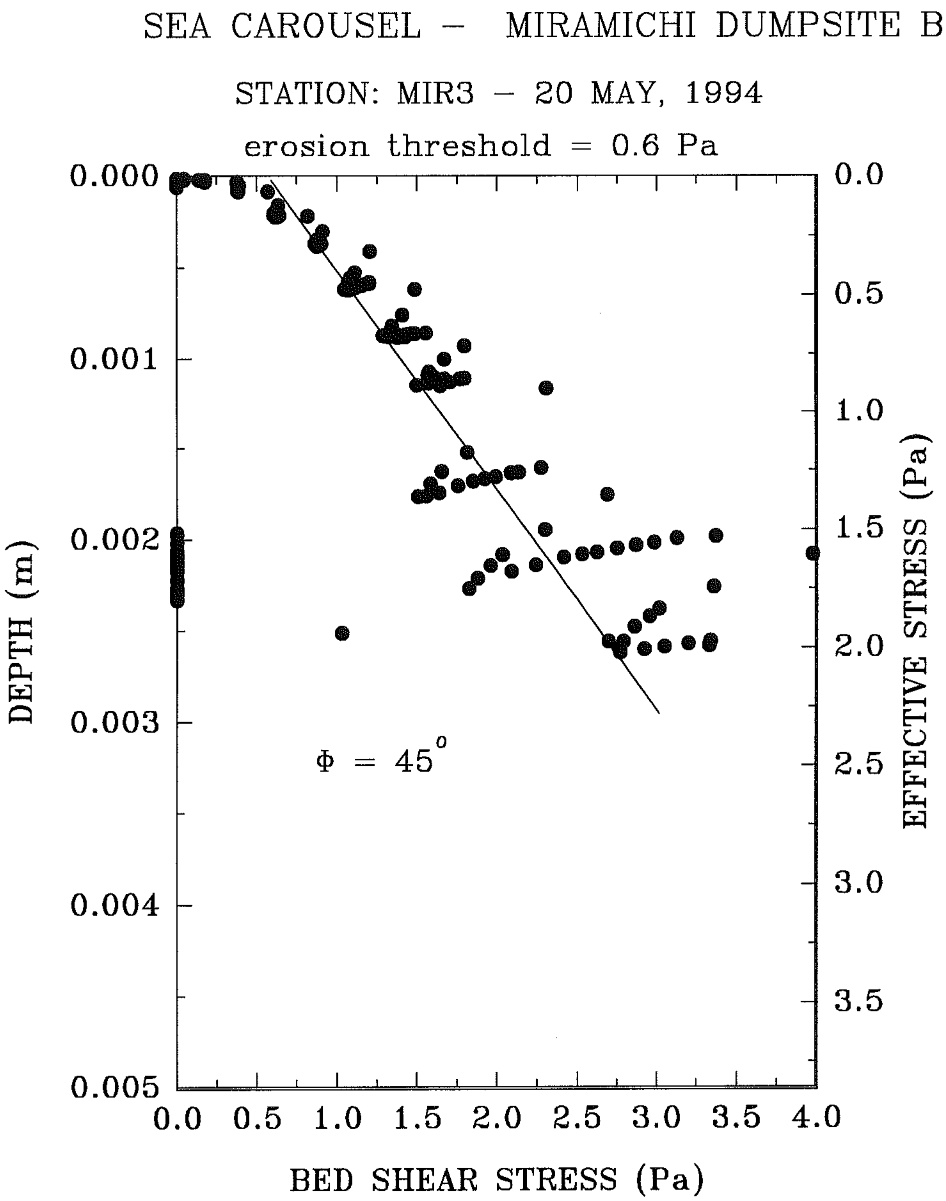

FIGURE 3.2.2.4. A synthetic core from station MIR3 computed from the Sea Carousel time-series data on eroded mass. The erosion threshold is 0.6 Pa, and the substrate is stable yielding a friction angle of 45°.

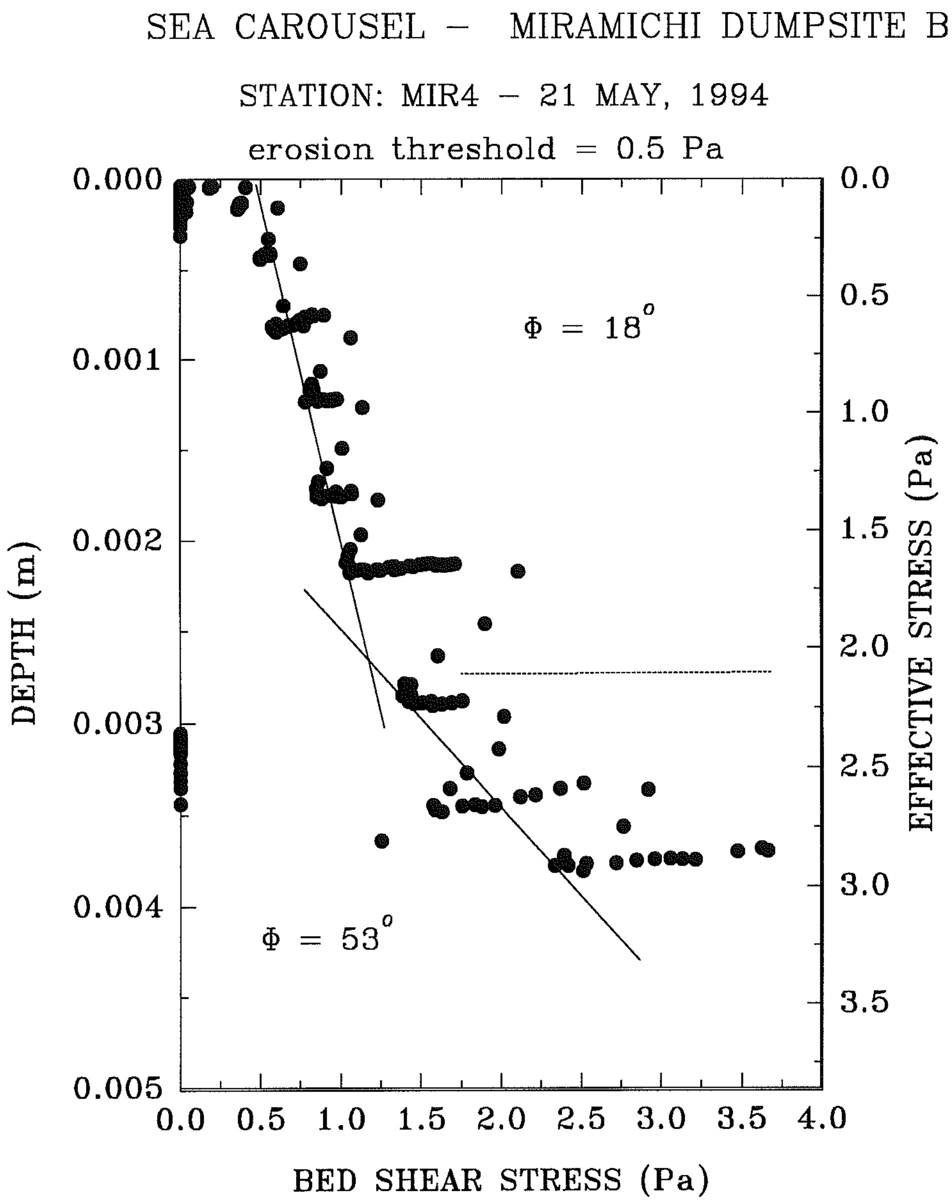

FIGURE 3.2.2.5. A synthetic core from station MIR4 computed from the Sea Carousel time-series data on eroded mass. The erosion threshold is 0.5 Pa, and the substrate is stable yielding friction angles of 18° and 53°.

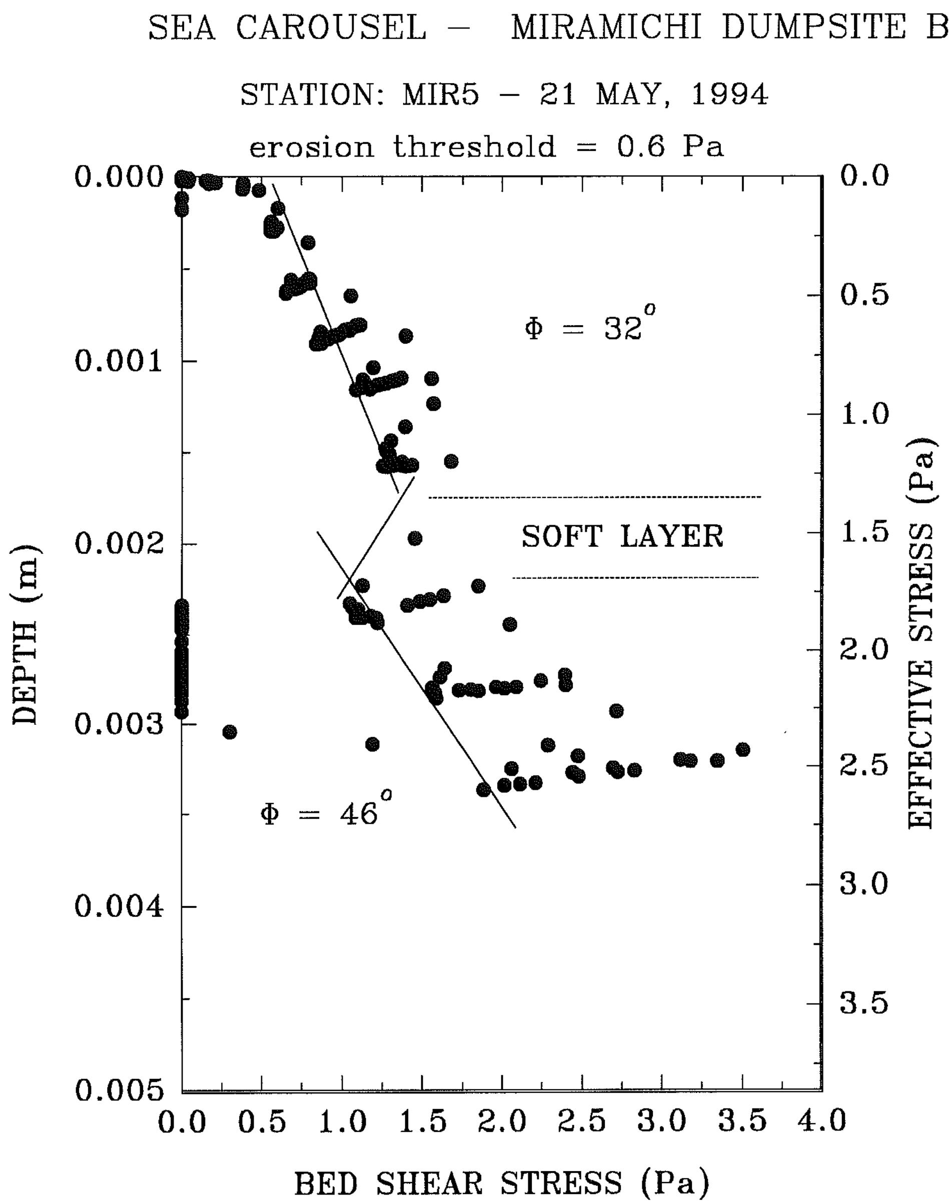

FIGURE 3.2.2.6. A synthetic core from station MIR5 computed from the Sea Carousel time-series data on eroded mass. The erosion threshold is 0.6 Pa, and the substrate is of variable stability yielding a friction angle of 32° and 46° separated by a "soft" at a depth of 0.002 m.

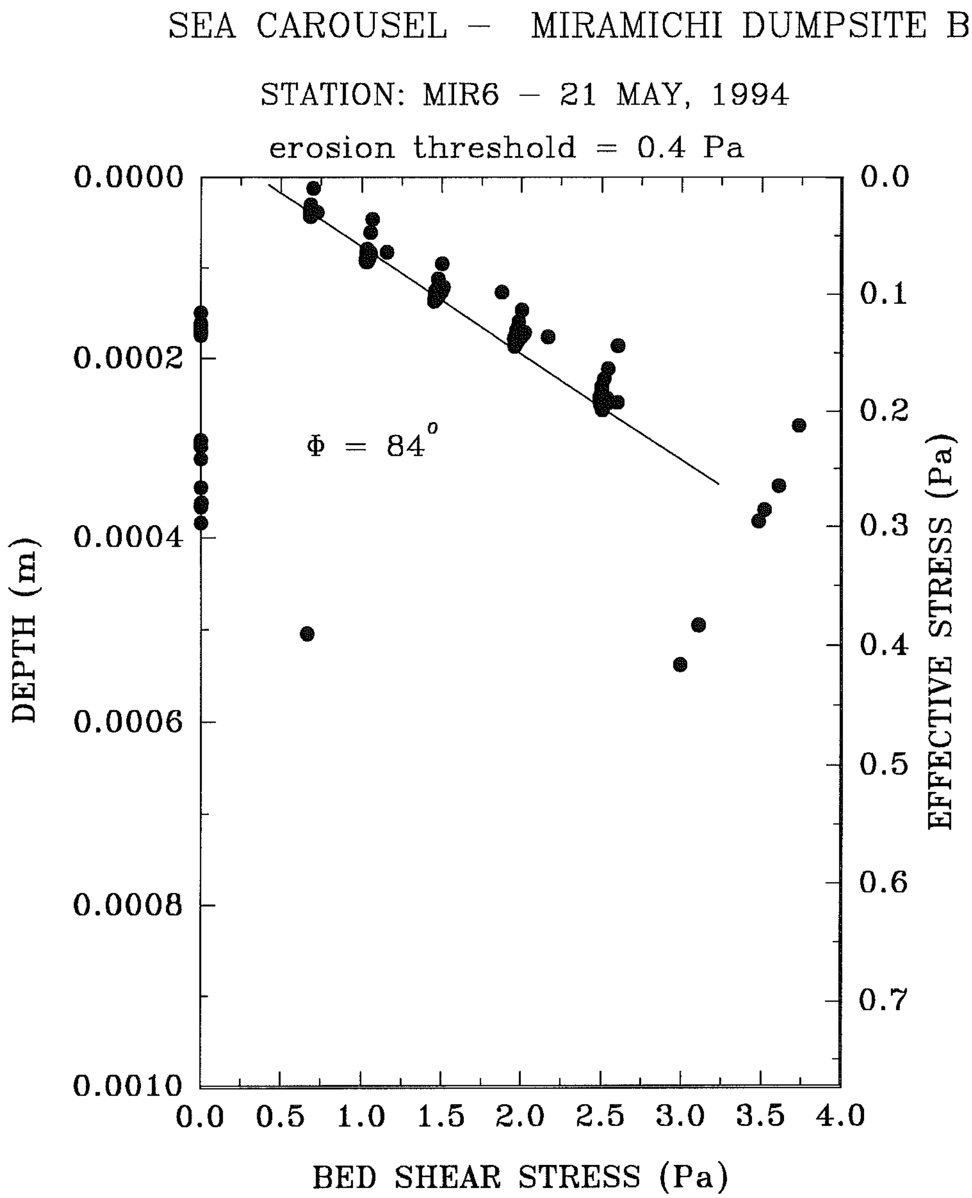

FIGURE 3.2.2.7. A synthetic core from station MIR6 computed from the Sea Carousel time-series data on eroded mass. The erosion threshold is 0.4 Pa, and the substrate is stable yielding a friction angle of 84°.

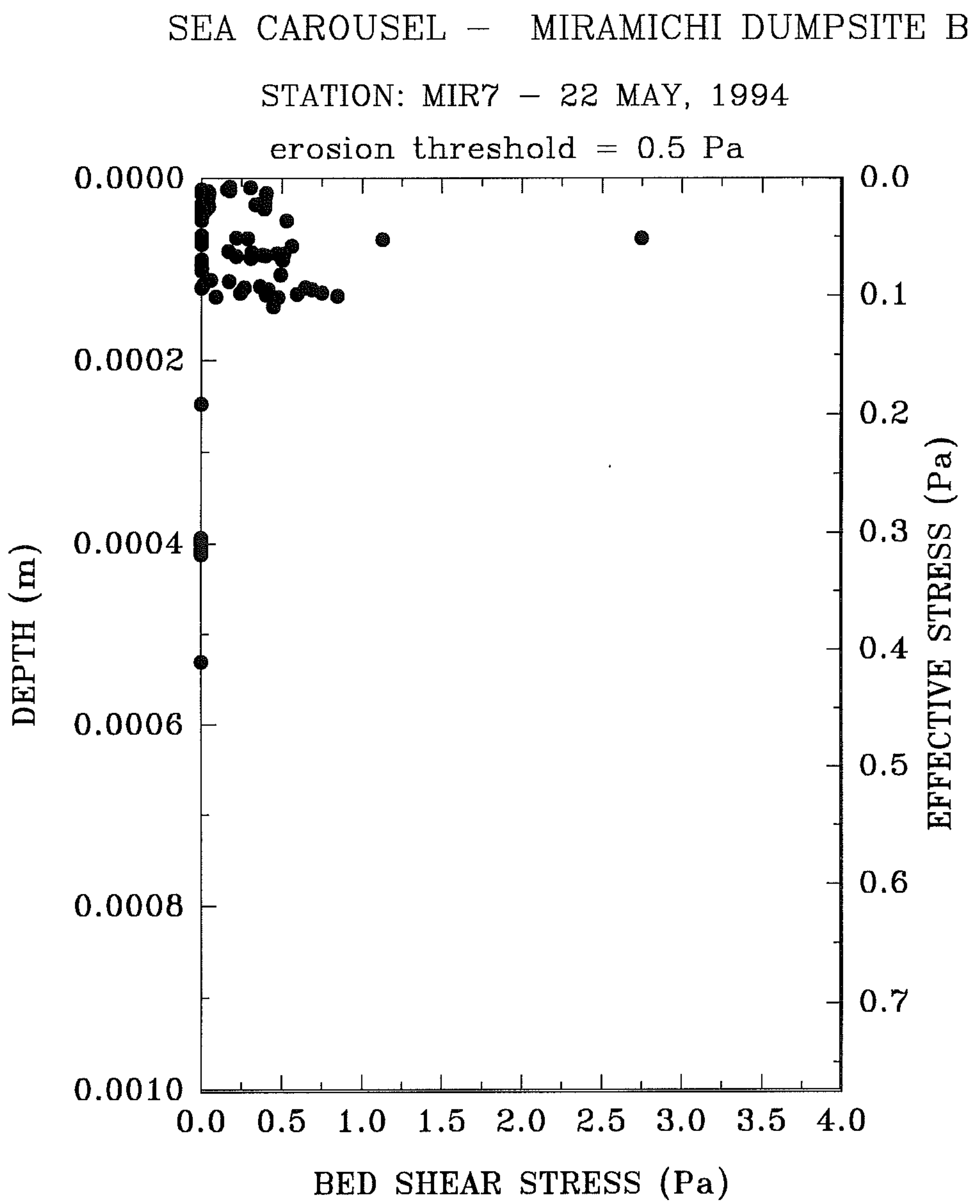

FIGURE 3.2.2.8. A synthetic core from station MIR7 computed from the Sea Carousel time-series data on eroded mass. The erosion threshold is 0.5 Pa.

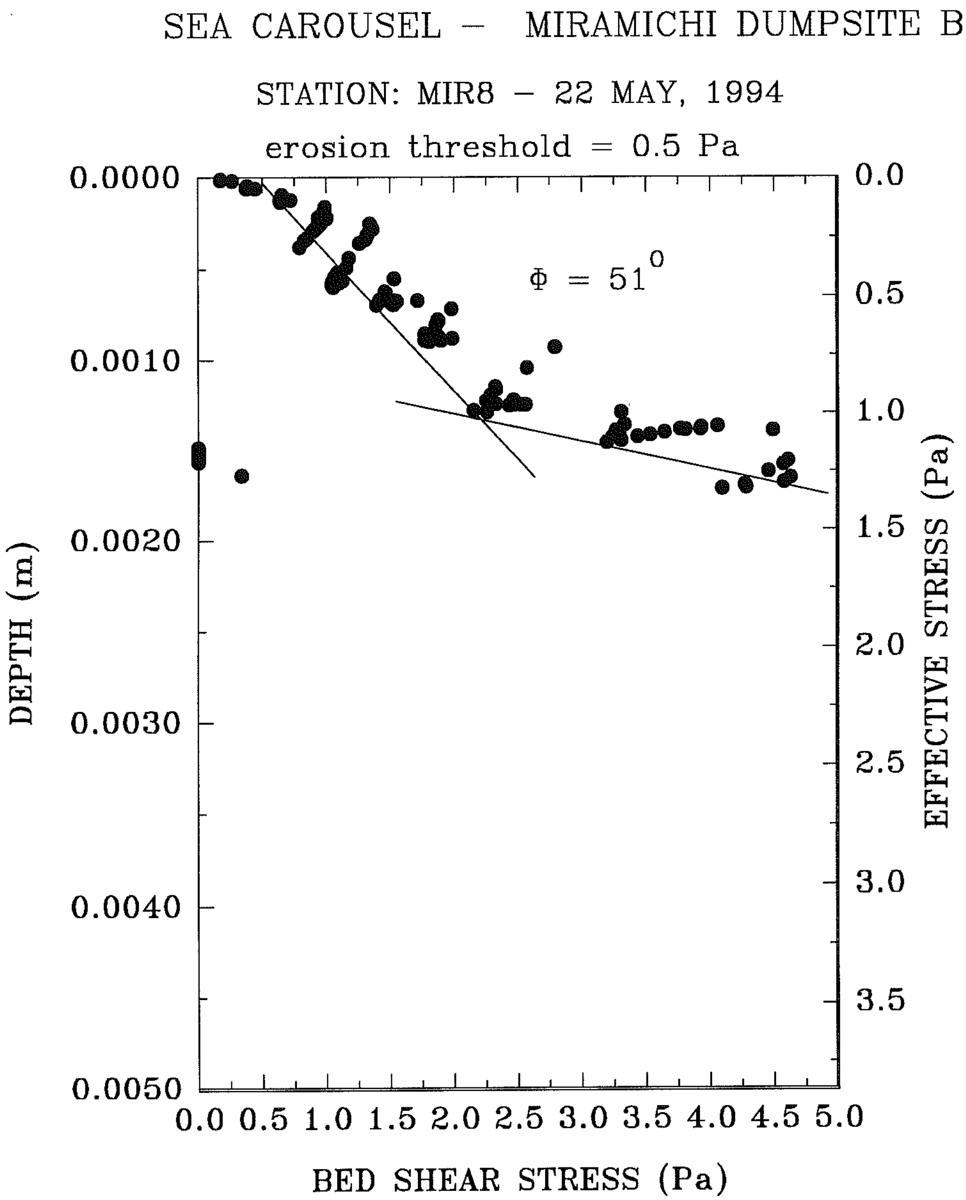

FIGURE 3.2.2.9. A synthetic core from station MIR8 computed from the Sea Carousel time-series data on eroded mass. The erosion threshold is 0.5 Pa, and the substrate is stable yielding a friction angle of 51°.

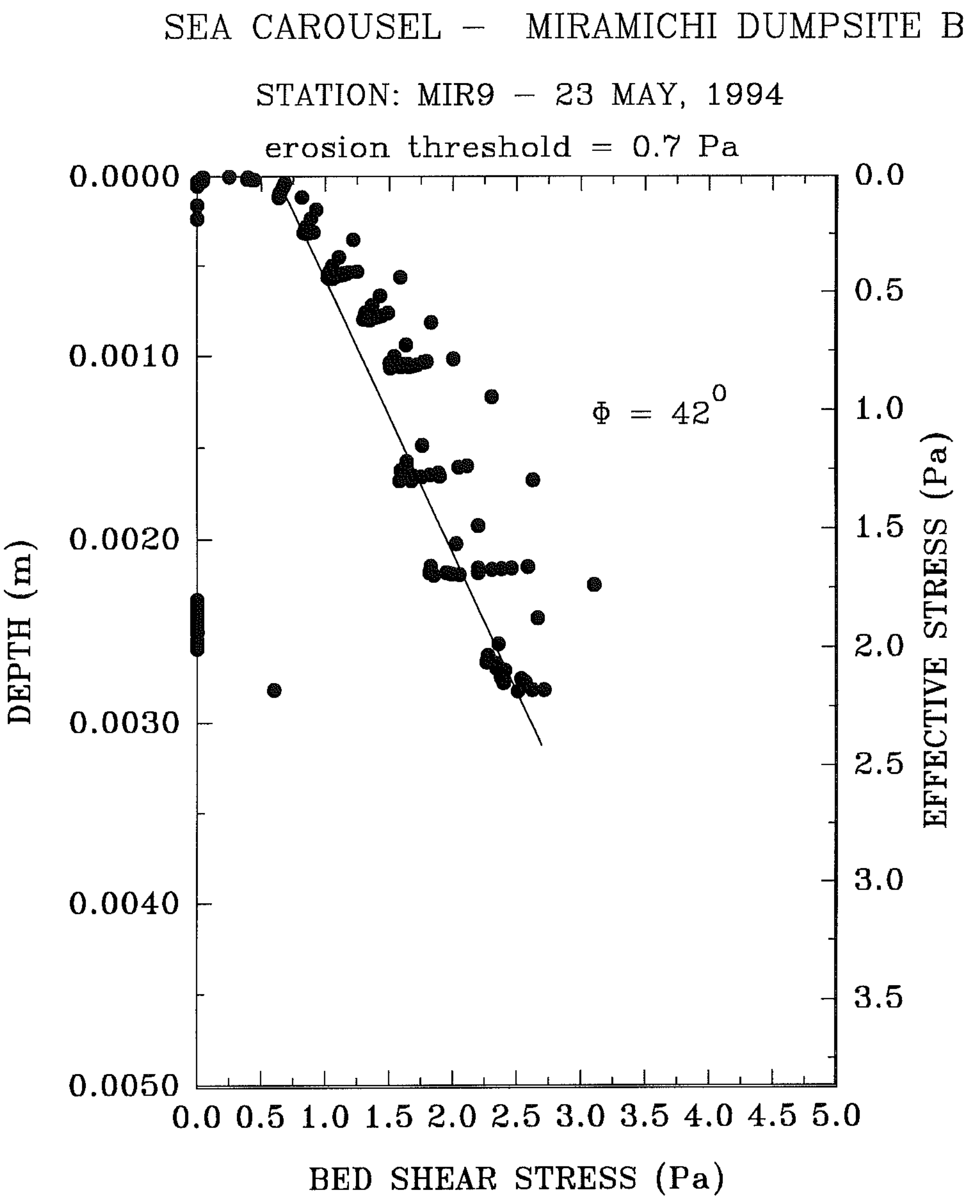

FIGURE 3.2.2.10. A synthetic core from station MIR9 computed from the Sea Carousel time-series data on eroded mass. The erosion threshold is 0.7 Pa, and the substrate is stable yielding a friction angle of 42°.

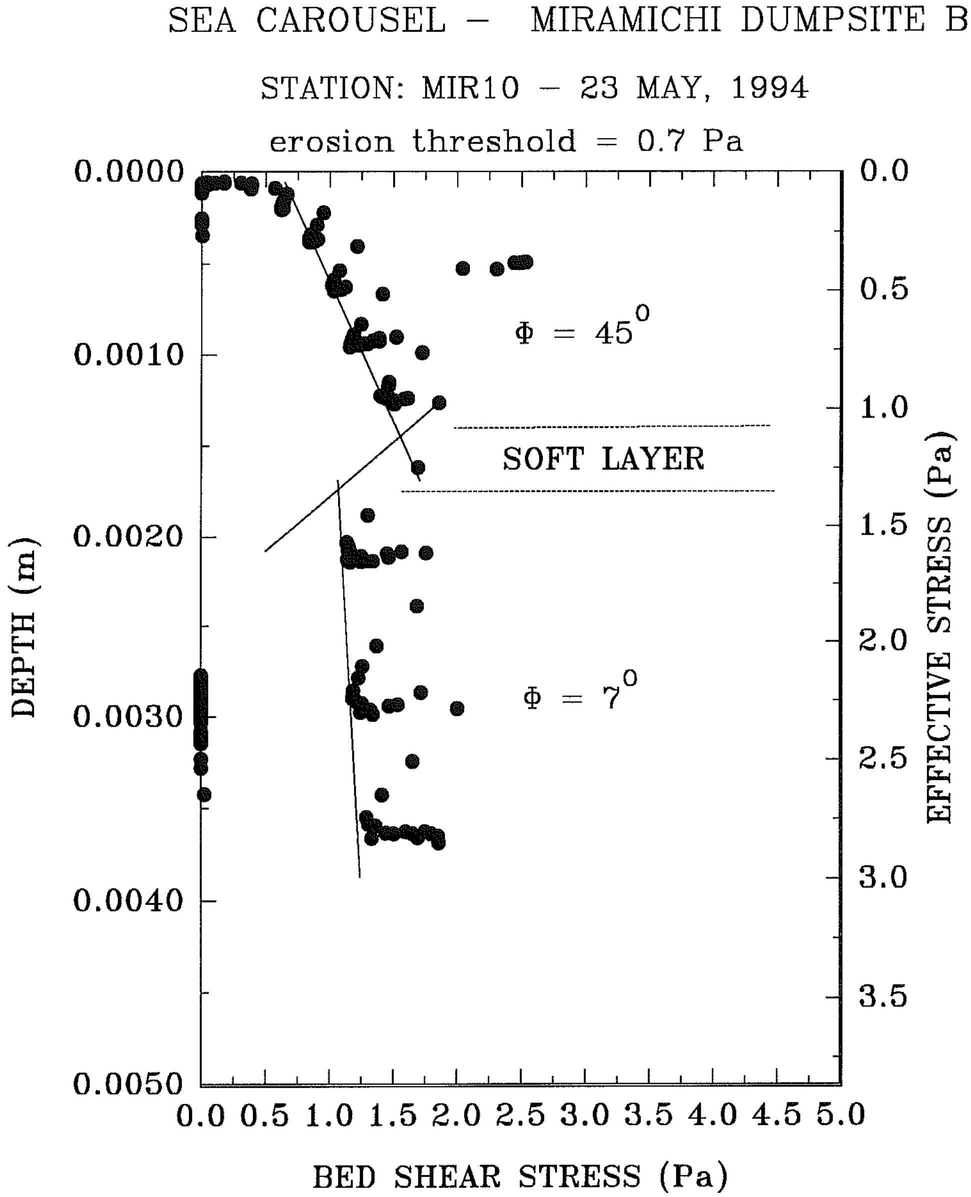

FIGURE 3.2.2.11. A synthetic core from station MIR10 computed from the Sea Carousel time-series data on eroded mass. The erosion threshold is 0.7 Pa, and the substrate is of variable stability yielding friction angles of 45° and 7° separated by a "soft" at a depth of 0.0015 m.

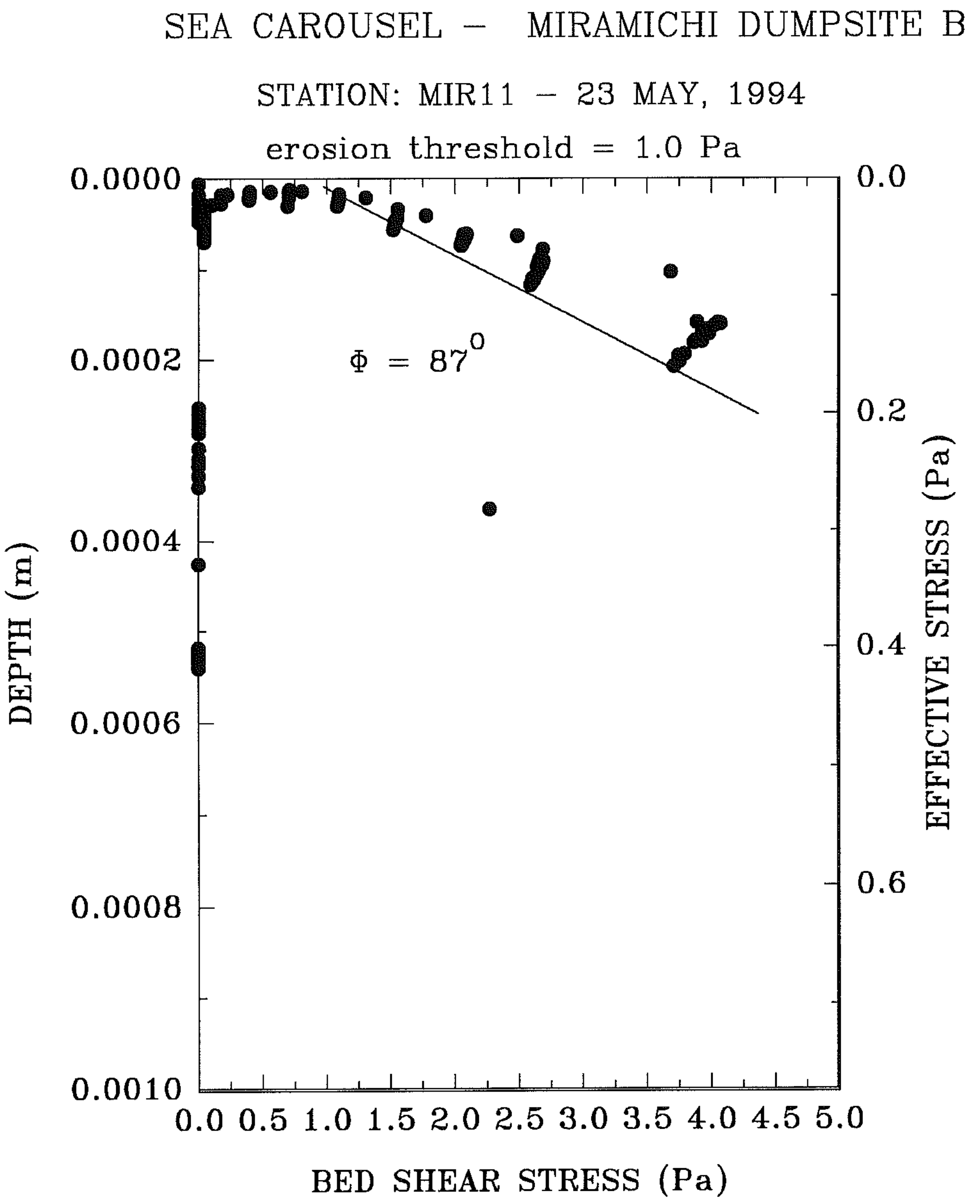

FIGURE 3.2.2.12. A synthetic core from station MIR11 computed from the Sea Carousel time-series data on eroded mass. The erosion threshold is 1.0 Pa, and the substrate is stable yielding a friction angle of 87°.

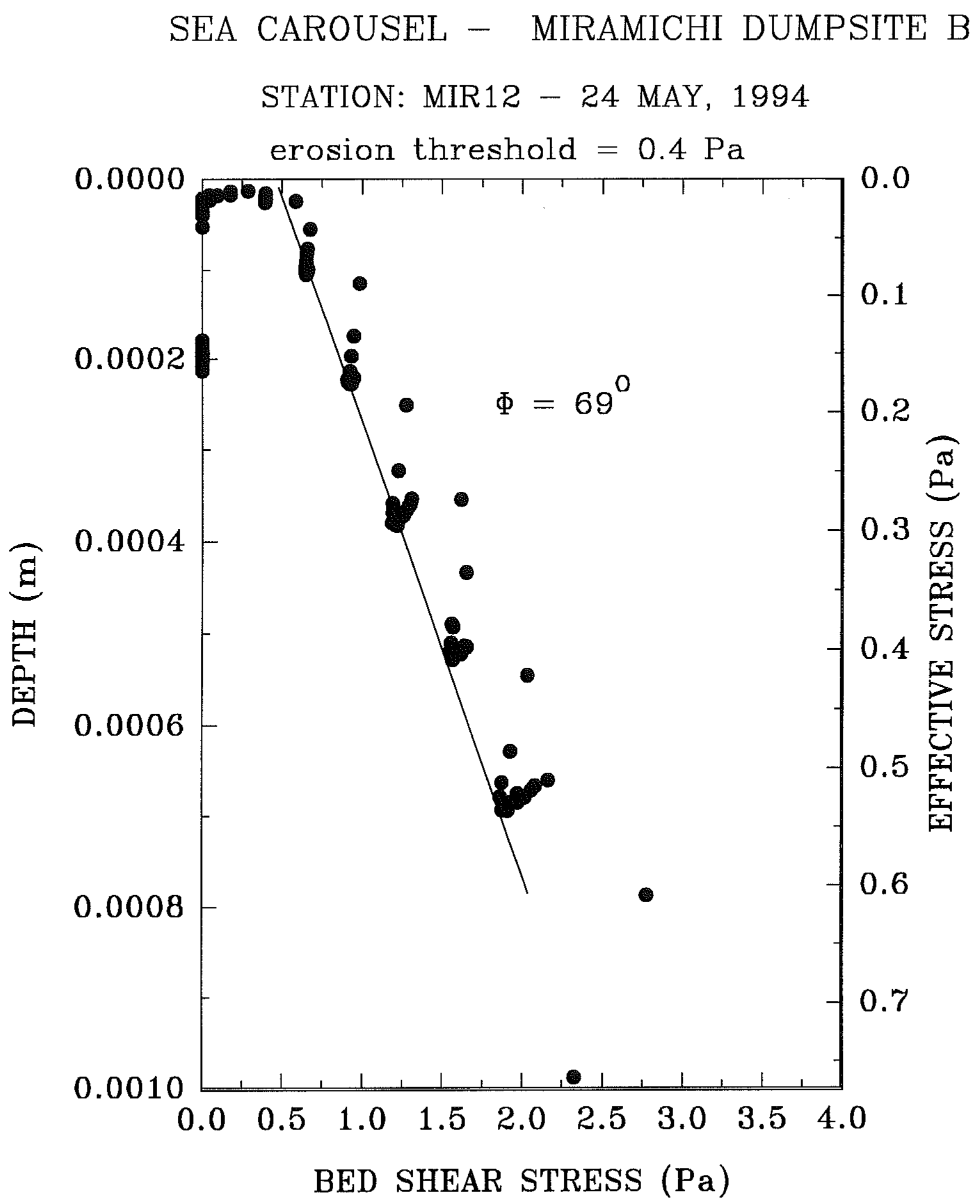

FIGURE 3.2.2.13. A synthetic core from station MIR12 computed from the Sea Carousel time-series data on eroded mass. The erosion threshold is 0.4 Pa and the friction angle is 69°.

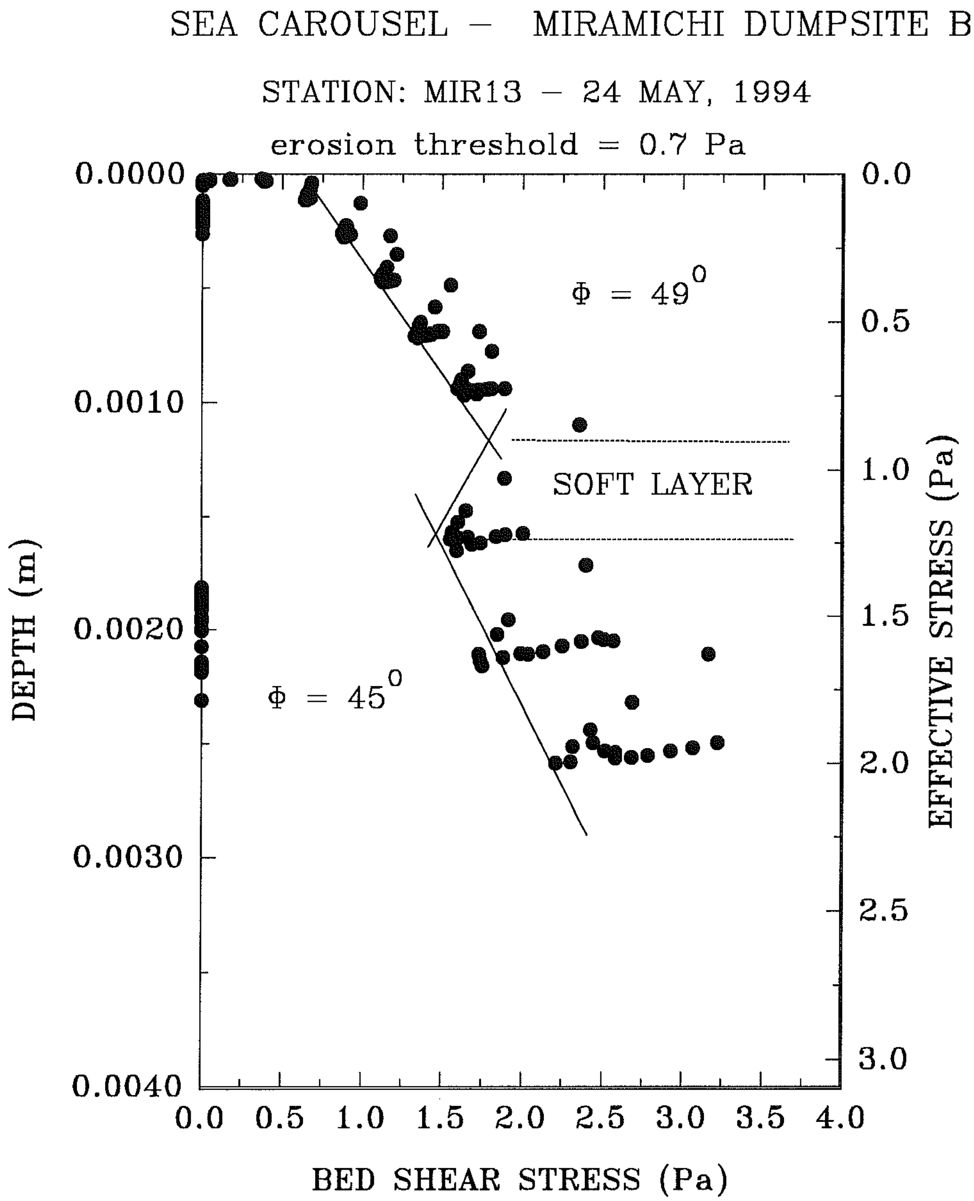

FIGURE 3.2.2.14. A synthetic core from station MIR13 computed from the Sea Carousel time-series data on eroded mass. The erosion threshold is 0.7 Pa, and the substrate is of variable stability yielding friction angles of 49° and 45° separated by a "soft" at a depth of 0.0015 m.

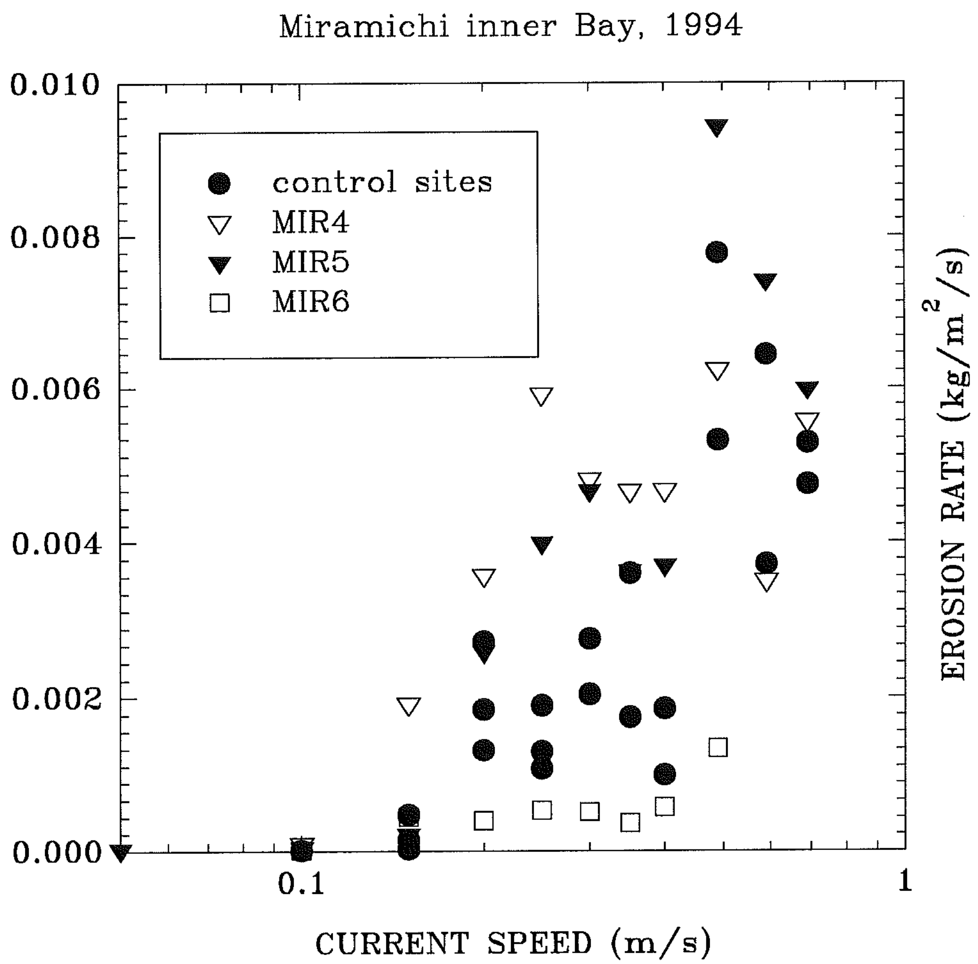

FIGURE 3.2.3.1. A scattergram of current speed (U_y) versus peak seabed erosion rate ($\delta M/\delta t$; $kg/m^2/s$) for the control sites (MIR1 - MIR3) and for stations MIR4 - MIR6. These stations exhibited Type I erosion. A positive exponential relationship was evident of the form $\delta M/\delta t = 0.006 + 0.006[\log_{10}(U_y)]$; $r^2 = 0.49$.

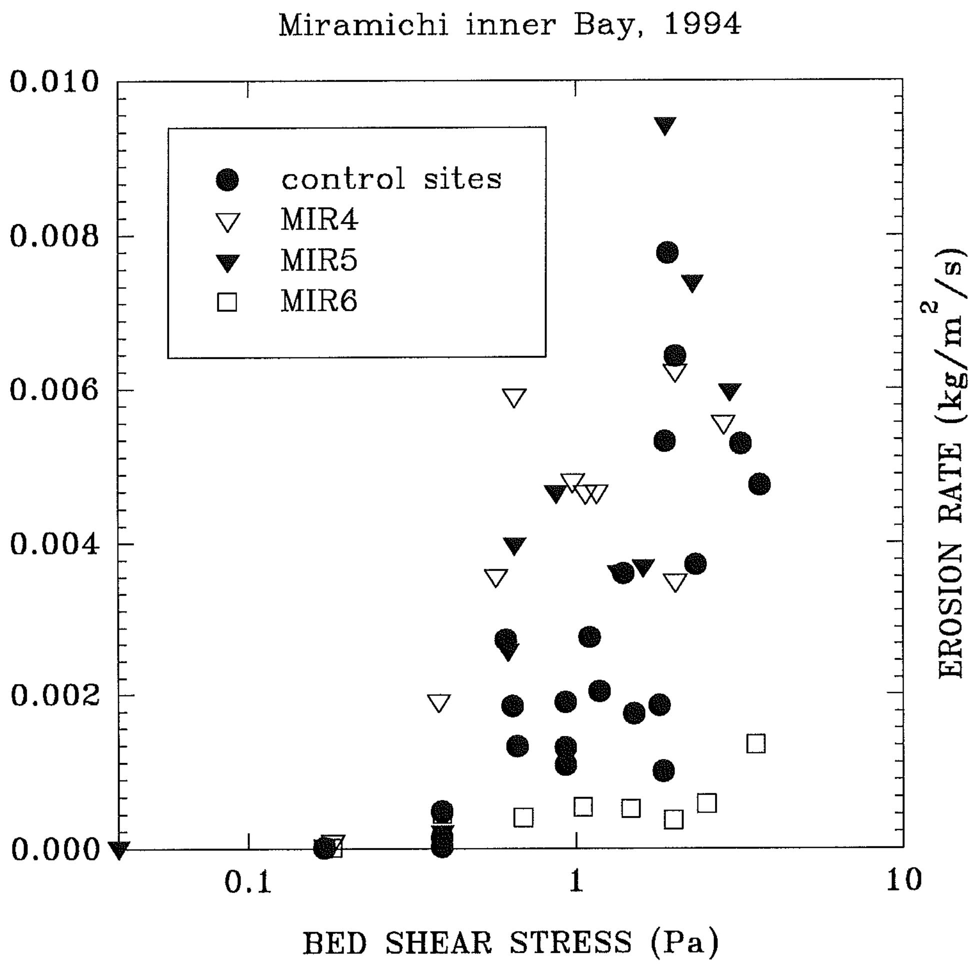

FIGURE 3.2.3.2. A scattergram of bed shear stress (τ) versus peak seabed erosion rate ($\delta M/\delta t$; $kg/m^2/s$) for the control sites (MIR1 - MIR3) and for stations MIR4 - MIR6. These stations exhibited Type I erosion. A positive exponential relationship was evident of the form $\delta M/\delta t = 0.003 + 0.003[\log_{10}(\tau)]$; $r^2 = 0.32$.

MIRAMICHI DISPOSAL SITE B – 1994

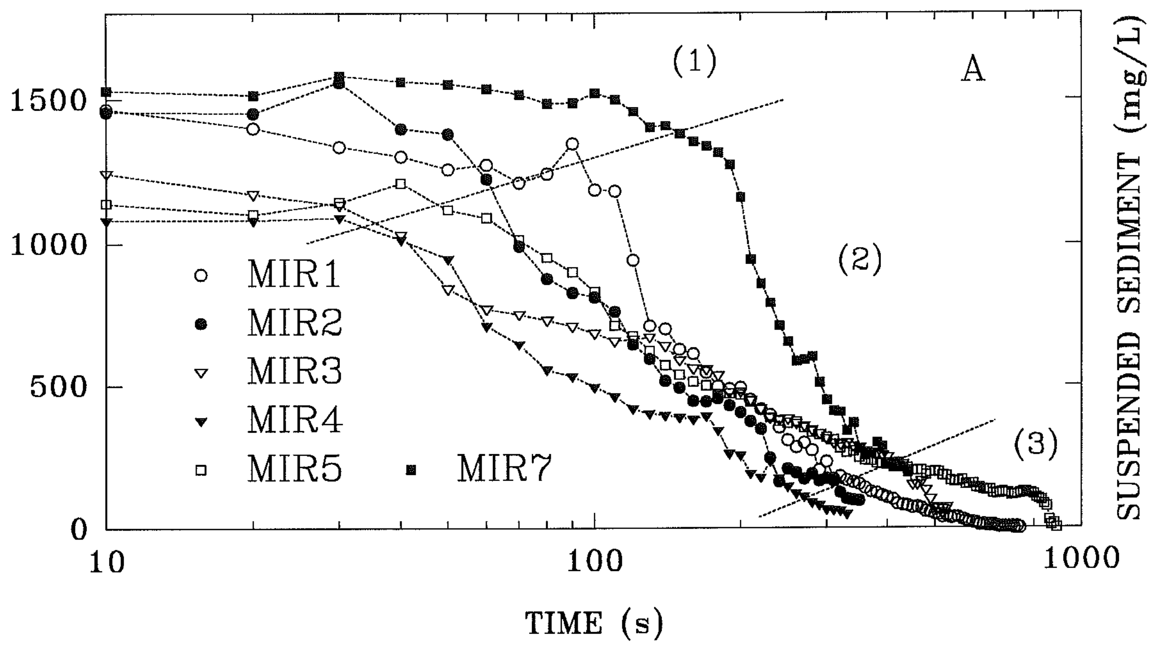

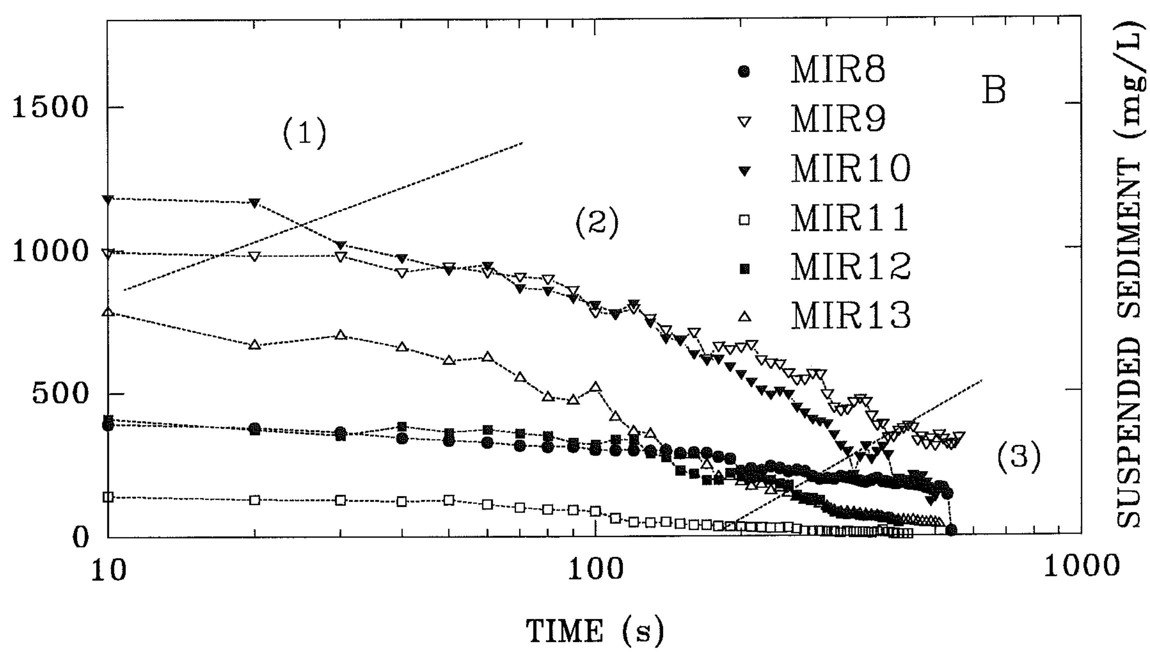

FIGURE 3.2.4.1. The still-water settling of material eroded from the seabed in stations (A) MIR1 - MIR7, and (B) MIR8 - MIR13. The concentration change with time falls into three phases (1) an initial period of inhibited settling; (2) a period of rapid settling; and (3) a final period of low settling.

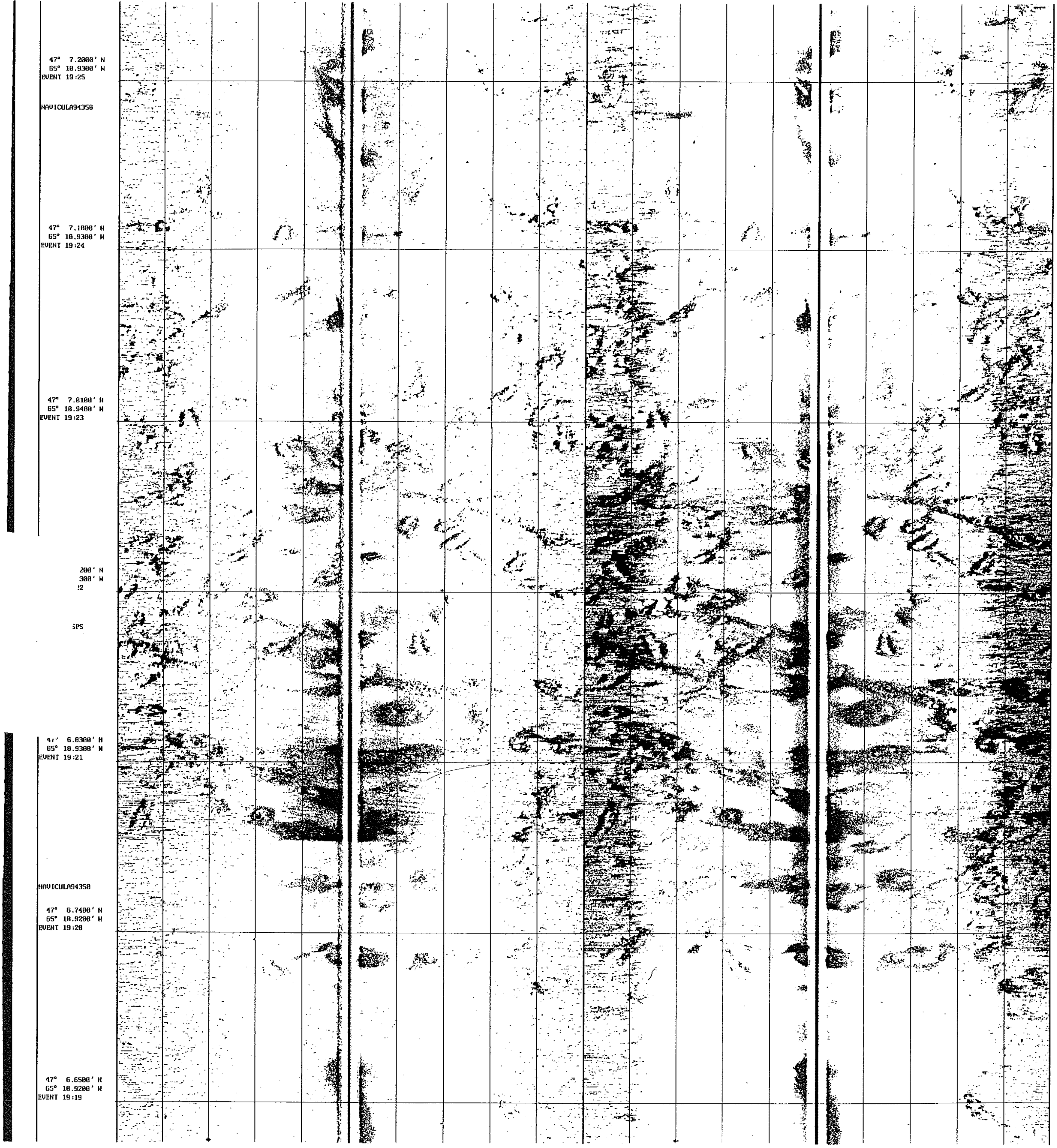

FIGURE 3.2.6.2. A detailed example of the sidescan record of the 1993 scow-dumps. The distance between fixes is approximately 100 m. The channel swath width is 100 m per channel. The two traces give results from two frequencies (120 - left, and 320 kHz - right).

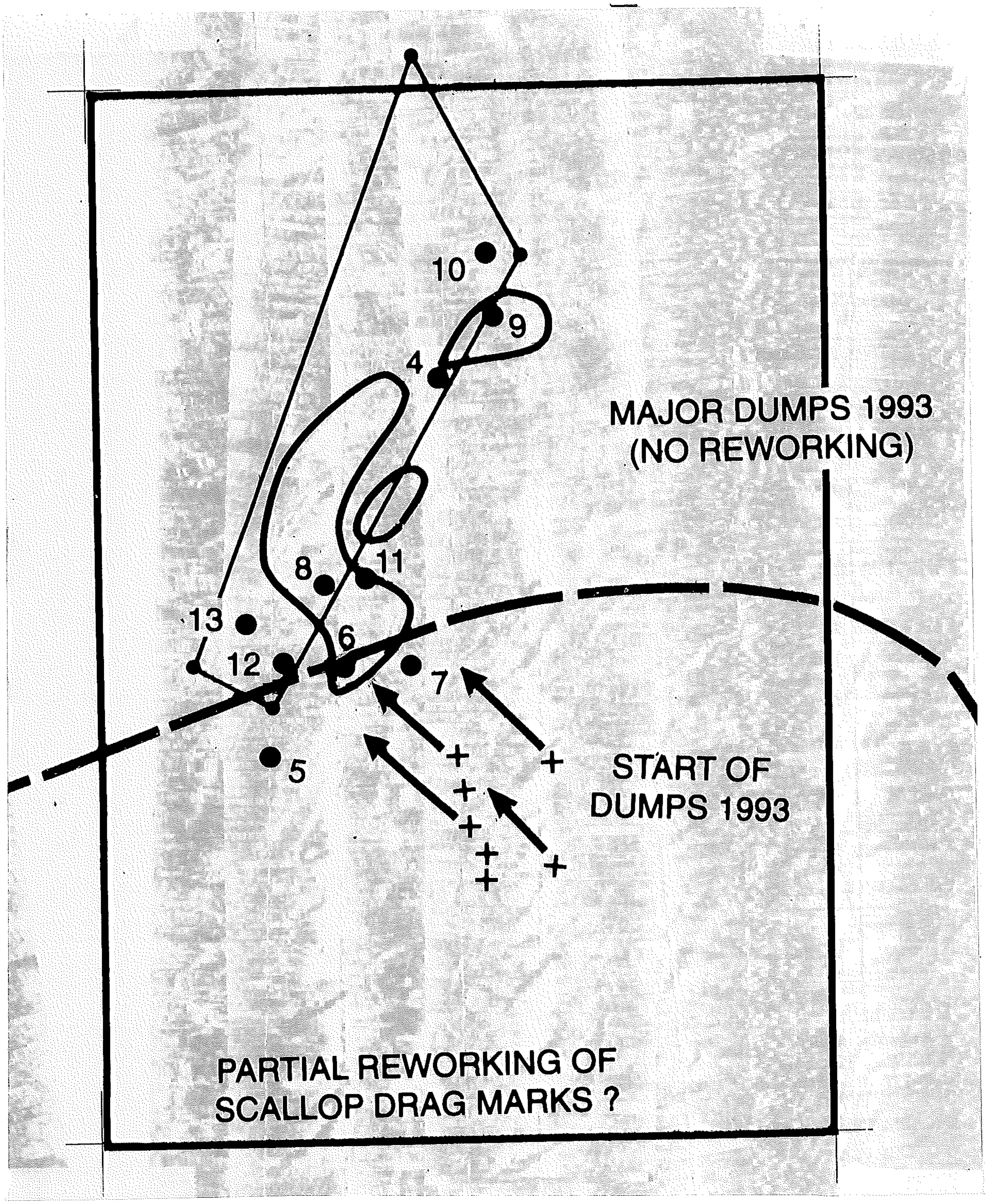

FIGURE 3.2.6.3. A detailed inset of the dumpsite B exclusion zone monitored in this study. The Sea Carousel stations are shown on and around the major region of dumping in 1993. The crosses show the positions at the beginning of dumping and the arrows show the scow paths. The location of the majority of the dumped material is shown by the solid curved oblongs. The northeast-southwest trending lineaments in the mosaic are interpreted to be scallop trawl marks. Notice one such marks appears to cross the 1993 dump material.

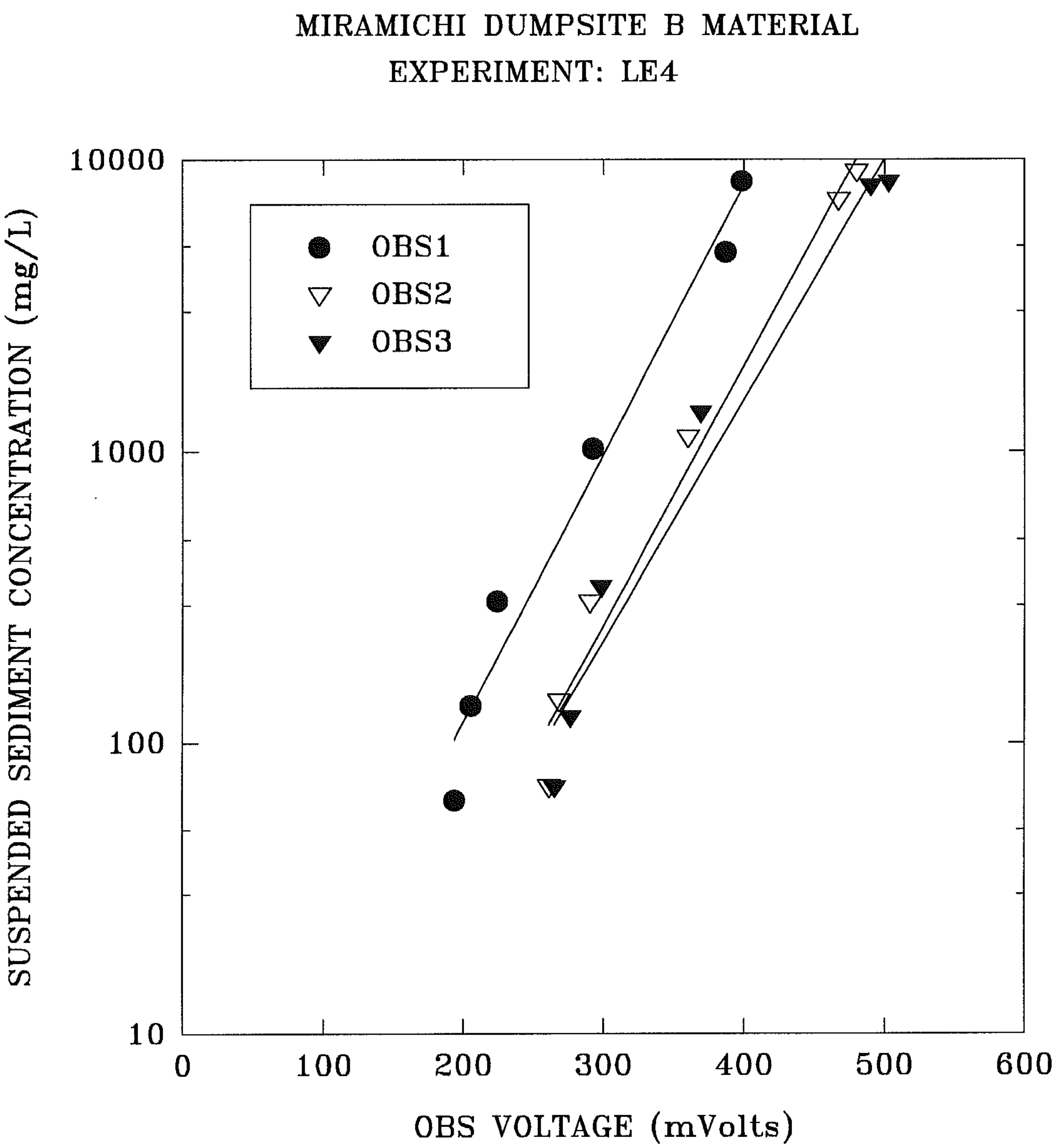

FIGURE 4.1.1. The calibration of the three Optical Backscatter Sensors (OBS) in the Laboratory Carousel against suspended sediment concentration for experiment LE4.

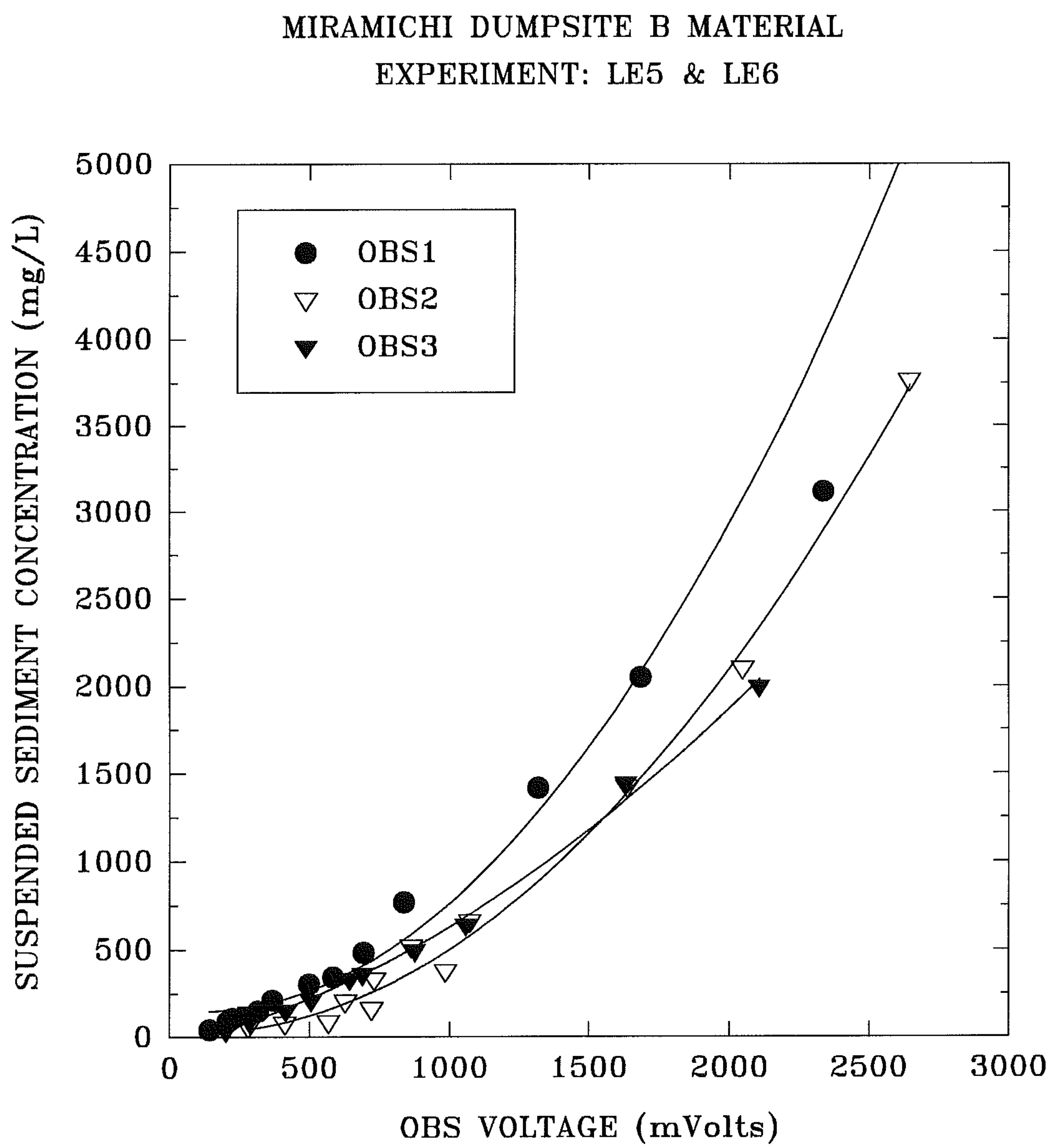

FIGURE 4.1.2. The calibration of the three Optical Backscatter Sensors (OBS) in the Laboratory Carousel against suspended sediment concentration for experiments LE5 and LE6.

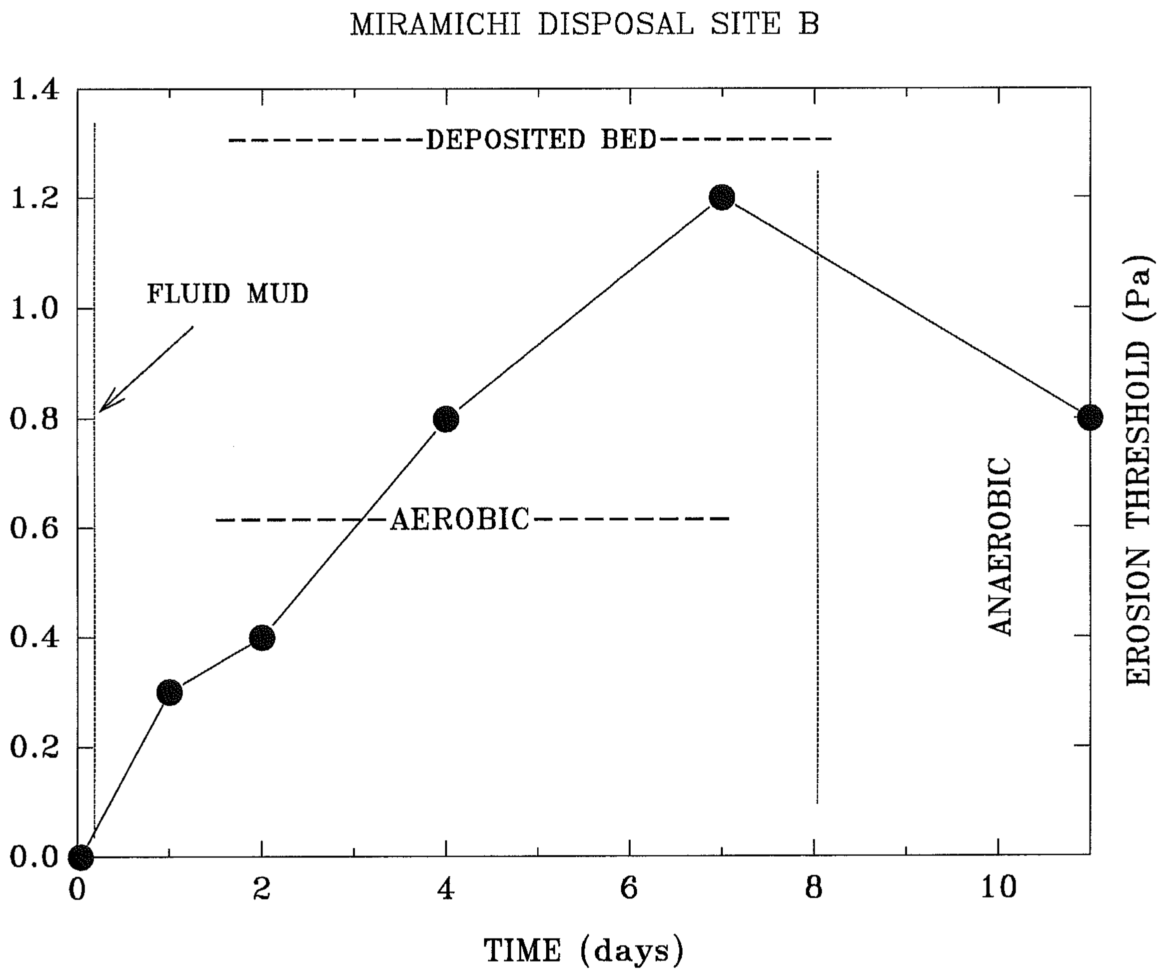

FIGURE 4.2.1.1. A time-series of erosion threshold derived from the Laboratory Carousel analysis of dumpsite B material. Notice the linear increase in erosion threshold with time over the first 7 days. The reveral in trends after 8 days reflects a change from oxygenated to anoxic conditions, associated with the collapse of the benthic macrofauna and development of anaerobic bacteria.

FIGURE 4.2.1.2. A time-series plot of the Laboratory Carousel experiment LE4, on dumpsite B material, Miramichi bay. (A) azimuthal and vertical current speed (m/s); (B) suspended sediment concentration (mg/L); and (C) erosion rate (kg/m^2/s).

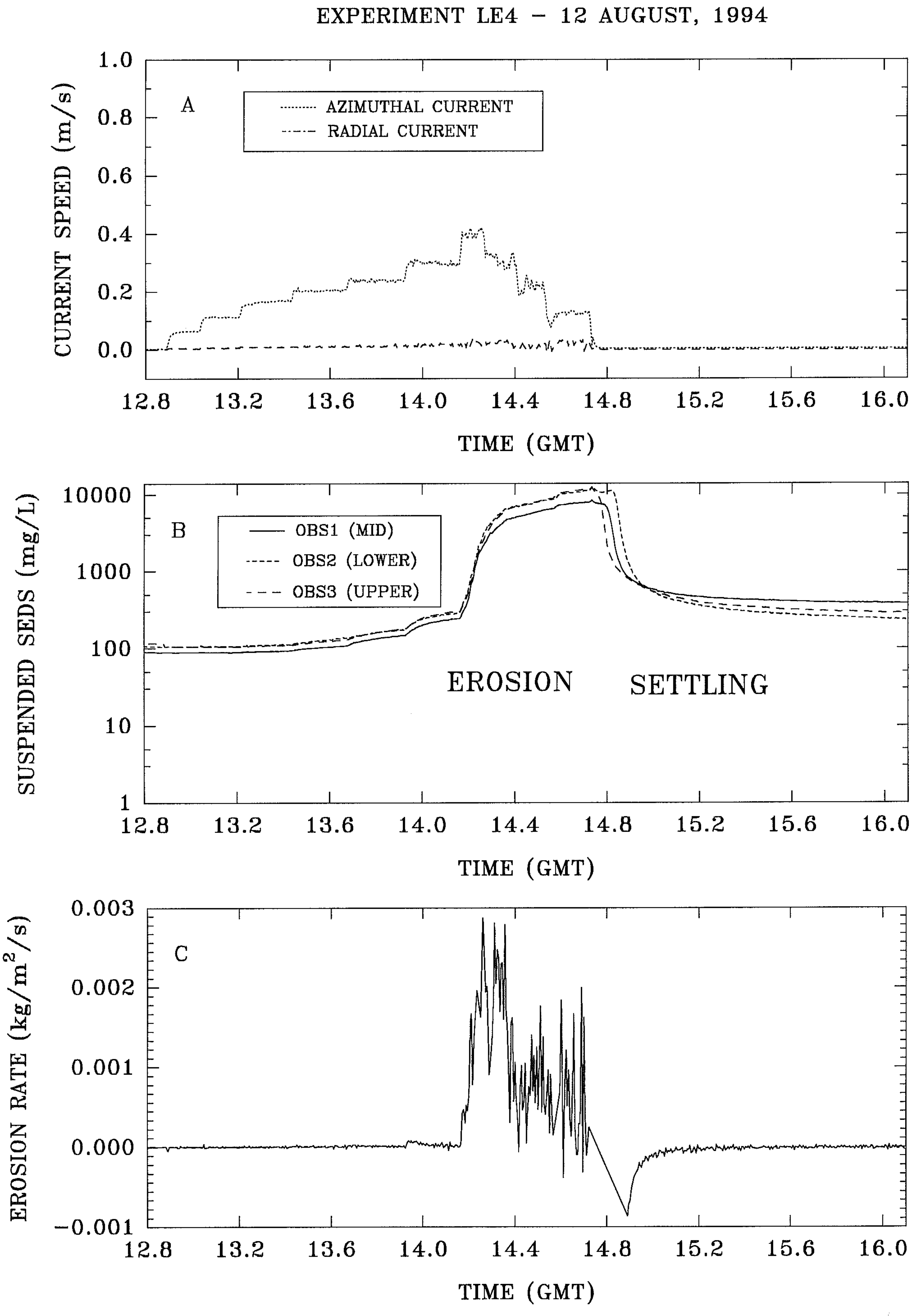

FIGURE 4.2.1.3. A time-series plot of the Laboratory Carousel experiment LE5, on dumpsite B material, Miramichi bay. (A) azimuthal and vertical current speed (m/s); (B) suspended sediment concentration (mg/L); and (C) erosion rate (kg/m²/s).

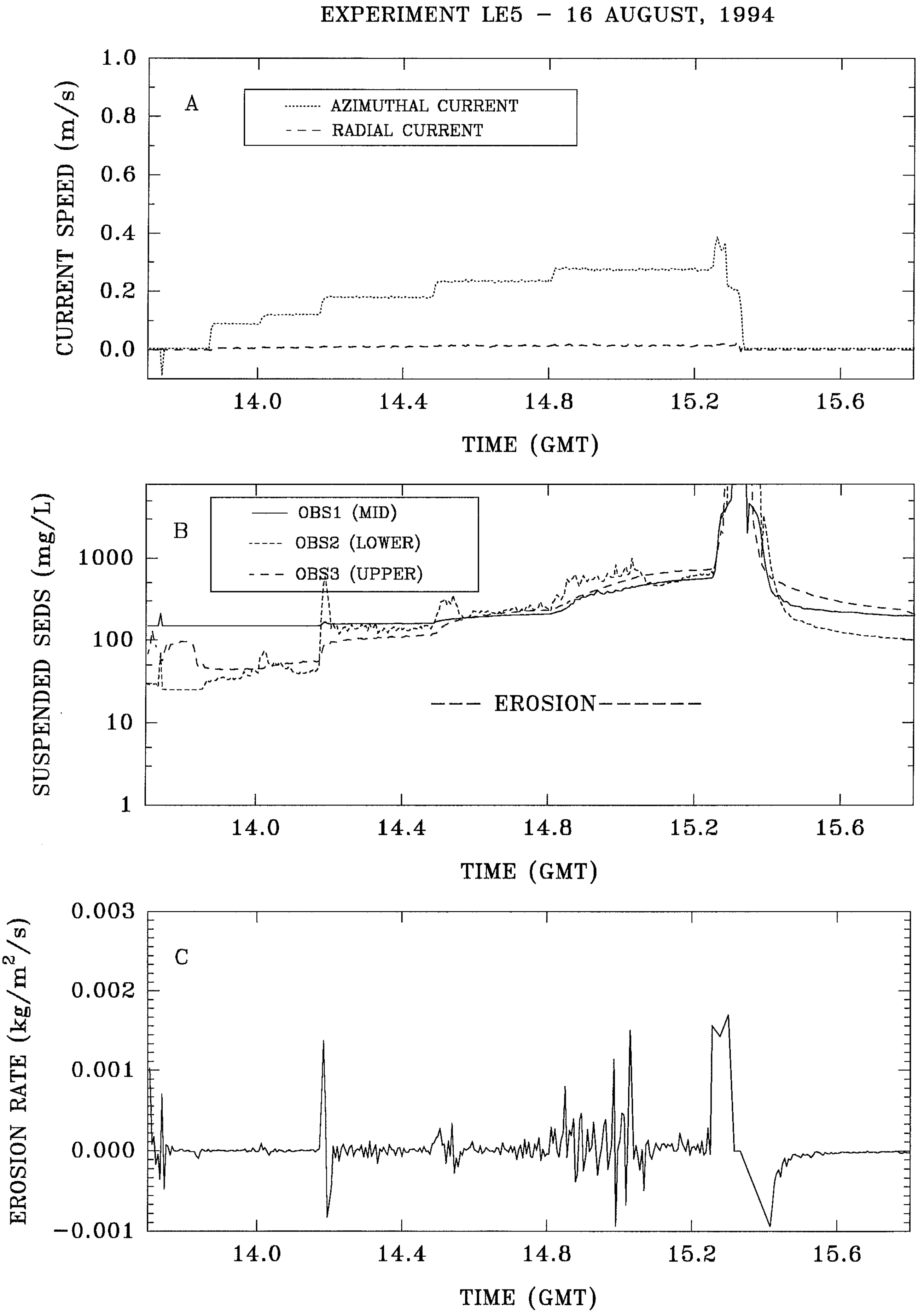

FIGURE 4.2.1.4. A time-series plot of the Laboratory Carousel experiment LE6, on dumpsite B material, Miramichi bay. (A) azimuthal and vertical current speed (m/s); (B) suspended sediment concentration (mg/L); and (C) erosion rate ($kg/m^2/s$).

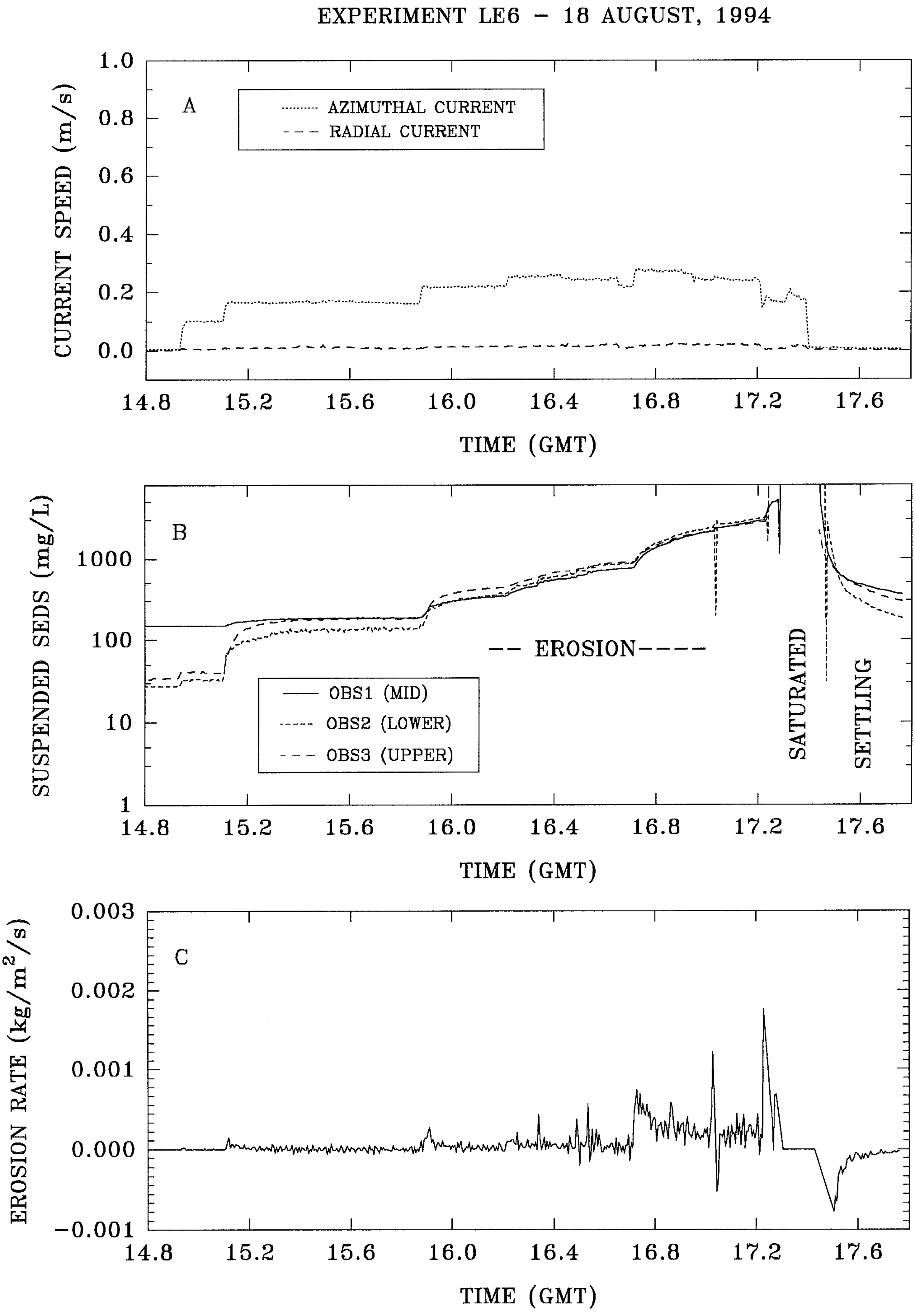

FIGURE 4.2.1.5. A time-series plot of the Laboratory Carousel experiment LE7, on dumpsite B material, Miramichi bay. (A) azimuthal and vertical current speed (m/s); (B) suspended sediment concentration (mg/L); and (C) erosion rate (kg/m²/s).

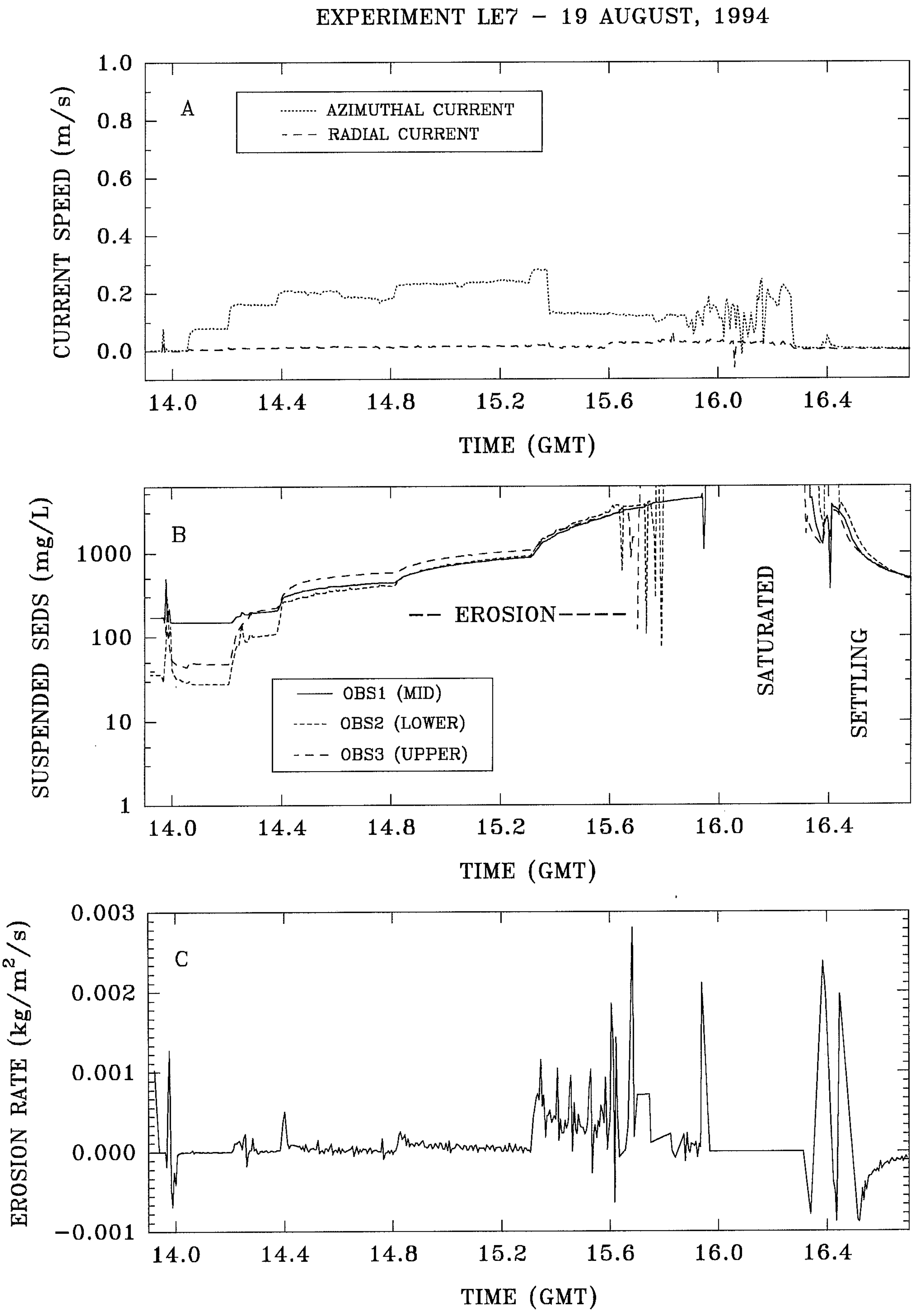

FIGURE 4.2.1.6. A time-series plot of the Laboratory Carousel experiment LE8, on dumpsite B material, Miramichi bay. (A) azimuthal and vertical current speed (m/s); (B) suspended sediment concentration (mg/L); and (C) erosion rate ($kg/m^2/s$).

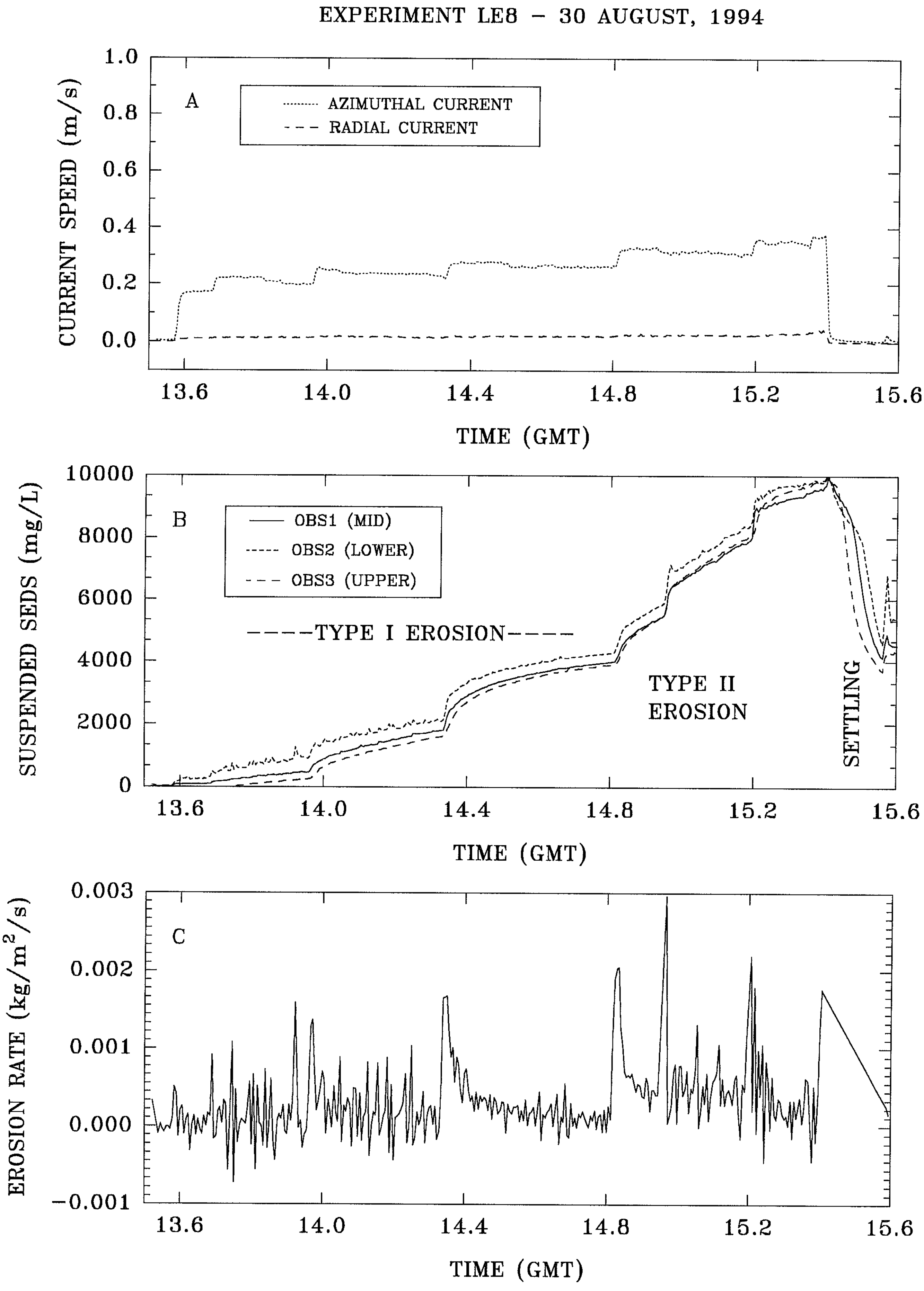

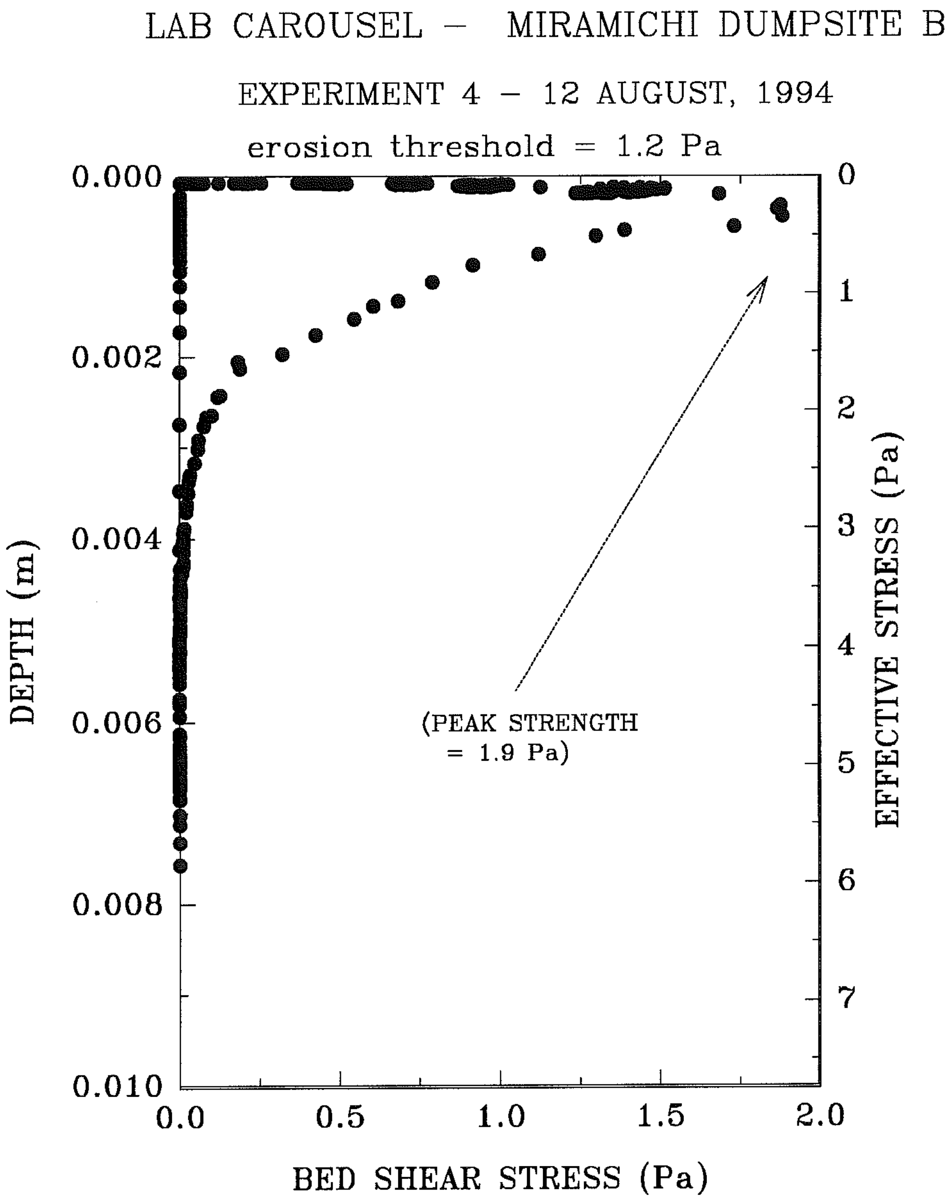

FIGURE 4.2.2.1. A synthetic core from experiment LE4 computed from the Laboratory Carousel time-series data on eroded mass. The experiment was undertaken after 7 days of consolidation/biostabilization. The erosion threshold is 1.2 Pa. Notice the peak in bed strength (1.9 Pa) within the topmost 2 mm, which is diagnostic of biostabilization.

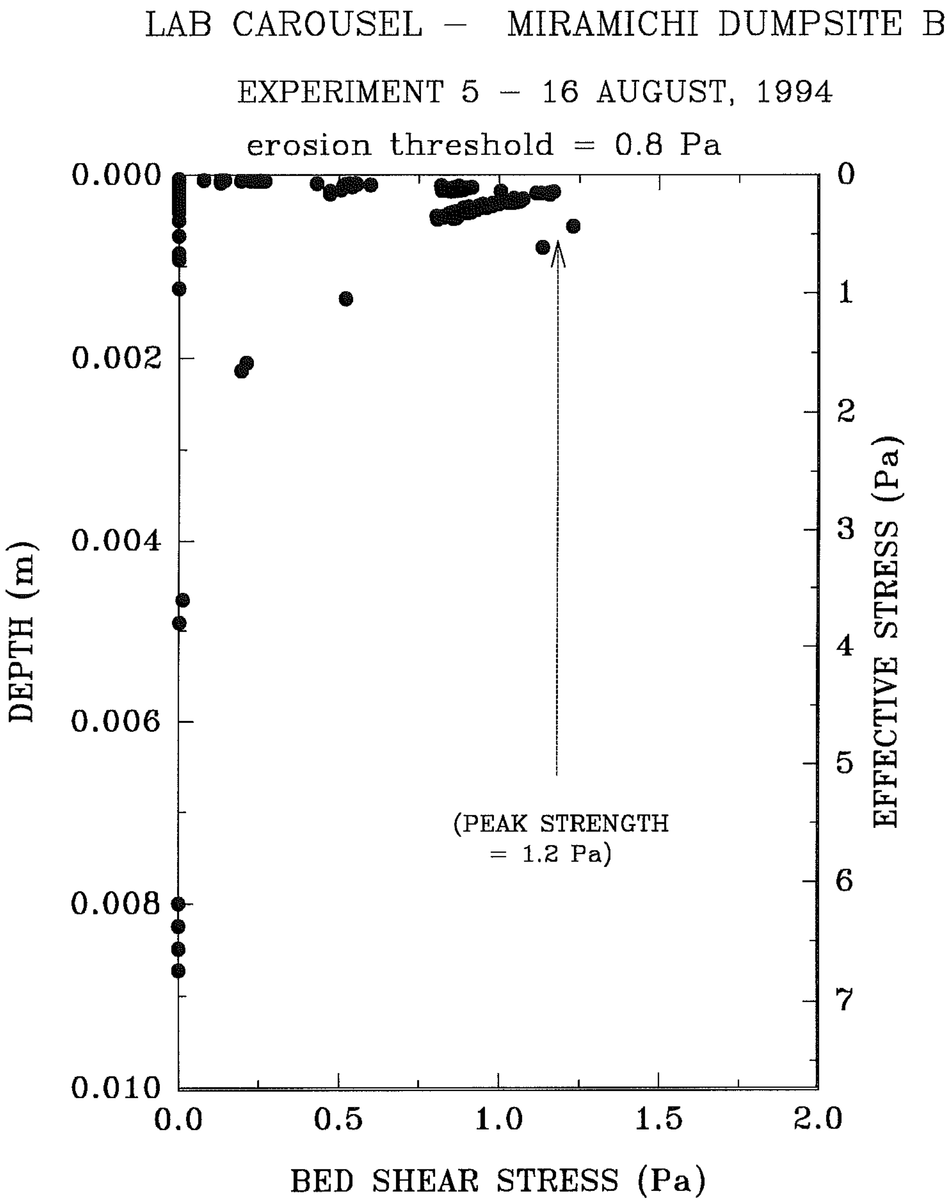

FIGURE 4.2.2.2. A synthetic core from experiment LE5 computed from the Laboratory Carousel time-series data on eroded mass. The experiment was undertaken after 4 days of consolidation/biostabilization. The erosion threshold is 0.8 Pa. Notice the peak in bed strength (1.2 Pa) within the topmost 2 mm, which is diagnostic of biostabilization.

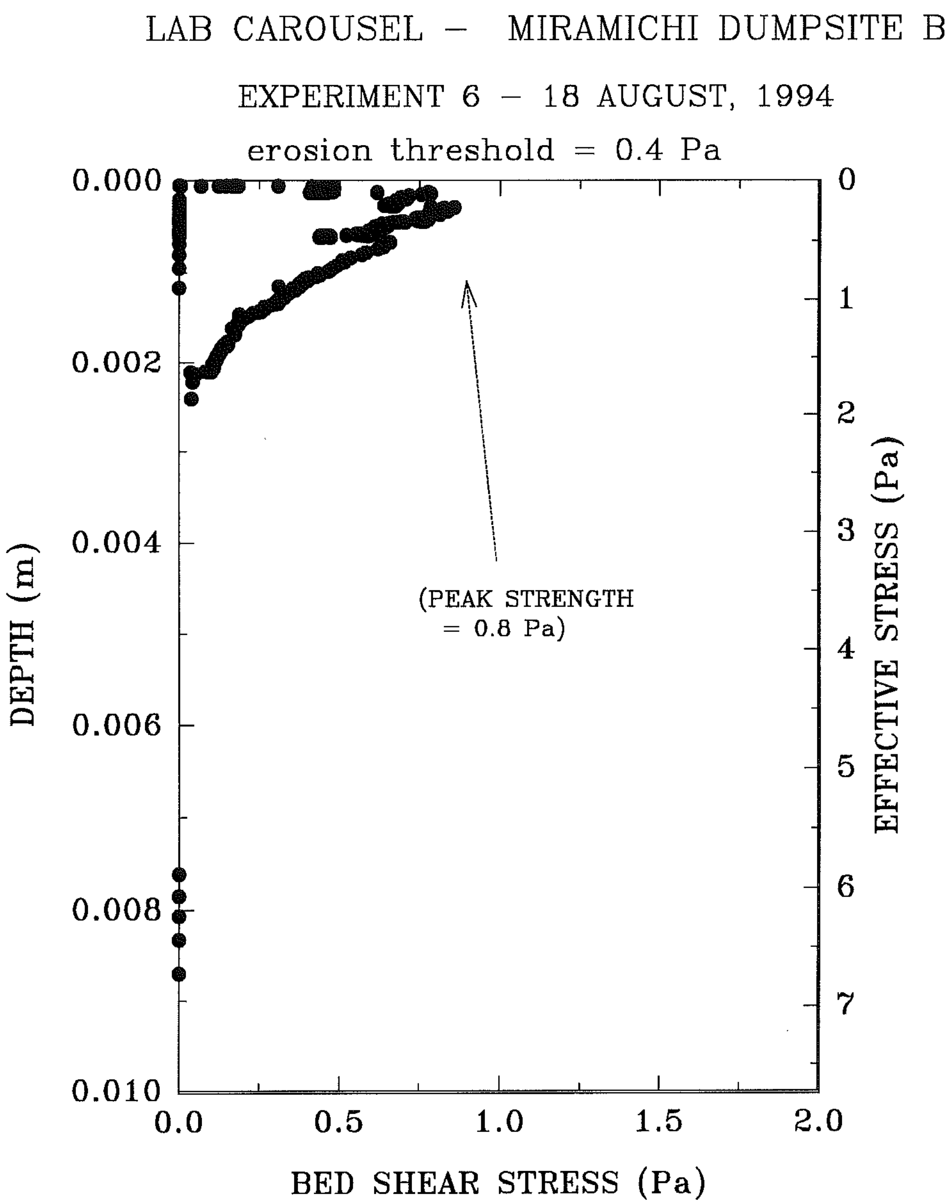

FIGURE 4.2.2.3. A synthetic core from experiment LE6 computed from the Laboratory Carousel time-series data on eroded mass. The experiment was undertaken after 2 days of consolidation/biostabilization. The erosion threshold is 0.4 Pa. Notice the peak in bed strength (0.8 Pa) within the topmost 2 mm, which is diagnostic of biostabilization.

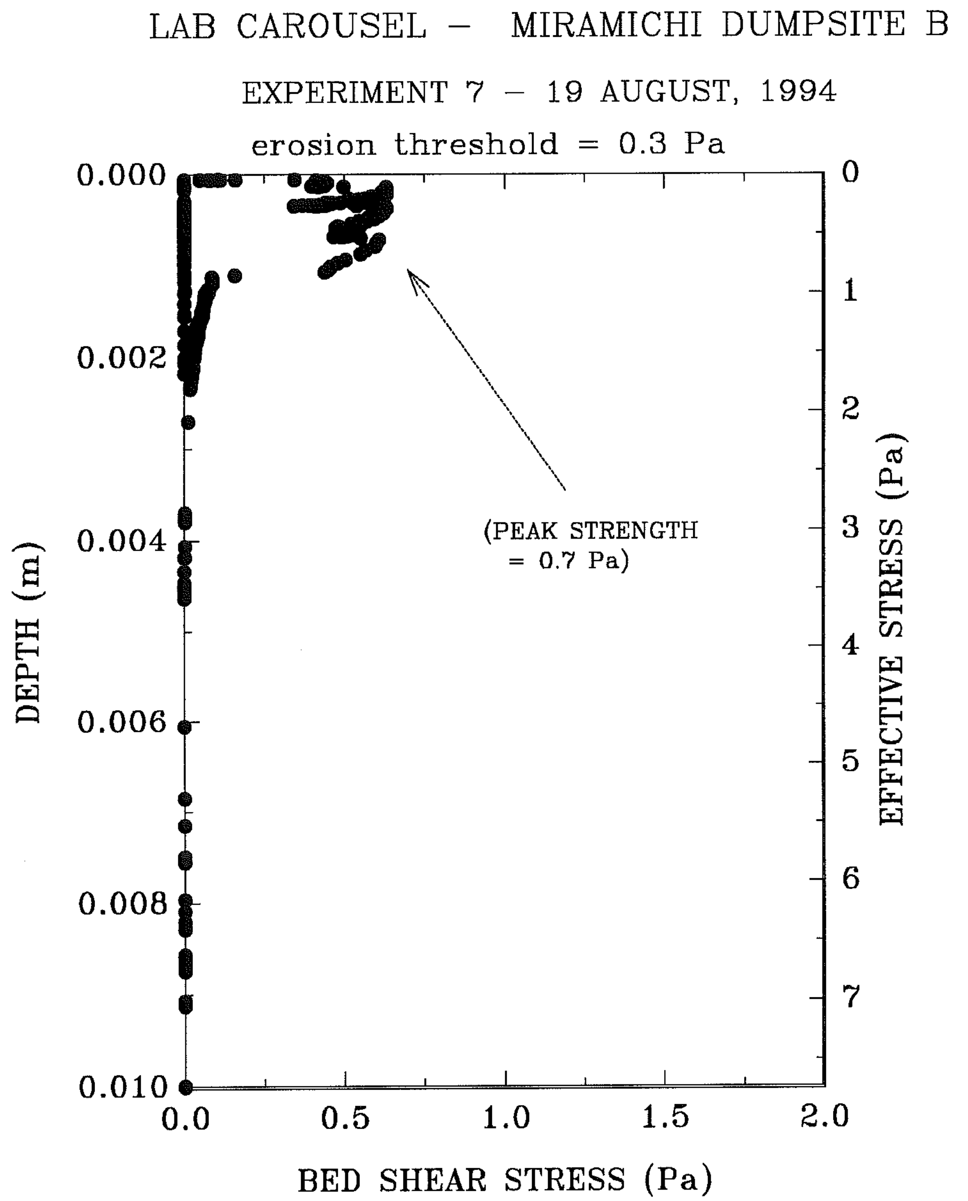

FIGURE 4.2.2.4. A synthetic core from experiment LE7 computed from the Laboratory Carousel time-series data on eroded mass. The experiment was undertaken after 1 day of consolidation/biostabilization. The erosion threshold is 0.3 Pa. Notice the peak in bed strength (0.7 Pa) within the topmost 1 mm, which is diagnostic of biostabilization.

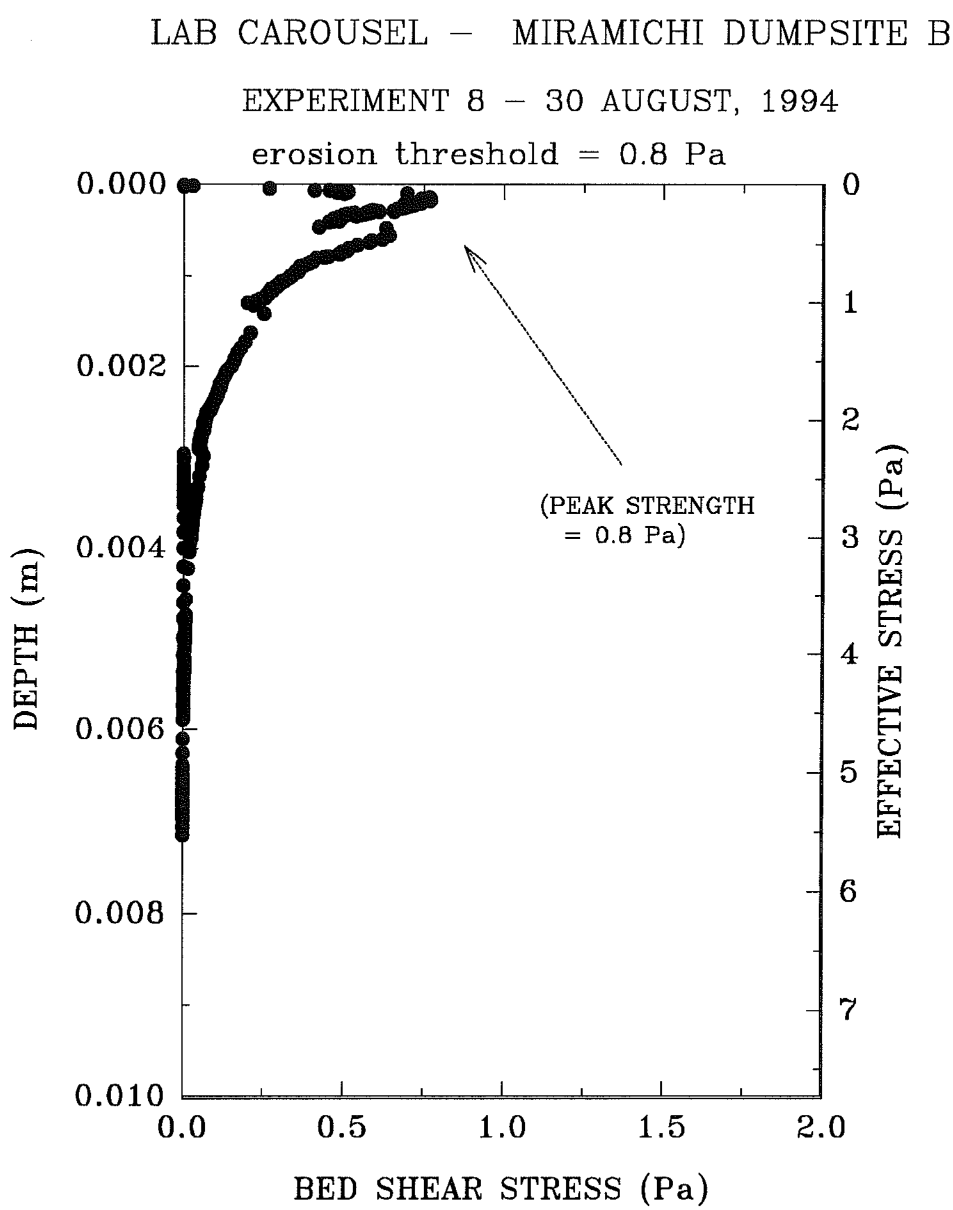

FIGURE 4.2.2.5. A synthetic core from experiment LE8 computed from the Laboratory Carousel time-series data on eroded mass. The experiment was undertaken after 11 days of consolidation/biostabilization and the system had gone anoxic. The erosion threshold is 0.8 Pa. Notice the peak in bed strength (0.7 Pa) within the topmost 1 mm, which is diagnostic of biostabilization.

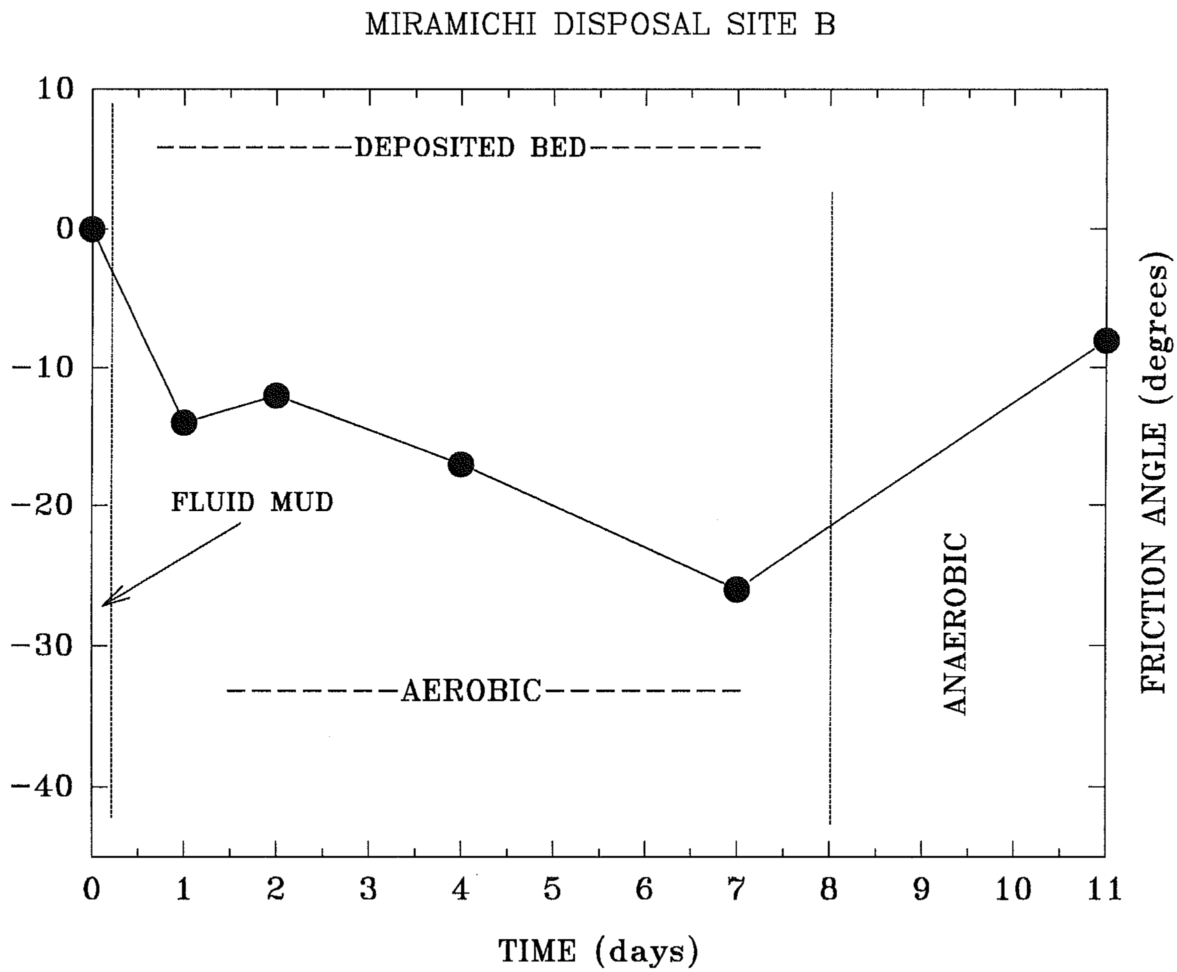

FIGURE 4.2.2.6. A time-series of the friction angle derived from the Laboratory Carousel analysis of dumpsite B material. The decrease in value with time is diagnostic of a systematic development of a biofilm (surface strengthening). The reveral in trends after 8 days reflects a change from oxygenated to anoxic conditions, associated with the collapse of the benthic macrofauna and development of anaerobic bacteria.

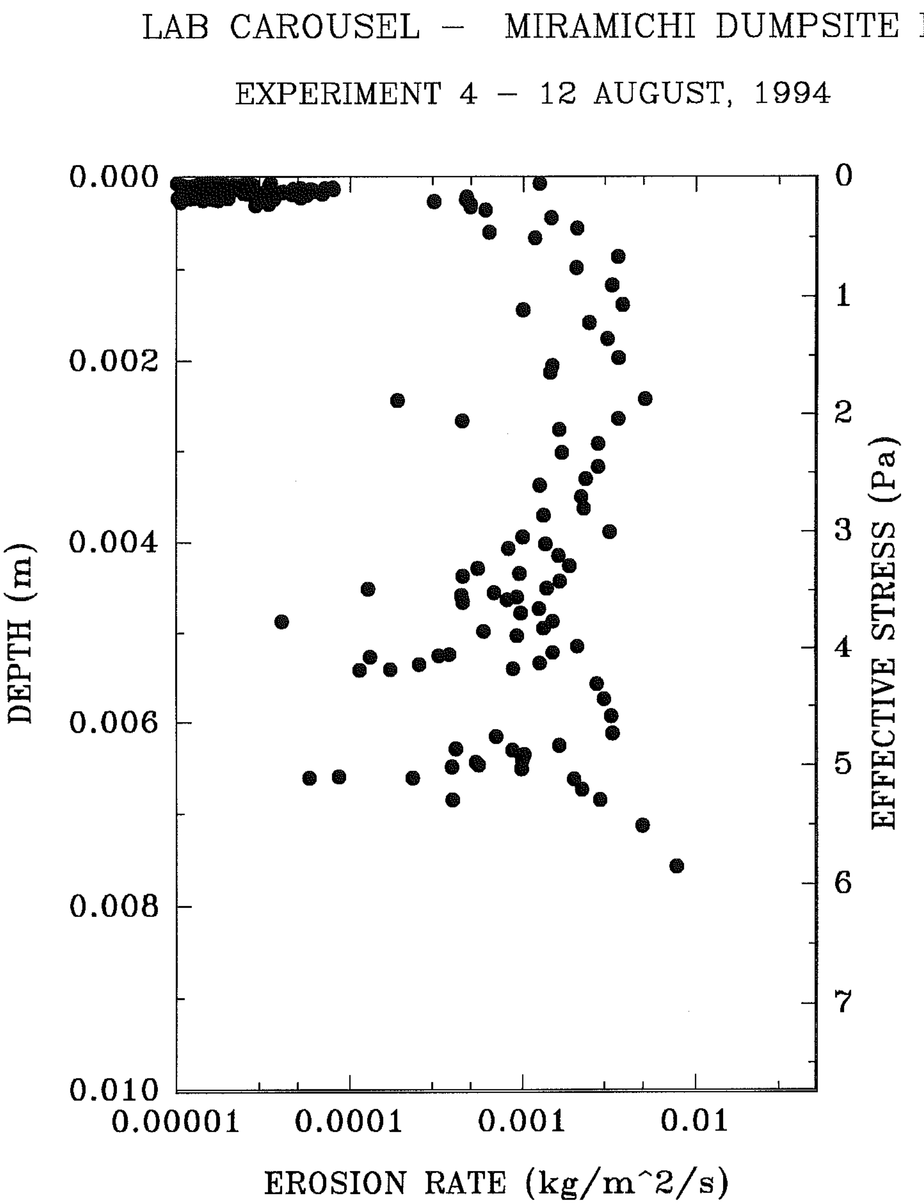

FIGURE 4.2.3.1. A synthetic core developed from Laboratory Carousel experiment LE4 showing the erosion rate (δM/δt) as a function of eroded depth. Notice that δM/δt is virtually constant at 1×10^{-3} kg/m^2/s.

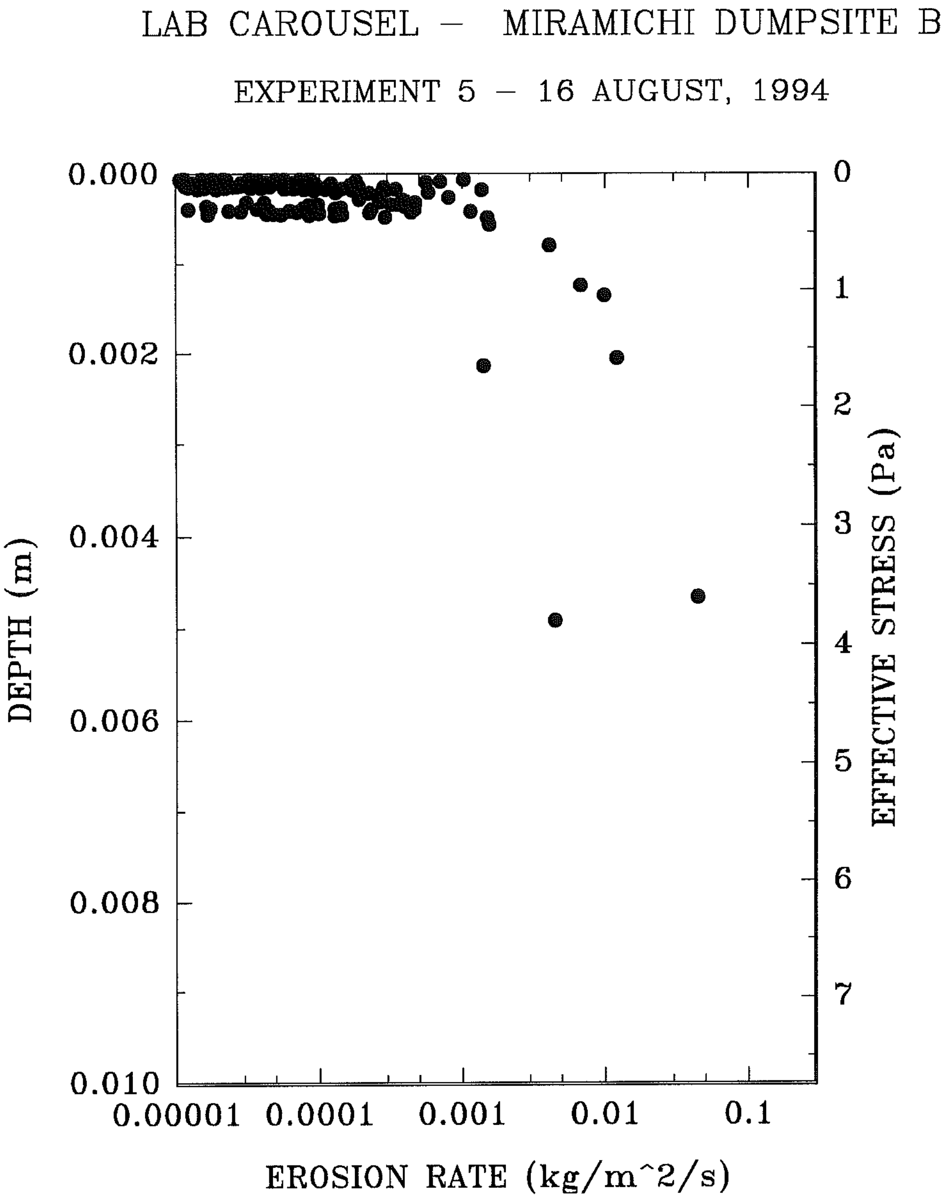

FIGURE 4.2.3.2. A synthetic core developed from Laboratory Carousel experiment LE5 showing the erosion rate (δM/δt) as a function of eroded depth. No clear trends emerged.

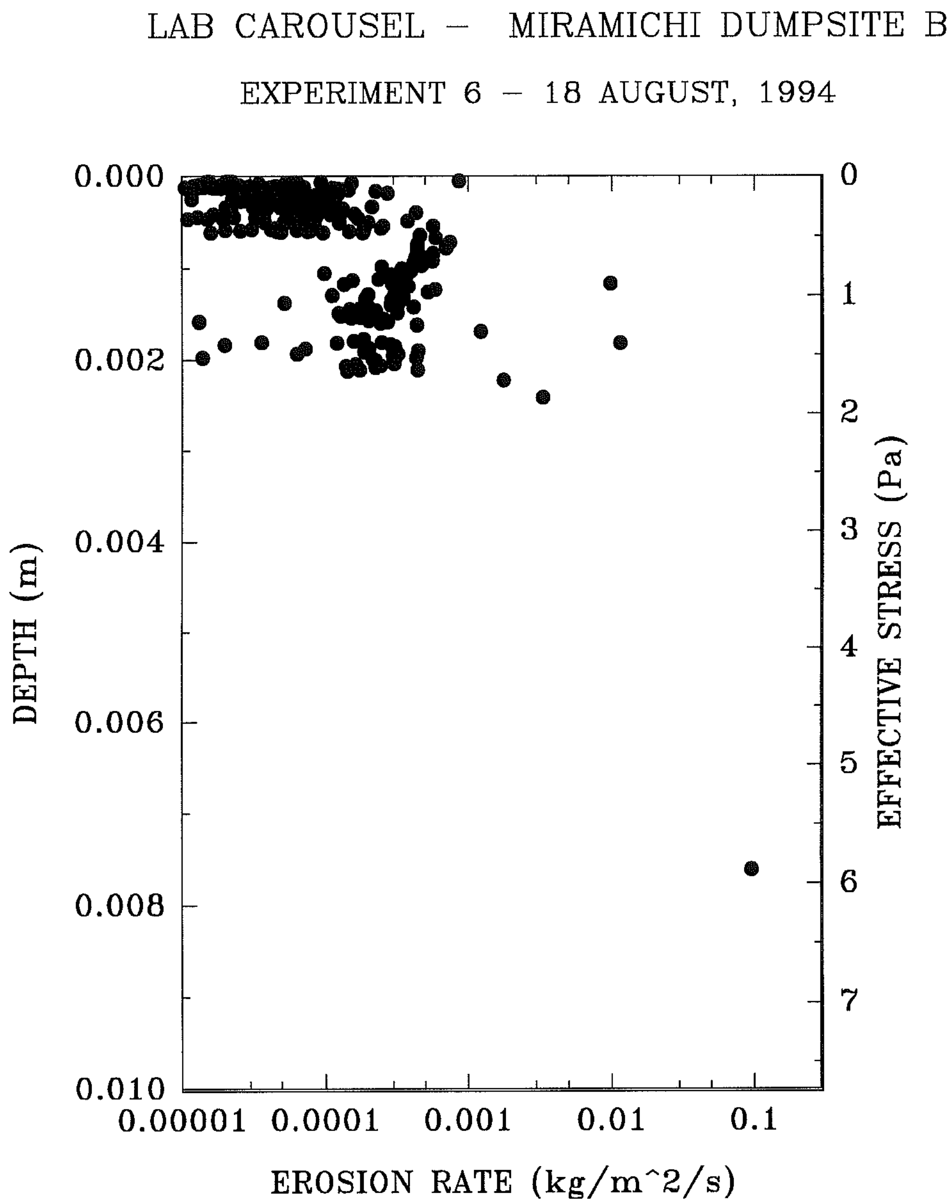

FIGURE 4.2.3.3. A synthetic core developed from Laboratory Carousel experiment LE6 showing the erosion rate (δM/δt) as a function of eroded depth.

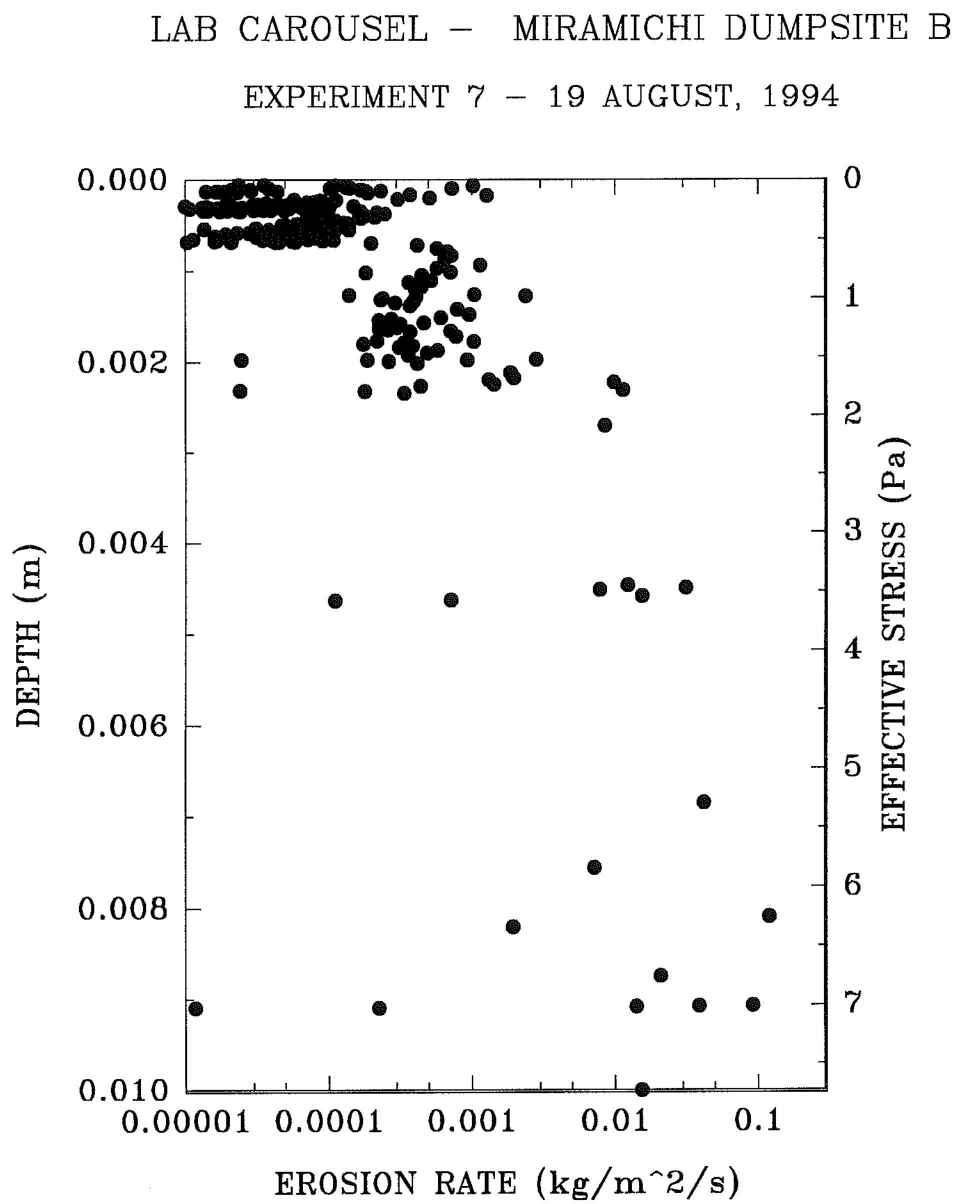

FIGURE 4.2.3.4. A synthetic core developed from Laboratory Carousel experiment LE7 showing the erosion rate ($\delta M/\delta t$) as a function of eroded depth. $\delta M/\delta t$ appears to increase with depth due to the lack of sediment consolidation (1 day only) but the data are scattered.

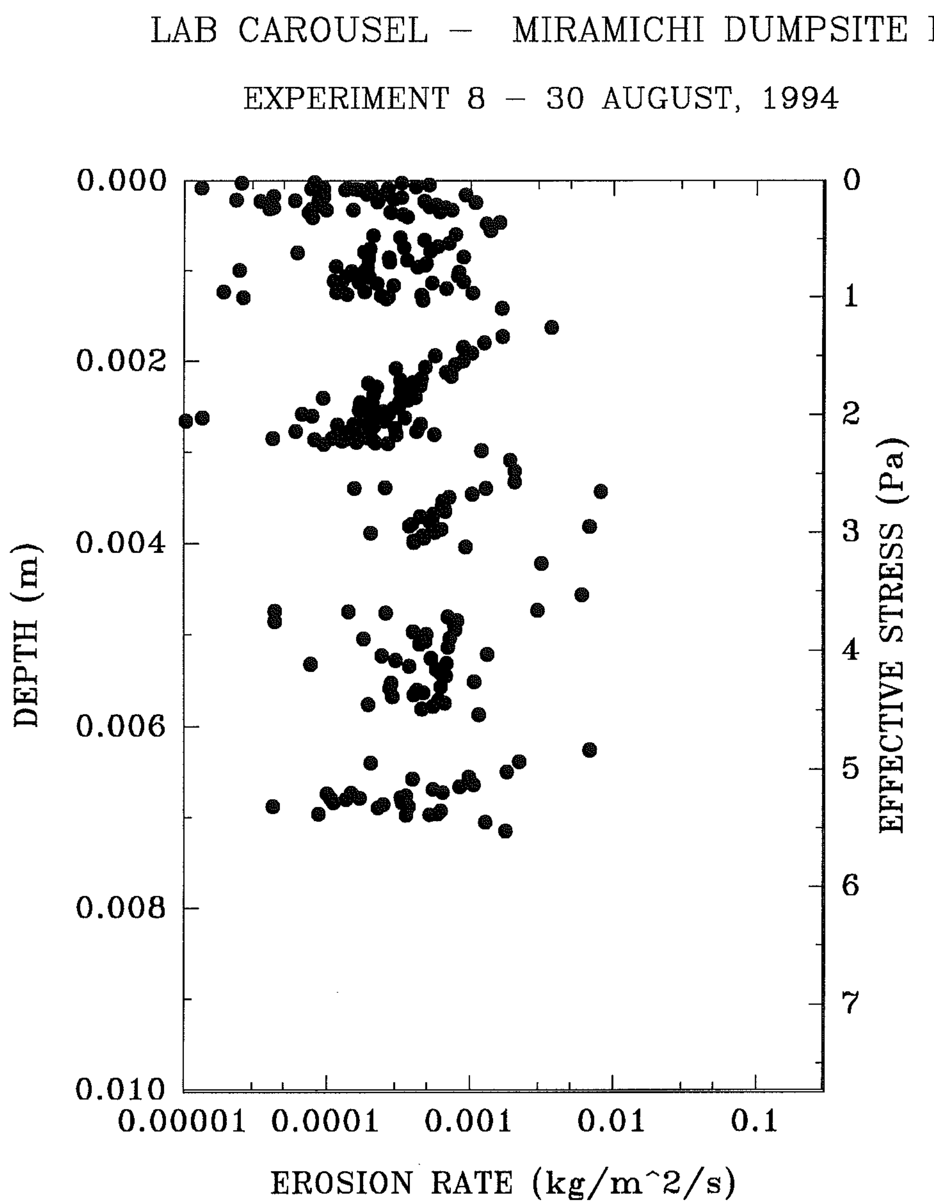

FIGURE 4.2.3.5. A synthetic core developed from Laboratory Carousel experiment LE8 showing the erosion rate ($\delta M/\delta t$) as a function of eroded depth. Notice that $\delta M/\delta t$ is virtually constant at 2×10^{-4} $kg/m^2/s$.

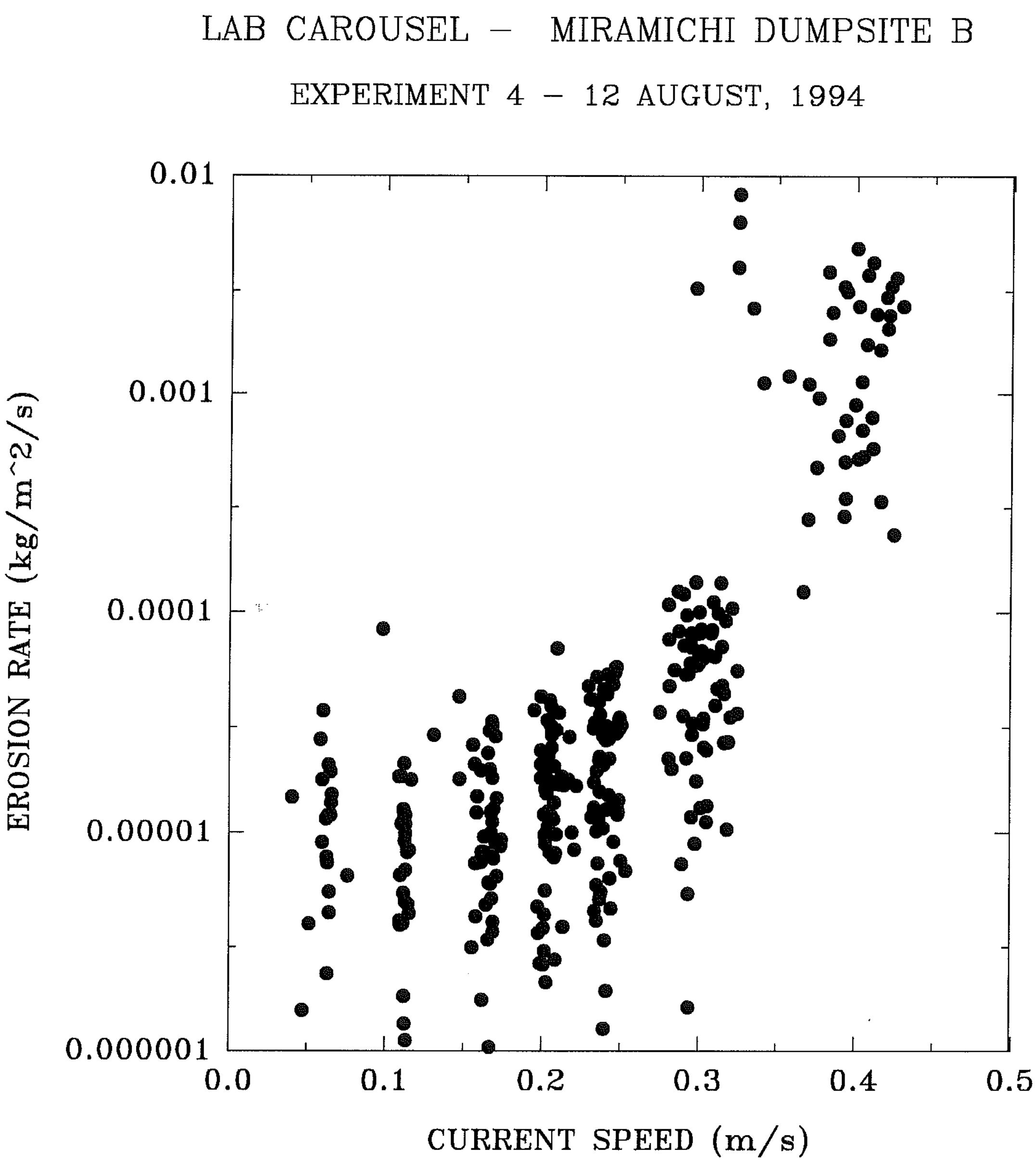

FIGURE 4.2.3.6. A scattergram of current speed against erosion rate ($\delta M/\delta t$) for Laboratory Carousel experiment LE4. $\delta M/\delta t$ appears to increase exponentially with current speed.

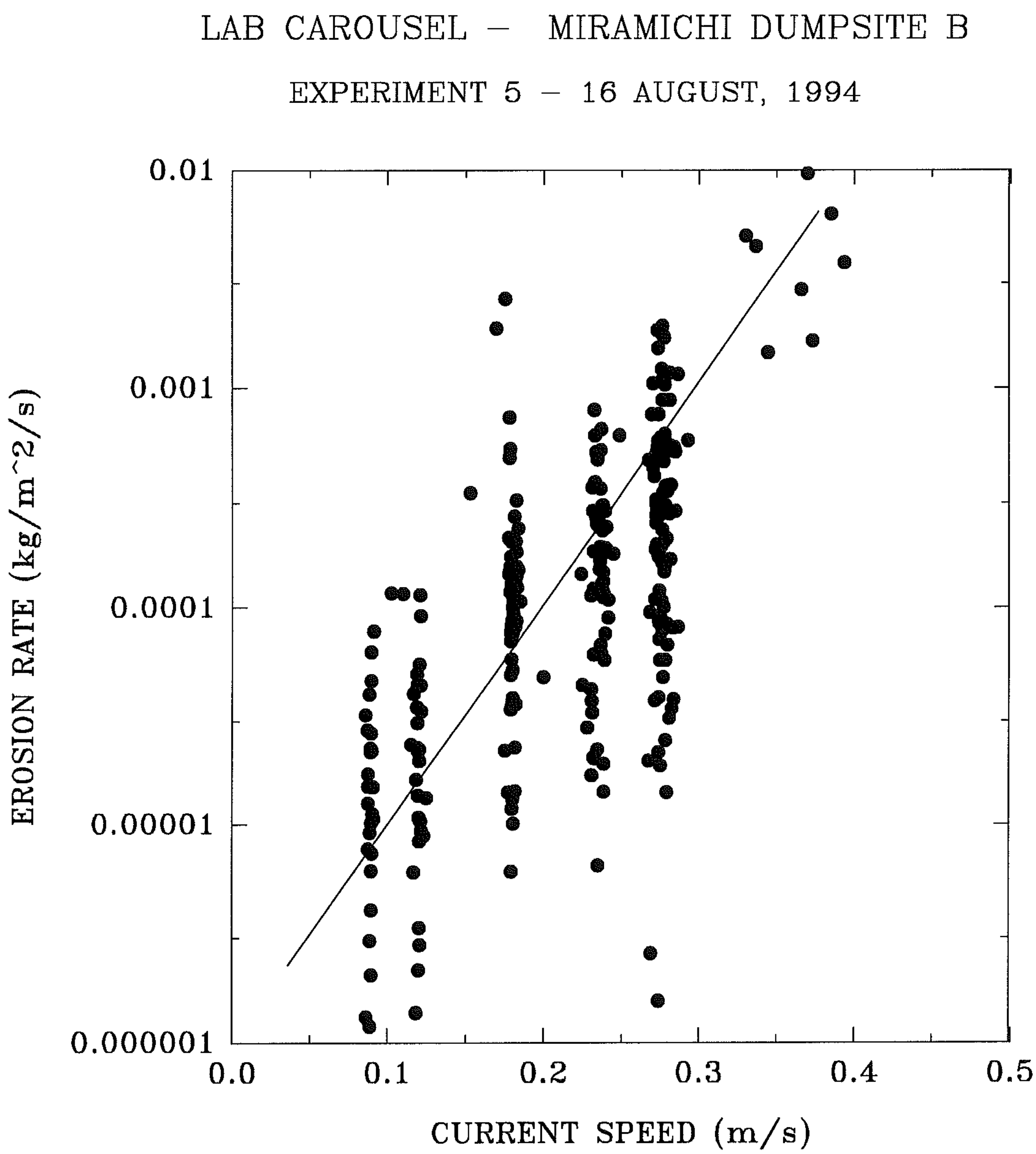

FIGURE 4.2.3.7. A scattergram of current speed against erosion rate (δM/δt) for Laboratory Carousel experiment LE5. δM/δt appears to increase exponentially with current speed.

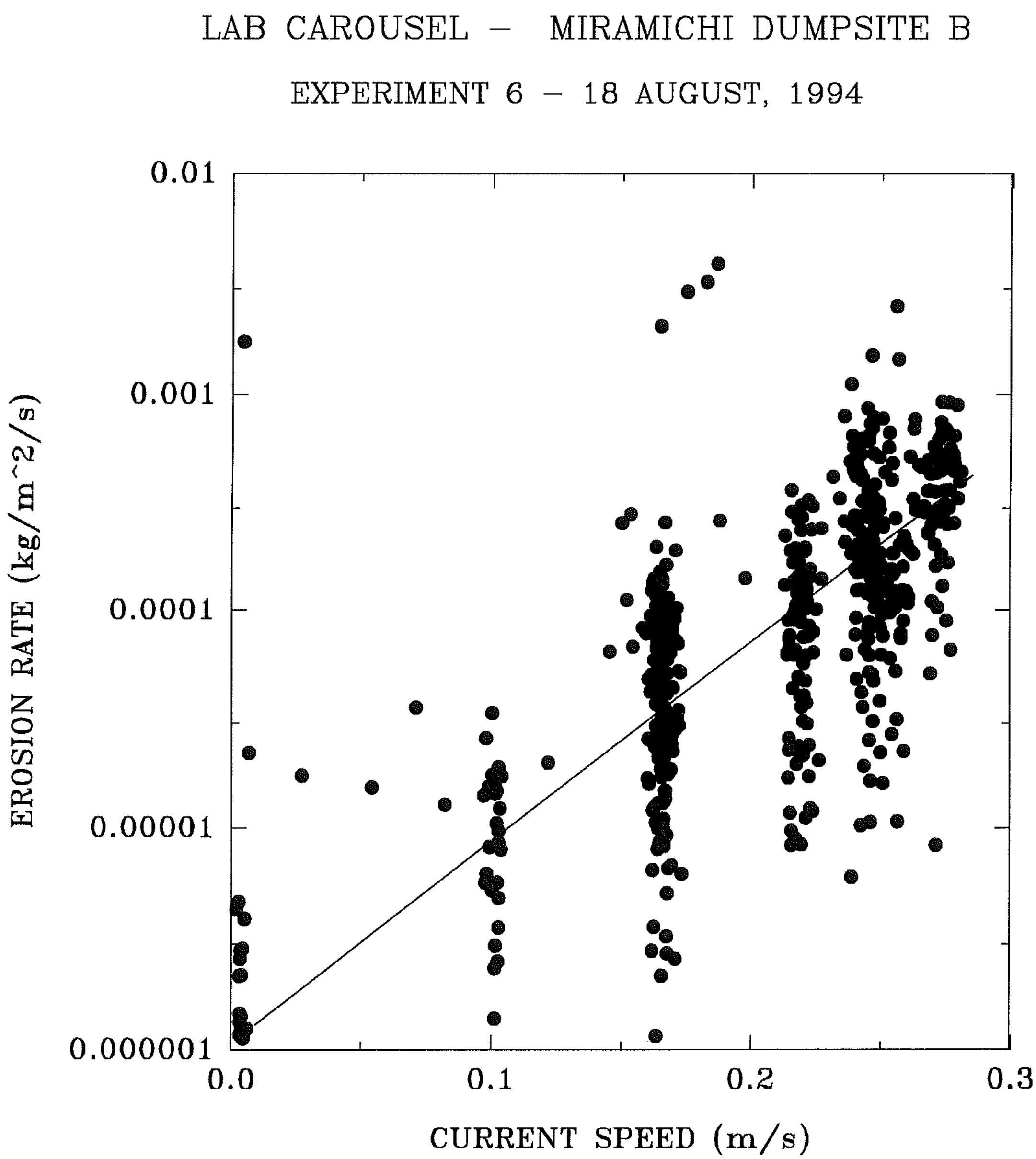

FIGURE 4.2.3.8. A scattergram of current speed against erosion rate (δM/δt) for Laboratory Carousel experiment LE6. δM/δt appears to increase exponentially with current speed.

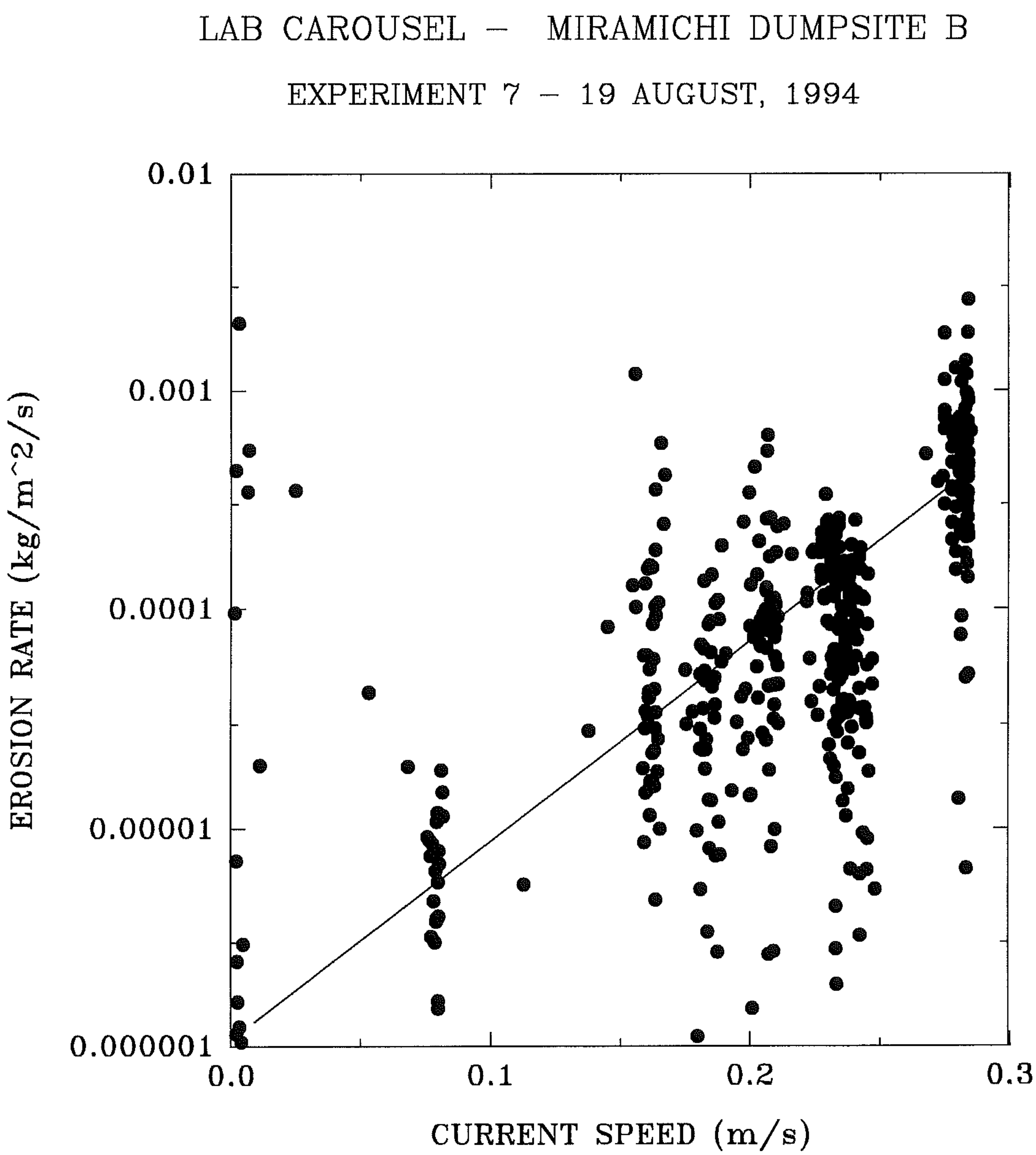

FIGURE 4.2.3.9. A scattergram of current speed against erosion rate (δM/δt) for Laboratory Carousel experiment LE7. δM/δt appears to increase exponentially with current speed.

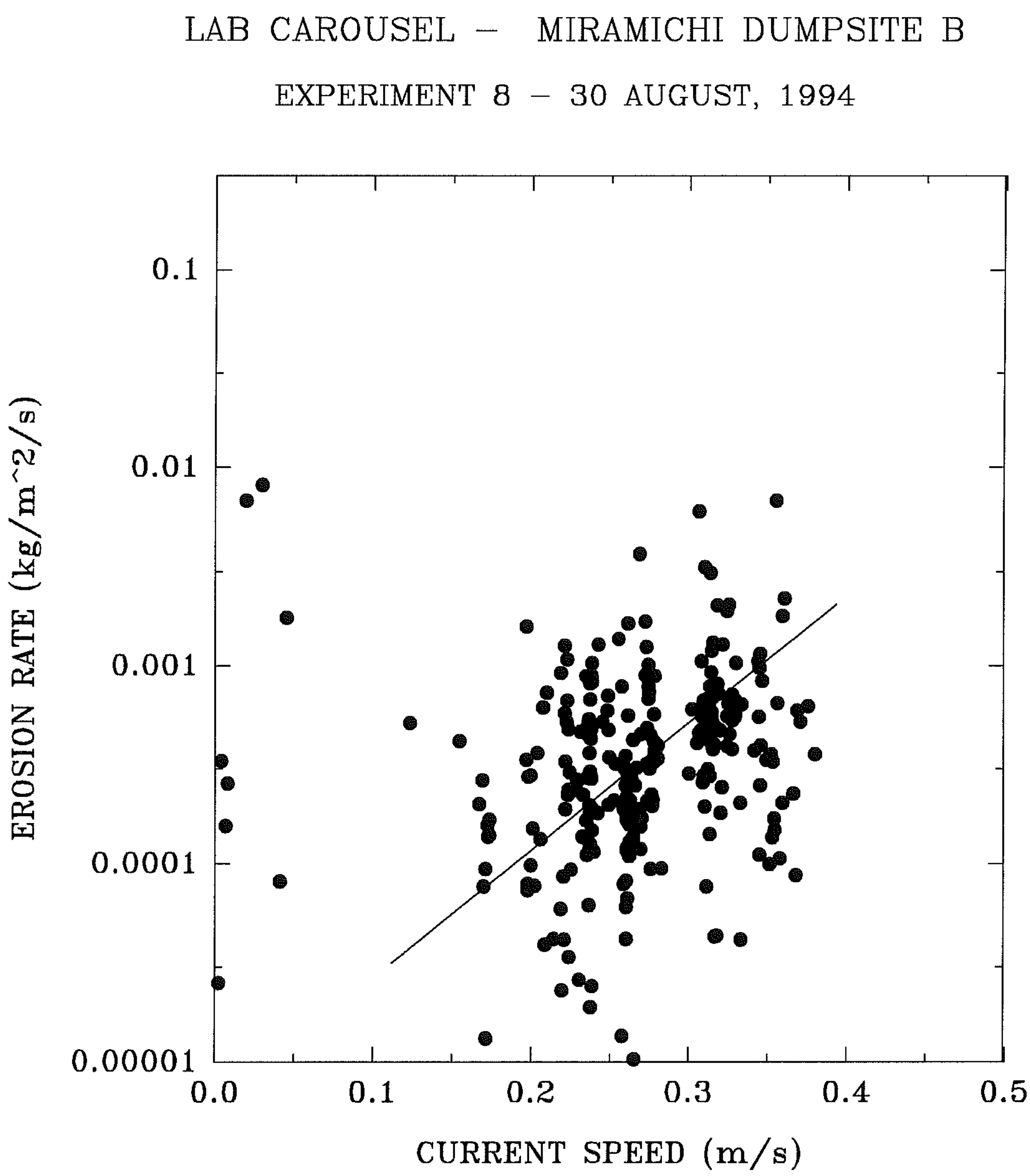

FIGURE 4.2.3.10. A scattergram of current speed against erosion rate (δM/δt) for Laboratory Carousel experiment LE8. δM/δt appears to increase exponentially with current speed.

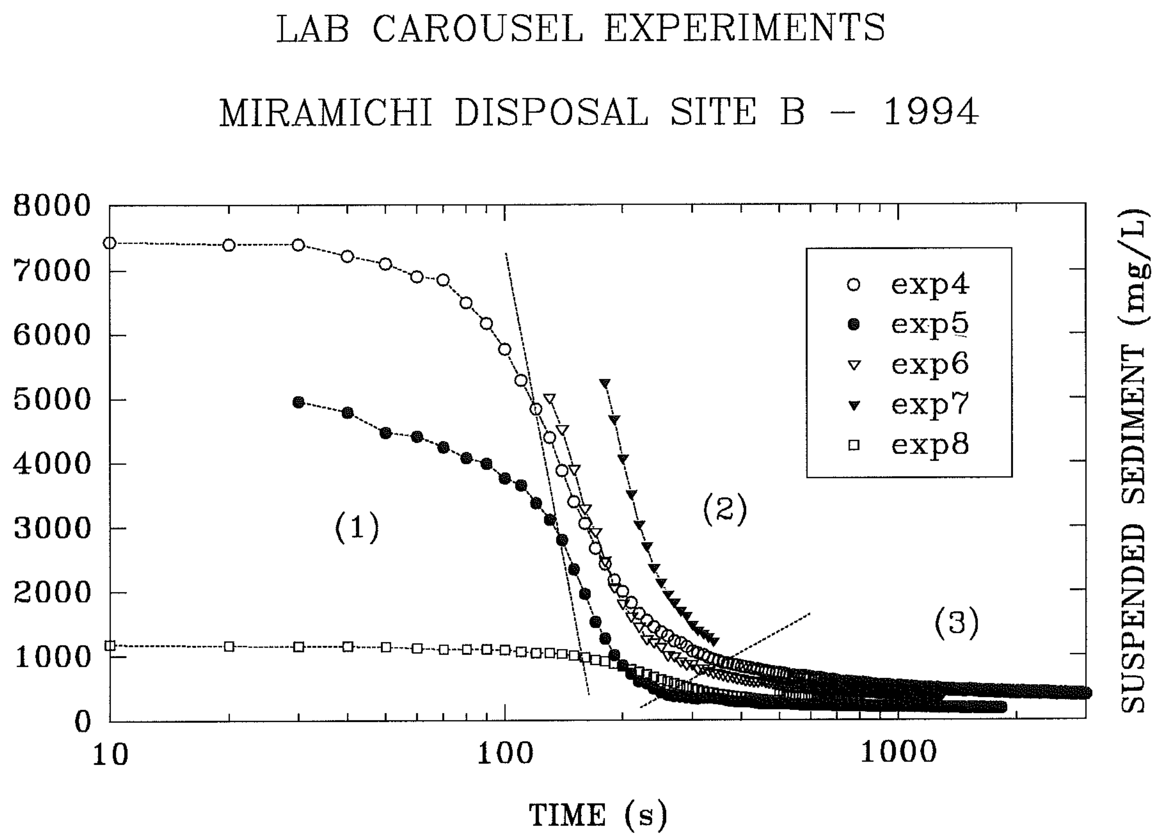

FIGURE 4.2.4.1. A time-series of still-water settling in the Laboratory Carousel for experiments LE4 - LE8. Notice they all show similar trends with time. These are: (1) an initial period of inhibited settling; (2) a period of rapid exponentially-decaying settling; and (3) a period of slow settling. These trends mirror those from the Sea Carousel *insitu* surveys.

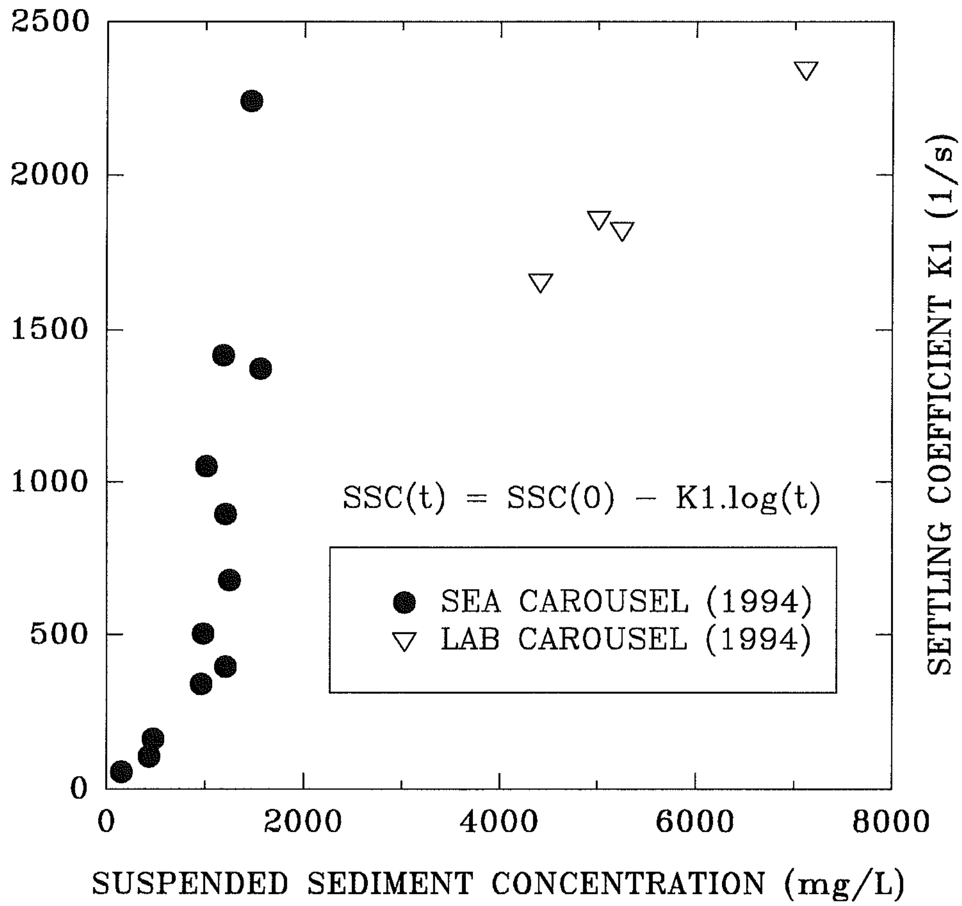

FIGURE 4.2.4.2. A scattergram of suspended sediment concentration against the settling decay constant (K_1). The Sea Carousel data indicates that settling was much greater *in situ* than was found under laboratory conditions.

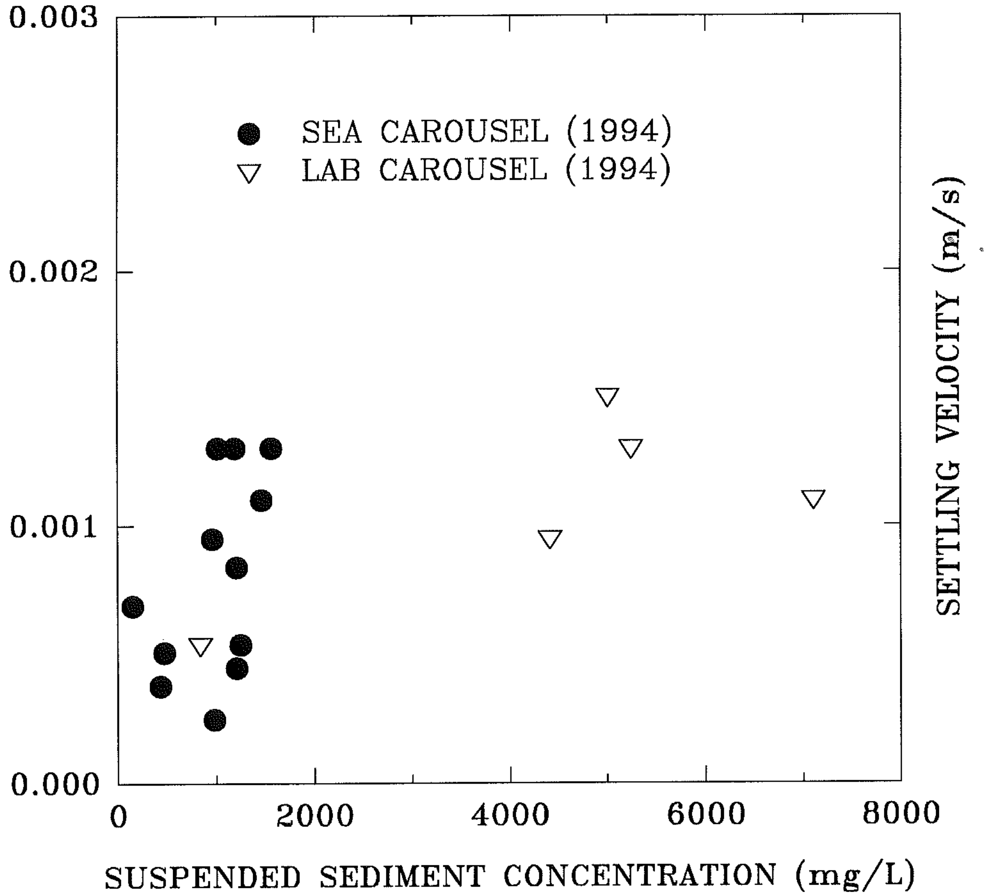

FIGURE 4.2.4.3. A scattergram of suspended sediment concentration (SSC) against mean mass settling velocity (W_s). Notice that W_s appears to reach a constant value of 0.0012 m/s at SSC's > 2000 mg/L, and is scattered, but less, at lower concentrations.

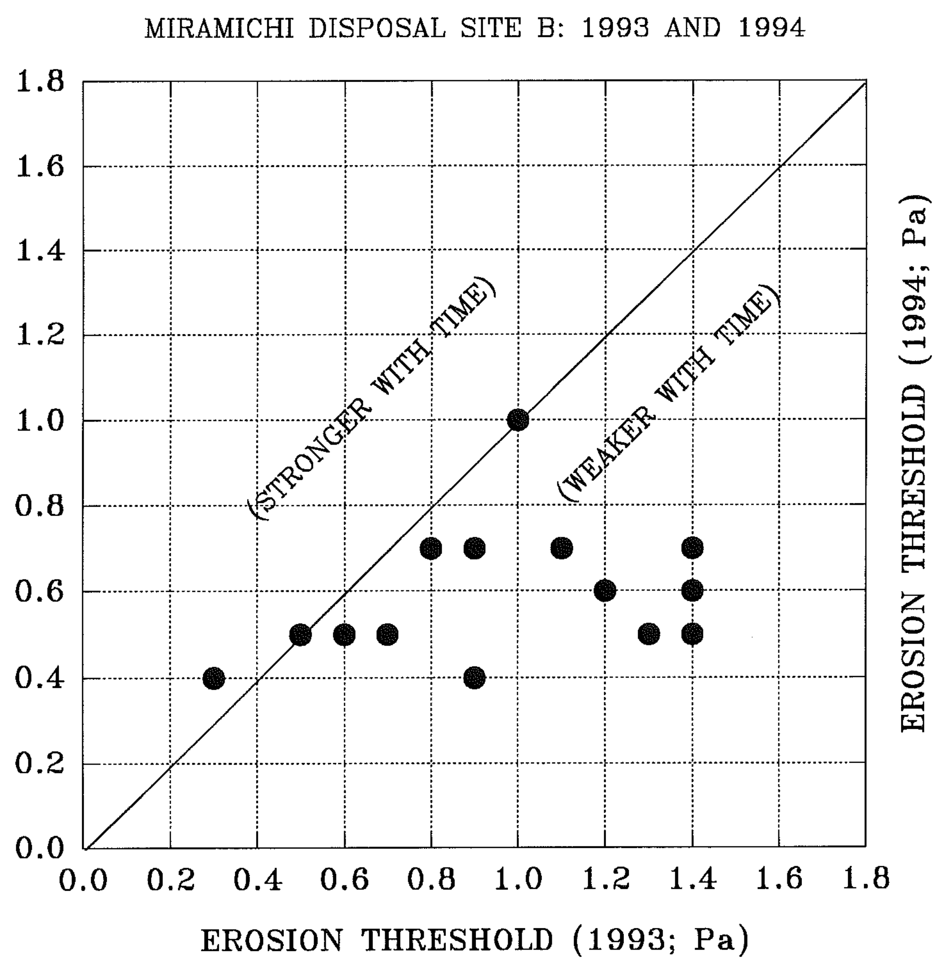

FIGURE 5.1. A scattergram of the erosion thresholds for Sea Carousel stations occupied on dumpsite B during 1993 and 1994. Notice that the seabed has become weaker during the year or so between surveys, even though no obvious change in physical bed properties was detected. This is attributed to seasonal fluctuations in bed strength related to benthic biological productivity.

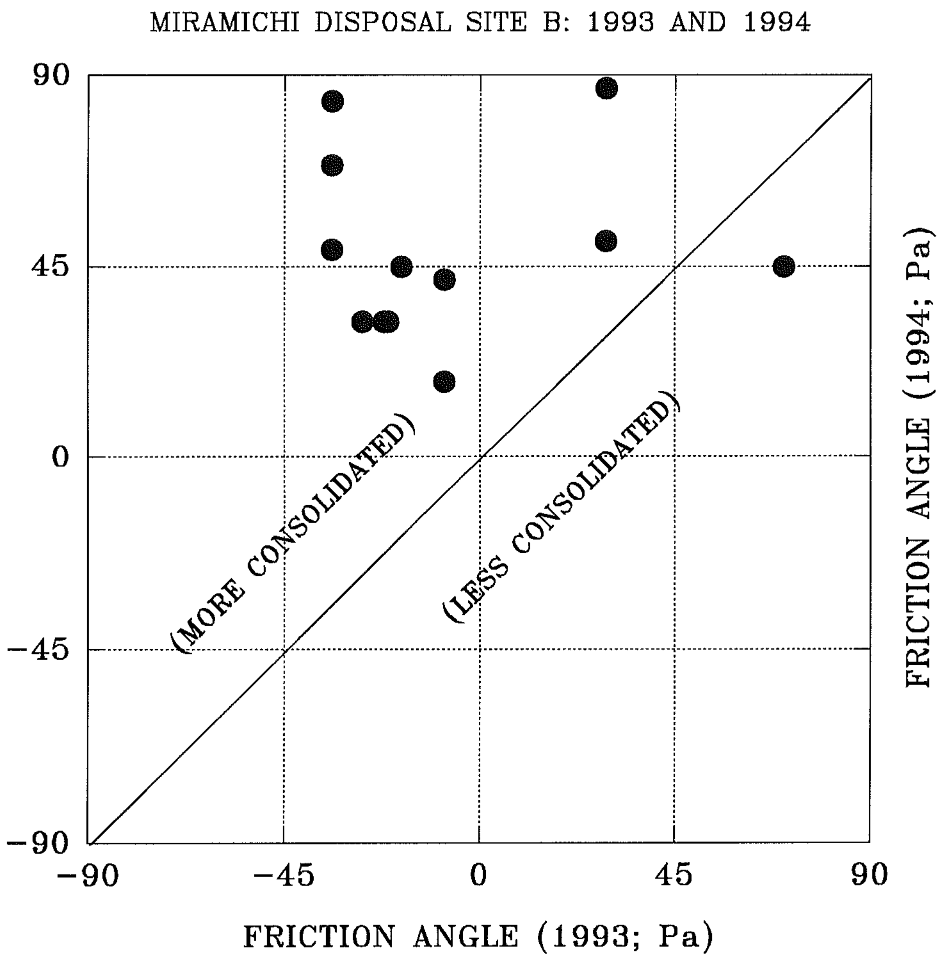

FIGURE 5.2. A scattergram of the friction angles for Sea Carousel stations occupied on dumpsite B during 1993 and 1994. Notice that the seabed has become more consolidated during the year or so between surveys as would be expected. This appears to have little effect on the erosion threshold as evidenced in Figure 5.1.

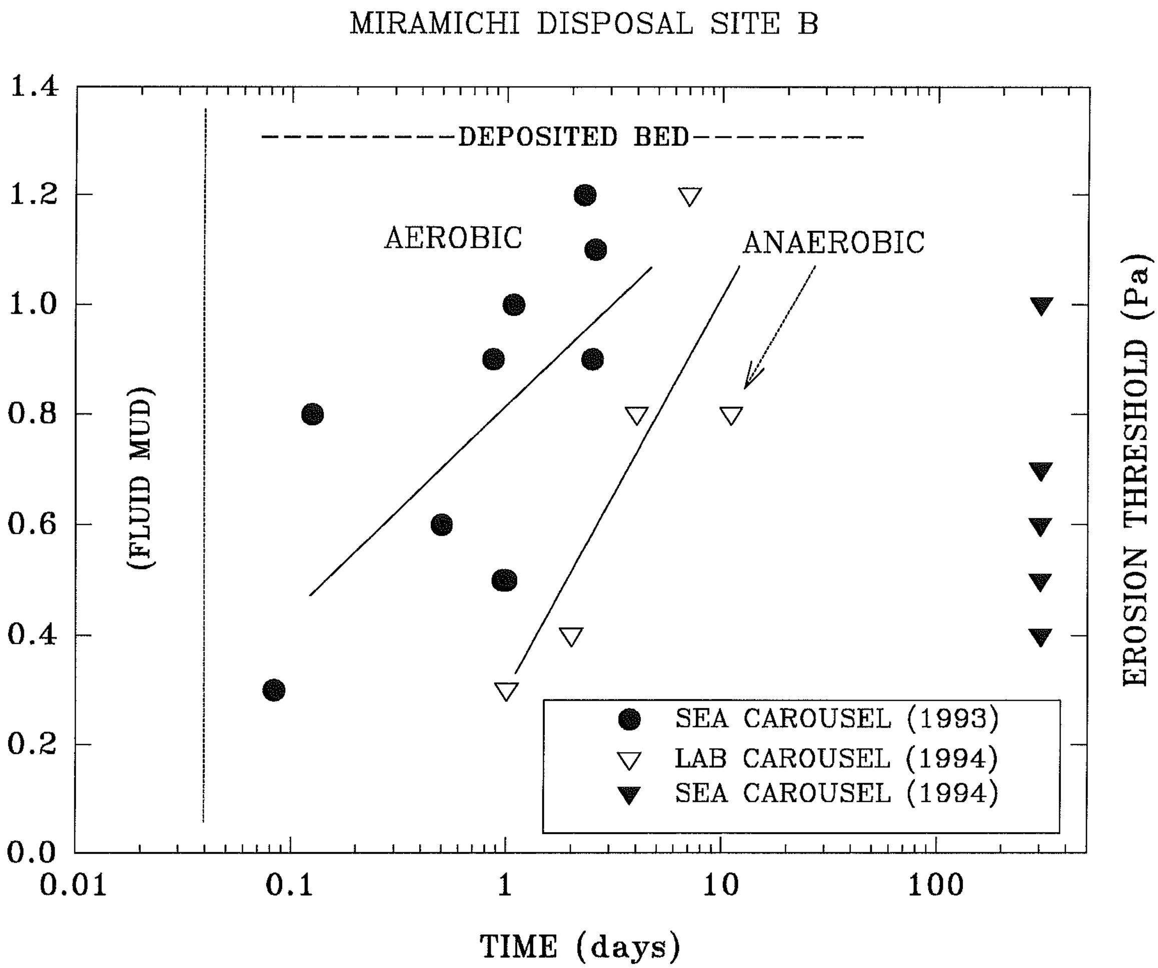

FIGURE 5.3. The observed increase in bed strength for three surveys of dumpsite B material: (1) the *insitu* 1993 Sea Carousel survey (water temp = 16°C); (2) the *insitu* 1994 Sea Carousel survey (water temp = 6°C); and (3) the laboratory study reported herein (water temp = 24°C). The solid lines show the best-fit increase in bed strengths for surveys (1) and (3). Notice that strength increase appears to be related to water temperature, which would agree with the concept of biostabilization.

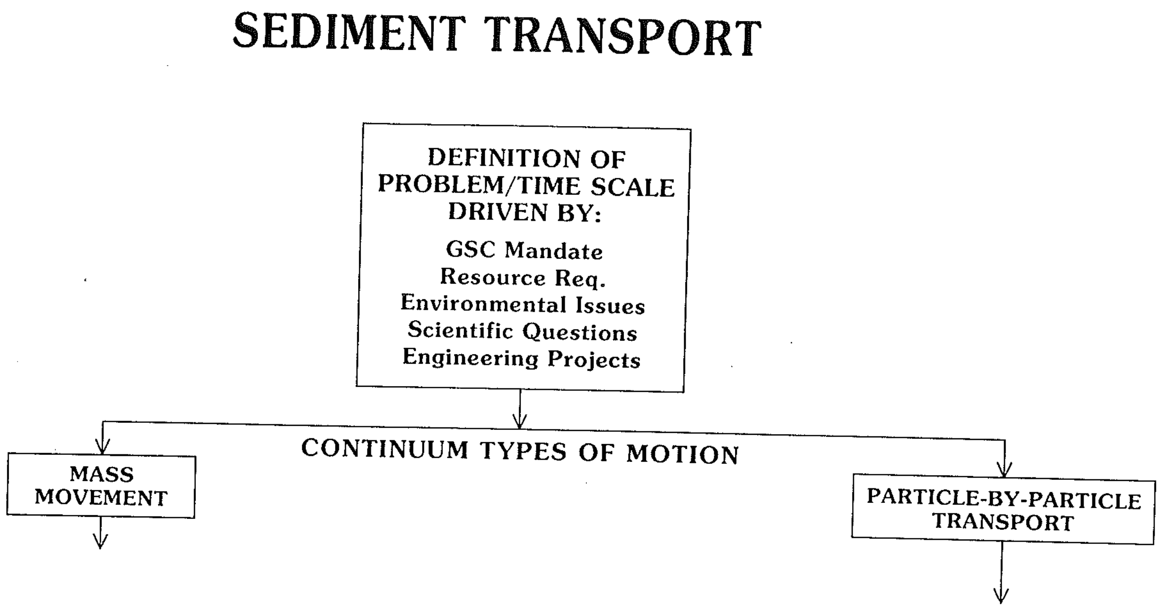

FIGURE 1.1. A schematic representation of the sediment transport process. It shows that erosion takes place over a continuum of scales from individual particles (particle-by-particle transport) to mass movements on the km scale.


94350
C.AMOS
001A
030
MUNSELL® SOIL COLOR CHART

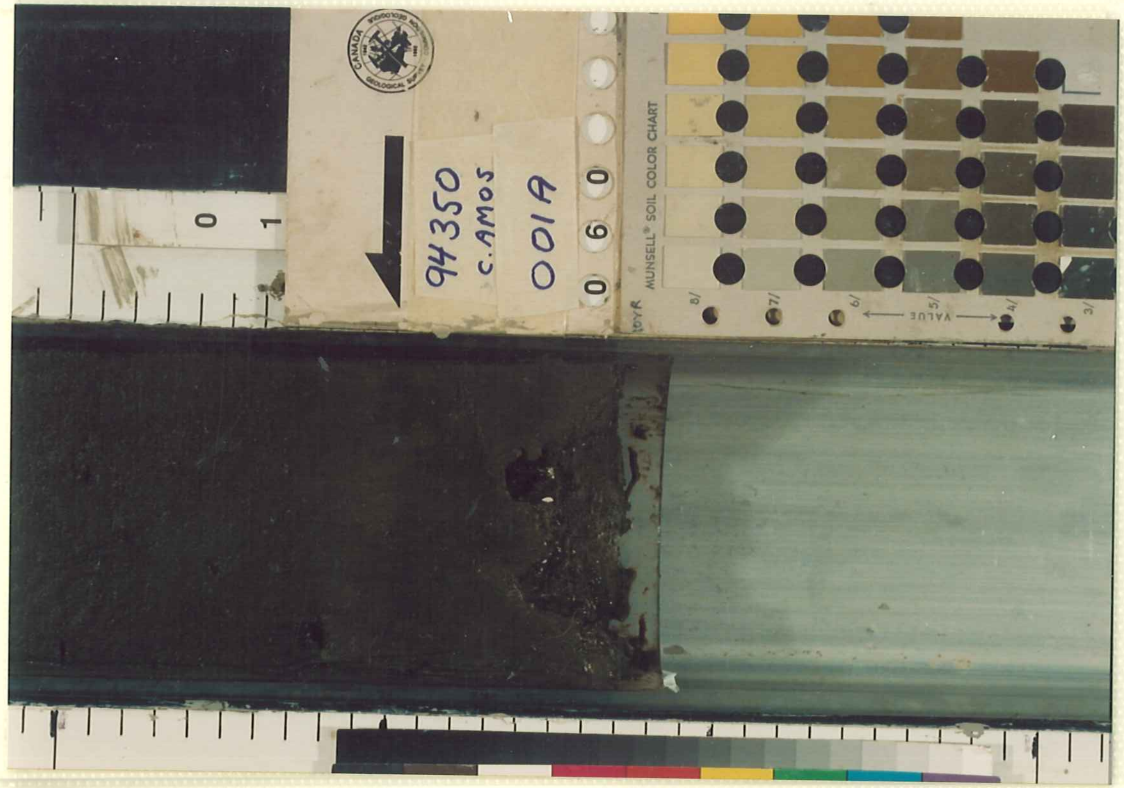
94350
C.AMOS
001A
060
MUNSELL® SOIL COLOR CHART


94350
C.AMOS
001A
000
MUNSELL® SOIL COLOR CHART


94350
C.AMOS
004A
000
MUNSELL® SOIL COLOR CHART


94350
C.AMOS
004A
MUNSELL® SOIL COLOR CHART


94350
C.AMOS
005A
MUNSELL® SOIL COLOR CHART


94350
C.AMOS
004A
MUNSELL® SOIL COLOR CHART

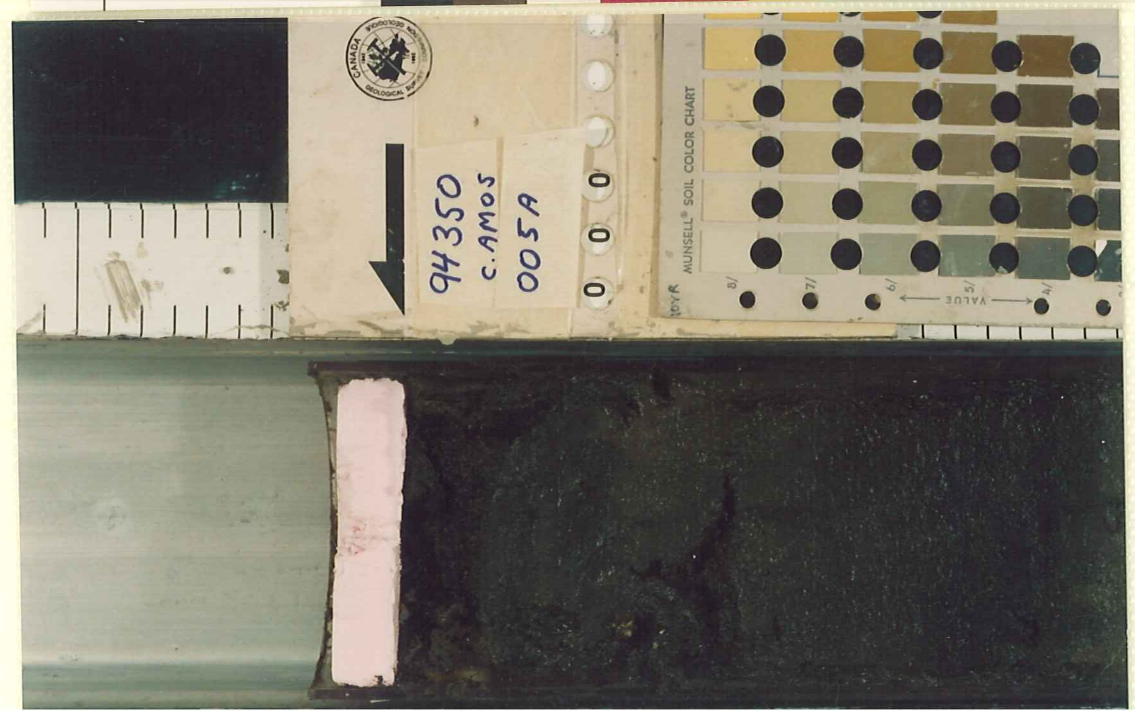
94350
C.AMOS
005A
MUNSELL® SOIL COLOR CHART

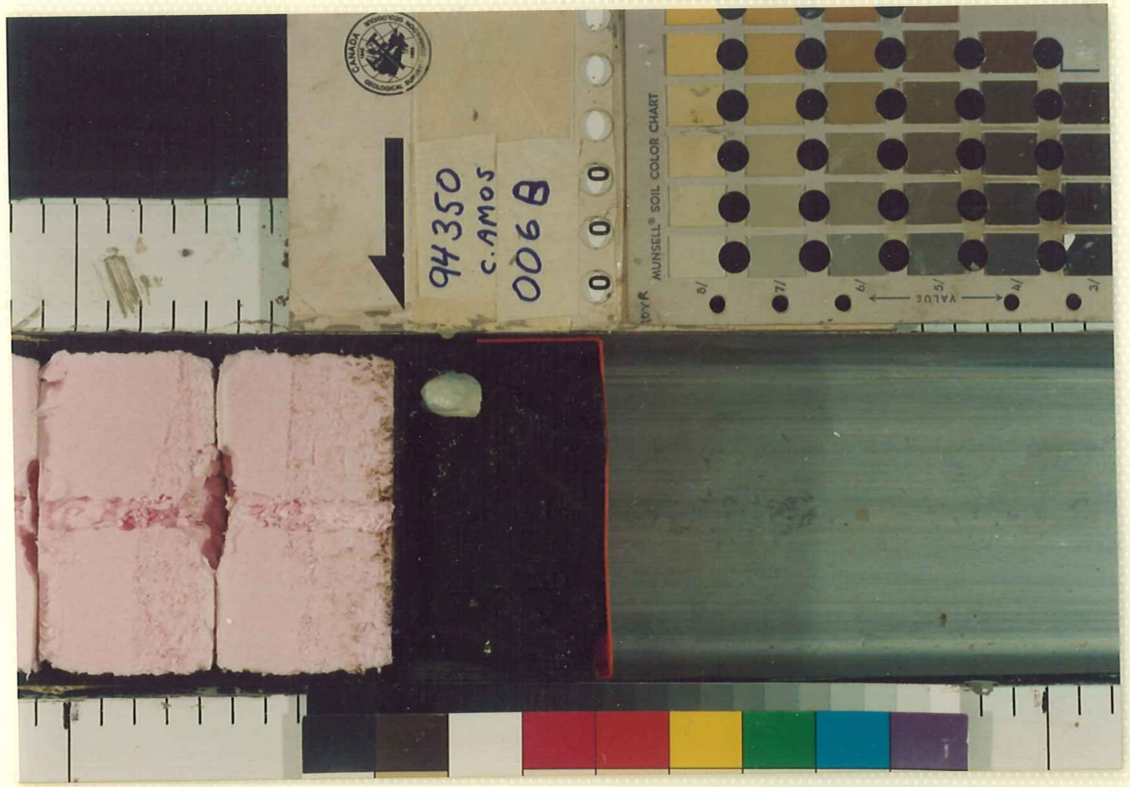
94350
C.AMOS
006B
000
MUNSELL® SOIL COLOR CHART

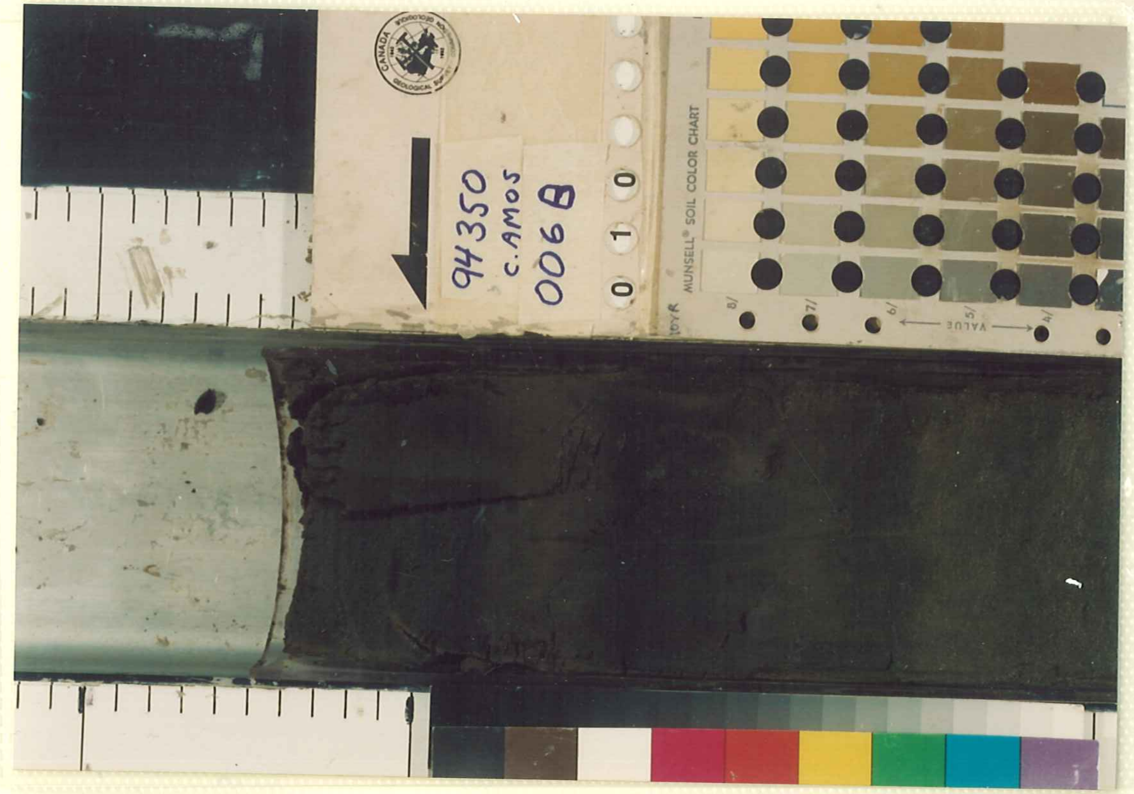
94350
C.AMOS
006B
010
MUNSELL® SOIL COLOR CHART


94350
C.AMOS
005A
050
MUNSELL® SOIL COLOR CHART


94350
C.AMOS
006A
000
MUNSELL® SOIL COLOR CHART

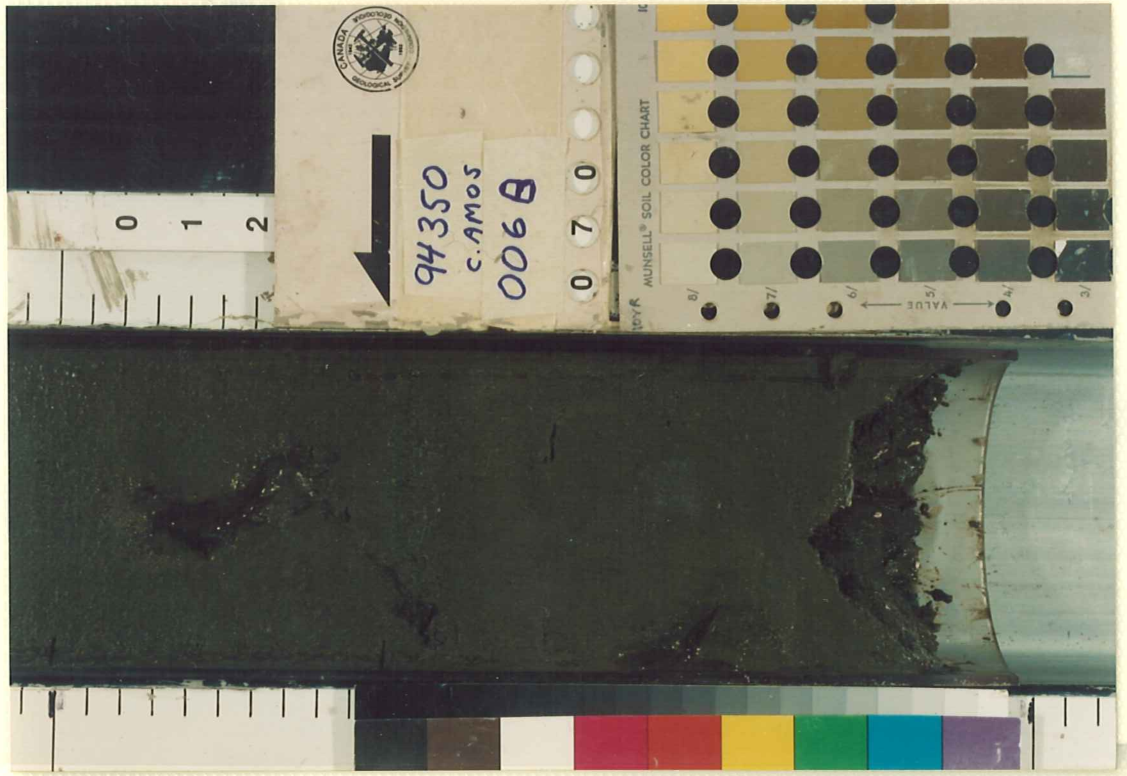
94350
C. AMOS
006B
070
MUNSELL® SOIL COLOR CHART


94350
C. AMOS
007A
000
MUNSELL® SOIL COLOR CHART


94350
C. AMOS
006B
030
MUNSELL® SOIL COLOR CHART

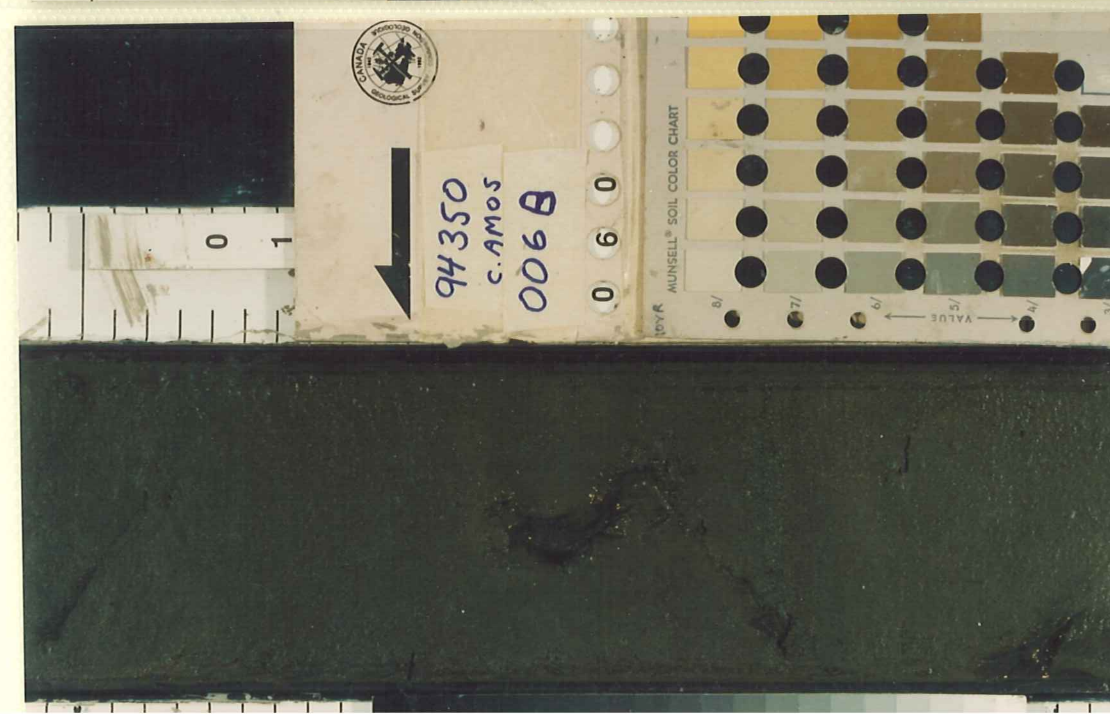
94350
C. AMOS
006B
060
MUNSELL® SOIL COLOR CHART


94350
C. Amos
007A
060
MUNSELL® SOIL COLOR CHART


94350
C. Amos
007A
020
MUNSELL® SOIL COLOR CHART

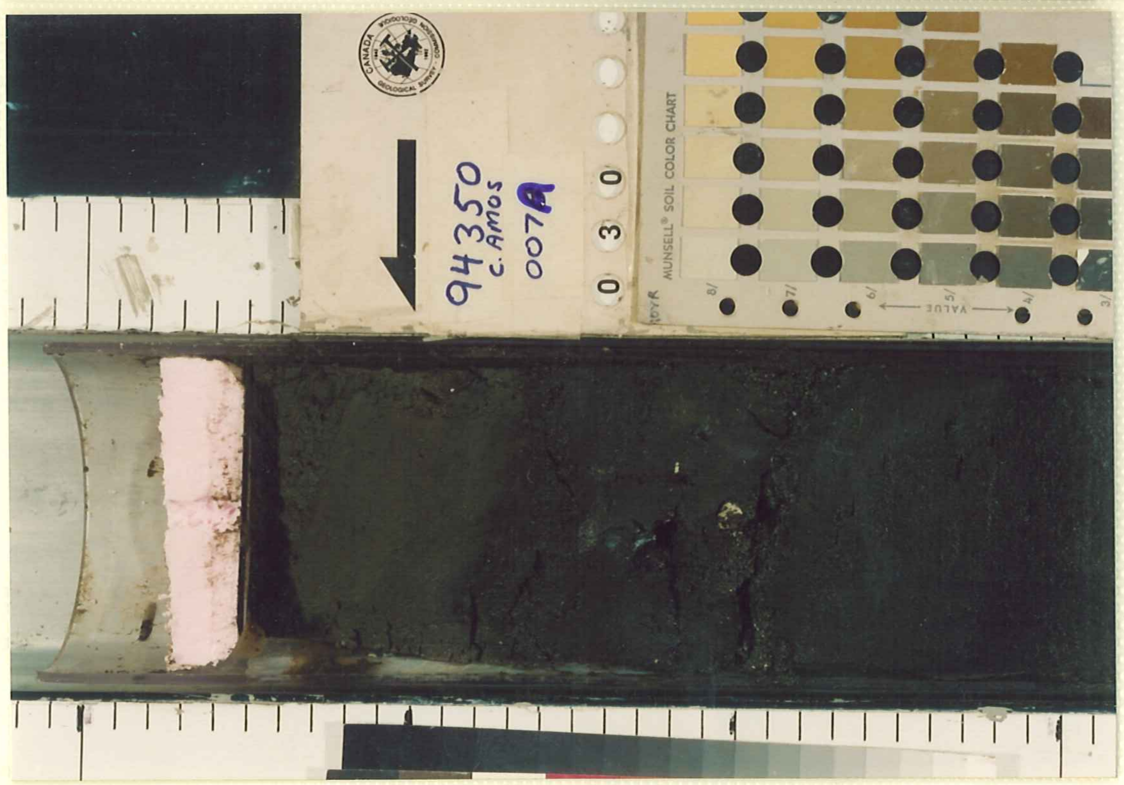
94350
C. Amos
007A
030
MUNSELL® SOIL COLOR CHART

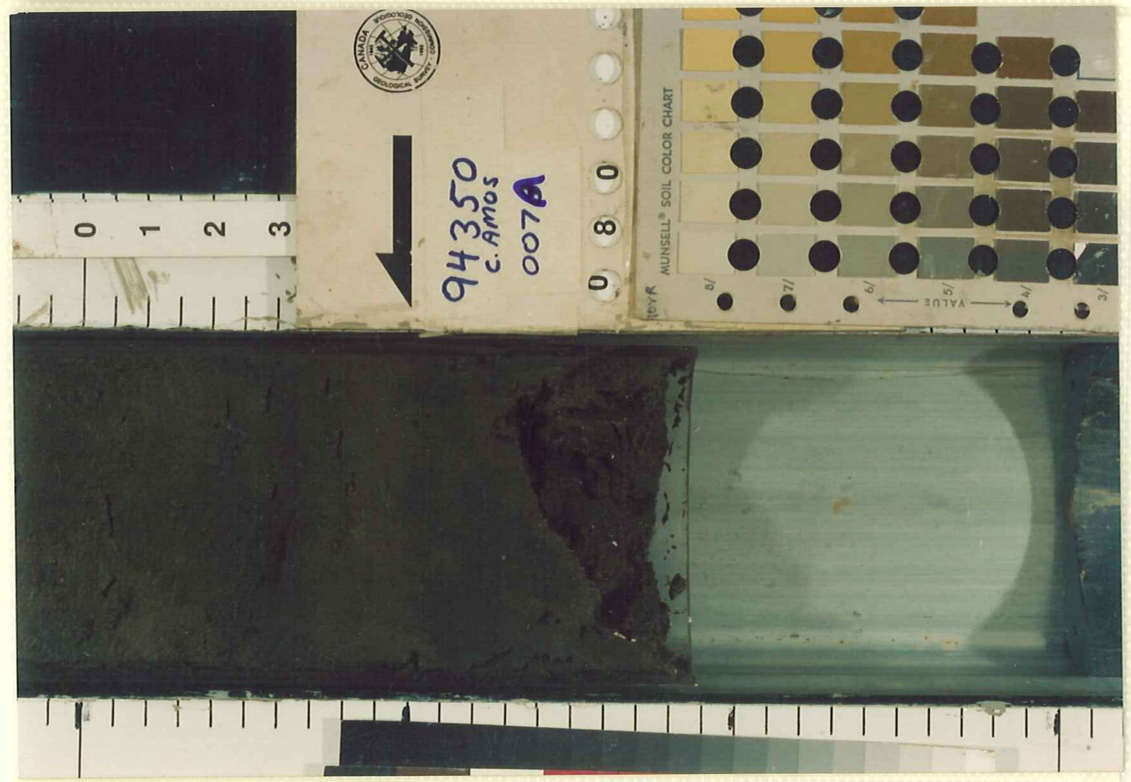
94350
C. Amos
007A
080
MUNSELL® SOIL COLOR CHART

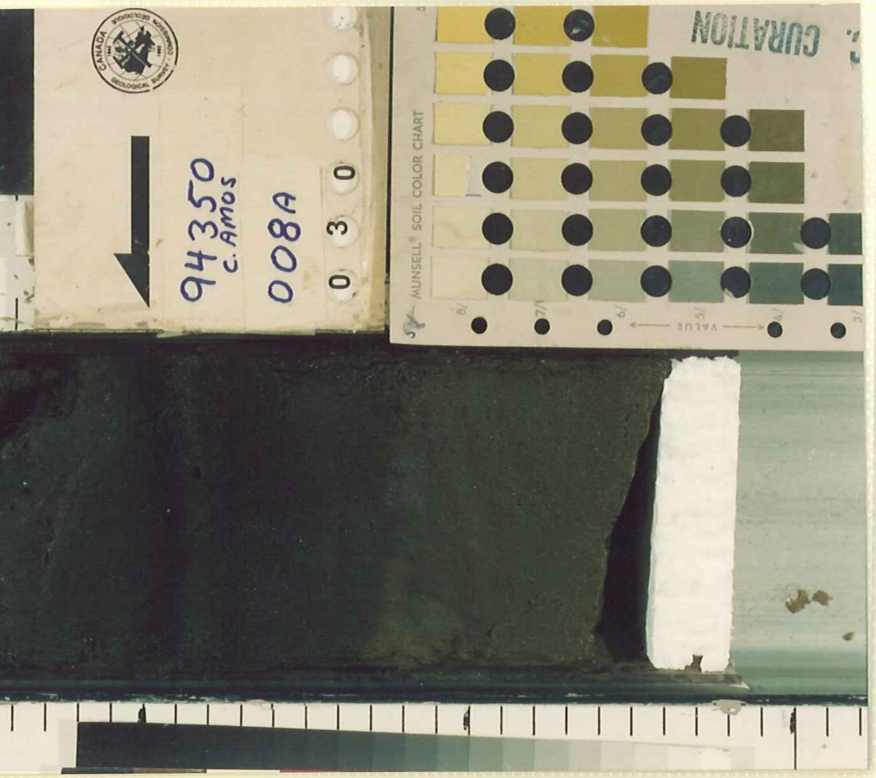
94350
C. Amos
008A
0 3 0
MUNSELL® SOIL COLOR CHART
CURATION
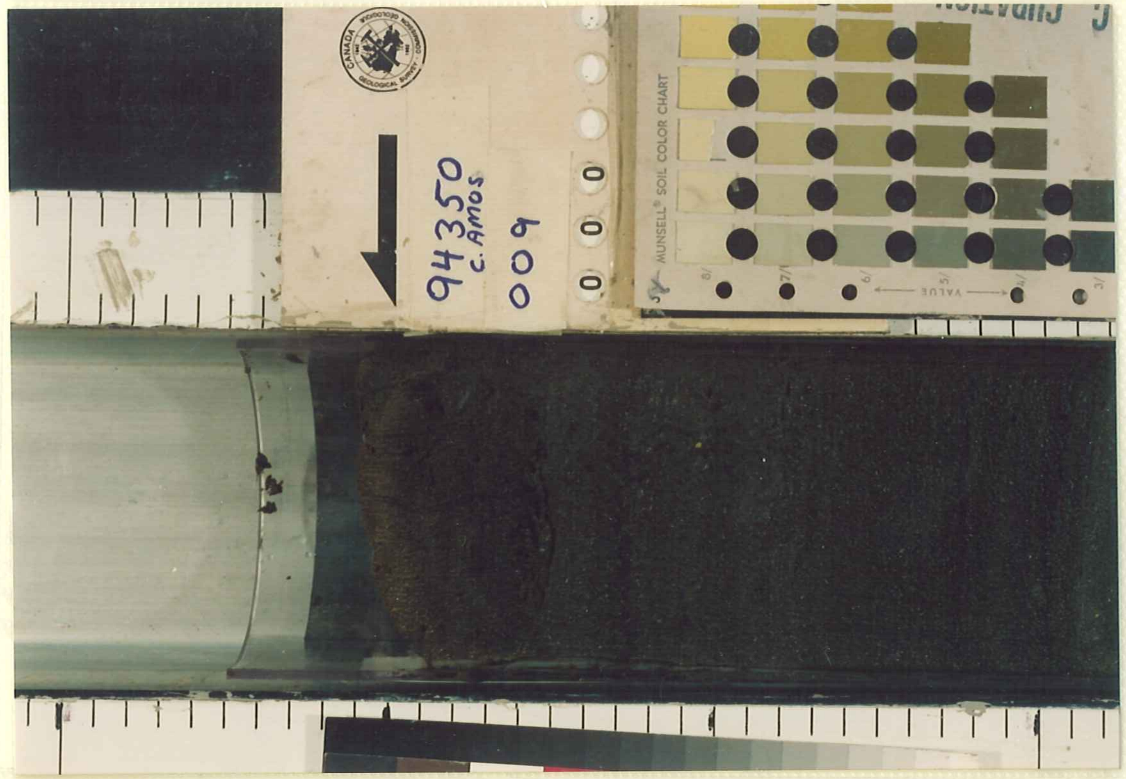
94350
C. Amos
009
0 0 0
MUNSELL® SOIL COLOR CHART
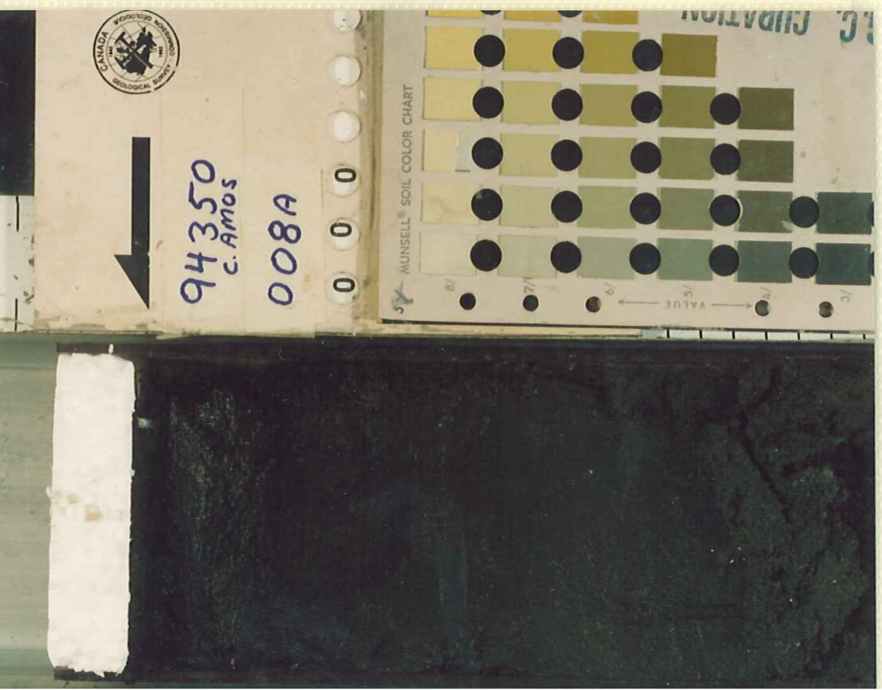
94350
C. Amos
008A
0 0 0
MUNSELL® SOIL COLOR CHART
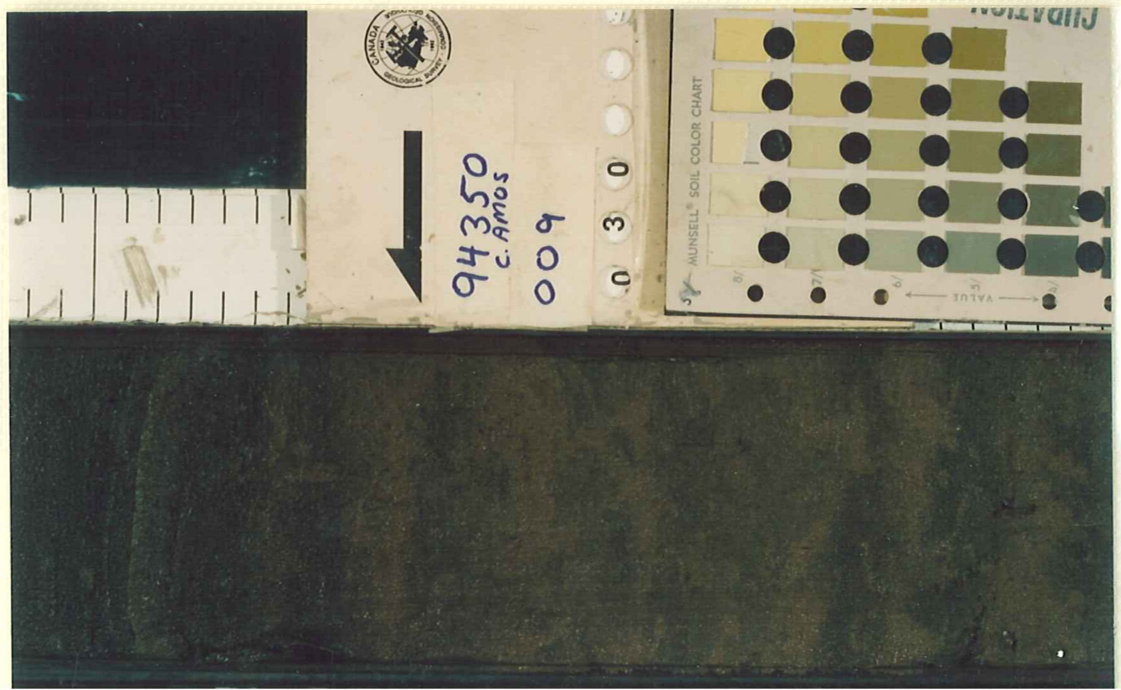
94350
C. Amos
009
0 3 0
MUNSELL® SOIL COLOR CHART

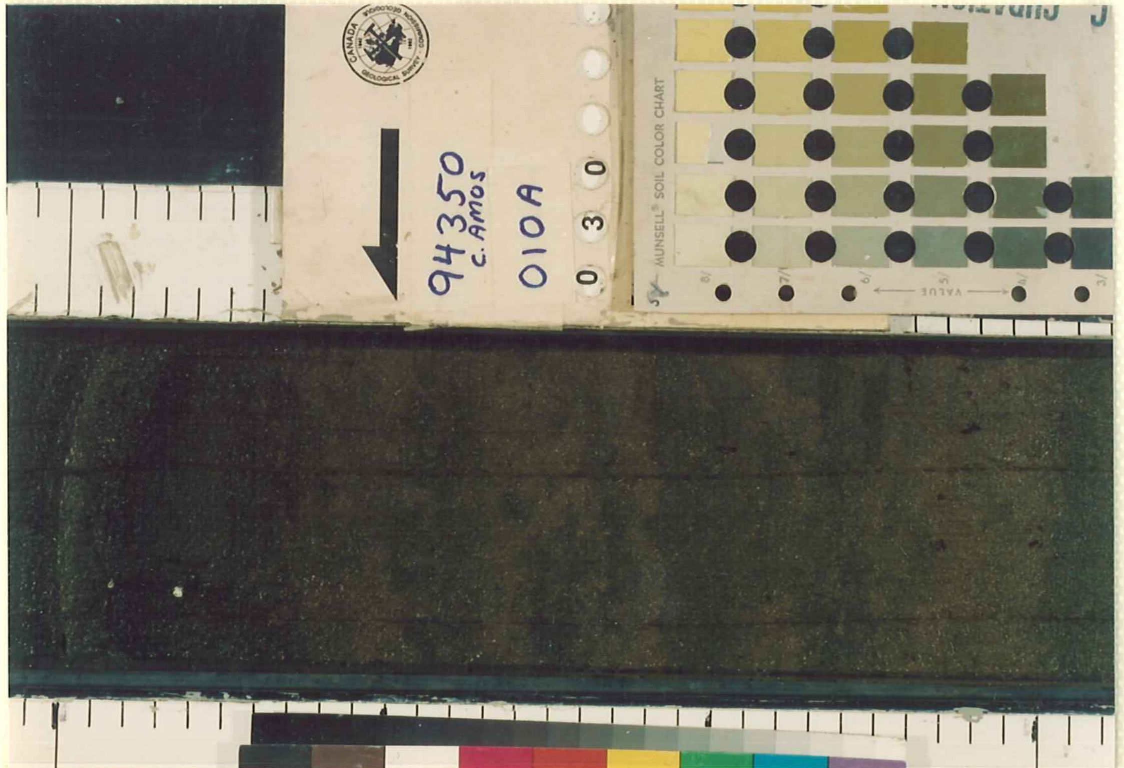
94350
C. Amos
010A
030
MUNSELL SOIL COLOR CHART

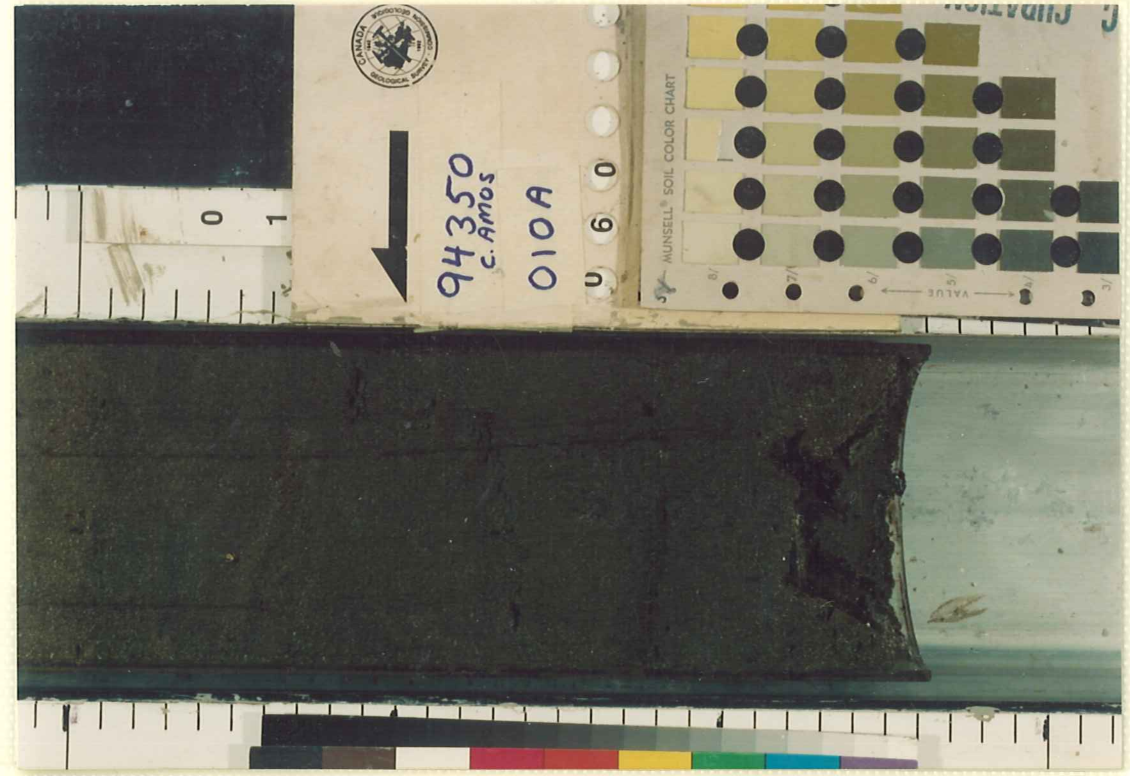
94350
C. Amos
010A
060
MUNSELL SOIL COLOR CHART

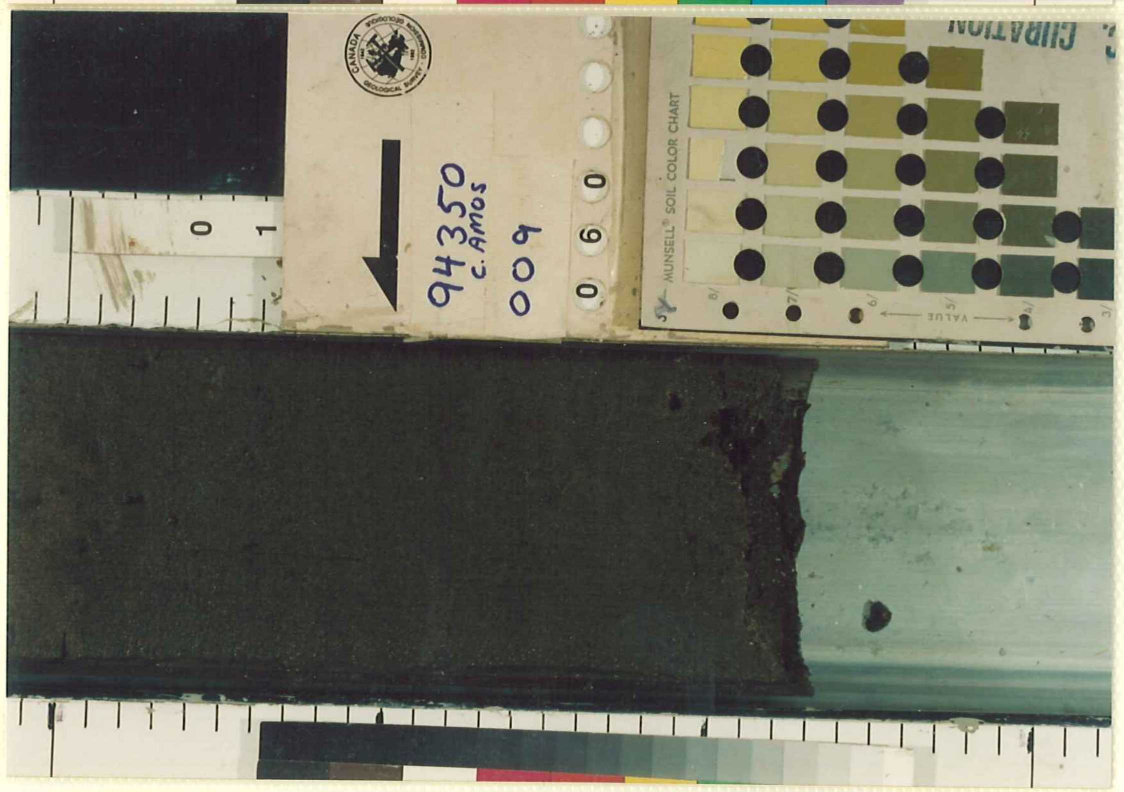
94350
C. Amos
060
MUNSELL SOIL COLOR CHART


94350
C. Amos
010A
000
MUNSELL SOIL COLOR CHART


94350
C. Amos
011
000
MUNSELL® SOIL COLOR CHART
CURATION

94350
C. Amos
012
000
MUNSELL® SOIL COLOR CHART
C. CURATION
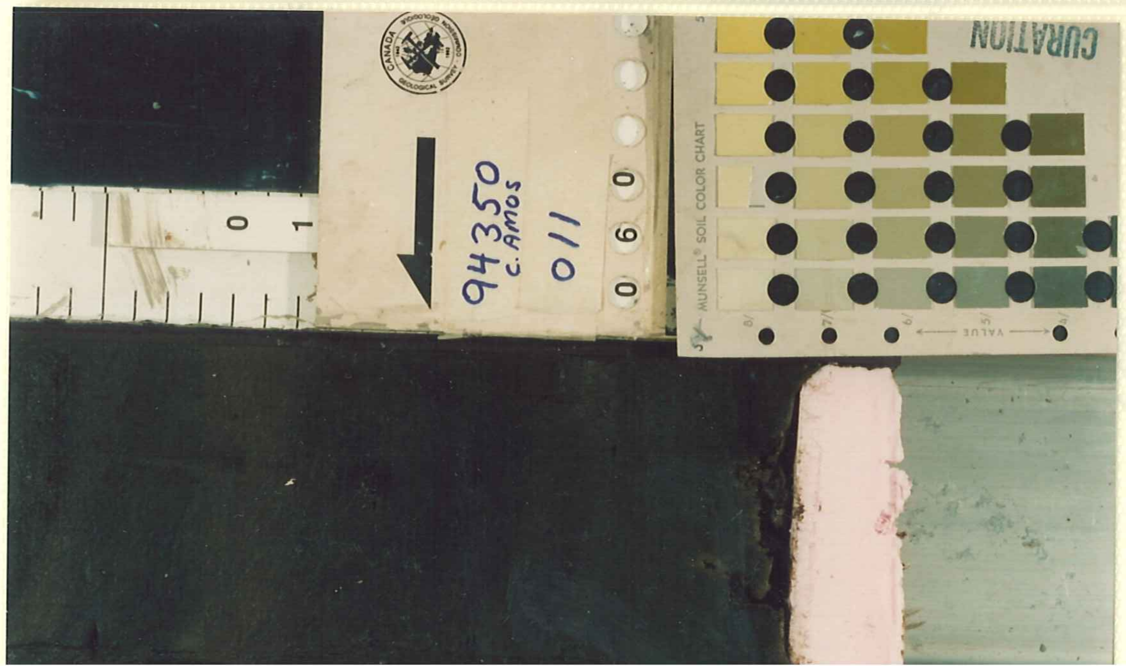
94350
C. Amos
011
060
MUNSELL® SOIL COLOR CHART
CURATION

94350
C. Amos
011
030
MUNSELL® SOIL COLOR CHART

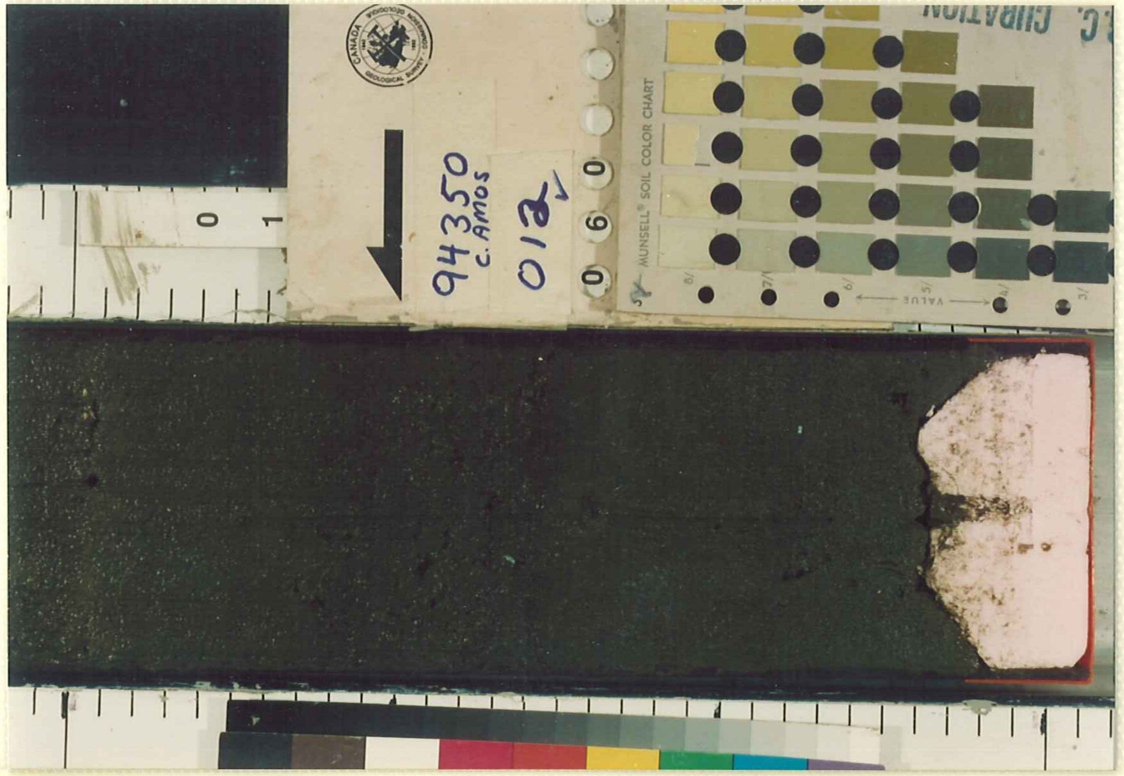
94350
C. Amos
012
MUNSELL® SOIL COLOR CHART

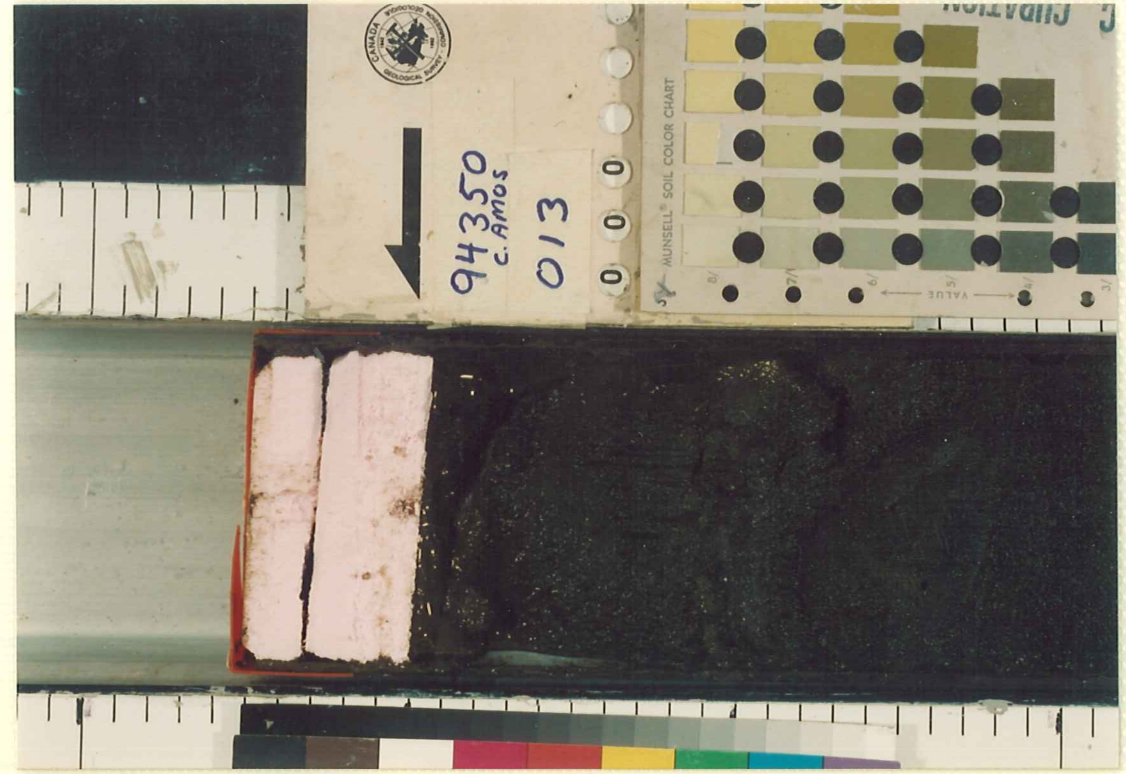
94350
C. Amos
013
MUNSELL® SOIL COLOR CHART


94350
C. Amos
012
MUNSELL® SOIL COLOR CHART

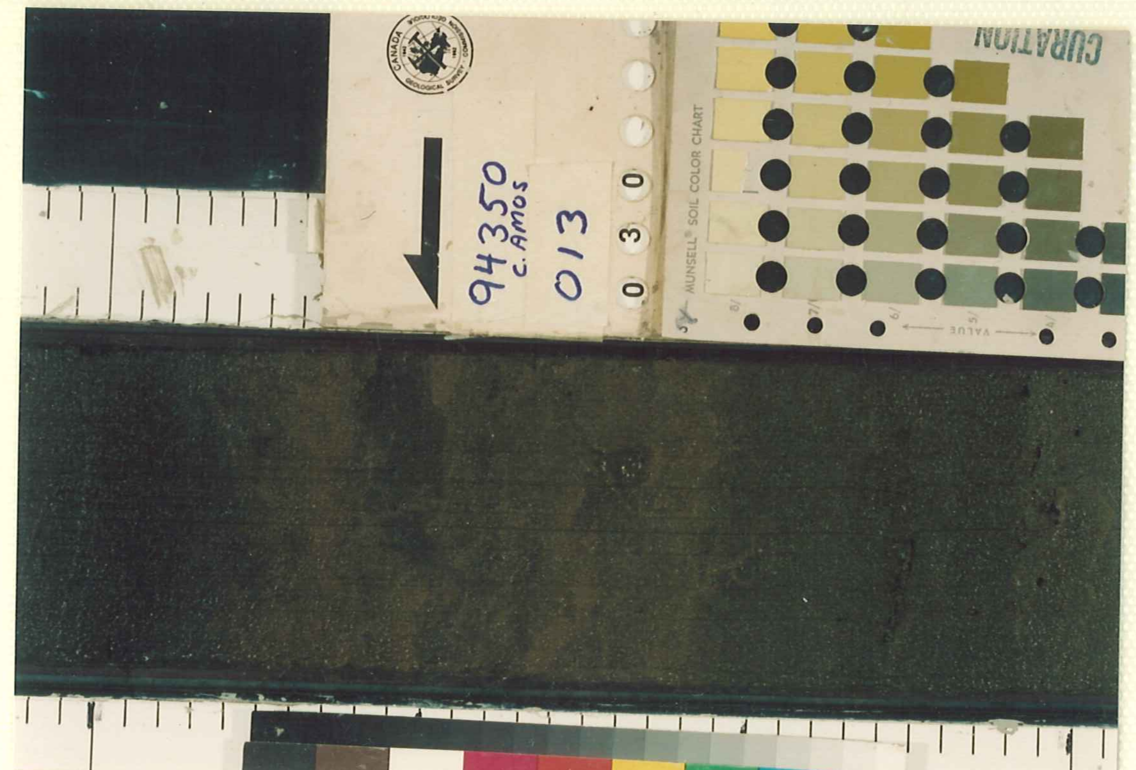
94350
C. Amos
013
MUNSELL® SOIL COLOR CHART


94350
C. Amos
013
MUNSELL® SOIL COLOR CHART
CURATION